Wadhams Amanatidis gp eudor WEB KINA22416ENC 002.pdf.en

Book · March 2021

CITATIONS
0

READS
751

2 authors:

P. Wadhams
University of Cambridge
301 PUBLICATIONS **11,181** CITATIONS
SEE PROFILE

Rasmus Tonboe
Technical University of Denmark
165 PUBLICATIONS **3,797** CITATIONS
SEE PROFILE

This book represents the proceedings of the International Workshop on Arctic Sea Ice Thickness: Past, Present and Future, held at Rungstedgaard Conference Centre, near Copenhagen, Denmark, on 8-9 November 2005.
The conference was a timely effort to bring together scientists from Europe, North America and Japan who are concerned with the problem of measuring and understanding the thinning of the Arctic sea ice cover. This thinning is dramatic, more than 40% in the last 25 years, and it promises to turn the Arctic Ocean into a seasonal sea ice zone by the 2080s, according to most climate models, but significantly earlier according to some others. Given that the thinning rate is faster than the rate of shrinkage of ice extent, it seems likely that in its final stages the ice cover will fragment and disappear quite suddenly, either through mechanical weakness or because the summer melt rate exceeds the winter growth rate.

KI-NA-22416-EN-C

Publications Office
Publications.europa.eu

ISBN 92-79-02803-0
9 789279 028038

Arctic sea ice thickness past, present & future

EUR 22416

PROCEEDINGS

EUR 22416

EUROPEAN COMMISSION

Community research

Arctic sea ice thickness

past, present & future

International workshop
Rungstedgaard, Denmark, 8-9 November 2005

Interested in European research?

RTD info is our quarterly magazine keeping you in touch with main developments (results, programmes, events, etc.). It is available in English, French and German. A free sample copy or free subscription can be obtained from:

European Commission
Directorate-General for Research
Information and Communication Unit
B-1049 Brussels
Fax (32-2) 29-58220
E-mail: rtd-info@ec.europa.eu
Internet: http://ec.europa.eu/research/rtdinfo

EUROPEAN COMMISSION

Directorate-General for Research
Directorate I — Environment
Unit I.5 — Climate Change and Environmental Risks

E-mail: rtd-climate-change@*ec.europa.eu*

European Commission
Office CDMA 3/128
B-1049 Brussels

Tel. (32-2) 29-84625
Fax (32-2) 29-95755
E-mail: georgios.amanatidis@*ec.europa.eu*

European Commission

EUR 22416 — International Workshop on Arctic Sea Ice Thickness: Past, Present and Future

Luxembourg: Office for Official Publications of the European Communities

2006 — 293 pp. — 16 x 24 cm

ISBN.92-79-02803-0

EUROPEAN COMMISSION

International Workshop

Artic Sea Ice Thickness: Past, Present and Future

Rungstedgaard Conference Centre, near Copenhagen, Denmark, 8-9 November 2005

SCIENTIFIC REPORT

edited by:

Peter Wadhams[1] and Georgios Amanatidis[2],

[1] Department of Applied Mathematics and Theoretical Physics (DAMTP), University of Cambridge, United Kingdom

[2] Climate Change and Environmental Risks Unit, Environment Directorate, Directorate-General for Research, European Commission

CONTRIBUTORS

Søren Andersen
Lawson W. Brigham
Kerry Claffey
Bruce C. Elder
Rene Forsberg
Martin Gade
Cathleen A. Geiger
Sebastian Gerland
Rashpal S. Gill
Sibylle Goebell
Jari Haapala
Christian Haas
Richard Hall
Edmond Hansen
Stefan Hendricks
Jürgen Holfort
Nick E. Hughes
Sine M. Hvidegaard
Lars Kaleschke
Chandra Kambhamettu
Stefan Kern
Yngve Kristoffersen
Susanne Juul Lassen
Terje Brink Løyning
Torge Martin
Naja Mikkelsen
Gerd Müller
Leif Toudal Pedersen
Niels Nørgaard-Pedersen
Donald K. Perovich
Andreas Pfaffling
Jacqueline A. Richter-Menge
James E. Reid
Angelika Renner
João Rodrigues
Carola von Saldern
Emma Sheldon
Henriette Skourup
John M. Snyder
Gunnar Spreen
Detlef Stammer
Mani V. Thomas
Rasmus T. Tonboe
Peter Wadhams
Jeremy Wilkinson

Climate Change and Natural Hazards series 10

2006 Directorate-General for Research Sustainable Development, Global Change and Ecosystems EUR 22416 EN

Europe Direct is a service to help you find answers to your questions about the European Union

Freephone number:
00 800 6 7 8 9 10 11

A great deal of additional information on the European Union is available on the Internet.
It can be accessed through the Europa server (http://europa.eu).

Cataloguing data can be found at the end of this publication.

Luxembourg: Office for Official Publications of the European Communities, 2006

ISBN.92-79-02803-0

Printed in Belgium

PRINTED ON WHITE CHLORINE-FREE PAPER

PREFACE

The European Commission has supported research on climate change and impacts for more than 20 years through its Framework Programmes. The aim is to provide expert scientific advice so that the European Union can meet its commitments in preserving the environment and ensuring sustainable development. Moreover, this research has been closely linked to the development of the international regulatory framework which led to the United Nations Framework Convention on Climate Change (1992) as well as the Kyoto Protocol (1997). As part of their obligation under these international agreements and in response to the scientific and public concerns about the impacts of climate change, both the European Commission and the Member States co-finance complementary research programmes to support policy actions at European and international level.

The persisting scientific uncertainties, the global dimension of the climate problem and the political leadership of the European Union in environmental legislation are calling for stronger European research programmes to further advance our understanding and to ensure effective interventions where appropriate. The new 7th Framework research programme 2007-2013 is the main implementation instrument to address the issues. Climate change research is a key priority area in this programme for the years to come.

The organisation of the International Workshop on Arctic Sea Ice Thickness fits into the overall European Commission strategy to provide a platform to present past achievements, latest research results and future approaches in specific areas of climate change and impacts.

On behalf of the European Commission I would like to express my sincere thanks to the authors, contributors and reviewers for their hard work in preparing this volume, as well as the organisers who helped to make this Workshop successful. I am confident that the outcome of this workshop will be useful for the scientific community, policy makers and research managers.

Georgios Amanatidis
Climate Change and Environmental Risks Unit
Directorate-General for Research, European Commission

1	Søren Andersen	14	Christian Haas	27	Andreas Pfaffling
2	Olivia Benham	15	Stefan Hendricks	28	Andy Ridout
3	Lawson W. Brigham	16	Sine M. Hvidegaard	29	João Rodrigues
4	Thomas Busche	17	Stefan Kern	30	Bert Rudels
5	Martin Doble	18	Takashi Kikuchi	31	Carola von Saldern
6	Rene Forsberg	19	Ron Kwok	32	Stein Sandven
7	Cathleen Geiger	20	Seymour Laxon	33	Torben Schmith
8	Sebastian Gerland	21	Wieslaw Maslowski	34	Henriette Skourup
9	Katharine Giles	22	Naja Mikkelsen	35	Norman Snow
10	Rashpal Gill	23	Martin Miles	36	John Snyder
11	Sibylle Goebell	24	Peter Minnett	37	Rasmus Tonboe
12	Preben Gudmandsen	25	David Peddie	38	Peter Wadhams
13	Jari Haapala	26	Leif Toudal Pedersen	39	Jeremy Wilkinson

Participants at the International Workshop on Arctic Sea Ice Thickness: Past and Present, Rungstedgaard Conference Centre, Copenhagen, Denmark, 8-9 November 2005

FOREWORD

This book represents the proceedings of the International Workshop on Arctic Sea Ice Thickness: Past, Present and Future, held at Rungstedgaard Conference Centre, near Copenhagen, Denmark, on 8-9 November 2005.

The conference was a timely effort to bring together scientists from Europe, North America and Japan who are concerned with the problem of measuring and understanding the thinning of the Arctic sea ice cover. This thinning is dramatic, more than 40% in the last 25 years, and it promises to turn the Arctic Ocean into a seasonal sea ice zone by the 2080s, according to most climate models, but significantly earlier according to some others. Given that the thinning rate is faster than the rate of shrinkage of ice extent, it seems likely that in its final stages the ice cover will fragment and disappear quite suddenly, either through mechanical weakness or because the summer melt rate exceeds the winter growth rate.

The wide-ranging papers in the book cover the methods used to measure ice thickness, on scales from basinwide down to local; the results obtained; the modelling of ice thickness; and the implications for Man's activities. Palaeoclimatic studies are also described, which reveal periods during the past 100,000 years when the Arctic Ocean has been ice-free, a challenge to our understanding of Earth system processes. Since the disappearance of the Arctic sea ice is literally the most visible aspect of global warming in action – we can see the change in the face of the planet from space - it is appropriate that the European Commission should take the initiative in seeking to understand this phenomenon.

The organisers of the meeting were the European Commission, and it was funded primarily through the project GreenICE (Greenland Arctic Shelf Ice and Climate Experiment) of the Fifth Framework Programme, code EVK2-CT-2002-00156. The organising committee comprised Peter Wadhams (co-ordinator, GreenICE), and Naja Mikkelsen, of GEUS, the Geological Survey of Denmark and Greenland, Copenhagen. I am deeply grateful to Naja for proposing Rungstedgaard and for making local arrangements.

The beautiful site of the Rungstedgaard Conference Centre is close to Rungstedlund, the family home of Karen Blixen, and is situated beside Øresund, some 12 miles north of Copenhagen. We are grateful to the staff of the conference centre for the smooth running of the meeting and the excellent facilities provided. Olivia Benham (née Low) co-ordinated both the conference and the production of this book, and her contribution is greatly appreciated.

The onerous task of technical editing and layout of the book was carried out by Nick Hughes (Scottish Association for Marine Science, Oban), and we also wish to thank the many referees who read the manuscripts and suggested changes.

Peter Wadhams
Department of Applied Mathematics and Theoretical Physics
University of Cambridge

CONTENTS

PREFACE **5**

FOREWORD **7**

CONTENTS **9**

REVIEW

1. Arctic Sea Ice Thickness – A Review of Current Techniques and Future Possibilities
Peter Wadhams 12

PART 1. HOW WE MEASURE SEA ICE THICKNESS

2. Ice Mass Balance Buoy: An Instrument to Measure and Attribute Changes in Ice Thickness
Jacqueline A. Richter-Menge, Donald K. Perovich, Cathleen Geiger, Bruce C. Elder and Kerry Claffey 24

3. A Review of the Use of Sonar on Underwater Vehicles to Obtain Information on Sea Ice Draft
Jeremy P. Wilkinson, Peter Wadhams and Nick E. Hughes 30

4. Key Characteristics of Helicopter Electromagnetic Sea Ice Thickness Mapping Resolution, Accuracy and Footprint
Andreas Pfaffling, Christian Haas and James E. Reid 46

5. The Simulated Seasonal Variability of the Ku-band Radar Altimeter Effective Scattering Surface Depth in Sea Ice
Rasmus T. Tonboe, Søren Andersen, Rashpal S. Gill and Leif Toudal Pedersen 57

6. SAR Motion Products: Tools for Monitoring Changes in Sea Ice Mass Balance and Thickness Distribution
Cathleen A. Geiger, Mani V. Thomas, and Chandra Kambhamettu 64

7. Classification of GreenICE SAR Data Using Fuzzy Screening Method
Rashpal S. Gill and Rasmus T. Tonboe 74

8. Sea Ice Freeboard from ICESat – A Comparison with Airborne Lidar Measurements
Henriette Skourup and Rene Forsberg 82

9. On the use of helicopter-borne Radar Backscatter Polarization Ratio measurements at L-Band to estimate the ice thickness
Stefan Kern, Martin Gade, Christian Haas, Andreas Pfaffling, and Gerd Müller 93

10. Satellite Thermal Microwave Sea Ice Concentration Algorithm Comparison
Søren Andersen, Rasmus T. Tonboe and Lars Kaleschke 104

PART 2. WHAT DO WE KNOW ABOUT THICKNESS CHANGES?

11. GreenICE Sediment Cores Reveal Reduced Last Interglacial Arctic Sea Ice Cover
Niels Nørgaard-Pedersen, Naja Mikkelsen, Susanne J. Lassen,
Emma Sheldon, Yngve Kristoffersen 114

12. Airborne Electromagnetic Measurements of Sea Ice Thickness: Methods and Applications
Christian Haas, Sibylle Goebell, Stefan Hendricks, Torge Martin,
Andreas Pfaffling, Carola von Saldern 136

13. Recent Changes in the Sea Ice Thickness Distribution in the Russian Arctic
João Rodrigues 149

14. Spring Sea Ice Thickness in the Western Fram Strait: Preliminary Results
Sebastien Gerland, Christian Haas, Richard Hall, Jürgen Holfort,
Edmond Hansen, Terje Brink Løyning, and Angelika Renner 158

15. Sea Ice Thickness, Geoid and Ocean Topography in the Arctic Ocean from ICESat and GRACE
Rene Forsberg, Henriette Skourup 165

16. Utilization of Multiple Satellite Sensors to Estimate Sea Ice Volume Flux through Fram Strait
Gunnar Spreen, Stefan Kern, and Detlef Stammer 176

17. Sea ice Thickness Estimates from Airborne Laser Scanning
Sine M. Hvidegaard, Rene Forsberg, and Henriette Skourup 193

18. Effect of the Physical Description of Sea Ice on the Modelled Mean Sea Ice Thickness on the Arctic Ocean
Jari Haapala 207

PART 3. SEA ICE EXTENT CHANGES AND IMPLICATIONS FOR SOCIETY

19. The Arctic Marine Shipping Assessment: Changing Marine Access and a Critical Need for Improved Sea Ice Thickness Information
Lawson W. Brigham 220

20. Arctic Sea Ice Thickness: Implications for Arctic Tourism
John M. Snyder 229

21. Recent Changes in the Sea Ice Distribution in the Russian Arctic: Ice Extent, Area and Length of the Ice-free Season
João Rodrigues 244

REVIEW

Arctic Sea Ice Thickness – A Review of Current Techniques and Future Possibilities

Peter Wadhams
Department of Applied Mathematics and Theoretical Physics (DAMTP),
University of Cambridge, Centre for Mathematical Sciences, Wilberforce Road, Cambridge CB3 0WA, UK.

Keywords: Ice thickness, climate change

ABSTRACT: We review the techniques currently being employed to measure sea ice thickness and consider what techniques, or combination of techniques, can be most effective for various roles in sea ice thickness measurement in future.

1 INTRODUCTION

The Arctic Ocean represents one of the most serious challenges for scientific monitoring and measurement techniques. Difficult of access, and containing extreme conditions of temperature and danger, it is one of the fastest-changing parts of the Earth's surface, and already the retreat of sea ice is the aspect of global change which is most clearly visible from space. The very face of our planet is changing. We need to understand the changes in ocean dynamics, water mass transformations, sea ice dynamics and ocean-ice-atmosphere energy exchanges, as well as interactions between these physical processes and the ecosystem. The palaeoceanography of the Arctic will also give us valuable lessons about how climate and ice interact.

The Arctic Ocean is the only ocean permanently covered by ice, of a thickness to make research by surface vessel difficult and expensive. It therefore represents an opportunity to deploy many of the new technologies being developed for ocean research which eliminate the need for a conventional surface ship. The deployment of the best and most cost-effective mix of new technology to solve the scientific problems of the Arctic represents an exciting challenge for the oceanographic community of Europe and the world. Nowhere is this more important than in the field of ice thickness measurement, since it is the dramatic thinning of Arctic sea ice which threatens to turn the Arctic from a frozen ocean into an open sea, with unsuspected consequences for the climate and way of life of Europe and the world.

2 ICE THICKNESS PARAMETERS

The fundamental parameter which we seek to measure is the ice thickness distribution and its variability over the Arctic Basin both in space and time. This is a real challenge to technology since no fully adequate and accessible method exists at present to achieve this aim.

It is important to measure not just the mean thickness but the entire probability density function *g(h)* of thickness. This is because:

(i) *g(h)* determines the ocean-atmosphere heat exchange, with thin ice dominating;

(ii) together with the ice velocity, it gives mass flux;

(iii) its downstream evolution gives the melt rate, i.e. the fresh water flux;

(iv) the shape of *g(h)* is a measure of the degree of deformation of the ice cover;

(v) if multi-year fraction is also known, *g(h)* can be used to give ice strength and other statistically definable mechanical properties of the ice cover;

(vi) its variability is a test of model outputs;

(vii) its long term trend indicates the nature of the climate response.

In addition to *g(h)* it is also valuable to have a measure of the ice bottom shape or roughness. This implies recording ice bottom surface profiles rather than simply sampling the draft at fixed time intervals as is done with moored sonar. The extra advantages of knowing ice surface shape are:

(i) it is a determining factor for the aerodynamic and hydrodynamic drag coefficients;

(ii) the deepest ridges are responsible for generating internal wave activity which may lead to a significant internal wave drag;

(iii) seabed scour by the deepest ridges defines the limit of fast ice on shelves and the extent of the stamukhi zone (Reimnitz et al., 1994);

(iv) ridges are an important component in the calculation of the force exerted by an icefield on offshore structures;

(v) the scattering of underwater sound by ridges defines the range to which acoustic transmission can be accomplished in the Arctic, since upward refraction leads to repeated surface reflection;

(vi) ridged ice provides a different habitat for sea ice biota from undeformed ice.

In this paper we review the methods that have been used, or could be used, to measure ice thickness distribution in the Arctic. We begin with existing well-tried techniques and then consider new methods. Current methods comprise:- submarine sonar profiling; moored upward sonar; airborne laser profilometry; airborne electromagnetic techniques; drilling; radar altimetry; laser altimetry.

3 CURRENT METHODS

Submarine sonar, reviewed in Chapter 2 of this book (Wilkinson et al., 2006), gives us the ability to obtain synoptic data on ice draft and under-ice topography in a rapid and accurate fashion, and most of our knowledge of the general distribution of *g(h)* over the Arctic comes from such profiles (e.g. Figure 1, a typical Arctic ice thickness distribution). Sidescan sonar (Wadhams, 1988; Sear and Wadhams, 1992) or swath sounding sonar (Wadhams et al., 2006) can be added to give extra information about ice type and two-dimensional bottom topography. However, military submarines are not always available frequently enough to obtain repeated profiles at a sufficient density to test for climate-related trends, nor are they necessarily able to profile over a desired systematic grid since ice profiling is an addendum to their operational task. Conversion of draft to ice thickness is a simple and accurate procedure, and in applications related to mass flux it is in fact useful to deal with draft as the relevant parameter, since this defines ice mass per unit surface area.

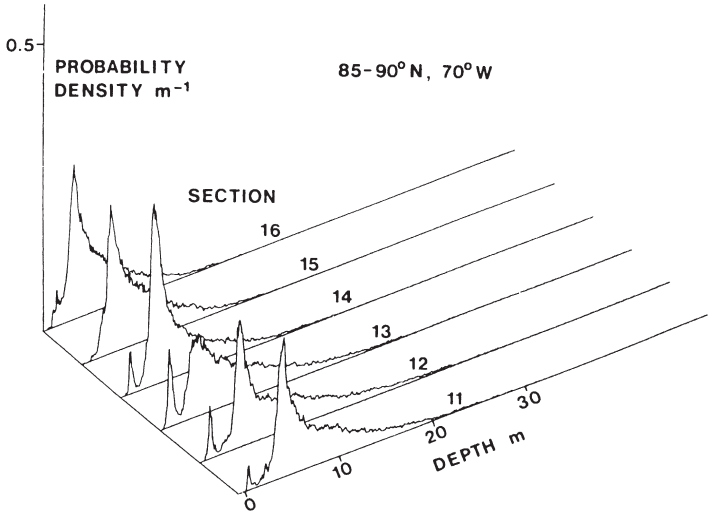

Figure 1. Some typical probability density functions of ice draft from the Arctic Basin (after Wadhams, 1981). Each function is derived from 100km of submarine sonar profile.

AUV sonar solves the problem of military data availability by placing the profiling sonar on an unmanned vehicle; this also enables the vehicle to work in shallow water and other unsafe situations. For short-range surveys the vehicle could be a cable-controlled ROV (Remotely Operated Vehicle), but for mesoscale and basinwide surveys it would have to be an AUV (Autonomous Underwater Vehicle). The earliest AUV operation under ice was carried out by Francois (Francois and Nodland, 1972) using an AUV in the Beaufort Sea; other early work is reviewed by Tonge (1992), while three recent deployments are described by Brierley et al. (2002) and Wadhams et al. (2004, 2006). The latter experiments featured sidescan and multibeam sonar, of which the latter offers full 3-dimensional quantitative mapping capability of the ice underside, the best quality data yet obtained under Arctic sea ice.

Drifting sonar involves placing a local sonar system on a drifting buoy, and intensively studying the time-dependent development of ice and snow thickness of a single floe (see Chapter 1 of this book). By using an upward sonar under the ice and a downward pinging sonar in air over the ice surface (together with thermistor chains) it is possible to separate the development of the upper and lower surfaces. Data are transmitted back by satellite.

Moored upward sonar solves the problem of systematic data collection by obtaining long-term information from a single point. It is invaluable for assessing the time variation of ice flux through critical regions such as Fram Strait. However, the ping rate is usually inadequate to resolve bottom topography, while the cost and difficulty of deployment and recovery preclude its general use over the whole Arctic on some systematic measurement grid.

Airborne laser profilometry yields freeboard distribution which can be converted to draft distribution if the mean density of ice plus overlying snow is known (Wadhams et al., 1991). This varies with time and space over the Arctic, implying that seasonal and regional validation is needed before this otherwise rapid and efficient technique can be used for basinwide surveys. Recent developments include swath sounding lasers, which give a three-dimensional image of the freeboard, making validation easier by facilitating matching with other types of profile (see chapters 7 and 16 of this book).

Airborne electromagnetic techniques consist of generating and sensing eddy currents under ice by VLF (10-50 kHZ) EM induction from a coil towed behind a helicopter, with simultaneous laser to give range to the snow surface. The early development of the technique was reviewed by Rossiter and Holladay (1994). The wide footprint involves some loss of resolution of individual ridges and a need to fly very low. The first packaged system fixed-wing aircraft use in the Arctic appears to be the system mounted in a Twin Otter by the Finnish Geological Survey (Hautaniemi et al., 1994), and recently the Alfred Wegener Institute Dornier has been fitted with antennas. Its use towed from a helicopter does, however, permit improved resolution. The AWI EM31 system and its applications are described in chapters 3, 11 and 13 of this book.

Drilling is the most accurate, but slowest, technique, the ultimate validation for all others. The use of a hot water drill increases the speed over that of a drill with a petrol-driven power head, and the replacement of the drill bit by a core barrel enables the ice to be directly sampled for salinity and other physical properties.

Radar altimetry involves the use of a radar beam from an aircraft or satellite; the time difference between the radar echo from the ice surface and from nearby thin ice or open water lying within the beam gives the freeboard. From this a conversion must be made to thickness from a knowledge of the mean density of sea ice and the thickness and density of the overlying snow. Results from the Envisat altimeter have been used to estimate the variability of mean ice thickness over the Arctic (Laxon et al., 2003), and a new type of altimeter was planned for use in the ESA CryoSat satellite which did not enter orbit in 2005 (CrtyoSat-2 is planned for 2009). The problem, as in laser profiling, is to use the correct conversion factor for the large multiplier needed to turn freeboard into thickness. An additional problem is that it is not clear where the reflection horizon lies; it is often assumed to be the snow-ice interface, but recent experimental research described in Chapter 4 of this book indicates that the horizon can lie within the snow layer, causing additional uncertainty.

Satellite laser altimetry operates in the same way as airborne laser altimetry. The first and only current laser altimetry satellite is ICESat of NASA (Kwok et al., 2004), which is also described in chapters 7 and 14 of this book. The same problem of conversion from freeboard to thickness occurs as in airborne laser altimetry, but it is at least clear that the echo is coming from the top of the snow layer.

4 FUTURE REQUIREMENTS

To accomplish the monitoring needs for the Arctic Ocean, two kinds of technology development are needed. One is to develop the above techniques further to give them the capability for routine basinwide use. The second is to develop and apply novel techniques that will permit the Arctic Basin to be surveyed rapidly and repeatedly. Examples of the first kind of development are:

(i) To carry out a regional and seasonal survey of mean snow-ice column density over the Arctic in order to allow laser and radar altimetry to be used systematically. At present data on ice density are rather sparse (Timco and Frederking, 1996). This could be done in conjunction with airborne altimetry measurements, e.g. using the ASIRAS altimeter which resembles that of CryoSat, in order to achieve a full validation test.

(ii) To carry out further basic research on the scales of variability, both horizontal and vertical, of such parameters as temperature, salinity and crystal fabric in first- and multi-year ice as well as densities as above; and also the scales of such larger-scale features as melt ponds, ridges and leads.

(iii) To carry out submarine surveys by a manned submarine dedicated to civilian use. This could occur through temporary reassignment from the military; through full conversion of a decommissioned military submarine to civilian research vessel (the so-called ‘white submarine’ concept); or by use of a commercially designed small submarine. There are a number of small commercial submarines available, but cost and safety considerations are major factors as is the limited submerged range of which such submarines are presently capable. A submarine is also a vital instrument for mapping the Arctic seabed.

(iv) To develop AUVs with basinwide capability, basically a problem of battery technology.

Examples of the second kind of development are:

(i) Mounting sonar on a neutrally buoyant float, to construct a g(h) over, say, a week’s drift, the data being transmitted acoustically to a readout station. This requires only a modest extension of the existing technology of under-ice SOFAR and RAFOS floats and is planned as a component of the 2006-9 EU DAMOCLES project.

(ii) The use of acoustic techniques. It has been shown that travel time changes for an acoustic path are reduced by the presence of an ice cover, in most cases by an amount approximately proportional to the ice thickness (Guoliang and Wadhams, 1989; Jin et al., 1993). In long range acoustic propagation experiments this can be used to give a single mean value for ice thickness along a path.

(iii) Increased efforts to obtain empirical correlations between ice thickness and the output of satellite sensors such as passive and active microwave or altimeter. Already a partial positive correlation between SAR backscatter and ice thickness has been demonstrated (Comiso et al., 1991; Wadhams and Comiso, 1992; Massom et al., 1999). Further advance requires extensive validation studies. A different approach involves matching some informational property of the SAR image, e.g. connectedness of sectors of similar brightness, or distribution of brightness gradients, to g(h) in validated studies between SAR and submarines, in search of quantitative relationships of mathematic form. An example is the work of Kerman et al. (1999). For one specific ice type, pancake ice, it has been found that the thickness can be successfully inferred from the change in dispersion for ocean waves passing into the ice from the open sea, detected by the Fourier analysis of SAR subscenes (Wadhams et al., 2004b).

(iv) Novel airborne electromagnetic techniques. An example, included as chapter 8 of this book, is the use of the radar backscatter co-polarisation ratio at a frequency of 1 Ghz (L-band) to obtain the thickness of thin ice.

(v) Deriving ice thickness as a by-product of some other measurement. For instance, long distance swell propagation in ice is subject to a slow attenuation due to creep (Wadhams, 1973). The attenuation rate is frequency dependent but also thickness dependent. In principle one could obtain the spectrum of flexure from a set of strainmeters or tiltmeters along a wave vector across the Arctic, and derive a mean value of ice thickness from the attenuation rate. This has already been attempted during the EU FP5 GreenICE project, in which the presence of a resonant frequency in flexural-gravity wave propagation has been used as a means of estimating the modal ice thickness along a track from the ice edge to the location of the tiltmeter system (Doble, 2006).

(vi) Until the advent of fully-validated polar orbiting altimetry satellites, the best way to achieve the reliable, synoptic and repeatable ice thickness measurements over the Arctic Basin is a combination of frequently repeated under-ice sonar profiles over a grid covering the Basin, accompanied by a programme of moored upward sonar measurements spanning key choke points for ice transport, i.e, Fram Strait, the Svalbard-Franz Josef Land gap and a small number of specimen points within the Trans Polar Drift Stream and Beaufort Gyre. Sonar moorings could well be combined with current meter moorings and sediment traps.

The use of a military submarines is necessary for these profiles, until or unless AUVs of sufficient range are developed. Valuable additional information can come from airborne laser surveys (again with validation needed) and airborne electromagnetic induction.

5 NEW TECHNOLOGY FOR THE STUDY OF ICE DEFORMATION

The study of Arctic sea ice thickness is also aimed at understanding sea ice processes which occur on scales of metres to hundreds of metres, where processes are concerned not with the microstructure of an ice sheet but rather with physical, geochemical and biological couplings associated with sea ice features such as pressure ridges, meltwater pools and leads. Pressure ridges constitute up to half of the volume of the ice in the Arctic. They are important biologically since they provide three-dimensional structure one scale up from the brine channel system, offering a substrate for algal growth and a feeding area and protected habitat

for larger species. Meltwater pools reduce the albedo at a time when short-wave solar radiation is near its annual maximum. Biological processes are affected by the downflow of fresh water into the near-bottom environment, while the variable albedo needs to be known for thermodynamic modelling. Leads involve massive heat exchanges and local convection in winter.

A study of individual pressure ridges, using first-year and multi-year ridges, would be very valuable, focusing on the structure and morphology of the ridges rather than their strength or the stresses involved in their formation. The required measurements each involve the use of new technology:

(i) The three-dimensional structure of ridges should be studied, including top and bottom shapes, block sizes, arrangements of voids, salinity and temperature profiles. The topography of the ridge underside can now be measured successfully using multibeam sonar (Wadhams et al., 2006), but to map the three-dimensional distribution of voids in a ridge it may be necessary to develop in-ice acoustic tomography or borehole video. Small–scale (of order 1 m range) in-ice tomography has been used to measure sound velocities in ice, but by scaling up a factor of ten it may be possible to observe individual voids.

(ii) Gradients of velocity, turbulence and oceanographic properties very close to the ridge surface require measurement. This will require small-scale chains of probes to be attached to the ice bottom by divers.

(iii) Biological and geochemical studies of the cavities are then needed to determine the significance of the cavities for primary and secondary production, and the utilisation of ridges by higher trophic levels. This requires the use of probes and sensors for penetrating the cavities.

(iv) Sedimentation rates under ridges require sediment traps to be deployed under ridges and then recovered.

For the study of melt season processes it is essential to be present through the whole melt season, from the time of snow melt beginning to the time of autumn freeze-up (July – October). The study would cover the initiation, development and draining of meltwater pools, their effect in flushing salt out of the ice as well as biological material and sediments, their effect in changing the surface and bottom topography of first-year ice in the transition towards multi-year, their role in defining the summer albedo, their absorption of radiation, and the fate of the meltwater as it is injected into the water column.

To implement such a programme on ridges and melt season processes it will be necessary to use either a drifting ship or a small drifting ice station, as will occur in the Damocles project with “Tara” in 2007 and in other programmes associated with the International Polar Year (2007-9). The work then involves collaborative top surface and ice underside work using, for instance, a small AUV for the underside coupled to top surface manual and EM measurements.

6 APPENDIX

International Workshop on Arctic Sea Ice Thickness: Past and Present
Rungstedgaard Conference Centre, Copenhagen, Denmark
8-9 November 2005
Organisers: European Commission. Organising committee: P. Wadhams (Cambridge), N. Mikkelsen (GEUS, Copenhagen)

Summary of recommendations for sea ice thickness measurement

1. Techniques available at present.

The most useful *synoptic technique*, i.e. a method for giving sea ice thickness distribution accurately over large areas, is **upward sonar from submarine vehicles** because this offers (a) basinwide coverage, (b) the complete shape of the draft distribution, which is very close to the thickness distribution. Military submarines have the greater range at present, but tend to be fitted with single-beam upward sonar and sidescan sonar. Recommendation: to fit a multibeam sonar system to a submarine to combine synoptic coverage with 3-D quality of thickness distribution along a swath. AUVs (e.g. Autosub) already have multibeam sonar but are limited in range and thus useful at present mainly for regional thickness distributions. Recommendation: to seek to use AUVs with the longest possible range for under-ice application.

Other valuable synoptic techniques are:-

Electromagnetic sounding from helicopters (e.g. EM31 of AWI). Advantages: gives a thickness (as opposed to draft) distribution. Problems: can be affected by porosity of ridges (EM sees first high conductivity horizon); beamwidth is function of helo height; limited by range of helo.

Laser freeboard swath sounding from aircraft (e.g. Danish National Space Centre). Advantage: range, swath capability. Problem: gives freeboard of ice plus snow, which is difficult to convert to ice thickness unless we know the snow depth and density (external variables which have to be measured by some other means or else estimated) and ice density (a fundamental quantity which, surprisingly, is not well enough known to permit good inference of thickness from freeboard, which involves a large multiplier).

Laser freeboard from satellite (ICESat). Advantage: global coverage. Problems: all those listed above, plus fact that it gives values over single pixels rather than a swath.

A synoptic technique which requires further validation is:-

Radar altimetry from satellite (e.g. Envisat now, Cryosat in future). Advantage: global coverage up to latitude limit of satellite orbit (81.5 degrees for Envisat). Problems: all those listed above for laser, plus a further problem in that laboratory studies carried out by Tonboe during GreenICE have shown that the radar reflection does not necessarily come from the ice-snow interface (as commonly assumed) but from some intermediate depth within the snow layer which is a function of temperature and wetness of the snow and which needs to be resolved before an appropriate multiplier can be applied to convert freeboard to thickness. Recommendation: a serious calibration-validation effort is needed before the launch of the next altimetry satellite (CryoSat 2).

Available *time-dependent techniques* (i.e. that measure thickness at a point, whether Eulerian or Lagrangian, over a period of time), include

Satellite-tracked buoys using acoustic pingers or thermistor chains for upper and lower snow and ice surfaces (well proven) or tiltmeter arrays for thickness inference from wave dispersion (tested on GreenICE but still under development).

Moored upward looking sonar, well proven in critical areas like Fram Strait (NPRI), Weddell Sea (AWI) and areas scheduled for oil development (e.g. Sakhalin).

Drilling, the most accurate of all but slow and tedious.

2. Future techniques

There was much interest in techniques whereby inference from satellites (e.g. SAR imagery, passive microwave data) is combined with model outputs to achieve a synthetic view. More work on these is recommended, together with new ideas on parameters that can be effectively measured from satellites.

7 REFERENCES

Brierley, A.S., N.W. Millard,, S.D. McPhail, P. Stevenson, M. Pebody, J. Perrett, M. Squires and G. Griffiths (2002). Antarctic krill under sea ice: elevated abundance in a narrow band just south of ice edge. *Science*, **295**, 1890-1892.

Comiso, J.C., P. Wadhams, W.B. Krabill, R.N. Swift, J.P. Crawford and W.B. Tucker (1991). Top/bottom multisensor remote sensing of Arctic sea ice. *J. Geophys. Res.*, **96**(C2), 2693-2709.

Doble, M. (2006). In GreenICE Final Rept., Contract EVK2-CT-2002-00156, European Commission.

Francois, R.E. and W.K. Nodland (1972). Unmanned Arctic Research Submersible (UARS) system development and test report. Univ. Washington, Applied Physics Lab., Tech. Rept. APL-UW 7219, 88pp.

Guoliang, J. and P. Wadhams (1989). Travel time changes in a tomography array caused by a sea ice cover. *Prog. Oceanogr.*, **22**(3), 249-275.

Hautaniemi, H., M. Oksama, J. Multala, M. Leppäranta, K. Riska and O. Salmela (1994). Airborne electromagnetic mapping of ice thickness in the Baltic Sea. Proc. IAHR Symp., Trondheim, Norway.

Jin, G., J.F. Lynch, R. Pawlowicz and P. Wadhams (1993). Effects of sea ice cover on acoustic ray travel times, with applications to the Greenland Sea Tomography Experiment. *J. Acoust. Soc. Amer.*, **94**(2), 1044-1056.

Kerman, B., P. Wadhams and J. Comiso (1999). Informational equivalence between synthetic aperture radar imagery and the thickness of Arctic pack ice. *J. Geophys. Res.*, **104**(C12), 29721-29731.

Kwok, R., H.J. Zwally and D. Yi (2004). ICESat observatyions of Arctic sea ice: a first look. *Geophys. Res. Lett.*, **31**, L16401, doi:10.1029/2004GL020309.

Laxon, S., N. Peacock and D. Smith (2003). High interannual variability of sea ice thickness in the Arctic region. *Nature*, **425**, 947-949.

Massom, R.A., J.C. Comiso, A.P. Worby, V.I. Lytle and L. Stock (1999). Regional classes of sea ice cover in the East Antarctic pack ice from satellite and in situ data during the winter tie period. *Remote Sens. Envt.*, **68**(C1), 61-76.

Reimnitz, E., D. Dethleff and D. Nürnberg, (1994). Contrasts in Arctic shelf sea-ice regimes and some implications: Beaufort Sea versus Laptev Sea. Marine Geol. 119, 215-225.

Rossiter, J.R. and J.S. Holladay (1994). Ice-thickness measurement. In: S. Haykin, E.O. Lewis, R.K. Raney and J.R. Rossiter (eds.) *Remote Sensing of Sea Ice and Icebergs*. Wiley, New York, 141-176.

Timco, G.W., and R.M.W. Frederking (1996). A review of sea ice density. *Cold Regions Res. & Technol.*, **24**, 1-6.

Tonge, E.M. (1992) An incremental approach to AUVs. Proc. Oceanology International '92, Brighton, 10-13 March 1992. Spearhead Exhibitions 1.

Wadhams, P. (1973). Attenuation of swell by sea ice. *J. Geophys. Res.*, **78** (18), 3552-3565.

Wadhams, P. (1988). The underside of Arctic sea ice imaged by sidescan sonar. *Nature*, Lond. **333**, 161-164.

Wadhams, P. and J.C. Comiso (1992). The ice thickness distribution inferred using remote sensing techniques. In *Microwave Remote Sensing of Sea Ice* (ed. F. Carsey), Geophys. Monograph 68, Amer. Geophys. U., Washington, 375-383.

Wadhams, P., W.B. Tucker III, W. Krabill, R. Swift, J.C. Comiso and N.R. Davis (1991). Relationship between sea ice freeboard and draft in the Arctic Basin, and implications for ice thickness monitoring. *J. Geophys. Res.*, **97**(C12), 20325-20334.

Wadhams, P., J.P. Wilkinson and A. Kaletzky (2004). Sidescan sonar imagery of the winter marginal ice zone obtained from an AUV. *J. Atmos. Oceanic Technol.*, **21**(9), 1462-1470.

Wadhams, P., F. Parmiggiani, G. de Carolis, D. Desiderio and M. J. Doble (2004b). SAR imaging of wave dispersion in Antarctic pancake ice and its use in measuring ice thickness. *Geophys. Res. Lett.*, **31**(L15305): doi:10.1029/2004GL020340.

Wadhams, P., J.P. Wilkinson and S.D. McPhail (2006). A new view of the underside of Arctic sea ice. *Geophys. Res. Lett.*, **33**, L04501, doi:10.1029/2005GL025131.

PART 1.
HOW WE MEASURE SEA ICE THICKNESS

HMS Tireless surfaced in a lead at the North Pole, 19 April 2004.
(Photo: Nick Hughes)

Ice Mass Balance Buoy: An Instrument to Measure and Attribute Changes in Ice Thickness

Jacqueline A. Richter-Menge, Donald K. Perovich, Cathleen Geiger,
Bruce C. Elder and Kerry Claffey
ERDC Cold Regions Research and Engineering Laboratory, 72 Lyme Road, Hanover, NH 03755, USA

Keywords: ice thickness, ice buoys, acoustic sounding, ice temperature, ocean heat flux

ABSTRACT: An ice mass balance buoy (IMB) is described, which measures the positions of the top and bottom surfaces of the ice, as well as a time series of snow accumulation and ablation, ice mass balance, internal ice temperature fields, and temporally-averaged estimates of ocean heat flux. 32 buoys have been deployed to date, and a summary of results so far is presented.

1 INTRODUCTION

We have developed the Ice Mass Balance buoy (IMB) in response to the need for monitoring changes in the thickness of the Arctic sea ice cover. The IMB is an autonomous, ice-based system. IMB buoys provide a time series of ice mass balance, snow accumulation and ablation, internal ice and snow temperature fields, temporally averaged estimates of ocean heat flux, sea level pressure (SLP), surface air temperature (SAT), and ice drift. The unique feature of the IMB is that it also allows us to determine whether changes in the thickness of the ice occur at the top or bottom of the ice cover. This information provides important insight on the driving sources behind the change and is necessary for extending the results from these individual sites to a broader region. The value of the IMB is further enhanced when it is coupled with other tools.

2 APPROACH

Autonomous IMB buoys provide an inexpensive alternative to field campaigns (Richter-Menge et al., accepted for publication). These ice-based systems provide a means of routinely monitoring the ice mass balance at many locations for durations as long as a few years. Each drifting buoy is equipped with thermistor strings, which extend through the snow and ice cover and into the upper ocean, and acoustic sensors monitoring the position of the top and bottom surfaces of the ice (Figure 1). These instruments provide a time series of snow accumulation and ablation, ice mass balance, internal ice temperature fields, and temporally-averaged estimates of ocean heat flux (Figure 2). Taken together these data delineate whether there has been a change in the mass balance of the ice due to ice growth, surface melt, bottom ablation, or snow accumulation. Observed changes can be correlated with driving forces, such as the start and duration of the summer melt season, the length of the growth season, and the ocean heat flux. The IMB buoys are also equipped to measure position, sea level pressure (SLP), and surface air temperature (SAT). The drift pattern of the buoys provides information on the circulation pattern of the sea ice cover. Data on SLP and SAT are designed to be compatible with similar data collected from the more basic drifting buoys deployed under the International Arctic Buoy Programme (IABP).

The IMB, like all other existing instrumentation, is not a perfect tool, primarily because of its spatial limitations. However, judicious selection of the measurement site combined with spatiotemporal correlation relationships can facilitate an interpretation of the data relative to larger regions (Perovich and Richter-Menge, accepted for publication). Since undeformed, unponded multiyear ice is the predominant ice type within the perennial zone, a site that reflects this ice type will optimize the impact of the deployment. Results from the Surface Heat Budget of the Arctic (SHEBA) experiment (Perovich et al., 1999) indicated that roughly two-thirds of the entire ice cover consisted of undeformed, unponded ice. More than half of these cases exhibited similar ice growth, surface melt, and bottom melt behaviour, with values falling in a 20 cm range.

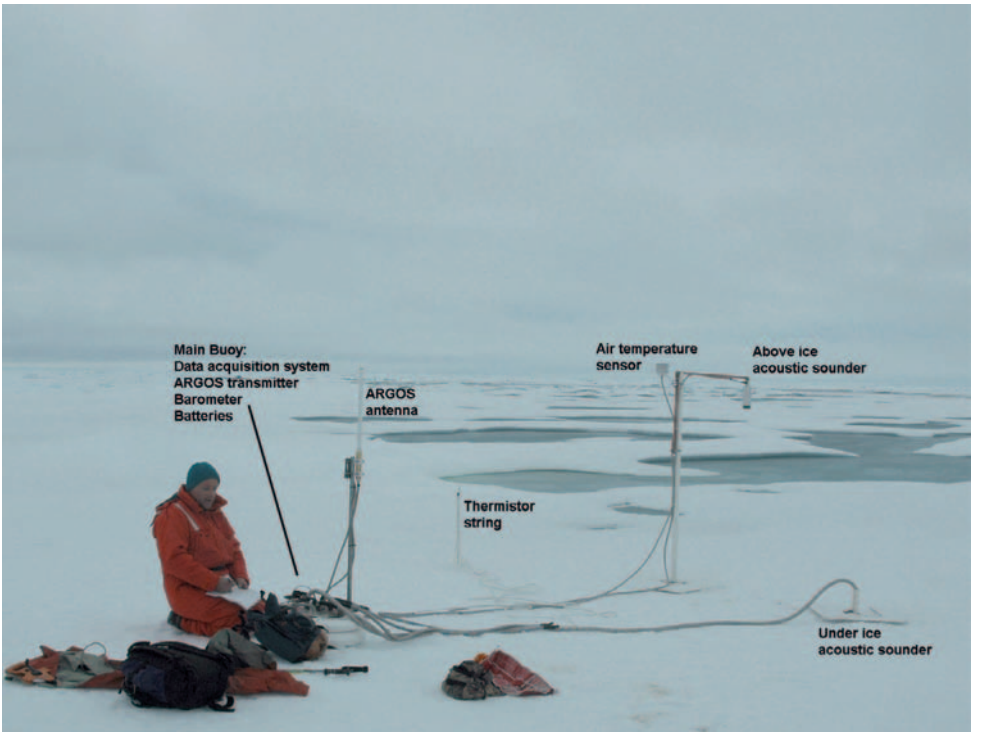

Figure 1. Ice mass balance (IMB) buoy, installed in a multiyear ice floe.

Another key to fully exploiting the time series information of mass balance measurements from IMB deployments is to couple and complement them with other tools which measure ice thickness with more spatial coverage. These tools include satellite-based altimeters (Laxon et al., 2003; Kwok et al., 2004); submarine and mooring-based ice profiling sonar (Rothrock et al., 1999; Melling, 2005), and helicopter-borne, ship-based or on-ice electromagnetic induction devices (Haas, 2004; Eicken et al., 2001). The central role of the IMB is to provide time series measurements of the mass balance of the ice over long periods at a high temporal resolution. These data provide critical insight on the driving forces governing variations in the state of the snow and ice cover. Common among many of the other tools is the ability to extend the spatial scales. For example, mooring-based ice profiling sonar provide time series information on the spatial variability of ice thickness. These systems are complementary in that the IMB is a drifting platform and the mooring-

based ice profiling sonar is a fixed platform, hence combined they provide both the Eulerian and Lagrangian perspectives. A network of IMB buoys and moorings can be located in regions where submarine and helicopter-borne electromagnetic surveys are conducted. The IMBs and moorings would provide a temporal link between survey missions. The submarine and helicopter-based surveys would extend the spatial coverage of the IMBs and moorings. Data from all of these instruments can be used to validate and calibrate remote sensing tools, including satellite-based instrumentation design to measure ice thickness or the onset and end of surface melt. Numerical models can be used to assimilate these data, present a context for the data, and provide a predictive capability.

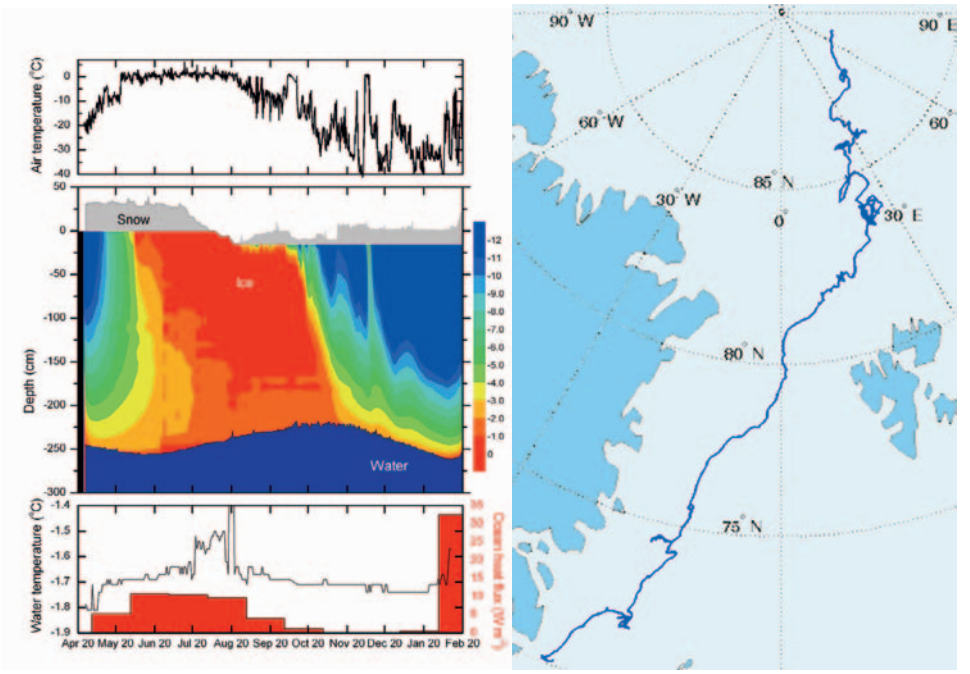

Figure 2. Results from ice mass balance buoy installed at the North Pole in April 2002.

3 DEPLOYMENTS

Since 1993, we have deployed 32 ice mass balance buoys (Figure 3). The majority of these deployments occurred after 2000, when the IMB became routinely deployed as part of the North Pole Environmental Observatory (NPEO). There was another notable increase in the number of deployments in 2003, associated with the National Oceanic and Atmospheric Administration's (NOAA) commitment to support a network of in situ ice thickness measurement platforms. When ever possible, the deployments of IMB buoys are coordinated with other projects. In addition to our ongoing coordination with the NPEO, IMBs are used to augment the buoy network established and maintained by the IABP, and deployed as part of the Japan Marine Science and Technology Center (JAMSTEC) (Kikuchi et al., 2002) and Woods Hole Oceanographic (WHOI) (Kemp et al., 2005) Arctic research programmes. Coordination of these activities also has the advantage of maximizing the cost-to-benefit ratio of the high logistical expenses that are associated with Arctic deployments.

Reflecting the availability of deployment platforms, there has been a concentration of buoy deployments in the vicinity of the North Pole and in the Beaufort Sea. The influence of the general circulation of the sea ice cover is immediately evident from the drift tracks. Buoys deployed in the vicinity of the North Pole are affected by the Transpolar Drift and eventually transported out of the basin via Fram Strait. These buoys typically drift out of the Arctic Basin 1-1.5 years after deployment. The drift tracks of the buoys deployed in the Beaufort Sea are more circuitous, reflecting the influence of the Beaufort Gyre. Depending on the strength of the gyre, the buoys either move in a circle within the basin (e.g. SIMI) or move toward the pole as they become incorporated into the Transpolar Drift (e.g. SHEBA).

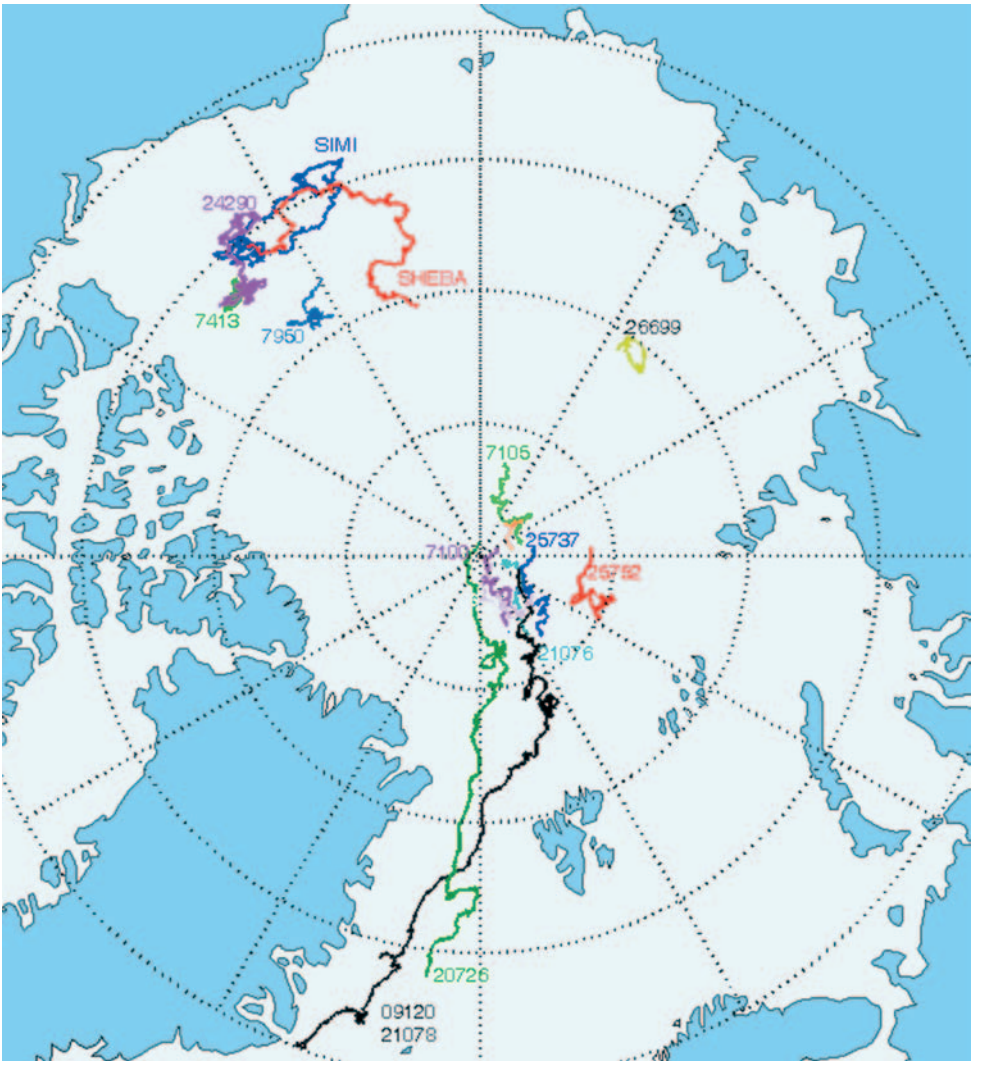

Figure 3. Initial location and drift of IMB buoys deployed near the North Pole and in the Beaufort Sea, beginning in 1993.

4 RESULTS

At this point, the collective time series is too short to draw significant and specific conclusions regarding interannual and regional variability in ice mass balance. Comparisons of the limited data do suggest the emergence of regional variations (Table 1). The ice surface ablation is greater in the Beaufort region relative to the North Pole. Not surprisingly, this is consistent with a longer average period of ice surface melt observed at the Beaufort buoys (76 days) compared to the North Pole buoys (59 days). The longer period of melt at the Beaufort buoys is a function of the surface heat flux, which is greater at the comparatively lower latitudes. Interestingly, ablation at the bottom of the ice surface, maximum ice thickness and maximum snow depth were comparable in the two regions.

Data from all of the IMB buoys that have been deployed is available at the website http://www.crrel.usace.army.mil/sid/IMB/index.htm.

Table 1. Summary of data collected from IMB buoys deployed in the Beaufort Sea and in the vicinity of the North Pole, beginning in 1993.

	Surface Ablation (cm)	**Bottom Ablation (cm)**	**Mean Maximum Ice Thickness (cm)**	**Mean Maximum Snow Depth (cm)**
NPEO (9 buoys)	0-30	10-37	232	27
Beaufort (3)	67-80	25-30	238	30

5 FUTURE WORK

As currently designed, the IMB buoy is best suited for deployment in the multiyear ice of the perennial ice zone. This is a significant limitation. One focus of our future work is to improve the versatility of the IMB, developing a system that is robust and can be placed in any ice type in both the perennial or seasonal ice zones. Another focus is the development of the associated website. The site will be upgraded to provide near-real time data from IMB buoys that are actively reporting and easy access to archival data. Our primary focus will be to continue efforts to coordinate the deployment of the IMB with other programs. By maintaining and further developing the buoy network, it is our intention to contribute to the efforts to provide a more consistent record of change, necessary for improving our understanding of this complex and important component of the global climate system.

6 ACKNOWLEDGEMENTS

This work has been supported by the United States National Oceanic and Atmospheric Administration, the U.S. National Science Foundation, and the U.S. Office of Naval Research. We acknowledge the gracious cooperation of many organizations which have assisted with the deployment of the autonomous ice mass balance buoys.

7 REFERENCES

Eicken, H., W.B. Tucker III, and D.K. Perovich (2001) Indirect measurements of the mass balance of summer Arctic sea ice with an electromagnetic induction device, *Ann. Glaciol.*, 194-200.

Haas, C. (2004) Late-summer sea ice thickness variability in the Arctic Transpolar Drift 1991--2001 derived from ground-based electromagnetic sounding, *Geophys. Res. Lett.*, **31**(L09402), doi: 10.1029/2003GL019394.

Kemp, J., Newhall, K., Ostrom, W., Krishfield, R., and A. Proshutinsky (2005) The Beaufort Gyre Observing System 2004: Mooring Recovery and Deployment Operations in Pack Ice, *WHOI Technical Report* WHOI-2005-5.

Kikuchi, T., K. Hatakeyama, K. Shimada, T. Takizawa and J. Morison (2002) Oceanographic observation under the multi-year ice of the Arctic Ocean using J-CAD, *The 17th International Symposium on Okhotsk Sea & Sea Ice*, 24-28 February 2002, Hokkaido, Japan.

Kwok, R., H.J. Zwally and D. Yi (2004) ICESat observations of Arctic sea ice: A first look, *Geophys. Res. Lett.*, **31**(L16401), doi: 10.1029/2004GL020309.

Laxon, S., N. Peacock and D. Smith (2003) High interannual variability of sea ice thickness in the Arctic Region, *Nature*, **425**, 947-950.

Melling H., D. A. Riedel, Z. Gedalof (2005), Trends in the draft and extent of seasonal pack ice, Canadian Beaufort Sea, *Geophys. Res. Lett.*, **32**, L24501, doi:10.1029/2005GL024483.

Perovich, D.K. and J.A. Richter-Menge (accepted for publication) From Points to Poles: Extrapolating point measurements of sea ice mass balance, *Ann. Glaciol*.

Perovich, D.K. et al. (1999) Year on ice gives climate insights, *EOS, Trans. of AGU*, **80**, 481, 485-486.

Richter-Menge, J.A, D.K. Perovich, B.C. Elder, K. Claffey, I. Rigor and M. Ortmeyer (accepted for publication) Ice Mass Balance Buoys: A tool for measuring and attributing changes in the thickness of the Arctic sea ice cover, *Ann. Glaciol*.

Rothrock, D.A., Y. Yu and G.A. Maykut (1999) Thinning of the Arctic sea-ice cover, *Geophys. Res. Lett.*, **26**, 3469-3472.

A Review of the Use of Sonar on Underwater Vehicles to Obtain Information on Sea Ice Draft

Jeremy P. Wilkinson[1], Peter Wadhams[2] and Nick E. Hughes[1]
[1]*Scottish Association for Marine Science, Dunstaffnage Marine Laboratory, Oban, Argyll PA37 1QA, Scotland*
[2]*Department of Applied Mathematics and Theoretical Physics, University of Cambridge, Centre for Mathematical Sciences, Wilberforce Road, Cambridge CB3 0WA, UK.*

Keywords: Sonar, submarines, AUV, pressure ridges

ABSTRACT: The history of the use of the submarine for ice thickness profiling is reviewed, and current trends in new types of sonar and new strategies for under-ice operation are considered, including joint submarine/aircraft/satellite experiments and the use of autonomous underwater vehicles.

1 INTRODUCTION

Despite new advances in obtaining information on sea ice thickness from satellite-mounted sensors (e.g. radar and laser altimeter), and airborne sensors (e.g. EM sounding and laser altimetry), under-ice mapping using sonar is still the most direct, and commonly used technique available. Since all parts of the Arctic Ocean have now been mapped at various times by under-ice sonar, it is from sonar profiling that the main information on sea ice thinning over the past decades has come (Rothrock et al., 1999; Wadhams and Davis, 2000, 2001; Rothrock et al., 2003).

Under-ice mapping with sonar falls into two categories; (1) upward-looking sonar from moorings, which offers data only at fixed locations, even though these may be critical choke points (e.g. Fram Strait); or (2) from moving platforms, i.e. submarines and autonomous underwater vehicles (AUVs). It is only moving platforms, in particular submarines, that can offer true synoptic ice thickness mapping of the Arctic. The continued availability of submarines (US and British) is therefore essential to the task of monitoring Arctic ice thickness through the present period of rapid change. Since the end of the Cold War, however, the deployment of British submarines in the Arctic has become more sporadic, and the US civilian Scientific Ice Expeditions (SCICEX) programme of 1990-99, which produced much valuable data on Arctic sea ice from submarines, has been reduced in scope. Given the possible shortage of submarine availability, the use of AUVs under sea ice is clearly an option that needs to be pursued vigorously, as AUVs offer the only platform which will definitely be available for scientifically controlled missions.

Here we review how the use of upward-looking sonar on submarines has evolved since it was first utilised, as well as the emerging role of AUVs for ice mapping and the need to shift from single-beam and side scan sonar to the multibeam swath mapping of the underside of sea ice.

2 BACKGROUND TO SUBMARINE OPERATIONS IN THE ARCTIC

A review of the early history of submarines under ice can be found in McLaren (1984). The first dive of a submarine under ice, followed by a successful surfacing through the ice, was by the submarine *Protector*, built by the American inventor Simon Lake, under ice 20 centimetres thick in Narragansett Bay during the winter of 1903-4. Subsequently the British, German and Russian navies gained experience operating in ice-covered waters, especially in the Baltic Sea, during World War I. This prompted the Australian explorer Sir Hubert Wilkins to lead an expedition to reach the North Pole in 1931 using an obsolete U.S. Navy O-class submarine renamed the *Nautilus*, originally built by Simon Lake and subsequently modified by him for the expedition (Wilkins, 1931; Casarini-Wadhams, 1989; Williams, 1998). Although the vessel failed to reach the Pole due to mechanical problems and probable sabotage, she was able to conduct tentative ice diving, despite the loss of the aft hydroplanes. Harald Sverdrup was the leader of the scientific staff, and the vessel did useful oceanographic work within the pack ice zone north of Svalbard (Sverdrup, 1933). Wilkins attempted to construct a new purpose-built polar submarine in 1937 (Casarini-Wadhams, 1989), but further progress was stopped by World War II, which involved limited operational use of submarines under ice as an evasion tactic during combat operations in the North Atlantic.

From 1946-53 the U.S. Navy undertook several important projects which led to the development of true Arctic-capable submarines under the direction of Dr. Waldo Lyon, the founder of the Arctic Submarine Laboratory (ASL). These experiments are summarised in McLaren (1984) and described in the biography of Lyon (Leary, 1999) as well as Williams (1998). The first upward-looking sonar was operated on *USS Atule* in 1946 between Baffin Island and Greenland. During Operation Highjump in the Antarctic the following year *USS Sennett* developed techniques for acoustically tracking pieces of floating ice, resulting in the first specifications for what components were required for a basic under-ice sonar navigation and piloting system. In August 1947 *USS Boarfish* made the first excursions under Arctic pack ice, the longest of which was of some 12 miles, in the Chukchi Sea and obtained the first ULS profiles of the underside of the ice canopy as well as demonstrating the utility of a mechanically-scanning forward-looking sonar for obstacle avoidance. This was a huge psychological boost, and over the next decade the honing of skills needed for under-ice navigation and ice discrimination continued. However the intrinsic limitations of diesel-electric submarine meant that these vessels could not safely manoeuvre very far from the ice edge, as they needed to surface at regular intervals to charge batteries.

The advent of the nuclear-powered submarines in the mid-1950s revolutionised under-ice operations as they were freed from the need to surface. In the International Geophysical Year the first nuclear powered submarine *USS Nautilus* conducted the first under-ice transit of the Arctic Ocean, being the first vessel to reach the North Pole on 3 August 1958 (Anderson, 1959). *Nautilus* was followed, a mere 9 days later, by the *USS Skate* which then surfaced within 40 miles of the Pole (Calvert, 1961). In the following years until 1962 *Skate* and her sister ships, *Sargo* and *Seadragon*, conducted further cruises in the Arctic to refine under-ice operations techniques including the first under-ice transits of the North West Passage (Mclaren et al., 1984). The first upward sonar datasets were analysed to yield estimates of sea ice thickness (Lyon, 1961, 1963). During this period U.S. submarines travelled over 50,000 km under the Arctic Ocean, leading Dr. Waldo Lyon to state that:

'The Arctic Ocean has become the private sea of the submariner, who is free to move in any direction and at any speed under the ice covering the sea'.

Despite warming and subsequent ice thinning, this is still the case. U.S. Arctic submarine development culminated with the development of the 637/*Sturgeon* class nuclear attack submarine in the late 1960's (Leary, 1999).

Surfacing within an ice covered ocean

Leads and thin ice are the obvious choice when a submarine needs to surface within an ice covered ocean. It is possible to identify areas of thinner ice directly above the submarine visually during daylight hours with the use of a periscope or camera because areas of thinner ice allow more light to be transmitted into the water column, and as such take on the appearance of a skylight in a darker-looking ice canopy. However, the only instrument available to submariners that can reliably and accurately give the thickness and extent of thin ice or a lead is sonar. An example of a submarine surfacing through a lead can be seen in figure 1.

Figure 1. HMS Tireless at the North Pole, 19 April 2004.

For these reasons submarines have a forward-looking sonar to detect objects located at or near the submarine's cruise depth, for example pressure ridges or icebergs that are extending deeply downwards; a downward-looking sonar to determine the clearance above the sea bed which can also be used to identify bathymetric features; and a number of upward-looking sonars mounted on the hull to continuously determine the separation distance of the

submarine from the ice bottom, or in the case of open water the sea surface. Typically there will be upward sonars at the bow, fin and stern, to determine whether a lead in which the submarine is attempting to surface has the necessary dimensions.

Over the years a significant number of under-ice missions have been performed and with the cooperation, openness and foresight of both the UK Royal and US Navy submarine fleet from which the sonar and navigational data have been stored, declassified and released to scientists. It was the analysis of ice draft data from submarines that first alerted the world that the summer sea ice within the Arctic was thinning at an astonishing rate, by some 40% since the 1970s (Rothrock et al., 1999; Wadhams and Davis, 2000; Rothrock et al., 2003), amounting to a reduction in mean thickness of 1 – 1.3 m with an accompanying reduction of some 73% in the frequency of deep pressure ridges (Wadhams and Davis, 2001), which is already having observable consequences in permitting surface ships to reach the North Pole more readily.

The pressure ridge reduction in particular indicates a radical change in ice dynamics. Satellite data has shown a reduction in the area of perennial (multi-year) ice throughout the Arctic (Comiso, 2002); while there has been a steady decline in the total area of Arctic ice since 1979, with some evidence of a recent acceleration (Parkinson et al., 1999; Stroeve et al., 2005). With fundamental change now occurring in the Arctic the need to continue to monitor ice thickness within the Arctic by submarine is a high priority.

3 THE EVOLUTION OF SONAR ON UK SUBMARINES

The earliest type of sonar that was employed on UK submarines was the Kelvin-Hughes Type 776 echo sounder which operated at 48 kHz and had a beam width of 20°. This sonar was installed onboard *HMS Dreadnought* during her cruise to the North Pole in March 1971, the first UK Arctic ice profiling operation. C.W.M. Swithinbank sailed aboard *Dreadnought* and obtained ice thickness distributions (Swithinbank, 1972; Williams et al., 1975) while P Wadhams sailed aboard the diesel-electric submarine *Oracle* which obtained upward-looking sonar data of wave penetration into the ice off NE Greenland (Wadhams, 1972, 1978a) at the same time. Records of the ice canopy were recorded on 150 mm wide sensitised paper and were digitised manually.

For the next Arctic deployment, of *HMS Sovereign* in October-November 1976, Wadhams was the on-board scientist and procured commercial sonar equipment of two kinds. A Kelvin-Hughes MS45 sonar was fitted as the upward sonar. This sonar operated at a slightly lower frequency, 45 kHz, but more importantly operated with a narrower beam width, 17° in the fore-and-aft direction and 5° in the athwartships direction (Wadhams and Lowry, 1977). This made it possible to make a correction for sonar beamwidth effects (Wadhams, 1980, 1981). The data were still recorded on Teledeltos paper, although on an x-y plot rather than a semicircular plot as on *Dreadnought* and early US submarines. Secondly, sidescan sonar, a 100 KHz Offshore Acoustics Ltd. model, was fitted for the first time to a submarine to give two-dimensional imagery of the underside of the ice. These data were also recorded on paper rolls using a Klein Associates chart recorder. Unfortunately the instrument only operated on one channel but still gave the first-ever under-ice sidescan record ever (Wadhams, 1978b). The voyage was organised as a joint expedition with support from the Defence Research Establishment, Ottawa, which flew an Argus research aircraft along the track of the submarine, equipped with laser profilometer and side-looking airborne radar

(SLAR). Ice thickness data are reported in Wadhams (1981), and the joint sonar-laser analysis in Wadhams (1980) and Wadhams and Lowry (1977).

The sidescan sonar deployed on *Sovereign* was developed into the Waverley operational system which was first deployed in the Arctic on *HMS Superb* in 1987. This recorded sidescan image and pulse timing information on an Edo chart plotter and as an FM analogue signal on 4-track tape. This highly successful experiment generated a large quantity of sidescan data, reported by Wadhams (1988). It was found that two valuable quantitative analyses can be carried out from sidescan data: discrimination between first-year and multi-year ice (Wadhams and Martin, 1990; Sear and Wadhams, 1992) from the small-scale roughness of the ice cover which is very pronounced in multi-year ice; and determination of the orientation of pressure ridges being crossed by the submarine, so that the apparent slope angles of the ridge measured by upward sonar could be turned into real slopes, thus yielding for the first time an experimental distribution of ridge slopes (Davis and Wadhams, 1995).

The 1987 cruise, by reproducing much of the track of the 1976 cruise, produced the first evidence of ice thinning in the Arctic, detecting a 15% loss of volume within the western Eurasian Basin (Wadhams, 1990). It was also the first cruise in which a valid joint top- and bottom- survey of the ice was carried out with the submarine operating on a track coincident with NASA P-3 Orion and Canadian aircraft carrying laser altimeter, passive microwave radiometer and X-band synthetic aperture radar (SAR). The sidescan sonar imagery when superimposed on the SAR record enabled individual ice floes, ridges and leads to be identified and this enabled the sonar and aircraft tracks to be matched so that true quantitative comparisons could be made. The very important discovery that the freeboard distribution has the same functional form as the draft distribution but subject to a density ratio factor (Wadhams et al., 1992) was made on this cruise. Other comparisons of the outputs of different sensors are given by Comiso et al. (1991) and Wadhams et al. (1991), with the basic ice thickness distributions reported by Wadhams (1992).

The use of sonar on UK submarines continued to evolve and in September 1996 *HMS Trafalgar* carried out an under-ice mission to the North Pole with new upward-looking sonar instruments, as well as a new sidescan sonar and oceanographic package (Wadhams and Davis, 2000, 2001). The upward-looking sonar was a new narrow-beam digital system, the 2077, which recorded depth versus distance directly onto digital tape, since both a pressure sensor and the boat's log were coupled to the sonar. In 1987 *Superb* had used an Admiralty-pattern 780 system, which was essentially identical to the system mounted on *Sovereign* in 1976 and recorded directly on to paper charts, so that both depth and speed variations had to be incorporated in the analysis of the manually digitised data. In addition *Trafalgar* carried an along-track oceanographic sensing system, the 2081, based on the Chelsea Instruments Aquapack system, which also recorded digitally, thus enabling along-track ocean data to be coupled to the under-ice sonar data. These instruments were used again in April 2004 aboard the most recent UK under-ice mission, that of *HMS Tireless* (Hughes and Wadhams, in press).

4 OBTAINING ICE DRAFT FROM UPWARD LOOKING SONAR

In the simplest terms single beam sonars work by transmitting a narrow beam of acoustic energy (sound) outwards from a single point or transducer. As the energy radiates conically outwards a proportion is reflected from objects intercepted at a distance from the sonar. The intensity of the returning energy or echo is a function of the distance the object is from the sonar from the sonar, as well as the shape and density of the objects encountered. As sea ice contains many minute bubbles it gives ice the acoustical characteristics of volume scattering and hence is a good reflector of sound.

After each pulse the sonar waits for a predetermined time for the sound to be reflected back before transmitting another pulse. The software within the sonar measures the time taken for the sonar pulse to return to the instrument. This is known as the travel-time.

In order to turn the travel-time into an absolute measurement of ice draft the following parameters are needed: depth of the sonar; average sound velocity in the water column above the sonar; the attitude of the sonar, i.e. pitch and roll, as it is unlikely that the sonar will be situated looking directly upwards; and finally the offset between the depth of the pressure sensor and the depth of the sonar. If a pressure sensor is being used as the primary measure of depth of the sonar below the surface, then it may even be necessary to apply a correction for variation of atmospheric pressure (e.g. a 50 mb drop in air pressure due to the passage of a low gives a 5 cm change in the apparent water depth measured by a pressure sensor). If all the above mentioned parameters are known then an ice draft can be calculated, but is still subject to sonar beam footprint effects (section 5). Because the submarine is constantly moving horizontally through the water a one-dimensional image of the ice canopy, draft vs. distance, is continuously built up one sonar ping at a time. The distance between pings is a function of the ping frequency of the sonar and the speed of the submarine.

In reality however, it is unlikely that all the parameters needed to convert travel-time to ice thickness are recorded sufficiently accurately, both temporally and spatially, to allow the direct conversion from travel-time to an accurate ice draft. This is especially true during early submarine missions. Therefore a different technique has been developed to obtain ice draft from submarine sonar data.

For submarine missions run during the summer months there are significant numbers of open water regions between the melting ice floes which can be used as zero reference points if they can be identified within the sonar record. It is fortunate that the ocean-atmosphere interface is highly reflective to sound and it return a strong sharply defined trace, even if only a small part of the insonified area is open water (Lyon, 1961). The specular reflection of open water can easily be identified in a sonar trace by a trained user. This is a long and laborious task but once all the open water areas within a sonar mission have been identified an accurate zero reference level (sea surface) is known for the whole mission. From this an accurate ice draft can be determined by calculating the distance between the ice bottom as identified by the sonar and the zero reference level or sea surface as identified by the trained user. This method is more problematic during the winter months when open water regions can freeze over quickly, but even narrow cracks and leads give characteristic hyperbola-shaped returns each of which gives a zero datum. Example of hyperbola-shaped returns in a sonar trace can be seen in figure 2.

The techniques used to derive ice draft from US submarine records are slightly different, and are described by Wensnahan and Rothrock (2005) and Rothrock and Wensnahan (in press).

5 DIFFICULTIES WITH ANALYSING SINGLE BEAM SONAR FROM SUBMARINES

Even though the difficulties of obtaining accurate ice draft measurements from submarines have been overcome through the zero reference level technique there are still limitations with the interpretation of ice draft from the sonar record. These are due to; (1) the characteristics of the sonar beam, i.e. its width and side lobes, (2) the unknown crossing angle of the submarine with respect to sea ice features and leads.

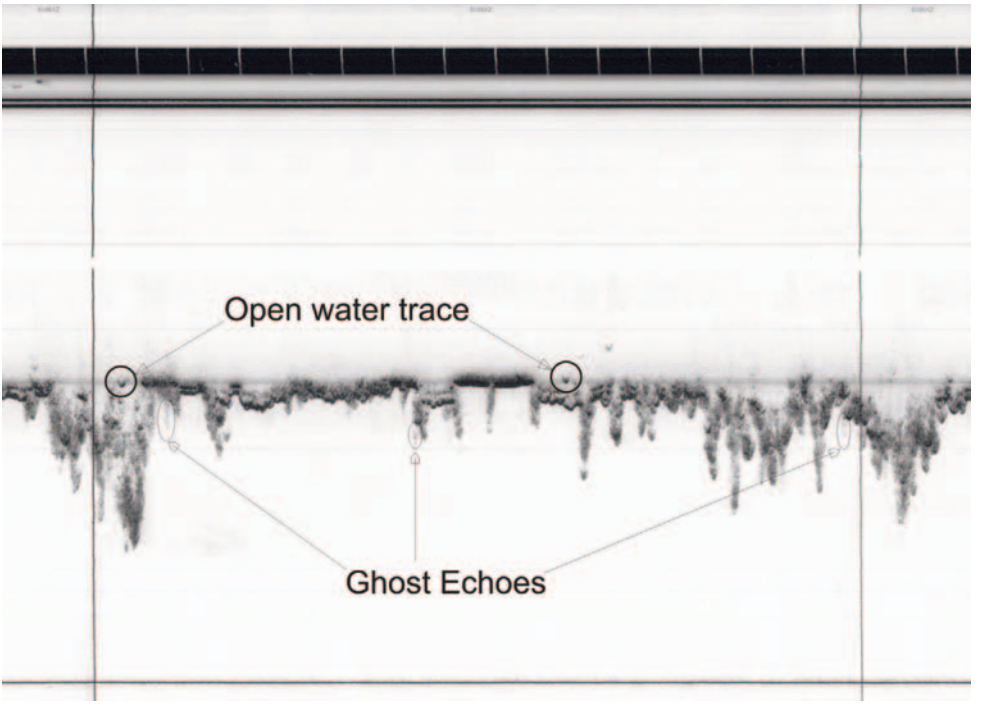

Figure 2. Example of a paper chart recording of an upward looking sonar profile of the underside of sea ice from a submarine. Identified in the image are both the hyperbola-shaped returns from open water as well as the ghost echoes from ice not directly above the submarine.

Sonar beam characteristics

Each sonar has a unique beam pattern which describes how the sound energy is radiated in different directions. The main features of the beam pattern are the main lobe, the side lobes and back radiation. For most applications the side lobes and back radiation should be minimal. Sonar systems are normally classified as wide beam i.e. wide main lobe or narrow beam, narrow main lobe. A narrow beam concentrates the sound energy and as such has a higher signal to noise ratio than wider beams. It also covers a smaller area and therefore provide a more detailed and accurate mapping capability.

The area insonified by the sonar is a function of the operating depth of the sonar and the width of the beam. The sonar that was fitted on early UK submarine missions had an effective along-track beamwith of 20°. Thus if a submarine was travelling at a depth of 50 m it would insonify an area on the sea surface of approximately 18 m in diameter and if travelling at 100 m it would insonify an area approximately 36 m in diameter. The effect of beamwidth with respect to ice draft is minimal when running under level ice but it smoothes out the profile under deformed ice i.e. ridges appear shallower and wider than they are. This necessarily implies an over-estimate of the mean ice draft.

A further complication with a wide beam sonar or side lobe effects is the receiving of sonar returns from ice keels that may not be immediately overhead or do not originate from the main lobe. The sonar record is dominated by first return signals from any reflecting surface. Late arriving signals, which may include those from points vertically overhead, may be lost if they are not the first to arrive. Multiple returns cause what is known as ghost echoes in the sonar profile.

To overcome these problems a sonar with a combination of a narrow beam width with limited side lobes is ideal for under ice operations. An example is the sonar used in the 1976 UK *Sovereign* cruise. With a wide beam in the fore-and-aft sense but a narrow (5°) athwartships beamwidth it was possible to devise an empirical correction technique for mean draft, and also for the percentages of ice in different depth ranges, using a calibration from another sonar (Wadhams, 1981). The principle here was that a record existed from a very narrow beam US sonar, used experimentally for a survey by *USS Gurnard* in the Beaufort Sea in 1976 (Wadhams and Horne, 1980). This was assumed to give an accurate profile. A model beam with the characteristics of the wide-beam UK sonar was run over the US ice record at the appropriate range, and the profile of first returns obtained and analysed. This gave a set of calibration curves relating statistics of the original narrow beam record to those of the model wide beam record, and so when used in reverse this enables the wide beam statistics to be reduced. Interestingly, it was found to make a 16% difference to the mean draft. Because the UK sonar was narrow beam to the side, it was possible to ignore "ghost" echoes from features not on the direct submarine track (see figure 2).

The effect of beamwidth on US profiles has been examined by Rothrock and Wensnahan (in press).

Crossing Angle

We know from the one-dimensional profile obtained from the upward looking sonar that much information can be obtained regarding the apparent shapes of pressure ridges and the apparent widths of leads. However a disadvantage is that we know nothing about the crossing angle of the submarine with respect to these features. An extreme case would be if the submarine were running under a long lead that was just wider than the sonar footprint. It would give the impression of open water where the surrounding ice cover at either side of the lead may be 100%. With respect to ice draft the submarine intersects a series of ice keels at unknown angles and therefore the true width and slope angle of a keel can only be computed if its orientation is known. Wadhams (1978c) showed that it is possible to overcome the lack of information regarding crossing angles if one assumes that ridge orientation is random; this allows an experimentally measured distribution of slope angles from a sonar profile to be turned into a "real" distribution of slope angles. A better method, of course, if sidescan is available, is to measure each individual ridge or lead orientation from the sidescan and thus

convert the upward sonar-derived slope into a real slope, apparent lead width into a real lead width etc. This was first carried out by Davis and Wadhams (1995).

One thing we can say is that if all morphological features (ridges, leads) are randomly oriented, then a one-dimensional profile of sufficient length will give an unbiased estimate of mean ice draft and, indeed, of ice draft distribution.

6 SIDESCAN SONAR

Sidescan sonar is a well proven acoustic technique for mapping features on the seafloor (e.g. Blondel and Murton, 1997). It works by transmitting a fan-shaped beam of acoustic energy outwards from port and starboard transducers so as to sweep the seabed or in our case the sea surface in a line-scan fashion as the vehicle carrying the transducers (submarine, ship or towfish) advances. A target with relief will result in an absence of sound, or shadows, behind the object, just as shining a beam of light at a low angle along the ground will create shadows behind objects that it hits. This intensity variation manifests itself as tonal variations, with light and dark portions representing strong or weak echoes respectively. After each pulse the sonar waits for a predetermined time for the sound to be reflected back before transmitting another pulse. Thus declination must be inferred from target distance only, using the assumption that the target field is essentially flat and horizontal.

Although the raw swath from the sidescan appears to be a real representation of the target area it is in fact distorted, with greatest distortion occurring in the near range of the record. This is due to the geometry of the system, as the initial return to the sidescan transducer is approximately vertical and the return from far range is approaching horizontal. An example of a side scan image of the underside of sea ice can be seen in figure 3.

It should be stressed that side scan sonar produces a qualitative 2-dimensional ‘photographic’ image with no quantitative information on ice thickness; it can be thought of as a photograph of the underside of the ice. It is possible to back out a one-dimensional ice thickness profile directly above the sidescan by assuming that the first sonar return is from ice immediately above the sonar (Wadhams et al., 2004), see bottom image of figure 3. Recently it has become possible to obtain an approximate measurement of ice draft from a sidescan system using phase detection through interferometric principles. However this only works well when the angle of incidence is large or the object being insonified is relatively flat. No three-dimensional data with this product has been obtained with respect to under ice mapping.

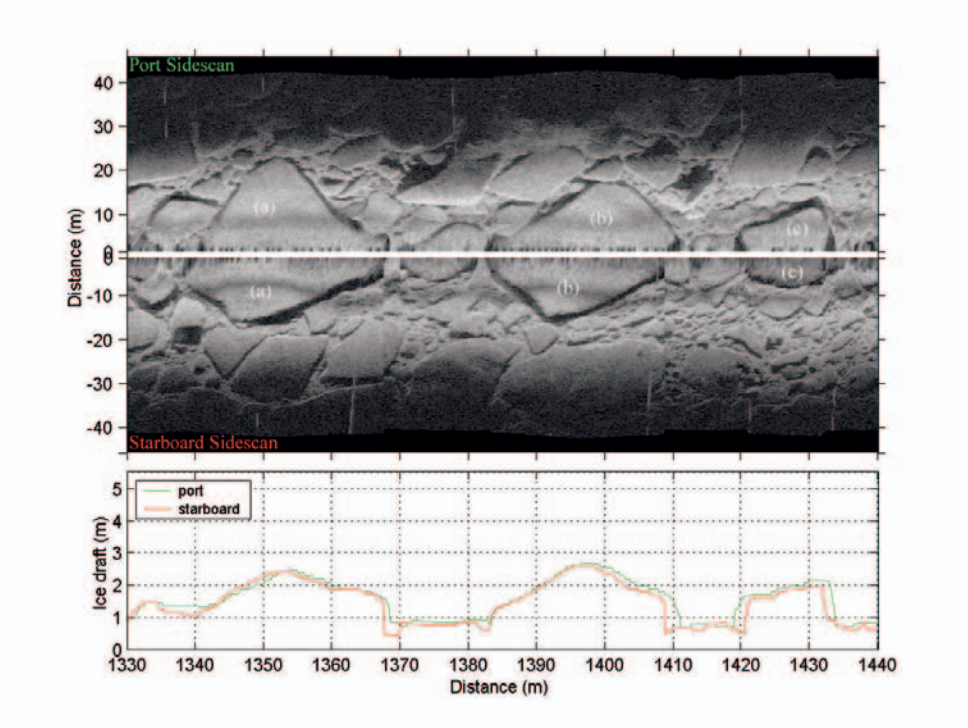

Figure 3. Section of sidescan from showing a high concentration of all ice types: frazil, brash/pancake and floes. Three angular multi-year floes (labelled (a), (b) and (c)), each up to 2.5 m thick and be seen in the central region of the image. No open water is visible in the image. Bottom plot shows the ice draft as seen directly above the port and starboard sidescan sensors (Wadhams et al., 2004).

7 MULTIBEAM SONAR

The next major leap in sonar technology with respect to under ice measurement did not materialise until 2004 when the first true three-dimensional imagery of the underside of sea ice was obtained using multibeam sonar mounted on an AUV (Wadhams et al., 2006). We have demonstrated how a single-beam sonar can obtain ice draft directly above the submarine. In theory we could mount many single-beam sonar systems at different angle to create a fan of beams perpendicular to the submarine's track, which when interpolated produces a three-dimensional image of the ice surface as the submarine moves through the water. In practice this is not feasible as the cost would be high and there would be interference between beams.

However, advances in technology in recent years have enabled multiple beams to be formed from a single transducer array. Hand–in-hand with this development has been advances in receiver design which has allowed the simultaneous detection of all beam echoes. This is known as electronic beam forming and detection and is the basis for multibeam sonar. The parameters associated with converting travel time to an accurate ice draft for multibeam sonar are the same as in any sonar, except that a detailed knowledge of how the sound speed varies with depth in the water column above the sonar is required. This is because the sound paths from the oblique parts of the beam are usually not straight, and ray path analysis may

be needed to calculate the correct depth and location of soundings taken away from the vertical.

In August 2004 the Autosub-II AUV operating off NE Greenland, obtained the first successful multibeam sonar measurements under sea ice, showing in unprecedented detail the three-dimensional nature of the under-ice surface. The multibeam sonar used was the Kongsberg Simrad EM-2000 swath multibeam bathymetric mapping system, mounted looking upwards. This system collects the equivalent of 111 independent beams equally spaced on a horizontal plane perpendicular to the direction of motion. It operates at 200 kHz, has a depth resolution of 1 cm, and beam widths of 1.5° along track and 2.5° across track. The overall angular coverage for the 111 beams for this mission was 120° and the beam spacing was set to equidistant, although it is operator adjustable and can be set equi-angle or any value in-between, but in such a way that the usable number of beams is always retained. The combination of phase and amplitude detection results in a measurement accuracy of 8 cm RMS being achievable practically independent of beam pointing angle. Useful information was obtained across a swath 100 m wide when the vehicle was running at 40 m depth (e.g. Figure 4).

There are many advantages to having 111 beams for sea draft measurements. One is that statistically valid probability density functions (pdfs) can be obtained over much shorter distances than the 50 km commonly employed for single-beam upward-looking sonar. The advantage is not quite a factor of (111)1/2 (=10.5) as expected from simple statistics, because of coherence of the ice draft over finite distances, but even if we assume a correlation length of 50 m the swath is still equivalent to 3 independent beams which gives a factor of √3, so that only 30 km or less are required to generate a pdf of equivalent quality to a 50 km upward sonar record.

The AUV, operated from *RRS James Clark Ross*, obtained more than 450 track-km of under-ice multibeam data over the NE Greenland shelf. Further information regarding the mission and associated data can be found in Wadhams et al. (2006). Some examples of EM-2000 multibeam ice draft data in perspective views, as if illuminated by a sun of elevation 20° can be seen in figure 4. Each image is accompanied by a probability density function (pdf) of ice draft compared to the pdf of the mission as a whole (lin-log scale, 5 cm bins).

8 SUMMARY

Despite it being almost 50 years since the first transect across the Arctic by submarine their observations are still the only direct measurement of ice draft and underside topography available to us on a synoptic scale, and as such the only benchmark we have at present to identify secular changes in Arctic ice thickness and in associated morphological parameters such as ridge spacings and depths. Furthermore the time series of ice draft data available to us is growing all the time as the UK Ministry of Defence and US Department of Defense release historical missions that were until now classified. The analysis of these data is a priority if we are to understand the fundamental changes that have occurred within the past few decades.

Whilst it is true that both the UK and US have cut the number of submarine missions in the Arctic substantially since the end of the cold war, when they do go the quality of the data they now obtain is far superior than was available during early missions. This is especially true with respect to the real-time digitisation of sonar data with the corresponding

oceanographic, depth and navigational data. The prevalence of civilian Arctic experiments using ice camps, surface ships and aircraft, and the increased use of ice-sensing satellites, now permits maximum value to be obtained from every submarine voyage in the way of cross-validation of sensor types.

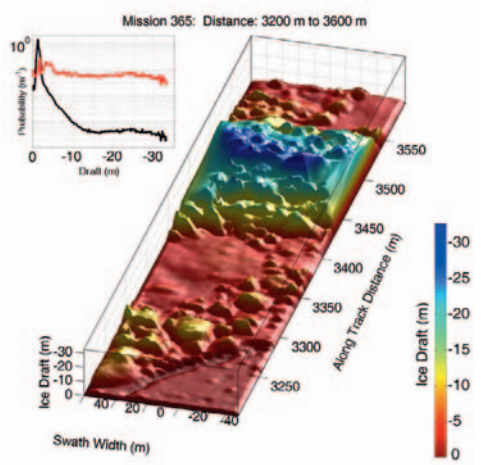

(a) Deep 33 m pressure ridge on Belgica Bank (marked A in figure 5), with shallower ridge in foreground, both surrounded by undeformed ice.

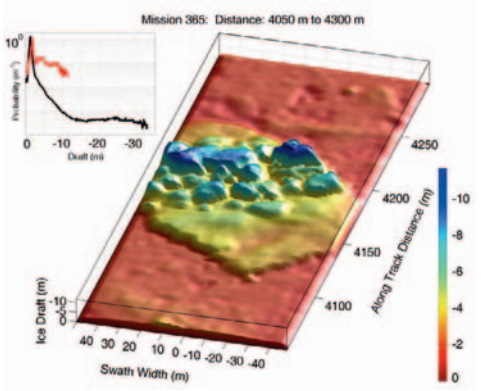

(b) Pressure ridge, marked B in figure 5, from western side of Norske Trough. Maximum draft 6 0. m. Smooth undeformed ice has peaks at 1.7 m and 1.3 m. Vertical exaggeration 1.75:1.

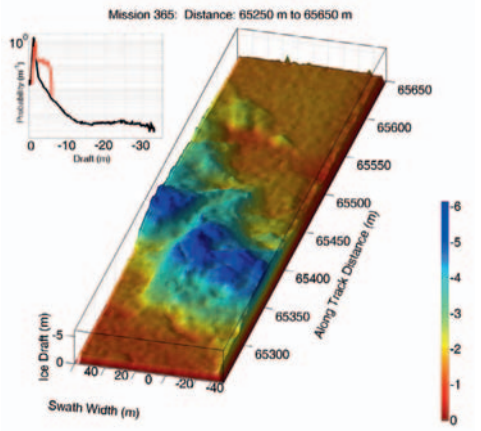

(c) Thick multi-year ridged floe of draft 3-5 m, with linear edges suggesting production from fracture of larger ice sheet, embedded in undeformed fast ice of draft 1.8 m. Fast ice shows pattern of depressions due to mirroring of surface melt pools. Thicker ice contains pressure ridge of maximum draft 11 m which has partly disintegrated into individual ice blocks of diameter 5-20 m. Evidence is that thicker floe came from MIZ.

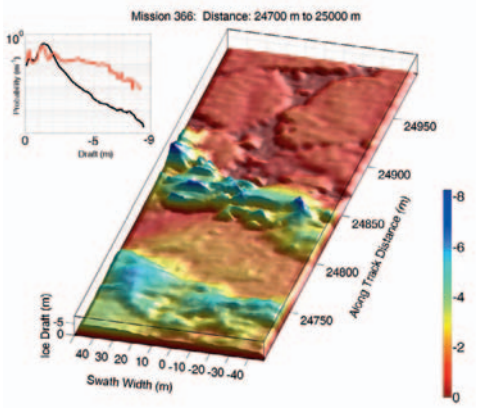

(d) Image showing in background first-year floes of 1.2 m draft with rounded edges embedded in young ice of 0.25 m draft. . In centre is young linear ridge, possibly shear ridge formed between the first-year ice and thicker floe in foreground. Foreground floe is multi-year ice of 1.85-2.25 m draft and in front a worn-down multi-year hummock. Vertical exaggeration 1.25:1.

Figure 4. Some examples of EM-2000 multibeam ice draft data in perspective views, as if illuminated by a sun of elevation 20°. Data points fill 2 m x 2 m grid. No vertical exaggeration unless otherwise stated. Each image is accompanied by a probability density function (pdf) of ice draft (red) compared to the pdf of the mission as a whole (black), lin-log scale, 5 cm bins (Wadhams et al., 2006).

However there are many regions within the polar seas to which submarines cannot venture. For example, the operation of military submarines is prohibited in the Antarctic (without full openness to inspection) by the Antarctic Treaty. Manned submarines also avoid very shallow waters at continental margins where coastal polynyas and fast ice can be found; the 2004 work of Autosub would have been highly unsafe for a manned submarine. Furthermore military submarines do not have the flexibility demanded by scientists who would like to choose the time and place of scientific missions under the ice. In these respects AUVs are the tool of choice for ice draft measurements, their greatest current disadvantage being their limited range.

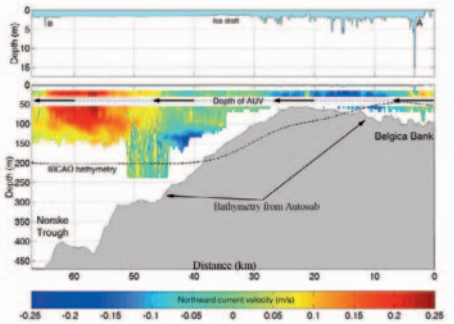

(a) The outward track of an Autosub mission off NE Greenland 21-22 August 2004, run at 40 m depth. The top profile is ice draft measured at crude resolution by upward-looking ADCP. Note smooth undeformed ice over Norske Trough. The bottom profile is the seabed topography measured by Autosub compared with the IBCAO bathymetry (dashed line). The coloured masses are N-S velocity components measured by the downward looking ADCP aboard Autosub. The red area is a strong northward current in the Trough, the Northeast Greenland Coastal Current (NEGCC); the blue area is a hitherto unrecognised southward current on the western flank of Belgica Bank. This image displays graphically the extra value obtained by carrying a number of oceanographic instruments on the AUV.

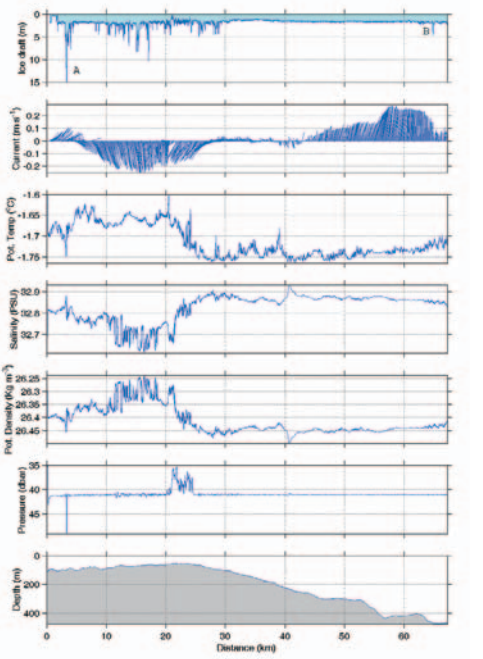

(b) Summary of the main oceanographic measurements onboard Autosub during its outward leg i.e. run towards the coast of Greenland. (a) Ice draft from upward-looking ADCP (b) Velocity and direction of the currents from the upward and downward-looking ADCP (c) Potential temperature (d) Salinity (e) Potential density (f) depth of Autosub during the mission (g) water depth from downward-looking ADCP.

Figure 5. Results from the outward run towards the coast of Greenland.

Autonomous underwater vehicles or AUVs are unmanned robotic submarines that can be programmed to complete a mission without human interference. AUVs have been used in the past for mine detection, open ocean oceanography, marine archaeology, but only recently for polar oceanography and sea ice research, although a deployment in the Beaufort Sea by a University of Washington vehicle in 1972 was decades ahead of its time (Francois, 1977). Ice-covered seas are particularly hazardous for an AUV as it has to work at freezing temperatures, have a collision avoidance system because of ice obstacles, and must also have an acoustic homing system in case the programmed recovery point becomes covered with

drifting ice during a given survey. The additional homing system will shepherd the AUV to a safe ice-free area for surfacing and recovery.

Besides the missions mentioned above, previous reported AUV operations under sea ice comprise an Autosub cruise under Antarctic sea ice with a single beam sonar (Brierley et al., 2002); and an operation off East Greenland by the Danish Maridan Martin AUV which yielded sidescan sonar imagery of the ice underside (Wadhams et al., 2004).

The combination of an AUV with a multibeam sonar is a huge leap forward for under-ice studies, and is important for work on the role of ice in climate change. Both the ice thickness profiling and the multisensor validation studies done up to now by military submarines can in principle be done from AUVs if the range problem can be solved. A combination of scientific instruments can be fitted to an AUV, and this in turn will allow researchers to simultaneously investigate the sea ice, oceanographic and biological properties under sea ice. An example of this multisensor approach can be seen in fig. 5. AUV technology will certainly play a role in obtaining data in critical regions of the world's polar oceans, especially the Antarctic.

9 REFERENCES

Anderson, W.R. (1959). *Nautilus 90 North*. Hodder and Stoughton.

Blondel, P. and Murton, B.J. (1997). *Handbook of Seafloor Sonar Imagery*. Wiley, 314pp.

Brierley, A.S., N.W. Millard,, S.D. McPhail, P. Stevenson, M. Pebody, J. Perrett, M. Squires and G. Griffiths (2002). Antarctic krill under sea ice: elevated abundance in a narrow band just south of ice edge. *Science*, **295**, 1890-1892.

Calvert, J. (1961). *Surface at the Pole*. Hutchinson.

Casarini-Wadhams, Maria Pia. (1989). By Submarine to the Arctic: Sir Hubert Wilkins' Nautilus Expedition of 1931. *Masters Thesis. Scott Polar Research Institute, University of Cambridge*.

Comiso, J.C., P. Wadhams, W. Krabill, R. Swift, J. Crawford, and W. Tucker (1991). Top/bottom multisensor remote sensing of Arctic sea ice. *J. Geophys. Res*. **96**(C2):2693-2711.

Comiso, J.C. (2002). A rapidly declining perennial sea ice cover in the Arctic *Geophys. Res. Lett.*, **29**(20), 17-1/4.

Davis, N.R. and P. Wadhams (1995). A statistical analysis of Arctic pressure ridge morphology. *J. Geophys Res.*, **100**(C6), 10915-10925.

Francois, R.E. (1997). High resolution observations of under-ice morphology. Univ. Washington, Applied Physics Lab., Tech. Rept. APL-UW 7712, 30pp.

Hughes, N and P. Wadhams (2006). Measurement of Arctic sea ice thickness by submarine 5 years after SCICEX. *Ann. Glaciol.*, 44, in press.

Leary, W.M. (1999). *Under Ice: Waldo Lyon and the Development of the Arctic Submarine*. Texas A & M University Press.

Lowry, R. T. and P. Wadhams (1979). On the statistical distribution of pressure ridges in sea ice. *J. Geophys. Res.*, **84**(C5), 2487-2494.

Lyon, W. (1961). Ocean and sea-ice research in the Arctic Ocean via submarine. *Trans. NY Acad. Sci,*. **23**(8), 662-674.

Lyon, W. (1963). The submarine and the Arctic Ocean. *Polar Rec.*, **11**(75), 699-705.

McLaren, A.S. (1984). The evolution of the Arctic submarine. *J. Navigation*, **37**(3), 380-397.

Mclaren, A. S., P. Wadhams and R. Weintraub (1984). The sea ice topography of M'Clure Strait in winter and summer of 1960 from submarine profiles. *Arctic*, **37**(2), 110-120.

Parkinson, C.L., D.J. Cavalieri, P. Gloersen, H.J. Zwally and J.C. Comiso (1999). Arctic sea ice extents, areas and trends, 1978-1996. *J. Geophys. Res.*, **104**(C9), 20837-20856.

Rothrock, D.A. and M. Wensnahan (2006). The accuracy of sea-ice drafts measured by U.S. Navy submarines. *J. Atmos. Oceanic Technol.*, in press.

Rothrock, D.A., Y. Yu and G.A. Maykut (1999). Thinning of the Arctic sea-ice cover. *Geophys. Res. Lett.*, **26** (23), 3469-3472.

Rothrock, D.A., J. Zhang and Y. Yu (2003), The arctic ice thickness anomaly of the 1990s: A consistent view from observations and models. *J. Geophys. Res.*, **108**(C3), 3083, doi:10.1029/2001JC001208.

Sear, C.B. and P. Wadhams (1992). Statistical properties of Arctic sea ice morphology derived from sidescan sonar images. *Prog. Oceanogr.*, **29**, 133-160.

Stroeve, J.C., M.C. Serreze, F. Fetterer, T. Arbetter, W. Meier, J. Maslanik and K. Knowles (2005). Tracking the Arctic's shrinking ice cover: another extreme September minimum in 2004. *Geophys. Res. Lett.*, **32**, L04501, doi:10.1029/2004GL021810.

Sverdrup, H. U. (1933). General report of the expedition. The Norwegian North Polar Expedition with *the "Maud" 1918–1925, Scientific Results*. Vol. II, *Meteorology*, Part I, *Discussion*, Geofysisk Institutt, 331 pp..

Swithinbank, C.W.M. (1972). Arctic pack ice from below, in *Sea Ice* (ed. T. Karlsson), Proc. Intl. Conf., Reykajvik. May 10-12 1971. Nat. Res. Counc. of Iceland, 246-254.

Wadhams, P. (1972). Measurement of wave attenuation in pack ice by inverted echo sounding. In *Sea Ice* (ed. T. Karlsson). Proc. Intl. Sea Ice Conf., Reykjavik, May 10-13 1971. Nat. Res. Counc. of Iceland, 255-260.

Wadhams, P. (1978a). Wave decay in the marginal ice zone measured from a submarine. *Deep-Sea Res.*, **25**(1), 23-40.

Wadhams, P. (1978b). Sidescan sonar imagery of sea ice in the Arctic Ocean. *Can. J. Remote Sensing*, **4**(2), 161-173.

Wadhams, P. (1978c) Characteristics of deep pressure ridges in the Arctic Ocean. *Proc. 4th Intl. Conf. on Port & Ocean Engng. Under Arctic Condns.*, St. John's, 26-30 Sept. 1977 (ed. D. B. Muggeridge). Memorial Univ. of Nfld., St. John's, 1, 544-555.

Wadhams, P. (1980). A comparison of sonar and laser profiles along corresponding tracks in the Arctic Ocean. In *Sea Ice Processes and Models*, Proc. AIDJEX/ICSI Symp., Seattle, 6-9 Sept. 1977 (ed. R. S. Pritchard), Univ. Washington Press, Seattle, 283-299.

Wadhams, P.(1981) . Sea-ice topography of the Arctic Ocean in the region 70°W to 25°E. *Phil. Trans. Roy. Soc.*, London, A302(1464), 45-85.

Wadhams, P. (1988). The underside of Arctic sea ice imaged by sidescan sonar. *Nature*, Lond., **333**, 161-164.

Wadhams, P. (1990) Evidence for thinning of the Arctic ice cover north of Greenland. *Nature*, Lond., **345**, 795-797.

Wadhams, P. (1992) Sea ice thickness distribution in the Greenland Sea and Eurasian Basin, May 1987. *J. Geophys. Res.*, **97**, 5331-5348.

Wadhams, P. and N.R. Davis (2000). Further evidence of ice thinning in the Arctic Ocean. *Geophys. Res. Lett.*, **27**, 3973-3975.

Wadhams, P. and N.R. Davis (2001). Arctic sea-ice morphology characteristics in summer 1996. *Ann. Glaciol.*, **33**, 165-170.

Wadhams, P. and R. J. Horne (1980). An analysis of ice profiles obtained by submarine sonar in the Beaufort Sea. *J. Glaciol.*, **25**(93), 401-424.

Wadhams, P. and R.T. Lowry (1977). A joint topside-bottomside remote sensing experiment on Arctic sea ice. *Proc. 4th Canadian Symp. on Remote Sensing*, Quebec, 16-18 May 1977. Canadian Remote Sensing Soc., 407-423.

Wadhams, P. and S. Martin (1990). Processes determining the bottom topography of multiyear Arctic sea ice. In *Sea Ice Properties and Processes* (eds. S. F. Ackley, W. F. Weeks), Monograph 90-1, US Army Cold Regions Res. & Engng Lab., Hanover, NH., 136-141.

Wadhams, P., N.R. Davis, J.C. Comiso, R. Kutz, J. Crawford, G. Jackson, W. Krabill, C.B. Sear, R. Swift and W.B. Tucker (1991). Concurrent remote sensing of Arctic sea ice from submarine and aircraft. *Int. J. Remote Sensing*, **12**(9), 1829-1840.

Wadhams, P., W.B. Tucker III, W.B. Krabill, R.N. Swift, J.C. Comiso and N.R. Davis (1992). Relationship between sea ice freeboard and draft in the Arctic Basin, and implications for ice thickness monitoring. *J. Geophys. Res.*, **97**(C12), 20325-20334.

Wadhams, P., J.P. Wilkinson and A. Kaletzky (2004). Sidescan sonar imagery of the winter marginal ice zone obtained from an AUV. *J. Atmos. Oceanic Technol.*, **21**(9), 1462-1470.

Wadhams, P., J.P. Wilkinson and S.D. McPhail (2006). A new view of the underside of Arctic sea ice. *Geophys. Res. Lett.*, **33**, L04501, doi:10.1029/2005GL025131.

Walker, E.R. and P. Wadhams (1979). Thick sea-ice floes. *Arctic*, **32**(2), 140-147.

Wensnahan, M. and D.A. Rothrock (2005). Sea-ice draft from submarine sonar: establishing a consistent record from analog and digitally recorded data. *Geophys. Res. Lett.*, **32**, L11502, doi:10.1029/2005GL022507.

Wilkins, H. (1931). *Under the North Pole: The Wilkins-Ellsworth Submarine Expedition*. New York: Brewer, Warren and Putnam.

Williams, E., C. Swithinbank and G. de Q. Robin (1975). A submarine sonar study of Arctic pack ice. *J. Glac.*, **15**(73), 349-362.

Williams, M.D. (1998). *Submarines Under Ice: The U.S. Navy's Polar Operations*. Naval Institute Press.

Key Characteristics of Helicopter Electromagnetic Sea Ice Thickness Mapping Resolution, Accuracy and Footprint

Andreas Pfaffling[1*], Christian Haas[1] and James E. Reid[2]
[1]*Alfred Wegener Institute for Polar and Marine Research, Climate Sciences Division, Sea Ice Physics Section, P.O. Box 120161, 27515 Bremerhaven, Germany.*
[2]*School of Earth Sciences, Private Bag 79, University of Tasmania, Hobart, Tasmania, 7001, Australia.*

Keywords: EM sounding, electromagnetic techniques, beam resolution

ABSTRACT: Helicopter electromagnetic (HEM) sea ice thickness profiling has become a widespread tool for regional mapping as well as for validation of remote sensing and modelling data. Here we give a detailed description of key quantitative parameters Comprising (1) resolution / precision and (2) accuracy estimates, being governed by technical noise and systematic biases respectively. Furthermore we study (3) the system footprint, providing lateral resolution quantities. For sea water and sea ice conductivies met in polar oceans as well as the Baltic Seas we derive sensitivities for the Alfred Wegener Institute's HEM system and show that for given noise levels, sea ice resolution better than 10 cm can be achieved at system altitudes smaller then 20 m above the ice surface. Accuracy losses due to data processing approximations stay within 10 cm for ice thickness up to 3 m. The modelled shape of the footprint size of 75 m for a bird height of 15 m is discussed and underlined by 3D modelling. The synthetically estimated precision, accuracy and footprint values are finally assessed with a ground truthed field data example where HEM level ice thickness agrees with drilling within 4 % or 2 cm.

1 INTRODUCTION

Frequency domain electromagnetic induction has become widely used to study changes in the sea ice thickness distribution (Haas, 2004). Regional mapping of the sea ice thickness distribution using helicopter electromagnetics (HEM) began in the late 1980s in North America, and was further developed in Canada prior to the latest research in Europe since the mid 1990's. Research on the applicability of helicopter EM for sea ice studies was initiated in 1985 by the U.S. Army Corps of Engineers' Cold Regions Research and Engineering Laboratory (CRREL, Kovacs et al., 1987). During those first attempts, using a conventional four-frequency mineral exploration HEM system, ice thickness profiles were retrieved with reasonable accuracy. The overall results were promising enough to develop sea ice dedicated sensors (Kovacs and Holladay 1990; Kovacs et al., 1995). Similar development took place at the Bedford Institute of Oceanography (BIO) in Canada cooperating with the Canadian Coast Guard (Holladay et al., 1990; Peterson et al., 1999; Prinsenberg et al., 2002). The first European airborne EM sea ice field programme was conducted in the Baltic Sea using the Geological Survey of Finland's (GSF) fixed wing EM system (Multala et al., 1996). The latest European development was initiated in 2000 by the Alfred Wegener Institute for Polar and Marine Research (AWI) in Bremerhaven, Germany. The AWI HEM system is a small scale, purpose built, adaptable, fully digital instrument which has been used on an operational basis during ship and land based expeditions in the Arctic Ocean, in Antarctic waters and the Baltic Sea (Haas et al., 2002; Haas et al., this volume; Pfaffling et al., 2004).

[*] Corresponding author: A. Pfaffling, andreas@pfaffling.net, Ph: +49 179 6733979

Here we discuss the main quantitative characteristics of HEM based ice thickness estimation. Error sources in HEM ice thickness are of random (A) as well as systematic (B) nature:

(A) Electronic noise in the technical parts of the system leads to random errors in ice thickness. Precision or resolution of the method are determined based on noise and sensitivity.

(B) The geophysical structure of sea ice allows to use a number of approximations in the sea ice thickness retrieval algorithm. As with all approximations a small bias is introduced into the ice thickness estimates. This systematic error governs the HEM ice thickness accuracy.

A quantitative discussion on precision and accuracy is given utilizing one-dimensional (1D) model data. However, being an inductive method, HEM integrates over a certain volume of sea ice and sea water and consequently ice thickness estimates represent a weighted average over a finite volume. The shape, size and influence of this HEM footprint are illustrated with 1D and 3D models.

Finally the theoretical estimates on precision, accuracy and footprint are underlined by a field example where HEM ice thickness is compared to ground truth data (thickness drillings).

2 METHODS

The basic principle of HEM sea ice thickness profiling is to estimate the bird-to-water distance from the EM data, while a laser altimeter in the bird determines the system height above the ice or snow surface (figure 1). The difference of these two distances consequently corresponds to the ice (or ice + snow) thickness. Whenever sea ice thickness is mentioned in this paper, it actually refers to the total thickness meaning ice thickness plus snow thickness. A detailed description of the AWI HEM system and ice thickness retrieval is given by Haas et al. (this volume) and Pfaffling et al. (2006).

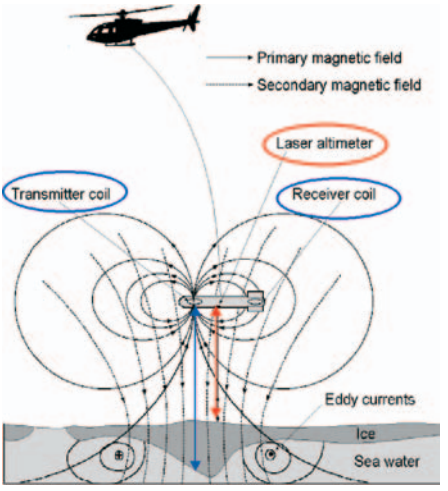

Figure 1. Basic principle of helicopter EM ice thickness profiling. As the induced eddy currents mainly occur in the highly conductive sea water the EM fields correspond to the bird – water distance, while the laser altimeter determines the height above the ice or snow surface (Adapted from Holladay et al., 1990).

Level ice versus pressure ridges

In interpreting electromagnetic data for sea ice thickness, generally two different ice types are considered. The first and more complicated case is deformed ice, so called pressure ridges, where the ice floes are broken up, crushed against each other and finally piled up into distinct topographic features. Attempts to process HEM data dedicated to these 3D features have been performed at the University of California at Berkeley by Liu and Becker (1990), who compiled interpretation charts for common pressure ridge shapes resulting in an elaborate 2D inversion scheme (Liu et al., 1991). However, due to the necessary extensive and advanced computing and only minor improvements in field results, multi dimensional data processing is not yet used on an operational basis. Furthermore the geometry of real world pressure ridges is rarely as presumed by the 2D model involved in inversion. Being composed of a mixture of single, broken blocks of ice and ocean water, pressure ridges are very difficult to describe even by drill hole thickness measurements. Therefore also ground truth data to validate processing algorithms cannot be acquired with the desired accuracy and detail. The underestimation of pressure ridge thickness due to 1D EM processing is discussed by Reid et al (2003).

In contrast to deformed ice, most sea ice is composed of homogeneous level ice, representing a computationally-simpler 1D situation. Level ice thickness mainly depends on the thermodynamic growing conditions while pressure ridges are linked to short-term events like storms. All approximations considered in this study focus on the determination of level ice thickness.

Direct inversion – the transformation from HEM data to ice thickness

A semi empirical processing technique has been developed to directly estimate sea ice thickness from HEM data (Pfaffling et al., 2006). The data transform has been used operationally since 2001, and has been successfully applied to interpretation of HEM data from the Arctic, Antarctic and Baltic. The method relies on three main approximations:

(1) The seawater conductivity is assumed to be known and constant. This assumption is generally satisfied, as within a certain region the conductivity hardly varies within geophysical scales and it is always possible to obtain a water sample to measure the conductivity for that particular region. However, the variation between different geographical regions can be dramatic, being ~2.7 S/m for Arctic or Antarctic seawater, but only 0.3 S/m for the brackish Baltic Sea.

(2) The sea ice conductivity is assumed to be zero. The contrast between water and sea ice is so pronounced (2.7 S/m to < 0.01 S/m) that varying the ice conductivity in 1D forward modelling hardly changes the modelled fields, for ice thickness up to 3 metres.

(3) The ice bottom is considered to be one-dimensional. As long as level sea ice is considered, this is true. It has been shown, that the HEM data transform provides very reliable level ice thickness estimates.

Taking into account the discussed approximations, the analytical model equation for the 1D HEM response simplifies to a series of exponentials allowing us to directly determine the distance between bird and water surface from the measured EM field. The difference to the laser determined bird height over the ice surface is consequently the ice thickness.

Footprint estimation

In a homogeneous half-space, the induced eddy current systems diffuse downward and outward from the transmitter (Tx) with decreasing frequency (e.g., Reid and Macnae, 1998). We therefore define the footprint to be the side length of the cube which contains the induced currents responsible for 90 % of the secondary field picked up by the receiver (Rx). This definition was chosen in order to be consistent with the original two-dimensional footprint defined by Liu and Becker (1990). Reid et al. (2006a) provide a detailed description of the footprint determination and consequences for HEM ice thickness mapping.

3D footprint assessment

In order to further test 1D estimates of the HEM footprint, we have calculated a series of three-dimensional (3-D) EM models using the code MARCO_AIR version 2.6.2 developed by Art Raiche and Zonghou Xiong (e.g. Xiong, 1992). Simulating level ice between two linear pressure ridges enables us to assess the 1D footprint definition by increasing the ridge separation until the response over the level ice meets the layered half-space solution. Details on the 3D footprint description are described in Reid et al. (2006a).

3 RESULTS

By analyzing analytical system resolution and accuracy ruled by geophysical sensitivity as well as assessing synthetic data we study the quantitative potential of HEM sea ice thickness mapping. Two profoundly different data quality measures are described in this section, resolution and accuracy. The former is governed by technical system noise, translated to resolution using sensitivity estimates. Furthermore the bias introduced by the approximations made for the HEM ice thickness retrieval algorithm relate to the method's accuracy. Quantitative information on the footprint size and its meaning is given towards the end of the section

Resolution / precision due to technical noise

The tandem of sensitivity and noise level is used to define two geophysical parameters, resolution and precision. Assuming 5 ppm random technical noise and 50 ppm/m sensitivity leads to 10 cm resolution or precision. The resolution implies that 10 cm is the smallest change in ice thickness which can be discriminated from the noise. Further, precision suggests, that for a given model ice thickness, the retrieved HEM ice thickness may lay within +/- 10 cm from the true model value.

To investigate the theoretically achievable precision in sea ice thickness estimates, sensitivity studies have been conducted for the major sea ice environments. Highly saline Arctic and Southern Ocean water as well as brackish Baltic Sea water was considered (water conductivities of 2.7 S/m and 0.3 S/m respectively). Sensitivity was analytically determined at typical flying heights and consequently 'distance to water' (dtw in Figure 2) for the AWI HEM system. Additionally, sensitivity with respect to first layer thickness for a set of two layer cases (ice layer over ocean half-space) was investigated. Ideally the two layer results coincide with the half-space solution, which is generally the case for the chosen channels (Figure 2).

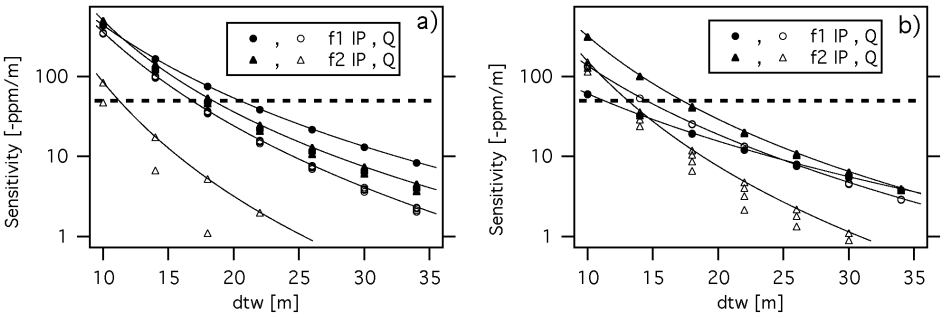

Figure 2. AWI bird sea ice thickness sensitivities for a) Arctic/Antarctic and b) Baltic conditions versus system distance to water (dtw), for both homogeneous half-space models with dtw = bird height (h) (line) and suites of two layer cases for dtw = ice thickness + h (markers). The dashed line is at a potential noise level threshold of –50 ppm/m (10 cm resolution at 5 ppm ambient noise).

Given a desired ice thickness precision of 10 cm and presuming a technical noise level of 5 ppm leads to a sensitivity threshold of 50 ppm/m to meet the required resolution. The dashed line in Figure 2 shows the 50 ppm/m threshold and consequently illustrates the maximum bird heights for the distinct channels.

Sensitivity results underline the significantly different character of the four system channels (two frequencies with in-phase (IP) and quadrature (Q) component). The maximum sensitivity channel is the 3.68 kHz IP for Arctic/Antarctic and 112 kHz IP for Baltic waters respectively, which is governed rather by the higher coil spacing than the lower frequency for the AWI system's geometry (Pfaffling et al., 2006). Consequently the identified maximum sensitivity channel is used for ice thickness estimation depending on whether we are confronted with saline or brackish conditions.

The accuracy of an approximation

The bias in ice thickness due to treating sea ice as electromagnetically transparent can be quantified using the determined sensitivities. Neglecting the sea ice conductivity introduces a residual, which leads to an HEM ice thickness transform accuracy. The resulting accuracy is mainly influenced by the system frequency, combined with a minor effect of flying height. For Baltic and Caspian Seas the influence of the finite ice conductivity is negligible and for the Arctic and Antarctic the accuracy stays better than 10 cm for ice up to 3 m thick using the 3.68 kHz in-phase component (Pfaffling et al., 2006).

Synthetic assessment of the HEM ice thickness transform

To study the discussed effects of accuracy and resolution on the HEM method, synthetic HEM data were ice thickness transformed and are analyzed here. The EM response was modelled for a sinusoidally varying flying height between 10 and 20 m (Figure 3) over a 3 m thick ice layer floating on saline ocean water.

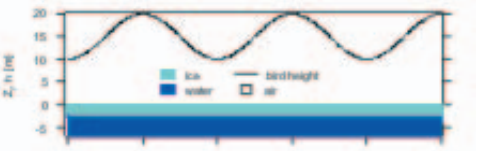

Figure 3. Sketch of model parameters used for synthetic HEM ice thickness assessment. System height varies sinusoidally between 10 and 20 m over a 3 m thick ice layer. A total of 1000 data points is calculated.

Three different cases were studied: In case (I) the ice conductivity was set to zero, simulating the half-space approximation, then (II) conductive ice was included with 50 mS/m and finally (III) Gaussian noise was added to the fields obtained for case (II) with standard deviation 6.4 ppm representing measured field conditions.

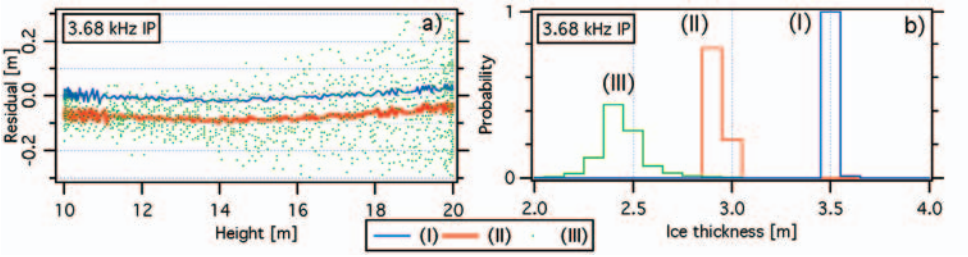

Figure 4. HEM ice thickness results from synthetic data with 3 m model ice thickness for varying bird altitudes. Panel a) shows the residual between HEM thickness results and the model thickness. Each panel includes three different model runs. (I) Electromagnetic transparent ice (0 S/m), (II) conductive ice (50 mS/m) and (III) conductive ice as in (II) with Gaussian noise added. Panel b) shows the ice thickness distribution obtained from f1 IP thickness in panel a). For improved clarity in Panel b), type (III) data is shifted -0.5 m and type (I) data +0.5 m along the ice thickness axis.

For clarity the model ice thickness was subtracted from the ice thickness transform results in Figure 4a, consequently showing the thickness residual. Case (I) reveals the numerical accuracy of the exponential curve fitting, laying in the cm-range. The neglected ice conductivity in (II) introduces a residual decreasing the accuracy, as concluded from the precision and accuracy analysis earlier. Although fairly thick and conductive ice is modelled, the accuracy is better than 10 cm for f1 IP. Finally the highly noisy data - passing the HEM ice thickness transform unfiltered – introduces a large scatter in the resulting ice thickness estimates, increasing with height, due to the decreasing sensitivity.

To get a final, quality approval of synthetic HEM ice thickness, the sea ice thickness distribution or histogram is analyzed. Here we focus on the mode of the distribution, ideally identifying the original 1D level ice thickness used for the forward modelling. For all three described model cases, the histograms peak at the correct thickness within a tolerance of 10 cm. The high noise added in case (III) broadens the distribution but does not bias the mode.

Footprint

Generally the HEM footprint is a function of flying height and sub-surface conductivity. Figure 5 shows the HEM induction pattern on a horizontal slice through a 2.77 S/m ocean water half-space at a depth of 3 m below the surface. The magnetic field contributions of each cell at the Rx are shown as a colour scale image, with yellow-red colours indicating stronger contributions. The lateral extents of the calculated footprints for the in-phase and quadrature components are indicated on Figures 5(a) and (b) by heavy black squares. The more compact pattern of the Q footprint is immediately apparent.

Figure 5 also clearly shows that the maximum induced current density is located in a ring roughly half the size of the conventional footprint definition.

3D modelling results are given in figure 6, alongside a sketch of the model geometry including level ice and two 50 m long pressure ridges in panel 6e. The ridge separation in the

model was increased until the response in the middle met the layered half-space response (horizontal dotted lines). This agreement was met at 75 m and 45 m separation for IP and Q respectively, both times slightly larger than the theoretical footprints. Thus, the 3D modelling supports the calculated half-space footprint sizes for the AWI HEM geometry and especially underlines the difference between IP and Q footprint size.

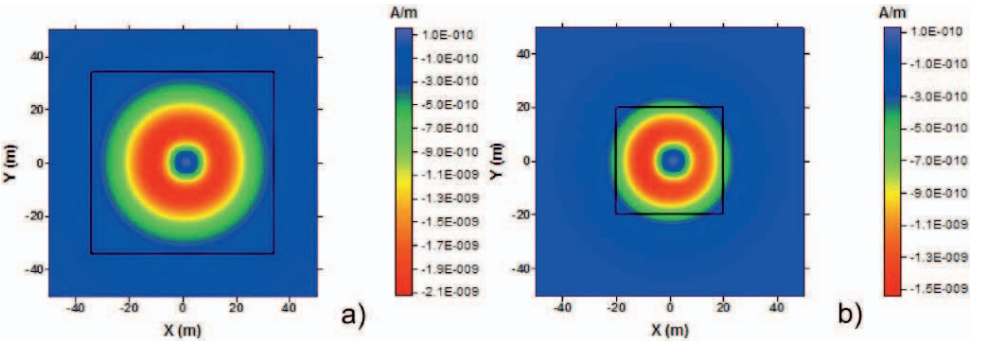

Figure 5. HCP in-phase (a) and quadrature (b) magnetic field contributions from induced currents at a depth of 3 m below the surface of a 2.77 S/m homogeneous half-space for the 3.68 kHz frequency of the AWI HEM system. The bold square on each panel indicates the lateral extent of the AEM footprint calculated as described in the main text.

4 FIELD DATA

In September-October 2003, an Australian-led international experiment dedicated to sea ice remote sensing validation (Massom et al., 2006), took place aboard the icebreaker *RV Aurora Australis* in the east Antarctic marginal sea ice zone. During a three-day long ice station almost one thousand drill hole ice thickness measurements were made on three parallel 500-meter long, 20 m spaced profiles, offering a unique data set for ground truthing of airborne EM data. For optimum validation data, a level ice floe with a prominent pressure ridge was chosen for this experiment. Ice core analyses and DC-soundings (Reid et al., 2006b) showed that the internal sea ice structure was homogeneous, lacking any disturbing features like highly conductive surface or slush layers.

HEM sea ice thickness estimates from raw and filtered (5 point running average) data agree with drilled thickness data particularly along the ~0.5 m thick level ice areas (Figure 7). Being fairly thin and moderately saline, the level ice introduces no residual affecting the accuracy of the HEM sea ice thickness transform. As anticipated, the massive 3D pressure ridge is underestimated in thickness by 50 % using the 1D processing method.

Note the steeper slope of the quadrature thickness in the vicinity of the major pressure ridge at 300 - 400 m due to the smaller footprint of Q compared to IP. However, though smaller than the footprint, the narrow ridge at 80 m is observable in the derived ice thickness. This is solely due to the sail topography, profiled by the laser, rather than the EM induction process.

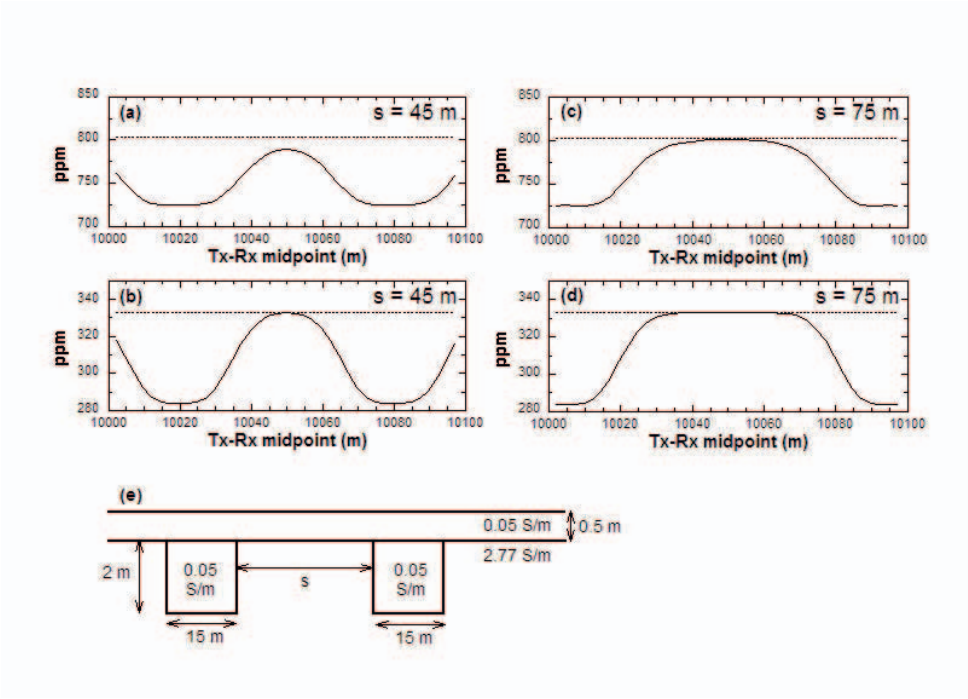

Figure 6. MARCO_AIR 3-D EM model results for a sea ice model containing two identical block targets (pressure ridges) embedded in a two-layered host medium (sea ice over sea water). Responses were computed for the AWI HEM-Bird system at frequency 3680 Hz at flight height 15 m above the surface. The panels (a) and (b) show in-phase and quadrature responses for a target separation of 45 and panels (c) and (d) the corresponding responses for 75 m separation. The horizontal dotted lines show the response of the level ice. The model geometry is shown in (e).

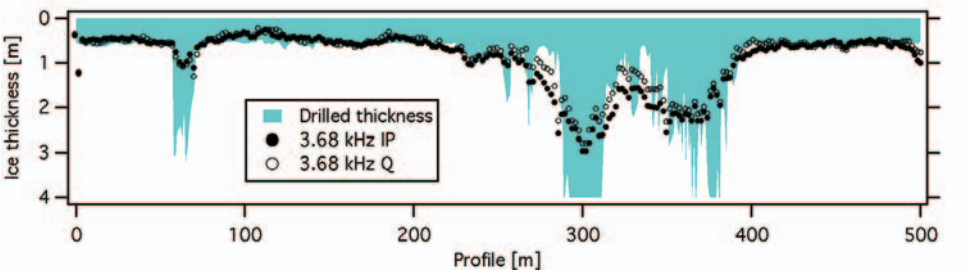

Figure 7. ARISE 2003 field data: Comparison of ice thickness estimates from auger measurements and HEM data. Drill spacing varied between 2 m and 1 m along level ice or pressure ridge sections respectively. The sampling frequency of the AWI bird is 10 Hz corresponding to ~ 3 m point spacing. Two parallel drillhole profiles, 20 m apart to both sides of the plotted line, and aerial photography imply strong lateral in homogeneities in the main ridge structure. The graph does not display the maximum 5.8 m drilled ridge thickness at 305 m.

Finally, comparing ice thickness histograms from drilling data and HEM estimates proves the overall accuracy of HEM ice thickness profiles (Figure 8). Even at 2 cm bin size the modes of the HEM and drilling histograms agree on the same thickness. Filtering the raw HEM data has a smaller effect on field data than on synthetic data, as technical and "glaciological" noise interfere.

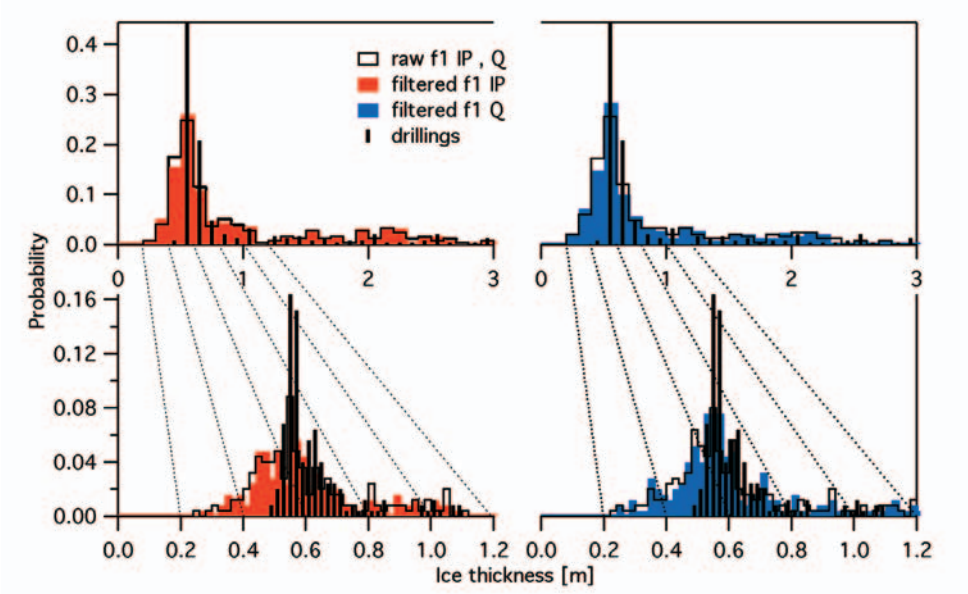

Figure 8. ARISE 2003 field data: Ice thickness distributions of drilling data compared to raw and filtered HEM thickness estimates for 3.68 kHz IP and Q. Histograms in the upper row use 10 cm sized bins, while the lower row provides a close-up with 2 cm bins.

5 DISCUSION AND RECOMMENDATIONS FOR HEM DATA USAGE

Both synthetic model data and field validations show that helicopter electromagnetic profiling is a suitable tool to retrieve high quality level ice thickness estimates. The overall accuracy of HEM derived level sea ice thickness is within 10 cm, governed by technical noise and systematic biases. In contrast to level ice, highly porous, three-dimensional pressure ridges are very challenging to map with electromagnetic methods. The spatial size of ridges is often smaller than the EM-footprint and therefore the maximum keel thickness is underestimated by 50-60 %.

The ice thickness accuracy and precision estimates presented here account solely for systematic biases (processing approximations) and random, technical noise. However, there may be additional effects, distorting the EM field. Potential problems include nonlinear base level drift and dynamic bird movements. The latter is influencing the laser height and induction geometry. Random noise is generally removed by the filter effect when using ice thickness histograms for further cross validation with other measurements. Though on a point-by-point scale, the accuracy of HEM ice thickness estimates may be worse than analysed in this work. This has to be taken into account when comparing HEM thickness profiles with data from other platforms. The suggested way to compare datasets with different

spatial resolution and also footprint sizes is to compile averages over finite regions, significantly larger than the largest footprint size of the platforms to compare. Doing this it has to be considered that the HEM footprint is not an average but rather involves a weighting function according to the induced current pattern. Using the HEM quadrature component rather than the commonly used in-phase, would make the footprint smaller, but difficulties arise due to the less favourable accuracy.

Future research is needed to improve the point-by-point accuracy of HEM ice thickness estimates. Tackling non-linear base level drift is a technical challenge asking for higher thermal stability in the involved bird components. Bird movement problems can be overcome by measuring bird pitch and roll and accounting for them in data handling and processing.

6 ACKNOWLEDGMENTS

Parts of this research have been funded by the EC research project "SITHOS" as well as by Australian Antarctic Science Advisory Committee Grant 2381. We thank the ARISE 2003 shipboard party for conducting almost 1000 drill-hole measurements of sea ice thickness, the officers and crew of the *RV Aurora Australis* for field support and the pilots and technicians of Helicopter Resources Pty Ltd.

7 REFERENCES

Haas, C., H. Edeler, M. Schürmann, J. Lobach, and K.-P. Sengpiel (2002). First operation of AWI HEM-bird for sea-ice thickness sounding, 62. Jahrestagung der Deutschen Geophysikalischen Gesellschaft DGG, Hannover, Germany, Conference Proceedings, 36-38.

Haas, C. (2004). Late-summer sea ice thickness variability in the Arctic Transpolar Drift 1991-2001 derived from ground-based Electromagnetic Sounding. *Geophys. Res. Lett.*, **31**, L09402, doi:10.029/2003GL019394.

Haas, C., S. Goebell, S. Hendricks, T. Martin, A. Pfaffling, and C. von Saldern (2006). Airborne electromagnetic measurements of sea ice thickness: methods and applications, in *European Commission, Arctic Sea Ice Thickness: Past, Present and Future*, ed. P. Wadhams and G. Amanatidis, Climate Change and Natural Hazards Series, Brussels.

Holladay, J.S., J.R. Rossiter and A. Kovacs (1990). Airborne measurements of sea-ice thickness using electromagnetic induction sounding. 9th Conf. of Offshore Mechanics and Arctic Engineering. Houston, USA, Conference Proceedings, 309-315.

Kovacs, A., N.C. Valleau and J.C. Holladay (1987). Airborne electromagnetic sounding of sea-ice thickness and subice bathymetry. *Cold Regions Science and Technology*, **14**, 289–311.

Kovacs, A. and J.S. Holladay (1990). Sea ice thickness measurement using a small airborne electromagnetic sounding system. *Geophysics*, **55**, 1327-1337.

Kovacs, A., J.S. Holladay and C.J.J. Bergeron (1995). The footprint/altitude ratio for helicopter electromagnetic sounding of sea ice thickness: comparison of theoretical and field estimates. *Geophysics*, **60**, 374–380.

Liu, G. and A. Becker (1990). Two-dimensional mapping of sea ice keels with airborne electromagnetics. *Geophysics*, **55**, 239-248.

Liu, G., A. Kovacs and A. Becker (1991). Inversion of airborne electromagnetic survey data for sea-ice keel shape. *Geophysics*, **56**, 1986–1991.

Massom, R., A.P. Worby, V. Lytle, T. Markus, I. Allison, T. Scambos, H. Enomoto, K. Tateyama, T. Haran, J. Comiso, A. Pfaffling, T. Tamura, A. Muto, P. Kanagaratnam, B. Giles, N. Young and G. Hyland (2006). ARISE (Antarctic Remote Ice Sensing Experiment) in the East 2003: Validation of satellite-derived sea-ice data products. *Ann. Glaciol.*, **44**, in press.

Multala, J., H. Hautaniemi, M. Oksama, M. Lepparanta, J. Haapala, A. Herlevi, K. Riska and M. Lensu (1996). An airborne system on a fixed-wing aircraft for sea ice thickness mapping. *Cold Regions Science and Technology*, **24**, 355–373.

Peterson, I.K., S.J. Prinsenberg and S. Holladay (1999). Using a helicopter-borne EM-induction system to validate RADARSAT sea ice signatures. 28th International Conference on Port and Ocean Engineering under Arctic Conditions (POAC), Helsinki, Finland, Conference Proceedings, Vol.1, 275-284.

Pfaffling, A., C. Haas, and J.E. Reid (2004). Empirical processing of HEM data for sea ice thickness mapping. 10th European Meeting of Environmental and Engineering Geophysics, Utrecht, The Netherlands, Expanded abstracts, A037.

Pfaffling, A., C. Haas and J. E. Reid (2006). A direct helicopter EM – sea ice thickness inversion, assessed with synthetic and field data, *Geophysics*, submitted.

Prinsenberg, S.J., S. Holladay and J. Lee (2002). Measuring ice thickness with EISFlowTM, a fixed-mounted helicopter electromagnetic-laser system. 12th International Offshore and Polar Engineering Conference, Kitakyushu, Japan, Conference Proceedings, Vol. 1, 737-740.

Reid, J.E., and J.C. Macnae (1998). Comments on the electromagnetic 'smoke ring' concept. *Geophysics*, **63**, 1908-1913.

Reid, J.E., J. Vrbancich and A.P. Worby (2003). A comparison of shipborne and airborne electromagnetic methods for Antarctic sea ice thickness measurements. 16th ASEG Geophysical Conference and Exhibition, Adelaide, Australia, Extended Abstracts.

Reid, J.E., A. Pfaffling and J. Vrbancich (2006a). Airborne electromagnetic footprints in 1D earths. *Geophysics*, **71**, G63-G72.

Reid, J.E., A. Pfaffling, A.P. Worby and J.R. Bishop (2006b). In-situ measurements of the direct-current conductivity of Antarctic sea ice: implications for airborne electromagnetic sounding of sea ice thickness. *Ann. Glaciol.*, **44**, in press.

Xiong, Z. (1992). Electromagnetic modeling of 3-D structures by the method of system iteration using integral equations. *Geophysics*, **57**, 1556-1561.

The Simulated Seasonal Variability of the Ku-band Radar Altimeter Effective Scattering Surface Depth in Sea Ice

Rasmus T. Tonboe[1]*, Søren Andersen[1], Rashpal S. Gill[1] and
Leif Toudal Pedersen[2]
[1]*Danish Meteorological Institute, Lyngbyvej 100, DK-2100 Copenhagen Ø, Denmark*
[2]*Ørsted, bld. 348, Technical University of Denmark, DK-2800 Kgs. Lyngby, Denmark*

Keywords: Radar altimetry, sea ice, seasonal variation, radiative transfer modelling, effective scattering surface, radar penetration

ABSTRACT: Radiative transfer simulations show that the Ku-band radar altimeter sea ice effective scattering surface depth is sensitive to snow density, thickness and the snow and ice surface roughness. In order to reduce the errors in sea ice freeboard estimation and the derived ice thickness to acceptable levels it will be necessary to have access to these snow and ice parameters. Here a thermodynamic and mass model is used to simulate the seasonal snow cover at 82.5°N, 0.0°E in the Arctic Ocean using the European Centre for Medium-range Weather Forecast (ECMWF) re-analysis meteorological data as input. The simulated seasonal snow profiles are used as input to a backscatter model. The seasonal variability of the effective scattering surface depth is discussed in terms of the simulated snow cover properties.

1 INTRODUCTION

Submarine sonar is widely used to measure sea ice thickness in the Arctic Ocean (Wadhams, 1990; Rothrock et al., 2003). This is the most significant ice thickness dataset today even though the coverage is sporadic and seasonal, inter-annual and spatial variations are poorly resolved (McLaren et al., 1992). Therefore, significant interest is being paid to alternative methods for monitoring sea ice thickness such as laser and radar altimetry (Kwok et al., 2004; Laxon et al., 2003; Wingham, 1999). However, estimating sea ice thickness by measuring its freeboard is disputed for two reasons: 1) the ice floe is not in hydrostatic equilibrium on a point-by-point basis. "*Therefore the relief of the underside of the ice and its thickness cannot be judged by the relief of the upper surface of the ice.*" (Doronin & Kheisin, 1977), and 2) "*... to estimate the ice surface ht and then multiply by ... 10 to obtain thickness h introduces unsatisfactory errors.*" (Rothrock, 1986). Indeed, simple calculations of sea ice buoyancy show that the freeboard, in addition to thickness, is also a function of snow density and thickness and ice density. If these additional snow and ice properties are known, the error due to buoyancy can be reduced and it can be argued that although the floe is not in hydrostatic equilibrium on small scales there is a correlation between freeboard and ice thickness on larger scales. Nevertheless, to further reduce the error to "acceptable" levels (see 2 above) it is also necessary to minimize the freeboard measurement error. This paper addresses the latter by using a radiative transfer backscatter model for identifying sensitivities of the space borne radar altimeter effective scattering surface depth used for snow/ice surface elevation and freeboard measurements.

* E-mail: rtt@dmi.dk, Tel.:+45 39 15 73 49.

Laboratory experiments, for dry snow on smooth sea ice, suggest that the total nadir looking radar backscatter is dominated by ice surface scattering and that snow and ice volume scattering are negligible (Beaven et al., 1995). Our model reproduces these observations. Yet the link between the backscatter mechanisms and the effective scattering surface is not established experimentally. The radiative transfer backscatter model is used to simulate the sea ice radar altimeter effective scattering surface variability as a function of a seasonal snow cover. The model is described in Tonboe et al. (2006) and hereafter called the backscatter model. Snow and ice profiles collected during the GreenICE project are used as input to the backscatter model and output from a mass and thermodynamic sea ice model (Tonboe, 2005) is used to assess the seasonal variability of these parameters in the central Arctic Ocean. This model is hereafter called the thermodynamic model.

Nadir looking radar backscatter

Surface scattering dominates backscatter in sea ice for a space borne Ku-band radar altimeter (Beaven et al., 1995). The nadir looking surface backscatter is a function of the nadir reflection coefficient $|R(0)|$ and the surface roughness (flat-patch area) F (Fetterer et al., 1992), i.e.

$$\sigma_{surf} = 0.9F\left|R(0)\right|^2 \frac{H}{u\tau} \tag{1}$$

where H is the satellite height, u the pulse propagation speed (speed of light in air, snow and ice) and τ the pulse length. A typical value for snow permittivity is about 1.5 and about 3.5 for sea ice (Ulaby et al., 1986). The reflectivity at the air/snow interface and the snow/ice interface is then about 0.1 and 0.2 respectively. Not accounting for extinction, this makes the ice surface backscatter nearly 5 times larger than snow surface backscatter using Eq. 1 (the same roughness for snow and ice). The dry snow permittivity and surface reflection coefficient is primarily a function of snow density. The relative importance of the snow surface backscatter is influenced by snow surface density, snow and ice surface roughness (F), snow extinction (deep snow and large scatterers or liquid water/ brine in the snow), and ice density and salinity. These parameters and processes are described in the backscatter model.

Snow on sea ice energy and mass balance

During precipitation events, the density of new snow is primarily a function of air temperature and wind speed (Jordan et al., 1999), and the snow gradually increases in density after deposition (Sturm & Holmgren, 1998). New snow is usually fine grained but the result of snow metamorphosis is always snow grain growth. The snow grains grow in dry snow as a function of temperature, temperature gradient, density and time (Marbouty, 1980). The short wave radiation snow albedo and extinction coefficient are functions of density and density and grain size respectively. The thermal snow conductivity is a function of density and temperature and these snow parameters are therefore important for the snow and ice energy balance. Both the thermal conductivity and specific heat of snow and ice are functions of temperature and the thermodynamic model therefore uses a finite difference scheme with a 10-minute time step.

2 RESULTS AND DISCUSSION

Simulated return pulse power for two measured snow and ice profiles

During the 2003 GreenICE campaign, two snow and first-year ice microphysical and temperature profiles were measured in Fram Strait near 76.26°N, 23.28°E. The ice thickness in the two profiles was identical (1.5m) while the snow thicknesses are 7 cm and 36 cm respectively. These profiles shown in Table 1 were used as input to the backscatter model and the simulated return pulse power is shown in Fig. 1. Surface roughness was not measured in the field and all layers have been assigned an equal flat-patch area of 1%.

Table 1. Snow and ice parameters used as input to the backscatter model: Temperature, T, Density, Layer thickness, correlation length (a measure of scatterer size) pec salinity S.

Thin snow profile

Layer No.	T [K]	Dens. [kg/m3]	Thick [m]	pec [mm]	S [ppt]	Type
1	254	400	0.04	0.07	0.10	snow
2	257	250	0.03	0.15	0.10	snow
3	259	920	0.05	0.19	7.00	ice
4	264	920	1.45	0.17	7.00	ice

Thick snow profile

Layer No.	T [K]	Dens. [kg/m3]	Thick [m]	pec [mm]	S [ppt]	Type
1	252	300	0.140	0.07	0.00	snow
2	262	920	0.002	0.10	0.00	snow
3	262	500	0.160	0.10	0.00	snow
4	265	300	0.060	0.15	0.00	snow
5	265	920	0.050	0.22	13.60	ice
6	267	920	0.100	0.21	11.30	ice
7	264	920	1.350	0.17	7.00	ice

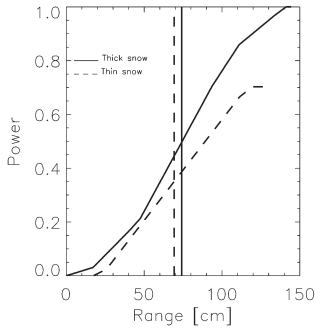

Figure 1. The simulated return pulse power as a function of apparent range. The vertical solid and dashed lines show the effective scattering surface. The thin (7cm) and thick (36cm) snow profiles shown in Tab. 1 are used as input.

The snow freeboards of the thick and the thin snow profile are 34 cm and 17 cm respectively giving the thick snow profile if in equilibrium (snow thickness 36cm) a slightly negative ice freeboard. The brine in the thin snow profile increases attenuation and reduce the total backscatter coefficient by 1.8 dB compared to the thick snow profile with no brine. We simulate the water as a dielectric slab at sea level and compare this simulated range measurement with the effective scattering surfaces of the two snow/ice profiles. The simulated effective scattering surface for the thin snow profile is then 11.4 cm above the water, i.e. just above the ice surface and the thick ice effective scattering surface is 6.6 cm above the water inside the snow. The simulated range measurement is about 5 cm longer for the thick snow profile than the thin snow profile while their respective ice surfaces are 12 cm apart.

Seasonal variability of the effective scattering surface

Figure 2, snow cover vs. time, shows the simulated snow surface density and snow accumulation in a single profile on multiyear ice at 82.5°N; 0.0°E between Fram Strait and the North Pole during the 2000/2001 winter season. ECMWF reanalysis data are input to the thermodynamic model. The simulations begin with a bare ice surface on September 1, which is approximately the end of the melt season. The effective scattering surface is aligned with the ice surface on Sep. 1. Since the surface roughness is not a prognostic variable in the thermodynamic model, the flat-patch area is set to 1% for both the snow and ice. Ice growth is disabled during the simulation, i.e. the ice thickness is a constant 3.5 m. Precipitation events of less than 1 kg/m^2 (<1mm SWE) are not included. The backscatter model is coupled to the thermodynamic model and the seasonal variability of both the effective scattering surface and the penetration depth are shown. The penetration depth increase during winter as a function of decreasing ice temperature and brine volume. During most of the season, except for a period during Jan/Feb 2001, the simulated effective scattering surface follows the snow/ice interface closely. On Jan. 23. snow precipitation (Fig. 3) combined with winds of about 14 m/s deposited a surface snow layer of 290 kg/m^3 on top of the existing 130 kg/m^3 surface layer. The new surface layer gradually compacted to 330 kg/m^3. Later on Feb. 13. light snow fall combined with winds about 5 m/s deposited a new surface snow layer of 190 kg/m^3. These snow surface density variations explain the simulated effective scattering surface depth variations during this period. The effective scattering surface depth is affected by the distribution of backscattering magnitude between the snow and ice surface and the snow depth. The ice surface scattering magnitude is a function snow layer extinction and the parameters in Eq. 1. It seems from the single point simulation in figure 2 that the ½-power time is rather robust to the simulated natural snow cover variations during winter and that the effective scattering surface follows the ice surface closely. At the same time, there are several natural parameters not included in the model, which play a role for the effective scattering surface variability:

1. *The snow and ice surface roughness.* For a case in Tonboe et al. (2006) the simulated effective scattering surface depth varies by 12 cm for varying roughness values. The different snow and ice roughnesses used represent extremes of this variation.

2. *Saline snow. Saline snow on sea ice is common in the Antarctic.* Though it is much less abundant in the Arctic even small amounts of brine can change the snow extinction significantly. An example is given in figure 1.

None of these important parameters are mapped systematically and it is therefore difficult to assess their spatial and temporal variability in the Arctic. The next section discusses future possibilities for snow and sea ice cover mapping by satellite.

Need for hemispheric snow and ice mapping

Sea ice freeboard is a function of snow/ ice thickness and density. The effective scattering surface depth (dry snow) is primarily a function of snow surface density, snow depth and snow/ice surface roughness. These parameters are needed when estimating the radar altimeter effective scattering surface depth and further using the sea ice freeboard as a proxy for ice thickness. Sensitivity studies with quantification of the error is given in Tonboe et al. (2006).

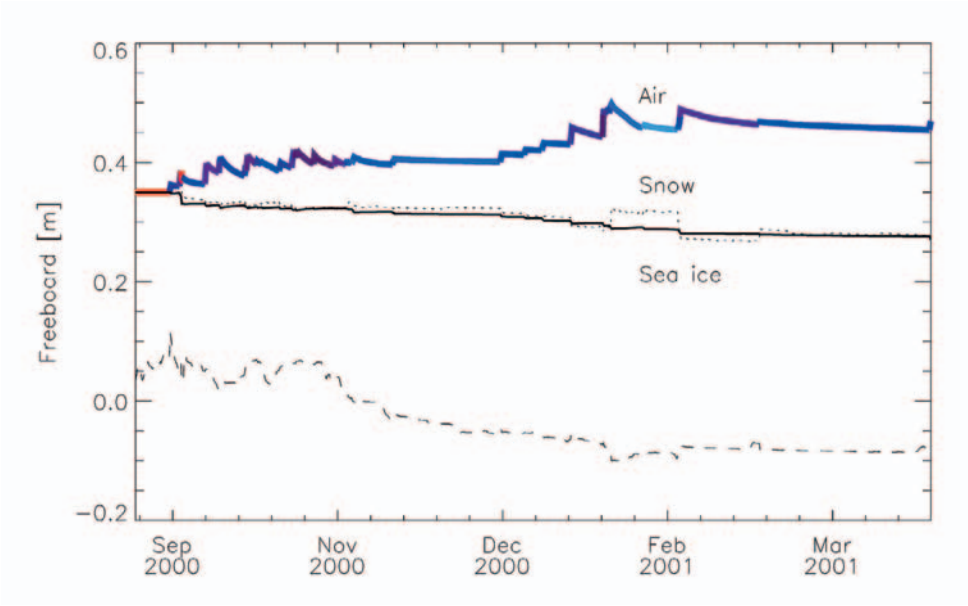

Figure 2. The simulated accumulation of snow in a single profile at 82.5°N 0.0°E during winter 2000/2001. The dashed line show the penetration depth at Ku-band and the dotted line show the depth of the effective scattering surface. The full line is the snow/ice interface. The colours of the snow surface line indicate the snow surface density. 

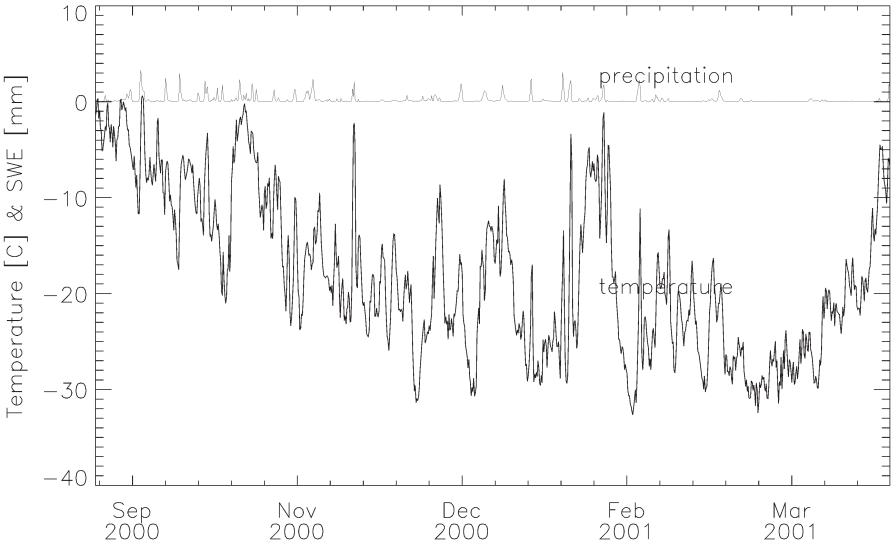

Figure 3. The ECMWF reanalysis air temperature and precipitation, (snow water equivalent, SWE), at 82.5°N 0.0°E, 2000/2001. These and other meteorological parameters are input to the thermodynamic model.

Field campaigns and drifting stations have measured the sea ice snow cover during the last 50 years in the Arctic Ocean. These measurements are continued today during selected periods and locations e.g. the GreenICE project field activities 2003-2005. The measurements can be used to build a snow climatology (Warren et al., 1999). However using climatology to correct freeboard measurements makes it difficult to distinguish snow and ice thickness anomalies when interpreting satellite altimeter data. Algorithms for hemispheric mapping of snow on sea ice are therefore urgent and the possibilities for using satellite remote sensing for mapping snow depth and density as well as snow/ice surface roughness is discussed below.

Passive microwave radiometer data contain information on dry snow volume on land. High correlations are found locally between snow water equivalent (SWE) and microwave brightness temperature signatures (Mätzler et al., 2006). Markus & Cavalieri (1998) further derived an empirical relationship between snow cover depth on Antarctic sea ice and the spectral gradient between 19 and 37 GHz in spaceborne SSM/I radiometer data. However, a universal SWE algorithm for snow on ice does not exist because the brightness temperature signature is also affected by layering, crusts and volume scattering (Mätzler et al., 2006). Pulliainen et al. (1999) demonstrated how physical models including several snow parameters might be inverted to derive single snow parameters (SWE) using spaceborne radiometer data. This approach seems promising also for future sea ice snow cover mapping. Surface roughness mapping using satellite data is even less established than snow cover mapping, but it is clear that the surface roughness play a significant role for C-band (e.g. Radarsat; Envisat ASAR; METOP ASCAT) and perhaps L-band (e.g. ALOS-PALSAR) SAR and scatterometer signatures (Onstott, 1992). Density of sea ice is related to the porosity and salinity (Doronin & Kheisin, 1977) and Ku-band and X-band backscatter is particularly sensitive to these ice parameters (Onstott, 1992). The QuikScat SeaWinds Ku-band scatterometer has now been operational since 1999 and proposed and near future satellite SAR missions will operate at these frequencies e.g. CoReH2O; TerraSAR. A significant effort is needed to bring these snow and ice cover mapping algorithms up to operational standard. Until these measures are taken the radar altimeter freeboard estimation errors remain high.

3 ACKNOWLEDGEMENTS

This work was supported by the European Commisions 5th framework programme; GreenICE (EVK2-2001-00280). Christian Haas of AWI measured and provided snow and ice profiles.

4 REFERENCES

Beaven, S.G., G.L. Lockhart, S.P. Gogineni, A.R. Hosseinmostafa, K. Jezek, A.J. Gow, D.K. Perovich, A.K. Fung, and S. Tjuatja (1995). Laboratory measurements of radar backscatter from bare and snow-covered saline ice sheets. *Int. J. Remote Sensing*, **16**(5), 851-876, 1995.

Doronin, Y.P. and D.E. Kheisin (1977). *Sea ice*. Amerind Publ. Co. Pvt. Ltd., New Delhi.

Fetterer, F.M., M.R. Drinkwater, K.C. Jezek, S.W.C. Laxon, R.G. Onstott, and L.M.H. Ulander (1992). Sea ice altimetry. In: F.D. Carsey (ed.), *Microwave Remote Sensing of Sea Ice*, Geophysical Monograph 68 (pp. 111-135). Washington DC: American Geophysical Union.

Jordan, R., E. Andreas, and A. Makshtas (1999). Heat budget of snow covered sea ice at North Pole 4. *J. Geophys. Res.*, **104**(C4), 7785-7806.

Kwok, R., H.J. Zwally, & D. Yi (2004). ICESat observations of Arctic sea ice: A first look. *Geophys. Res. Lett.*, **31**, L16401, doi:10.1029/2004GL020309.

Laxon, S., N. Peacock and D. Smith (2003). High interannual variability of sea ice thickness in the Arctic region. *Nature*, **425**, 947-949.

Marbouty, D. (1980). An experimental study of temperature gradient metamorphism. *J. Glaciol.*, **26**(94), 303-312.

Markus, T. and D.J. Cavalieri (1998). Snow depth distribution over sea ice in the southern ocean from satellite passive microwave data. *Antarctic Sea Ice*, Antarctic Research Series, **74**, 19-39.

Mätzler, C., P.W. Rosenkranz, A. Battaglia and J.P. Wigneron (eds.) (2006). *Thermal Microwave Radiation - Applications for Remote Sensing*, IEE Electromagnetic Waves Series, London, UK.

McLaren, A.S., J.E. Walsh, R.H. Bourke, R.L. Weaver, and W. Wittmann (1992). Variability in the sea-ice thickness over the North Pole from 1977 to 1990. *Nature*, **358**, 224-226.

Onstott, R.G. (1992). SAR and scatterometer signatures of sea ice. In: F.D. Carsey, (ed.) *Microwave remote sensing of sea ice*, Geophysical monograph 68 (pp. 73-104). Washington DC: American Geophysical Union.

Pulliainen, J., J. Grandell and M. Hallikainen (1999). HUT snow emission model and its applicability to snow water equivalent retrieval. *IEEE Trans. Geosci. and Remote Sensing*, **37**, 1378-1390.

Rothrock, D.A., J. Zhang and Y. Yu (2003). The arctic ice thickness anomaly of the 1990s: A consistent view from observations and models. *J. Geophys. Res.,* **108**(C3), 3083, doi: 10.1029/2001JC001208.

Sturm, M. and J. Holmgren (1998). Difference in compaction behaviour of three climate classes of snow. Ann. Glaciol., **26**, 125-130.

Tonboe, R. (2005). *A mass and thermodynamic model for sea ice*. Danish Meteorological Institute Scientific Report 05-10.

Tonboe, R., S. Andersen, and L. Toudal Pedersen (2006). Simulation of the Ku-band radar altimeter sea ice effective scattering surface. *IEEE Geoscience and Remote Sensing Letters*, **3**(2), 237-240.

Ulaby, F.T., R.K. Moore and A.K. Fung (1986). *Microwave Remote Sensing, from Theory to Applications*, vol. 3. Dedham MA: Artech House.

Wadhams, P. (1990). Evidence for thinning of the Arctic ice cover north of Greenland. *Nature*, **345**, 795-797, 1990.

Warren, S.G., I.G. Rigor, N. Untersteiner, V.F. Radionov, N.N. Bryazgin, Y.I. Aleksandrov and R. Colony (1999). Snow Depth on Arctic Sea Ice. *Journal of Climate*, **12**, 1814-1829.

Wingham, D. (1999). The first of the European Space Agency's opportunity missions: CryoSat. *Earth Observation Quarterly*, **63**, 21-24.

SAR Motion Products: Tools for Monitoring Changes in Sea Ice Mass Balance and Thickness Distribution

Cathleen A. Geiger[1,3], Mani V. Thomas[2], and Chandra Kambhamettu[2]
[1]*Snow and Ice Branch, Cold Regions Research and Engineering Laboratory, Hanover, NH, USA*
[2]*VIMS Lab, Computer and Information Science, University of Delaware, Newark, DE, USA*
[3]*Center for Climatic Research, University of Delaware, Newark, DE, USA*

Keywords: high-resolution SAR products, discontinuous material, thickness variability, mass balance, Arctic observing network

ABSTRACT: Sea ice is a discontinuous non-rigid material when viewed from microwave SAR imagery at scales of tens of kilometres. The discontinuous motion and behaviour of sea ice has a definitive impact on its thickness distribution. Techniques for resolving sea ice discontinuities are demonstrated as contributions toward an integrated Arctic Observing Network.

1 INTRODUCTION

The sea ice community has basic knowledge of how the ice thickness distribution varies regionally and seasonally throughout the Arctic. The fraction of ridged ice varies between 10-30% in the Laptev Sea (mean end-of-winter thickness ranges between 2 to 3 m) [Haas and Eicken, 2001] and 40-80% in the convergent region north of the Canadian Archipelago [Melling et al., submitted] (mean end-of-winter ice thickness is 6-8 m). We also know that ice thickness has large decadal and interannual variability. For example, there is a decadal trend in multi-year ice thickness in the Beaufort Sea, with a decrease in thickness of 1.3 m between the 1960/70s and 1990s [Rothrock et al., 1999]. This has been related to changes in ice circulation regimes in observational [Rigor et al., 2002] and modelling [Lindsay and Zhang, 2005] studies. There is pronounced interannual variability, O($1x10^6$ km^3), in Fram Strait ice export [Kwok et al., 2004]. Melling et al. [2005] found the interannual variability of ice thickness in the Beaufort Sea to be up to 2.7 m. One cause of this variability is dynamic in nature, with changes in ice circulation resulting in (1) changes to the age of ice exiting the Arctic or entering a local region and (2) changes to the sea ice deformation rate.

Global Climate Model (GCM) projections of future ice extent show ice receding, and loss of the perennial ice zone, though models disagree on the rate of recession [ACIA, 2005]. Models used in the ACIA study all have very different constitutive models, thermodynamic models, and atmospheric dynamics. The sensitivity of ice thickness to thermodynamic parameterizations, dynamic parameterizations, and ocean/wind forcing variability is comparable (e.g., Steele and Flato [1999]; Kreyscher et al. [2000]). Thus, it is not possible to isolate the cause of the differences using only models. One way to improve these models is to identify the magnitude and direction of feedbacks on the ice mass balance, and build accurate parameterizations of ocean-ice-atmosphere coupling.

We do not know whether dynamic effects result in negative or positive feedback to sea ice mass decrease in a warming climate. For example, in a weakening ice pack, we could expect convergence to increase as resistance to closure decreases. Hence the ice ridging rate

could increase (a negative feedback). On the other hand, large scale changes in ice drift and increased surface wave activity, from an increase in fetch length, might result in less compression against the coast and multi-year ice zone, hence reducing the ridging height yet increasing the areal coverage and potentially total new ice growth; a positive feedback mechanism. To determine the sign and magnitude of this feedback we must improve our understanding of how new ice grows and how ridging and rafting will respond to such things as: (a) increasing storminess in the Arctic; (b) a seasonal ice pack of reduced thickness; and (c) large scale changes in drift modifying ice stress.

As we do not know whether current models adequately represent leads, we are uncertain of their ability to correctly represent observed sea ice strain rate and its impact on ice growth and redistribution. Models show that increasing deformation rates and variability result in increased total ice mass [Heil and Hibler, 2002; Kwok et al., 2003]. Yet, we lack quantitative validation of model estimates and the effect of deformation on ice mass. This is in part because the in situ data required for such validation are sparse and incomplete. As sea ice thickness is highly sensitive to modification of rheological and surface stress parameterizations, typically showing 10-20% sensitivity [Kreysher et al., 2000; Hutchings, 2001], it is very important to simulate the stress-strain rate relationships adequately.

In short, there is a need to improve our understanding of the interplay between ice dynamics and mass balance including necessary input for the design of an optimal set of observation methods for long-term monitoring of sea ice mass balance. This need addresses high priority research topics listed in recent program documents, including SIMBA [Hutchings and Bitz, 2005], SEARCH [SEARCH 2005], DAMOCLES (Gascard, pers. comm.), IPY [Perovich et al., 2005] and ACIA [ACIA, 2005]. To achieve the goals listed in these documents, a comprehensive set of sea ice measurements needs to be taken to develop and validate models of both thermodynamic and dynamic processes for sea ice, across all the scales over which dynamic and thermodynamic processes vary.

The SAR techniques described in this paper are important contributions to an optimal measurement network for Arctic-wide monitoring. Specifically we focus on integrating SAR products at the kilometre to regional scales for sea ice mass balance monitoring. This is the range where teams of scientists engage in localized coordinated programs involving models, remote sensing, and in situ measurements. It is important to understand the needs at this level, because these regional programmes are essential and fundamental nodes of a large Arctic-wide monitoring network.

2 BASICS OF TECHNIQUE

The basic technique of sea ice motion rendering using SAR imagery stems from a method known as region based motion estimation (or correlation method), which is derived from a fundamental principle called optic flow. This process tries to find the closest match in local image intensity between two time-lagged images. This has been an active area of research in the computer vision community [e.g., Barron, 1994 and references therein] with sea ice motion products basically developed from these principles with some modification [e.g., Fily and Rothrock, 1987; Kwok et al., 1990; Li et al., 1998; Liu and Cavalieri, 1998]. Unfortunately, this type of motion estimation is plagued by a problem known as the "generalized aperture problem", which represents the uncertainty principle in image analysis and additionally defines an upper bound on the possible accuracy in motion estimates [Kruger, 1996]. The main difficulty arises in determining the size of an analysis window.

Smaller analysis windows lead to high resolution estimates of the underlying motion, but the estimates may be biased due to insufficient gradient variation within the window. On the other hand, larger analysis windows come with the possibility to linearize the complex variations in the underlying motion field [Kruger, 1996]. In an effort to strike a balance between the computational complexity of large analysis windows and the optimality of small analysis windows, most algorithms proposed in the literature handle the aperture problem using multiple image resolutions of a single image [Anandan 1989; Thomas, 2000] or applying scaling techniques to the full resolution image such as the wavelet method by Liu and Cavalieri [1998].

A suite of tools already exist to explore several aspects of sea ice including 8 motion products (ice displacement, vorticity, divergence, shear, ice age, thickness and backscatter histograms, and melt onset) from a Lagrangian perspective at a 10 km by 10 km grid and from an Eulerian perspective (all but melt onset) at a 12.5 km by 12.5 km grid [Kwok et al., 1995; Kwok et al., 1999; Kwok and Cunningham, 2002; http://www-radar.jpl.nasa.gov/rgps/products.html]. There are also 5 km motion products during the SHEBA period (1997-1998) and 22 km products from the CASES 2003-2004 experiments. In all these cases, the correlation method assumes a sea ice continuum which imposes a threshold on the motion product resolution (~5 km).

The technique here is essentially another variant of the many methods that already exist, with a few added features. First, we make use of a SAR image as a complex microwave backscatter signal (i.e., there is both a magnitude/intensity and phase/direction to the backscatter signal). The Fourier transform of the SAR image's intensity renders both a magnitude and phase component of the intensity in the frequency domain. We refer to the correlation of the "whitened" frequency domain phase component of an image's intensity as image intensity phase correlation (IIPC), to distinguish it from the correlation of the phase of the complex signal received in a SAR satellite image [Thomas et al., 2004; 2005; Geiger et al., 2005]. This method is illumination invariant since the whitening filters perform the required signal normalization. The phase of the intensity is practical for this application because it is a powerful tool for isolating the boundaries of features. However, unlike normalized cross correlation, IIPC can be efficiently computed in Fourier space [Vernon, 2001; Foroosh, 2002 and references therein]. This provides the opportunity to utilize high-speed FFT methods to solve the motion in a computationally efficient manner. We handle the motion estimation process at multiple resolutions [Anandan, 1989] with the estimated information being percolated from coarse-to-fine resolutions based on a filtering of the image from its original resolution to more smoothed renditions.

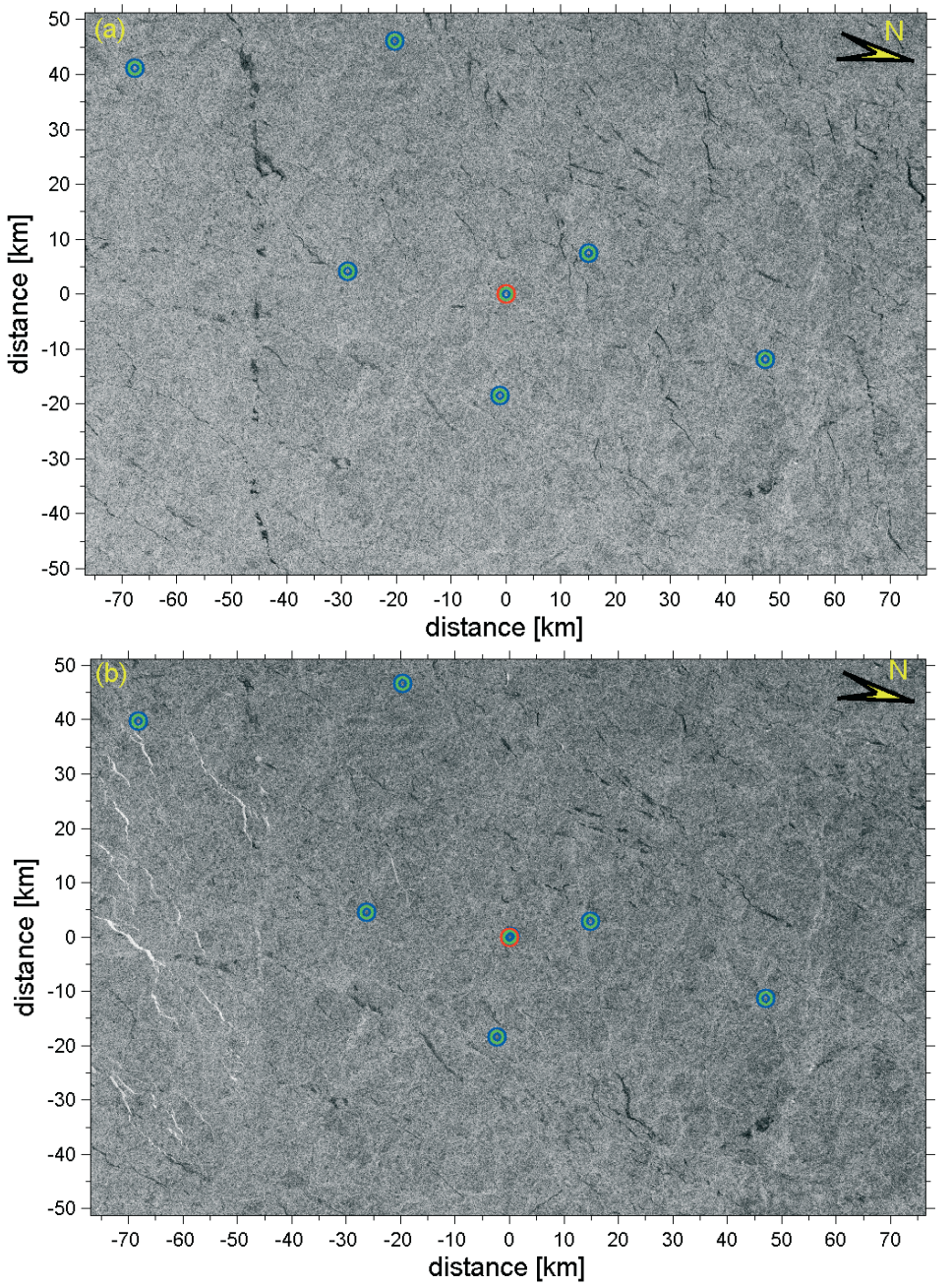

Figure 1. RADARSAT SAR images coincident with SHEBA buoys on multiyear sea ice floes. Shown are segments of RADARSAT SAR images (a) R110435256P3S013 and R110492261P3S013 on day 306 and (b) R110435256P3S013 and R110492261P3S013 on day 310 over the SHEBA research area in 1997. Coincident buoys (blue circles) and the drifting ship (red circle) are equipped with GPS units recording hourly position. Dark stripes are open water leads while bright white stripes are refrozen leads with very thin new ice.

As with all previous methods, we found that this processing method works well in regions where continuous motion exists. However, one sees clearly from SAR imagery that sea ice is not a continuous material, so we need to refine our method to resolve regions of discontinuity [Vernon, 2001]. This fact arises from the Affine Fourier Theorem [Bracewell, 1993] where the linear motion approximation is considered correct only under the assumption that the magnitude of distortion is much smaller than the translational motion. We turn this constraint from a problem to a solution by identifying the poor results (i.e., low values of correlation) as potential regions of discontinuities. We represent such results using a grey-scale map of the correlation coefficient. Visual inspection of such a correlation map reveals long linear features with distinctly different motion patterns on either side of the features. Making additional use of the velocity gradient observed across these regions, we are able to further refine and identify the discontinuities using a masking scheme to define regions of continuous versus discontinuous flow. In this way we are able to map a discontinuous material by defining boundaries of discontinuities, and then computing the velocity in the continuous regions where the Affine Fourier Theorem is valid. This technique is essential in our efforts to understand the behavior of sea ice as a discontinuous non-rigid material. A detailed description of this process from a geophysical perspective is described in Geiger et al., [2006].

3 RESULTS

As an example, Figure 1 shows SAR imagery segments in the vicinity of the SHEBA buoy array during the 1998 field season in the Beaufort Sea [Richter-Menge et al., 2002]. In particular, we direct the reader to the presence of short and long dark narrow features which divide the ice into fragments or aggregates. Some of these delineations behave as slip lines along which aggregates plates of sea ice move. This is the basic composition of sea ice as a discontinuous material which we are trying to understand further.

Figure 2 is an estimate of the motion of this region when resolved to the continuum resolution of 4.8 km. There is good agreement between the velocity derived from the buoy displacement and that of the SAR image as independent calculations of the motion (Figure 2). This is the typical product developed from SAR image processing methods and it provides a wealth of information about the large-scale motion of the region. However, there is more information to be gained from these images if one looks beyond the constraint of a continuum approximation.

The remote sensing products shown in Figure 3 incorporate a series of SAR ice motion analysis tools developed by Thomas, Geiger, and Kambhamettu [2004, 2005]. These new computational methods resolve the discontinuous non-rigid motion of sea ice [Geiger and Drinkwater, 2001; 2005; Thomas et al., 2004; 2005; Geiger et al., 2006]. This work is motivated by a need to provide SAR motion products as input and validation for lead-resolving sea ice models and to advance the understanding of fundamental sea ice processes and interactions. In particular, we are interested in the capabilities of this system to (1) aid in the deployment strategy of buoy arrays, (2) compute the mechanical thickness redistribution along 10 km and 100 km 1D strain rate transects coincident with GPS buoys and thickness measurements, and (3) provide high spatial resolution global and relative motion, and strain rate fields of divergence and shear over a regional research area (hundreds of kilometres). The approach distinguishes itself from existing efforts by assuming a priori that the image is from a discontinuous non-rigid material. By marking the discontinuities, a very high resolution product (as small as 400 m resolution) can be produced (Figure 3). This capability

encourages us to make more detailed investigations between high temporal resolution ice drifting buoys and high spatial resolution all-weather SAR-based motion products with the hope of developing an effective synthesis from a combination of these two data sets.

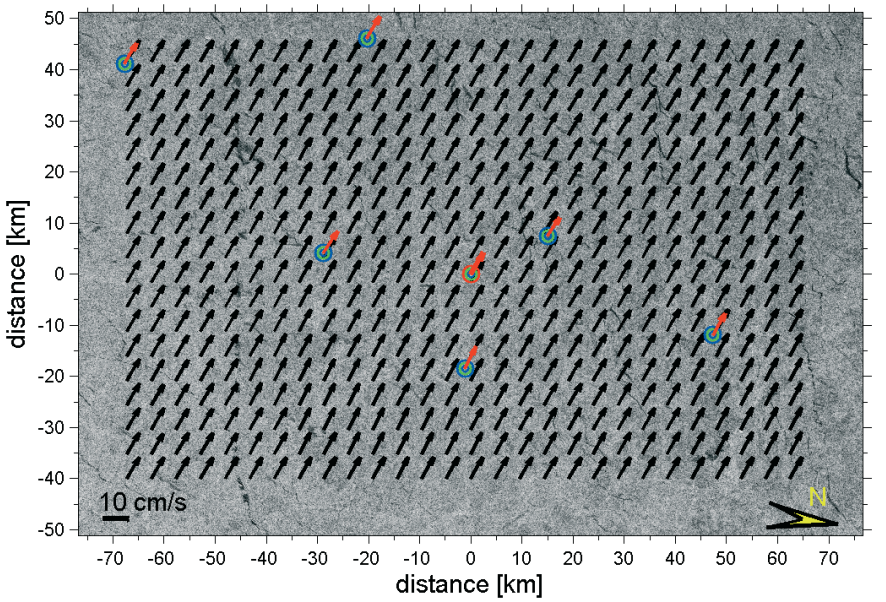

Figure 2. Standard motion products. The SAR scenes and buoy positions from Figure 1 are used to compute velocity vectors to a resolution of 4.8 km which is close to the smallest reasonable continuum scale. Buoy motion vectors (red) are computed from the buoy positions at times corresponding to the SAR scenes for independent comparison of motion products.

4 CORRELATIONS WITH OTHER TECHNIQUES

Figure 5 in Thomas et al. [2004] shows the scatter map from 12 ERS-1 image pairs from the Weddell Sea (a particularly difficult region to track sea ice motion). When compared with the 2650 motion vectors rendered from those images by Drinkwater [1998a, b], 72.8% of the estimated motion vectors were within a 400 m displacement difference. We choose this threshold because of the SAR geolocation uncertainty of 323 m described by Holt et al. [1992]. We can account for 93.5% of all the data points when we identify remaining flagged points in discontinuous regions (which do not compare to within 400 m using continuum-based methods because of the discontinuities). The remaining 6.5% of data are displacement results greater than 400 m which we cannot account for using a correlation map and velocity gradient demarcation scheme. These points correspond to regions where the gradient of the velocity is high but the correlation is not low (infinitesimal discontinuities relative to image resolution) which, in principle, requires a higher-order motion model to localize the position of a potential discontinuity. Hence, initial comparisons with other SAR motion products yield encouraging results and accuracies to within the measuring capabilities of the SAR instrument itself. However, for an independent measurement, we require a comparison against in situ measurements of sufficiently high density to test the location and motion of sea ice discontinuity features. We currently seek such opportunities to test our methodology further.

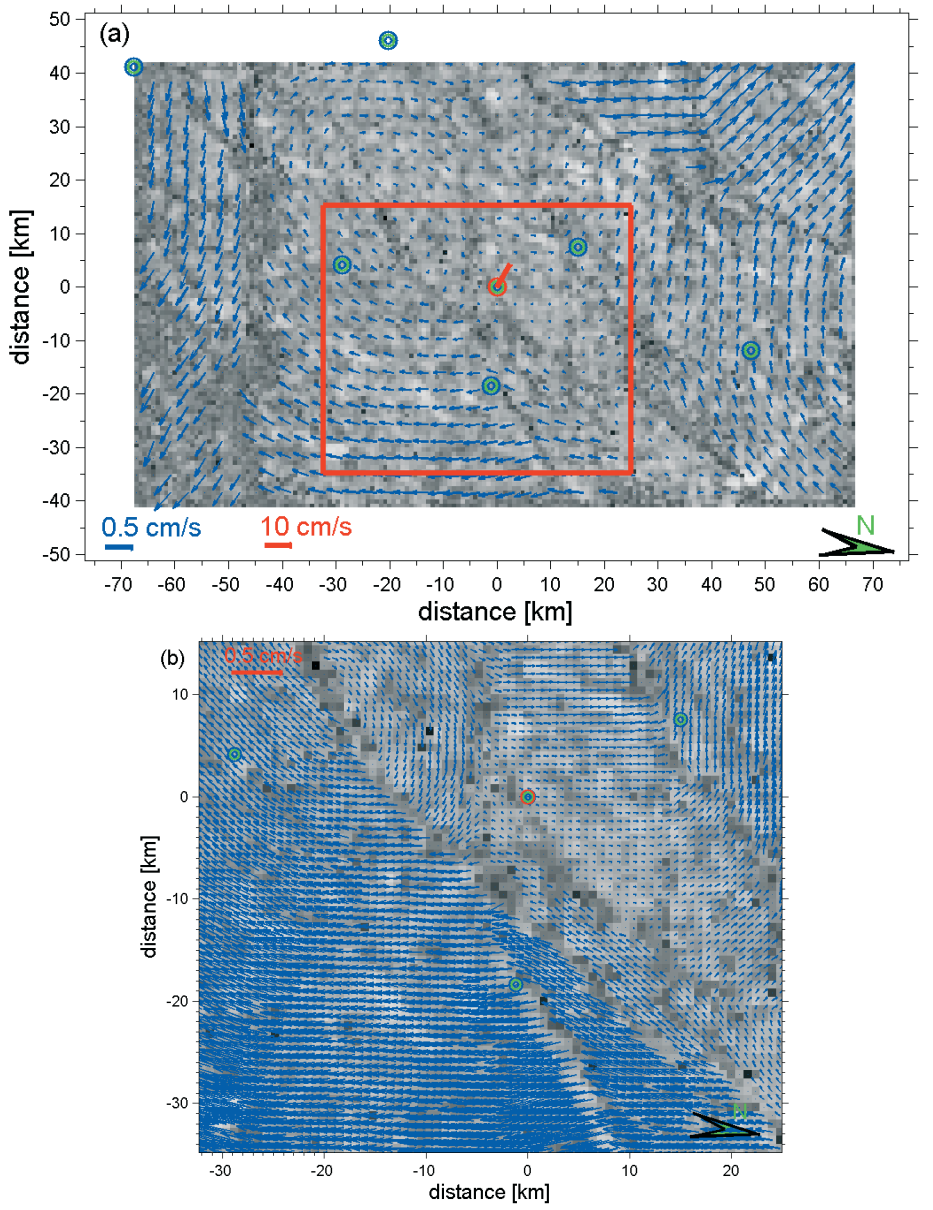

Figure 3 (Opposite). Sea ice mesoscale structure. Global motion is shown for the ship (red vector) with relative motion shown at all other points (blue vectors). This representation displays both global and local motion and illustrates the discontinuous behavior of sea ice as a material (low correlation, as likely discontinuities, are notated by the darker shaded boxes). Detailed flow structure within individual continuous regimes as seen in (b) referenced from the red box in (a). Every 4th vector shown in (a) while every vector (400m resolution) shown in (b). Despite their close distances, the buoys are located within different aggregates separated by shear zones, leads, and ridges. There is a clockwise (anticyclonic) eddy-scale circulation resolved in a fractured form in the upper left. Ice-ice interactions due to aggregate plate dynamics modify the ice circulation pattern away from a smoothly varying continuum.

5 RECOMMENDATIONS AND CONCLUSIONS

The method identified in this paper requires further validation using independent sources especially in the confirmation of discontinuity location and local-motion accuracy. We currently seek means to test this method, especially opportunities to compare such results with high-density buoy deployment programs. We also seek to understand and validate this method in the context of sea-ice thickness distribution, so as to combine a buoy-SAR program with sea-ice thickness observations to validate the location of leads and ridges found in the method presented here. Such testing also provides an incredible opportunity to combine all three recently evolved technologies (GPS buoys, new SAR processing techniques, and new ice thickness instrumentation) to explore the behavior of sea ice at the regional scale in a way that has never been possible before.

6 ACKNOWLEDGEMENTS

Support for this paper was made possible through NASA grant NNH05AB76I. The authors also wish to thank and acknowledge the ALASKA SAR facility in Fairbanks for the downloading and processing of the RADARSAT images used in this study. The authors also wish to thank and acknowledge the many scientists who participated in, collected, and archived the buoy data during the SHEBA program in 1998.

7 REFERENCES

Arctic Climate Impact Assesment (ACIA) (2005). Impacts of a warming climate: Arctic climate impact assessment, S.J. Hassol, University of Cambridge Press, 139pp.

Anandan, P. (1989). A computational framework and an algorithm for the measurement of visual motion, *International Journal of Computer Vision*, **2**(3), 283-310.

Barron, J., D. Fleet, and S. Beauchemin (1994). Performance of optical flow techniques, *International Journal of Computer Vision*, **12**(1), pp 43-77.

Bracewell, R.N., K.-Y. Chang, A.K. Jha, and Y.-H. Wang (1993) Affine Theorem for two-dimensional Fourier Transform, *Electronics Letters*, **29**(3), 304.

Drinkwater, M.R. (1998a). Active microwave remote sensing observations of Weddell sea ice, in *Antarctic Sea Ice: Physical Processes, Interactions and Variability*, Antarct. Res. Ser. 74, edited by M. O. Jeffries, pp.187-212, AGU, Washington, D.C.

Drinkwater, M.R. (1998b). Satellite microwave radar observations of Antarctic sea ice, Chapter 8 in *Analysis of SAR Data of the Polar Oceans*, edited by C. Tsatsoulis and R. Kwok, pp. 145-187, Springer-Verlag, New York.

Fily, M. and D.A. Rothrock (1987). Sea-ice tracking by nested correlations, *IEEE Trans. Geosci. Remote Sens.*, GE-25(5):570-580.

Foroosh, H., J.B. Zerubia, and M. Berthod (2002). Extension of phase correlation to sub pixel registration, *IP*, **11**(3), 188-200.

Geiger, C.A., and M.A. Drinkwater (2001). Impact of temporal-spatio resolution on sea ice drift and deformation. *IUTAM Symposium on Scaling Laws in Ice Mechanics and Ice Dynamics*, J.P. Dempsey & H.H. Shen (eds), Kluwer Academic Publishers, 407-416.

Geiger, C.A., and M.A. Drinkwater (2005). Coincident buoy- and SAR- derived surface fluxes in the western Weddell Sea during Ice Station Weddell 1992. *J. Geophys. Res.*, **110**, C04002, doi:10.1029/2003JC002112.

Geiger, C.A., M.V. Thomas, and C. Kambhamettu (2006). Identification of continuous and discontinuous sea ice motion. *J. Geophys. Res.*, submitted

Holt, B., D.A. Rothrock, and R. Kwok (1992) Determination of sea ice motion from satellite images, Chapter 18 in *Microwave Remote Sensing of Sea Ice*, Geophysical Monograph 68, ed. F. Carsey, pp. 343-354, AGU, Washington, D.C.

Haas, C., and H. Eicken, 2001: Interannual variability of summer sea ice thickness in the Siberian and central Arctic under different atmospheric circulation regimes. J. Geophys. Res., 106(C3), 4449-4462.

Heil, P and WD Hibler, III (2002). Modelling the high-frequency component of Arctic sea-ice drift and deformation. *J. Phys. Oc.*, **32**(11), 3039-3057.

Hutchings, J.K. (2001). On modelling the mass of Arctic sea ice. Ph.D. Thesis, University of London., 153pp.

Hutchings, J.K., and C. Bitz, (2005). Sea ice mass budget of the Arctic (SIMBA) Workshop: Bridging regional to global scales. University of Alaska Fairbanks, August 2005. 80pp.

Kreyscher, M., M. Harder, P. Lemke, and G. Flato (2000). Results of the sea ice model intercomparison project: Evaluation of sea ice rheology schemes for use in climate simulations, *J. Geophys. Res.*,**105**(C5): 11299-11320.

Kruger, S.A., and A.D. Calway (1996). A Multi-resolution frequency domain method for estimating Affine Motion parameters, in *International Conference on Image Processing*, pp. 113-116.

Kwok, R., J.C. Curlander, R. McConnell, and S. Pang (1990). An ice motion tracking system at the Alaska SAR facility, *IEEE J. Oceanic Eng*., **15**(1):44-54.

Kwok, R., D.A. Rothrock, H.L. Stern and G.F. Cunningham (1995). Determination of Ice Age using Lagrangian Observations of Ice Motion, *IEEE Trans. Geosci. Remote Sens.*, **33**(2), pp. 392-400.

Kwok, R., G.F. Cunningham, N. LaBelle-Hamer, B. Holt, and D.A. Rothrock (1999). Sea ice thickness from high-resolution SAR imagery, *EOS, Trans. AGU*, **80**(42), 495-497.

Kwok, R. and G.F. Cunningham (2002). Seasonal ice area and volume production of the Arctic Ocean: November 1996 through April 1997, *J. Geophys. Res.*, **107**(C10): art. no. 8038.

Kwok, R., G.F. Cunningham, W.D. Hibler III (2003). Sub-daily sea ice motion and deformation from RADARSat observations, *Geophys. Res. Lett.*, **30**, 2218, doi: 10.1029/2003GL018723.

Kwok, R., G.F. Cunningham and S.S. Pang (2004). Fram Strait sea ice outflow, *J. Geophys. Res.*, **109**, C01009, doi:10.1029/2003JC001785.

Li, S., Z. Cheng, and W.F. Weeks (1998). Extraction of intermediate scale sea ice deformation parameters from SAR ice motion products, in *Analysis of SAR Data of the Polar Oceans*, Springer-Verlag, New York, pages 69-90.

Lindsay, R.W., and J. Zhang (2005). The thinning of arctic sea ice, 1988-2003: have we passed a tipping point? *J. Climate*, in press

Liu, A.K., and D.J. Cavalieri (1998). On sea-ice drift from the wavelet analysis of the defense meteorological satellite program DMSP special sensor microwave imager SSM/I data. *Int. J. Remote Sens.*, **19**(7):1415-1423.

Melling, H., D.A. Riedel, and Z. Gedalof (2006). Trends in thickness and extent of seasona pack ice, Canadian Beaufort Sea. *Geophys. Res. Lett.*, under review

Perovich, D., H. Eicken, J.K. Hutchings & 58 others, (2005). The state of the Arctic sea ice cover: Physical and biological properties and processes in a changing environment. Full proposal I.D. 95, submitted to International Polar Year International Programme Office.

Richter-Menge J.A., S.L. McNutt, J.E. Overland, and R. Kwok (2002b). Relating Arctic pack ice stress and deformation under winter conditions. *J. Geophys. Res.*, **107**(C10), 8040, doi:10.1029JC00477.

Rigor, I.G., J.M. Wallace, and R.L. Colony (2002). Response of Sea Ice to the Arctic Oscillation, *J. Climate*, **15**(18):2648-2668

Rothrock, D.A., Y. Yu and G.A. Maykut (1999). Thinning of the Arctic sea-ice cover, *Geophys. Res. Lett.*, **26**, 3469-3472.

Study of Environmental Change (SEARCH), 2005: Study of Environmental Arctic Change: Plans for Implementation During the International Polar Year and Beyond. Fairbanks, Alaska: Arctic Research Consortium of the United States (ARCUS). 104pp.

Steele, M. and G.M. Flato (1999). Sea ice growth, melt, and modeling: a survey. In *The Arctic Ocean Freshwater Budget*, NATO ARW. 70, 549-587.

Thomas, M.V., A. Shah, and G.C. Reddy (2000). A fast block motion estimation algorithm based on motion adaptive partitioning, in *Proc. Indian conference on Computer Vision, Graphics and Image Processing*.

Thomas, M.V., C.A. Geiger, and C. Kambhamettu (2004). Discontinuous Non-Rigid Motion Analysis of Sea Ice using C-Band Synthetic Aperture Radar Satellite Imagery, IEEE Workshop on Articulated and Nonrigid Motion (ANM) (In conjunction with CVPR'04), held June 27, 2004 in Washington, D.C., 9 pages.

Thomas, M.V., C.A. Geiger, and C. Kamhamettu (2005). Mesoscale sea ice features derived from discontinuous nonrigid motion SAR products, Proceedings of the 18th International Conference on Port and Ocean Engineering Under Arctic Conditions (POAC), June 26-30, Potsdam, New York, USA (in press).

Vernon, D. (2001). *Fourier Vision - Segmentation and Velocity Measurement using Fourier Transform*, Kluwer Academic Publishers.

Classification of GreenICE SAR Data Using Fuzzy Screening Method

Rashpal S. Gill* and Rasmus T. Tonboe
Danish Meteorological Institute, Lyngbyvej 100, 2100-Copenhagen, Denmark.

Keywords: SAR, sea ice types, fuzzy logic

ABSTRACT: A semi-automatic SAR sea ice classification algorithm is described. It is based on combining the information in the original SAR data with those in the 'image' products derived from it, such as Power-to-Mean Ratio (PMR), the Gamma distribution and the second order texture parameter entropy, inertia and uniformity. The technique used to fuse the information in these products is based on a method called Multi Experts – Multi Criteria Decision Making (ME-MCDM) fuzzy screening. The Multiple Experts in this case are the above six 'image' products. The two criteria used currently for making decisions are the Kolmogorov-Smirnov (KS) distribution matching and the statistical means. The algorithm classifies an image into any number of pre-determined surface classes. The representative classes of the latter are manually identified by the user in the individual images.

In the context of the GreenICE project, this algorithm was tested using the Radarsat SAR acquired during the GreenICE 2003 – 2004 field campaigns. In this case the algorithm was used to estimate the percentage of open water, leads, ridges, new ice and old ice in the individual SAR images which have pixel size in the range 6.25 m – 25.0 m. The results obtained using the classification scheme were consistent with expectations such as, for example, detecting significantly more ridges in the 2004 data from north of Greenland (~ 80 ºN) than in the 2003 ice camp from north of Spitsbergen. Further, ice types are indicators of ice thickness and it was found that the region near the ice camps consists of ~75 % - 85 % multiyear ice which typically has thickness ~ 3 m- 6 m. The possible strengths and weakness of the cur-rent classification algorithm and those based on SAR images in general are discussed.

1 INTRODUCTION

In recent years satellite image classification and multi sensor data fusion based on neural networks (NN) and fuzzy set theory have received much attention in the open literature (Zadeh, 1965, Kohonen et. al., 1995, Masselli et. al., 1995, Atkinson and Tatnall, 1997, Chanussot et. al., 1999, Solaiman et. al., 1999, Tupin et. al., 1999, Andrefouet et. al., 2000, Pal et. al., 2000, Melgani et. al., 2000, Wu and Linders, 2000, Moore et. al., 2001, Zhang and Foody, 2001). One of the main reason why NN has gained popularity over the more traditional statistical approaches is that the former is distribution-free i.e., no prior knowledge of the distribution(s) underlying the different surface classes is needed for classification, only the actual data. There are several different types of NN and one thing they all have in common is that they all require the training of the network (Atkinson and Tatnell, 1997). The training can be supervised or unsupervised. The supervised training algorithms include those based on Multi-Layer Perception (MAL) using a feed - forward concept and those using a feedback neural network, for example the so-called Hopfield network (Atkinson

* E-mail: rsg@dmi.dk, Tel.: +45 39 15 73 42.

and Tatnell, 1997). In these algorithms prior data sets of known classes are required. In the case of MAL, training of the network involves the fine tuning of the weights of the connections, while in the case of the Hopfield network, the output from the nodes are fed back into the input. In the unsupervised training network no prior information is provided about the desired classification; the network learns itself so to speak. The Organising Topological Map is an example of this type of unsupervised network (Atkinson and Tatnell, 1997).

In the neural network approach a given unknown pixel or a region is classified into one of the pre-defined classes. In other words, a given pixel is either a full member of a particular class or is not a member. This is one disadvantage with using a NN approach, as in many cases data are mixed i.e., an unknown pixel may partially belong to several classes as the boundary between them may not be sharp. Fuzzy set theory explores this concept. In the fuzzy classification schemes, a given pixel can partially belong to several classes. In this case the contribution of each class in the pixel or a region must be estimated. Some of the most well-known algorithms based on fuzzy theory are the hard and fuzzy-c means (HCM, FCM) clustering algorithms used for image segmentation (Pal et. al., 2000). Since its first introduction by Zadeh (1965), fuzzy set theory has invaded many other fields beside fuzzy classifications, which include fuzzy control systems and fuzzy image processing (Melgani et. al., 2000).

One of main aims of the EU financed GreenICE project is to measure the thickness of sea ice (Wad-hams, 2001). In the context of this project, satellite Radarsat SAR data are used to relate sea ice thick-ness to that measured by other sensors, such as airborne laser profiling. Direct measurement of sea ice thickness using SAR is not possible, though if the age of the ice is known it can be used to infer its typical thickness, since first, second and multi - year ice are approximately 1m , 2m, and 3 – 5 m thick respectively. This task of determining the observed ice types is best carried out using a reliable SAR image classification algorithm.

The scheme used to classify SAR images acquired during the GreenICE field 2003 - 2004 campaigns is called the Multi Experts – Multi Criteria Decision Making (ME-MCDM) (Gill, 2002a) fuzzy screening method. This method was selected as it was found to be very flexible, with potential to include auxiliary information which could be relevant for image classification. In particular, it allowed for having multiple experts (the texture image products discussed below), any number of image surface classes (called alternatives), the possibility to use multiple decision making criteria and to associate importance to each of them. The scheme also allowed the user to determine how many experts have to agree before a region is reliably classified. The method is originally due to Yager (1993) and "is useful in environments in which we must select, from a large class of alternatives, a small subset to be further investigated". It is well suited for SAR image classification because it allows for fusing the information in the original SAR image with that contained in the statistical and texture image products derived from it, namely, Power-to-Mean Ratio (PMR), Gamma probability distribution function (Gamma-pdf) and the second order texture parameters such as entropy, inertia and uniformity (Gill, 2001, 2002b, Gill and Valuer, 1999). The latter products are found to contain useful supplementary information which is often useful in discriminating between the different surface cover types (Gill, 2001).

The full details of the ME-MCDM fuzzy screening method are described in Gill, 2002 (a). The main components of ME-MCDM classification scheme are summarised below, together with the computational procedure.

Main components of the ME-MCDM fuzzy screening method:

1. **Experts –** the image products (e.g., AMPLITUDE, GAMMA-pdf, PMR, ENTROPY (ENT), INERTIA (INER), UNIFORMITY (UNIF)) used in the image classification.
2. **Alternatives/Classes –** The number of different surface classes into which the SAR image is to be classified. In the present case five surface classes were chosen: open water, leads including leads infested with thin ice such as nilas, ridges, new (first year) and old (multi year) sea ice.
3. **Criteria –** necessary to make decisions by the experts about the possible alternatives. Currently two criteria are used, Kolmogorov – Smirnov (KS) distribution matching and statistical means comparison tests.

Computational procedure.

1. Compute the six image product (AMP; GAMMA-pdf, PMR, ENT, INER and UNIF).
2. Manually identify on a computer screen the surface classes into which the SAR image is to be classified. Store the values of these different classes.
3. By using a N × N test window in each of the six products, compute the scores of each of the above class using each of the above two criteria.
4. Use the fuzzy screening rules to aggregate the scores for each class from each of the 6 products for the test window. This will result in the overall scores for each class for the test window.
5. Hard classify the overall scores for the test window by de-fuzzying the results. This is achieved by taking the class that has the maximum overall score.
6. Steps 3 – 5 are repeated for the entire image by sliding the above N × N window across the image.

The SAR classification scheme discussed above is sketched in figure 1 below.

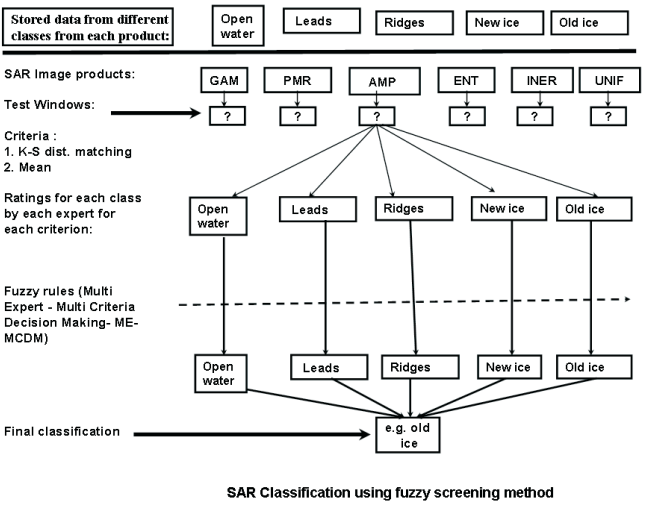

Figure 1. Shows the sketch of the SAR image classification using the fuzzy screening method. In the figure these are surface classes 5 (open water, leads, ridges, new and old ice), and 6 experts (AMP, PMR, GAM (=GAMMA_pdf), ENT, INER and UNIF. Criteria used a re the KS and the statistical means. For the sake of illustration only the ratings for each class by AMP are shown in the figure.

2 RESULTS AND DISCUSSION

We give an example using a classification of the Radarsat Standard Mode (SGF) image from 11th April 2003 shown in Fig. 2 (top). This image is from North of Spitsbergen acquired during the GreenICE 2003 ice camp. The image product is approximately100 km x 100 km in size with 12.5 metre pixel size. It has been chosen because it is relatively easy to interpret manually and can then be used to ascertain the performance of the algorithm qualitatively. Detailed examination of the image shows that it contains essentially three surface types: old multiyear ice floes, new ice and open leads. The classified image is shown at the bottom of fig. 2. Qualitative comparison of the classified image with the original image shows that the classification appears to be reasonable.

According to the classification algorithm the image contained c. 64 % of old multi year ice, c.34% new first year ice, c. 0.7% ridges, c. 1.5% leads including those infested with thin ice such as nilas.

Classification of the entire Radarsat dataset acquired during the GreenICE 2003 (north of Spitsbergen) and 2004 (north of Greenland at ~ 80 ºN) ice camps was carried out in a similar manner. The results are summarised in Table 1. In interpreting these results, it is important to bear in mind that the ice regimes and their dynamical movements during the periods of the two camps were very different. The 2003 ice camp was established relatively close to the ice edge and was facilitated by the Polarstern cruise, while the 2004 ice camp was established 200 km north of the Canadian Forces Station Alert in nearly 100 % sea ice regime. This is reflected in the overall classified results for the two ice regimes. The percentage of new ice is higher in the 2003 data than in the 2004 data. The percentage of ridges, defined as regions with very high backscatter values, is much higher in the data from north of Greenland than from north of Spitsbergen. In particular, the percentage of ridges in the sea ice regime in north Greenland was in the range ~ 3 % - 17 % while in the north of Spitsbergen it was < 1.4 % in all the Radarsat images. Finally, at first glance the classification results for the 14th April 2003 appear suspect as they only give ≈ 58 % for old ice and ~ 27 % for open water. However, the SAR image for that date was a lower resolution 25 m pixel size ScanSAR narrow image of a much larger area (~ 300 km x 300 km) at the sea ice – open water boundary and contained significant open water regions.

Excluding the classification results from 14th April 2003 for the reason listed above, it can be seen from the table that the percentage of old multi-year ice in the vicinities of the ice camps was typically in the range ~ 75 % - 85 %. These ice types are typically ~ 3 m – 6 m in thickness, with average ~ 3m for the entire Arctic. New ice types, ridges, and leads were in the range ~ 3 % - 34 %, ~ 0 % - 17 %, 0 % - 9%, respectively.

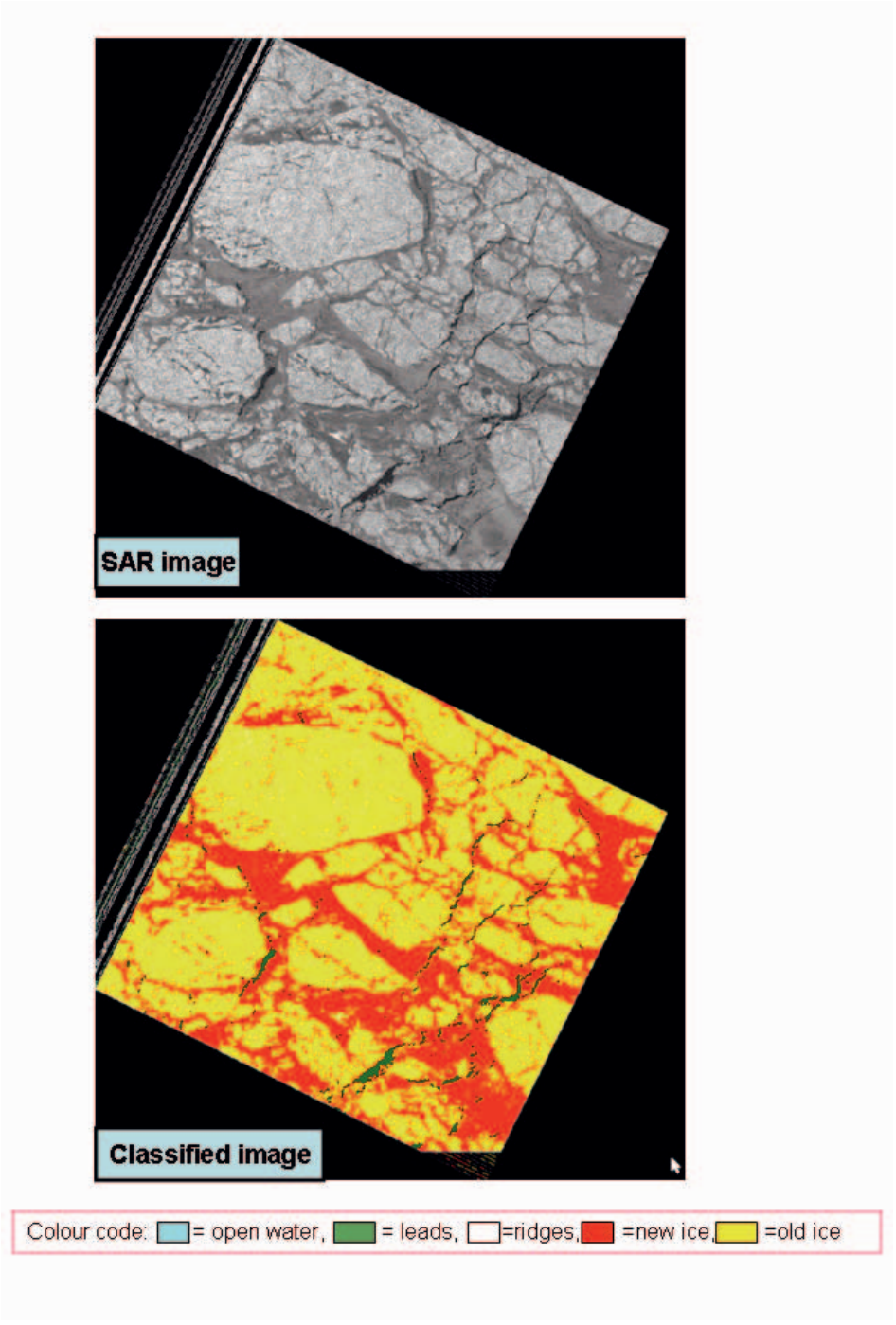

Figure 2. Shows the geo-coded original SAR from 11th April, 2003 and its classification into 5 surface types. The image is ap-proximately 100 km x 100 km in size.

Table 1. Classification of RADARSAT data for 2003 – 2004 ice camps into 4 surface types in percentages. Radarsat product FN3 is of size 50 km x 50 km. S7, W3 and SGF are ˜100 km X 100 km. Finally SCN are of 300 km X 300 km.

	Radarsat Product and pixel size (m)	Open water %	Leads or ice infested leads %	Ridges or ice infested ridges %	New ice %	Old ice %
2003-04-11_A	SGF (12.5 m)	0	1.5	0.7	33.9	63.9
2003-04-11_B	SGF (12.5 m)	0	0.4	1.4	9.3	88.9
2003-04-12	SGF (12.5 m)	0	1.0	0.2	15.6	83.2
2003-04-14	SCN (25.0 m)	27	8.5	0.0	6.6	58.0
2003-04-16	SGF (12.5 m)	0	0.2	0.1	11.7	88.0
2003-04-17	SGF (12.5 m)	0	5.8	0.04	20.0	74.2
2004-05-05	SCN (25.0 m)	0	4.5	7.5	4.8	83.3
2004-05-07 – badly processed	SCN (25.0 m)	0	3.8	17.3	6.3	72.7
2004-05-10	SCN (25.0 m)	0	2.2	16.4	16.1	65.3
2004-05-12	SCN (25.0 m)	0	4.2	9.3	12.6	73.9
2004-05-13	S7 (12.5 m)	0	0.8	3.4	14.8	81.1
2004-05-15	SGF (12.5 m)	0	1.3	11.4	2.9	84.4
2004-05-15	FN3 (6.25 m)	0	0.04	13.8	3.5	82.3
2004-05-20	W3 (12.5 m)	0	2.7	7.9	6.8	82.6

Concerning the accuracy of the classification scheme it is important to ensure that the representative classes, identified manually by the user, do not contain impurities from other classes. This was clearly seen during the classification of the SAR images from the 15th May 2004 where two images, one a fine beam product (FN 3) with pixel size of 6.25 m and the other SGF image (pixel size = 12.5 m), were acquired over the same ground area but different acquisition times. It was found that the initial classification of the same sea ice regime observed in the two images did not agree too well. It was later found that the reason for this disagreement was that the representative classes of some ice types, identified by the user, were contaminated by impurities from other classes. Based on this experience the representative classes used to classify images were re-examined to ensure that they did not contain impurities from other classes. The main point to conclude from this is that the performance of the algorithm is only as good as the quality of the representative classes identified by the user.

Further, it was found that the classification results are not very reliable in the near range of the SAR images due to high pixel values arising from the steep radar incidence angles. This is one of the reasons (the other is the low resolution of the SAR image product used) why the estimates of the ridges based on ScanSAR narrow images from 7th and 10th May 2004 are unusually high and should be treated with caution. The SGF and other high resolution Radarsat products acquired for the ice camps had radar surface incidence angles greater than the ≥ 30 ° which are sufficient for reliable classification. For improved classification the radar images should be corrected for this incidence angles effects prior to classification.

It was found that the KS criterion was more effective at discriminating between the different ice classes than the simple statistical means. To account for this fact more importance was accorded to the KS criterion in the algorithm. However, the KS test has its own limitations: (i) it is most sensitive around the median of the cumulative distribution

function and less sensitive at the tail ends, and (ii) it cannot discriminate between all types of distributions, such as a distribution with two maxima.

One of the main weaknesses of the current (or for that matter any other SAR image classification scheme based on single polarisation or frequency data), is that unambiguous criteria or texture parameters that discriminate between different surface types in different meteorological surface weather conditions have, so far, not been identified. All the parameters used in the current classification; amplitude, power-to-mean ratio, Gamma-pdf, entropy, uniformity and inertia (and others), are also ambiguous. More specifically, none of them have unique values for the different ice types during the different weather conditions observed in the region, especially in different surface winds conditions and surface temperatures. Thus until more robust criteria and or parameters are found that are better at discriminating between the different surface types in different weather conditions, situations will arise when the classification schemes, such as the one used in here, do not give very reliable results.

The effectiveness of using surface types identified in one SAR image to classify a SAR image of the same (and different) region, from another day, was also investigated. The results were not very encouraging. The main reason for this is that the different image classes are too sensitive to the radar incidence angles, i.e., their position in the across range direction. Another important reason is that the statistical characteristics of the surface classes can, in the time between the two images, undergo significant changes (due to meteorological conditions).

Finally it should be recalled that in the ME-MCDM model it is assumed that all experts are independent and have the same importance. This assumption is not strictly satisfied as all the six products are derived from the same original SAR image. In the future it is planned to undertake combined Radarsat and ENVISAT -ASAR image classification, thus relaxing the above assumption. Results of this investigation will be reported in the near future.

3 ACKNOWLEDGEMENTS

This work was supported by the European Commission 5th Framework Programme GreenICE Project (EVK2-2001-00280).

4 REFERENCES

Andrefouet S., Roux L., Chancerelle Y., and Bonneville A., (2000). A fuzzy-possibilistic scheme of study for objects with indeterminate boundaries: application to French Polynesian reefscapes. *IEEE Trans. Geoscience and Remote Sensing*, 38(1), p. 257.

Atkinson P.M., and Tatnall A.R.L. (1997). Neural networks in remote sensing, *Int. J. Remote Sensing*, 18(4), pp.669 – 709.

Chanussot J., Mauris G., and Lambert P. (1999). Fuzzy fusion techniques for linear features detection in multitemporal SAR. *IEEE Trans. Geoscience and Remote Sensing*, 37(3), p. 1292.

Gill R.S. and Valeur H.H. (1999). Ice cover discrimination in the Greenland waters using first-order texture parameters of ERS SAR images. *Int. J. Remote Sensing*, 20(2), pp. 373-385.

Gill R.S. (2001). Sea Ice Edge and Icebergs Detection using routine operations. *Canadian J. Remote Sensing*, special issue on Sea Ice and Icebergs, 27(5), pp. 411-432.

Gill R.S. (2002a). SAR ice classification using fuzzy screening method. *Danish Met. Scientific Report*, 02 -12.

Gill R.S. (2002b). SAR surface classification using distribution matching. *Danish Met. Scientific Report*, 02 -08.

Kohonen, T., Hynninen, J., Kangas, J., Laaksonen, J., and Torkkola, K. (1995). LVQ-PAK: the learning vector quanitsation program package, version 3.1. *Technical Report, Laboratory of Computer and Information Science*, Helsinki University of Technology, Finland.

Masselli F., Conese C., Filippis F.D., and Norcini S. (1995). Estimation of forest parameters through fuzzy classification of TM data, *IEEE Trans. Geoscience and Remote Sensing*, 33(1), p. 77.

Melgani F., Bakir A.R., Al Hasheny, and Taha S.M.R. (2000). An explicit fuzzy supervised classification method for multispectral remote sensing images. *IEEE Trans. Geoscience and Remote Sensing*, 38(1), p. 287.

Moore T.S., Campbell, J.W., and Feng, H. (2001). A fuzzy logic classification scheme for selecting and blending satellite ocean colour algorithms, *IEEE Trans. Geoscience and Remote Sensing*, 39(8), p. 1764.

Pal, S.K., Ghosh, A., Shankar, B.U. (2000). Segmentation of remotely sensed images with fuzzy thresholding and quantitative evaluation. *Int. J. Remote Sensing*, 21(11), pp. 2269-2300.

Solaiman, B., Pierce, L.E., and Ulaby, F.T. (1999). Multisensor data fusion using fuzzy concepts: application to land-cover classification using ERS-1/JERS-1 SAR composites. *IEEE Trans. Geo-science and Remote Sensing*, 37(3), p. 1316.

Tupin, F., Bloch, I., and Maitre, H. (1999). A first step toward automatic interpretation of SAR images using evidential fusion of several structure detectors. *IEEE Trans. Geoscience and Remote Sensing*, 37(3), p. 1327.

Wadhams, P. (2001). Greenland Artic Shelf ice and climate experiment, acronym GreenICE, EU proposal number EVK2-2001-00280.

Wu, D. and Linders, J. (2000). Comparison of three different methods to select feature for discriminating forest cover types using SAR imagery. *Int. J. Remote Sensing*, 10(10), pp. 2089-2099.

Yager, R.R. (1993). Fuzzy screening systems. In: R. Lowen and M. Roubens (eds.), *Fuzzy Logic: State of the Art* (Kluwer, Dordrecht), pp. 251-261.

Zadeh, L.A. (1965). Fuzzy sets. *Inform. Contr.*, 8, pp. 338-353.

Zhang J., and Foody, G.M. (2001). Fully-fuzzy supervised classification of suburban land cover from remotely sensed imagery: statistical and artificial neutral network approaches. *Int. J. Remote Sensing*, 22(4), pp. 615-628.

Sea Ice Freeboard from ICESat – A Comparison with Airborne Lidar Measurements

Henriette Skourup† and Rene Forsberg
Geodynamics Dept, Danish National Space Center, Juliane Maries Vej 30, DK–2100 Copenhagen Oe, Denmark.

Keywords: ICESat, satellite laser, airborne laser, lidar

ABSTRACT: In connection with the GreenICE ice camp in the Arctic Ocean north of Alert, May 2004, airborne sea ice laser scanner data was measured on transits to the drifting ice camp, as well as in dedicated laser scanner flights. Two lines were flown along ICESat ground tracks, in order to do a near-coincident underflight of the ICESat satellite. In this paper we report on the intercomparison of the freeboards estimated by high-resolution airborne swath laser data and the laser altimetry from ICESat. Our results show that the satellite laser measurements have good agreement with the airborne laser scanner, but due to the larger footprint and lower along-track laser shot sampling, ridges and leads are significantly underestimated, when using a lowest-level filtering method to estimate the mean sea level. In the very rough and thick sea ice region north of Greenland, this bias is found to be around 35 cm for our specific filtering algorithm, thus providing a possible systematic error in ICESat derived freeboards. We conclude the paper by deriving Arctic Ocean-wide freeboard maps for two ICESat periods in 2003 (laser 1 and laser 2A). The derived ice freeboards (and implied thicknesses) show good qualitative agreement with the distribution of thick multi-year sea ice, obtained from QuikSCAT backscatter maps.

1 INTRODUCTION

The utilization of satellite altimeter missions to measure sea ice thickness is very important in order to monitor large-scale changes of the Arctic sea ice. Methods to determine sea ice thickness from radar altimetry were originally developed for ERS by Laxon et al (2003) covering up to 81.5°N. The launch of NASA's ice, cloud, and elevation laser altimeter satellite (ICESat) in January 2003 has expanded the satellite coverage up to 86°N, and has given new possibilities for research in deriving sea ice thickness from satellite altimetry. First published investigations includes Kwok et al (2006), and Forsberg and Skourup (2005). In this paper, we report on the first direct underflight of ICESat over sea ice covered waters with a high-resolution airborne lidar system.

The airborne lidar data were collected as part of the Danish National Space Center (DNSC) GreenICE/SITHOS field campaign in 2004 carried out to measure the sea ice thickness north of Greenland. A more detailed description of the operations and data processing is reported in the DNSC technical report by Dalå et al (2005). Two dedicated partially cloud-free tracks were flown on May 25 to do a near-coincident underflight of ICESat, see Figure 1 for the track location. Both sub-tracks span approximately 50 km each corresponding to approximately 300 ICESat observations.

† E-mail: hsk@spacecenter.dk

Unfortunately a timing error for the aircraft scheduling gave an 8 hr delay in the underflight compared to the ICESat passage. However, the sea ice both along the western and eastern flight tracks showed essentially no movement in the period due to calm wind conditions, as verified by drift vectors estimated from successive ENVISAT ASAR images, cf. Figure 2.

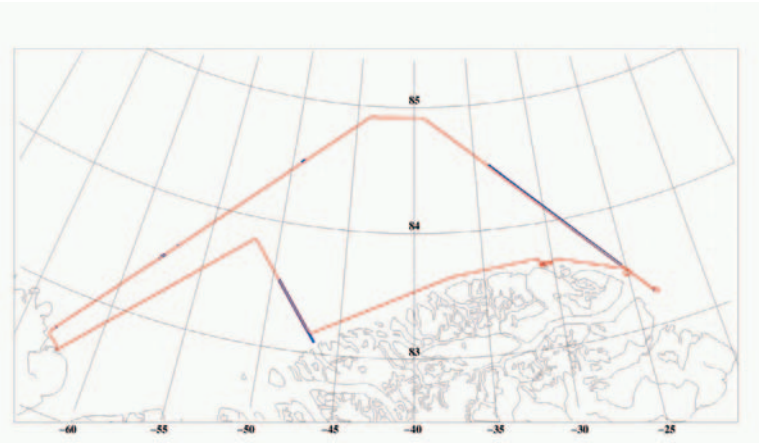

Figure 1. The red line is the Twin-Otter flight track of May 25, lined up along several ICESat tracks. The blue lines are the cloud-free near-coincident ICESat sub-tracks.

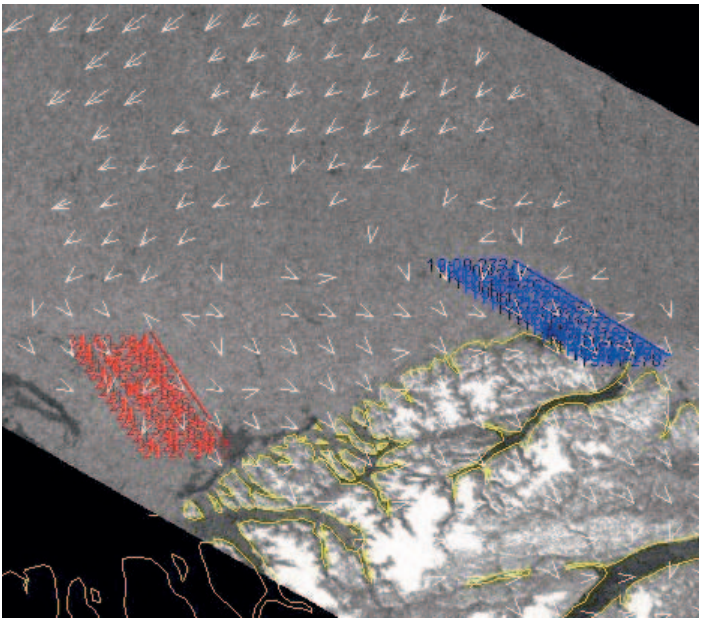

Figure 2.ENVISAT ASAR imagery for May 25, with estimated ice drift vectors from repeated ASAR scenes. The maximum velocity is roughly 3 km/day to be found in the northwestern area of the image. The random nature of the velocities off the coast of northern Greenland confirms the essentially no-drift condition in the survey area. Figure courtesy Leif Toudal, Danish Technical University.

2 DESCRIPTION OF THE LASER ALTIMETER SYSTEMS

The ICESat laser altimeter (GLAS) operates at two wavelengths, an infrared channel (1064 nm), primarily used for surface altimetry, and a green (532 nm) channel primarily used to measure the vertical distribution of clouds and aerosols (Zwally et al, 2002). The infrared channel wavelength is almost identical to the DNSC airborne laser scanner system working at a wavelength of 900 nm. The pulse repetition frequency for ICESat is 40 Hz corresponding to an along-track separation of the centers of the footprints by approximately 172 m, and the footprint diameter is approximately 70 m wide. The accuracy of the ICESat ellipsoidal heights of the sea ice surface is in the order of 15 cm.

In this paper we compare sea ice freeboards obtained from the ICESat laser data to freeboards derived from the DNSC high-resolution airborne laser scanner data. In the airborne system a swath scanner is used, with a basic laser footprint size of 1 x 1 m at flight altitude ~300 m. The lidar system gathers data in an across-track swath of width roughly equal to the flight height, with an inherent relative precision of a few cm. Absolute errors in determining the sea ice ellipsoidal heights are estimated to be 20-30 cm due to errors in the long-range kinematic aircraft positioning. For more information on the airborne instrumentation and the system setup, see the paper by Hvidegaard et al (this volume).

3 FREEBOARD ESTIMATION FROM ICESAT AND AIRBORNE LIDAR

The sea ice freeboard (F) including snow for both ICESat and the airborne laser measurements, is given by

$$F = h - N - MDT - e \tag{1}$$

where h is the ellipsoidal height of the altimeter measurements (where the ICESat measurements have been corrected for tides), N is the geoid, MDT the mean dynamic topography, and e measurement errors. To a first approximation a geoid model is used to represent the mean sea surface (MSS). The first step is therefore to remove the geoid from the ellipsoidal heights of the altimeter measurements (h-N). However, due to ocean mean dynamic topography and measurement errors, it is necessary to apply a lowest-level filtering scheme. The filtering scheme selects the lowest levels from the heights (h-N) and these are fitted to a smooth curve. As the lowest levels are assumed to represent open water or leads covered by thin ice, the smooth curve is supposed to reflect the instantaneous sea surface height (SSH).

For airborne laser data this method was originally described in Hvidegaard and Forsberg (2002), using a polynomial-fit scheme to define the smooth SSH surface. In the ICESat investigations, this scheme has been updated to use a smooth least-squares collocation (optimal estimation) function, yielding nearly equivalent results to the polynomial scheme, but allowing a more flexible fitting to the assumed “lowest-level” points. The typical distance used between such points is 5-15 km, and will in practice be chosen based on ice properties and geoid model errors. An example of the lidar swath freeboard data, and coincident nadir imagery, is shown in Figure 3.

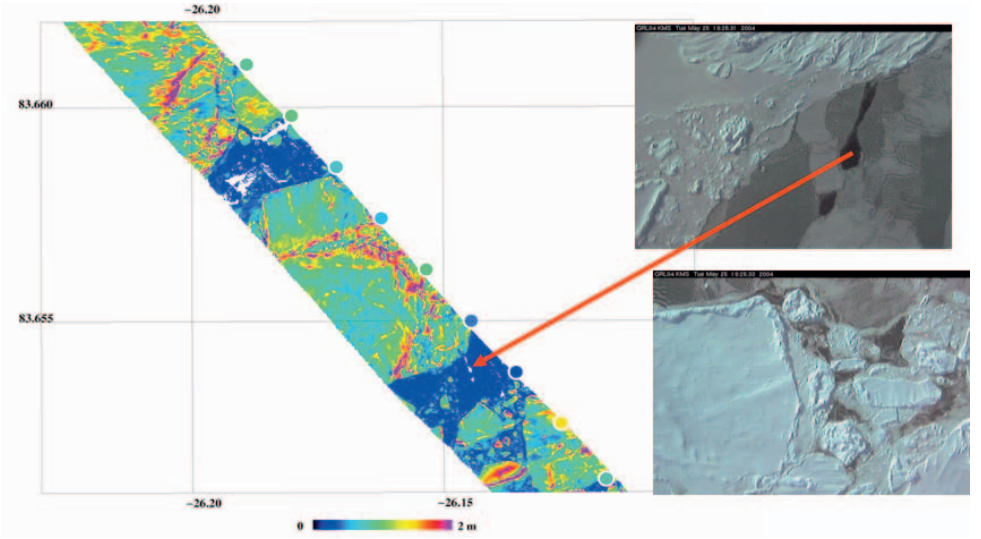

Figure 3. Example of lidar swath freeboard data (width approx. 250 m) after lowest-level filtering. ICESat measurements shown with circles, same color coding. A good qualitative agreement is seen.

In this study, the observations from the satellite and the airborne systems have been converted to sea ice freeboards by applying the above described techniques. We use an Arctic geoid model (version December, 2004) derived by spherical FFT methods from the Arctic Gravity Project terrestrial data (Forsberg and Kenyon, 2004) and GRACE satellite data, for more details see Forsberg and Skourup (2005). The volume of the raw airborne data has been decreased by averaging across-track and thinning along-track to a resolution of approximately 5 by 5 m. For the ICESat-derived freeboards we have used the GLA13 data product, specially designed for sea ice applications. The May 25, 2004, ICESat data were from laser 2C, release 17.

The lowest-level algorithm was applied to ICESat taking the average value of the three lowest-levels for each interval of 10 km. For the airborne lidar data, with the much higher spatial resolution, the lowest-level of the vertical component is used within an average interval of 10 km along the swath. We also made tests with 5 km resolution "lowest-level" filtering, yielding changes in the lowest-level surface of typically 5 cm. Therefore algorithm-dependent biases in the freeboard results could be at a similar level.

4 COMPARISON OF ICESAT AND AIRBORNE LIDAR

Figure 4 displays the freeboards from the vertical component of the airborne scanner data plotted together with the ICESat freeboards (upper plot), and the corresponding reflectivity of the surface (uncorrected for atmospheric effects) measured by ICESat (lower plot). The reflectivity (R) can be used as an indicator of the presence of open water and newly formed lead ice, as these are represented by low values in the reflectivity (R~0), which has been shown to increase rapidly with ice thickness (Kwok et al, 2004).

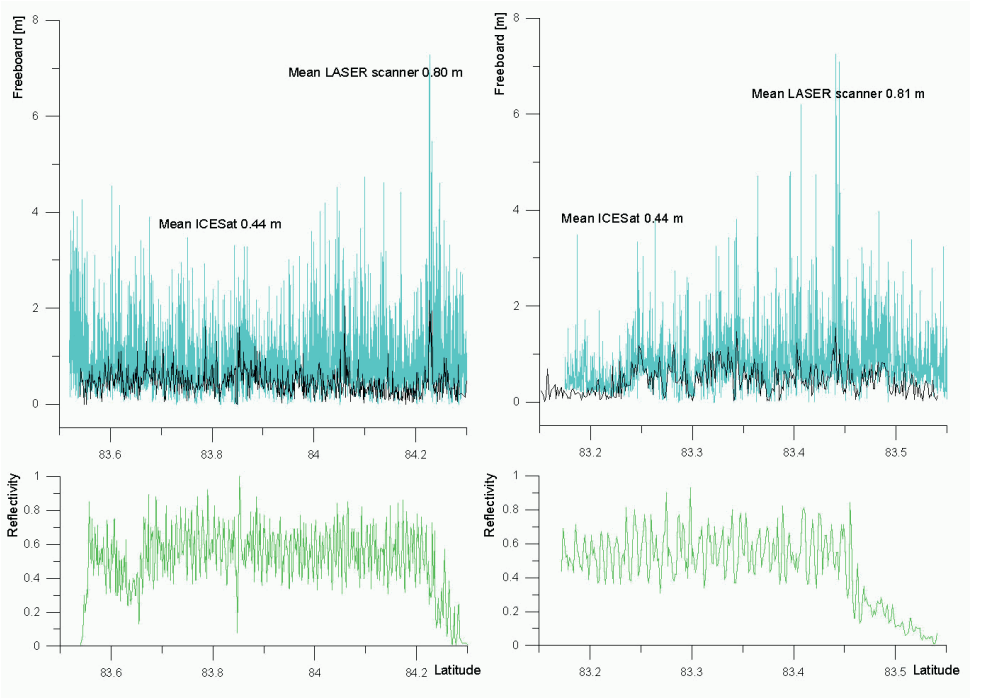

Figure 4. Sea ice freeboard heights from ICESat (black), and the vertical component from airborne lidar (blue) for the eastern (left) and the western flight (right). In the lower plot (green) is the reflectivity of ICESat displayed. It is seen, that the sea ice has thicknesses up to 6 m in the region north of Greenland.

By averaging the freeboards in the upper plots, an offset of 36 cm for the eastern-most track and 37 cm for the western-most track, were found between the two measurement methods. The lowest-level technique applied here to estimate the freeboards is highly dependent on open water and thin lead ice, as the lowest values are assumed to represent the sea surface height. For each ICESat sample the freeboard heights are averaged over the relatively large ICESat footprint (~70 m in diameter). To detect an open lead with ICESat the size of the lead should be wide enough to contain the full ICESat footprint. Otherwise, the measured freeboard height is higher, than the level of the open lead, due to averaging over the footprint. This effect results in an overestimated sea surface height, and thus an overall underestimation of sea ice freeboards.

The effect of smoothing across the ICESat footprint can also be detected in the freeboard distributions, see Figure 5, where the probability density functions (pdf) of freeboard heights for ICESat and the lidar data are plotted. In these plots we have added the biases obtained above to the ICESat freeboards to be able to compare the distribution of sea ice features. It is seen that the thinnest ice classes and ridges are almost absent in the ICESat freeboard pdf, but present in the laser scanner freeboard pdf.

Another issue, which might bias the ICESat freeboard heights in the lowest-level filtering scheme, is due to the relatively coarse along-track resolution (~172 m) of ICESat, when compared to the airborne system. According to this fact, ICESat may not detect all of the leads. Especially, in the region north of Greenland the sea ice cover is primarily

composed of thick perennial ice with heavy ridges and rubble fields with very few or no open leads (see Figure 6). In these heavy ice conditions it is unlikely, that ICESat observe any open leads, causing the lowest-levels to be biased. This is also sustained by the reflectivity profiles of Figure 4, where no major leads, expressed by low reflectivity (R~0), are seen. The airborne system is expected to pick up even the most narrow lead features due to the smaller footprint (~1m) and the higher along-track resolution (~1m).

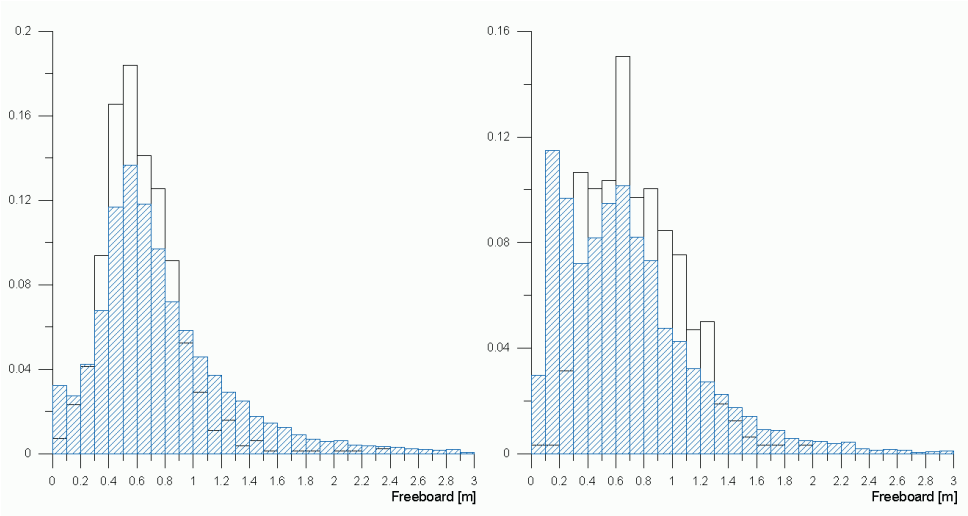

Figure 5. Probability functions for sea ice freeboard heights from ICESat (open bars) and airborne lidar (hatched bars), for the western subtrack (left) and the eastern subtrack (right).

Thus, the biases observed here are believed to originate from an overestimation of the lowest-level points as seen by ICESat, due to the larger footprint and the coarser along-track resolution, compared to the narrow leads measured by the airborne lidar. The bias problem is expected to be less pronounced in other regions of the Arctic Ocean, where the ice is thinner and more leads are found.

To further compare the airborne scanner and ICESat derived freeboards the airborne scanner data has been modeled to match ICESat footprints. The modeled footprint is assumed to be circular, and has been weighted by the far field beam pattern taken to be near Gaussian in shape with 1/e-width set to 35 m to match the footprint size. Figure 7 shows the result of this comparison for the western track. The correlation between the two data sets has a correlation coefficient r = 0.65, which is fairly good. In the northern-most end of the track the freeboard heights of the two data sets seem to diverge. At latitudes higher than 83.46 N a high gain (G > 50) is observed in the ICESat measurements. According to Kwok et al (2006) a high gain indicates a low signal to noise ratio (SNR), and thus the likelihood of a reduced surface return, explained by scattering by atmospheric constituents (clouds, water vapor etc.). A reduced surface signal might cause the location of the surface to be misinterpreted causing biases in the measured ICESat heights. This could explain the divergence between the ICESat freeboard heights and the airborne freeboard heights north of 83.46°N.

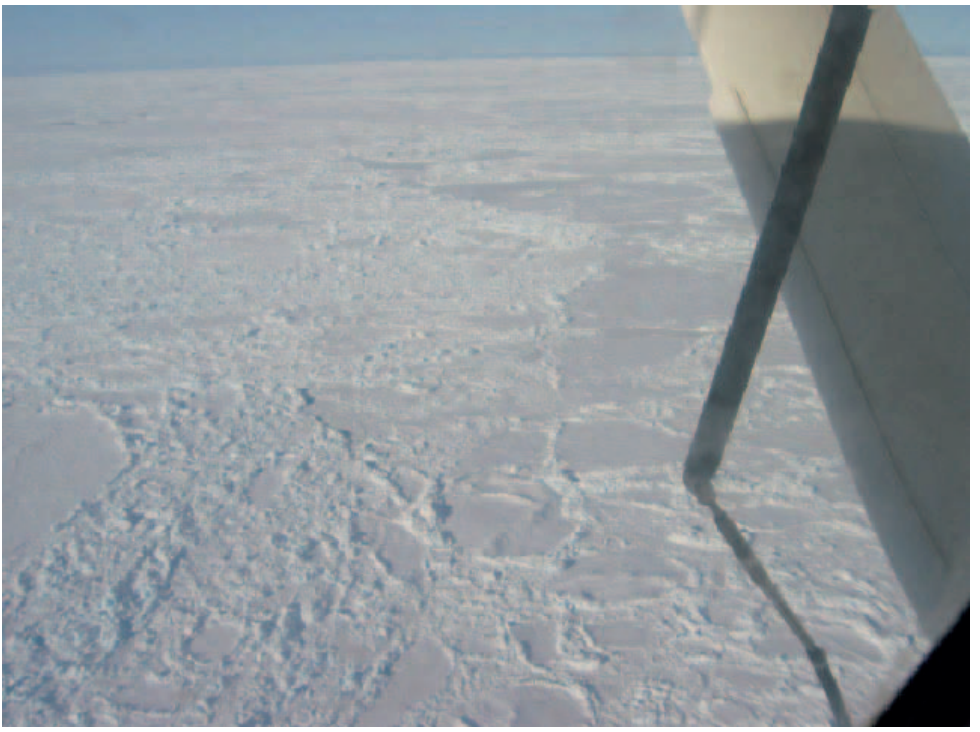

Figure 6. Typical sea ice north of Greenland (eastern subtrack), May 25, 2004.

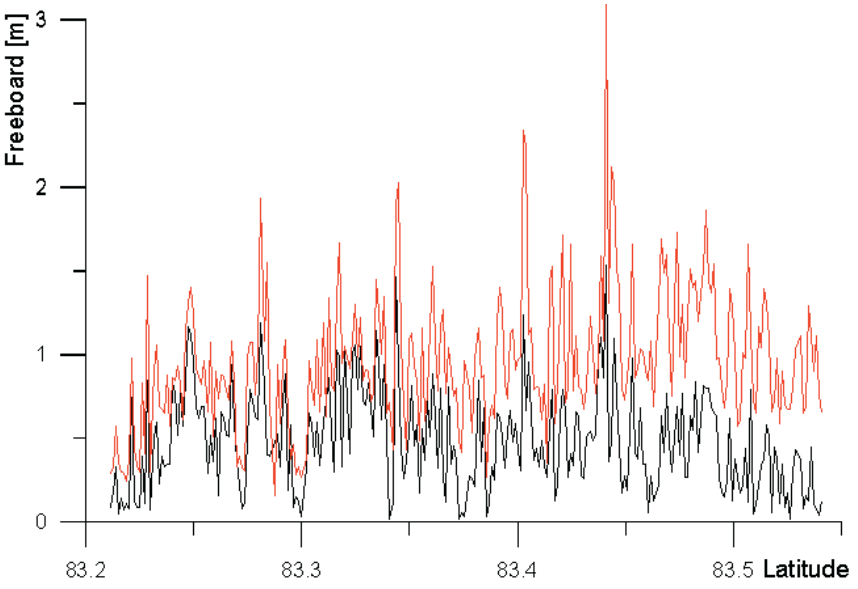

Figure 7. Comparison of ICESat freeboard heights (black) and averaged airborne lidar data (red) for the western subtrack. Due to lack of leads the ICESat values are biased.

5 ARCTIC OCEAN-WIDE SEA ICE FREEBOARD MAPS

The procedure described above to estimate the sea ice freeboards has been applied to two periods of ICESat data to estimate Arctic Ocean-wide sea ice freeboard maps. We have here used ICESat data from laser 1 release 18 (February 20 – March 29, 2003) and laser 2A release 21 (September 25 – November 18, 2003).

The above described technique to calculate the freeboards from laser altimetry has been applied to each ICESat track in a given period, taking the three lowest-levels averaged for each interval of 20 km. To reduce systematic errors, which might cause uncertainties in the measured ICESat heights, data has been rejected according to the threshold criteria listed in Table 1. In order to reduce the "trackiness" originating from differences in atmospheric sea level pressure (SLP) the altimeter data are corrected for the inverse barometer (IB) effect. This can be expressed as:

$$IB(mm) = \alpha \times (SLP - 1013 \cdot 3) \tag{2}$$

where the constant 1013.3 mbar represent the global mean sea level pressure calculated over the oceans, and the proportionality constant α is taken to be -13.1 mm/mbar (Kwok, pers. comm.). The sea level pressure (SLP) fields used here to obtain the IB correction for each ICESat sample is linearly interpolated from 6-hourly NCEP/NCAR reanalysis products (http://www.cdc.noaa.gov/). Spatial and temporal differences due to the IB effects are in the order of a few decimeters.

Table 1. Threshold criteria to reduce systematic errors, which might cause uncertainties in the measured ICESat heights.

Parameters	Threshold Criteria
Standard deviation of Gaussian fit to the waveform (S)	S < 60 mV
Reflectivity (R)	1 ≤ R ≤ 1
Ellipsoidal height of the altimeter measurements (h), geoid (N)	-1.5 m ≤ (h-N) ≤ 1.5 m

The resulting Arctic Ocean sea ice freeboard maps are plotted in Figure 8, together with backscatter maps obtained by SeaWinds ku-band scatterometer, QuikSCAT. Kwok (2004) have shown that high backscatter (σ > -14.5 dB) values obtained from ku-band scatterometer data correspond to multi-year sea ice, explained by enhanced volume scattering. Multi-year sea ice is defined by the World Meteorological Organization (WMO) to be ice thicker than 2 m. Thus, a high backscatter value in the QuikSCAT backscatter maps indicates areas with ice thicker than 2 m. In Figure 8 the ICESat estimated freeboards shows qualitatively the same features as in the backscatter data obtained from QuikSCAT, with thicker sea ice north of Greenland (with freeboards up to 1 m, corresponding to a sea ice thickness of 6 m), forced against the coast by the Beaufort Gyre, and thinner sea ice in the Russian Arctic.

In addition the ICESat freeboard maps show seasonal variations with winter conditions present in the laser 1 data set, represented by a large extent of sea ice, e.g. off the coast of east Greenland. Laser 2a represents fall conditions, just after the minimum extent of sea ice occurring in September. The freeboard map shows here much less ice, both in extent but also in freeboard heights, especially in the Siberian Arctic (Chukchi Sea).

6 CONCLUSIONS

The airborne underflight of ICESat shows that lowest-level filtering techniques for ICESat may produce a bias in the estimated sea ice freeboard heights, when compared to high-resolution airborne lidar measurements. We found a bias of approximately 35 cm in the region north of Greenland for a 10 km-resolution lowest-level filtering algorithm. We believe the bias is due to the lower spatial sampling of ICESat, with fewer points to hit the open leads, and also due to averaging the freeboard across the footprint. The smoothing features in ICESat was also seen in the comparison of the probability density functions, where thin ice, and ridges are absent in the ICESat data, but present in the laser scanner data. By modeling the high-resolution scanner data to match the ICESat footprint return, a fairly good correlation is found, and the short-wavelength ICESat features representing ridges and leads are mapped well in the modeled data.

Only very few cases of low reflectivity are found in the two ICESat sub-tracks, indicating that ICESat only picks up very few open or thin-ice leads to represent the lowest-levels. This information can be implemented in future sea ice thickness products based on ICESat data, where a combination of lowest-level estimation and reflectivity probably would give better results. The bias problem is expected to be less in other regions of the Arctic Ocean, where the ice is thinner and more leads are found.

We also used the lowest-level filtering method to analyse the ICESat data for 2003, and presented two Arctic Ocean-wide freeboard maps. The freeboard maps show thick ice (~6 m in thickness) north of Greenland with thinner ice classes in the Chukchi Sea, as well as seasonal variations. These conditions are consistent with the distribution of multi-year sea ice corresponding to high backscatter values obtained from QuikSCAT.

Future work should include a more accurate recovery of sea ice freeboards from ICESat. We believe that a combination of lowest-level filtering and reflectivity could be useful. More coincident airborne data in other parts of the Arctic would also be useful for a more detailed characterization of possible biases as a function of sea ice roughness and dynamics.

7 ACKNOWLEDGEMENTS

We thank B. Schutz, Univ. of Texas, for providing the ICESat orbit information. The ICESat data used for the airborne comparison were obtained from NASA-GSFC (D. Yi and J. Zwally). The 2003 ICESat data were obtained from NSIDC. L. Toudal, DTU, provided the Envisat SAR interferometry ice drift vectors for the ICESat tracks. NCEP/NCAR Reanalysis data were provided by the NOAA-CIRES Climate Diagnostics Center, Boulder, Colorado, USA, from their Web site at http://www.cdc.noaa.gov/ The QuikSCAT data were obtained from CERSAT, at IFREMER (France). Nynne S. Dalå and Sine M. Hvidegaard, DNSC, have contributed to the processing of the lidar data.

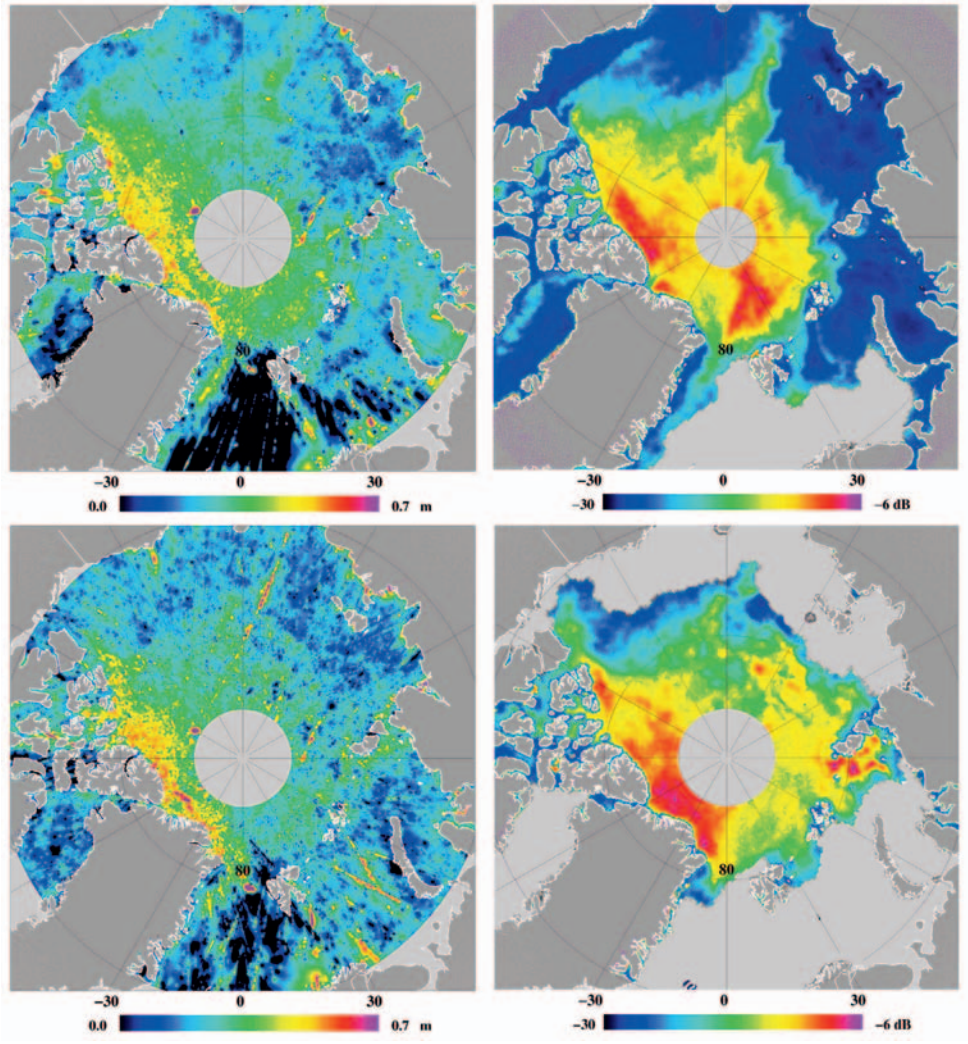

Figure 8. Left column: ICESat derived sea ice freeboards in the Arctic Ocean, upper image laser 1 February 20 – March 29, 2003 and lower image laser 2A September 25 – November 18, 2003. Right column: QuikSCAT backscatter maps for the Arctic Ocean with ocean mask (light grey), upper image February 21, 2003 and lower image October 15, 2003.

8 REFERENCES:

Dalå, N.S., R. Forsberg, K. Keller, H. Skourup, L. Stenseng, and S. M. Hvidegaard: Airborne lidar measurements of sea ice north of Greenland and Ellesmere Island 2004. GreenICE/SITHOS/CryoGreen/A76 projects, Final Report. Technical Report, Danish National Space Center, 2005.

Forsberg, R., K. Keller, S. M. Jacobsen: Airborne Lidar measurements for Cryosat validation. *Proc. IEEE IGARSS-2002*, Toronto, vol. III pp. 1756-1758, 2002.

Forsberg, R. and S. Kenyon: Gravity And Geoid in The Arctic Region – The Northern Polar Gap Now Filled. 6 pp., *Proc. GOCE Workshop*, ESA-ESRIN, March 2004.

Forsberg, R., and, H. Skourup: Arctic Ocean Gravity, Geoid and Sea ice Freeboard Heights from ICESat and GRACE. *Geophysical Research Letters*, 32, L21502, 2005.

Hvidegaard, S.M., and R. Forsberg: Sea ice thickness from airborne laser altimetry over the Arctic Ocean north of Greenland, *Geophysical Research Letters*, 29, no. 20, pp.1952-1955, 2002.

Kwok, R., G. F. Cunningham, H. .J. Zwally, and D. Yi: ICESat over Arctic sea ice: Interpretation of altimetric and reflectivity profiles. *Journal of Geophysical Research*, 111, L06006, 2006.

Kwok, R.: Annual cycles of multiyear sea ice coverage of the Arctic Ocean: 1999-2003. *Journal of Geophysical Research*, 109, C11004, 2004.

Kwok, R., H.J. Zwally, and D. Yi: ICESat observations of Arctic sea ice: A first look. *Geophysical Research Letters*, 31, L16401, 2004.

Zwally, H.J., B. Schutz, W. .Abdalati, J. Abshire, C. Bentley, A. Brenner, J. Bufton, J. Dezio, D. Hancock, D. Harding, T. Herring, B. Minster, K. Quinn, S. Palm, J. Spinhirne, and R. Thomas: ICESat's laser measurements of polar ice, atmosphere, ocean, and land. *Journal of Geodynamics*, 34, pp. 405-445, 2002.

Laxon , S., N. Peacock, and D. Smith, High interannual variability of sea ice thickness in the Arctic region, *Nature*, 425, 947-950, 2003.

On the use of helicopter-borne Radar Backscatter Polarization Ratio measurements at L-Band to estimate the ice thickness

Stefan Kern[1], Martin Gade[1], Christian Haas[2], Andreas Pfaffling[2], and Gerd Müller[3]
[1] *Centre for Marine and Atmospheric Research, Institute of Oceanography, Bundesstr. 53, 20146 Hamburg, Germany*
[2] *Alfred-Wegener Institute for Polar and Marine Research, Bussestr. 24, 27570 Bremerhaven, Germany*
[3] *Center for Marine and Atmospheric Research, Institute for Meteorology, Bundesstr. 55, 20146 Hamburg, Germany*

Keywords: Sea Ice, Remote Sensing, Arctic, Sea-Ice Thickness, Radar Backscatter

ABSTRACT: Climate warming makes an increasing thin-ice fraction likely to occur in the Arctic, underpinning the need for its regular observation. Synchronous helicopter-borne measurements of the sea-ice thickness and like-polarized radar backscatter carried out along identical flight tracks north of Svalbard, Arctic, during late winter 2003 are combined to develop an algorithm to estimate the thin-ice thickness solely from the radar backscatter co-polarization ratio at a frequency of 1 GHz (L-Band). The airborne ice thickness and co-polarization ratio data are smoothed along track to reduce noise, co-located and compared. A linear and a logarithmic fit are applied using thickness values between 0.0 and 0.6 m and 0.0 and 1.0 m, respectively. The thin-ice thickness is derived from the co-polarization ratio data using the above fits, first for dependent data, i.e. those used to obtain the fits, and subsequently for independent data. The results are compared to airborne ice thickness measurements for ice-thickness values between 0.0 and 0.6 m using linear regression. The logarithmic fit gives the most reliable results with a correlation of 0.72, and a RMS-difference of 8 cm. It offers the potential to get an estimate of the thickness of thin ice (below 40-60 cm thickness) from airborne measurements of the radar backscatter co-polarization ratio at L-Band with an uncertainty of about 10 cm.

1 INTRODUCTION

Satellite observations indicate a decrease in Arctic sea ice extent, particularly at the end of summer (Cavalieri et al., 2003; Stroeve et al., 2005), and a decrease in the sea-ice thickness (Rothrock et al., 1999; Rothrock and Zhang, 2005). Numerical models predict a further decrease of the summer Arctic ice extent due to a longer melt period (up to an almost complete loss) while it will remain nearly unchanged during winter (ACIA, 2004). Consequently, the seasonal ice cover can be expected to become thinner, and an increase of the thin-ice fraction is likely to occur in the near future. This is important for the winter-time ocean-atmosphere energy exchange in ice-covered regions, which is largest over leads and polynyas, where open water and thin ice are abundant; it is in particular sensitive to the thickness of the thin ice. The sea-ice thickness can be obtained from measurements from various platforms, e.g., satellite observations in the visible, infrared (IR) and microwave frequency range (radiometry, radar and laser altimetry), upward looking sonar (ULS) either from a mooring or from a submarine, and from airborne and in-situ observations (e.g. Yu and Lindsay, 2003; Rothrock et al., 2003; Laxon et al., 2003; Kwok et al., 2004; Haas, 2004). But, except for in-situ and some airborne measurements, quantities such as the snow depth have to be assumed in order to obtain the ice thickness from the observed draft or freeboard - a major limitation (Kwok et al., 2004). Moreover, typical values of thin-ice draft (a few to

about 25 centimetres) or freeboard (a few millimetres to centimetres) lie within the error range of the used sensors. An alternative is to combine satellite observations with numerical models. This requires a high accuracy of model input data (e.g. air temperature), good availability and high quality of satellite data (e.g. fine spatial resolution), and the ability to unambiguously identify thin ice (e.g. Yu and Lindsay, 2003; Drucker et al., 2003). Another way is to use only remote sensing data. Attempts to obtain the thin-ice thickness from airborne radar imagery have been made, e.g., by Kwok et al. (1995), and Wakabayashi et al. (2004). They utilize a neural network trained with radar backscatter measurements obtained at L- and C-Band using a fully polarimetric Synthetic Aperture Radar (SAR) and coincident IR-temperature observations, and a simple empirical relationship between ULS observed ice thickness and the radar backscatter co-polarization ratio at L-Band, respectively. Approaches, which are similar to the one of Wakabayashi et al. (2004), were made by Matsuoka et al. (2002) and Nakamura et al. (2005), who used cross-polarized radar backscatter observations at L-Band and the radar backscatter co-polarization ratio at X-Band, respectively. Dierking et al. (2003) suggested that the classification of different types of thin ice and the retrieval of its thickness could benefit from using fully polarimetric data. However, although encouraging, these attempts reveal very different values for the maximum obtainable ice thickness: 10 to 100 cm. In this article, synchronous measurements carried out by two helicopter-borne sensors, an electromagnetic (EM) induction ice-thickness sounder (EM-Bird) and a multi-frequency, multi-polarization scatterometer (HELISCAT) are combined to form a unique data set to estimate the thickness of thin ice similar to the approach of Wakabayashi et al. (2004).

2 BACKGROUND

The HELISCAT is a helicopter-based microwave scatterometer operating at frequencies of 1.0 GHz, 2.4 GHz, 5.3 GHz, 10.0 GHz, and 15.0 GHz (L, S, C, X, and Ku band, respectively). It permits us to measure the radar backscatter quasi-simultaneously at the above frequencies at all like- and cross-polarizations from 50-150 m altitude. The HELISCAT uses a single broadband 96 cm parabolic dish antenna both for transmission and reception. The antenna is aft-looking and can be tilted during the flight from 23° to 65° nominal incidence angle (Gade et al., 1998; Wismann et al., 1998). HELISCAT data are complemented by the helicopter's pitch and roll measured by a gyro, CCD-camera imagery of the antenna's footprint on the ground, GPS, and handheld digital photography. Data used in this paper were acquired from an altitude of 65 m at an incidence angle of 40°, resulting in a footprint size at L-Band of 20 m x 27 m (+/- 5 to 10 m due to variations in altitude and incidence angle during the flight) and at Ku-Band of 1.3 m x 1.7 m. The average flight speed was 30-35 m/s. Time series of the HELISCAT measurements at each frequency band were sampled at 10 kHz. Subsequently, Döppler spectra (of length 1000) were calculated and the integral of the spectral Döppler peak was integrated within its 6 dB limits with a sample rate of 10 Hz (time step of 0.1 s). The instrumental noise was calculated from a part of the spectrum well off the Döppler peak with the same sample rate, and was used to obtain the signal-to-noise (SNR) ratio. This paper focuses on observations at L-Band, because its long wavelength promises the largest penetration depth into thin ice and therefore a maximum obtainable thickness.

The EM-Bird is a purpose built, small, lightweight sea-ice thickness profiler used operationally since 2001 at the Alfred-Wegener Institute for Polar and Marine Research, Bremerhaven (AWI). It is a 3.5 m long, 100 kg towed sensor suspended 20 m below a helicopter and operated at heights of 10 to 20 m above the ice surface. In short, the EM Bird

consists of an assembly of coils for the transmission and reception of low-frequency electromagnetic fields (3.69 and 112 kHz) and a laser altimeter. While the EM system is sensitive to the sensor's height above the conductive sea water, the sensor's altitude above the ice surface is determined with the laser altimeter. Over sea ice, the water surface coincides with the ice underside. Therefore, the difference of the height measurements of both components corresponds to the ice-plus-snow thickness. The method is calibrated over open water, where ice thickness is known to be zero. On a point-by-point basis, the estimates of the ice thickness agree within +/- 0.1 m with drill-hole data, whereas statistically determined level ice thickness can reach accuracies in the cm range (Pfaffling and others, 2004). However, due to the diffusive nature of the low-frequency EM induction field, its strength represents some average thickness of an area of two to four times the instrument's altitude above the ice surface, i.e. of an area of 30 to 80 m diameter. Due to this "footprint", maximum ridge thickness can be underestimated by as much as 50% in the worst cases, depending on the geometry and consolidation of the ridge keel (Reid and others, 2005).

During the expedition ARK XIX/1 of the R/V Polarstern (Feb. 28 – Apr. 24, 2003, (Schauer and Kattner, 2004)), sea-ice and snow properties and distributions were observed north of Svalbard in-situ and by helicopter-borne laser-altimetry, video imagery, EM surveying and scatterometer measurements. Ice conditions were characterized by vast multiyear ice floes, intersected by regions of first-year ice. Thin and first-year ice formed in prominent, long and wide leads extending from the Northwest towards the ice edge in the Southeast, as a result of shear and divergence in the marginal ice zone (see Figure 1 a). On April 19, 2003, a tandem flight of the EM Bird and the HELISCAT was carried out revealing a unique combination of data from both instruments. The synchronous flight was conducted using two helicopters, one towing the EM-Bird at 50 ft height immediately followed by the second one along the same track carrying the HELISCAT at 150-200 ft altitude. In order to reduce the scatter inherent in the data due to small-scale sea-ice heterogeneities and instrument noise both time series are smoothed spatially along the flight track with a running mean. A window width of 150 m (50 data points) turned out to effectively remove outliers and scatter while keeping the spatial resolution at a reasonable level to resolve major leads. Only HELISCAT data (at L-Band) with a SNR above 20 dB are used (see Kern et al., 2006).

Figure 1 shows the location of the tandem flight in Fram Strait together with the sea ice situation as observed by the Advanced Very High Resolution Radiometer (AVHRR) aboard NOAA-17 at channel 1 on April 20, 2003, 12:46 UTC (panel a), and the sea-ice thickness as measured by the EM-Bird during the tandem flight on April 19, 2003, at about 17 UTC (panel b) – together with a zoom of the same AVHRR image. In order to demonstrate the sea-ice dynamics in our region of interest, the AVHRR image in panel a) is superposed with the track of two ARGOS drift buoys (ID 20755 and 20811) between the time of the tandem flight and the acquisition of the AVHRR image. The total displacement during this time period is about 10 km. Although the track of the tandem flight superposed on the AVHRR image in Figure 1 b) has been corrected for this drift, the agreement between areas of low ice thickness as measured by the EM-Bird and low albedo values observed by the AVHRR, which indicate also thinner ice or open water, is not convincing. This can be explained by several factors: leads observed during the tandem flight could have closed, new ones could have opened, the ice could have gained in thickness, which causes albedo values similar to the surrounding thick ice, and frost flowers could have developed causing a similar albedo increase; all is likely to occur under the observed north-easterly cold air flow. This underlines that the combination of HELISCAT measurements with the ice thickness

measured by the EM-Bird is indeed unique and that this dataset forms an ideal basis to investigate the relationship between the ice thickness and radar backscatter measurements.

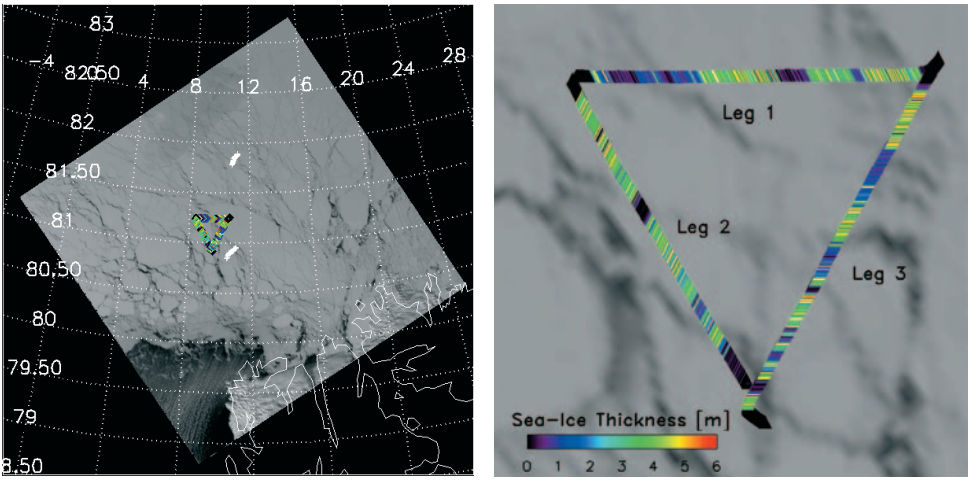

Figure 1. a) AVHRR-NOAA17 image of the broadband albedo (channel 1) obtained north of Svalbard on April 20, 2003, 12:46 UTC. The red star marks the position of the R/V Polarstern, the coloured triangle marks the flight track of the helicopters (see b). Lines of white plus signs mark the sea ice drift measured by ARGOS buoys 20755 and 20811 between the helicopter flights (at about 17 UTC, April 19, 2003) and AVHRR image acquisition. b) Sea-ice thickness measured by the EM-Bird during this tandem flight; initial flight direction from the Polarstern (see red star) was to the west, i.e. to the left. Black areas at the beginning and end of each leg can be interpreted as missing data.

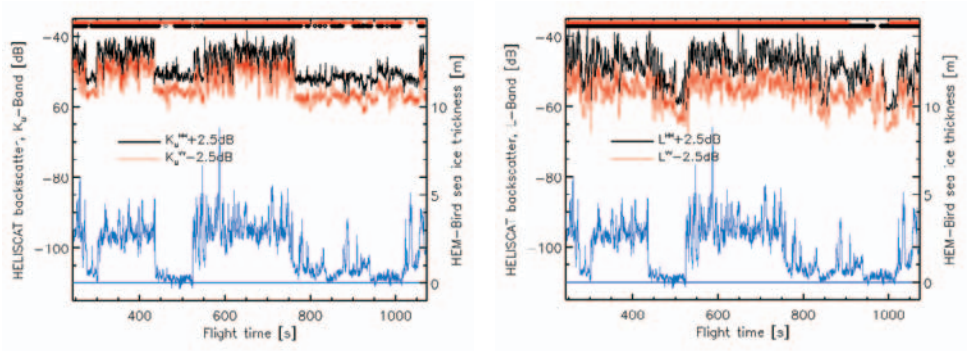

Figure 2. EM-Bird ice thickness (blue) and HELISCAT Ku-Band (a) and L-Band (b) relative radar backscatter values along a part of leg 1 of the tandem flight (see Figure 1 b); only the values obtained at like-polarization shown are (HH: black, VV: red) offset by p lus / minus 2.5 dB relative to measured values for better visibility. Gaps in the line of diamonds at the top indicate where the SNR falls below 5 dB at Ku-Band (a) and below 20 dB at L-Band (b).

Figure 2 shows a comparison between the co-located time series of EM-Bird ice-thickness measurements and the relative radar backscatter measured by the HELISCAT at L-Band and Ku-Band, HH- and VV-polarization, along the same track along leg 1 (Figure 1 b). Figure 2 a) reveals clearly the expected decrease in radar backscatter at Ku-Band between multiyear ice, which can be easily identified by its thickness of around three meters as measured by the EM-Bird, and first-year or young ice. This decrease is also evident in Figure

2 b) for L-Band but is less clearly defined due to the smearing of the radar backscatter values because of the considerably larger footprint at L-Band compared to Ku-Band.

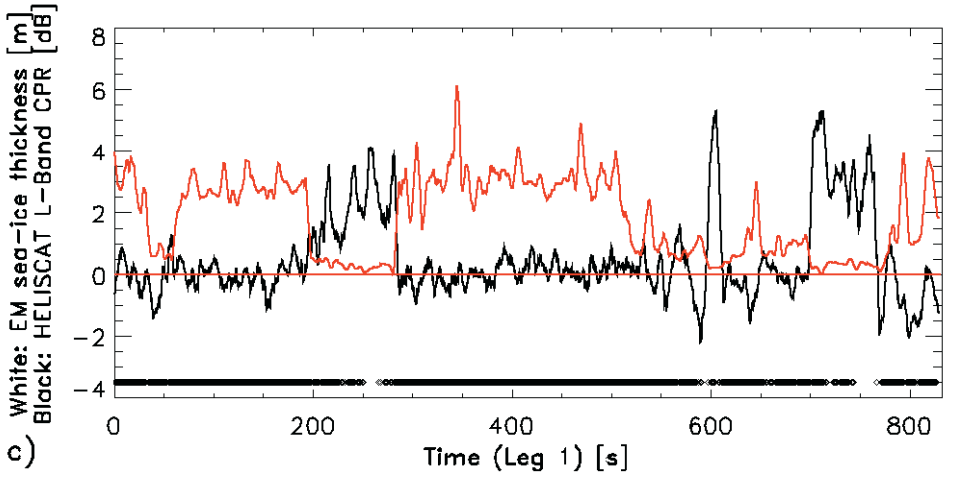

Figure 3. EM-Bird ice thickness (black) and HELISCAT radar backscatter co-polarization ratio at L-Band (red) along leg 1 (Figure 1 b) - averaged over 150 m. Gaps in the line of diamonds at the bottom indicate a SNR below 20 dB.

Figure 3 shows the radar backscatter co-polarization ratio (radar backscatter at VV-polarization divided by the one at HH-polarization) obtained from HELISCAT measurements at L-Band along leg 1 (Figure 1b), averaged over 150 m (see previous section and Kern et al., 2006 for further details). Changes in the observed like-polarized radar backscatter at L-Band take values of up to 15 dB between thin ice and multiyear ice. This agrees with earlier observations, e.g. by Rignot and Drinkwater (1994). The obtained radar backscatter co-polarization ratio at L-Band takes values around zero decibels for multiyear ice and thick first-year ice and increases to values up to five decibels over thin ice or to even higher values over open water. This is also in agreement with earlier observations, e.g. Wakabayashi et al. (2004).

3 THIN-ICE THICKNESS ESTIMATION METHOD

Radar backscatter measurements carried out in the laboratory over thin saline ice (e.g. Nghiem et al., 1997) reveal low like-polarization radar backscatter values, which increase with thickness during initial growth above a threshold thickness of about three centimetres (by about 6-10 dB at L- and C-Band). However, single polarization radar backscatter values can change not only because of changes in ice thickness but also due to a change in the degree of deformation of the ice or due to changes in the surface or near-surface properties (Onstott, 1992). Therefore it might be difficult to associate a change in the single polarization radar backscatter uniquely to a change in ice thickness. Onstott (1992) and Wakabayashi et al. (2004) showed a decrease of the radar backscatter co-polarization ratio with increasing thickness of thin ice below a certain threshold thickness, and that this decrease is particularly pronounced at large incidence angles, i.e. above 40°. This can be explained by changes in surface/near-surface backscattering characteristics of thin saline ice during its growth, causing the radar backscatter to increase – especially at horizontal polarization. This behavior

can be used to derive the sea-ice thickness – however, only below a threshold ice thickness, which is determined by the surface roughness, the bulk salinity, the vertical salinity profile, and the liquid fraction of the ice. An approach similar to the one of Wakabayashi et al. (2004) was developed, which uses a simple empirical relationship between EM-Bird ice thickness and HELISCAT L-Band radar backscatter co-polarization values obtained simultaneously along the same flight track (Figure 3) to derive the thin-ice thickness solely from this ratio (Kern et al., 2006).

Our analysis of co-located EM-Bird thickness measurements and HELISCAT radar backscatter co-polarization ratio (RBCOPR) observations indicates that this ratio tends to take values typical for multiyear ice or thick first-year ice above a thickness of approximately 0.6 m. This ratio increases towards values close to six decibels for thickness values approaching zero. By using a logarithmic fit applied to the scatterplot of the ice thickness observed by the EM-Bird and the RBCOPR obtained from HELISCAT measurements at L-Band:

$$D_h = b_0 + \left(\log\left(RBCOPR\right) \times b_1 + 0 \cdot 02\right) + \left|\log\left(0 \cdot 02\right)\right| \times \left(-b_0\right) / \left(\left|\log\left(0 \cdot 02\right)\right| + \left|\log\left(b_2\right)\right|\right) \quad (1)$$

The radar backscatter co-polarization ratio (RBCOPR) values can be inverted into the ice thickness. DH is the HELISCAT derived ice thickness, and b0= 1.0, b1= 0.7, and b2 = maximum RBCOPR value are the coefficients of the logarithmic fit. A simple linear fit was also applied in order to investigate the need for the logarithmic approach given above (see Kern et al., 2006 for details). The two fits were derived and optimised using data of leg 1 and subsequently applied to data of all legs (Figure 1 b).

4 RESULTS AND DISCUSSION

Figure 4 presents the thin-ice thickness estimated from the radar backscatter co-polarization ratio obtained from HELISCAT measurements at L-Band (SNR > 20 dB, averaging window: 150 m) using the linear (a, c) and the logarithmic (b, d) fit. Figure 4 (a, b) show the results of the thickness estimation for leg 1, i.e. using dependent data. Figure 4 (c, d) show the results of this estimation for leg 3, i.e. using independent data. Table 1 summarizes the results of regression analyses of HELISCAT derived and EM-Bird observed ice thickness for the tandem flight (see Figure 1 b) together with the correlation between both datasets (assuming a linear relationship) and the standard deviation of the mean thin-ice thickness of the range 0.0 to 0.6 m.

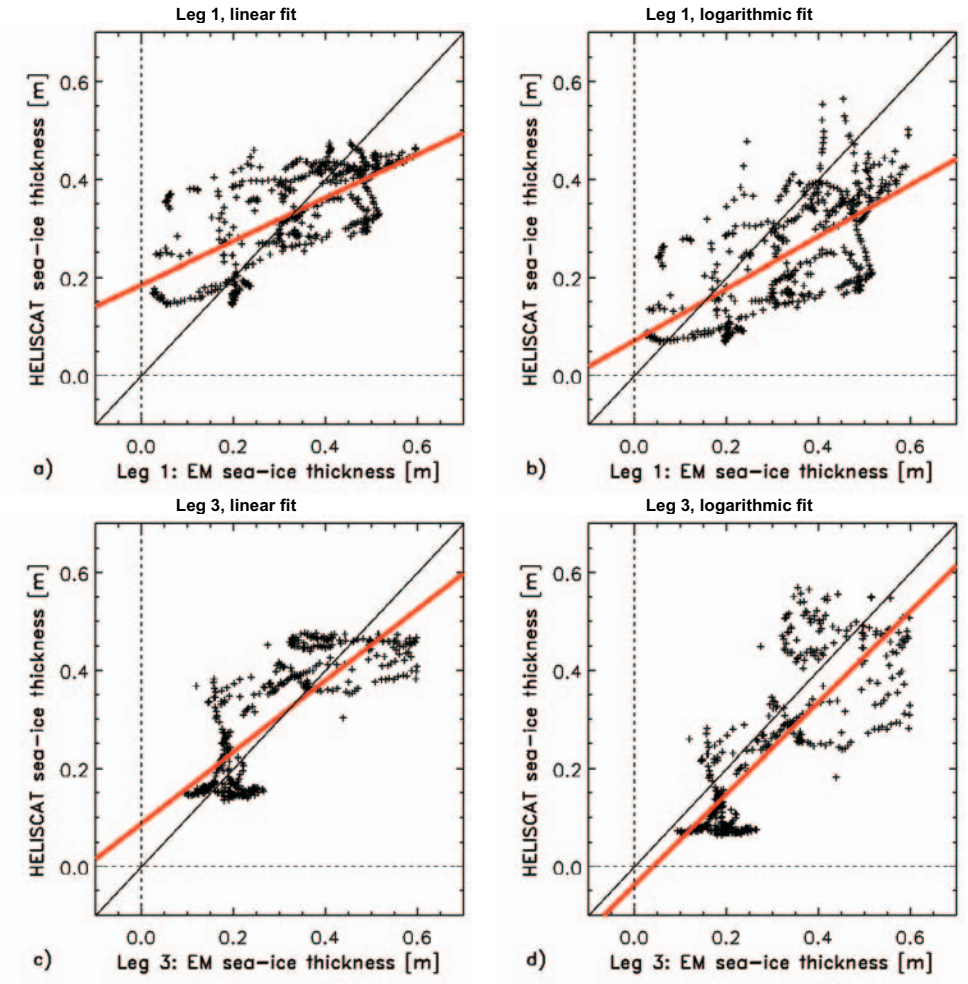

Figure 4. HELISCAT derived vs. EM-Bird observed ice thickness for leg 1 (top) and leg 3 (bottom) using an averaging window of 150m and a SNR > 20 dB; the used fits are derived from data of leg 1. Panel a) shows the thickness for leg 1 using the linear fit, b) is for leg 1 using the logarithmic fit, c) and d) are for the independent data of leg 3 using the linear and the logarithmic fit, respectively. Red lines denote the linear regression between each of the shown thickness data sets. Thin black diagonals denote perfect agreement.

Table 2. Comparison between the ice thickness derived from HELISCAT data and EM-Bird measurements for thickness values between 0.0 and 0.6 m for the logarithmic (top) and the linear (bottom) fit. Given are the number of involved data pairs, correlation, RMS-difference and intercept for the regression between the derived and the measured thickness, and, standard deviation (SD) of the mean derived and the mean measured thickness.

Fit	Number of Data Pairs	Correlation	RMS-Difference [m]	Intercept [m]	SD of mean thickness [m]	
					derived	measured
Logarithmic	1729	0.723	0.08	0.06	0.13	0.13
Linear	1729	0.724	0.07	0.17	0.10	0.13

HELISCAT derived and EM-Bird observed ice thickness are in reasonable agreement with each other within the uncertainties given by the two sensors involved: about +/- 0.05 m for EM-Bird measurements averaged over a reasonable number of single measurements, and +/- 0.14 m for the radar backscatter co-polarization ratio at L-Band. Correlations are similar for the linear (0.724) and the logarithmic fit (0.723). The RMS-difference of the regression (for thickness values between 0.0 and 0.6 m) between HELISCAT derived and EM-Bird observed ice thickness is similar for both fits, while the intercept of the regression line is substantially higher for the linear fit: 0.17 m compared to 0.06 m. The standard deviation of the mean HELISCAT derived ice thickness is in closer agreement to the measured ice-thickness variability for the logarithmic fit. Because of this and because the achieved intercepts are substantially lower (compare e.g. Figure 4 a) and b)), we suggest that a logarithmic fit is indeed required to get ice-thickness estimates from the L-Band radar backscatter co-polarization ratio (RBCOPR). This agrees with earlier findings about the relationship between the RBCOPR and the thickness of thin ice (e.g. Onstott, 1992; Wakabayashi et al., 2004).

Our maximum obtainable thickness seems to be around 50 cm, which agrees to some extent with the findings of Wakabayashi et al. (2004, see their Fig. 11b). They used an airborne fully polarimetric L-Band SAR (Pi-SAR, spatial resolution: 3 m) to observe sea-ice radar backscatter in the Sea of Okhotsk just north of Hokkaido. They averaged the RBCOPR at L-Band (calculated from the scattering matrix) over grid cells of 20 m x 20 m size with a sampling distance of 10 m along a track, which is given by ice draft and drift observed by a moored ULS. These draft measurements were combined with the RBCOPR (time difference less than 10 h), both averaged along 100 m intervals, in order to obtain an empirical fit used to map the ice thickness from the Pi-SAR L-Band observations (Wakabayashi et al., 2004). The main difference between their and our approach is, among differences in the instrumentation, that we benefit from quasi-simultaneous (within seconds) measurements of ice thickness and radar backscatter along the same flight track and thereby keep such errors in the developed fit functions to estimate the ice thickness at a minimum, which result from a time difference between the two involved data sets.

The HELISCAT measurements were carried out at an incidence angle of 40°. Owing to the fact that the RBCOPR change per unit change in thin-ice thickness (1 cm) is larger at higher incidence angles than at low ones, our approach could be improved using radar backscatter measurements carried out at larger incidence angles. However, an important drawback of larger incidence angles is that the radar backscatter of level surfaces is closer to the noise level compared to smaller incidence angles. Another improvement would be to enhance the accuracy of the independent ice-thickness measurements involved to develop the fit function, particularly for very thin ice, for which the accuracy of the EM-Bird measurements decreases. Such an improvement could be to additionally calculate the thin-ice thickness via the heat-flux method of Drucker et al. (2003) using simultaneous IR-temperature measurements as obtained, e.g. by AVHRR. However, due to the coarse (compared to HELISCAT or SAR data) spatial resolution of this data, such an attempt would only make sense for large thin ice areas such as observed in the vicinity of large-scale polynyas (Ross Sea Polynya), or in the Sea of Okhotsk, and of course at the beginning of the freezing season. Again, it has to be stressed that the time difference between the involved data sets has to be small enough to keep changes in the ice properties due to drift or melt/freeze events at a minimum level.

Kwok et al. (1995) noted that a highly saline brine skim could be present particularly on very thin ice (below 10 cm). Such a skim is responsible for the high co-polarization values observed here. However, when the thin ice becomes covered with snow, already a layer of a few millimetres thickness would be sufficient to destroy this skim, the co-polarization ratio would decrease and consequently the ice thickness would be overestimated. A natural step to avoid this error source using our data would be to include the simultaneous video imagery in the analysis by classifying the thin ice into bare and snow/slush covered and develop the approach separately for different thin-ice classes.

So three main shortcomings can be identified: a) the possible influence of any change in the surface properties (snow, water, slush, frost flowers, …), b) the possible deterioration of the radar backscatter signal when looking at a shallow incidence angle at a very smooth surface such as level bare thin ice, and c) the need for simultaneous independent ice thickness estimates in order to develop and tune the approach for different regions and seasons.

5 CONCLUSIONS

The relationship between sea-ice thickness and like-polarized L-Band radar backscatter has been investigated by synchronous helicopter-based measurements carried out north of Svalbard, Arctic, in April 2003, during a tandem flight of an electromagnetic (EM) induction ice-thickness sounder (EM-Bird), and a multi-frequency, multi-polarization scatterometer (HELISCAT). These are combined to derive a method to estimate the thickness of thin ice solely from L-Band radar backscatter co-polarization ratio (RBCOPR) data. Co-located EM-Bird thickness observations and the L-Band RBCOPR from HELISCAT are compared after smoothing with a 150 m running mean along track. A linear and a logarithmic fit are applied to the scatterplots of the two data sets. These fits are used to infer the thickness of thin ice (below about 60 cm) from dependent (i.e. used to obtain the fits) and independent L-Band RBCOPR data obtained by HELISCAT. Subsequently, the HELISCAT derived and the EM-Bird observed ice thicknesses are compared for values below 60 cm using a linear regression. The logarithmic fit turned out to give the most reliable results: correlation 0.72, intercept of regression 6 cm, RMS-difference 8 cm.

We stress here, however, that the approach can only be applied to thin ice, i.e., below about 50 cm thickness, and that the role that snow, slush, or frost flowers may have on the retrieval needs still to be investigated. Consequently, the next step is to apply the method to other HELISCAT data obtained during ARK XIX/1 or forthcoming campaigns to further test the method. This should be done particularly with regard to the presence of snow, slush, or frost flowers and also with regard to the temperature-dependent liquid water fraction of the thin ice, as can be measured, e.g. using the approach suggested by Notz et al. (2005), because of the influence on the dielectric properties and roughness of the ice surface. In this context, it is essential to numerically model the radar backscatter of thin ice for large incidence angles (above 40°) for the frequency range 1-15 GHz, HH, VV, and HV-polarization with particular emphasis on the influence of snow, slush, and/or frost flowers, building on the experience of earlier studies (e.g. Nghiem et al., 1997).

The launch of ALOS-PALSAR in early 2006 will provide space-borne L-Band data to which our method could be applied after some modification - provided that the RBCOPR will be available from this sensor and that requirements regarding the SNR and the incidence angle will be met. Moreover, TerraSAR-X is scheduled for launch in 2006 as well. Data of these two sensors in conjunction with observations carried out by RADARSAT-2 SAR and

Envisat ASAR at C-Band might open the opportunity to obtain estimates of the thickness of thin ice on a regular basis or might at least allow us to investigate the potential of using data of these sensors in more detail – independent of weather, daylight, and limitations of numerical models.

6 ACKNOWLEDGEMENTS

This work was supported by the German Science Foundation (DFG): Me-487/40-1, SFB 512–E1, and the European Union via EVG1-CT-2000-00029 (MARSAIS) and EVK2-CT-2002-00146 (SITHOS). The authors wish to thank the crew of the R/V Polarstern, the helicopter team, and J. Lieser, S. Willmes, and T. Martin. Provision of AVHRR data by NOAA's Comprehensive Large Array-Data Stewardship System (CLASS) is also greatly acknowledged.

7 REFERENCES

ACIA, Impacts of a Warming Arctic: Arctic Climate Impact Assessment, Cambridge University Press, 2004, http://www.acia.uaf.edu.

Cavalieri, D.J., C.L. Parkinson, and K.Y. Vinnikov, 2003: 30-Year satellite record reveals contrasting Arctic and Antarctic decadal sea ice variability. *Geophys. Res. Lett.*, 30(18), 1970, doi:10.1029/2003GL018031.

Dierking, W., H. Skriver, and P. Gudmandsen, 2003: On the improvement of seai classification by means of radar polarimetry. *Proc. Workshop on SAR Polarimetry for Sea Ice Classification*, ESA-ESRIN, Frascati, Italy, ESA-SP-529.

Drucker, R., S. Martin, and R. Moritz, 2003: Observations of ice thickness and frazil ice in the St. Lawrence Island polynya from satellite images, upward looking sonar, and salinity/temperature moorings. *J. Geophys. Res.*, 108(C5), 3149, doi: 10.1029/2001JC001213.

Gade, M., W. Alpers, H. Hühnerfuss, V. Wismann, and P.A. Lange, 1998: On the reduction of the radar backscatter by oceanic surface films: scatterometer measurements and their theoretical interpretation. *Rem. Sens. Environ.*, 66, 52-70.

Haas, C, 2004: Late-summer sea ice thickness variability in the Arctic Transpolar Drift 1991-2001 derived from ground-based electromagnetic sounding. *Geophys. Res. Lett.*, 31, L09402, doi:10.1029/2003GL019394.

Kern, S., M. Gade, C. Haas, and A. Pfaffling, 2006: Retrieval of thin-ice thickness using the L-Band polarization ratio measured by the helicopter-borne Scatterometer HELISCAT. *Annals of Glaciology*, accepted.

Kwok, R., S.V. Nghiem, S.H. Yueh, and D.D. Huyngh, 1995: Retrieval of thin ice thickness from multi-frequency polarimetric SAR data, *Rem. Sens. Environ.*, 51, 361-374.

Kwok, R., H.J. Zwally, and D. Yi, 2004: ICESat Observations of Arctic sea ice: A first look. *Geophys. Res. Lett.*, 31, L16401, doi:10.1029/2004GL020309.

Laxon, S. N. Peacock, and D. Smith, 2003: High interannual variability of sea ice thickness in the Arctic Region. *Nature*, 425, 947-950.

Matsuoka, T., S. Uratsuka, M. Satake, A. Nadai, T. Umehara, H. Maeno, H. Wakabayashi, F. Nishio, and Y. Fukamachi, 2002: Deriving sea-ice thickness and ice types in the Sea of Okhotsk using dual-frequency airborne SAR (Pi-SAR) data, *Annals of Glaciology*, 34, 429-434.

Nakamura, K., H. Wakabayashi, K. Naoki, F. Nishio, T. Moriyama, and S. Uratsuka, 2005: Observation of sea-ice thickness in the Sea of Okhotsk by using dual-frequency and

fully polarimetric airborne SAR (Pi-SAR) data. *IEEE Trans. Geosci. Rem. Sens.*, doi: 10.1109/TGRS.2005.853928.

Notz, D., J.S. Wettlaufer, and M.G. Worster, 2005: A non-destructive method for measuring the salinity and solid fraction of growing sea ice in situ. *J. Glaciology*, 51(172), 159-166.

Nghiem, S.V., R. Kwok, S.H. Yueh, A.J. Gow, D.K. Perovich, J.A. Kong, and C.C. Hsu, 1997: Evolution in polarimetric signatures of thin saline ice under constant growth. *Radio Sci.*, 32(1), 127-151.

Onstott, R.G., SAR and Scatterometer Signatures of Sea Ice. 1992. In: Carsey, F.D., ed., *Microwave Remote Sensing of Sea Ice*. Washington, DC, American Geophysical Union, 73-104. (Geophysical Monograph Series 68.).

Reid, J., A. Pfaffling and J. Vrbancich, 2005: Airborne electromagnetic footprints in one-dimensional earths. *Geophysics*, in press.

Pfaffling, A., C. Haas, and J. Reid, 2004: Empirical inversion of HEM data for sea ice thickness mapping: Extended abstracts, *10th European Meeting of Environmental and Engineering Geophysics (EAGE`s Near Surface 2004)*, Utrecht, The Netherlands, A037.

Rignot, E. and M.R. Drinkwater, 1994: Winter sea-ice mapping from multi-parameter synthetic-aperture radar data. *J. Glaciol.*, 40(134), 31-45.

Rothrock, D.A., Y. Yu, and G.A. Maykut, 1999: Thinning of the Arctic sea-ice cover. *Geophys. Res. Lett.*, 26(23), 3469-3472.

Rothrock, D.A., J. Zhang, and Y. Yu, 2003: The Arctic ice thickness anomaly of the 1990s: A consistent view from observations and models. *J. Geophys. Res.*, 108(C3), 3083, doi: 10.1029/2001JC001208.

Rothrock, D.A., and J. Zhang, 2005: Arctic Ocean sea ice volume: What explains its recent depletion? *J. Geophys. Res.*, 110, doi :10.1029/2004JC002282.

Schauer, U. and G. Kattner, 2004: The Expedition ARKTIS XIX/1 a, b and XIX/2 of the Research Vessel POLARSTERN in 2003, *Reports on Polar and Marine Research*, 481.

Stroeve, J.C., M.C. Serreze, F. Fetterer, T. Arbetter, W. Meier, J. Maslanik, and K. Knowles, 2005: Tracking the Arctic's shrinking ice cover: Another extreme September minimum in 2004. *Geophys. Res. Lett.*, 32, L04501, doi: 10.1029/2004GL021810.

Wakabayashi, H., T. Matsuoka, K. Nakamura, and F. Nishio, 2004: Polarimetric characteristics of sea ice in the Sea of Okhotsk observed by airborne L-Band SAR. IEEE Trans. *Geosci. Rem. Sens.*, 42(11), 2412-2425.

Wismann,V., M. Gade, W. Alpers, and H. Hühnerfuss, 1998: Radar signatures of marine mineral oil spills measured by an airborne multi-frequency multi-polarization microwave scatterometer. *Int. J. Rem. Sens.*, 19, 3607-3623.

Yu, Y., and R.W. Lindsay, 2003: Comparison of thin ice thickness distributions derived from RADARSAT Geophysical Processor System and advanced very high resolution radiometer data sets. *J. Geophys. Res.*, 108(C12), 3387, doi :10.1029/2002JC001319.

Satellite Thermal Microwave Sea Ice Concentration Algorithm Comparison

Søren Andersen[1*], Rasmus T. Tonboe[1] and Lars Kaleschke[2]
[1] *Center for Ocean & Ice, Danish Meteorological Institute, Lyngbyvej 100, DK-2100 Copenhagen Ø, Denmark*
[2] *University of Hamburg, Center of Marine and Atmospheric Research (ZMAW), Institute of Oceanography (IfM), Germany*

Keywords: Sea ice concentration, radiometer algorithms, sea ice surface emissivity and temperature, sea ice extent and area trends

ABSTRACT: Seven of the most common radiometer algorithms, used to compute the sea ice concentration, are compared to ScanSAR data estimates of ice concentration. Our focus is on the near 100% ice cover in winter. The sensitivity of the algorithms to the variable sea ice surface emissivity and temperature is the most significant hindrance for correct estimates of ice concentration in this ice regime. The skill of the best radiometer algorithms is significantly better than the worst set, but all correlate poorly to and display higher variability than the SAR data at high ice concentrations. On a climatological time scale the differences between algorithms amounts to 14% and 22% of the down-going trend in winter Arctic sea ice extent and area, respectively. The climatological changes in atmospheric and water surface emissivity primarily affects the extent trend while the changes in sea ice surface emissivity affects the sea ice area trend.

1 INTRODUCTION

The use of thermal microwave data for mapping the sea ice extent and area is perhaps the most successful application of satellite remote sensing for sea ice monitoring. Today time-series, covering the arctic regions daily from the early 1970s, are most significant for estimating inter-annual and decadal trends in this important climate parameter. Applications also include climate oriented coupled general circulation and numerical weather prediction models. These data are important input to numerical sea ice models where the ice thickness is estimated. Ice concentration is not directly linked with ice thickness, but the minimum ice extent in summer is a measure of the amount of thick multiyear ice. The reduction over the past decades in the multiyear ice extent is an indication of an ongoing climate change process that affects the ice thickness as well.

> *"…a thick slab of arctic pack ice reduces the wintertime sensible heat loss from ocean to atmosphere by a factor of 100 to 1000, compared to fluxes from open water." (Moritz, 1988, p. 1).*

Even small changes in the sea ice concentration thus have a significant impact on energy fluxes between the ocean and the atmosphere, i.e. a change from 100% to 99% may double the fluxes. Once sea ice cover the ocean surface, the impact of ice thickness on heat flux is relatively small. From a climate change perspective, the key question is how fast the total volume of sea ice is changing. This requires reliable estimates of ice concentration for the derivation of the sea ice area. Therefore, ice concentration is an important ice cover

[*] Email: san@dmi.dk, Tel.:+45 39 15 75 00, Fax.: +45 39 15 73 00.

parameter and must be estimated accurately (Steffen & Schweiger, 1991). The Mean accuracy of some of the more common algorithms, used to compute ice concentration from SSM/I data, such as NASA Team (Cavalieri et al., 1984) and Bootstrap (Comiso, 1986) are reported to be 1-6 % in winter (Steffen & Schweiger, 1991; Emery et al., 1994; Belchansky & Douglas, 2002). These uncertainties are in general caused by atmospheric opacity, wind roughening of open water areas, sensor noise and anomalous ice surface emissivity.

Table 1. Radiometer ice concentration algorithm overview and their acronyms used in the text.

Acronym	Algorithms	Channels used	Tie-points ref.	Reference
BRI	Bristol	19V, 19H, 37V, 37H	Comiso et al. (1997)	Smith (1996)
CF	Bootstrap frequency mode	19V, 37V	Comiso et al. (1997)	Comiso (1986)
CP	Bootstrap polarisation mode	37V, 37H	Comiso et al. (1997)	Comiso (1986)
N90	Near 90 GHz algorithm	85V, 85H	Kaleschke et al (2001)	Svendsen et al. (1987)
NT	NASA TEAM	19V, 19H, 37V	Comiso et al. (1997)	Cavalieri et al. (1984)
NT2	NASA TEAM2	19V, 19H, 37V, 37H, 85V ,85H	Markus and Cavalieri (2000)	Markus and Cavalieri (2000)
TUD	Technical University of Denmark hybrid	19V, 37V, 85V, 85H	Pedersen (1998)	Pedersen (1998)

Each of the algorithms may perform better under certain conditions (Emery et al., 1994). Their sensitivity to emissivity and thermometric temperature of the target depends on the selection of brightness temperatures at different polarisations and frequencies (Comiso et al., 1997). The computed ice concentration accuracy is further degraded by particular atmospheric constituents like cloud liquid water, where NASA Team ice concentration can increase by erroneously by 10 % (Oelke, 1997), and changes in the ice emissivity, where the computed concentration can be depressed by about 20 % (Tonboe et al., 2003). The sensitivity of the different ice concentration algorithms to the two main error sources in the ice covered ocean, i.e. atmospheric- and ice brightness temperature variability, is not the same. Here a set of seven different sea ice concentration algorithms are compared with wide swath SAR. The analysis draws largely on the results presented in Andersen et al. (2006) and focuses on the near 100% ice cover, typical for the Arctic Ocean in winter. The ice concentration algorithms considered, their acronyms and channel combinations are summarised in table 1. Note that the NT2 algorithm is also run in a modified version, NT2u, that allows solutions to be found in an extended concentration interval [0%,120%]. This is to capture the full variability of the retrievals at the 100% limit.

2 OBSERVING SEA ICE CONCENTRATION WITH SPACE-BORNE RADIOMETERS

Microwave radiometers have continuously monitored arctic regions daily since the 1970s. The spectral and polarisation information makes it possible to derive the ice concentration for every pixel independently. Other data can be used to monitor ice concentration, e.g. visual or infrared scanner (VIS/IR) and SAR data. The use of VIS/IR is limited by cloud cover and the visual data further by darkness (during winter). The coverage is therefore not continuous and in some regions it is only sporadic. The coverage with SAR in the Arctic Ocean is not continuous and the classification of the data still requires manual guidance. SAR data are very useful in case specific comparisons, such as this study.

Reliable estimates of atmospheric cloud liquid water and the ice brightness temperature variability are not readily available and it is therefore important to find ice concentration algorithms that are least sensitive to these atmospheric and surface properties. Other parameters, such as atmospheric water vapour and open ocean surface wind, are quantified rather well by numerical weather prediction models. It is therefore feasible to correct brightness temperatures for the influence of these effects using radiative transfer models before computing the ice concentration (Breivik et al. 2001). This is not done here since we would like to evaluate the true natural variability of different ice concentration algorithms.

3 COMPARISON OF RADIOMETER ICE CONCENTRATION WITH SAR DATA

During winter, the variability of the SSM/I concentration estimates in the perennial ice is larger than the true variability of the ice concentration (Kwok, 2002). This is confirmed by extensive SAR comparisons in Andersen et al. (2006). The ice concentration estimates from the seven algorithms within the near 100% ice cover have large regional differences. Figure 1 shows these differences. The N90, NT2U, NT and CP have a negative bias stretching from the Fram Strait across the North Pole. The CF has a negative bias near land, e.g. north of Greenland and Canada. These depressions are consistent while other patterns change from year to year.

The ice concentration estimates from the seven different algorithms are compared to SAR data classified into areas of ice and open water. The RADARSAT-1 and ENVISAT SAR wide swath scenes from 2003 and 2004 in locations with near 100% ice cover are distributed geographically across the Arctic. 68 scenes were analysed and 59 scenes were found to be useful after classification and masking. Trained ice analysts from the operational Greenland ice service did the selection of useful scenes and the classification procedure. Andersen et al. (2006) describes the details. Figure 2 shows the correlation between the SAR and radiometer derived ice concentrations. The correlation coefficient between the datasets is about 0.9 at lower concentrations giving justification to both methods in this ice regime. However, at higher concentrations this high correlation is reduced. In the near 100% ice regime, assuming a constant ice concentration actually matches SAR ice concentrations better than radiometer ice concentrations. The color code in Figure 2 shows that the small correlation coefficient at high concentration is not only dependent on the smaller variability of the SAR concentrations.

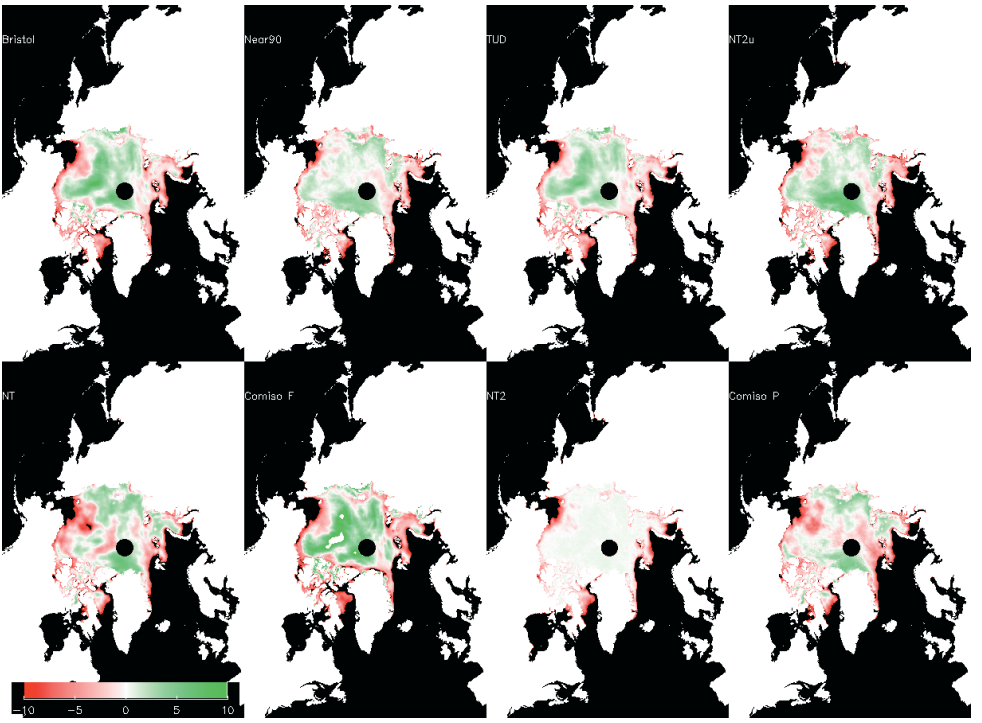

Figure 1. Radiometer ice concentration anomalies Σ(daily field - seasonal average) winter 2003-2004 for the 7 different algorithms and the 2 versions of the NT2 algorithm.

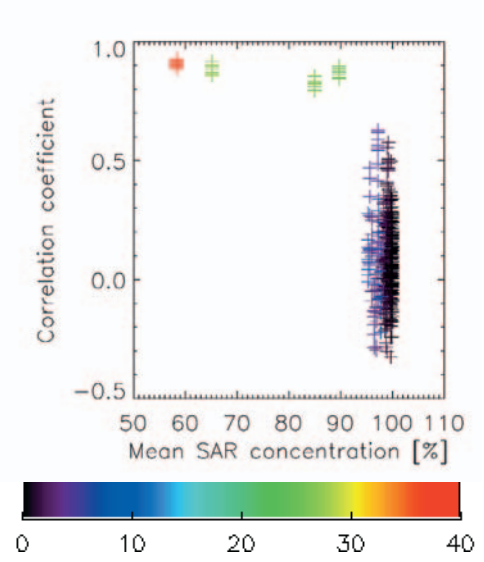

Figure 2. Scene correlations between SAR and SSM/I derived ice concentrations as function of average SAR scene ice concentration. Colour is assigned according to the standard deviation of the concentrations within the SAR scene.

Table 2 shows the results of the comparison in the winter Arctic Ocean where ice concentrations are near 100%. The SAR ice concentration estimate is 99.7% for this dataset with a STDEV of only 0.7 for coincident pixels. Error standard deviations (STDEV) from the seven algorithms range from 2.5-4.9%. The correlation coefficient is not a meaningful measure with the near constant SAR concentration. The primary error source in these comparisons are the thin ice types whose radiative properties mimic a mixture of sea ice and water in most radiometer ice concentration algorithms and is ambiguous in the SAR data. The SAR concentrations are biased towards high variability by the misclassification of thin ice as open water. Even then, the variability of the SAR ice concentrations is significantly lower than the radiometer ice concentrations STDEV. Therefore, the high STDEV of the radiometer ice concentration cannot be explained only by sea ice concentration variability. The fact that the 85GHz algorithms, i.e. N90 and TUD, have lower STDEV than algorithms using 19 and 37GHz channels indicates that atmospheric variability is not significant. It suggests that it is the ice emissivity variation that leads to the high radiometer ice concentration STDEV. The skill of the best radiometer algorithms including TUD, N90 and Bristol are significantly better than the worst set including the CP, CF and NT, but none of them seems adequate at high concentration.

Table 2. Comparison between coincident SAR and SSM/I radiometer ice concentrations. The SAR scenes are all located inside the Arctic Ocean from November 2003 to April 2004.

	Average	**Stdev**	**No. obs.**
SAR (lores):	99.7	0.7	3669

	Bias	**Error stdev**	**Correlation**	**Sensor noise**
BRI	2.1	3.0	-0.02	1.4
CF	3.5	4.6	-0.10	1.7
CP	-0.3	4.9	0.11	1.8
N90	-2.1	3.9	0.10	2.6
NT	-1.5	4.5	0.21	1.7
NT2	-0.4	1.4	0.03	1.7
NT2u	6.9	4.7	0.07	1.7
TUD	4.4	2.7	0.05	2.5

4 SEA ICE EXTENT AND AREA TRENDS

Trends in sea ice extent and area use the radiometer ice concentration data from the 1970s to the present day. Parkinson et al. (1999), using the NT, show that the Arctic sea ice extent and area are shrinking by -34000 km2/yr and -29300 km2/yr respectively. The ice area is the sum of all ice concentration pixels multiplied by the area of these pixels while the extent is the extent of ice pixels. At the same time the arctic atmosphere and sea ice surface properties are changing. Different satellite microwave radiometer ice concentration algorithms used to map sea ice extent and area have different sensitivities to the atmosphere and the ice surface properties. The sea ice trend mapped with different algorithms is therefore different. The ice surface emissivity variability is in fact the primary error source for the microwave radiometer ice concentration estimate over the near 100% ice cover in the Arctic Ocean. Figures 3 show the sea ice area and extent trends using SSM/I time series and the 7 different algorithms. The independent variations between the algorithms are larger for ice area than extent consistent with the more complicated sensitivities to trends in ice surface parameters, that influence the ice area estimates. In contrast it is mainly atmospheric

humidity and water surface roughness that affects the extent. The long time series trend including all SSM/I data (1987-2004) shown with grey bars in figures 3 a) have a smaller annual ice area reduction than the shorter time series trend with functional 85GHz channels on SSM/I (1991-2004) shown with black bars indicating that the reduction has accelerated. For example the Bristol extent trend is -32700km2/yr and -46900km2/yr for the long and short period respectively. Similarly the area trend is -27400k2/yr and -41100km2/yr, respectively.

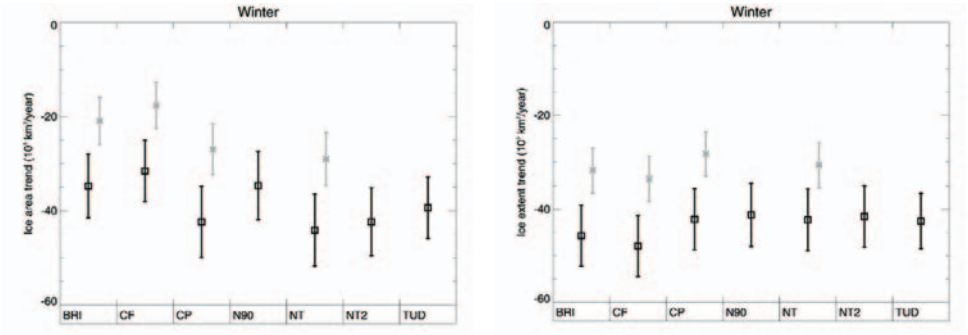

Figure 3. Observed trends in a) ice area and b) ice extent during winter (Oct. – Apr.) for the SSM/I dataset excluding the F8 satellite (1991-2004, black) and the entire dataset (1987-2004, grey). The 85GHz channels were not reliable on F8. Bars show ±1 STDEV.

To study the accelerated retreat, 35 years of average monthly sea ice extent is constructed from two datasets: 1) the 30 year record of Cavalieri et al (2003), and 2) the continuously updated sea ice index at the NSIDC (Fetterer and Knowles, 2002 updated 2006). The first record includes the ice extent derived from the Nimbus 5 Electrically Scanning Microwave Radiometer (ESMR) and the National Ice Center (NIC) digital sea ice data set as well as SMMR and SSM/I data. The second record is based on SMMR and SSM/I data only. The overlap of both records was used to merge both datasets by fitting mean and standard deviations. This new merged record goes from January 1972 to July 2006. The sea ice extent increase slightly during the 1970's, reaching its maximum in 1978, the same year when the first space borne multi-channel microwave instrument, SMMR, was launched. The trends are highly dependent on the selected period. Changing the starting point of the linear trend calculations from 1972 to 1987 results in an accelerated rate of retreat of approximately 8000 km2/y, whereas the change in period from 1991-2004 to 1996-2006 results in a change in rate of 39000 km2/y. This change is large in comparison to the differences between algorithms recorded above and is mainly the result of the large near present accelerated reduction.

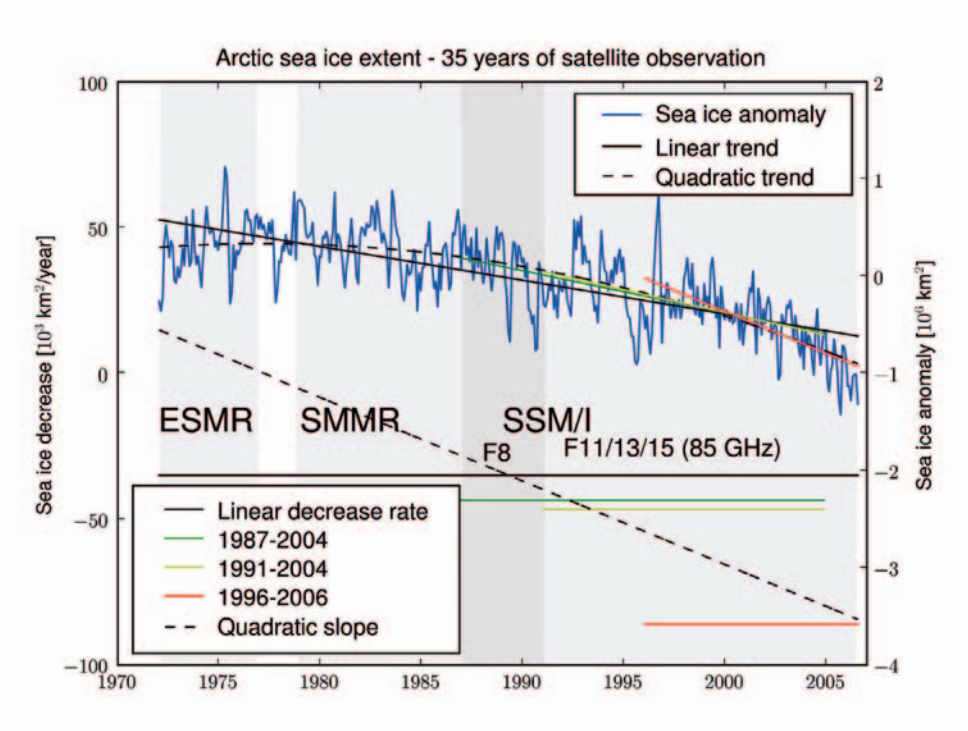

Figure 4. Observed sea ice extent anomaly over the combined ESMR, SMMR and SSM/I time series. Linear trends with different start and end points as well as a quadratic fit to the extent anomalies are shown along with their associated rate of decrease.

5 CONCLUSIONS

For all algorithms during winter, the STDEV exceed the STDEV of the coincident SAR ice concentrations and there is no correlation between the datasets at high concentration. In the perennial winter sea ice, the prevailing ice concentrations are very high (>99%) and the variability in radiometer ice concentration is mainly due to variations in ice brightness temperature. In this ice regime, a constant ice concentration actually matches SAR ice concentrations better than radiometer ice concentrations. However, at intermediate concentrations, the correlation between SAR and radiometer is between 0.8 and 0.9.

Analysis of the entire SSM/I time series (1987-2004) shows that there are significant differences between trends in both area and extent using the 7 different radiometer ice concentration algorithms. All algorithms compute a significant ice retreat consistent with earlier studies. For the ice extent trend the algorithm sensitivity to atmosphere seems crucial for the differences. The differences between the CF and N90 extent trend amounts to 14% of the total down-going trend in winter. The differences between the N90 and NT area trend are 22% of the total trend in winter. The differences are similar for extent if summer data are included but the differences in area trend (NT and N90) are smaller 16%. This indicates that all algorithms have comparable (poor) skills during summer melt.

Applications using ice concentrations within the perennial ice during winter, e.g. for estimation of ice volume and in numerical weather prediction modelling, should not rely exclusively on radiometer ice concentrations. Since the high ice concentration variability is primarily due to ice brightness temperature variations, high-resolution observations such as SAR and VIS/IR observations should be important supplements. Particular care should be exercised when temporal trends are analysed, since the trends in radiometer ice concentrations are significantly different depending on the algorithm. However, it is beyond discussion that the Arctic ice extent and area is retreating and is doing so with an increased pace in later years. In the past, much effort has been invested in the development of radiometer sea ice concentration algorithms with low sensitivity to atmospheric opacity and open water roughness. In the near future, it is necessary to minimize sensitivity to ice surface brightness temperatures at high ice concentrations. In the longer term it should be investigated if the wide spectral range on AMSR and the fully polarimetric WindSat may be useful in distinguishing surface emissivity effects from true ice concentration variations.

6 REFERENCES

Andersen, S., R. Tonboe, L. Kaleschke, G. Heygster, L. Toudal Pedersen, 2006: Intercomparison of passive microwave sea ice concentration retrievals over high concentration Arctic sea ice. Submitted to *J. Geophys. Res.*, 2006.

Belchansky, G. I., & D. C. Douglas, 2002: Seasonal comparisons of sea ice concentration estimates derived from SSM/I, OKEAN, and RADARSAT data. *Rem. Sens. Env.*, 81, 67-81.

Breivik, L.-A., S. Eastwood, Ø. Godøy, H. Schyberg, S. Andersen & R. Tonboe (2001) Sea ice products for EUMETSAT satellite application facility. *Can. J. Rem. Sens.*, 27(5), 403-409.

Cavalieri, D.J, P. Gloersen, & W. J. Cambell, 1984: Determination of sea ice parameters with the NIMBUS 7 SMMR. *J. Geophys. Res.*, 89(D4), 5355-5369.

Cavalieri, D. J., C. L. Parkinson, and K. Y. Vinnikov, 2003: 30-Year satellite record reveals contrasting Arctic and Antarctic decadal sea ice variability, *Geophys. Res. Lett.*, 30(18), 1970, doi:10.1029/2003GL018031.

Comiso, J.C., 1986: Characteristics of arctic winter sea ice from satellite multispectral microwave observations. *J. Geophys. Res.*, 91(C1), 975-994.

Comiso, J.C., D. J. Cavalieri, C. L. Parkinson, & P. Gloersen, 1997: Passive microwave algorithms for sea ice concentration: a comparison of two techniques. *Rem. Sens. Env.*, 60, 357-384.

Emery, W. J., C. Fowler, & J. Maslanik, 1994: Arctic sea ice concentrations from special sensor microwave imager and advanced very high resolution radiometer satellite data. *J. Geophys. Res.*, 99(C9), 18329-18342.

Fetterer, F., and K. Knowles. 2002, updated 2006. Sea ice index. Boulder, CO: National Snow and Ice Data Center. Digital media

Kaleschke, L., C. Lüpkes, T. Vihma, J. Haarpaintner, A. Bochert, J. Hartmann, G. Heygster, 2001: SSM/I Sea Ice Remote Sensing for Mesoscale Ocean-Atmosphere Interaction Analysis. *Can. J. Remote Sensing*, 27(5), 526-537.

Kwok, R., 2002: Sea ice concentration estimates from satellite passive microwave radiometry and openings from SAR ice motion. *Geophys. Res. Lett.*, 29(9), doi:10.1029/2002GL014787.

Markus, T., D.J. Cavalieri, 2000: An enhancement of the NASA Team sea ice algorithm. *IEEE Trans. Geosci. Rem. Sens.*, 38(3), 1387-1398.

Moritz, R. E., 1988: The ice budget of the Greenland Sea. (Ph.D. thesis) University of Washington technical report APL-UW TR8812.

Oelke, C., 1997: Atmospheric signatures in sea-ice concentration estimates from passive microwaves: modelled and observed. *Int. J. Rem. Sens.*, 18(5), 1113-1136.

Parkinson, C. L., D. J. Cavalieri, P. Gloersen, H. J. Zwally, & J. C. Comiso, 1999: Arctic sea ice extents, areas and trends, 1978-1996. *J. Geophys. Res.*, 104(C9), 20837-20856.

Pedersen, L.T., 1998: Chapter 6.2 in Sandven et al. IMSI report no. 8. Development of new satellite ice data products (Chapter 6.2). Bergen, Norway: NERSC Technical Report no. 145, Nansen Environmental and Remote Sensing Center, Bergen, Norway.

Smith, D.M., 1996: Extraction of winter sea-ice concentration in the Greenland and Barents Seas from SSM/I data. *Int. J. Rem. Sens.*, 17(13), 2625-2646.

Steffen, K., & A. Schweiger, 1991: NASA Team algorithm for sea ice concentration retrieval from Defence Meteorological Satellite Program Special Sensor Microwave Imager: comparison with Landsat satellite imagery. *J. Geophys. Res.*, 96(C12), 21971-21987.

Svendsen, E., C. Mätzler, T.C. Grenfell, 1987: A model for retrieving total sea ice concentration from spaceborne dual-polarized passive microwave instrument operating near 90 GHz. *Int. J. Remote Sensing*, 8(10), 1479-1487.

Tonboe, R. T., S. Andersen, & L. Toudal, 2003: Anomalous winter sea ice backscatter and brightness temperatures. Danish Meteorological Institute Scientific Report 03-13.

PART 2. WHAT DO WE KNOW ABOUT THICKNESS CHANGES?

Drilling a survey line across summer sea ice on Belgica Bank, East Greenland.
(Photo: Nick Hughes)

GreenICE Sediment Cores Reveal Reduced Last Interglacial Arctic Sea Ice Cover

Niels Nørgaard-Pedersen[1], Naja Mikkelsen[1], Susanne J. Lassen[1], Emma Sheldon[1], Yngve Kristoffersen[2]
[1] *Geological Survey of Denmark and Greenland, DK-1350 Copenhagen, Denmark*
[2] *Department of Earth Science, University of Bergen, N-5007 Bergen, Norway*

Keywords: Arctic Ocean, Late Quaternary, paleoceanography, glacial-interglacial, sea ice, planktic foraminifera

ABSTRACT: We present a sediment record of the last ca. 200,000 years from the southernmost part of the Lomonosov Ridge off the northern Greenland/Canada continental margin. Evident cyclic changes in hemipelagic sediment types and microfossil content reflect changing glacial-interglacial ice cover characteristics and shifting paleoceanographic circulation patterns. Increased input of coarse ice-rafted debris, from mainly northern Canada, appears to be related to glacial marine isotope stages 6, 4, and late 3. Interglacial stages 7, 5e, and 1, as well as warm interstadial 5a and mid stage 3 were characterised by deposition of fine-grained sediment with abundant planktic foraminifera suggesting less severe ice conditions. The occurrence of abundant small (>63µm) subpolar *Turborotalita quinqueloba* in the intervals representing substages 5e (last interglacial) and 5a (warm interstadial) implies that last interglacial sea ice concentrations were considerably reduced off some areas of northern Greenland/Canada. Whether this was part of a larger regional pattern or it represents the influence of extensive polynya areas with locally increased primary productivity remains to be solved.

1 INTRODUCTION

Major changes have been reported during the last decade concerning the Arctic Ocean, its atmospheric and oceanic circulation and its sea-ice cover's seasonal cycles and interannual variability. The reduction and thinning of Arctic sea ice (e.g. ACIA Overview Report, 2004; Rothrock et al, 1999) has drawn attention to whether this environmental change is an early reaction to global warming, or if it is part of a natural multi-decadal variation of the Arctic environment. Modelling studies indicate that the Arctic is likely to show a large temperature increase, and that sea ice cover could almost disappear during peak summer seasons by the end of this century, (Hadley Centre, 2004; Johannessen et al., 2004). Such a scenario would not only have a dramatic impact on the Arctic ecosystem, navigation, and indigenous people, but could also influence the thermohaline circulation and regional climate in the sub-Arctic and North Atlantic region. In this discussion, there is an urgent need for high latitude Arctic records of climate, oceanography and sea ice cover representing long time periods and, in particular, records of natural environmental change during earlier warm periods.

In the Arctic today, sediment inclusions in sea ice that forms over shallow shelf regions may be incorporated in the Arctic Ocean ice pack and delivered several years later to the deep sea (Pfirmann et al., 1990; Eicken, 2003; Eicken et al., 2000). Some sediment is lost by drifting ice floes during summer melting and ice rafting and contributes to sedimentation along the drift trajectories. However, the bulk of the sediment load is likely to be deposited

when the floe reaches the marginal ice zone in e.g. Barents Sea, Fram Strait or Greenland Sea (Pfirman et al., 1997). At the marginal ice zone and areas characterised by extensive open water leads or polynyas, primary production is enhanced by algae blooms (Berner and Wefer, 1990). Fine grained particles at the ice underside and in the upper water column are incorporated in faecal pellets of e.g. copepods, leading to enhanced sedimentation near ice margins (Hebbeln and Wefer, 1991). Through the planktic-benthic coupling of productivity, benthic life and its fossil remains is also to a large degree dependent on the sea ice cover characteristics. Thus, Arctic Ocean sediment core data analysed in a chronostratigraphic framework can reveal data about changing sea ice conditions through the geological past. Apart from a major impact on the character and extent of sea ice cover, glacial-interglacial climate changes had a profound influence on the extent of continental ice sheets, sea level, and oceanic and atmospheric heat transport and circulation (e.g. Dyke et al., 2002; Svendsen et al., 2004; Chappel and Shackleton, 1986, Dansgaard et al., 1993; Dokken and Hald, 1996).

The recent geological record of the Arctic Ocean is still poorly known and hampered by difficult access, controversial chronostratigraphic models and limits in the applicability of traditionally used proxies. Time control for Arctic Ocean sequences beyond the range of 14C-dating has mostly been based on crude magnetostratigraphy combined with lithostratigraphic correlation of characteristic sediment units (Clark et al., 1980; Phillips and Grantz, 1997; Spielhagen et al., 1997). Recently, progress was made by extending the established nannofossil stratigraphy from the northernmost Atlantic (Gard, 1988; Gard and Backman, 1990) to central Arctic records (Jakobsson et al., 2000, 2001; Backman et al., 2004; Spielhagen et al., 2004). The central Arctic records can be further correlated to distant mid-depth Amerasian basin records by means of unique benthic foraminifera biostratigraphic events (Polyak et al., 2004).

Our study documents a record from a hitherto unexplored, heavily ice-covered region of the Arctic Ocean: the southernmost part of the Lomonosov Ridge facing the Lincoln Sea north of Greenland and Ellesmere Island (Fig. 1). Sediment coring and seismic reflection measurements were part of the multidisciplinary Greenland Arctic Shelf Ice and Climate Experiment (GreenICE) to study the structure and dynamics of the sea ice cover and attempt to relate these to a longer term record of climate variability retrieved from the sediment cores. The field work was carried out during a two week campaign in May 2004 on drifting sea ice at 85° N, 65° W, ca. 170 km north of Ellesmere Island. Wind stresses from persistent easterly winds (opposite to dominant westerlies in the area) resulted in a drift trajectory of 245 +/-15° from a water depth of 500 m to about 1100 m over the southernmost part of the Lomonosov Ridge.

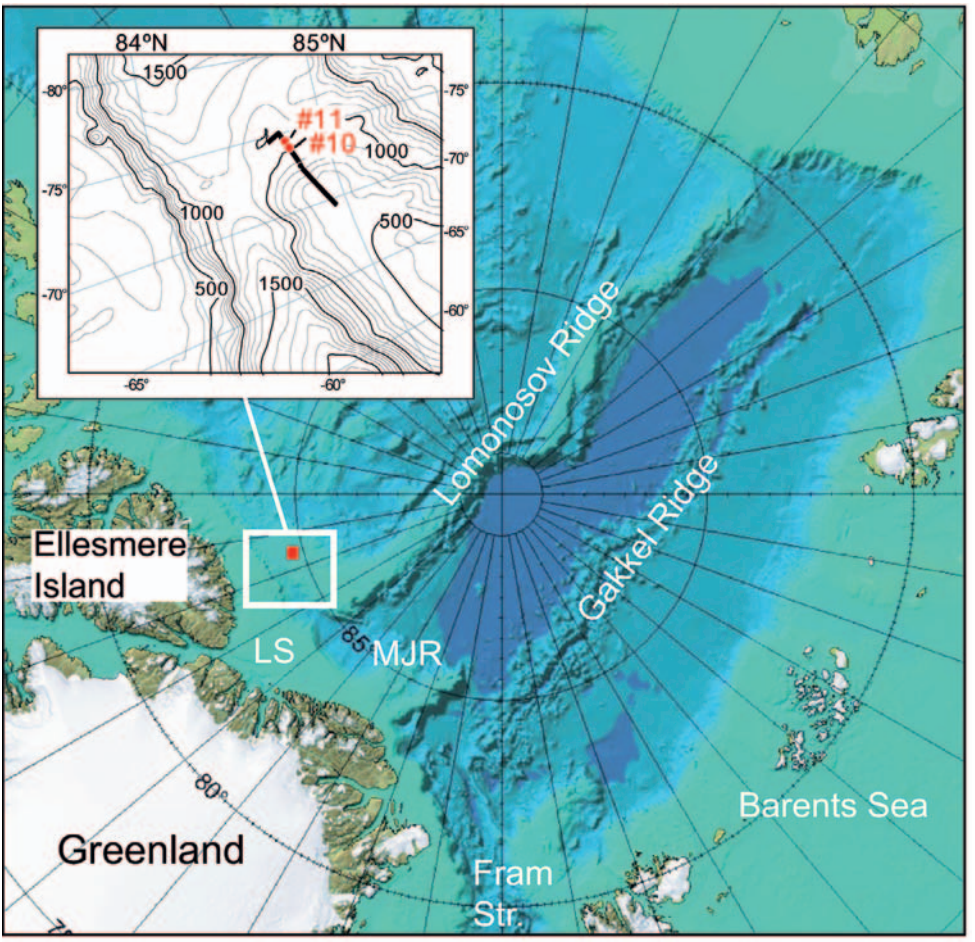

Figure 1. Arctic Ocean bathymetry and location of GreenICE study area. Detailed insert map shows the drift track of the GreenICE station and location of coring sites 10 and 11. LS: Lincoln Sea. MJR: Morris Jesup Rise. Map source: International Bathymetric Chart of the Arctic Ocean (IBCAO).

2 STUDY AREA

The Lincoln Sea and the adjacent Arctic Ocean are generally considered to have some of the thickest sea ice cover of the entire Arctic Ocean, with mean ice thicknesses of 4 m or more (Wadhams, 1997; Wadhams and Davis, 2000). Ice thickness measurements from helicopter flights over the GreenICE study area by low frequency electromagnetic induction (EMI) confirmed mean sea ice thicknesses of 4-5 m during May 2004 (Haas et al., this volume). The present ice drift and surface water circulation over the study area either recirculates in the Beaufort Gyre over the Canada Basin or bends off towards the east with the Transpolar Drift Current when approaching the north Greenland shelf, leading to ice convergence and heavy ice conditions. The stratified water mass structure of the Arctic Ocean includes the low salinity surface water, several intermediate water layers, and the bottom waters (Aagaard et al., 1985). Surface water salinity in the study area is in the range

31-32 psu (EWG Atlas, 1997; Falkner et al., 2005). Below the surface flow and halocline layer, relatively warm (>0ºC) and saline (34.75 or greater) modified Atlantic Water flows as a boundary current counter clockwise around the Arctic Ocean continental margin. The Atlantic Water enters the Arctic Ocean either across the Barents Shelf or as a branch of the West Spitsbergen Current (Aagaard et al., 1985; Rudels et al., 1991, 1994, 1999).

Seismic single channel reflection measurements were carried out parallel to coring along the drift of the GreenICE station (Kristoffersen and Mikkelsen, 2006). The seismic results show that the top of southern Lomonosov Ridge is bevelled (550 m water depth) and only thin sediments (< 50 ms) cover acoustic basement. About 1 km of sediments is found at the western entrance to the deep passage between southern Lomonosov Ridge and the Lincoln Sea continental margin. Here, the uppermost part (+ 0.3 s thick) of the section probably reflects increased sediment input during the Plio–Pleistocene. Erosion and/or non-deposition of sediment on the top of the Lomonosov Ridge contrasts with the presence of about 400 m thick hemipelagic sediment drape observed over the remaining length of the trans-Arctic Lomonosov Ridge (Jokat, 1992, 1999; Kristoffersen et al., 2004; ACEX Shipboard Scientific Party, 2005).

3 METHODS AND MATERIAL

A 2 m long gravity corer with 200 kg core head was suspended from a tripod and handled by a custom made hydraulic winch through a hole drilled in the sea ice (Fig. 2). The corer was fitted with a 25 cm long cone beneath the core catcher in order to enhance recovery of surface sediments. A 9 cm inner diameter core liner was used. Several short gravity cores and surface samples were taken along the ice camp drift path between 650-1100 m water depth (Fig. 1, Table 1). Core 10 and 11 recovered the longest sediment records of 176 cm and 65 cm, respectively. The other shorter cores did not penetrate an IRD-rich sandy layer at about 20-40 cm sub-bottom depth.

Figure 2. The GreenICE sediment cores were retrieved by a 2 m long gravity corer (200 kg core head) suspended from a tripod and handled by a custom made hydraulic winch through a hole drilled in the sea ice. Photos by Yngve Kristoffersen (a) and Sibylle Göbell (b).

Table 1. GreenICE coring and surface sediment sampling stations.

Station No.	Latitude °N	Longitude °W	Water depth (m)	Sample type	Core length (cm)
1	84° 49.79	71°42.47	650	surface	-
2	84° 51.51	72° 08.91	691	surface	-
3	84° 51.40	72° 13.05	ca. 710	surface	-
4	84° 51.24	72° 19.79	730	surface	-
5	84° 50.23	72° 59.14	830	surface	-
6	84° 50.19	73° 07.25	845	core	10
7	84° 50.23	73° 17.05	902	core	24
8	84° 49.68	73° 51.42	1026	Core (double penetration)	105
9	84° 49.58	73° 59.00	1006	surface	-
10	84° 48.76	74° 16.96	1040	core	176
11	84° 48.86	74° 15.75	1089	core	65
12	84° 48.16	75° 03.50	1117	surface	-
13	84°48.02	75° 10.50	1101	core	18
14	84° 47.90	75° 17.53	1086	surface	-
15	84° 47.61	75° 28.48	1071	core	22

Shore based laboratory work concentrated on detailed investigations of core 10 and 11. Magnetic susceptibility was measured in cm steps on core sections. After splitting of the core sections, subsamples of 3-4 cm3 were taken every 1-2 cm downcore. The samples were wet-sieved (>63µm, >1mm) and the 63-1000µm fraction was dry-sieved in subfractions (63-125µm, 125-250µm, 250-1000µm). These samples were used for coarse fraction analysis, counting of ice-rafted debris (IRD) content, microfaunal analysis, and oxygen and carbon isotope measurements. Accelerator mass spectrometry (AMS) 14C dating was carried out on ~10 mg samples of the planktic foraminifera *Neogloboquadrina pachyderma* (sinistral) at the Leibniz AMS laboratory, University of Kiel. Reservoir correction applied is -440 yr (Mangerud and Gulliksen, 1975); however, actual reservoir time could be larger in the Arctic Ocean, especially during glacial periods (cf. Voelker et al., 1998; Haflidason et al., 2000). The total planktic foraminifera abundance (specimens/g) and planktic foraminifera species assemblages (polar/subpolar) were determined on representative sample splits of the >63µm size fraction. Between 300 and 400 individuals per sample were identified using a binocular microscope. Oxygen and carbon isotope measurements were carried out on planktic foraminifera *N. pachyderma* (s) from the 125-250 µm fraction (about 20 individuals per sample) at the Goodwin Laboratory, Cambridge. Nannofossil smear slides were prepared for selected sample intervals and examined using the light microscope. Due to the scarcity of coccoliths in Arctic sediments only about 50-100 specimens per sample were counted. Thus, as done by Jakobsson et al. (2000, 2001), occurrences of *Gephyrocapsa muellerae* and *Emiliania huxleyi* were primarily used to identify marine isotope stage (MIS) 5. Ice rafted debris (IRD) grains >250µm were counted on representative sample splits of core 11 and IRD grains/g were quantified. Moreover, the downcore occurrence of IRD clasts with a diameter > 0.5cm ("dropstones") were noted during core description and later subsampling of core sections. The fraction >250µm was used also to quantify the abundancy of larger specimens of benthic foraminifera *Cibicides wuellerstorfi* and *Bulimina aculeata*.

For an overview of the stratigraphical subdivision into marine isotope stages (MIS), a diagram is shown in Fig. 3, relating marine isotope stages 7-1 to a time line, with an associated global oxygen isotope curve and an insolation curve for 90°N.

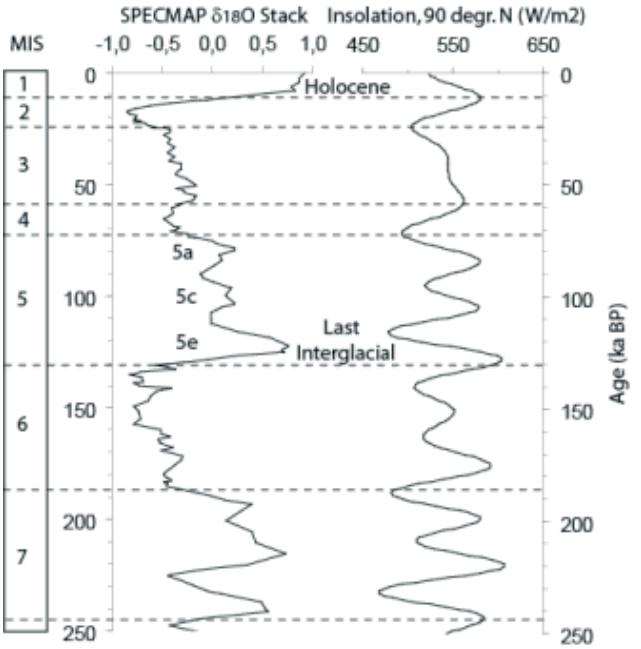

Figure 3. Climate records related to global climate changes through the last 250.000 years with marine isotope stages (MIS) indicated to the left. The SPECMAP stack from Martinson et al. (1987) shows the generel pattern of $\delta^{18}O$ variation based on foraminifera samples in a large number of global ocean sediment cores. The June insolation curve for 90°N is from Berger and Loutre, 1991).

4 RESULTS

Sediment core stratigraphy

All seven cores recovered appear to correlate visually, which indicate they are representative for the regional, hemipelagic sediment succession in the area. The core sections consists of alternating greyish brown and light yellowish brown beds of clayey and sandy muds with occasional occurrence of dropstones, up to several cm in diameter (Fig. 4). Indications of current winnowing and iron-manganese coating of grains can be observed in the coarse fraction peak at about 15 cm subbottom depth. Greyish brown (10 YR 5/2) layers are bioturbated silty clays which are rich in calcareous microfossils such as planktic and benthic foraminifera and ostracods. This supports interglacial or warm interstadial conditions with dominant sea ice sediment rafting, open water leads during summer, and oxygenated bottom water conditions (cf. Nørgaard-Pedersen et al., 1998; Polyak et al., 2004). Light yellowish brown (2.5Y 6/4) and light olive brown (2.5Y 5/4) layers are in general more sandy with occasional granule to small pebble-sized IRD and a sparse microfossil content, supporting glacial conditions, with iceberg sediment rafting, a closed sea ice cover, and poorly oxygenated bottom water conditions. Calcareous planktic and benthic foraminifera, and late Quaternary nannofossils are very well-preserved in core 10 and 11. This is also true for intervals showing low foraminifera abundances. The basal part of core 10, though,

appears to be barren of calcareous specimens, and contains a sparse assemblage of agglutinated benthic foraminifera.

The age models for core 10 and 11, described in detail below, are based on a combination of AMS-14C dating from planktic foraminifera, nannofossil assemblage stratigraphy, and characteristic benthic foraminifera biostratigraphic markers. Furthermore, characteristic colour changes and variable microfossil content have been used to correlate with radiocarbon dated cores from the interior Arctic Ocean (Darby et al, 1997; Nørgaard-Pedersen et al., 1998) and mark transitions between marine isotope stages (MIS) 1-3.

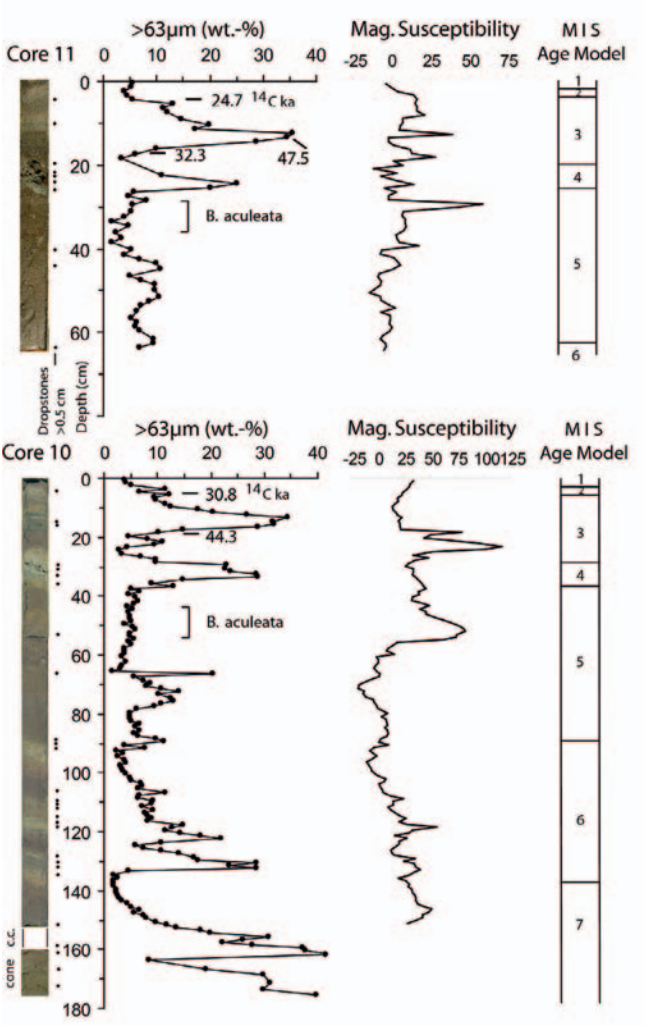

Figure 4. GreenICE cores 10 and 11: Core photos, coarse fraction content >63µm (wt.-%), occurrence of "dropstones" >0.5 cm, magnetic susceptibility, and age model (marine isotope stages (MIS) 1-7). The stratigraphic levels with AMS-^{14}C dates (^{14}C ka) and peak oc currence of benthic foraminifera Bulimina aculeata are indicated. The sediment stratigraphy in the cone below the core catcher (c.c.) in core 10 was intact.

Core 11: At 5-6 cm, an AMS-14C date of 24.7 14C kyr BP was obtained (Table 2). Accordingly, the light brown, fine-grained layer from 5-2 cm corresponds to peak glacial MIS 2 (24-12 ka), based on correlation with central Arctic records (Darby et al, 1997; Nørgaard-Pedersen et al., 1998, 2003). The topmost greyish brown sediment is of Holocene age, based on its elevated content of planktic foraminifera and benthic foraminifera *C. wuellerstorfi* (Fig. 5). However, we suspect that the younger part of the Holocene record was lost during the coring process. The two dates at 13-14 cm (IRD-rich unit: 47.5 14C kyr BP) and 17-18 cm (dark brown planktic foraminifera rich unit: 32.3 14C kyr BP) reveal an age reversal. The corresponding dark brown unit in Core 10 gave an AMS-14C age of 44.3 14C kyr BP. The influence of very low sedimentation, bioturbation and larger uncertainty of AMS dates close to the dating limit (about 50 kyr BP), possible can explain the scatter of ages obtained. From interior Arctic Ocean box cores, ages of 50-30 14C kyr have been obtained in a similar foraminifera-rich greyish brown unit (Darby et al., 1997; Nørgaard-Pedersen et al., 1998). On the basis of stratigraphic evidence from the bounding units, the IRD-rich unit from 26-20 cm probably represents MIS 4 to early MIS 3. The thick brown section from 26 cm to the base of core 11 contains common calcareous nannofossils dominated by Gephyrocapsa mullerae (80-90%) with subordinate *Emiliania huxleyi*, and occasionally, *Gephyrocapsa oceanica* and *Gephyrocapsa carribeanica* (Fig. 5). From this section upwards to the nannofossil-bearing units at 20-16 cm, 8-5 cm, and 2-0 cm, there is a clear shift towards a decrease in *G. mullerae* (20-60%) and a marked increase in *E. huxleyi* (30-80%). This corresponds with the transition seen between the MIS 5/4 transition (74 ka) and MIS 4/3 (59 ka) in the nannofossil biozonation scheme for high northern latitudes (Gard 1988, Gard and Backman, 1990). The validity of the aforementioned scheme for interior Arctic records was recently demonstrated by Jakobsson et al. (2000, 2003), Spielhagen et al. (2004), and Backman et al. (2004). Furthermore, abundance peaks of the benthic foraminifera *Bulimina aculeata* at 30-28 cm supports that this stratigraphic level corresponds to late MIS 5 (cf. Backman et al., 2004; Polyak et al., 2004). Considering that the interval from 62-53 cm reveals a prominent peak in subpolar planktic foraminifera and benthic foraminifera *C. wuellerstorfi* (Fig. 5, 6), this level is assigned to the last interglacial (substage 5e). The lowermost trend in the core 11 record, demonstrating a sharp reduction downwards in total planktic foraminifera/g sediment and percentage subpolar foraminifera, likely represents the transition to the penultimate glacial period (MIS 6). This is supported also by data from core 10.

Table 2. AMS-^{14}C dates of GreenICE cores 10 and 11. Reservoir correction applied is –440 yr (Mangerud and Gulliksen, 1975).

Core No.	Depth (cm)	Lab. ID	Delta ^{13}C	Conventional ^{14}C Age (yr BP)	Reservoir Corrected ^{14}C Age (kyr BP)
GreenICE 10	5-6	KIA 25763	0.82 ± 0.04	31210 + 500 / -470	30.8
GreenICE 10	18-19	KIA 25764	0.39 ± 0.14	44760 + 390 / -380	44.3
GreenICE 11	5-6	KIA 25760	-0.06 ± 0.06	25170 + 240 / -230	24.7
GreenICE 11	13-14	KIA 24847	-0.16 ± 0.30	47910 + 1540 / -1290	47.5
GreenICE 11	17-18	KIA 25761	-2.06 ± 0.10	32690 + 600 / -550	32.3

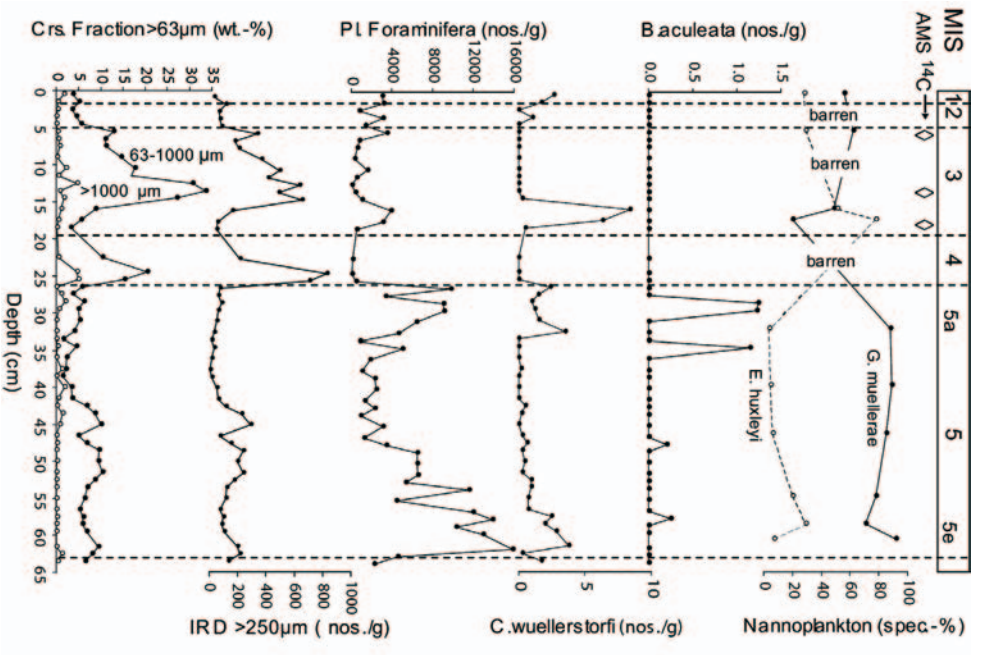

Figure 5. Basic stratigraphic data of core 11: coarse fraction content >63µm (wt.-%), IRD>250 µm (grains/g), planktic foraminifera abundance (specimens >63µm/g), selected benthic foraminifera C. wuellerstorfi and B. aculeata (specimens>250µm/g), nannofossil assemblage: E. huxleyi and G. muellerae (% of total assemblage). Marine isotope stage (MIS) age models with substages 5e (last interglacial) and 5a (warm interstadial) are shown to the right.

Core 10: The lithostratigraphic and biostratigraphic data of core 10 (Fig. 4) indicate that the record of the upper 90 cm in detail can be correlated to the record of core 11, encompassing MIS 5-1. Two AMS 14C dates at 5-6 cm (30.8 14C kyr BP) and 18-19 cm (44.3 14C kyr BP) corroborate the stratigraphic framework of MIS 3 sediments, overlain by condensed MIS 2 (light greyish brown) and MIS 1 (greyish brown) sediments. An abundance peak of *Bulimina aculeata* at 54-53 cm support the finding in core 11, and a MIS 5a age is assigned to the upper part of the thick brown unit. As the light yellowish brown units between 140-90 cm are enriched in IRD supporting dominantly glacial conditions, this unit is tentatively assigned to MIS 6. The greyish brown unit below (160-140 cm) contains moderate high numbers of planktic and benthic foraminifera and nannofossils and it is suggested that it represents the penultimate interglacial MIS 7. This is corrobated by the occurrence of *Pullenia* sp. benthic foraminifera, exclusively occurring in the MIS 7 interval in Amerasian Basin and central Lomonosov Ridge cores (Jakobsson et al., 2001; Backman et al., 2004). Coccolith species *Emiliana huxleyi* are found in the lower part of the core (rare specimens), and it can be inferred that the oldest sediment recovered is younger than (or equal to) late MIS 8, as its first evolutionary appeareance is dated to about 0.26 Ma (Thierstein et al., 1977).

Foraminifera record

In core 11, high planktic foraminifera abundances are found in the fine-grained, greyish brown beds (5000-15000 specimens/g) and very low abundances are found in the

light yellowish to olive IRD-rich units (<1000 specimens/g) (Fig. 4, 5, 6). The assemblages are in general dominated by *Neogloboquadrina pachyderma* (sinistral). In specific intervals, however, subpolar small *Turborotalita quinqueloba* (=*Globigerina quinqueloba*) comprise a significant part of the assemblage (20-50%). *Neogloboquadrina pachyderma* (dextral) are found throughout the core (3-15%), but do not appear to show any significant co-variation with other parameters. Other species like *Globigerina glutinata* and *Globigerina bulloides* occur rarely. Small *T. quinqueloba* are particularly abundant in two intervals also revealing peak abundances in planktic foraminifera; the lower and upper section of the thick brown bed assigned to MIS 5 (Fig. 6). The lower abundance peak representing substage 5e (last interglacial) reveals approximately 40-50% *T. quinqueloba*, whereas the upper peak representing substage 5a contains 20-35% *T. quinqueloba*. The upper part of core 11 assigned to MIS 3-1 contains a relatively unimodal planktic foraminifera assemblage with ≥90% *N. pachyderma* (s), 5-10% *N. pachyderma* (d), and <5% *T. quinqueloba*. All surface samples recovered along the drift track of the GreenICE station contain a planktic foraminifera assemblage (>63µm) totally dominated by *N. pachyderma* (s). For comparison, late Holocene surface sediment samples (>63µm) from central Lomonosov Ridge and Morris Jesup Rise (cf. Nørgaard-Pedersen et al., 1998) reveal a similar pattern, with a clear *N. pachyderma* (s) dominance (≥90%).

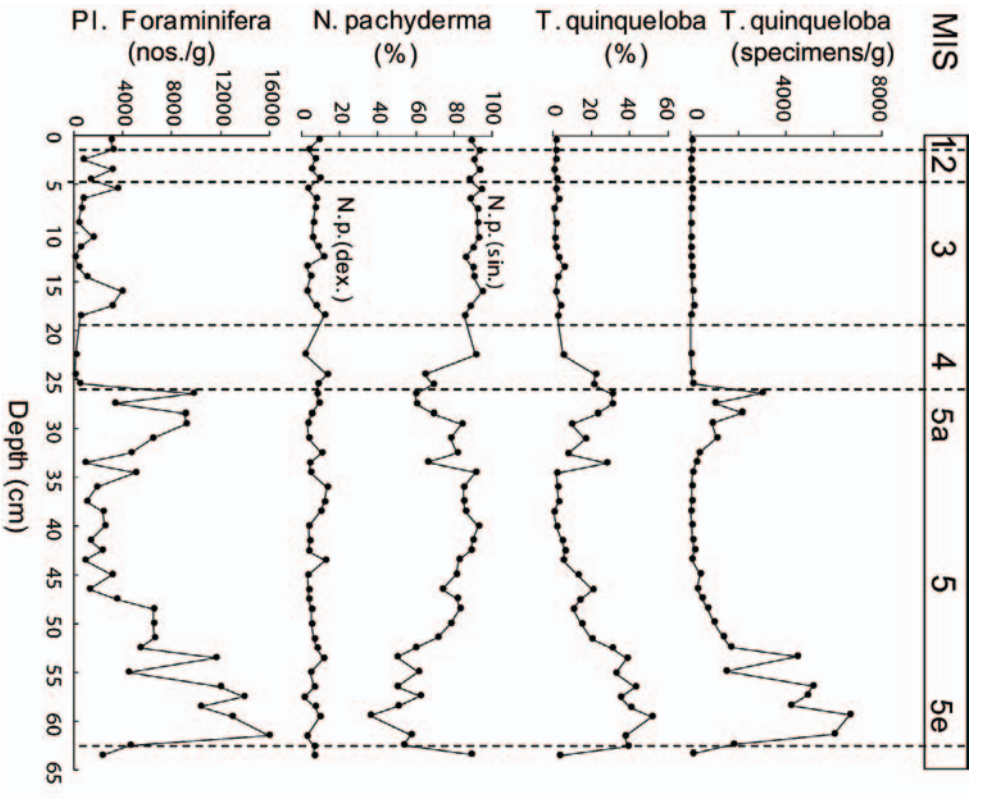

Figure 6. Planktic foraminifera assemblage record (specimens >63µm) of core 11. The two intervals assigned to substages 5e and 5a are characterised by abundant subpolar foraminifera T. quinqueloba, whereas polar species N. pachyderma (s) dominate totally in the other part of the record.

The down-core abundance of two selected benthic foraminifera species in the >250 µm size fraction was quantified in core 11. *Cibicidoides wuellerstorfi* is an epifaunal suspension-feeder found in intermediate waters of Atlantic Water affinity below 1000 m (Polyak, 2004; Wollenburg et al., 2001). Moderately high numbers of *C. wuellerstorfi* occur in the intervals assigned to MIS 5e, 5a, mid MIS 3, and the Holocene (Fig. 5). *Bulimina aculeata* occurs in high numbers in a narrow stratigraphic interval in several cores from the central and Amerasian Arctic Ocean taken at water depths between 1000 and 2000 m (Poore et al., 1993; Ishman et al., 1996; Jakobsson et al., 2001, Polyak et al., 2004). This species is virtually absent from the Arctic Ocean today, enabling its peak in abundance to be a distinct biostratigraphic marker. Abundant *B. aculeata* are observed in core 11 in the 35-28 cm interval with only few specimens found elsewhere (57-56 cm and 47-46 cm) in the core (Fig. 5). A similar abundance peak is seen in the adjacent core 10, in the correlative level 55-45 cm. Together with the nannofossil data, it can be inferred that *B. aculeata* can be used as a stratigraphic marker for MIS 5a in mid-depth Arctic Ocean records (cf. Backman et al., 2004, Polyak et al., 2004).

Planktic foraminifera δ18O and δ13C data

The δ18O and δ13C record of *N. pachyderma* (s) in core 11 (Fig. 7) exhibits significant variability, as we might expect for an interior Arctic Ocean site, where the global ice-volume glacial-interglacial pattern (cf. Lea et al., 2002) is masked by the influence of surface water salinity changes (Spielhagen and Erlenkeuser, 1994; Nørgaard-Pedersen et al., 1998; Polyak et al., 2004). In the interior Arctic Ocean, *N. pachyderma* (s) calcify mainly in surface/halocline water (Spielhagen and Erlenkeuser, 1994; Bauch et al., 1997; Volkmann and Mensch, 2001) thereby reflecting mainly surface water salinity changes rather than temperature changes (present day surface/halocline waters close to freezing point –1.8°C of sea water). There appear be no evident co-variation with observed foraminifera assemblage changes (Fig. 7). Relatively low δ18O values (1.0-2.0‰) associated with low δ13C values are observed in the early to mid MIS 5 record. During mid to late MIS 5 and MIS 4, intervals of very high δ18O values (2.5-3.5‰) and relatively high δ13C characterise the record. The sudden increases of δ18O values with up to 1‰ are well above the values that can be explained by global δ18O-water changes. It implies a remarkable increase in surface water salinity at the site. Similar trends have been reported in δ18O records from the Mendeleev Ridge (Polyak et al., 2004), the central Lomonosov Ridge, and the Morris Jesup Rise (Spielhagen et al., 2004). Polyak et al. (2004) suggested that the maxima of δ18O values occurring in some interstadials could be due to the cessation of low salinity Pacific Water inflow, when the Bering Strait was closed due to global sea level fall. The present sill depth of the Bering Strait is about 40-50 m and critical reductions of sea level during the last interglacial-glacial cycle were reached in MIS substages 5d, 5b and stage 4-2 (cf. Lea et al., 2002). The MIS 3-1 record exhibits relatively low δ18O values (1.0-2.0‰) associated with low δ13C values, but the very low resolution may preclude detection of salinity changes related to the last glacial-interglacial transition. Comparing δ18O values of the MIS 5e interval (about 1.8-2.0‰) to core top values and interior Arctic Ocean mid to late Holocene δ18O values (*N. pachyderma* (s)) showing values of about 1.5 ‰ (Nørgaard-Pedersen et al., 1997, 1998, 2003), it appears that last interglacial surface water/halocline properties at the GreenICE site may have been slightly more saline than present day conditions (assuming a similar global ice volume during the two interglacials).

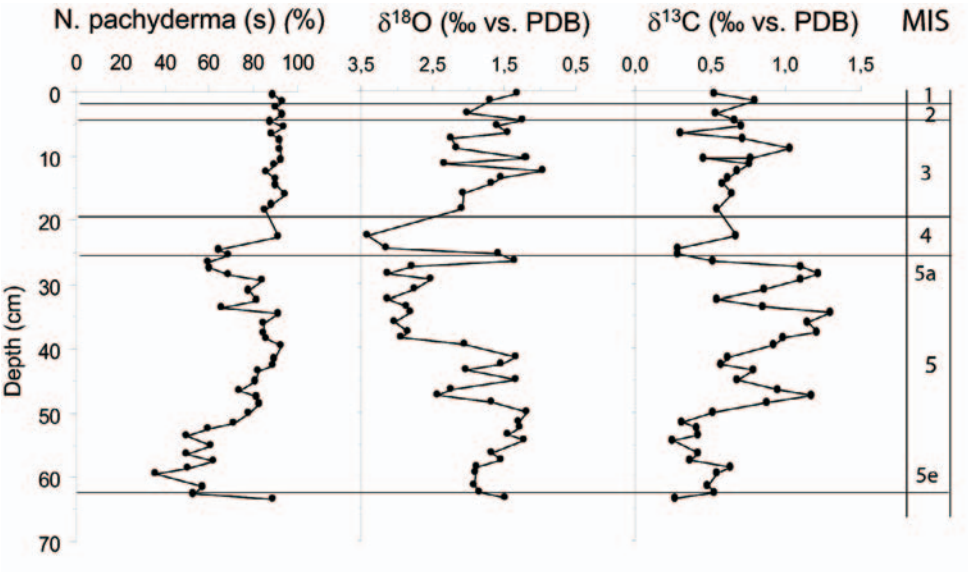

Figure 7. Oxygen and carbon isotope record of N. pachyderma (s), core 11. For comparison, the N. pachyderma (s) content (%) is shown also. Marine isotope stage (MIS) age model with substages 5e (last interglacial) and 5a (warm interstadial) is shown to the right.

Ice-rafted debris (IRD) record

From the quantification of IRD>250 µm in core 11, it is evident that peaks in coarse fraction (>63µm) content (including biogenic remains and authigenic aggregates) parallel peaks in the IRD content (Fig. 4, 5). Based on this and the occurrence pattern of dropstones >0.5cm, intervals of increased IRD content can be inferred also for core 10. Peak values of 500-2000 grains/g are found in the units assigned to MIS 6, 4 and late MIS 3. The IRD concentration in the late MIS 3 unit, however, appears to have been influenced by current winnowing, as indicated by iron-manganese coatings of grains and dark colour banding. A low IRD content (10-100 grains/g) characterises the greyish brown beds with abundant foraminifera, i.e. early and late MIS 5, mid-MIS 3, and Holocene. The early mid-MIS 5 (?substage 5d) section contains an elevated IRD content (200-300 grains/g). A semi-quantitative evaluation of the >1000µm grain lithology indicates a relatively uniform IRD composition throughout most of the record with abundant quartz, detrital carbonate (mostly dolomite), sandstone, and metamorphic rock fragments. Small detrital carbonate pebbles are common in the MIS 4 unit, also containing abundant authigenic carbonate material. Noteworthy, the basal part of core 10 show IRD enriched in quartz with almost no detrital carbonate rocks. Detrital carbonate IRD is very common in Quaternary records from the Amerasian Basin (Phillips and Grantz, 1997) as well as the central Lomonosov Ridge and the Morris Jesup Rise (Nørgaard-Pedersen et al., 1997, 1998; Vogt, 1997).

5 DISCUSSION

The GreenICE sediment records, from a hitherto unexplored area of the Arctic Ocean, reveal new data on variable Arctic Ocean paleoceanographic conditions during the last two glacial-interglacial cycles. The records contain very well-preserved calcareous foraminifera and nannofossils allowing the establishment of a reliable age model and fix points for correlation with other interior Arctic Ocean late Quaternary records. The stratigraphic framework used relies on recent progress in central Arctic Ocean late Quaternary stratigraphy (cf. Jakobsson et al., 2000, 2003; Backman et al., 2004; Spielhagen et al., 2004; Polyak et al., 2004). Our age models for core 11 and 10 indicate that sedimentation rates for the GreenICE site have been in the range 0.5-1.0 cm /kyr for the last two glacial-interglacial cycles. This is about half the rate determined for sites on the central part of the Lomonosov Ridge (cf. Backman et al., 2004 and references therein). The youngest Holocene deposits were probably lost during the coring process, so we cannot make an estimate of recent sedimentation rates. Interior Arctic Ocean box cores and multicores from elevated highs reveal Holocene sedimentation rates of about 1 cm/kyr (0.5-1.0 g cm-3 kyr-1) (Stein et al., 1994; Darby et al., 1997; Nørgaard-Pedersen et al., 1998). The severe ice conditions over the GreenICE site, compared to e.g. central Lomonosov Ridge sites, support lower recent hemipelagic sedimentation rate at the site.

The IRD records of core 11 and 10 reveal specific periods of intensified deposition of IRD material related to glacier collapse events during the last glacial-interglacial cycles. At the GreenICE site increased IRD deposition appear to have taken place during MIS 6 (early part and 6/5 transition, early-mid MIS 5 (5d?), MIS 4, and late MIS 3. For MIS 2 (incl. the last glacial maximum) there is no evidence of intensified ice-rafting. This is in accordance with other interior Arctic Ocean MIS 2 records indicating extremely low sedimentation rates of clayey muds more or less barren in microfossils (Darby et al., 1997; Nørgaard-Pedersen et al., 1998, 2004). It is notable that a few dropstones >0.5 cm were found in the MIS 2 section of the GreenICE cores, indicating that icebergs occasionally were drifting and melting over the site. The IRD material in core 10 and 11 contains abundant dolomitic carbonates. This support a dominant terrestrial source from North Canada/Greenland where palaeozoic platform carbonates extensively crop out (Okulitch, 1991; Phillips and Grantz, 1997, 2001). In relation to GreenICE seismic records showing possible glacial erosion of the top of the shallow Lomonosov Ridge about 45 km from the core sites (Kristoffersen and Mikkelsen, 2006), there is no indication in the GreenICE sediment core record supporting that this took place during the last two glacial-interglacial cycles. However, core 10 and 11 are from deeper water (>1000 m) limiting the burden of proof for the timing of such erosion events.

Abundant well-preserved calcareous planktic and benthic foraminifera are found in specific intervals of interglacial MIS 7, 5, 1, as well as some interstadials of MIS 3 and 6. Subpolar foraminifera, *T. quinqueloba*, occur in high numbers in two intervals, most likely representing substages 5e (last interglacial) and 5a (warm interstadial). This is a new discovery for interior Arctic late Quaternary records. Usually larger size fractions (>125µm or >150µm) have been studied and a total dominance of polar foraminifera *N. pachyderma* (s) with subordinate *N. pachyderma* (d) has been reported for late Quaternary records (e.g. Poore et al., 1993; Hommers, 1998; Polyak et al., 2004). A few studies, however, mention species assemblages in the finer fraction >63µm, still with a total dominance of polar specimens (e.g. Poore et al., 1993; Backman, 2004). All surface sediment samples taken along the GreenICE drift transect reveal planktic foraminifera assemblages (>63µm) totally dominated by *N. pachyderma* (s). Radiocarbon-dated late Holocene surface sediment samples (>63µm) from

interior Arctic mid-depth box core sites with excellently preserved calcareous microfossils also reveal a clear dominance of polar *N. pachyderma* (s).

At present, *T. quinqueloba* shows maximum abundance in the Nordic seas along oceanic fronts, in particular the Arctic Front that separates Atlantic and Arctic water masses (Johannesen et al., 1994). The Fram Strait and the south-western Eurasian Basin, currently characterised by strong subsurface advection of Atlantic water below colder and lower salinity polar surface water, contain abundant small subpolar *T. quinqueloba* in the water column (Carstens and Wefer, 1992; Carstens et al., 1997; Volkmann, 2000a, 2000b). The abundance of *T. quinqueloba* declines steadily further to the north (Fig. 8). Despite the high abundance of *T. quinqueloba* in the water column, sediment surface samples along the Barents Sea margin and the adjacent deep Arctic Ocean show an assemblage totally dominated by *N. pachyderma* (s) (Volkmann, 2000b). This is explained by selective dissolution of the subpolar *T. quinqueloba* by corrosive shelf-derived waters (Aagaard et al., 1985; Steinsund and Hald, 1994; Volkmann, 2000b). Studies investigating the <150µm fine fraction in the subpolar to temperate Nordic seas, have revealed that *T. quinqueloba*, that is dominant during peak interglaciations, seems to become reduced in size under a cooler temperature regime (Bauch, 1994). Persistence of these smaller *T. quinqueloba* in the Nordic seas and the Fram Strait during interstadial periods and certain glacial stadials, allows relatively warm Atlantic Water advection to this region to be traced during periods other than peak interglaciations (Hebbeln et al, 1994; Dokken and Hald, 1996; Bauch et al., 2001; Kandiano and Bauch, 2002).

The oxygen and carbon isotope data on *N. pachyderma* (s) do not appear to reveal changes in the surface ocean salinity and ventilation rate co-varying with the planktic foraminifera species changes within MIS 5. However, a comparison of last interglacial δ18O values with average mid- to late Holocene values (including other interior Arctic records (cf. Stein et al., 1994; Nørgaard-Pedersen, 1997, 1998) suggests that surface/halocline water salinities at the GreenICE site were somewhat higher during the last interglacial period. Higher salinity values of surface near water masses may have been supported by a vigorous Atlantic Water circulation. However, sudden increases of δ18O values with up to 1 ‰ during the later part of MIS 5 and 4 indicate even higher salinities in the area. As suggested by Polyak et al. (2004), cessation of low salinity Pacific Water inflow through the Bering Strait during periods of global sea level reduction may have influenced the salinity balance and halocline structure of the Arctic Ocean and, in particular, Amerasian Basin conditions.

The discovery of a large numbers of small *T. quinqueloba* in the early and late MIS 5 record at the GreenICE site indicates paleoceanographic conditions in the area different from today. At present the area is heavily ice-covered and remote from sea ice margins. Could this imply that advection of Atlantic Water to the interior Arctic Ocean was much stronger during the last interglacial MIS 5e and warm interstatial MIS 5a? Or was the sea ice margin placed further to the north so that the GreenICE site was situated at an ice-marginal position? Nordic Sea studies have shown that, when exclusively small sized specimens of *T. quinqueloba* are found, there is most likely a relation to advection processes (Kandiano and Bauch, 2002). Indeed, a submerged Atlantic Water layer, below an ice-covered halocline can also carry and transport abundant numbers of subpolar foraminifera into the Arctic Ocean. However, the consistent reduction of subpolar specimen abundances in the downstream, mostly ice-covered areas of the two Atlantic Water inflow branches (Spitsbergen Current and Barents Sea Current) indicate that present day oceanographic circulation cannot explain the high *T. quinqueloba* abundance during MIS 5 warm periods. Thus, the percentage of *T. quinqueloba*

are reduced from ≥50% in the Barents Sea Branch to <10% along the Laptev Sea margin (Volkmann, 2000a). From the northern Barents Sea margin (influenced by the core of the West Spitsbergen Current) abundances of *T. quinqueloba* ≥50% are reduced to less than 20% over the Gakkel Ridge at 86˚N (Fig. 8) (Carstens and Wefer, 1992). Subpolar foraminifera carried to the GreenICE site via the present day subsurface Atlantic Water boundary current (from high productive ice margin or ice free sites like the Fram Strait) would have to travel several thousand kilometres and probably only traces of an original assemblage would arrive at the destination.

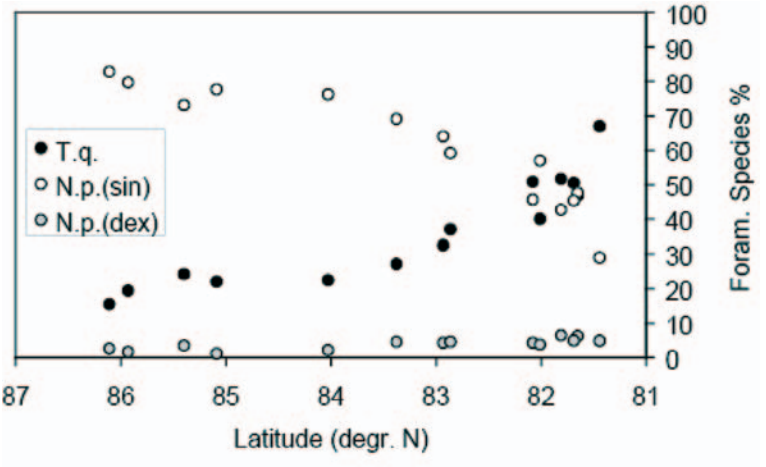

Figure 8. Recent distribution of planktic foraminifera (species >63µm) in the upper 500 m water column of the Nansen Basin along a S-N transect from the northern Barents Sea margin (81°N) to the Gakkel Ridge (86°N). Subpolar species T. quinqueloba are found abun dantly in the southern region characterised by strong advection of Atlantic Water. Data from Carstens and Wefer (1992).

Another explanation to consider is if a reduction in sea ice cover (as inferred for substages 5e and 5a) is a regionally restricted phenomenon forced by a polynya-type setting (similar to the modern NorthEast Water Polynya, NE Greenland). Without detailed studies of further records from north of Greenland and interior Arctic sites we cannot rule this explanation out. It should be noted, however, that preliminary studies of MIS 5 sediments from the Morris Jesup Rise also indicate abundant small subpolar foraminifera in foraminifera peaks assigned to early and late MIS 5 (following the age model of Spielhagen et al. (2004)). If a polynya setting (or extensive flaw leads) along the Lincoln Sea continental margin caused the high productivity events, it is unlikely that the actual polynya area reached the GreenICE site at the southern Lomonosov Ridge (almost 100 km to the north of the Lincoln Sea continental margin).

Dinocyst and benthic foraminifera studies from the northern Barents Sea margin suggest that Atlantic Water advection to the Arctic Ocean was somewhat stronger during the last interglacial (Mathiessen and Knies, 2001; Wollenburg et al., 2001) and, during MIS 5a, possibly comparable to present conditions. Evidence of relative warm last interglacial conditions at the northern Barents Sea margin contradicts the data on bulk carbonate, planktic foraminifera, and coccolith abundance from Fram Strait, which suggest a less intense Atlantic Water inflow than in the Holocene (Gard and Backman, 1990; Köhler and Spielhagen, 1990; Hebbeln and Wefer, 1997; Bauch et al., 1999). An explanation for this discrecancy could be

that low biogenic carbonate contents may be explained by dissolution and/or dilution with terrigeneous sediments. Mollusc and benthic foraminiferal data from last interglacial coastal deposits of Svalbard indicate conditions slightly warmer than the present (Mangerud et al., 1998; Bergsten et al., 1998). These works and Bauch et al. (1999), however, also argue that the last interglacial in that region appear to have been colder than the Holocene climatic optimum. A number of last interglacial records from the circum-arctic shelf regions indicate a period of warmer conditions than today and a reduced sea ice cover (Hamilton and Brigham-Grette, 1991; Brigham-Grette and Hopkins, 1995; Funder et al., 1998; Kelly et al., 1999). The sea ice limit in the Amerasian Basin north of the Bering Strait has been estimated to have been placed at least 800 km north of its present position during the last interglacial (Brigham-Grette and Hopkins, 1995). Ice core data from the NGRIP core, Greenland, support a stable last interglacial climate with temperatures about 5°C warmer than today at the ice sheet summit (North Greenland Ice Core Project members, 2004).

Together, most of the climate proxy data mentioned above indicate a reduced sea ice cover in the Arctic Ocean during the last interglacial, supporting that subpolar foraminifera should be found in higher abundances higher to the north than the present day pattern. An actualistic approach supports that conditions during the last interglacial at the GreenICE site were comparable to the present day south-western Eurasian Basin close to the Fram Strait. This would imply that extended periods of seasonally open water conditions possibly prevailed at distances not too far from the GreenICE site. The scarcity of high resolution data and reliable dated records of the last interglacial from the Arctic continental margin and interior ocean, at the present stage precludes reconstructions of the Arctic circulation pattern of surface and subsurface water masses.

6 CONCLUSIONS

The GreenICE record represent hemipelagic sedimentation through the last ca. 200.000 years. The lithological and faunal changes reflect shifting environmental conditions related to glacial-interglacial changes in sea ice concentration, sediment rafting, biological productivity and paleoceanographic circulation. Glacial conditions with a massive sea ice cover and periodically increased sediment ice rafting characterised stage 6, 4, late stage 3, and 2. The provenance of the iceberg-rafted material appears to have been mainly the northern Canada archipelago. Interglacial conditions with reduced sea ice conditions and a higher planktic/benthic productivity characterised marine isotope stages 7, 5, mid 3, and 1. This is in general in accordance with other recent studies on the Arctic Ocean late Quaternary development. Our study, however, reveals high abundances of small subpolar planktic foraminifera *T. quinqueloba* in the early and late interval of marine isotope stage 5. The abundance peaks are assigned to substage 5e (last interglacial) and 5a (warm interstadial). This subpolar species occurs present day abundantly in subsurface Atlantic Waters close to the sea ice margin north of Svalbard and in the Barents Sea Branch. However, only a small percentage of subpolar specimens reach the interior Arctic Ocean as evidenced by living assemblages in the water column and late Holocene surface sediment samples from interior Arctic sites with excellent carbonate preservation. Even with an enhanced Atlantic Water boundary current system during the last interglacial period, it is unlikely that abundant subpolar specimens were advected several thousands kilometres to the interior Arctic Ocean. We therefore conclude that sea ice conditions near the GreenICE site must have been much reduced during the last interglacial. Whether this was related to a polynya-type setting or whether it reflects a generally reduced sea ice cover of the interior Arctic Ocean is not known

at the present stage. Circum-arctic climate proxy data support interglacial conditions warmer than the present, but the few well-dated interior Arctic Ocean records preclude detailed paleoceanographic interpretation.

7 ACKNOWLEDGEMENTS

This contribution is a result of the EU GreenICE Project (No. EUK-2001-00280). We would like to thank all those that contributed with logistical assistance during the ice camp field campaign in May 2004. Special thanks go to John Boserup (GEUS) for his skillful technical assistance and hard work under very difficult conditions. We extend our thanks to Robert Spielhagen (IFM-GEOMAR, Kiel) for allowing us to study radiocarbon-dated core top material from interior Arctic Ocean sites.

8 REFERENCES

Aagaard, K., J.H. Swift, and E.C. Carmack, 1985: Thermohaline circulation in the arctic mediterranean seas. *Jour. Geophys. Res.*, 90, 4833–4846.

ACEX Shipboard Scientific Party, 2005: Arctic Coring Expedition (ACEX): paleoceanographic and tectonic evolution of the central Arctic Ocean. *IODP Prel. Rep*, 302, http://www.ecord.org/exp/acex/302PR.pdf.

ACIA Overview Report, 2004: *Impacts of a Warming Arctic - Arctic Climate Impact Assessment*. 144 pp., Cambridge University Press, New York.

Backman, J., M. Jakobsson, R. Løvlie, L. Polyak, and L.A. Febo, 2004: Is the Central Arctic Ocean a sediment starved basin? *Quaternary Science Reviews*, 23(11-13), 1435-1454.

Bauch, D., Carstens, J., and Wefer, G., 1997: Oxygen isotope composition of living Neogloboquadrina pachyderma (sin.) in the Arctic Ocean. *Earth Planet. Sci. Lett.*, 146, 47-58.

Bauch, H.A., 1994: Significance of variability in Turborotalita quinqueloba (Natland) test size and abundance for paleoceanographic interpretations in the Norwegian-Greenland Sea. *Marine Geology*, 121, 129-141.

Bauch, H.A., 1999: Planktic Foraminifera in Holocene sediments from the Laptev Sea and the Central Arctic Ocean: Species distribution and paleobiogeographical implication. In: *Land-Ocean Systems in the Siberian Arctic: Dynamics and History*, edited by H. Kassens, H.A. Bauch, I. Dmitrenko, H. Eicken, H.-W. Hubberten, M. Melles, J. Thiede, and L. Timokhov, pp. 601-614, Springer, New York.

Bauch, H.A., H. Erlenkeuser, R.F. Spielhagen, U. Struck, J. Matthiessen, J. Thiede, and J. Heinemeier, 2001: A multiproxy reconstruction of the evolution of deep and surface waters in the subarctic Nordic seas over the last 30,000 years. *Quaternary Science Reviews*, 20 (4), 659-678.

Berger, A., and M.F. Loutre, 1991: Insolation values for the climate of the past 10 million years. *Quaternary Science Reviews*, 10, 297-317.

Bergsteen, H., Anderson, T., and Ingólfsson, 1998: Foraminiferal stratigraphy of raised marine deposits, representing isotope stage 5, Prins Karls Forland, western Svalbard. *Polar Research*, 17, 81-91.

Berner, H. und G. Wefer, 1990: Physiographic and biological factors controlling surface sediment distribution in the Fram Strait. In: *Geological History of the Polar Oceans: Arctic versus Antarctic*. In U. Bleil and J. Thiede, NATO ASI Series, Dordrecht (Kluwer Academic Publishers), C308, 317-335.

Brigham-Grette, J., and D.M. Hopkins, 1995: Emergent marine record and paleoclimate of the last interglaciation along the northwest Alaskan Coast. *Quaternary Research*, 43, 159-173.

Carstens, J., and G. Wefer, 1992: Recent planktonic foraminifera in the Nansen Basin, Arctic Ocean. *Deep-Sea Research*, 39(2), 507-524.

Carstens, J., D. Hebbeln, and G. Wefer, 1997: Distribution of planktic foraminifera at the ice margin in the Arctic (Fram Strait). *Marine Micropaleontology*, 29, 257-269.

Chappell, J. and N. J. Shackleton, 1986: Oxygen isotopes and sea level. *Nature*, 324, 137 - 140

Clark, D.L., R.R. Whitman, K.A. Morgan, and S.D. Mackey, 1980: Stratigraphy and glacial-marine sediments of the Amerasian Basin, central Arctic Ocean. *Geol. Soc. Am. Spec. Pape*, 181, pp. 57.

CLIMAP Project Members, 1976: The surface of Ice-Age Earth. *Science*, 191, 1131-1137.

Dansgaard, W., S.J. Johnsen, H.B. Clausen, D. Dahl-Jensen, N.S. Gundestrup, C.U. Hammer, C.S. Hvidberg, J.P. Steffensen, A.E. Sveinbjörnsdottir, J. Jouzel and G. Bond, 1993: Evidence for general instability of past climate from a 250-kyr ice-core record. *Nature*, 364, 218-220.

Darby, D.A., J.F. Bischof, and G.A Jones, 1997: Radiocarbon chronology of depositional regimes in the western Arctic Ocean. *Deep-Sea Research II*, 44 (8), 1745–1757.

Dokken, T.M., and M. Hald, 1996: Rapid climatic shifts during isotope stages 2-4 in the polar north Atlantic. *Geology*, 24, 599–602.

Dyke, A.S., J.T. Andrews, P.U. Clark, J.H. England, G.H Miller, J. Shaw, and J.J. Veilette, 2002: The Laurentide and Innuitian ice sheets during the Last Glacial Maximum. *Quaternary Science Reviews*, 21, 9-31.

Eicken H, J. Kolatschek, J. Freitag, F. Lindemann, H. Kassens, I. Dmitrenko, 2000: Identifying a major source area and constraints on entrainment for basin-scale sediment transport by Arctic sea ice. *Geophys. Res. Lett.*, 27, 1919-1922.

Eicken, H., 2003: The role of Arctic sea ice in transporting and cycling terrestrial organic matter. In: *The Organic Carbon Cycle in the Arctic Ocean: Present and Past*, edited by R. Stein and R. W. Macdonald, Berlin, Springer-Verlag, pp. 45-53.

England, J., 1999: Coalescent Greenland and Innuittian Ice during the Last Glacial Maximum: revising the Quaternary of the Canadian High Arctic. *Quaternary Science Reviews*, 18, 421-556.

EWG Atlas, 1997: Environmetal Working Group Joint U.S.-Russian Atlas of the Arctic Ocean (CD-ROM), Natl. Snow and Ice Data Cent., Boulder, Colorado.

Falkner, K.K., M. Steele, R. A. Woodgate, J. Swift, K. Aagaard, and J. Morison, 2005: Dissolved oxygen extrema in the Arctic Ocean halocline from the North Pole to the Lincoln Sea. *Deep-Sea Research I*, 52, 1138-1154.

Foley, K.M., and R. Poore, 1993: Planktic foraminifera census data from Northwind Ridge core 5 Arctic Ocean, *U.S. Geological Survey Open-File Report 91-346*, U.S. Geological Survey, Reston, VA.

Funder, S., C. Hjort, J.Y. Landvik, S.-I. Nam, N. Reeh, and R. Stein, 1998: History of a stable ice margin – East Greenland during the Middle and Upper Pleistocene, *Quaternary Science Reviews*, 17, 77-123.

Gard, G., 1988: Late Quaternary calcareous nannofossil biozonation, chronology and palaeo-oceanography in areas north of the Faeroe-Iceland Ridge. *Quaternary Science Reviews*, 7, 65–78.

Gard, G., and J. Backman, 1990): Synthesis of Arctic and Sub-Arctic coccolith biochronology and history of North Atlantic Drift water influx during the last 500,000 years. In: *Geological History of the Polar Oceans: Arctic versus Antarctic*, edited by

U. Bleil and J. Thiede, J., NATO ASI Series C, 308, 417–436, Kluwer Academic Publishers, Dordrecht.

Haas, C. et al., this volume: Airborne electromagnetic measurements of sea ice thickness: methods and applications

Hadley Centre, 2004: http://www.metoffice.com/research/hadleycentre//models/modeldata.html

Haflidason, H., J. Eiriksson, and S. Van Kreveld, 2000: The tephrachronology of Iceland and the North Atlantic region during the middle and late Quaternary: A review. *Journal of Quaternary Science,* 15, 3–22.

Hamilton, T.D., and J. Brigham-Grette, 1991: The last interglaciatio in Alaska: stratigraphy and paleoecology of potential sites. *Quaternary International*, 10-12, 49-71.

Hebbeln, D., T. Dokken, E.S. Andersen, M. Hald, and A. Elverhøi, 1994: Moisture supply for northern ice-sheet growth during the Last Glacial Maximum. *Nature*, 370, 357–360.

Hebbeln, D., and G. Wefer, 1991: Effects of ice coverage and ice-rafted material on sedimentation in the Fram Strait, *Nature*, 350, 409-411.

Hommers, H., 1998: Gehäuseuntersuchungen an planktischen Foraminiferen hoher Breiten, Hinweise auf Umweltveränderungen während der letzten 140.000 Jahre. *Reports on Polar Research*, 295, 96pp., Alfred Wegener Institute for Polar and Marine Research, Bremerhaven.

Ishman, S.E., L. Polyak, and R.Z. Poore, 1996: An expanded record of Pleistocene deep Arctic change: Canada Basin, western Arctic Ocean. *Geology*, 24, 139–142.

Jakobsson, M., R. Løvlie, H. Al-Hanbali, E. Arnold, J. Backman, and M. Mörth, 2000: Manganese and color cycles in Arctic Ocean sediments constrain Pleistocene chronology. *Geology*, 28 (1), 23-26.

Jakobsson, M., R. Løvlie, E. Arnold, J. Backman, L. Polyak, L. Knutsen, and E. Musatov (2001), Pleistocene stratigraphy and paleoenvironmental variation from Lomonosov Ridge sediments, central Arctic Ocean. *Global and Planetary Change*, 31, 1-21.

Jakobsson, M., J. Backman, A. Murray, and R. Løvlie, 2003: Optically Stimulated Luminescence dating supports central Arctic Ocean cm-scale sedimentation rates. *Geochemistry, Geophysics, Geosystems*, 4 (2), 1-11.

Johannesen, T., E. Jansen, A. Flatoy, and A.C. Ravelo, 1994: The relationship between surface water masses, oceanographic fronts, and paleoclimatic proxies in surface sediments of the Greenland, Iceland Norwegian seas. NATO ASI Ser. 117, 61-85.

Johannessen, O.M., L. Bengtson, M.W. Miles, S.I. Kuzmina, V.A. Semenov, G.V. Alekseev, A.P. Nagurnyi, V.F. Zakharov, L.P. Bobylev, L.H. Pettersson, K. Hasselmann, and H.P. Cattle, 2004: Arctic climate change: observed and modeled temperature and sea-ice variability. *Tellus A*, 56 (5), 559-560.

Jokat, W., G. Uenzelmann-Neben, Y. Kristoffersen, and T. Rasmussen, 1992: ARCTIC'91: Lomonosov Ridge - a double sided continental margin. *Geology* 20, 887-890.

Jokat, W., 1999: The Expedition ARK-XIV/1a of RV Polarstern in 1998. *Reports on Polar Research*, 308, 159 pp., Alfred Wegener Institute for Polar and Marine Research, Bremerhaven.

Kandiano, E.S., and H.A. Bauch, 2002: A case study on the application of different planktic foraminiferal size fractions for interpreting late Quaternary paleoceanographic changes in the polar North Atlantic. *Jour. Foram. Res.*, 32 (3), 245-251.

Kelly, M., S. Funder, M. Houmark-Nielsen, K.L. Knudsen, C. Kronborg, J. Landvik, and L. Sorby 1999: Quaternary glacial and marine environmental history of northwest Greenland: a review and reappraisal. *Quaternary Science Reviews*, 18, 373-392.

Knies, J., N. Nowaczyk, C. Müller, C. Vogt, and R. Stein, 2000: A multiproxy approach to reconstruct the environmental changes along the Eurasian continental margin over the last 150.000 years. *Marine Geology*, 163, 317–344.

Köhler, S.E.I., and R.F Spielhagen, 1990: The enigma of oxygen isotope stage 5 in the central Fram Strait. In: *Geological History of the Polar Oceans: Arctic versus Antarctic*, edited by U. Bleil, and J.Thiede, NATO ASI Series C, 308, pp. 489–497, Kluwer Academic Publishers, Dordrecht.

Kristoffersen, Y., B. Coakley, W. Jokat, M. Edwards, H. Brekke, J. Gjengedal, 2004: Seabed erosion on the Lomonosov Ridge, central Arctic Ocean: A tale of deep draft icebergs in the Eurasia Basin and the influence of Atlantic water inflow on iceberg motion, *Paleoceanography*, 19, PA3006.

Kristoffersen, Y., and N. Mikkelsen, 2006: On sediment deposition and nature of the plate boundary at the junction between the submarine Lomonosov Ridge, Arctic Ocean and the continental margin of Arctic Canada/North Greenland. *Marine Geology*, 225, 265-278.

Lea, D.A., P.A. Martin, D.K. Pak, and H. Spero, 2002: Reconstructing a 350 ky history of sea level using planktonic Mg/Ca and oxygen isotope records from a Cocos Ridge core. *Quaternary Science Reviews*, 21, 283-293.

Mangerud, J., and S. Gulliksen, 1975: Apparent radiocarbon ages of recent marine shells from Norway, Spitsbergen, and Arctic Canada. *Quaternary Research*, 5, 263–273.

Martinson, D.G., N.G. Pisias, N.D. Hays, J. Imbrie, T.C. Moore, and N.J. Schackleton, 1987: Age dating and the orbital theory of the ice ages: development of a high-resolution 0 to 300.000 year chronostratigraphy. *Quaternary Research*, 27, 1-29.

Matthiessen, J., and J. Knies, 2001: Dinoflagellate cyst evidence for warm interglacial conditions at the northern Barents Sea margin during marine isotope stage 5. *Journal of Quaternary Science*, 16 (7), 727–737.

North Greenland Ice Core Project members, 2004: High-resolution record of Northern Hemisphere climate extending into the last interglacial period. *Nature*, 431, 147-151.

Nørgaard-Pedersen, N., 1997: Late Quaternary Arctic Ocean sediment records: surface ocean conditions and provenance of ice-rafted debris. *GEOMAR Report 65*, 115 pp., University of Kiel, Kiel, Germany.

Nørgaard-Pedersen, N., R.F. Spielhagen, J. Thiede, and H. Kassens, 1998: Central Arctic surface ocean environment during the past 80,000 years. *Paleoceanography*, 13(2), 193-204.

Nørgaard-Pedersen, N., R.F. Spielhagen, H. Erlenkeuser, P.M. Grootes, J. Heinemeier, and J. Knies 2003: The Arctic Ocean during the Last Glacial Maximum: Atlantic and Polar domains of surface water mass distribution and ice cover. *Paleoceanography*, 18 (3), 1063, doi:10.1029/2002PA000781.

Okulitch, A.V., 1991: Geology of the Innuitian Orogen and Arctic Platform of Canada and Greenland. In: *The geology of North America, vol. E., Geology of the Innuitian Orogen and Arctic Platform of Canada and Greenland*, edited by H.P Trettin, Geol. Survey Canada, Alberta.

Pfirman S.L., R. Colony, D. Nürnberg, H. Eicken, I. Rigor I, 1997: Reconstructing the origin and trajectory of drifting Arctic sea ice. *J Geophys Res.*, 102(C6):12575–12586.

Pfirman, S., Lange, M. A., Wollenburg, I., and Schlosser, P., 1990: Sea ice characteristics and the role of sediment inclusions in deep-sea deposition: Arctic - Antarctic comparisons. In: *Geological history of the Polar Oceans: Arctic versus Antarctic*, edited by U. Bleil and J. Thiede, Dordrecht, Kluwer Academic Publishers, 187-211

Phillips, R.L., and A. Grantz, 1997: Quaternary history of sea ice and paleoclimate in the Amerasia basin, Arctic Ocean, as recorded in the cyclical strata of Northwind Ridge. *Geol. Soc. Am. Bull.*, 109, 1101–1115.

Phillips, R.L., and A. Grantz, 2001: Regional variations in provenance and abundance of ice-rafted clasts in Arctic Ocean sediments: implications for the configuration of Late Quaternary oceanic and atmospheric circulation in the *Arctic. Marine Geology*, 172, 91–115.

Polyak, L., W.B. Curry, D.A. Darby, J. Bischof, and T.M. Cronin, 2004: Contrasting glacial/interglacial regimes in the western Arctic Ocean as exemplified by a sedimentary record from the Mendeleev Ridge *Palaeogeography, Palaeoclimatology, Palaeoecology*, 20, 73-93.

Poore, R.Z., R.L. Phillips, and H.J. Rieck, 1993: Paleoclimate record for Northwind Ridge, western Arctic Ocean. *Paleoceanography*, 8, 149–159.

Rothrock, D.A., Y. Yu, and G.A. Maykut, 1999: Thinning of the Arctic sea-ice cover. *Geophysical Research Letters*, 26(23), 3469-3472.

Rudels, B., H.J. Friederich, and D. Quadfasel, 1999: The Arctic Circumpolar Boundary Current. *Deep Sea Research II*, 46, 1023-1062.

Rudels, B., A.-M. Larsson, and P.-I. Sehlstedt, 1991: Stratification and water mass formation in the Arctic Ocean: some implications for the nutrient distribution. *Polar Research*, 10, 19-32.

Rudels, B., E.P. Jones, L.G. Anderson, G. Kattner, 1994: On the intermediate depth waters of the Arctic Ocean. In: *The Polar Oceans and their Role in Shaping the Global Environment*, Geophysical Monograph Series 85, edited by O.M., Johannesen, R.D Muench, and J.E. Overland, pp. 33-46, AGU, Washington D. C.

Spielhagen, R.F., K.-H. Baumann, H. Erlenkeuser, N.R. Nowaczyk, N. Nørgaard-Pedersen, C. Vogt, and D. Weiel, 2004: Arctic Ocean deep-sea record of northern Eurasian ice sheet history. *Quaternary Science Reviews*, 23, 1455-1483.

Spielhagen, R.F., G. Bonani, A. Eisenhauer, M. Frank, T. Frederichs, H. Kassens, P.W. Kubik, N. Nørgaard-Pedersen, N.R. Nowaczyk, A. Mangini, S. Schäper, R. Stein, J. Thiede, R. Tiedemann, and M. Wahsner, 1997: Arctic Ocean evidence for Late Quaternary initiation of northern Eurasian ice sheets. *Geology*, 25, 783-786.

Spielhagen, R.F., and H. Erlenkeuser, 1994: Stable oxygen and carbon isotopes in planktic foraminifers from Arctic Ocean surface sediments: reflection of the low salinity surface water layer, *Marine Geology*, 119 (3/4), 227–250.

Stein, R., C. Vogt, C. Schubert, and D. Fütterer, 1994: Stable isotope stratigraphy, sedimentation rates, and salinity changes in the latest Pleistocene to Holocene eastern central Arctic Ocean, *Marine Geology*, 119, 333–355.

Steinsund, P.I., and M. Hald, 1994: Recent calcium carbonate dissolution in the Barents Sea: paleoceanographic implications. *Marine Geology*, 117, 303–316.

Svendsen, J.I., H. Alexanderson, V. I. Astakhov, I. Demidov, J.A. Dowdeswell, S. Funder, V. Gataullin, M. Henriksen, C. Hjort, M. Houmark-Nielsen, H.W. Hubberten, Ó. Ingólfsson, M. Jakobsson, K.H. Kjær, E. Larsen, H. Lokrantz, J.P. Lunkka, A. Lyså, J. Mangerud, A. Matiouchkov, A. Murray, P. Möller, F. Niessen, O. Nikolskaya, L. Polyak, M. Saarnisto, C. Siegert, M.J. Siegert, R.F. Spielhagen, and R. Stein, 2004: Late Quaternary ice sheet history of northern Eurasia. *Quaternary Science Reviews*, 23, 1229-1271.

Thierstein, H.R., K. Geitzenauer, B. Molfino, and N.J. Shackleton, 1977: Global synchroneity of late Quarternary coccolith datum levels: Validation by oxygen isotopes. *Geology*, 5, 400-404.

Voelker, A.H.L., M. Sarnthein, P.M. Grootes, H. Erlenkeuser, C. Laj, A. Mazaud, M.-J. Nadeau, and M. Schleicher, 1998: Correlation of marine 14C ages from the Nordic Seas with the GISP2 isotope record: implications for 14C calibration beyond 25 ka BP. *Radiocarbon 40*, (1), 517–534.

Vogt, C., 1997: Zeitliche und räumliche Verteilung von Mineralvergesellschaftungen in spätquartären Sedimenten des Arktischen Ozeans und ihre Nutzbarkeit als Klimaindikatoren während der Glazial/ Interglazial-Wechsel. *Reports on Polar Research*, 251, 309 pp., Alfred Wegener Institute for Polar and Marine Research, Bremerhaven.

Volkmann, R., 2000a: Planktic foraminifers in the outer Laptev Sea and the Fram Strait – modern distribution and ecology. *Jour. Foram. Res.*, 30, 157-176.

Volkmann, R., 2000b: Planktic foraminifer ecology and stable isotope geochemistry in the Arctic Ocean: implications from water column and sediment surface studies for quantitative reconstructions of oceanic parameters, *Reports on Polar Research*, 361, 100 pp., Alfred Wegener Institute for Polar and Marine Research, Bremerhaven.

Volkmann, R., and M. Mensch, 2001: Stable isotope composition (δ18O and δ13C) of living planktic foraminifers in the outer Laptev Sea and the Fram Strait. *Mar. Micropaleontol.*, 42, 163-188.

Wadhams, P., 1997: Ice thickness in the Arctic Ocean: the statistical reliability of experimental data, *Jour. Geophys. Res.*, 102, 27951-27959.

Wadhams, P., and N.R. Davis, 2000: Further evidence of ice thinning in the Arctic Ocean. *Geophys. Res. Lett.*, 27, 3973-3975.

Wollenburg, J., W. Kuhnt, and A. Mackensen, 2001: Changes in Arctic Ocean paleoproductivity and hydrography during the last 145 kyr: The benthic foraminiferal record, *Paleoceanography*, 16(1), 65-77.

Airborne Electromagnetic Measurements of Sea Ice Thickness: Methods and Applications

Christian Haas, Sibylle Goebell, Stefan Hendricks, Torge Martin, Andreas Pfaffling, Carola von Saldern
Alfred Wegener Institute for Polar and Marine Research, Climate Sciences Division, Sea Ice Physics Section, 27515 Bremerhaven, Germany

Keywords: ice thickness, EM methods, electromagnetic sounding

ABSTRACT: Alfred Wegener Institute operates two helicopter-borne electromagnetic (EM) sounding devices dedicated to the measurement of sea ice thickness. With the method, level total (ice plus snow) thickness can be determined with an accuracy of ±0.1 m. However, due to the footprint of the method and due to the porosity of unconsolidated ridge keels, deformed ice thickness can be strongly underestimated. The paper summarizes the retrieval of ice thickness from the EM data, and shows some validation results. Applications of the methods show that level ice thickness has decreased by 20% in the Transpolar Drift between 1991 and 2001, but remained constant at 2.0 m between 2001 and 2004. Surveys in 2004 and 2005 in the Lincoln Sea revealed very thick ice with modal thicknesses between 3.9 and 4.2 m, and an increase of mean ice thickness from 4.67 m in 2004 to 5.18 m in 2005. As the EM instruments also comprise a laser altimeter and a differential GPS receiver (DGPS), independent measurements of ridge distributions and surface roughness can be obtained. In addition, coincident measurements of total thickness and surface elevation allow the retrieval of snow thickness.

1 INTRODUCTION

Sea ice thickness is one of the most important parameters for climate studies and ice engineering problems. Apart from upward looking sonar (ULS) profiling, electromagnetic induction (EM) thickness sounding has become an accurate and efficient method for thickness profiling and can be operated on the ice, from ships (Haas, 1998; Haas et al., 1999), or from structures like lighthouses or oil rigs (Haas and Jochmann, 2003). However, EM sounding is most powerful when operated from helicopters (Kovacs et al., 1987; Kovacs and Holladay, 1990; Prinsenberg and Holladay 1993; Haas, 2004; Haas et al., 2006) or fixed-wing aircraft (Multala et al., 1996).

At Alfred Wegener Institute for Polar and Marine Research in Bremerhaven, Germany, two helicopter EM (HEM) systems have been developed since 1999 (EM birds), based on good experience on the robustness and efficiency of EM thickness measurements in general (Haas et al., 1997; Haas and Eicken, 2001). Those two birds have since been widely operated in Arctic, Antarctic, and Baltic waters, providing unique new insights into regional ice thickness distributions and their temporal changes.

Here, we review the HEM method and discuss the accuracy of HEM thickness retrievals. Some of the most recent results are summarized. Then, a final section shows how HEM measurements can be applied for advanced studies of delineating ice regimes from surface or satellite remote sensing data, and for the determination of snow thickness if the thickness retrievals are combined with laser altimeter and GPS measurements. Most results

were obtained within the EU-funded GreenICE (Greenland Arctic Shelf Ice and Climate Experiment) and SITHOS (Sea Ice Thickness Observing System) projects between 2003 and 2005.

2 METHODS

HEM thickness sounding

An EM system consists of an assembly of coils for the transmission and reception of low-frequency EM fields, and a laser altimeter. The EM components are sensitive to the sensor's height above the conductive sea water surface, while the sensor's altitude above the ice or snow surface is determined with the laser altimeter. Over sea ice, the water surface coincides with the ice underside. Therefore, the difference of the height measurements of both components corresponds to the ice-plus-snow, or total thickness (Figure 1; Haas, 1998).

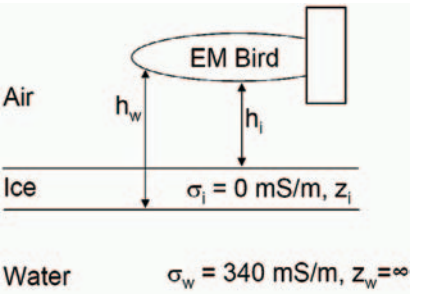

Figure 1. Principle of EM thickness sounding, using a bird with transmitter and receiver coils and a laser altimeter. Ice thickness z_i is obtained from the difference of measurements of the bird's height above the water and ice surface, h_w and h_s, respectively. H_w is obtained with the assumption of a negligible ice conductivity σ_i, known water conductivity σ_w, and horizontal layering (see below).

AWI EM birds

We have built two EM birds dedicated to scientific sea ice studies. They must be easily operable from any kind of helicopter capable of carrying an external load, and from aboard icebreakers (Figure 2). Therefore, our birds are only 3.5 m long and weigh 100 kg. They are suspended 20 m below the helicopter and are towed at heights of 10 to 20 m above the ice surface. One two-frequency EM bird operates at frequencies of 3.6 and 112 kHz, and our single-frequency bird uses a signal frequency of 4.1 kHz. Coil spacing is 2.77 m for the low frequency transmitting and receiving coils, and 2.05 m for the high frequency. Signal generation, reception, and processing are fully digital, maximising signal-to-noise ratio. The EM systems are calibrated by means of internal calibration coils with a known response. EM sampling frequency is 10 Hz, corresponding to a measurement point spacing of approximately 3 to 4 m. Measurements are interrupted every 15 to 20 minutes by ascents to high altitude, to monitor electrical system drift.

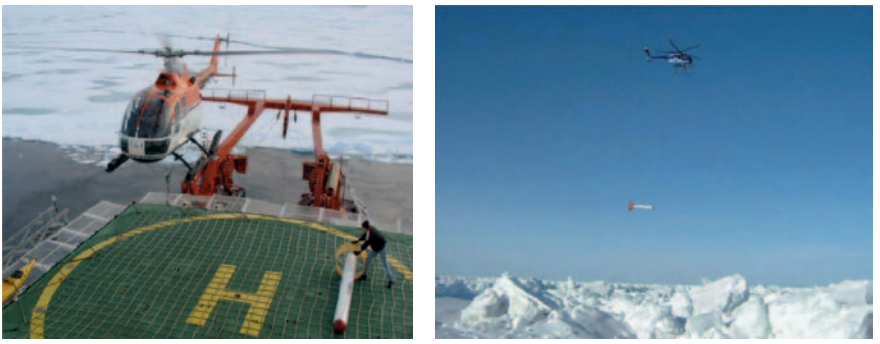

Figure 2. AWI HEM bird during take-off from the helicopter deck of an icebreaker, and during operation at 15 to 20 m above the ice surface (right photo courtesy J. Wilkinson).

Thickness retrieval

For the thickness computation over high salinity sea water, we use only data of the in-phase component of the complex EM signal, which is the strongest and most sensitive channel. Figure 3 shows the relationship between bird height above the ice surface and the measured and modelled EM responses for a flight over the Lincoln Sea. The model results (Ward and Hohmann, 1988) have been computed for open water (ice thickness 0 m) with a sea water conductivity of 2500 mS/m, representative of in-situ CTD measurements. The model curve provides the general means of computing the height of the bird above the water surface or ice underside from a measurement of in-phase EM field strength at a certain height above the water (Figure 1; Haas, 1998). Measurements at different heights are obtained because the altitude of the helicopter and bird vary between 10 and 25 m during the flight (Figure 3). The data can be separated into two branches: while open water measurements at different bird heights agree well with the model curves, the presence of sea ice leads to a reduction of the measured EM signal at a given laser height (Fig. 3). Therefore the scattered cloud of data points below the model curve represents measurements over ice. Ice thickness is computed by subtracting the laser height measurement over sea ice from the model curve (Haas, 1998). It can also be visually estimated from the horizontal distance between each EM measurement and the model curve (Fig. 3). The thickness computation assumes a negligible sea ice conductivity of < 20 mS/m, which is likely for the multiyear ice in the study region (Haas et al., 1997).

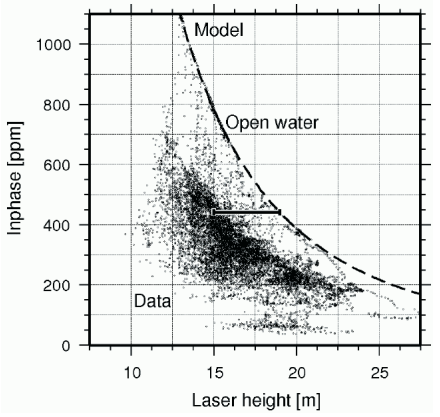

Figure 3. EM field strength (in-phase component of relative secondary field strength at 3.6 kHz) versus laser height measurement. A model curve and data over a typical ice surface with some leads are shown. The model curve has been computed for a sea water conductivity of 2500 mS/m. The horizontal bar illustrates how ice thickness (4 m) is obtained for a single data point from the difference between laser measurement and the model curve for a given EM field strength (see text).

Figure 4 illustrates the two steps of determining the height above the ice and water surfaces, and obtaining ice thickness from the difference of these measurements. The example is from the Transpolar Drift in August 2001. Figure 4c shows the thickness distribution computed from the resulting ice thickness profile, computed with a bin width of 0.1 m. The modes of the distribution represent the fraction of open water along the profile, first year ice with a modal thickness of 1.2 m, and 2 m thick second and multiyear ice. The narrowness of the modes demonstrates the low noise and high accuracy of our measurements, which we estimate to be better than ±0.1° m.

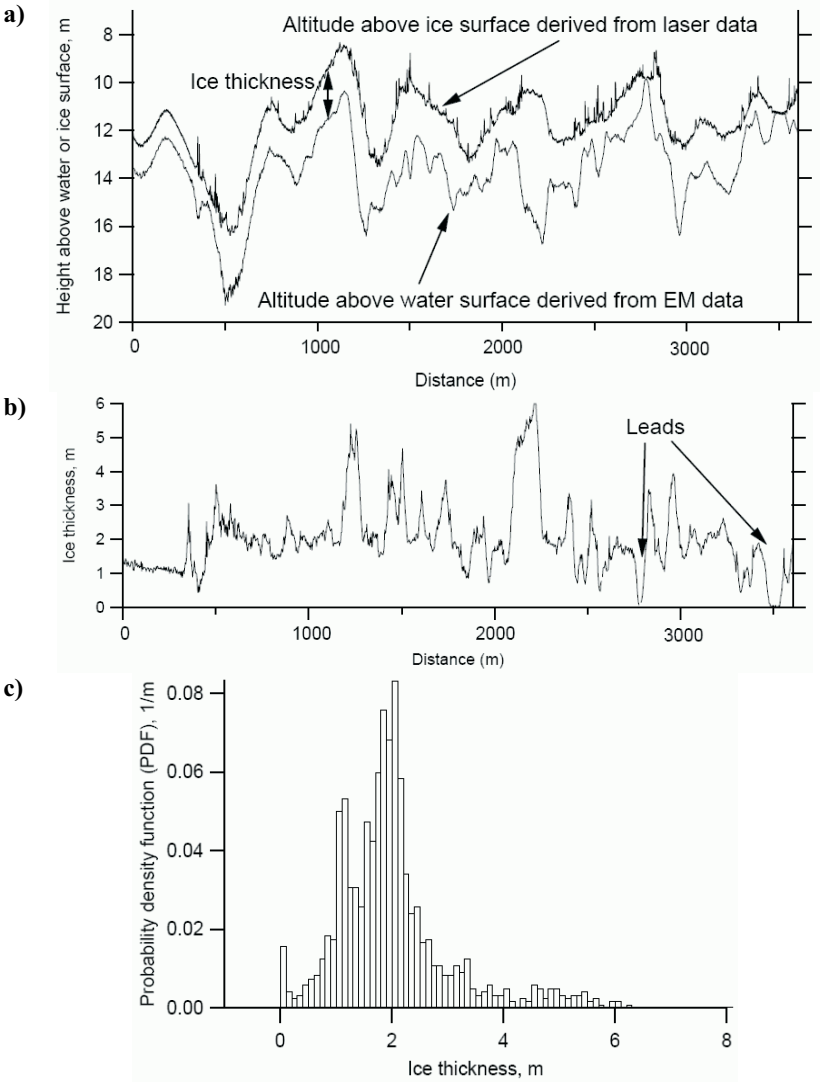

Figure 4. (a) EM and laser derived bird height above the water and ice surface, respectively, and (b) ice thickness profile resulting from subtraction of the latter from the former. (c) Resulting thickness distribution.

3 VALIDATION OF EM THICKNESS RETRIEVALS

Comparison with drill-hole data shows that the EM derived ice thicknesses agree well within ±0.1 m over level ice (e.g. Reid et al., 2006, Pfaffling et al., 2006; see also Fig. 8 below). Figure 5 shows an example of a 150 m long drill-hole profile compared to the HEM thickness retrievals. However, the accuracy is worse over ridges. Because the low-frequency EM field is diffusive, its strength represents the average thickness of an area of 3.7 times the instrument's altitude above the ice surface (Kovacs et al., 1995; Reid et al., 2006). Due to this "footprint" and the porous nature of ridge keels, the maximum ridge thickness can be strongly underestimated. A study by Reid et al. (2006) shows that the footprint of the Quadrature component of the EM signal amounts only to half or two-thirds of the In-phase footprint. This can also be judged from Figure 5. However, we normally use the In-phase component because it has a much better signal-to-noise ratio.

Haas and Jochmann (2003) have performed coincident ULS and EM measurements on a lighthouse in the Bay of Bothnia of the Baltic Sea, allowing for a direct comparison of ULS draft and EM thickness measurements of deformed ice thickness. These showed that the thickness of unconsolidated deformed ice is underestimated by the EM measurements by as much as 50 or 60% in the worst cases, depending on the geometry and consolidation of the keels (Figure 6). It should be noted, however, that the example of Figure 6 has been obtained over brackish sea water where the measurements are hampered by low EM responses. Other experience shows that the performance of the EM measurements over consolidated ridges under Arctic conditions is much better (Figure 5).

4 RESULTS AND APPLICATIONS

The main application of EM measurements is the determination of regional thickness distributions and their seasonal, interannual, and decadal variability. Unfortunately, systematic regional thickness monitoring programmes have only just been initiated, as shown below by the results of our measurements in the Lincoln Sea. Other applications focus on the validation of satellite data and the provision of ground-truth data for algorithm development. For example, we are working on algorithms to estimate surface roughness characteristics from SAR imagery, where the analysis and classification of laser profiler data plays a crucial role. HEM thickness soundings are also the only means for the validation of satellite altimeter data, where the transformation of profiles of freeboard (CryoSat) or surface elevation (ICESat) into ice thickness is the main challenge.

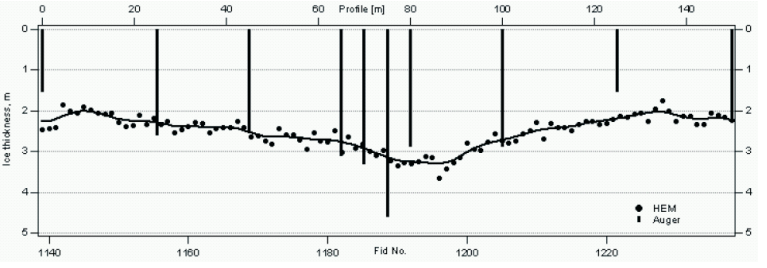

Figure 5. Comparison of helicopter EM thickness estimates with drill-hole measurements obtained over Arctic multiyear ice.

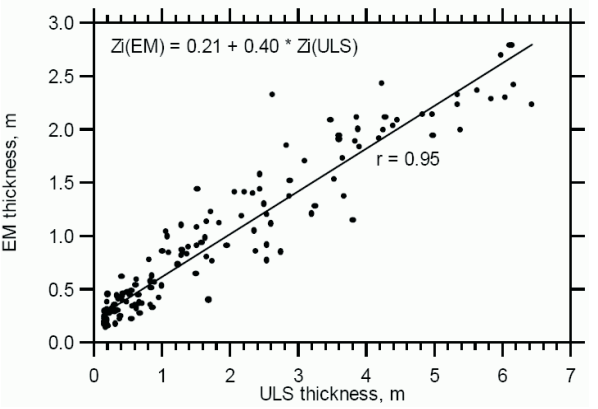

Figure 6. Comparison of coincident EM and ULS ice thickness measurements obtained from the northern Baltic Sea (Haas and Jochmann, 2003).

Ice thickness variability in the Transpolar Drift, 1991-2004

By means of EM sounding, we have irregularly observed the temporal sea ice thickness variability of the Transpolar Drift during August and September since 1991 (Figure 7). The data published by Haas (2004) were updated by HEM flights during cruise ARK 20/2 of RV *Polarstern* in the summer of 2004. Results showed that modal ice thickness decreased from 2.5 m in 1991 to less than 2 m in 2001, corresponding to a thickness decrease of more than 20% (Haas, 2004). In 2004, the observed modal ice thickness of 2.0 m was only 0.05 m thicker than in 2001 (Figure 7). Thus, there was no further thinning observed between 2001 and 2004. However, we do not know how ice thickness has varied in the meantime.

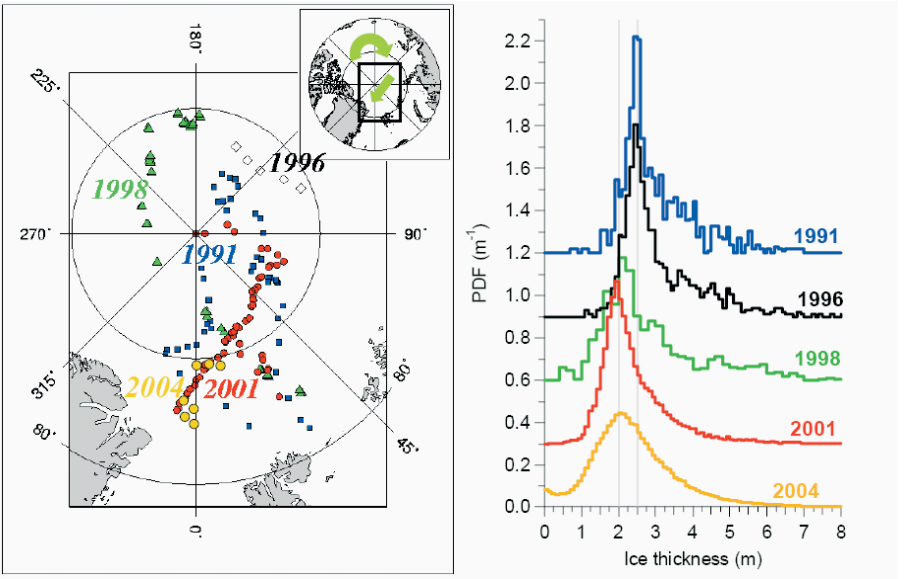

Figure 7. Map of ice thickness measurements performed during summers between 1991 and 2004 in the Transpolar Drift (left). In 2004, all measurements were performed with the EM Bird for the first time. Earlier measurements have been performed by ground-based EM profiling on single floes. Observed ice thickness distributions from the years 1991, '96, '98, 2001 and 2004 had modal thicknesses of 2.5, 2.5, 2.1, 1.95 and 2.0 m respectively (right).

Ice thickness distribution in the Lincoln Sea, May 2004 and 2005

Funded by the EU GreenICE project, systematic HEM thickness surveying has been initiated in the Lincoln Sea and adjacent Arctic Ocean, north of the Canadian Forces Station Alert on Ellesmere Island at 82.5°N, and between 60 and 70°W. First measurements have been performed in May 2004 and 2005 (Haas et al., 2006). Figure 8 compares the thickness distributions thus obtained. It can be seen that the ice is generally very thick, with modal multiyear ice thicknesses between 3.9 and 4.2 m. However, there are also significant amounts of thinner, likely first-year ice with modal thicknesses between 0.9 and 2.2 m. This ice has formed in the recurring Lincoln Polynya. Ice thickness was larger in 2005, with a mean of 5.18 m compared to 4.67 in 2004 (Haas et al., 2006). While the increased modal thickness is partially due to a 0.1 m thicker snow cover in 2005 (with a mode of 0.28 m), ice thickness did also increase by different thermodynamic boundary conditions as well as ice deformation, as can be seen from the longer tail of the 2005 thickness distribution in Figure 8. However, the observed thickness increase is much smaller than would have been expected from the strong southward ice drift towards the coasts of Ellesmere Island and Greenland, as was monitored by drifting GPS buoys (Haas et al., 2006). This is due to ice export through Nares Strait and narrow shear zones along the coasts.

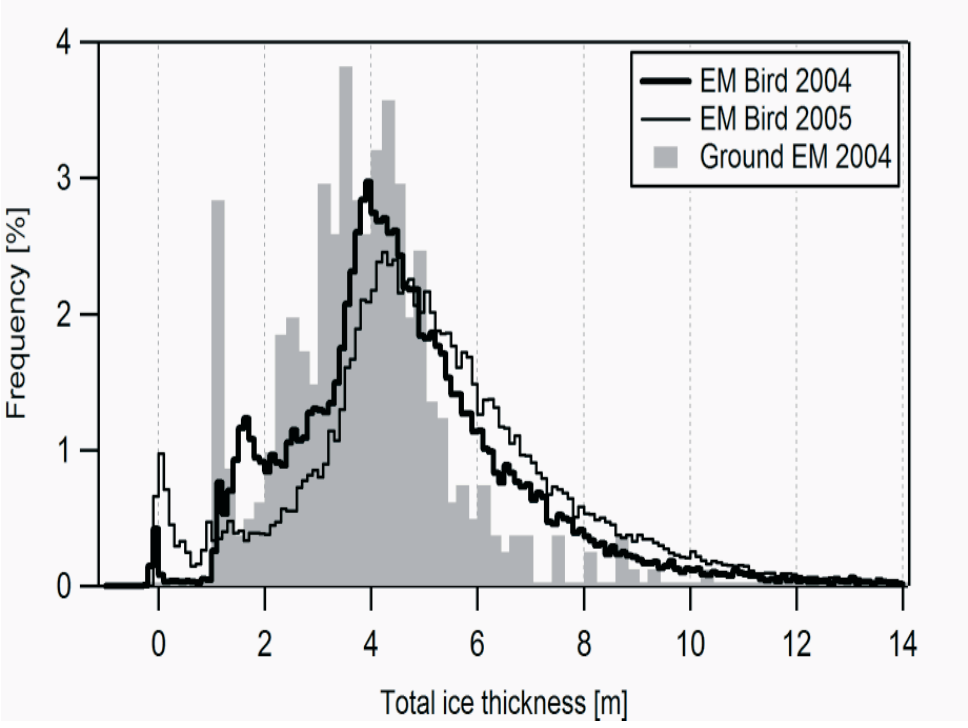

Figure 8. Sea ice thickness distributions of meridional profiles between Alert and 84°N in May 2004 and 2005. The grey-shaded distribution shows the results of the ground-based measurements in 2004 for comparison (Haas et al., 2006).

Laser profiling of surface roughness and ridge distributions

The laser altimeter included in the EM Bird can be used independently of the EM measurements to obtain information on surface roughness and ridge statistics. Originally, there was no DGPS receiver in the EM Bird to obtain measurements of bird altitude variations, which is necessary to extract the surface roughness profiles (Hvidegaard, xxx; Forsberg et al., this issue). However, the bird altitude variations can also roughly be removed by a combination of different high- and low-pass filters (Hibler, 1972). While this does not allow computation of absolute values of surface elevation, the small scale roughness on scales of some ten meters remains unaffected. Figure 9 shows typical roughness profiles thus obtained, for characteristically different ice types based on the WMO sea ice classification (von Saldern et al., 2006).

We have developed classification algorithms based on the laser data to distinguish between different ice types, and to relate them to ice thickness. A result of a clustering algorithm is shown in Figure 10, where the region around Svalbard is grouped into different degrees of deformation (von Saldern et al., 2006). Unfortunately, there was only weak agreement between roughness and thickness classes. The two thickest ice classes (Thick FY and Old ice) could be discriminated best with the classification technique, and it was also possible to distinguish these thicker classes from the three thinner classes. The three thinner ice classes could not be separated.

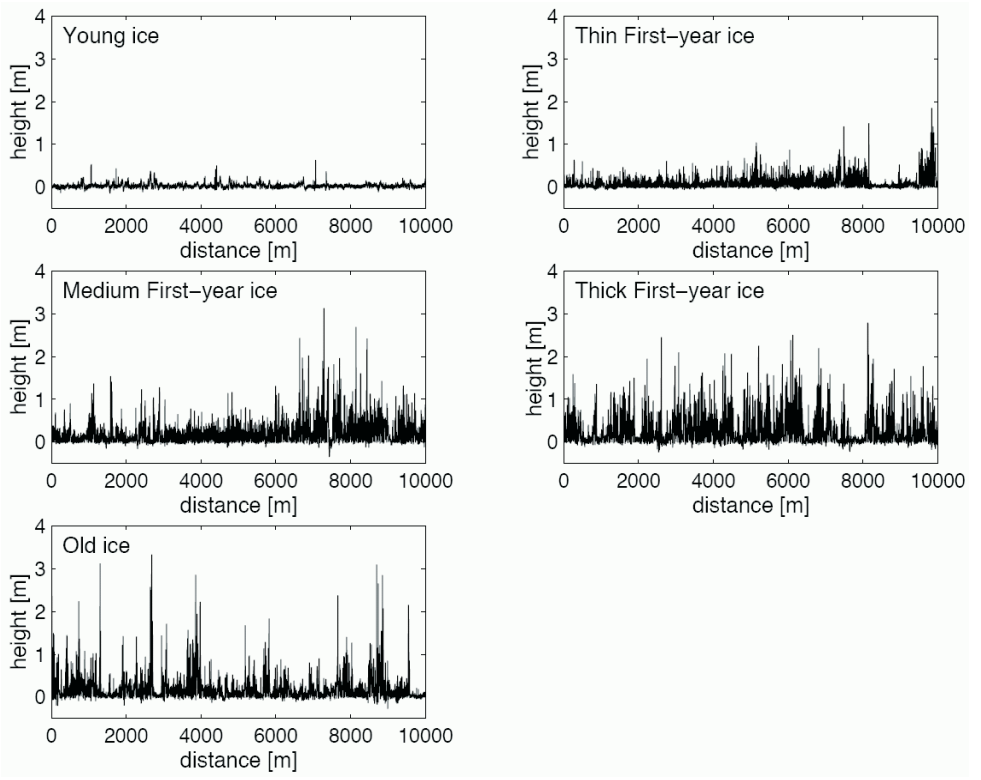

Figure 9. Surface roughness profiles of different ice types, which have been used to develop algorithms for their objective classification (von Saldern et al., 2006).

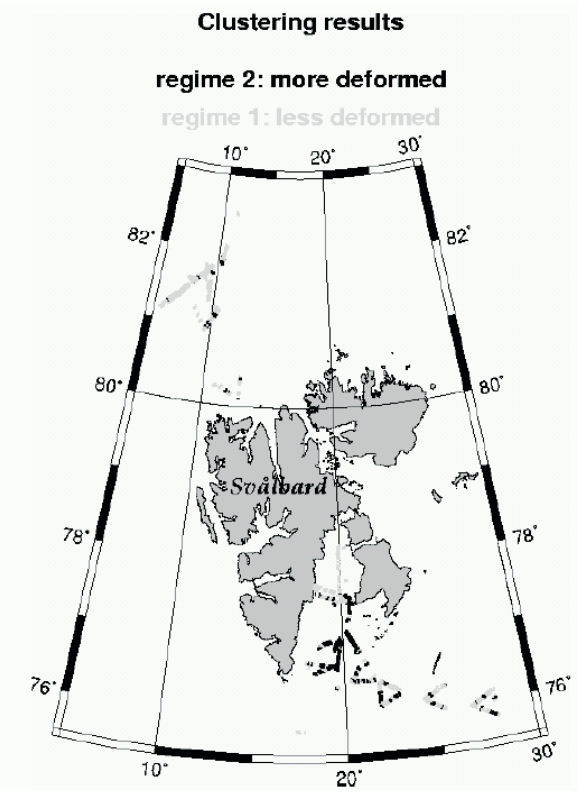

Figure 10. Geographical distribution of two roughness regimes around Svalbard in March and April 2003, in Storfjord and the Barents Sea, and in Fram Strait (von Saldern et al., 2006).

The surface roughness profiles can also be used to identify pressure ridges. This is routinely done with all EM-Bird data, as it provides additional information on the amount and thickness of deformed ice, which is underestimated from the EM thickness data alone. Figure 11 summarizes the results thus obtained during GreenICE and SITHOS HEM campaigns to the Lincoln Sea, Fram Strait, Barents Sea, and to the Baltic Sea. Sail height distributions possess the well-known exponential decline towards higher sails (Fig. 11, left panel). The distribution changes its steepness from the thin first year ice of the Baltic to the heavily deformed multiyear ice in the Lincoln Sea north of Greenland and the Canadian Archipelago. Barents Sea and Fram Strait feature ice regimes that are of intermediate deformation state, representing Arctic thick first-year and thin multiyear ice. Differences in the distributions of ridge density (Fig. 11, right panel) closely correspond to the characteristics of the respective ridge height distributions. Ridge density is the number of ridges per kilometre and is calculated from the sail spacing of 5 km long legs. The thin and thick first-year ice of the Baltic and Barents Seas shows rather small modal ridge densities of only 1 km-1, for a cut-off height of 0.8 m. In Fram Strait and the Lincoln Sea larger ridges are more frequent, up to 16 km-1. It is interesting to note that also in the Barents Sea a second, smaller mode occurs at 20 km-1. This mode originated from heavily deformed second-year ice in the entrance of Storfjord, which was advected into the Barents Sea by the East Spitzbergen Current in March 2003.

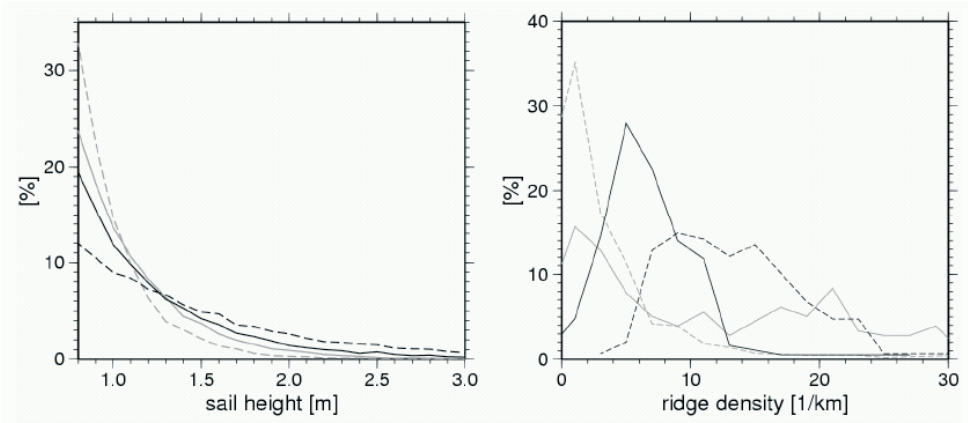

Figure 11. Frequency distributions of sail height (left panel) and ridge density (right panel) in Fram Strait (solid black), in the Lincoln Sea (dashed black), in the Barents Sea (solid grey), and in the Baltic Sea (dashed light grey) derived from HEM laser profiles. Ridge statistics have been computed for a cut-off height of 0.8 m.

Snow thickness measurements using laser altimetry, DGPS, and total thickness estimates

Since 2004, a DGPS receiver has been included in our EM-Bird for the accurate determination of surface elevation from laser and DGPS data. With the DGPS data, the bird altitude variations can be accurately removed from the laser measurements. Therefore, the EM-Bird now acquires coincident profiles of ice thickness and surface elevation, allowing validation of ICESat and CryoSat ice thickness retrievals.

Key to accurate thickness retrievals from satellite altimetry is the transformation of surface elevation to ice thickness by multiplying the former with a factor R, which is a function of snow depth and the densities of snow and ice (Wadhams et al., 1992). While these are generally not known with sufficient accuracy, the situation is even more complicated if different ice and snow thickness classes are present. Figure 12 shows an example from the Lincoln Sea, where thick MY ice and thinner FY ice were present in May 2005. The histogram of surface elevation can be transformed into a thickness distribution matching the EM-derived data, if varying R-factors are assumed for different surface elevations.

In the example of Figure 12, R-factors were computed from the modes of the thickness and surface-elevation distributions as given in the Figure. They were R = 6.3 and R = 5.74 for first-year and multiyear ice, respectively.

From the varying R-factors, different snow thicknesses can be calculated, if isostatic equilibrium and certain values for the densities of seawater, ice, and snow are assumed. In the example of Figure 12, modal snow thicknesses of 0.16 and 0.44 m result for the first-year and multiyear ice, with water, ice, and snow densities of 1024, 915, and 300 kg m-3, respectively. These results are in good agreement with direct measurements on the ground (Haas et al., 2006). However, our results show that R varies widely between values of 5 and 8, and that functions of R versus surface elevation have to be tuned for any different ice type.

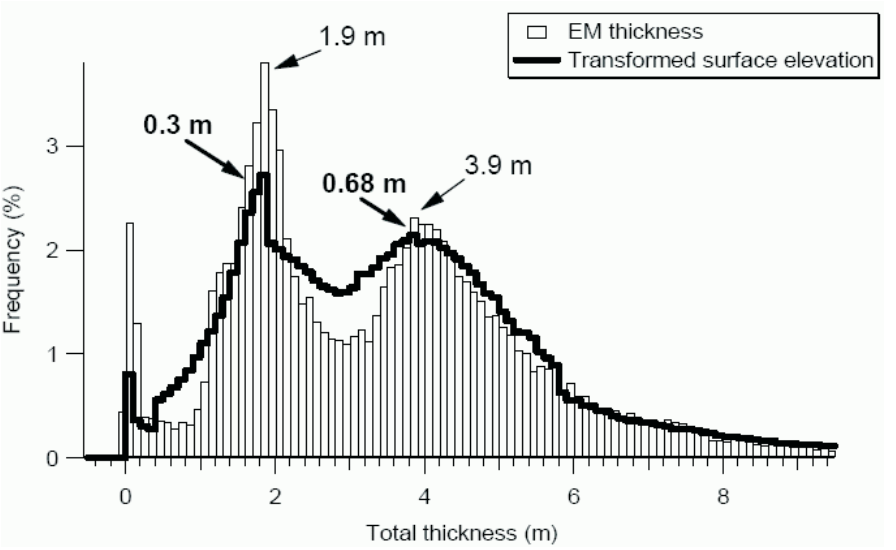

Figure 12. Comparison of ice thickness distributions in the Lincoln Sea in May 2005, derived from EM thickness sounding and from coincident laser/DGPS measurements of surface elevation. The distribution of surface elevations was transformed into an ice thickness distribution using R-factors derived from matching local modes of both distributions, given by the numbers (bold: surface elevation; plain: ice thickness).

5 CONCLUSION AND OUTLOOK

EM thickness sounding is a powerful tool for accurate thickness measurements. The accuracy of retrievals of level ice thickness is better than ±0.1 m. However, over deformed ice, the maximum thickness of ridge keels could be underestimated by as much as 50 or 60%. Nevertheless the measurements provide information about the amount of deformed ice in the survey region (Fig. 11), and ridge thicknesses can be distinguished relatively, as shown by our EM/ULS comparison (Fig. 6) and by the surveys in the Lincoln Sea in 2004 and 2005 (Fig. 8). The method is therefore well understood and robust, and can now be applied for more systematic measurements, e.g. for the thickness monitoring programme we have just initiated in the Lincoln Sea and adjacent Arctic Ocean.

To better understand and possibly correct for the underestimation of deformed ice thickness, 2- and 3D- EM modelling studies are required. These need to take into account not only the 3D structure of the ridges, but also the high ridge porosity, comprising of large seawater-filled, interconnected voids and large ice blocks. The connectivity of the voids leads to channelling effects of the eddy currents, which may prevent any deeper penetration of the EM fields. However, different EM channels will have variable sensitivity to these conditions, and therefore multi-channel inversion procedures could improve the thickness retrievals over deformed ice.

Ultimately, more coincident ULS and EM measurements under Arctic conditions should be performed to obtain profiles of ULS draft and EM ice thickness for direct comparison. Unfortunately, an attempt during RV *Polarstern* cruise ARK 20 in 2004 failed due to bad weather, when RV *Polarstern* and British RRS *James Clark Ross* met with the

intention to perform joint measurements with the UK Autosub. Therefore, any other opportunity would be highly appreciated.

Although HEM thickness surveying is a big step forward for systematic measurements, the limited range of helicopter operations of 300 to 400 km still poses a problem for larger scale studies. Therefore, we strongly encourage international cooperation, e.g. in the usage and joint deployment of fuel depots and other infrastructure in the Arctic to extend operation range. For example, during IPY 2007 and 2008 we plan to survey across the whole Arctic Ocean, jointly with logistical support from US, Danish, and Russian colleagues. We do also loan our birds to other groups who might have access to ship cruises and helicopter time. The operation range can also be extended by usage of fixed wing aircraft. For example, we are currently developing an EM system for our DO228 research aircraft at Alfred Wegener Institute. Similarly, jointly with French colleagues we plan to cross the Arctic Ocean with a Zeppelin airship in 2007. However, any survey based on EM sounding has to be performed at low system altitudes of < 30 m, which poses another limitation on the method.

EM surveys yield the total sea ice thickness, i.e. the sum of ice and snow thickness. Snow thickness is another important but extremely difficult to measure climate variable. Our new results using EM thickness surveying combined with laser profiling and DGPS flight-altitude measurements point to en exciting new possibility to retrieve both snow and ice thickness from a single bird flight. We will perform an extensive validation study of this technique during September 2006 in the Weddell Sea.

6 ACKNOWLEDGEMENTS

We are most gratefully to E. Augstein and H. Miller for initiating this work, and for AWI funding. Geophysical and technical contributions by K.P. Sengpiel, J. Lohbach, and staff of Aerodata and Optimare are greatly acknowledged. Numerous students improved the data processing procedures. All developments benefited from extensive tests flights with Helicopter Service Wasserthal and Helitransair.

7 REFERENCES

Forsberg, R., H. Skourup, 2006: Sea-ice thickness, geoid and ocean topography in the Arctic Ocean from ICESat and GRACE

European Commission, Arctic Sea Ice Thickness: Past, Present & Future, Edited by Peter Wadhams & Georgios Amanatidis, *Climate Change and Natural Hazards Series*, Brussels, 2006.

Haas, C., S. Gerland, H. Eicken, and H. Miller, 1997: Comparison of sea-ice thickness measurements under summer and winter conditions in the Arctic using a small electromagnetic induction device. *Geophysics*, 62, 749-757.

Haas, C., 1998: Evaluation of ship-based electromagnetic-inductive thickness measurements of summer sea-ice in the Bellingshausen and Amundsen Seas, Antarctica. *Cold Regions Science and Technology*, 27, 1-16.

Haas, C., K.-H. Rupp, and A. Uuskallio, 1999: Comparison of along track EM ice thickness profiles with ship performance data. *Proceedings of the 15th International Conference on Port and Ocean Engineering under Arctic Conditions*, Espoo, Finland, 1999, Helsinki Univ Techn, Ship Lab, 1, 343-353.

Haas, C., and H. Eicken, 2001: Interannual variability of summer sea ice thickness in the siberian and central Arctic under different atmospheric circulation regimes. *Journal of Geophysical Research*, 106 (C3), 4449-4462.

Haas, C., and P. Jochmann, 2003: Continuous EM and ULS thickness profiling in support of ice force measurements. *Proceedings of the 17th International Conference on Port and Ocean Engineering under Arctic Conditions, POAC ´03*, Trondheim, Norway, Department of Civil and Transport Engineering, Norwegian University of Science and Technology NTNU, Trondheim, Norway,2, 849-856.

Haas, C., 2004: Airborne EM sea-ice thickness profiling over brackish Baltic sea water. *Proceedings of the 17th international IAHR symposium on ice*, June 21-25, 2004, St. Petersburg, Russia, All-Russian Research Institute of Hydraulic Engineering (VNIIG), Saint Petersburg, Russia, 2, 12-17.

Haas, C., S. Hendricks and M. Doble, 2006: Comparison of the sea ice thickness distribution in the Lincoln Sea and adjacent Arctic Ocean in 2004 and 2005. *Annals of Glaciology*, 44, in press

Hibler, W.D. III, 1972: Removal of aircraft altitude variation from laser profiles of the Arctic ice pack. *J. Geoph. Res.*, 77(36), 7190-7195.

Hvidegaard S. M., and R. Forsberg, 2002: Sea-ice thickness from airborne laser altimetry over the Arctic Ocean north of Greenland. *Geophys. Res. Lett.*, 29 (20), 1952, doi:10.1029/2001GL014474.

Kovacs, A., N.C Valleau, and J.S. Holladay, 1987: Airborne electromagnetic sounding of sea ice thickness and sub-ice bathymetry. *Cold Regions Science and Technology*, 14, 289-311.

Kovacs, A., and J.S. Holladay, 1990: Sea-ice thickness measurements using a small airborne electromagnetic sounding system. *Geophysics*, 55, 1327-1337.

Kovacs, A., J.S. Holladay, and C.J. Bergeron, 1995: The footprint/altitude ratio for helicopter electromagnetic sounding of sea-ice thickness: Comparison of theoretical and field estimates. *Geophysics*, 60, 374-380.

Multala, J., H. Hautaniemi, M. Oksama, M. Leppäranta, J. Haapala, A. Herlevi, K. Riska, and M. Lensu, 1996: An airborne electromagnetic system on a fixed wing aircraft for sea ice thickness mapping. *Cold Reg. Sci. Techn.*, 24, 355-373.

Pfaffling, A., C. Haas, and J. Reid, 2006: Key characteristics of helicopter electromagnetic sea ice thickness mapping: Resolution, accuracy, and footprint. European Commission, *Arctic Sea Ice Thickness: Past, Present & Future*, Edited by Peter Wadhams & Georgios Amanatidis, Climate Change and Natural Hazards Series, Brussels, 2006.

Prinsenberg, S.J., and J.S. Holladay, 1993: Using air-borne electromagnetic ice thickness sensor to validate remotely sensed marginal ice zone properties. *Port and Ocean Engineering under Arctic Conditions (POAC 93)*, HSVA (Ed), Vol. 2, 936-948.

Reid, J., A. Pfaffling, and J. Vrbancich, 2006: Airborne electromagnetic footprints in one-dimensional earths. *Geophysics*, 71(2). G63-G72, doi: 10.1190/1.2187756.

Saldern, C., C. Haas, and W. Dierking, 2006: Parameterisation of Arctic sea ice surface roughness for application in ice type classification. *Annals of Glaciology*, 44, in press.

Wadhams, P., W.B. Tucker III, W.B. Krabill, R.N. Swift, J.C. Comiso, and N.R. Davis, 1992: Relationship between sea ice freeboard and draft in the Arctic Basin, and implications for ice thickness monitoring. *J. Geoph. Res.*, 97(C12), 20,325-20,334.

Ward, S. H., and G.W. Hohmann, 1988: Electromagnetic theory for geophysical applications. *Electromagnetic methods in applied geophysics-theory*, volume 1, SEG Monograph, (M.N. Nabighian, Ed.), Vol. 3, 131-313.

Recent Changes in the Sea Ice Thickness Distribution in the Russian Arctic

João Rodrigues
Polar Oceans Physics Group, Department of Applied Mathematics and Theoretical Physics, University of Cambridge, Cambridge, UK.

Keywords: Russian Arctic, ICESat, Aqua, snow on ice

ABSTRACT: We derive the winter ice thickness distribution in the Kara, Laptev, East Siberian and Chukchi Seas in 2003 from the measurements of the ice freeboard and snow depth by NASA's ICESat and EOS Aqua satellites and compare it with the direct measurements performed in the late 1970s and early 1980s.

1 INTRODUCTION

The Arctic is presently one of the most talked about regions of the Earth due to the much-reported global warming whose effects have been experienced here particularly intensely in the past few decades. Strong evidence of rapid changes in the Arctic climate is provided by the rise of the average air temperatures, at a rate which is almost twice that of the rest of the world, the substantial reduction of the extent and thickness of the sea ice cover, the increase of the length of the ice-free season in peripheral areas, the decrease of the snow cover over land, the widespread melting of glaciers and the shrinking of the Greenland ice sheet [ACIA 2004].

There are clear indications that in many regions of the Arctic, sea ice is now thinner than it was a few decades ago. The reduction of the average Arctic ice thickness between 1960 and 1990 is estimated in 10-15% in [ACIA 2004] but other studies [Rothrock 2000, Wadhams 2000] suggest that it could be higher than 40%. These estimates rely almost exclusively on measurements performed by British and American submarines in the Arctic Ocean and in the Canadian Basin. However, due to the sparsity of the observations and associated uncertainties, our knowledge of the present (and past) Arctic ice thickness distribution is still insufficient and global trends are difficult to evaluate. In spite of the undisputed quality of the submarine data, the relatively small number of cruises, the use of different methods of sonar operation, non-coincident cruise tracks and differences of seasonal timing among cruises, together with the interannual (and short term) fluctuations of the regional ice distributions, make it difficult to corroborate this apparently rapid thinning of the Arctic ice cover. Clearly, more data are needed, especially for the Siberian Basin, for which no submarine data are available.

However, systematic measurements of sea ice thickness in the Russian Arctic began a long time ago, in the early 1930s. For six decades the Soviet Union carried out extensive research programmes in the Arctic, collecting data on the thickness and other morphometric properties of the ice layer and on the depth of the snow cover. The measurements were mostly made during aircraft landings in March, April and May as well as at the end of summer. Data for the 1928-1989 period are available in digital format in the NSIDC archive [Romanov 2004] and in print [Romanov 1995]. The data set [Romanov 2004] contains measurements of 23 parameters, including ice thickness and snow depth, performed in the

Arctic Ocean and peripheral Russian Arctic seas from March to May only. In Section 3 we will use these data to construct a rough picture of the ice thickness distribution in the Russian Arctic around 1979 based on the average ice thickness (and corresponding deviations) for each region.

A continuous large scale determination of the sea ice thickness in the Arctic Ocean and surrounding seas can be done, at least in principle, by satellite altimetry. Laxon and collaborators [Laxon 2003] used radar altimetry measurements of ice freeboard by the ERS-1 and ERS-2 satellites to investigate the ice thickness distribution and its variability within the band of latitudes 65°N-81°30'N between October 1993 and March 2001. Data for the marginal ice zone were not available, which meant that the portion of the Barents Sea S of 75°N, a large fraction of the central and S sectors of the Kara Sea, the portion of the Laptev Sea S of 76°N and parts of the East Siberian Sea near the Novo Sibirskiye Ostrova were excluded from the study. The mean average winter ice thickness (excluding thin ice – less than 0.5-1.0m thick – and open water) for the region between 60°E and 150°E (which covers the NE sector of the Barents Sea, most of the NE Kara Sea, most of the Laptev Sea N of 76°N, the northeasternmost sector of the East Siberian Sea and the portion of the Arctic Ocean between those meridians) was estimated as 2.4m. The study indicated that there is a large interannual variability in the average Arctic winter ice thickness, which the authors correlated with the length of the melting season.

The launch of NASA's ICESat in January 2003 [Zwally 2002] allowed an unprecedented gathering of high quality laser altimetry data from which a global distribution of the ice freeboard in the Arctic (with the exception of the latitudes above 86°N) was derived. The data set released so far [Zwally 2003] cover the periods 21 February 2003 to 19 March 2003 and 27 September 2003 to 28 November 2003. Forsberg and Skourup [Forsberg 2005, Forsberg 2006] combined the ICESat altimetry data with an “extremely accurate” geoid model from the GRACE [Tapley 2004] and ArcGP [Kenyon 2001] to map the sea ice freeboard heights for those two periods.

The ice thickness can be retrieved from the ice freeboard assuming that the depth of the snow load, as well as the densities of the water (ρw), ice (ρi) and snow (ρs), are known. In fact, from hydrostatic equilibrium it is straightforward to derive the relation

$$h_i = \frac{\rho_w}{\rho_w - \rho_i} f - \frac{\rho_w - \rho_s}{\rho_w - \rho_i} h_s \tag{1}$$

between the ice thickness hi, the freeboard f (which includes the snow layer because the laser pulse is likely to be reflected at the snow-air interface) and the snow depth hs.

The above equation shows that the snow layer plays an important role in the determination of the ice thickness from freeboard measurements. Since 2002 the large-scale distribution of the snow depth over sea ice is being monitored daily by the Advanced Microwave Scanning Radiometer – Earth Observing System (AMSR-E) instrument on the NASA EOS Aqua satellite, which also provides global passive microwave measurements of brightness temperatures and sea ice concentrations. Data are mapped to a polar stereographic grid at 12.5km spatial resolution. The technique for retrieving snow depth from SSM/I data is described in [Markus 1998]. For the period relevant for our study, data have been processed with the so-called B02 Algorithm and archived in the NSIDC data base [Cavalieri 2004].

According to the authors of the algorithm, the extraction of Arctic snow depth is complicated by the presence of multi-year ice, which has a signature similar to snow cover on first-year ice. Therefore, the algorithm only retrieves snow depth in the seasonal sea ice zones and in regions where the ice concentration is between 0.2 and 1 and the concentration of multi-year ice below 0.2 [Cavalieri 2004]. Notice that concentrations less than 0.2 exist almost exclusively near the ice edge. The authors also point out that the main sources of error in the retrieval of snow depth on sea ice are inherent errors in sea ice concentration, uncertainty in the linear relationship between snow depth and the AMSR-E brightness temperatures, undetected snow wetness, snow grain size and snow density variability, and sensitivity to extreme weather effects.

2 WINTER 2003 ICE THICKNESS DISTRIBUTION FROM SATELLITE MEASUREMENTS

Altimetry data collected by ICESat between 21 February 2003 and 19 March 2003 [Zwally 2003] (the period of operation of Laser 1 in the winter of 2003) were analysed by Forsberg and Skourup [Forsberg 2005, Forsberg 2006], who provided the author with the file containing the average ice freeboard distribution in the Arctic for that period. The snow depth distribution for the same period was obtained from the dataset [Cavalieri 2004].

Derivation of the ice thickness from the ice freeboard and snow depth requires a knowledge of the water, ice and snow densities. While the values of the density of the water as functions of temperature and salinity are reasonably well established (we use 1.028 g cm^{-3}), there are non-negligible uncertainties in the values of the densities of the ice and snow. The density of the ice depends on the type of ice and the most likely type of ice to be found varies with the location and time of the year. According to Sandven [2003], the ice density is normally in the range 0.82-0.92 g cm^{-3} and one of the most used values is 0.887 g cm^{-3}, from Eicken [1995]. The density of freshly fallen snow is usually in the range 0.07-0.15 g cm^{-3} but compacted snow may have a much higher density, roughly between 0.30 g cm^{-3} and 0.40 g cm^{-3} [Granberg 1998]. In Sandven [2003] the value 0.36 g cm^{-3}, adequate for late winter, is used.

Combining the freeboard data with the snow data and using $\rho w=1.028 g cm^{-3}$, $\rho i=0.88$ g cm^{-3} and $\rho s=0.36$ g cm^{-3}, we derived the ice thickness charts shown in Figure 1 for the Kara, Laptev, East Siberian and Chukchi Seas. We hope that they offer a reliable description of the winter ice thickness distribution in the Russian Arctic in spite of the already mentioned year-to-year fluctuations and possible errors in the parameters.

Tables 1-4 show the average and the standard deviation of the ice thickness (in m) in several sectors of the Russian Arctic during the period of 27 days covered by this study as a function of the densities of the ice and snow (in g cm^{-3}); the median is almost always 3-10cm below the average. The different sectors that appear in this and next section's tables are defined as follows. The S, mid-latitudinal and N parts of the Laptev Sea are the waters S of 75°N, between 75°N and 78°N, and N of 78°N, respectively. The S, mid-latitudinal and N parts of the East Siberian Sea lie, respectively, S of 72°N, between 72°N and 75°N, and N of 75°N. For the Chukchi Sea, we define the S, mid-latitudinal and N sectors as the waters S of 69°N, between 69°N and 72°N, and N of 72°N. Notice that ICESat data were processed for the range of latitudes 70°N-86°N only.

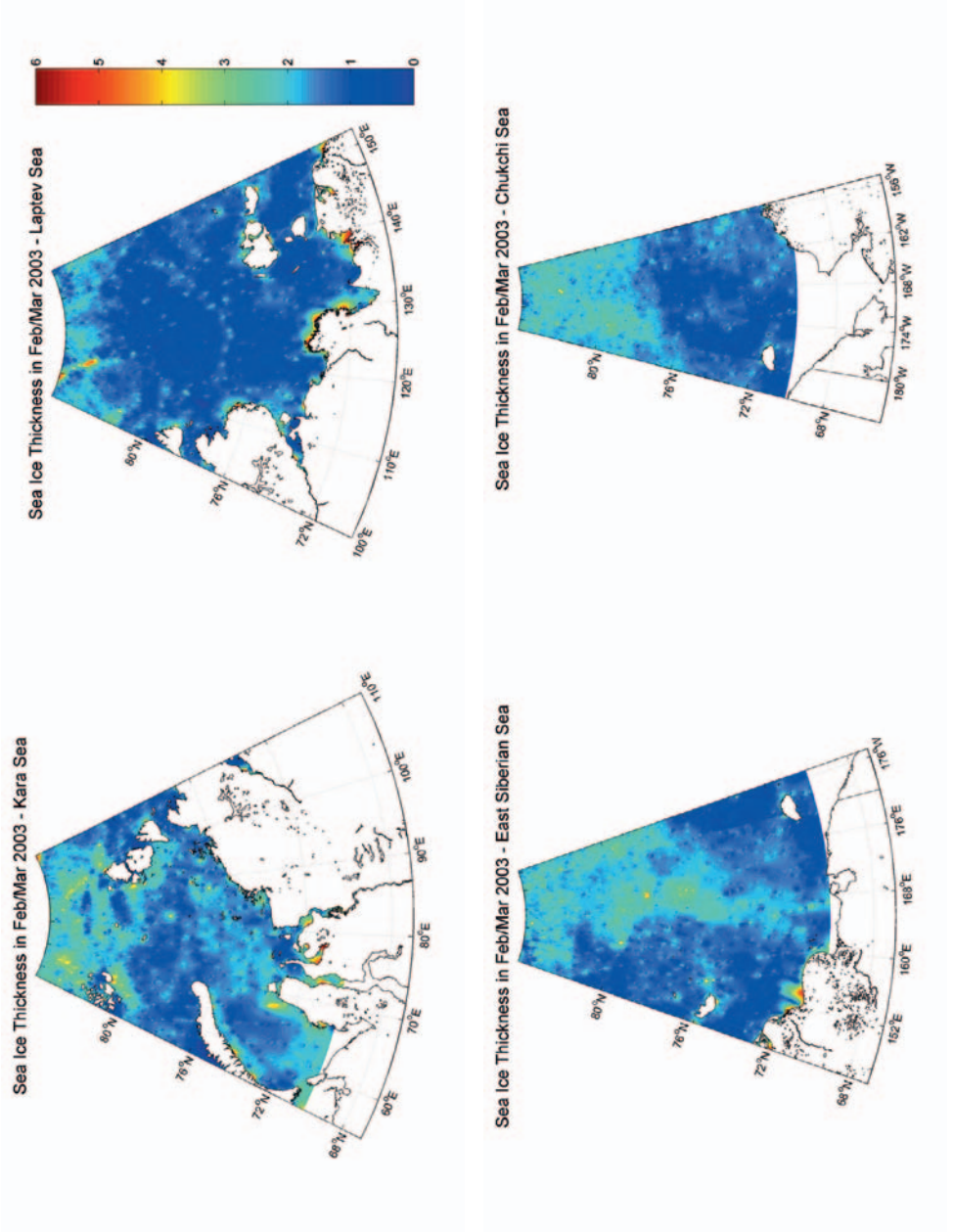

Figure 1. Average sea ice thickness from ICESat freeboard and Aqua snow depth during the period 21 February 2003 to 19 March 2003 in the Kara, Laptev, East Siberian and Chukchi Seas. The colour bar indicates the ice thickness in metres.

Table 1. Ice thickness in the Kara Sea in the period 21 February 2003 to 19 March 2003.

Ice Density	Snow Density	South		Mid-latitude		North	
		Average	S.D.	Average	S.D.	Average	S.D.
0.82	0.25	1.16	0.36	1.08	0.32	1.06	0.35
0.82	0.35	1.18	0.35	1.10	0.31	1.08	0.34
0.82	0.45	1.19	0.35	1.12	0.31	1.09	0.33
0.88	0.25	1.63	0.50	1.52	0.45	1.50	0.49
0.88	0.35	1.64	0.50	1.55	0.44	1.51	0.48
0.88	0.45	1.68	0.49	1.58	0.43	1.53	0.47
0.92	0.25	2.23	0.69	2.08	0.61	2.05	0.67
0.92	0.35	2.27	0.68	2.12	0.60	2.07	0.65
0.92	0.45	2.30	0.68	2.16	0.59	2.09	0.64

Table 2. Ice thickness in the Laptev Sea in the period 21 February 2003 to 19 March 2003.

Ice Density	Snow Density	South		Mid-latitude		North	
		Average	S.D.	Average	S.D.	Average	S.D.
0.82	0.25	0.87	0.50	0.70	0.32	0.69	0.31
0.82	0.35	0.88	0.50	0.71	0.32	0.71	0.31
0.82	0.45	0.90	0.49	0.73	0.32	0.74	0.31
0.88	0.25	1.22	0.70	0.98	0.45	0.97	0.44
0.88	0.35	1.24	0.70	1.00	0.45	1.00	0.44
0.88	0.45	1.27	0.69	1.03	0.45	1.04	0.43
0.92	0.25	1.67	0.96	1.34	0.62	1.32	0.61
0.92	0.35	1.70	0.96	1.38	0.62	1.37	0.60
0.92	0.45	1.74	0.95	1.41	0.61	1.42	0.59

Table 3. Ice thickness in the East Siberian Sea in the period 21 February 2003 to 19 March 2003.

Ice Density	Snow Density	South		Mid-latitude		North	
		Average	S.D.	Average	S.D.	Average	S.D.
0.82	0.25	0.94	0.44	0.93	0.28	1.00	0.34
0.82	0.35	0.96	0.44	0.94	0.27	1.02	0.33
0.82	0.45	0.99	0.43	0.95	0.26	1.03	0.32
0.88	0.25	1.32	0.62	1.30	0.39	1.41	0.47
0.88	0.35	1.36	0.61	1.32	0.38	1.43	0.46
0.88	0.45	1.39	0.61	1.33	0.36	1.45	0.46
0.92	0.25	1.81	0.85	1.78	0.53	1.93	0.65
0.92	0.35	1.86	0.84	1.81	0.51	1.96	0.63
0.92	0.45	1.90	0.84	1.83	0.50	1.99	0.62

Table 4. Ice thickness in the Chukchi Sea in the period 21 February 2003 to 19 March 2003.

Ice Density	Snow Density	Mid-latitude		North	
		Average	S.D.	Average	S.D.
0.82	0.25	0.81	0.25	0.67	0.22
0.82	0.35	0.83	0.25	0.70	0.21
0.82	0.45	0.86	0.24	0.72	0.21
0.88	0.25	1.14	0.36	0.94	0.31
0.88	0.35	1.17	0.35	0.98	0.30
0.88	0.45	1.21	0.34	1.01	0.29
0.92	0.25	1.56	0.49	1.29	0.43
0.92	0.35	1.61	0.48	1.34	0.41
0.92	0.45	1.65	0.47	1.39	0.40

3 EARLY DETERMINATIONS OF ICE THICKNESS

The average sea ice thickness distribution in the Russian Arctic around 1979 can be inferred from the (relatively sparse) observations made by Soviet researchers during the five year period between 1977 and 1981. The data set [Romanov 2004] is based on measurements made between March and May. However, in order to compare with the 2003 satellite data, we limit ourselves to the March data. Since the observations in the Barents Sea are very small in number and confined to Pechorskoy More, we exclude it from our analysis.

Figure 2 depicts the locations and the results of the ice thickness and snow depth measurements performed between 1977 and 1981. Tables 5-8 show the figures for the number of measurements (N), average thickness and standard deviation (in metres).

Table 5. Ice thickness in the Kara Sea in March between 1977 and 1981.

Sector	N	Average	S.D.
West	44	0.81	0.34
East	39	1.05	0.36
North	12	1.01	0.39

Table 6. Ice thickness in the Laptev Sea in March between 1977 and 1981.

Sector	N	Average	S.D.
South	10	1.27	0.39
Mid-latitude	15	1.16	0.36
North	8	1.35	0.33

Table 7. Ice thickness in the East Siberian Sea in March between 1977 and 1981.

Sector	N	Average	S.D.
South	24	0.99	0.36
Mid-latitude	23	1.25	0.42
North	6	1.41	0.29

Table 8. Ice thickness in the Chukchi Sea in March between 1977 and 1981.

Sector	N	Average	S.D.
South	18	1.05	0.30
Mid-latitude	40	1.03	0.32
North	27	1.25	0.32

4 CONCLUSIONS

Attempts to compare the results derived from recent satellite data (2003) with those obtained from early conventional measurements (around 1979) face several problems, starting from the fact that we are dealing with very different methods: old fashion drilling versus modern satellite technology.

The old Soviet observations span a period of a few decades but were made in scattered locations (though roughly uniformly distributed in space) and in specific periods. By contrast, the satellite offers a global coverage but so far the data released by the ICESat team is limited to two periods in 2003. In view of the high interannual variability of the ice thickness, it would be not be safe to take the 2003 values as representative of the current ice thickness distribution.

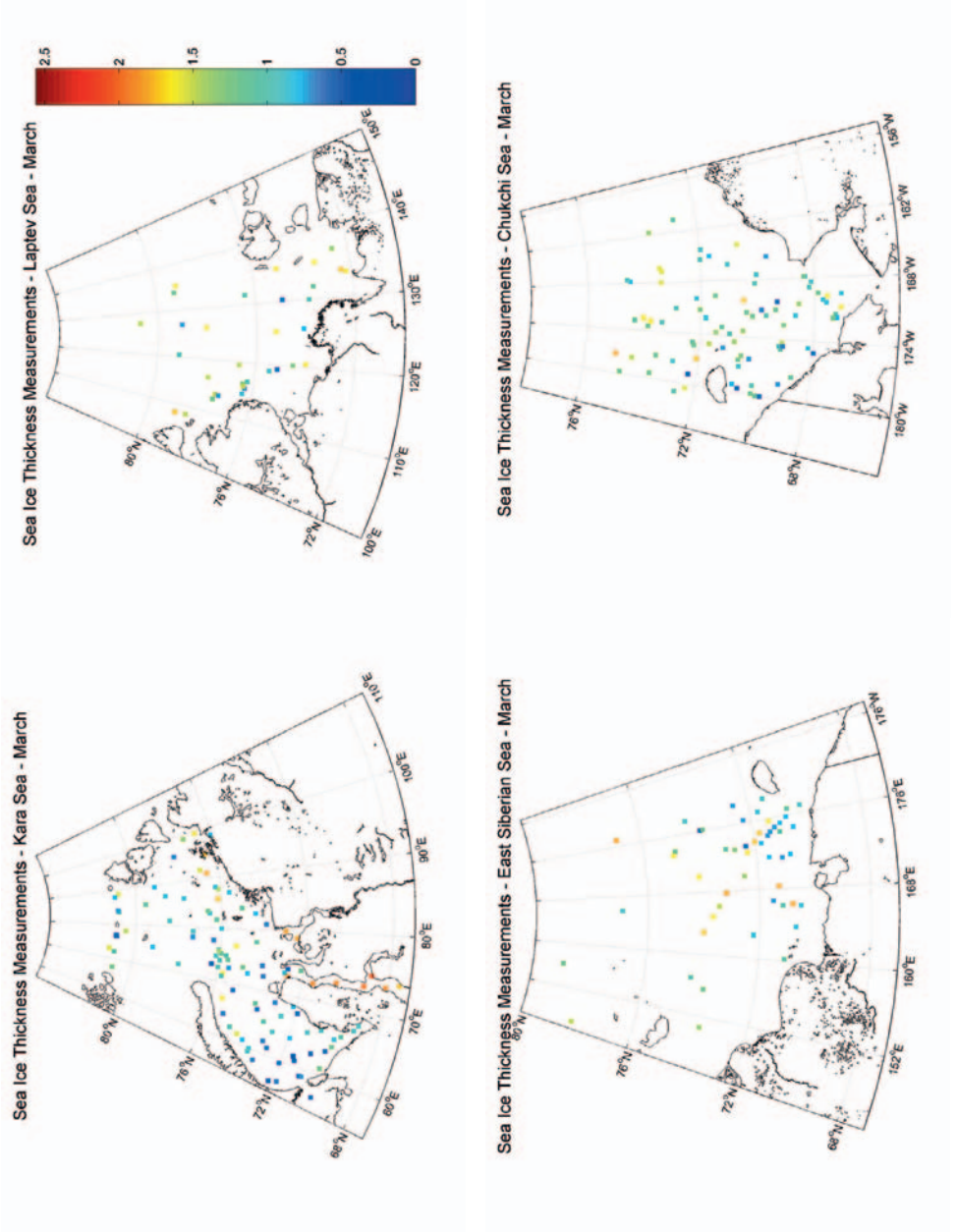

Figure 2. Measurements of sea ice thickness and snow depths in March between 1977 and 1981. The colour bar indicates the ice thickness in cm.

The values of the ice thickness that appear in Tables 5-8 refer to the ice thickness of the runway only and from them we can infer, at most, the thickness distribution of level ice. On the contrary, the ICESat altimetry measurements apply to all forms of ice.

When trying to get ice thickness from ICESat data we are confronted with insufficient knowledge of the spatial and temporal distributions of snow depth, snow density and sea ice density (apart from uncertainties inherent to altimetry measurements and geoid and ocean dynamic topography determinations). The problem concerning the uncertainty in the ice density is particularly severe because the retrieved ice thickness has a strong dependence on this quantity.

Finally, we have to take into account that the time of year during which the drill-hole measurements were made in the late 1970s and early 1980s does not exactly coincide with the period of operation of the ICESat laser in 2003. In fact, the old Soviet measurements of ice thickness in the Kara, Laptev and East Siberian Seas tended to start in mid-March (beginning of March in the Chukchi Sea).

In view of these difficulties, we consider that there is currently not enough evidence to support or to oppose the idea that the ice cover in the Russian Arctic is thinning, a well established fact in some other parts of the Arctic where submarine data are available. Instead, we regard our calculations as a contribution to the validation process that is now being applied to the new satellite measurements of ice thickness. In fact, in spite of uncertainties in essential parameters such as the ice density, the combination of the freeboard and the snow depth distributions obtained from ICESat and Aqua led to ice thickness values that are in a perfectly acceptable range and to an ice thickness distribution compatible with Romanov's direct measurements. For example, taking $\rho i=0.88$ g cm^{-3} and $\rho s=0.35$ g cm^{-3}, it is fair to say that there is a good agreement between the old and the recent measurements, except in the Kara Sea, where the thicknesses based on satellite data for the winter 2003 greatly exceed those obtained from drilling 25 years earlier.

With freeboard and snow depth data being now regularly collected by ICESat, Aqua (and, in the future, by CryoSat), more accurate geoid models being developed and more experimental determinations of the densities of the ice and snow planned, we will soon have an ice thickness time series for the whole Arctic from which the (widely expected) trends may be inferred.

5 ACKNOWLEDGMENTS

I am most grateful to Rene Forsberg for providing me with the processed ICESat freeboard data and to Peter Wadhams for valuable suggestions.

This work was partly supported by the GreenICE Project of the EU Fifth Framework Environment and Sustainable Development Programme.

6 REFERENCES

ACIA (2004); *Impacts of a Warming Arctic: Arctic Climate Impact Assessment*; Cambridge University Press.

Cavalieri, D.J. and J.C. Comiso (2004); *AMSR-E/Aqua daily L3 12.5 km Tb, Sea Ice Concentrations and Snow Depth Polar Grids*; National Snow and Ice Data Center, Boulder, CO; Digital Media (updated daily).

Eicken, H. et al. (1995); Thickness, structure, and properties of level summer multi-year ice in the Eurasian sector of the Arctic Ocean; *J. Geophys. Res.*, 100, 22697-22710.

Forsberg, R. and H. Skourup (2005); Arctic Ocean Gravity, Geoid and Sea-ice Freeboard Heights from ICESat and GRACE; *Geophysical Research Letters*, 32 L21502.

Forsberg, R. and H. Skourup (2006); Sea-ice thickness, geoid and ocean topography in the Arctic Ocean from ICESat and GRACE;

European Commission, *Arctic Sea Ice Thickness: Past, Present and Future*; Ed. by P. Wadhams and G. Amanatidis; Climate Change and Natural Hazards Series, Brussels.

Granberg, H.G. (1998); Snow Cover on Sea Ice; in: *Physics of Ice-covered Seas*; Ed. M. Leppäranta; Helsinki University Printing House.

Kenyon, S. and R. Forsberg (2001); Arctic Gravity Project - A status; in *Gravity, Geoid and Geodynamics 2000*, International Association of Geodesy Symposia, vol.123; Ed. by M.G. Sideris; Springer, New York.

Laxon, S., N. Peacock and D. Smith (2003); High interannual variability of sea ice thickness in the Arctic region; *Nature*, 425, 947.

Markus, T. and D. Cavalieri (1998); Snow depth distribution over sea ice in the Southern Ocean from satellite passive microwave data; *Antarctic Sea Ice: Physical Processes, Interactions, and Variability*. Antarctic Research Series 74, 19-39; Washington, DC, USA: American Geophysical Union.

Romanov, I.P. Ed. by A. Tunik (1995); *Atlas of Ice and Snow of the Arctic Basin and Siberian Shelf Seas*; Backbone Publishing Company.

Romanov, I.P. (2004); *Morphometric Characteristics of Ice and Snow in the Arctic Basin: Aircraft Landing Observations from the Former Soviet Union, 1928-1989*; National Snow and Ice Data Centre, Boulder, CO; Digital Media.

Rothrock, D.A., Y. Yu and G.A. Maykut (2000); Thinning of the Arctic sea ice cover; *Geophys. Res. Lett.*, 26, 3469-3472.

Sandven, S. et al. (2003); Sea ice thickness and freeboard as function of snow and ice properties; CryoSat Validation Experiment; http://www.cryovex.dk.

Tapley, D.B. et al. (2004); GRACE measurements of mass variability in the earth system; *Science*, 305, 503-505.

Wadhams, P. and N.R. Davis (2000); Further evidence of ice thinning in the Arctic Ocean; *Geophys. Res. Lett.*, 27, 3973-3975.

Zwally, J. et al. (2002); ICESat's laser measurements of polar ice, atmosphere, ocean and land; *Journal of Geodynamics*, 34, 405-445.

Zwally, J. et al. (2003); *GLAS/ICESat L1 and L2 Global Altimetry Data*; National Snow and Ice Data Centre, Boulder, CO; Digital Media (updated 2005).

Spring Sea Ice Thickness in the Western Fram Strait: Preliminary Results

Sebastien Gerland[1], Christian Haas[2], Richard Hall[1], Jürgen Holfort[1,3], Edmond Hansen[1], Terje Brink Løyning[1], and Angelika Renner[1,4]
[1] *Norwegian Polar Institute, The Polar Environmental Centre, 9296 Tromsø, Norway*
[2] *Alfred Wegener Institute for Polar & Marine Research, 27515 Bremerhaven, Germany*
[3] *Present address: Bundesamt für Seeschifffahrt und Hydrographie (BSH), 18057 Rostock, Germany*
[4] *Present address: British Antarctic Survey, High Cross, Madingley Road, Cambridge CB3 0ET, UK*

Keywords: sea ice thickness, Fram Strait, Greenland Sea, Arctic, electromagnetics, Transpolar Drift, upward-looking sonar, airborne measurements

ABSTRACT: The Fram Strait is the only deepwater connection between the central Arctic Ocean and the global ocean, and it is the main gateway for multi-year sea ice leaving the Arctic. Over a period of two weeks in May/June 2005 sea ice thickness was investigated in detail in the Western Fram Strait during the expedition FRAM 2005. The field work was conducted from two ships, KV "Svalbard", and RV "Lance", and from a helicopter. Except for ice draft data obtained from moored upward looking sonars and satellite remote sensing data very little data exist on snow and ice thickness, and related parameters for the period before the onset of melt in the western Fram Strait. Ice thickness was measured from drillings, ground electromagnetics and helicopter-borne electromagnetics. The main research area was at 79° N, between 10° W and 2° W.

Ground measurements were accompanied by snow thickness measurements using a snow stake. In drillholes, freeboard was also recorded. In total, 33 ice stations were completed; 15 of them included electromagnetic profiling. Usually, ground EM profiles were either 250 or 500 m long. The accumulative length of all ground EM profiles was 4150 m. More than 500 km of helicopter profiles were flown, using the AWI EM-bird instrument.

Ice conditions varied along the west-to-east transect. Multi-year ice thicknesses typically ranged between 2 and 3.50 m, with relatively deep snow. In addition, first-year ice, probably originating from refrozen leads, was also observed. We present preliminary results from this survey, including long ice thickness transects and histograms for snow and ice thickness in the research area. In the near future, the findings will be also used in connection with calibration and validation studies of both satellite altimetry data (CryoSat II) and upward looking sonar-derived ice draft data.

1 INTRODUCTION

The "lifetime" of sea ice in the Arctic can vary from days to years. Most of the sea ice in the Arctic responds quickly to changes in the energy fluxes at the atmosphere-ice-ocean interface. Recent indications of a reduction in sea ice thickness are discussed in a number of scientific publications (e.g. Wadhams, 1990; Wadhams and Davis, 2000; Rothrock et al., 1999, Holloway and Sou, 2002; Winsor, 2001, Laxon et al., 2003; Haas, 2004), which emphasises the relevance of this research subject.

The area of the northern Greenland Sea, located between Greenland and Svalbard, is usually referred to as the Fram Strait. It is the only deep connection between the Arctic Basin and the other world oceans. The Fram Strait is the main route for multi-year sea ice leaving the Arctic Basin. Roughly 10% of the total Arctic sea ice mass is exported each year through the Fram Strait (Kwok et al. 2004). Dense water formation in the sub-polar gyres is a component of the oceanographic circulation pattern transporting heat northward ("the global conveyor belt"), and is sensitive to the output of sea ice and freshwater through the Fram Strait.

Since 1990, ice thickness in the Fram Strait has been systematically and continuously monitored by the "Fram Strait monitoring programme" of the Norwegian Polar Institute (Vinje et al., 1998; 2001). The central part of that programme is a set of moorings located along 79°N in the western Fram Strait region (Fig. 1). The moorings are deployed for a year at a time, and consist of oceanographic equipment and upward looking sonars. Since 2003, the measurements have been supplemented with in situ ice thickness measurements every September, at the time of the lowest ice concentration and moorings re-deployment (Hansen et al., 2004). In May 2005, the Norwegian expedition "FRAM 2005" gave the possibility to investigate Fram Strait sea ice shortly after the maximum ice concentration, and prior to the onset of melt. About 30 ice stations were performed from the ships KV Svalbard and RV Lance, together with helicopter profiles and small ice stations. This research note summarizes the preliminary results of the sea ice mass balance part of FRAM 2005.

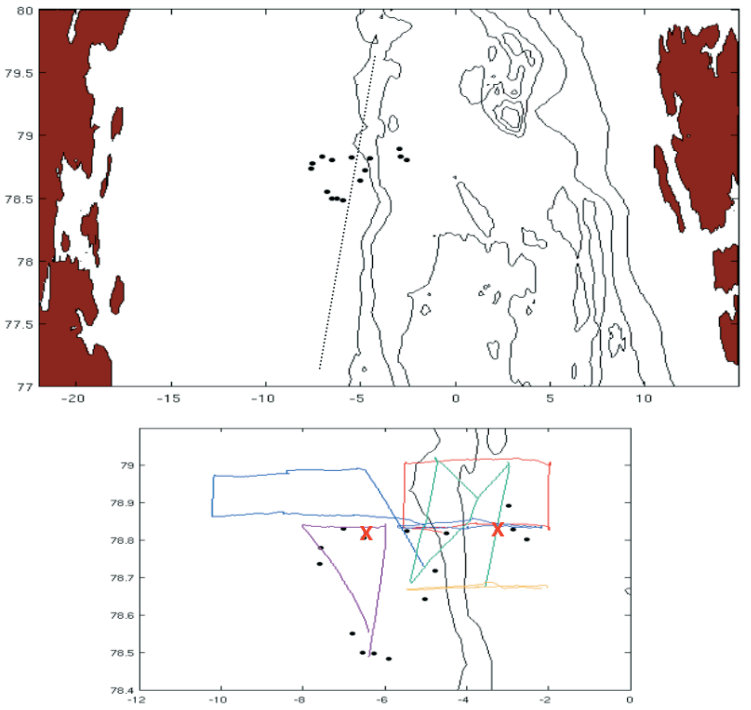

Figure 1. Map of Fram Strait with ground- EM stations (dots, see Figs. 2a and 3a) overlaid on bathymetry contours. The dotted line indicates the distinguishing of western and eastern stations (see Fig. 3a). The coloured lines in 1b show helicopter-EM flight trac ks (see Figs. 2b and 3b) , and the red crosses in 1b represent the two ULS positions F14 (see Fig. 3c) in the west and F11 (see Fig. 2c) in the east.

2 METHODS AND INSTRUMENTS

The methods used for ice thickness determination were i) direct thickness measurements in drillholes, ii) electromagnetic, indirect ice thickness measurements, and iii) thickness estimation from ice draft measurements by means of upward looking sonar.

The footprint of the direct thickness measurements is 5 cm (drill diameter) with a vertical accuracy of 1 cm, but the measurement preparation (drilling) is time consuming, and consequently only few of those measurements can be done at an ice station. The main purpose of the measurements was to calibrate ground electromagnetics.

All electromagnetic (EM) ice thickness measurement systems use the principle of EM induction. EM systems consist of a transmitting and a receiving coil (usually one per frequency) and provide an accuracy in the range of 10%, with the lateral resolution dependent on the coil geometries. Ground EM (e.g. Kovacs and Morey, 1991; Haas et al., 1997) were applied with a Geonics EM31 portable instrument (single frequency, Geonics Ltd., Missisauga, Canada). The instrument is placed on the snow surface and a reading is taken and the snow thickness was measured in parallel with a pole. Profiles were between 50 and 500 m long, and a reading was taken every 5 m. The lateral resolution is several metres. Helicopter-borne EM (Kovacs et al., 1987; Haas et al. 2006) is faster and flights with profile lengths of more than 100 km can be achieved. The instrument is a 2-frequency AWI-EM bird (Alfred Wegener Institute, Bremerhaven, Germany), that hangs below the helicopter during the flight. The instrument is calibrated over open water. The system consists also of a laser altimeter in order to correct for helicopter/EM-bird altitude variations. For this system, no corresponding snow thicknesses could be measured.

Upward looking sonars (ULS) are used to measure sea ice draft from moorings (Vinje et al., 1998). The ULS instrument is a CMR ES300 (Christian Michelsen, Bergen, Norway). The ULS is mounted on the top of a mooring, about 50 m below the water surface. The beam width of the sonar is 2°. Consequently, the lateral resolution of the system is similar to the ground EM. Data processing involves assumptions on water sound velocity (for the calculation from pulse travel time to distance) and snow and ice density assumptions (for the thickness calculation from draft. Ice situations with some open water improve the achievable accuracy. ULS readings are taken automatically every 3-4 minutes.

3 PRELIMINARY RESULTS

During the fieldwork based on KV Svalbard during FRAM 2005, 28 ice thickness drillings, 4150 m of ground EM measurements and more than 500 km of helicopter-borne EM were performed, together with the time series from 2 ULS instruments. Examples of the three types of ice thickness/draft profiles are presented in Fig. 2 (a: ground EM, b: helicopter EM, c: ULS). The range of typical profile lengths varies from hundreds of metres (ground EM) to 100-1000 km (helicopter EM and ULS). To illustrate the extent of the ULS in terms of distance: a hypothetic average drift speed of the ice of 0.5 km/h (see e.g. Kwok et al. 2004) would equal a profile of 4380 km for one year.

First ice thickness/draft distributions were calculated from the ice thickness profiles (Fig. 3). The distributions are a common tool to compare the ice thickness distribution in a region with data from either a different time and/or location. Here, ice thickness distributions allow comparison of different methods applied in the same area.

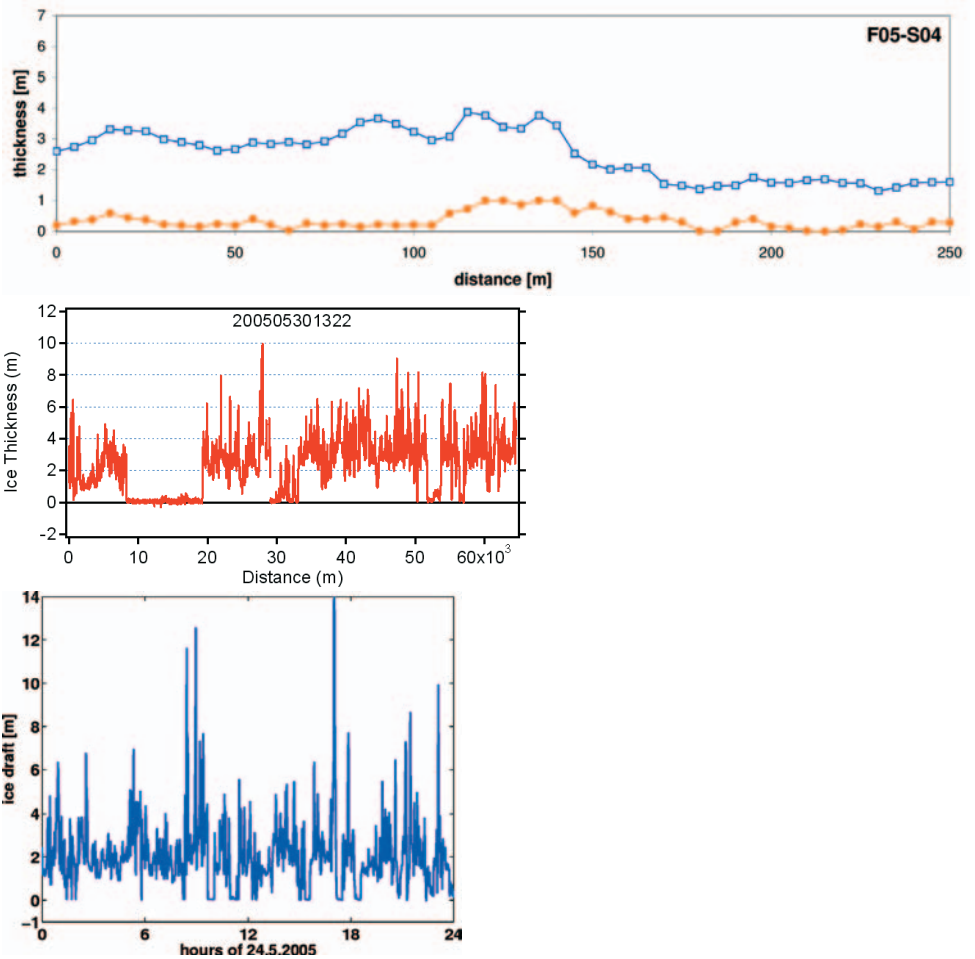

Figure 2. a) Profile of snow thickness (red) and snow plus ice thickness (blue), measured with ground electromagnetics. The part from 0 to 140 m covers multiyear sea ice, the part beyond that first year ice. b) Profile with preliminary ice thickness data from helicopter electromagnetics. The section from about 8 to 20 km was flown over open water.
c) Time series of preliminary ice draft from the ULS at the eastern mooring F11 from 24 May 2005. Flat sections at 0 m ice draft indicate open water, and peaks with maxima indicate pressure ridges.

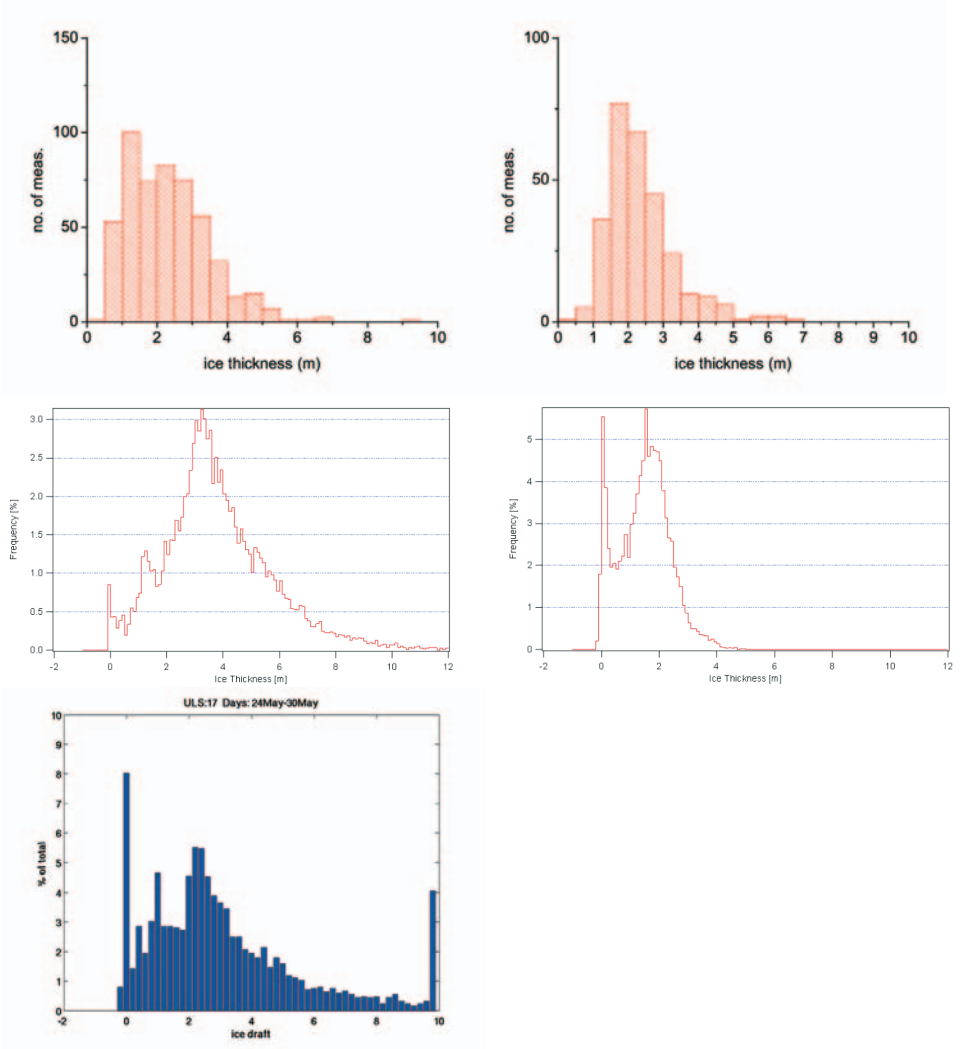

Figure 3. a) Ice thickness distributions from ground electromagnetics for the profiles in the western (left diagram) and the eastern (right diagram) part of the research area.
b) Ice thickness distribution for the western (left) eastern parts (right) of the research area from helicopter electromagnetics (preliminary data, selections from only one profile).
c) Ice draft distribution (preliminary data) from upward looking sonar at the western position F14 for the time 24 – 30 May 2005. Peaks at 0 m refer to open water, at 10 m to all data equal and larger than 10 m.

The histograms calculated for the western and eastern part of the research area in the Fram Strait (ground EM data in Fig. 3a and helicopter EM data in Fig. 3b) show that the ice thickness distribution varies significantly over a relatively limited area. This is evident in all the methods used (see helicopter EM data for a section in the eastern part of the research area in Fig. 3b, and ULS data for the western position F14 in Fig. 3c) . Ground EM data show that in the west, the thickness of the most abundant multi-year ice (incl. snow) was highest at 2.25 m, whereas in the east it was 1.75 m (see Fig. 3a). A first year ice peak appears more significant in the west (at the 1.25 m mode, Fig. 3a).

4 DISCUSSION AND INTERCOMPARISON OF METHODS

During FRAM 2005, extensive ice thickness data sets for the western Fram Strait area were collected. The main result was that ice thickness distribution there features a gradient in thickness across the Transpolar Drift along 79° N. Previously, the variability of ice thickness across the main drift route of the ice leaving the Arctic Basin has not been studied in detail. The ice thickness was investigated with three independent methods, and all methods gave preliminary results showing either the gradient (helicopter EM, ground EM) , or being consistent with a gradient (ground EM, ULS).

A methodical comparison of the data shows that all the methods are suitable for investigating multi-year ice thickness distribution in the Arctic. The methods have different possibilities and differ in flexibility and costs. Ground EM is relatively cheap, once a ship is in the ice-covered area of interest. However, the range of a survey line is limited by the measurement speed and by the size of floe under investigation. Helicopter EM is expensive and requires a helicopter, but it gives the most complete picture about the thickness (snow plus ice) distribution in a larger area at a given time. The ULS runs automatically, but maintenance of moorings in ice-covered regions with icebergs occurring is complex and costly.

The results shown here are preliminary, and at the time of writing, the final processing for the helicopter EM and ULS data in this study have not been completed. However, the changes from the results presented here will be minor, and therefore the two main conclusions about the ice thickness distribution and the method inter-comparison will be unaffected.

5 FUTURE WORK

After the processing of all data is completed, data for smaller regions within the research area will be investigated, with thickness observations (drillings) done from RV Lance during FRAM 2005 included. SAR images for the area from May 2005 will be analysed in order to investigate whether the ice regimes that can be distinguished by thickness distribution express some parallel unique signatures in radar images. It is expected that the thickness gradient already identified can be described in more detail. Using additional information from oceanographic measurements done in parallel to the thickness surveys could help to explain the observed ice thickness distribution and its variability.

6 ACKNOWLEDGEMENTS

We are grateful to the crew and captain of the KV Svalbard (Norwegian coast guard) and several helpers in the field. The team from Airlift AS is acknowledged for good collaboration regarding the helicopter EM survey.

7 REFERENCES

Haas, C. 2004. Late-summer sea ice thickness variability in the Arctic transpolar drift 1991-2001 derived from ground-based electromagnetic sounding. *Geophysical Research Letters*, 31 (L09402), doi:10.1029/2003GL019394.

Haas, C., S. Gerland, H. Eicken, and H. Miller 1997. Comparison of sea-ice thickness measurements under summer and winter conditions in the Arctic using a small electromagnetic induction device. *Geophysics*, 62 (3), 749-757.

Haas, C., S.Goebell, S. Hendricks, T. Martin, A. Pfaffling, and C. von Saldern 2006. Airborne electromagnetic measurements of sea ice thickness: methods and applications. This volume.

Hansen, E., T. Løyning, S. Gerland, and H. Goodwin 2004. Arctic sea ice thickness variability observed over a decade in the Fram Strait. Extended Abstract. *Arctic Climate System Study (ACSYS), 2004. Progress in Understanding the Arctic Climate System: The ACSYS Decade and Beyond. Proceedings of the ACSYS Final Science Conference*, St. Petersburg, Russia, 11-14 Nov 2003. WCRP-118 (CD); WMO/TD No. 1232. September 2004. 4 pages.

Holloway, G., and T. Sou 2002. Has Arctic sea ice rapidly thinned? Journal of *Climate*, 15, 1691-1701.

Kovacs, A., N. Valleau, and J. Holladay 1987. Airborne electromagnetic sounding of sea ice thickness and sub ice bathymetry. *Cold Regions Science and Technology*, 14, 289-311.

Kovacs, A., and R. M. Morey 1991. Sounding sea ice thickness using a portable electromagnetic induction instrument. *Geophysics*, 56 (12), 1992-1998.

Kwok, R., G. Cunningham, and S. Pang 2004. Fram Strait sea ice outflow. *Journal of Geophysical Research*, 109 (C01009, doi: 10.1029/2003JC001785).

Laxon, S., N. Peacock, and D. Smith 2003. High interannual variability of sea ice thickness in the Arctic region. *Nature*, 947-950.

Rothrock, D. A., Y. Yu, and G. A. Maykut 1999. Thinning of the Arctic sea-ice cover. *Geophysical Research Letters*, 26 (23), 3469-3472.

Vinje, T. 2001. Fram Strait ice fluxes and atmospheric circulation: 1950-2000. *Journal of Climate*, 14, 3508-3517.

Vinje, T., N. Nordlund, and Å. Kvambekk 1998. Monitoring ice thickness in Fram Strait. *Journal of Geophysical Research – Oceans*, 103 (C5), 10437-10449.

Wadhams, P. 1990. Evidence for thinning of the Arctic ice cover north of Greenland. *Nature*, 345 (28 June 1990), 795-797.

Wadhams, P., and N. R. Davis 2000. Further evidence of ice thinning in the Arctic Ocean. *Geophysical Research Letters*, 27, 3973-3975.

Winsor, P. 2001. Arctic sea ice thickness remained constant during the 1990s. *Geophysical Research Letters*, 28 (6), 1039-1041.

Sea Ice Thickness, Geoid and Ocean Topography in the Arctic Ocean from ICESat and GRACE

Rene Forsberg*, Henriette Skourup
Geodynamics Dept, Danish National Space Center
Juliane Maries Vej 30, DK–2100 Copenhagen Oe, Denmark

Keywords: sea ice thickness, geoid, topography, ICESat, GRACE, gravity missions

ABSTRACT: In the paper we outline sea ice freeboard height and sea level results in the Arctic Ocean from ICESat, derived from an updated geoid model based on Arctic Gravity Project data and GRACE. Knowledge of the sea surface heights above the ellipsoid is essential for mapping sea-ice freeboard by space and airborne methods. We additionally compare the mean dynamic topography of the Arctic Ocean, derived from a combination of ICESat and ERS altimetry and the geoid, to an independent oceanographic model. Our results show that it is possible by space methods not only to determine sea-ice freeboard heights, but also the Arctic Ocean mean dynamic topography, and thus overall ocean circulation. The combination of geoid and satellite sea level data forms the core of a new ESA-sponsored project – ARCGICE – a cooperation between several European and Canadian partners, aimed at characterizing errors in the Arctic Ocean mean sea surface, as needed for satellite sea ice thickness mapping (e.g. for CryoSat-2).

1 INTRODUCTION

With the launch of dedicated polar altimetry satellites - NASA's ICESat, launched 2003 (Zwally et al., 2002, cf. Figure 1) and the re-planned ESA Cryosat-2 (2009) - monitoring of sea-ice thickness and its changes over most of the Arctic Ocean appears possible. Preliminary results of ICESat-derived Arctic Ocean sea-ice thickness (up to 86°N), have thus recently been published by Forsberg and Skourup (2005).

Figure 1. The ICESat laser illuminates a ground footprint of approx. 70 m extent.

* E-mail: rf@spacecenter.dk.

Methods for satellite measurement of sea-ice thickness were originally developed for ERS pulse-limited radar altimetry (Laxon et al., 2003), which only cover parts of the Arctic (south of 81 N) due to orbit limitations. In the ERS investigations, the radar return pulse shape is used to discriminate between "specular" reflections from open water or leads in the ice pack, and reflections from ice floes. This allows a measurement of the sea-ice freeboard height, which under assumptions of isostatic balance of the ice floe in the water, and assumptions on snow, ice and water density, may be converted to sea ice thickness. The principle is illustrated in Fig. 2.

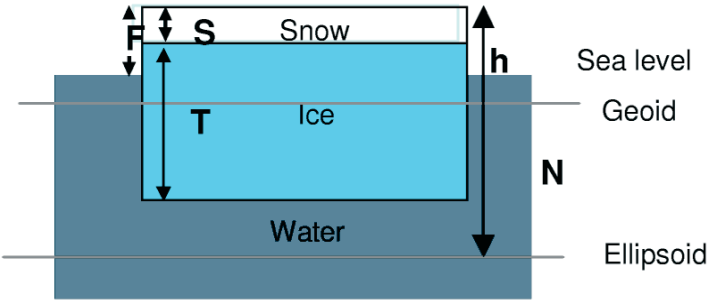

Figure 2. Schematic diagram of sea-ice snow freeboard height (F), sea-level and geoid height (N).

It should be pointed out that there are two types of freeboard heights: the freeboard including snow (F, as shown in. Fig. 2), and the freeboard height of the ice only (F-S). The latter is the freeboard height used for radar altimetry, since it is generally believed that the radar reflects off the snow/ice interface (except for the summer melting season). For airborne and satellite laser altimetry, the snow freeboard is measured.

For satellite altimetry the basic measurement is thus the ellipsoidal height of the snow surface (laser) or the ice (radar). With good orbit and pointing data, this measurement is accurate to few cm. Due to the developments in geoid determination, notably the launch of the GRACE satellite (Tapley et al., 2004), the accuracy of geoid models has become very high as well, at the absolute error level of a few cm at wavelength scales longer than a few hundred km.

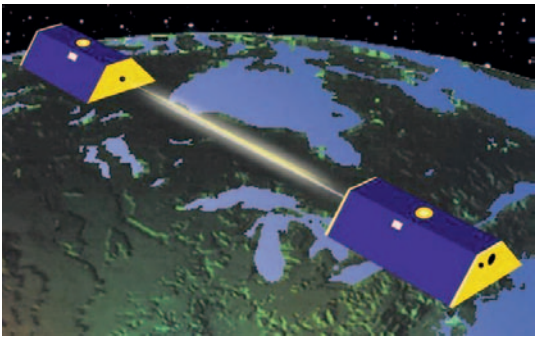

Figure 3. The GRACE satellite pair: measurement of inter-satellite range-rates gives a superior (cm) geoid model at long wavelengths.

If the deviation between the ocean surface and the geoid, i.e. the oceanographic mean dynamic topography (MDT) and the tides, can be modeled with sufficient accuracy, it should therefore in principle be possible to measure the sea-ice freeboard heights directly from space without special identification of measurements originating from leads and thin ice. This would be an advantage for laser altimetry, where there is at present no simple method to discriminate between laser returns from thin or thick ice (Kwok et al., 2004).

The basic equation for the measurement of sea-ice freeboard is thus

$$F = h - N - MDT + e \tag{1}$$

where the altimeter measurement of ellipsoidal heights h is assumed to by corrected for tides, and e is the errors from measurement, models and uncertainties in reference systems. To obtain sea-ice thickness T from F, this is usually done by assumption of a constant ratio approximation

$$T = KF \tag{2}$$

where the K-factor incorporates snow, ice and water density and snow depth assumptions, the latter typically from climatology. The K-factor uncertainty is large, especially for laser measurements, and calibration/validation on independent data, such as submarine upward-looking sonar or electromagnetic thickness measurements, are in practice necessary. The same uncertainty applies to airborne measurements, see e.g. Hvidegaard et al (this volume).

At present Equation (1) is too inaccurate to apply directly, and models for the error e must be estimated from such methods as lowest level filtering, as applied e.g. for airborne laser data (Hvidegaard and Forsberg, 2002), or through the identification of radar reflection waveform types (Laxon et al., 2003). In the latter case, no explicit geoid model was used at all, since the collection of nearly a decade of repeat-track ERS altimetry data has allowed for the determination of an average sea-level surface south of 81°N with great precision.

It is clear, however, that information on the dominant source of variability of the ocean sea surface ellipsoidal heights (SSH), i.e. the geoid variations, should make the detection of freeboard-related height changes more reliable. Numerous airborne gravity survey activities, especially in the last decade have resulted in geoid variations of the Arctic Ocean are known in many regions to an accuracy of 10-20 cm. In the sequel we will outline the current computation of the Arctic geoid, and illustrate the use of geoid models to derive sea-ice freeboard heights F (see also Skourup and Forsberg, this volume). From estimated freeboard heights, the sea surface height (SSH) can subsequently be determined. We will in the sequel focus on the determination of the MDT directly from remote sensing by

$$MDT = SSH - N + e, \quad SSH = H - F \tag{3}$$

and for the first time compare the results to an oceanographic model, providing an overall "consistency check" of the basic equation (1).

2 GEOID OF THE ARCTIC OCEAN FROM THE ARCTIC GRAVITY PROJECT AND GRACE

The Arctic Gravity Project has compiled a 5' gravity anomaly data grid for the Arctic region north of 64°N, based on all available surface, submarine and airborne gravity data, supplemented in some regions (mainly north of Siberia) with ERS- satellite altimeter-derived gravity (Laxon and McAdoo, 1998). Essentially the whole Arctic region is covered, with a typical resolution of underlying airborne gravity data of 10' (18 km). For details of the project and data coverage see the ArcGP web site (http://earth-info.nga.mil/GandG/agp). Figures 4 and 5 show some major recent airborne gravity data sets, which have entered the ArcGP computation, and Fig. 6 the computed gravity anomaly grid of the region, incorporating data sources from Russia and many other countries.

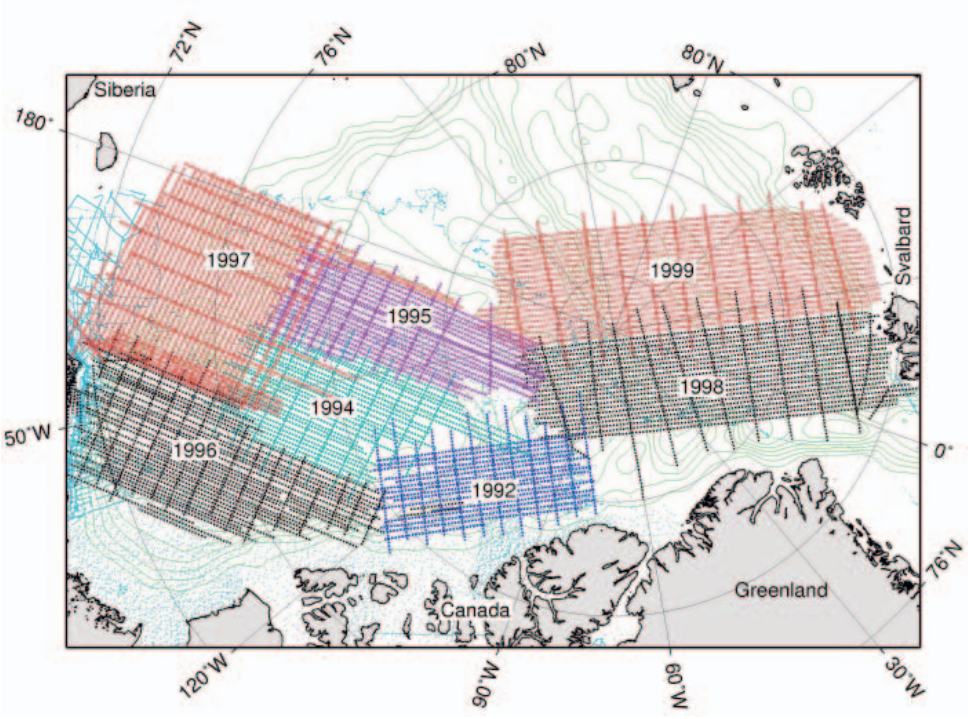

Figure 4. Long-range airborne gravity coverage of the west-central Arctic Ocean region. Within these data sets the propagated geoid error is often 10 cm or less. Figure courtesy J. Brozena, US Naval Research Lab.

We generated a new geoid model of the Arctic region on a corresponding 5' grid, using the GRACE GGM02S spherical harmonic model as a reference model, and using an updated, yet unpublished new ArcGP grid, incorporating new data sources, among others new high-resolution data for Siberia. We used the "remove-restore" method, transforming the residual ArcGP gravity anomalies into geoid residuals by spherical FFT methods (Forsberg and Sideris, 1993). The FFT methods implement Stokes' formula

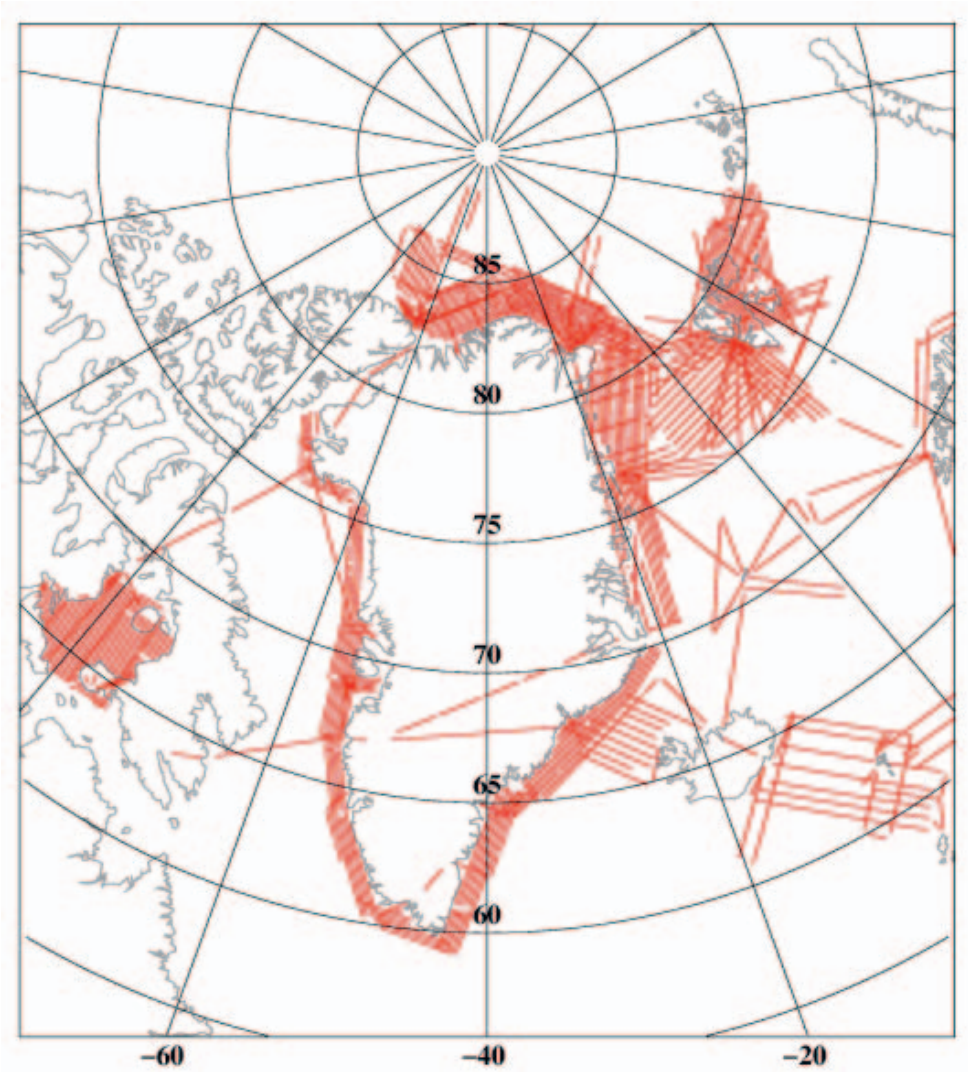

Figure 5. Example of high-resolution aerogravity data (2 mGal r.m.s., 5 km resolution) acquired by a Danish-Norwegian airborne gravity system, flown in an Air Greenland Twin-Otter at low altitudes.

$$N = \frac{R}{4\pi\gamma}\iint_{\sigma} \Delta g S'(\psi) d\sigma \tag{4}$$

where Δg is the gravity anomaly, R Earth radius, γ normal gravity, and ψ the spherical distance, with the integral in principle covering the whole earth. We used a modified Stokes' function given by:

$$S'(\psi) = \sum_{l=n}^{\infty} \frac{2l+1}{l-1} w_l P_l(\cos\psi) \tag{5}$$

only allowing the short-wavelength gravity anomalies to affect the computed geoid at spectral bands higher than spherical harmonic n. We used a 5' grid (10' in longitude), where spectral weights w_l were assigned to make a linear transition in the spherical harmonic band n = 100 to n = 110, implying spherical harmonic data are used fully below harmonic degree 100, and terrestrial data fully above degree 110. To reduce edge effects, we used a high-degree composite GRACE/EGM spherical harmonic reference model complete to degree 360, formed by merging GGM02S linearly with EGM96 in the same harmonic band. We believe that the new geoid represents a major improvement over the current ArcGP geoid, primarily due to the inclusion of GGM02S.

3 THE ARCGP GEOID COMPARED TO ICESAT: FREEBOARD HEIGHTS AND MDT

We have analyzed two periods of ICESat data, February 20 – March 29, 2003 (Laser 1, release 18) and September 25 – November 18, 2003 (Laser 2a, release 21). Fig. 7 shows the difference between the ICESat measured heights (h) and the geoid for the Laser 1 period. It is seen that the differences shows both orbit-related and more localized errors, and that a sea-ice freeboard signal is not very apparent. Some of the errors are due to track biases (e.g., due to errors in orbits, pointing, and inverted barometer effects), and others due to geoid errors (notably the outlier near 85°N, 120°W, which corresponds to the data gap in the airborne gravity data coverage, cf. Fig. 4).

To estimate freeboard heights, a lowest-level filtering must be done on the ICESat track data. This is outlined in detail in Skourup and Forsberg (this volume). Fig. 8 below shows the estimated freeboard heights from ICESat after application of the lowest-level filtering, and Fig. 9 the associated apparent MDT (= SSH – N) for both the analyzed periods (February/March and October/November, 2003). To limit the orbit-related errors, a cross-over adjustment have been applied to these data, estimating a bias for each orbit.

4 COMPARISON OF ARCTIC OCEAN MDT FROM ERS AND ICESAT TO AN OCEANOGRAPHIC MODEL

The ICESat MDTs, as shown in Fig. 9, only covers a limited time span, and are probably still offset by major biases, such as biases from the lowest-level filtering algorithm, as evidenced from airborne lidar underflights of ICESat (Skourup and Forsberg, this volume). To make an Arctic Ocean-wide MDT, covering a larger area and a longer time span, we have therefore merged the MDT data sets from ERS and ICESat. The ERS SSH data set span the period 1993-2001, and has been provided by UCL, UK. To merge the data sets, the difference in MDTs between ERS and ICESat across an overlapping band 80-81.5°N

$$\varepsilon = MDT_{\mathrm{ERS}} - MDT_{\mathrm{ICESat}} \tag{6}$$

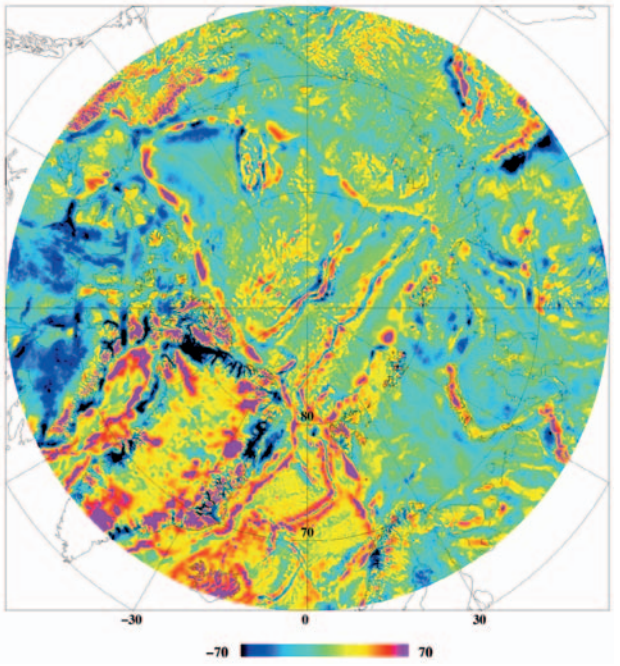

Figure 6. Compiled gravity anomalies in the Arctic Gravity Project. Range of colour scale –70 to 70 mGal.

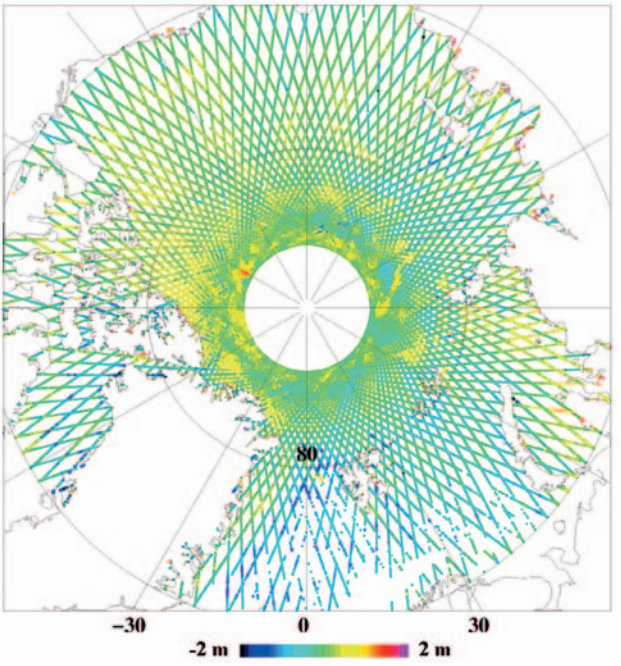

Figure 7. Difference between SSH from ICESat (laser 1) and the ArcGP geoid.

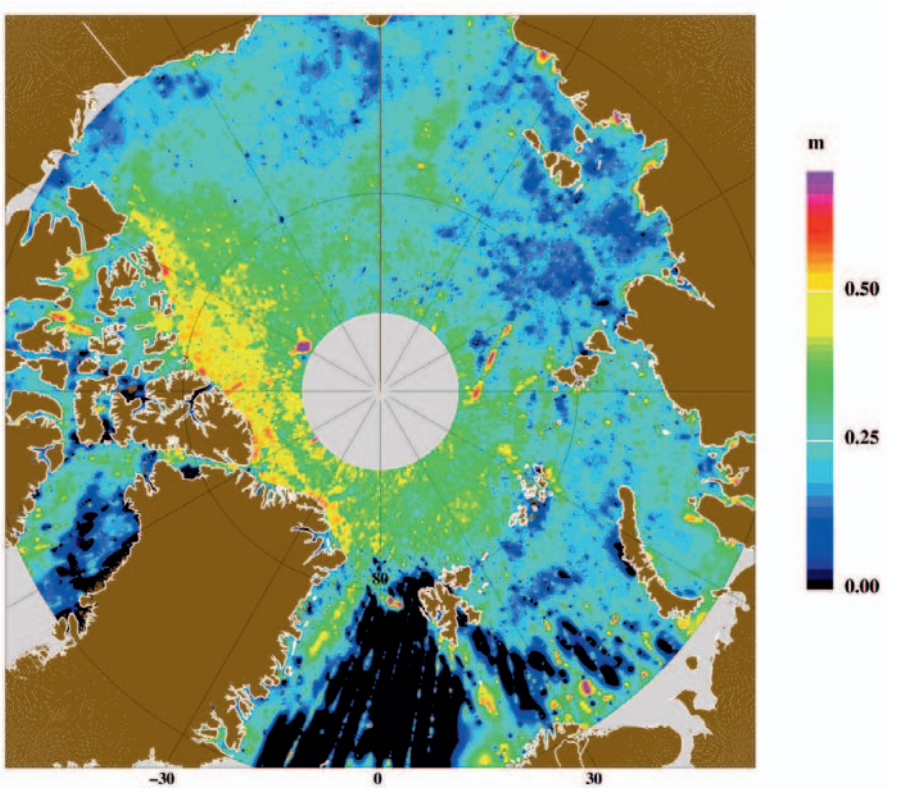

Figure 8. Sea-ice freeboard heights for February/March 2003 from ICESat. Unit m.

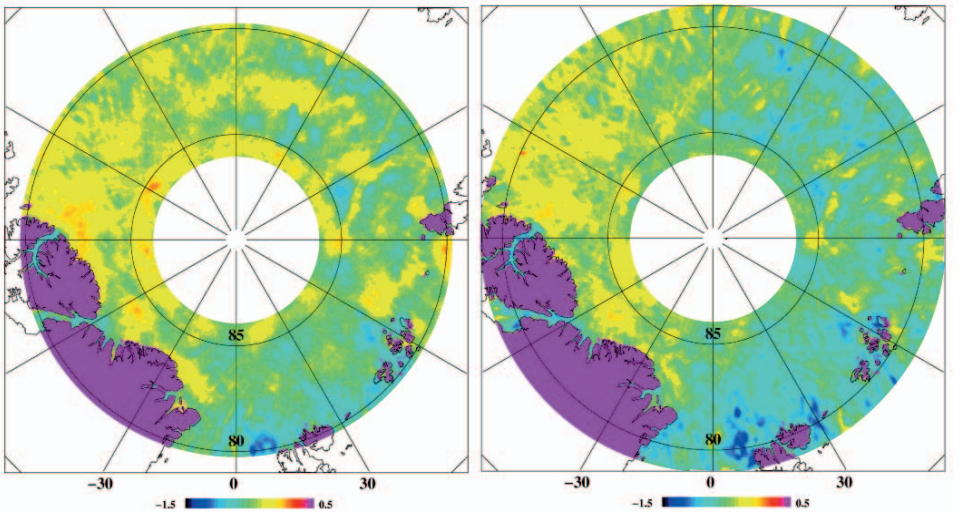

Figure 9. Apparent ICESat MDT (= SSH-geoid) for Feb-Mar 2003 (left) and Sep-Oct 2003 (right). Unit m.

has been interpolated outside the overlap zone with least-squares collocation (optimal estimation), using a correlation length of approx. 20 km, and an a priori noise of 20 cm. The predicted correction ε has subsequently been added to the ICESat data, effectively forcing these data to match the much longer ERS time span. A constant offset has at the same time been estimated, taking into account primarily the different reference systems (ICESat uses the Topex ellipsoid, while ERS ellipsoidal heights are given in WGS84; the difference between the semi-major axis of the two ellipsoids is 70 cm). Table 1 shows the statistics of the comparisons in the MDTs across the comparison band, and Fig. 10 shows the difference between the average ICESat and ERS, as well as the compiled Arctic-wide MDT, where a similar collocation draping has been used across the polar gap data void, north of 86°N.

Table 1. Statistics of difference between the SSH and geoid.

Unit: m	Mean	Std.dev.
ICESat – geoid (in the overlap band (80-81.5°N)	-0.52	0.19
ERS (UCL) – geoid (in overlap band)	-1.19	0.39
ERS – ICESat (do)	-0.71	0.28
Composite MDT – geoid in WGS84 (entire Arctic Ocean)	0.26	0.29

Fig. 10 (right) is the final estimate of the MDT from the space methods (satellite altimetry and geoid). For comparison Fig. 11 shows a plot of the MDT from a coupled oceanographic/sea-ice model (PIPS) of W. Maslowsky, NPS, USA, with a nearly identical colouring scheme as Fig. 10 (right). There is a good qualitative agreement in the observed and modelled MDTs, with e.g. the low in the Norwegian-Greenland sea seen to propagate northwards into Siberian Arctic Ocean consistently in both plots. It is therefore clear that the freeboard/MDT estimation is consistent with the independent MDT data, and the potential of the space-based methods is therefore highlighted. The ability to map changes in the MDT, and thus the underlying ocean circulation, could thus in principle provide new constraints on oceanographic models of the region. This could again provide insight into the basal melting process of the sea-ice, since the changing inflow of Atlantic and Pacific waters is believed to be a major source of currently observed sea-ice thickness changes.

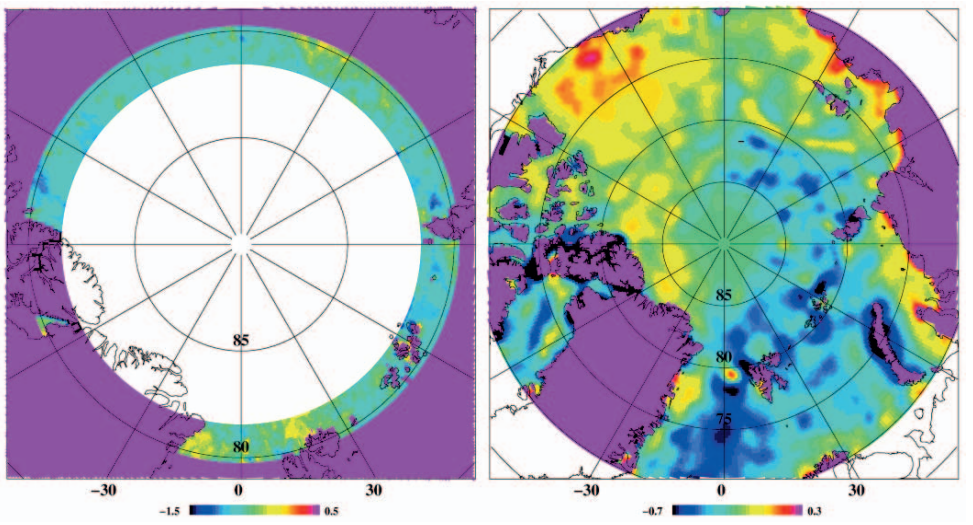

Figure 10. Left: Difference between MDT from ICESat (2003) and ERS (1993-2001). Right: Composite MDT made by "draping" of ICESat to ERS, and draping ArcGP geoid to ICESat north of 86°N. Units: metre.

We have outlined the estimation of Arctic Ocean sea-ice freeboard heights from two releases of ICESat laser altimetry data, using an updated geoid model of the Arctic Ocean, based on GRACE satellite gravity field data and local gravity from an updated Arctic Gravity Project 5' data grid. The estimated freeboards show a pattern consistent with the expected distributions of sea-ice thickness, with the thickest ice located north of Greenland and Ellesmere Island.

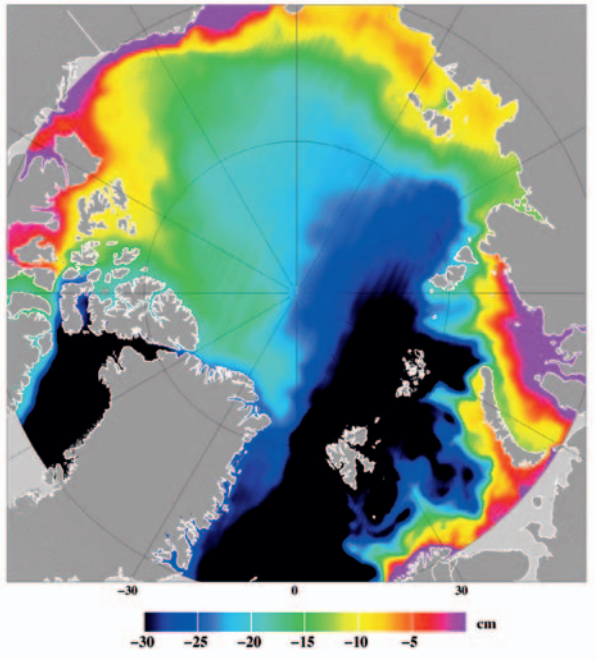

Figure 11. MDT from the PIPS oceanographic model (courtesy W. Maslowski, US Naval Postgraduate School).

From the estimated freeboard heights, the Arctic Ocean mean sea surface heights have been estimated, and merged with a nearly 10 year long MSS time series from ERS, by collocation draping techniques. The derived mean dynamic topography (MDT), obtained by subtracting the geoid model, shows a good quantitative agreement with a state-of-the-art MDT model, thus illustrating the potential application of satellite altimetry missions, especially the upcoming Cryosat-2, to estimate not only sea-ice thickness and its trends, but also ocean mean dynamic topography and its temporal changes, expressing changes in the overall ocean circulation.

5 ACKNOWLEDGEMENTS

We thank Seymour Laxon, University College London, for providing the ERS mean sea surface data, and W. Maslowski, Naval Postgradute School, USA, for providing the oceanographic results. The ICESat data was downloaded from the National Snow and Ice Data Center, Boulder, USA.

6 REFERENCES

Forsberg, R. and S. Kenyon: Gravity And Geoid in The Arctic Region – The Northern Polar Gap Now Filled. 6 pp., Proc. GOCE Workshop, ESA-ESRIN, March 2004.

Forsberg, R., and, H. Skourup: Arctic Ocean Gravity, Geoid and Sea-ice Freeboard Heights from ICESat and GRACE. *Geophysical Research Letters*, 32, L21502, 2005.

Forsberg, R., M. G. Sideris (1993): Geoid computations by the multi-band spherical FFT approach. *Manuscripta Geodaetica*, 18, pp. 82-90.

Hvidegaard, S.M., and R. Forsberg: Sea-ice thickness from airborne laser altimetry over the Arctic Ocean north of Greenland, *Geophysical Research Letters*, 29, no. 20, pp.1952-1955, 2002.

Kwok, R., H.J. Zwally, and D. Yi: ICESat observations of Arctic sea ice: A first look. *Geophysical Research Letters*, 31, L16401, 2004.

Laxon, S., D. McAdoo (1998): Satellites provide new insights into polar geophysics. *EOS*, Transactions AGU, 79 (6), 69-72.

Laxon , S., N. Peacock, and D. Smith, High interannual variability of sea ice thickness in the Arctic region, *Nature*, 425, 947-950, 2003.

Tapley, D. B., S. Bettadpur, J. Ries, P. Thomson, M. Watkins (2004): GRACE measurements of mass variability in the earth system. *Science*, 305, issue 5683, 503-505 [doi: 10.1126/science.1099192]

Zwally, H.J., B. Schutz, W. .Abdalati, J. Abshire, C. Bentley, A. Brenner, J. Bufton, J. Dezio, D. Hancock, D. Harding, T. Herring, B. Minster, K. Quinn, S. Palm, J. Spinhirne, and R. Thomas: ICESat's laser measurements of polar ice, atmosphere, ocean, and land. *Journal of Geodynamics*, 34, pp. 405-445, 2002.

Utilization of Multiple Satellite Sensors to Estimate Sea Ice Volume Flux through Fram Strait

Gunnar Spreen, Stefan Kern, and Detlef Stammer
Centre for Marine and Atmospheric Sciences, University of Hamburg, Inst. of Oceanography, Bundesstr. 53, 20146 Hamburg, Germany

Keywords: Sea Ice, Sea Ice Thickness, Remote Sensing, Laser Altimetry

ABSTRACT: The sea ice volume flux through Fram Strait is estimated using a combination of multiple satellite observations. These involve sea ice concentration and drift, combined to yield the area flux, determined from brightness temperature measurements of the 89 GHz channels of the Advanced Microwave Scanning Radiometer (AMSR-E), and estimates of the sea ice thickness distribution, inferred from elevation measurements of the ICESat GLAS instrument. The thickness is derived from ICESat data, by converting its surface elevation measurements into the sea ice freeboard height. Uncertainties in these freeboard height estimates due to geoid model errors are reduced by using the recent geoid from the Arctic Gravity Project (ArcGP). Missing information about the ocean circulation and ocean tides is approximated locally by interpolating the sea surface height linearly between leads for every ICESat orbit. This approach is evaluated using coincident Synthetic Aperture Radar imagery. The average freeboard height distribution is calculated for complete ICESat measurement periods using a standard polar-stereographic grid. Using typical average values for ice density and snow depth and density derived from a climatology in combination with in situ measurements, the freeboard height is converted into an average ice thickness distribution. Sea ice area flux and thickness are combined to get an estimate of the sea ice volume flux through Fram Strait. The meridional ice volume flux estimated for 79°N amounts to 168 km^3 and 62 km^3 for the Feb/Mar and Oct/Nov ICESat measurement periods in 2003, respectively, with a relative error of at least 20%. These values lie in the absolute range given by previous similar studies, but are considerably smaller than the average ice flux during the 1990s. There is evidence that this is caused by a smaller ice drift speed during 2003 compared to the 1990s – particularly during the autumn measurement period.

1 INTRODUCTION

Changes in the mass balance of Arctic sea ice have been shown to influence the global climate in various ways (Bamber and Payne, 2004). With respect to the ocean changes in the amount and location of the release of freshwater and brine are two of the most important.

Two main processes can be identified for a change in Arctic sea ice mass: a change in the net amount of sea ice production and in the export of sea ice out of the Arctic Ocean. The first process depends on the length of the freezing period, snow accumulation, ice production in polynyas and meteorological conditions. The second process is largely determined by the sea ice export through Fram Strait into the Greenland Sea, since export through Fram Strait is by far the largest portion of the total Arctic sea ice export. Currently the net annual sea ice volume exported through Fram Strait amounts to about 10% of the total sea ice volume of the Arctic Ocean and is the single largest source of freshwater in the Greenland-Icelandic-Norwegian (GIN) Sea (Aagaard and Carmack, 1989). Anomalies in this export are major

contributors to the freshening of surface waters in the Greenland and Labrador Seas and by this may enhance or hamper convective overturning and water mass modification. This in turn can result in significant changes in the export of dense water from the GIN Sea into the Atlantic Ocean and then impact the global ocean thermohaline circulation (Dickson et al., 1988; Karstensen et al., 2005).

While in sea ice model studies the ice volume or ice mass flux is one of the quantities of the most interest, it is difficult to get this flux from observations. Sea ice area and motion, ice thickness and ice density have to be known to derive the sea ice volume flux, and is not possible to obtain these with any one measurement technique. A multi sensor approach has therefore been chosen by other groups (e.g. Kwok et al., 2004a) and is also chosen for this study, with the goal to utilise only satellite measurements. The sea ice area and motion are measured routinely, daily (area) or every other day (motion), and globally, based on all-weather and daylight independent space-borne passive and/or active microwave sensors like the Special Sensor Microwave/Imager (SSM/I) or the SeaWinds QuikSCAT since late 1978 (e.g. Agnew et al., 1997; Kwok et al., 1998; Cavalieri et al., 2002). It became evident from this data that the sea ice extent of the Arctic Ocean is currently shrinking (Cavalieri et al., 2003). It is expected to further decrease in response to accelerated Arctic climate warming (Johannessen et al., 2004). Here we use data from the Advanced Microwave Scanning Radiometer (AMSR E) to obtain sea ice concentration and motion.

More crucial for the volume flux determination is the sea ice thickness measurement at a similar scale to the ice area measurements. Until recently, our knowledge of the sea ice thickness distribution in the polar regions was merely based on in-situ drillings, ice draft observations by upward looking sonar (ULS), and ground-based and airborne electromagnetic sounding (e.g. Wadhams, 2002, Haas, 2004). Such measurements have been used to infer the sea ice volume flux through Fram Strait with the limitation that the sea ice thickness across the Fram Strait has to be extrapolated from one point measurement. Laxon et al. (2003) were the first to publish at least an average sea ice thickness distribution of the Arctic Ocean derived from satellite radar altimetry. The averaging period, however, is too long to use this data to derive the sea ice volume flux. Nevertheless, these data sources reveal that the Arctic sea ice seems to have thinned substantially since the late 1950s (Rothrock et al., 2003 and 1999; Wadhams and Davis, 2000; Haas, 2004). Together with the shrinking ice area, this means a significant reduction of the Arctic sea ice volume. Whether this reduction will continue towards an ice free Arctic Ocean in the future, or whether the downward trend can be attributed to a multi-decadal oscillation (e.g. Divine and Dick, 2006), which will reverse into an upward trend in the future, has to be carefully monitored.

ICESat's (Ice, Cloud, and land Elevation Satellite) Geoscience Laser Altimeter System (GLAS) is the first space-borne instrument, which at least comes close to the needed spatial and temporal resolutions needed to monitor the sea ice thickness globally. Unfortunately this mission only started in 2003 and, due to a hardware malfunction, GLAS is only operating for up to three periods of about one month duration per year. Thus currently ICESat data cannot be used to make long-term estimates of the sea ice thickness variability, as the time series is interrupted and too short. Despite these limitations, we demonstrate that ICESat data can be used, in combination with other satellite data, to estimate the sea ice volume flux independently from in-situ measurements. Thus in the future, when the time series is longer and/or more sensors are measuring similar quantities, the sea ice volume flux can be estimated at least on a monthly scale globally.

We focus on Fram Strait sea ice volume flux. This is highly variable, e.g. Kwok et al. (2004a), and its amount is determined by the sea ice thickness at the northern entrance of the Fram Strait and the wind forcing. It was shown by Pfirman et al. (2004) that sea ice export through Fram Strait can occur in surge-like events, where large portions of the old, thick ice leave the Arctic Ocean. Depending on the strength and location of the Beaufort Gyre and the Transpolar Drift, it takes several years until ice of similar thickness has formed again. Estimates of Fram Strait sea ice volume flux (1970s to 1990s) range from 1600 km^3/year to 5000 km^3/year. During 1991-1999, averaged transports amount to (2218 ± 497) km^3/year (Kwok et al., 2004a). These estimates were obtained primarily using ULS data by extrapolating local thickness estimates across the entire Fram Strait to obtain a complete cross-strait ice thickness profile (e.g. Vinje et al., 1998). In this study, this cross-strait profile is measured by ICESat's GLAS, which measures its height above the Earth's surface, from which the sea surface height (SSH) and the sea ice freeboard height (called freeboard hereafter) can be inferred. Kwok et al. (2004b) provide a first estimate of the sea ice thickness distribution from ICESat data from selected satellite overpasses. Key problems are i) inaccurate sea surface height (SSH) estimates, ii) unknown snow depth and ice density, which are needed to convert freeboard to ice thickness, iii) contamination by clouds. Therefore, best results are expected to be obtained in regions with a stationary sea ice cover, which permits averaging over long/large periods/areas. These conditions are not met in the Fram Strait/Greenland Sea: sea ice is known to drift several kilometres per day, divergence and convergence can continuously change surface roughness, and snow accumulation can be very variable, and therefore careful error estimates are crucial to determine the reliability and accuracy of the estimated quantities – like sea ice freeboard height and volume flux.

In this study present state-of-the-art AMSR E distributions of sea ice concentration (area) and motion are combined with sea ice thickness distributions of two GLAS measurement periods in the Fram Strait region, to obtain the sea ice volume flux distribution.

2 DATA, CONCEPTS AND METHODS

For our estimates of sea ice volume flux, satellite information about sea ice area, its drift and thickness have to be combined (see Figure 1). Other information from in-situ and airborne sources are only used indirectly, e.g., as geoid model and as a priori information on sea ice density and as snow depth and density. All data are interpolated on a polar stereographic 25 km grid covering the Fram Strait region (e.g. Figure 3). Data sets are explained from left to right in Figure 1:

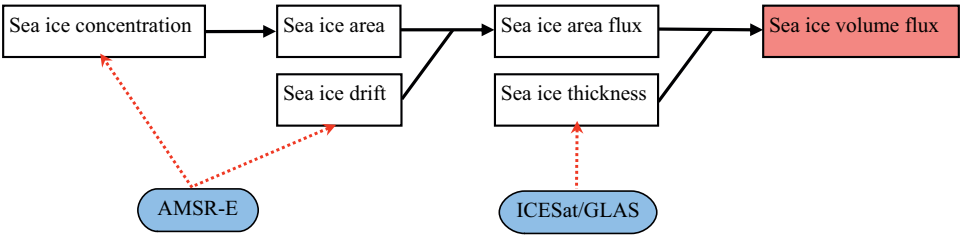

Figure 1. Schematic flow diagram of quantities (black boxes) and satellite sensors (blue ovals) involved in the estimation of the sea ice volume flux.

Sea Ice Concentration and Area

Sea ice concentration gives the percentage of a defined area, here the grid cell, covered with sea ice. By multiplying the sea ice concentration with the grid cell area the sea ice area per grid cell is obtained. We use data obtained by the Advanced Microwave Scanning Radiometer for EOS (AMSR-E) on board NASA's AQUA satellite. It measures the thermal radiation of the earth at 6 different microwave frequencies (7, 11, 19, 24, 37 and 89 GHz) at horizontal and vertical polarization. These microwave measurements are, in contrast to visual and infrared ones, almost independent of daylight and clouds. The Arctic region is completely covered each day at least once.

Sea ice concentrations are calculated with the ARTIST Sea Ice (ASI) algorithm (Spreen et al., 2005b; Kaleschke et al., 2001). It uses the 89 GHz channels, which offer the highest spatial resolution (~5 km) of all channels but are hampered slightly more by the water vapour and cloud liquid water in the atmosphere. A combination of the 19, 24 and 37 GHz channels are used to eliminate this atmospheric influence over the open ocean off the ice edge which otherwise may cause spurious ice concentrations. An example of ice concentration in the study region for February 26, 2003, is shown in Figure 2. Clearly, this ice concentration map shows the variable ice conditions typical for the Fram Strait during winter, with regions of a very compact but also a quite open ice cover along the ice edge. Moreover, the fine spatial resolution allows resolution of smaller scale features such as polynyas along the coast or downstream of huge multi-year ice floes, as well as the disintegration of the ice pack into ice patches and fingers in the marginal ice zone (MIZ) (see black box). The ice concentrations are sampled down onto the 25 km grid used for the final sea ice volume flux estimates. An example of this smoothed ice concentration data is shown as background in Figure 3 for the same day as Figure 2.

Sea Ice Drift and Sea Ice Area Flux

Sea ice drift can be obtained from satellite passive microwave radiometry by the cross-correlation of fields of time-lagged data (e.g. Kwok et al., 1998) in which recognizable features are tracked. As these features have to be correlated the already coarse resolution of passive microwave sensors is further reduced. We again use the 89 GHz channel data of AMSR-E, which currently offer the highest spatial resolution for passive microwave remote sensing. The French Research Institute for Exploitation of the Sea (IFREMER) provides a daily data set of ice drift on 31.25 km grid using AMSR E data with a time gap of two days (Ezraty et al., 2005). Ice drift is calculated separately for the vertically and horizontally polarized 89 GHz daily brightness temperature maps on a 6.25 km grid. The Laplacian motion of 5 x 5 pixel fields (31.25 x 31.25 km2) are calculated using a maximum correlation technique. Finally, the two derived drift vector maps (from horizontally and vertically polarized data) are merged to one consistent ice drift field. The error in ice drift speed is estimated by comparison to ice drift speeds from the International Arctic Buoy Program (IABP) and was 2.6 cm/s (2.2 km/day) for the complete Arctic (Ezraty et al., 2005). However, the error is expected to be larger in dynamic regions such as the Fram Strait. We interpolate the 31.25 km grid fields onto our 25 km grid. An example for the ice drift on February 26, 2003, is shown in Figure 3. In a small band east of Svalbard a strong outflow of sea ice is taking place. In the Fram Strait the ice motion increases from west to east. By multiplying the sea ice area of section 2.1 with the sea ice drift the sea ice area flux is determined.

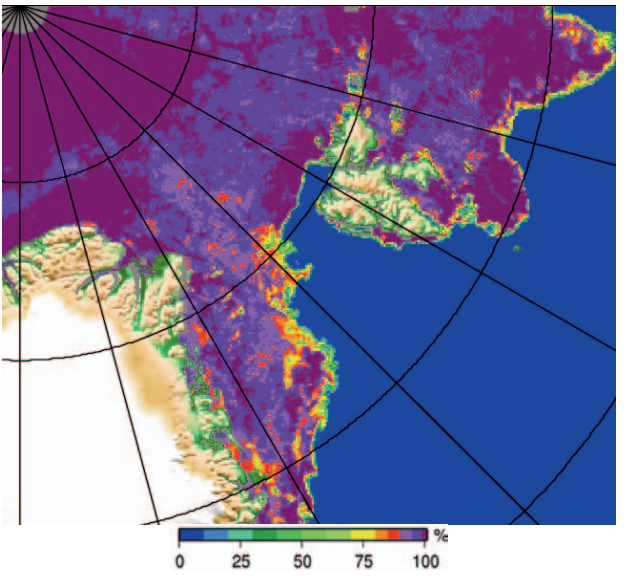

Figure 2. Sea ice concentration on 26 February 2003 in Fram Strait region obtained from AMSR E 89 GHz data (ARTIST Sea Ice (ASI) algorithm). Grid spacing is 6.25 km. The corresponding sea ice drift is shown in Figure 3.

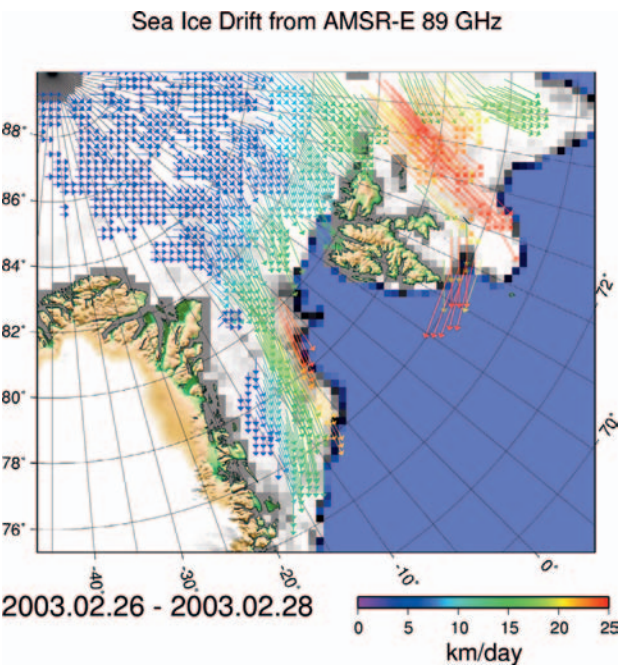

Figure 3. Two-day gap colour-coded sea ice drift in Fram Strait region obtained from merged vertically and horizontally polarised AMSR E 89 GHz data. 26-28 February 2003; grid spacing is 25 km (interpolated from 31.25 km grid). Background: ASI sea ice concentration, see Figure 2 for details.

Sea Ice Freeboard

As a prerequisite step to obtain the sea ice thickness the sea ice freeboard is determined. The GLAS instrument aboard ICESat permits observation of the sea ice up to 86° North. Here GLAS data for the first two ICESat measuring periods 20 February to 19 March 2003 (period I) and 26 September to 17 November 2003 (period II) is used (GLA13 datasets).

By measuring twice the laser pulse travel time at 1064 nm wavelength between the sensor and the surface, the height of the sensor, Dlaser, above the surface is obtained for a footprint of 64 m diameter every 170 m along track (see Fig. 4 and Zwally et al., 2002). ICESat's orbit and thus its height above a reference ellipsoid, hellip, is determined with an accuracy of 5 cm. By subtracting Dlaser from hellip the mean surface elevation in the footprint above the reference ellipsoid is obtained. After atmospheric and tidal corrections the total error budget for a single ICESat surface elevation measurement was estimated as 13.8 cm (Zwally et al., 2002). By subtracting the geoid height, hgeoid, and the contribution to SSH due to the ocean dynamics, Δh, an estimate of the sea ice freeboard height, F, can be obtained (see Figure 4). Δh contains contributions caused by ocean currents, steric SSH changes, atmospheric pressure loading, and ocean and Earth tides. Accordingly, the ice freeboard F is given as

$$F = h_{ellip} - D_{laser} - SSH = h_{ellip} - D_{laser} - h_{geoid} - \Delta h. \quad (1)$$

Similar to all altimeter studies, an accurate geoid is a necessary prerequisite to estimate the ice freeboard. In a preliminary study, Spreen et al. (2005a) found that using the project-provided geoid (EGM96), causes unrealistically large variations of the SSH (several metres) in some regions of the Greenland Sea. We therefore use a more recent gravity field compiled by the Arctic Gravity Project (ArcGP). It represents today's best geoid north of 64° latitude and combines gravity data from several airborne surveys, surface measurements (ground, helicopter, marine), submarine data, satellite altimetry and GRACE (Gravity Recovery and Climate Experiment) data on a 5'x5' grid (Forsberg and Kenyon, 2004; Forsberg and Skourup, 2005). Figure 5 demonstrates the significant improvement of the ArcGP geoid in comparison to the EGM96 geoid. In the Fram Strait differences of ±4 m between the two geoid models become apparent which compares well to the above mentioned discrepancies in the SSH (Spreen et al., 2005a). For our purposes, the ArcGP geoid heights are interpolated bi-linearly onto the locations of the ICESat measurements before they were subtracted from the surface elevation data. As explained in Figure 4, the dynamic part, Δh, of the ocean has to be removed next from the remaining SSH field before an estimate of the ice freeboard can be obtained. No measurements or models exist to date, which would provide an accurate estimate of the dynamic SSH field during period I and II. Instead, Δh has to be inferred from the ICESat data itself. For that purpose we use the “lowest level elevation method” proposed by Zwally and Yi (personal communication, 1st CryoSat Workshop, 2005, http://earth.esa.int/workshops/cryosat2005/, and IGARSS’05, July 25-29, Seoul, Korea) to get the absolute ice freeboard estimates. A similar method was used for airborne laser measurements by Hvidegård and Forsberg (2002) and recently adopted for ICESat data (Forsberg and Skourup, 2005).

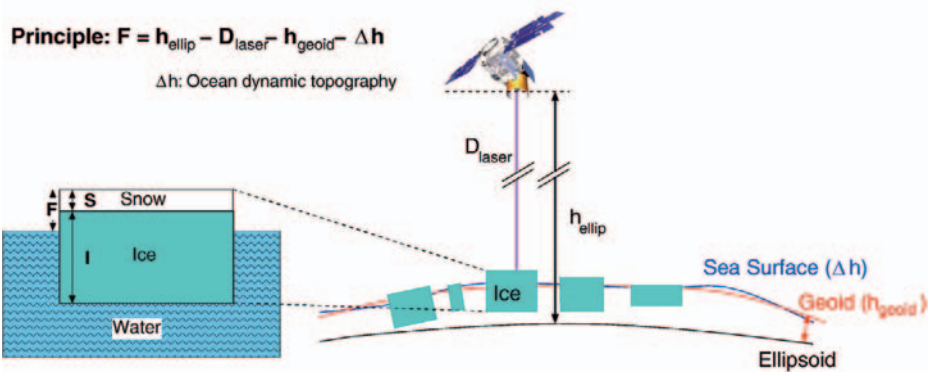

Figure 4. Schematic diagrams showing the interrelation of ice freeboard, F, snow depth, S, and sea ice thickness, I (left) and an artist's view of ICESat above the three involved surfaces: reference ellipsoid, geoid, and sea surface (right).

We adapted this method for our purpose as follows:

(1) We divided the daily GLA13 dataset into separate ICESat overpasses and took only elevation measurements with positive data-quality flags, and an uncorrected reflectivity between 0.1 and 0.9. Additionally we removed outliers and spikes by filtering.

(2) We removed elevation data which were located in open water by using sea ice concentrations calculated from AMSR-E data with the ASI algorithm described before. Elevations in areas with zero ice concentration are excluded from further analysis.

(3) We filtered out the large-scale dynamic variability of the SSH by smoothing the remaining elevations with a 50 km boxcar running mean and subtracting the smoothed from the original elevations. The lowest 2% of the data points in these residual minimum elevations are identified and assumed to represent areas of open water or young, thin ice. This assumption is reasonable, because such areas (leads) are abundant in the study region (sea ice concentrations calculated on a 25 km x 25 km grid rarely exceed 98%), and the combination of the frequent sampling (every 170 m along track) and the small footprint size (64 m) of the GLAS ensures that several leads are hit during one ICESat overpass. It should be mentioned that this 2%-rule certainly results in an underestimation of open water areas in the MIZ.

(4) We fit the remaining minima linearly using a least absolute deviation method to account for remaining trends in the elevations after boxcar averaging.

(5) The derived SSH was subtracted from the measured elevations to obtain the ice freeboard.

An example for a part of one orbit on 23 February 2003 demonstrating how this method works is shown in Figure 6. The black lines are the GLAS elevations after filtering with the 50 km running mean. The blue line connects the lowest 2% of data points. In red the finally fitted SSH is given. Subtracting the red line from the black elevation and setting all remaining negative values to zero yields the required sea ice freeboard height.

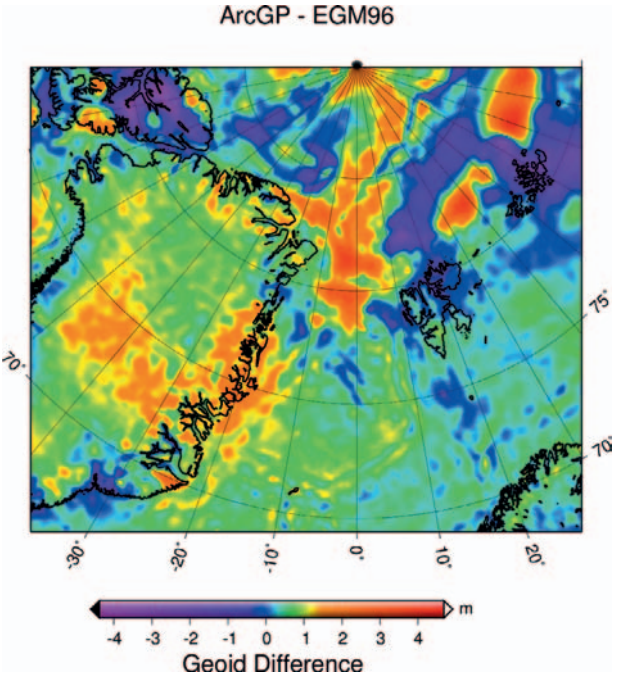

Figure 5. Difference between the more accurate ArcGP and ICESat's standard EGM96 geoid. Differences of ±4 m can be observed in the Fram Strait region.

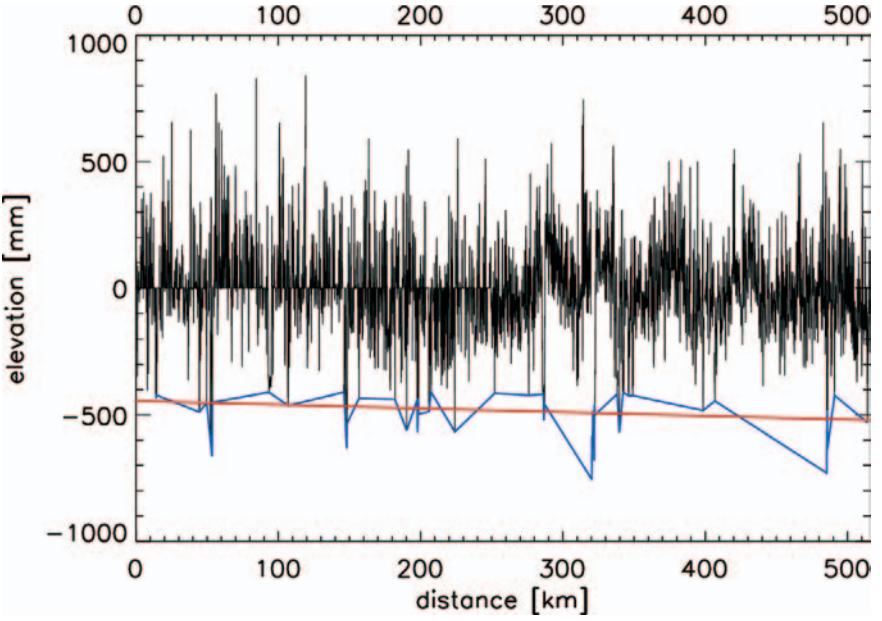

Figure 6. Example from 23 February 2003 showing the principle of the lowest level elevation method. Black: high-pass filtered GLAS elevations, blue: connected lowest 2% of elevation data; red: the resulting SSH.

Following this approach, the ice freeboard distribution is calculated on a 25 km grid as a mean of all overpasses for period I (Feb/Mar 2003) and II (Oct/Nov 2003), yielding a mean value of 55 ± 18 cm for period I and of 34 ± 19 cm for period II, respectively. The stated ± bands describe the variability of the ice freeboard in our study region.

To check if the lowest level elevation method works properly, we compared several Envisat ASAR scenes with our ICESat freeboard heights on a single orbit base. One example of this comparison is shown in Figure 7. In a typical winter-time SAR image of the Arctic Ocean sea ice cover the radar backscatter takes high values (grey-white in Figure 7) over multiyear ice and low values (black-dark grey in Figure 7) over smooth first-year ice, young ice and calm open water. In Figure 7 some of these dark regions are marked with red circles. The overlaid GLAS freeboard heights drop to near zero exactly in this region. The remaining shift in the location of the open water/thin ice areas identified between both datasets can be ascribed to the ice drift during the acquisition time difference of the two data sets. This difference causes the biggest problem for comparison of these datasets. If the time difference exceeds 2-3 hours in most cases no agreement between both datasets can be found; otherwise the match between these datasets in general is comparable to the example shown here. Additional problems might be caused by an inaccurate geo-location of the datasets. However, overall the comparison showed good agreement, underlining the feasibility of our approach.

Sea Ice Thickness

To retrieve ice thickness, I, from the ice freeboard, F, prior information about snow thickness, S, and the densities of ice, ρ_I, of snow, ρ_S, and of water, ρ_W, has to be known (see Figure 4). Because no reliable satellite snow depth measurements are available covering our study region and period, we used in-situ snow depth and density measurements available in the vicinity of our study area in combination with a snow climatology. Snow thickness, and snow and ice density measurements from R/V "Polarstern", which operated in April 2003, one month after period I, north of Svalbard, are taken as reference for period I. The observed mean snow thickness, S, was 20 cm (range: 0 – 70 cm) with a density, ρ_S, of 330 kg/m3. The mean ice density, ρ_I, was 850 kg/m^3 (range: 825 – 890 kg/m^3). Here the upper limit of ρ_I = 890 kg/m^3 is taken in order to account for the considerable fraction of first-year ice in the study area, which is not represented properly by these ice density measurements, of predominantly multi-year ice. Isostatic balance is assumed (on average), i.e. the snow depth on freely floating ice has to be always less than or equal to the ice freeboard. For thin ice the snow depth is therefore reduced. With these parameters the ice thickness I for period I can be calculated from the ice freeboard F according to Archimedes' principle as:

$$I = F\frac{\rho_W}{\rho_W - \rho_I} + S\frac{\rho_S - \rho_W}{\rho_W - \rho_I} = 7.65F - 5.18S. \tag{2}$$

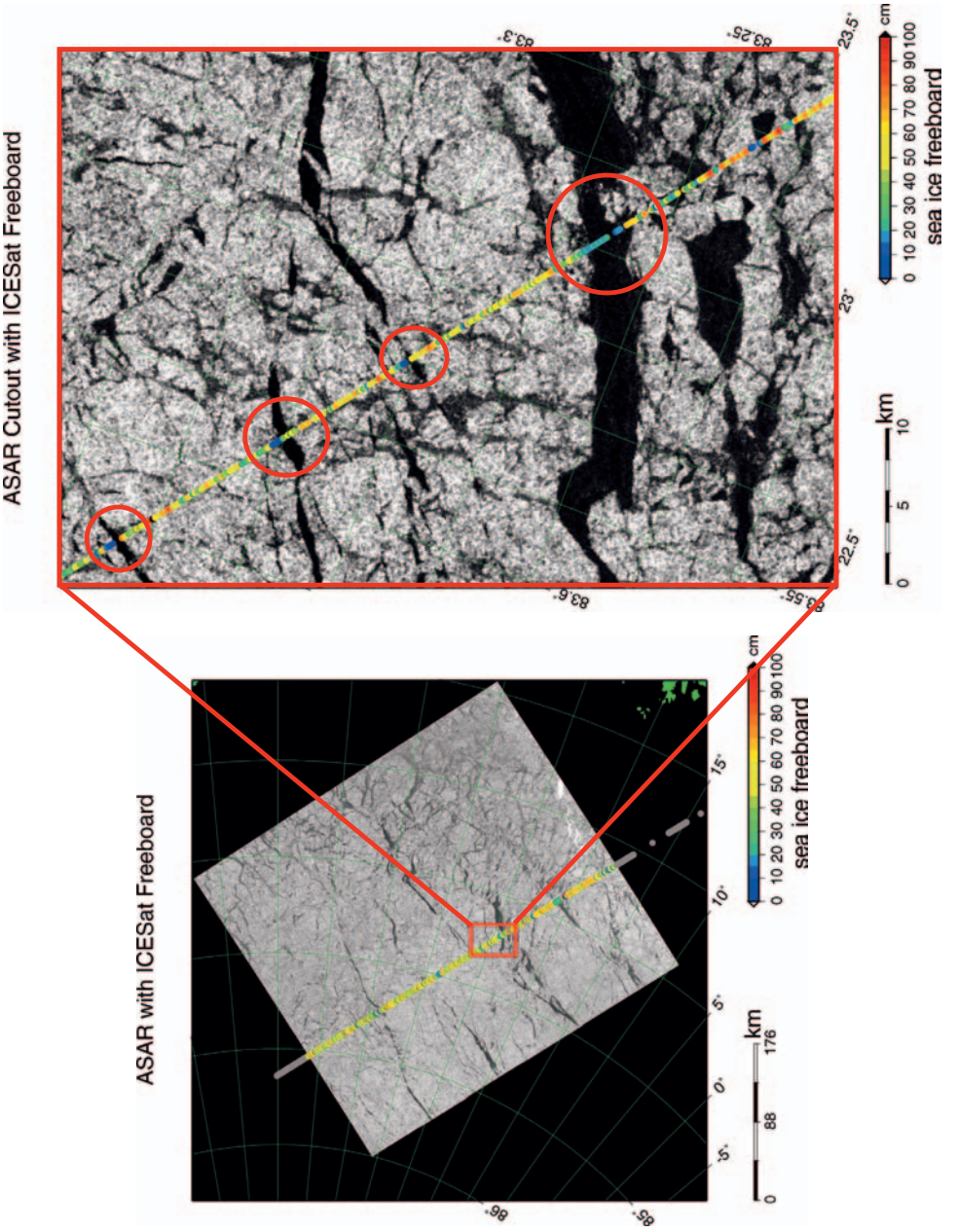

Figure 7. Envisat ASAR image from 09 March 2003, 16:52 UTC, overlaid by colour-coded GLAS sea ice freeboard heights (not to scale) of an ICESat overflight of the same day, 15:41 UTC. Left: complete 400 km x 400 km wide-swath ASAR scene north of Svalbard; right: zoom of the part enclosed by the red rectangle. Red circles mark regions where the SAR image shows leads (covered either by smooth first-year ice and/or thin ice and/or calm open water) and accordingly the ICESat freeboard drops down to values near zero. A slight shift in the location of the leads in the two datasets can be attributed to the ice drift during the 1:10 hour time difference.

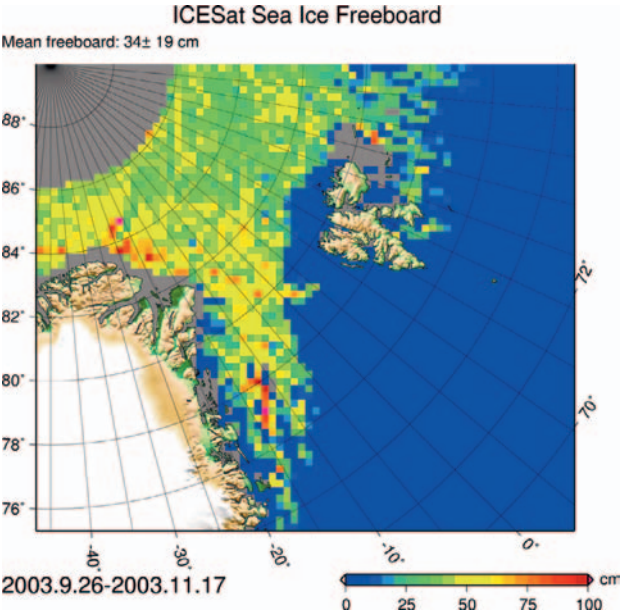

Figure 8. Sea ice freeboard height distribution derived from GLAS elevation data for the second ICESat measurement period in autumn 2003. All data of this 53 days period are averaged on a 25 km grid. Grey areas mark missing data.

For period II, snow parameters can be expected to substantially differ from those of period I (e.g. Warren et al., 1999). In-situ measurements representative of snow conditions during period II are not available. Alternatively climatological snow depths (Warren et al., 1999) could be used, revealing values in the range of 19 cm and 32 cm for October and March (resemble period II and I) for the complete Arctic, respectively. However, these values are based on observations made during 1954 to 1991 predominantly in the central Arctic. Meanwhile the ice age and thickness and presumably also the snow depth have changed but most likely not the seasonal cycle, i.e. the ratio between spring and autumn snow depths should be the same. Therefore, we estimated the snow depth of period II, by taking the snow depth S measured during spring as reference, as $S = 19/32*0.2$ m = 0.12 m. After Warren et al. (1999) the snow density in the Arctic varies seasonally rather than spatially so that their snow density estimate for October/November of $\rho_S = 280$ kg/m^3 is taken for period II. This is supported by their snow density measurements of 325 kg/m^3 for March/April, which match well with the measurements during CryoVEx of 330 kg/m^3. This leads to estimates of the ice thickness during period II as:

$$I = 7.65F - 5.56S. \tag{3}$$

The sea ice thickness distribution as derived from the GLAS ice freeboard estimates (Figure 8) using equation (3) for ICESat period II (Oct/Nov) is shown in Figure 9. They are scaled with ASI sea ice concentrations (section 2.1) sampled onto the 25 km grid. Thus the given thickness is the mean sea ice thickness in the corresponding grid cell, including the open water part. The mean sea ice thickness amounts to 3.0 m and 1.9 m, during periods I and II, respectively. The mean error budget of every grid cell is quite large and of the order of 1 m for both periods using conservative error assumptions for the individual variables. A more detailed error discussion can be found in Spreen et al. (2006).

Sea Ice Volume Flux

Finally the sea ice volume flux out of every grid cell was obtained by combining sea ice area flux (section 2.2) with the sea ice thickness estimates derived from ICESat data. The sea ice volume flux Vf is calculated by multiplying the sea ice thickness I of every grid cell with the grid size G and the absolute value of the sea ice motion M of this cell:

$$Vf = I \cdot G \cdot M. \tag{4}$$

The spatial distribution, mean amount and direction of the sea ice volume flux estimated with equation (4) using the AMSR E drift is shown for the Fram Strait region for autumn periods II in Figure 10. The zonal distribution of the meridional volume flux through a transect at 79°N (marked with a black line in the main panel of Figure 10) is shown in the inset of Figure 10.

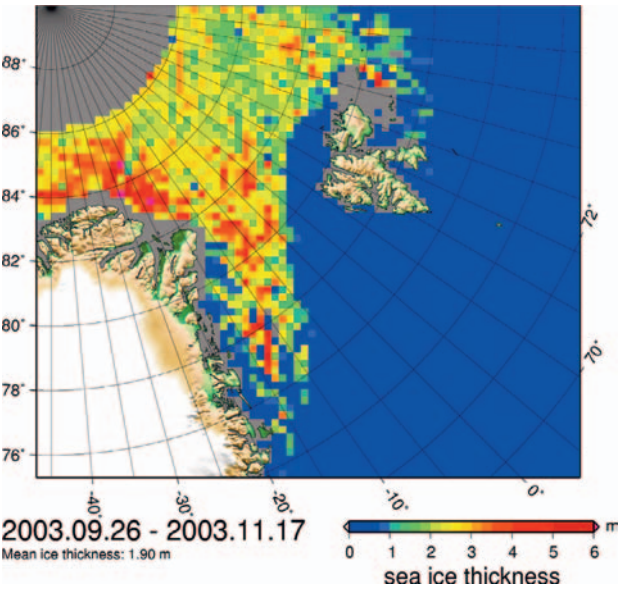

Figure 9. Mean sea ice thickness derived from ICESat GLAS observations for Oct./Nov. 2003 (ICESat measurement period II). Grey areas denote missing data.

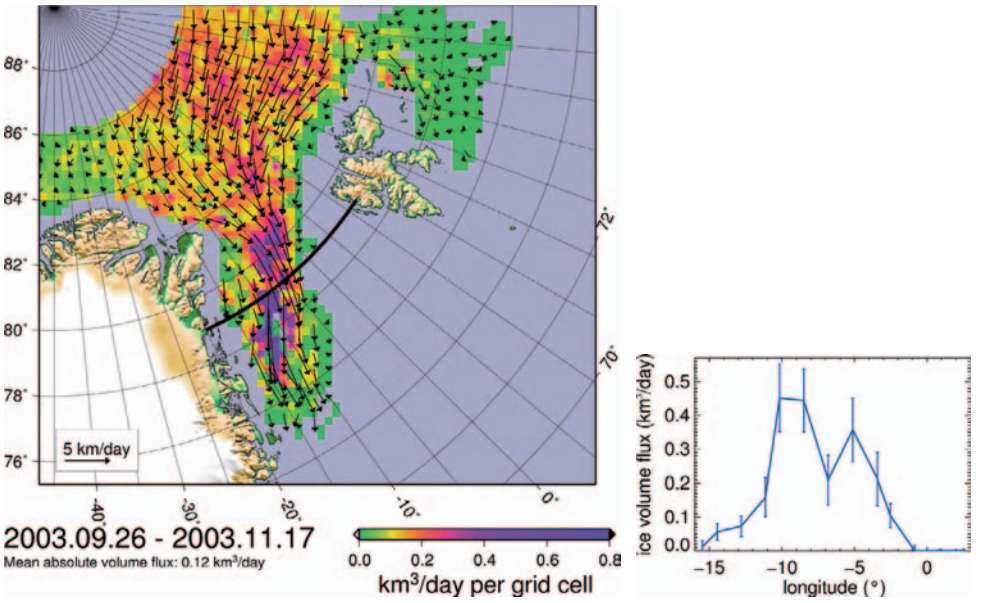

Figure 10. Main: Sea ice volume flux in the direction indicated by the ice motion vectors (AMSR-E ice drift, starting at every third grid cell) for Oct./Nov. 2003 (ICESat period II). Grid cells with either or both no ICESat or no AMSR-E data are marked gray. Inlay: Zonal distribution of the meridional sea ice volume flux across transect at 79°N (black line in main panel). Error bars denote the RMS error budget of the transect data points.

3 RESULTS AND DISCUSSION

The spatial distribution of sea ice volume flux has been obtained from solely satellite observations. For such estimates, sea ice parameters, obtained from various satellites, have to be combined. Figure 10 represents the mean daily flow of ice volume for every grid cell in the direction of the AMSR E based ice drift vectors during ICESat measurement period II. Analogous results were obtained for ICESat measurement period I (not shown here). Inflow from neighbouring grid cells is not considered. The figure clearly suggest that the ice volume flux through Fram Strait is not evenly distributed across the strait, but strongly concentrated toward its western portion. Near Greenland, thick, land-fast ice prevails. Accordingly, its ice motion and volume fluxes tend to be negligible. However, east of this region the volume flux reaches its highest values, coincident with the East Greenland Current (EGC) axis, which supports the transport of thick multi-year ice from the Fram Strait southward. Further eastward, the flux values decline towards the open water area. The mean ice thickness in period II is about 1 m smaller than in period I (1.9 m to 3 m). This can be explained to some extent by the thinning of ice through melting during summer months. Moreover, the ice drift distribution suggests that the ice in the Fram Strait region and the EGC during period I originates from a thick-ice region north of Greenland, while during period II the ice flux tends to originate from the transpolar drift with smaller ice thickness. The sea ice drift of period I appears, on average, about twice what is shown for period II.

The meridional ice volume flux across 79°N latitude for period I is displayed in the inlay of Figure 10. To calculate this meridional flux, data from three grid points around these latitudes (approximately one north, one at the latitude and one south) have been averaged. Also shown as error bars are the root mean square (RMS) values of the flux calculated by

error propagation (details in Spreen et al., 2006). The ice volume flux is maximum between -10° and -7°E. Calculating the total flux through the transect at 79° N gives 5.6 ± 1.0 km3/day for period I and 2.1 ± 0.4 km3/day for period II. From these values the monthly (30 days) volume fluxes result in 168 ± 31 km3 and 62 ± 13 km3, respectively.

Compared to the Fram Strait mean volume flux estimates of Kwok et al. (2004a) and Vinje et al. (1998) given for the 1990s, our estimates are small. Both studies used a combination of ice drift estimates from satellite microwave radiometry (SSM/I), together with ice thickness estimates obtained from ice draft measurements by ULS at near 79°N, 5°W. Their mean volume flux estimates in the 1990s averaged ~340 km^3 for March and ~230 km^3 for October in comparison to our one year estimates of 168 ± 31 km^3 and 62 ± 13 km^3 for 2003. Assuming that both datasets are comparable, both periods, but especially the second ICESat measurement period, showed lesser sea ice volume fluxes compared to the 1990s. Such low volume fluxes did occur in the 1990s, however, the minimum values reported by Kwok et al. (2004a) and Vinje et al. (1998) for the two months February/March and October/November are 94 km^3/month and -2 km^3/month, respectively. Therefore our estimates lie in the range of previously calculated values. Our relative uncertainty for the total ice volume flux through the 79°N transect is around 18% and comparable to the uncertainties of 12% to 20% published by Vinje et al. (1998) for their method.

It would have been nice to use their method also during the ICESat measurement periods to compare our results, but unfortunately the ULS time series distributed by the National Snow and Ice Data Centre (NSIDC) stops in 2002 before the ICESat launch. Data we have got from other institutions, which operate ULS instruments, e.g. the Norwegian Polar Institute (NPI) in Tromsø (Edmond Hansen, personal communication, 2005), also stop in 2001.

The largest part of the volume flux variability is caused by the variability of the ice drift. We therefore compared the ice drift used in our study to the mean ice drift for the corresponding months of the years 1991 to 2002 (Kwok et al., 2004a) at a zonal flux gate at 80°N. The maximum ice drift values along the gate for ICESat period I are more than 15% smaller than the corresponding mean drift values for 1991 to 2002. The zonal drift distribution is also much narrower. For ICESat period II (Oct./Nov.) the AMSR-E derived maximum ice drift values are more than 50% smaller than for October 1991–2002. This is a strong argument towards an extraordinary small ice volume flux during ICESat period II compared to previous years, which would explain our smaller result.

4 CONCLUSIONS

We presented here a multi-sensor satellite approach to estimating the sea ice volume flux, which allows - for the first time - calculations of the spatial distribution of this flux on a monthly basis. The approach combines surface elevation measurements obtained by the ICESat GLAS instrument with the sea ice area flux (combination of sea ice concentration and drift) obtained from brightness temperature measurements of the 89 GHz channels of the Advanced Microwave Scanning Radiometer (AMSR E). The thickness is derived from ICESat data by converting its surface elevation measurements into the sea ice freeboard height. Using the recent geoid from the Arctic Gravity Project reduces uncertainties in these freeboard height estimates due to geoid model errors. Missing information about the ocean circulation and ocean tides is approximated locally by interpolating the sea surface height linearly between leads for every ICESat orbit. The average freeboard height distribution is

calculated for single ICESat measurement periods using a standard polar-stereographic grid. Using typical average values for ice density and snow depth and density derived from a climatological dataset in combination with in-situ measurements, the freeboard height is converted into an average ice thickness distribution. Sea ice area flux and thickness are finally combined to get an estimate of the sea ice volume flux. The approach is applied to data of the first two ICESat measurement periods (Feb./Mar., period I, and Oct./Nov., period II, 2003) in the Fram Strait region. Estimated meridional ice volume fluxes across 79°N amount to approximately 170 km^3 and 60 km^3 for period I and II, respectively, with a relative error of about 20%. One reason for the fact that these values are at the lower bound of earlier observations during the 1990s using ULS-derived ice thickness, particularly for period II is certainly the significantly smaller ice drift speed observed during period II as compared to the 1990s. However, because of a large inter-annual variability in the ice drift, a direct comparison between our results and those of earlier studies is not meaningful.

The parameters sea surface height (SSH), ice density, snow density and depth, and ice drift, which determine the accuracy of our ice volume flux estimates, are highly variable and/or cannot be determined with sufficient accuracy. An error and sensitivity analysis (Spreen et al., 2006) reveals that SSH, ice drift speed, snow depth, and ice density can be of equal importance for the accuracy of the ice volume flux. Regarding SSH, improved estimates can be expected from a more accurate geoid and improved information about day-to-day variations in dynamic ocean surface topography, which together could allow a more accurate estimation of the ice freeboard height. Ice drift speed estimates could be improved by using an approach especially tuned for the highly dynamic Fram Strait region, e.g. an approach which is less vulnerable to the atmospheric influence, and which allows a finer spatial resolution. The usage of Synthetic Aperture Radar (SAR) data could be an alternative (Kwok et al., 2004a). A further validation and/or enhancement of the AMSR-E snow depth algorithm for Arctic sea ice (Comiso et al., 2003) would be required to use its results for our goals. At the time of writing the snow depth estimates available from AMSR E data for the Fram Strait region are significantly smaller than corresponding in-situ measurements and are thus not used in this study. Most difficult would be an improvement with respect to the ice density, which could be achieved, however, by distinguishing at least first- and multi-year ice, and assigning different density values for each class when converting the freeboard heights into ice thickness.

Unfortunately, ICESat is only operating 3 months a year at maximum. Therefore there will be always large gaps in this time series. Also, during summer months the ice drift retrieval using AMSR E data is hampered if not impossible due to melting conditions which cause a loss of the distinct surface features required for the maximum cross-correlation method. Thus for summer months our method would have to use alternative ice drift estimates.

We note that our approach of estimating sea ice volume transport is entirely satellite based and can therefore be applied to geographical regions other than the Greenland Sea. We anticipate that our method can easily be adapted to new freeboard measurements like the ones expected to be available from the upcoming CryoSat II mission. CryoSat II will measure continuously and thus the gaps in the time series could be significantly reduced by use of these data.

5 ACKNOWLEDGEMENTS

This work was supported by the German Research Foundation (DFG) project SFB 512-E1. The authors gratefully acknowledge the provision of ICESat and AMSR-E data by the National Snow and Ice Data Centre (NSIDC), Boulder, CO, USA. Especially we acknowledge the provision and support on sea ice drift data from AMSR-E data by Robert Ezraty and Fanny Ardhuin from IFREMER, Brest, France and the provision of the ArcGP geoid by Rene Forsberg from Danish National Space Centre, Copenhagen, Denmark.

6 REFERENCES

Aagaard, K. and E. Carmack, 1989: The role of sea ice and other fresh water in the Arctic Circulation, *J. Geophys. Res.*, 94(C10), 14,485-14,498.

Agnew, L., H. Le and T. Hirose, 1997: Estimation of large-scale sea ice motion from SSM/I 85.5 GHz imagery, *Ann. Glaciol.*, 25, 305-311.

Bamber, J.L. and A.J. Payne (editors), 2004: *The mass balance of the cryosphere : observations and modelling of contemporary and future changes*, Cambridge University Press, Cambridge, UK; New York.

Cavalieri, D.J., C.L. Parkinson and K. Y. Vinnikov, 2003: 30-year satellite record reveals contrasting Arctic and Antarctic decadal sea ice variability, *Geophys. Res. Lett.*, 30(18), L1970, doi:10.1029/2003GL018031.

Cavalieri, D.J., C. Parkinson, P. Gloersen and H. Zwally, 2002: Sea ice concentrations from Nimbus-7 SMMR and DMSP SSM/I passive microwave data, *Tech. Rep., National Snow and Ice Data Center*, Boulder, Colorado, USA.

Comiso, J.C., D.J. Cavalieri and T. Markus, 2003: Sea ice concentration, ice temperature, and snow depth using AMSR-E data, *IEEE Trans. Geosci. Rem. Sens.*, 41, 243-252.

Dickson, R.R., J. Meincke, S.-A. Malmberg and A.J. Lee, 1988: The "Great Salinity Anomaly" in the northern North Atlantic 1968-1982, *Prog. Oceanogr.*, 20, 103-151.

Divine, D.V. and C. Dick, 2006: Historical variability of sea ice edge position in the Nordic Seas, *J. Geophys. Res.-Ocean*, 111, C01001.

Ezraty, R., F. Ardhuin and D. Croizé-Fillon, 2005: Sea ice drift in the Central Arctic using the 89 GHz brightness temperatures of the Advanced Microwave Scanning Radiometer (AMSR-E), User's Manual, Version 1.0, Institut français de recherche pour l'exploitation de la mer (IFREMER), Brest, France.

Forsberg, R. and H. Skourup, 2005: Arctic ocean gravity, geoid and sea-ice freeboard heights from ICESat and GRACE, *Geophys. Res. Lett.*, 32, L21502, doi: 1029/2005GL023711.

Forsberg, R. and S. Kenyon, 2004: Gravity and geoid in the Arctic region – The northern polar gap now filled. *Proceedings Second International GOCE Workshop "GOCE, The Geoid and Oceanography"*, ESA-ESRIN, Frascati, Italy, 8-10 March 2004.

Haas, C., 2004: Late-summer sea ice thickness variability in the Arctic Transpolar Drift 1991-2001 derived from ground-based electromagnetic sounding, *Geophys. Res. Lett.*, 31, L09402, doi:10.1029/2003GL019394.

Hvidegård, S.M. and R. Forsberg, 2002: Sea-ice thickness from airborne laser altimetry over the Arctic Ocean north of Greenland, *Geophys. Res. Lett.*, 29(20), 1952-1955.

Johannessen, O.M., L. Bengtsson, M.W. Miles, S.I. Kuzmina, V.A. Semenov, G.V. Alekseev, A.P. Nagurnyi, V.F. Zakharov, L.P. Bobylev, L.H. Pettersson, K. Hasselmann and H.P. Cattle, 2004: Arctic climate change: observed and modeled temperature and sea-ice variability, *Tellus*, 56A(4), 328-341.

Kaleschke L., C. Lüpkes, T. Vihma, J. Haarpaintner, A. Bochert, J. Hartmann and G. Heygster, 2001: SSM/I sea ice remote sensing for mesoscale ocean-atmosphere interaction analysis, *Can. J. Rem. Sens.*, 27(5), 526-537.

Karstensen, J., P. Schlosser, D.W.R. Wallace, J.L. Bullister and J. Blindheim, 2005: Water mass transformation in the Greenland Sea during the 1990s, *J. Geophys. Res.*, 110, C07022, doi:10.1029/2004JC002510.

Kwok, R., G.F. Cunningham and S.S. Pang, 2004a: Fram Strait sea ice outflow, *J. Geophys. Res.*, 109, C01009, doi:10.1029/2003JC001785.

Kwok, R., H.J. Zwally and D. Yi, 2004b: ICESat observations of Arctic sea ice: A first look, *Geophys. Res. Lett.*, 31, L16401, doi:10.1029/2004GL020309.

Kwok, R., A. Schweiger, D.A. Rothrock, S. Pang and C. Kottmeier, 1998: Sea ice motion from satellite passive microwave imagery assessed with ERS SAR and buoy motions, *J. Geophys. Res.*, 103(C4), 8191-8214.

Laxon S., N. Peacock and D. Smith, 2003: High interannual variability of sea ice thickness in the Arctic region, *Nature*, 425, 947-950.

Pfirman S., W.F. Haxby, R. Colony and I. Rigor, 2004: Variability in Arctic sea ice drift, *Geophys. Res. Lett.*, 31, L16402, doi: 10.1029/ 2004GL020063.

Rothrock D. A., J. Zhang and Y. Yu, 2003: The Arctic ice thickness anomaly of the 1990s: A consistent view from observations and models, *J. Geophys. Res.*, 108, doi: 10.1029/2001JC001208.

Rothrock D. A., Y. Yu and G.A. Maykut, 1999: Thinning of the Arctic sea-ice cover, *Geophys. Res. Lett.*, 26(23), 3469-3472.

Spreen, G., S. Kern, D. Stammer, R. Forsberg and J. Haarpaintner, 2006: Satellite-based estimates of sea ice volume flux through Fram Strait, *Ann. Glaciol.*, 44, in press.

Spreen, G., S. Kern, R. Ezraty, H. Witte and D. Stammer, 2005a: Towards remote sensing of the net sea ice volume flux in the Greenland Sea, *Proc. 1st CryoSat Workshop*, March 8-10, 2005, ESA ESRIN, Frascati, Italy, http://earth.esa.int/workshops/cryosat2005/all.html.

Spreen, G., L. Kaleschke and G. Heygster, 2005b: Operational sea ice remote sensing with AMSR-E 89 GHz channels, *2005 IEEE International Geoscience and Remote Sensing Symposium Proceedings*, Seoul, Korea, July 25—29.

Vinje, T., N. Nordlund and A. Kvambekk, 1998: Monitoring ice thickness in the Fram Strait, *J. Geophys. Res.*, 103(C10), 10,437-10,449.

Wadhams, P., 2002: *Ice in the Ocean*, Gordon and Breach Science Publishers, London, 351pp.

Wadhams, P. and N. R. Davis, 2000: Further evidence of ice thinning in the Arctic Ocean, *Geophys. Res. Lett.*, 27, 3973-3975.

Warren, S.G., I.G. Rigor, N. Untersteiner, V.F. Radionov, N.N. Bryazgin, Y.I. Aleksandrov and R. Colony, 1999: Snow depth on Arctic sea ice, *J. Climate*, 12, 1814-1829.

Zwally, H.J., B. Schutz, W. Abdalati, J. Abshire, C. Bentley, A. Brenner, J. Bufton, J. Dezio, D. Hancock, D. Harding, T. Herring, B. Minster, K. Quinn, S. Palm, J. Spinhirne and R. Thomas, 2002: ICESat's laser measurements of polar ice, atmosphere, ocean, and land, *J. Geodyn*, 24, 405-445.

Sea ice Thickness Estimates from Airborne Laser Scanning

Sine M. Hvidegaard, Rene Forsberg, and Henriette Skourup
Geodynamics Department, Danish National Space Center, Juliane Maries Vej 30, DK-2100 Copenhagen Oe, Denmark

Keywords: airborne laser, ice sounding

ABSTRACT: We describe the extensive 2003 to 2005 laser scanner surveys in the Arctic Ocean by the Danish National Space Center (DNSC). The experimental work was co-funded by national and international projects, among these the EU 5th Framework projects GreenICE (Greenland Arctic Shelf Ice and Climate Experiment) and SITHOS (Sea Ice Thickness Observing Systems), and the European Space Agency. The observations consist of laser elevation measurements supplemented with GPS, inertial navigation systems, and photography from a Twin Otter aircraft. From these measurements the sea ice thickness can be estimated, assuming independent information on snow depth, and snow, ice, and seawater density to convert measured freeboard heights to thickness. The laser monitoring of the sea ice conditions in the Arctic Ocean has been coordinated with many other observations of the sea ice, including AWI helicopter-borne electromagnetic thickness measurements, as well as in situ groundwork. This paper outlines the airborne fieldwork, describes the laser scanner technique, and presents the main airborne lidar results from the 2003 to 2005 campaigns. In addition we present some preliminary results from inter-comparisons to independent sea ice thickness measurements, showing that the airborne lidar freeboard method can produce reasonable estimates of ice thickness.

1 INTRODUCTION

Monitoring of the Arctic sea ice conditions is highly important for e.g. navigation and climate change studies. Sea ice extent has been followed using passive microwave satellite techniques for decades, but systematic, year-round observations of sea ice thickness has been much more sporadic, except for the area south of 81°N with ERS satellite radar altimetry coverage (Laxon et al, 2003). North of this latitude, ice thickness information has come from submarines, icebreakers and ice camps.

The Geodynamics Department at the Danish National Space Centre, DNSC, (formerly a part of the National Survey and Cadastre, KMS) has since the late 1990's developed an airborne laser altimetry/laser scanner (lidar) system, used to measure surface elevations of ice and snow both over sea ice and inland ice. The first campaign took place in 1998 in connection with airborne gravity surveys, where data from a laser altimeter were used to generate sea ice freeboard heights north of Greenland (Hvidegaard and Forsberg, 2002). A number of later aerogravity campaigns similarly yielded airborne laser coverage, typically in the late spring. We here focus on activities in the 2003-05 period, where activities were done as part of the GreenICE, SITHOS and CryoSat cal/val projects.

The DNSC system was used in the three campaigns to gather sea ice elevation data to be used for sea ice thickness monitoring. An overview of the field campaigns is found in Table 1.

Table 1. Twin Otter lidar 2003-5 field campaign overview.

Date	Area	Aim	Main Tasks	Comments
April 1-23 2003	Fram Strait and Arctic Ocean north-east of Greenland.	Sea ice monitoring and CryoSat cal/val test.	Coincident laser scanner and helicopter EM flights. Long flights north of Greenland.	Coordinated effort with ground and helicopter work from *Polarstern.*
May 3-27 2004	Lincoln Sea and Arctic Ocean north of Greenland.	Sea ice monitoring and support of sea ice camp.	Repetition of previous lines Under-flight of ICESat. Transport to/from camp. Repeated laser and helicopter EM flights.	No coincident laser and EM flights were possible due to bad weather and medivac.
May 3-20 2005	Lincoln Sea and Arctic Ocean north of Greenland.	Sea ice monitoring and joint EM-laser inter-comparison.	Repetition of previous surveyed areas. Coincident laser and helicopter EM flights. Sea ice thickness and drift buoy deployment.	Buoy deployment by helicopter not Twin Otter since no suitable ice for landing was found.

The operations were based out of the military stations CFS Alert on Ellesmere Island, Canada, and Station Nord, Northeast Greenland. The airport in Longyearbyen, Svalbard, was also used in 2003. The specific flight tracks are seen in Figure 1. All flights were done as low-level flights at a maximum height above the sea ice of
300 m.

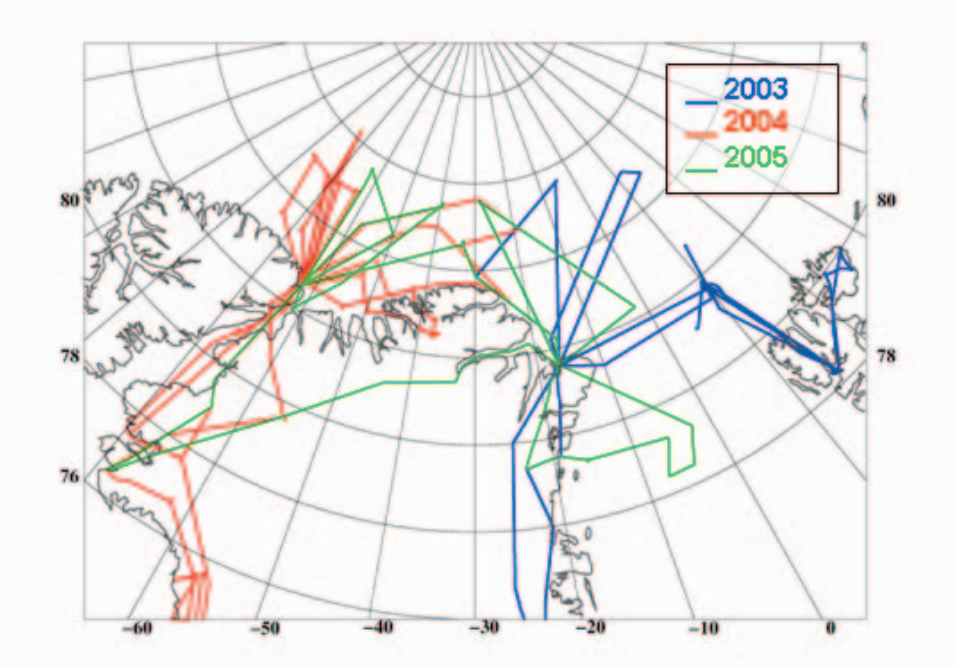

Figure 1. Flight tracks for 2003, 2004, and 2005 DNSC airborne laser scanner surveys.

2 THE AIRBORNE LIDAR SYSTEM AND FREEBOARD MEASUREMENT

The DNSC airborne lidar system consists of:

- A near-infrared laser scanner (LMS- Q140i-60) manufactured by Riegl, Austria.
- Several precise geodetic GPS receivers (Trimble, Ashtech, Javad), fed from different antennae on top of the aircraft
- A medium-grade, strap-down, GPS-aided inertial navigation system (Honeywell H764G), that provided precise observations of the aircraft accelerations and rotations.
- Nadir looking cameras for visual verification of the surface conditions
- Power system and PCs for instrument control and data storage

Figure 2 sketches the mounting of the instruments in the aircraft.

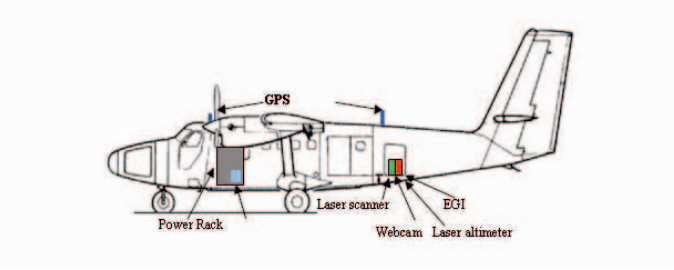

Figure 2. Sketch of DNSC instrument mounting in the Twin Otter.

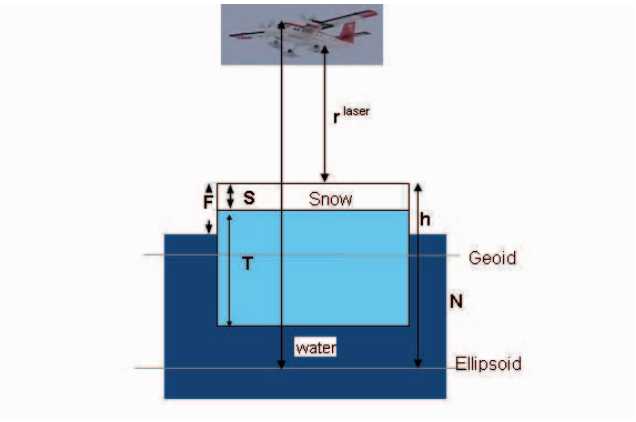

Figure 3. Illustration of the observation principle and principle of freeboard determination.

The method of observing the surface with laser altimetry from an airborne platform is shown in Figure 3. The aircraft is positioned using the GPS system, and the platform attitude changes are determined from the INS. The laser scanner measures the range between the platform and the surface at a particular epoch, as timed by GPS, with an accuracy of a few cm and a beam width of less than 1 m. By combining the laser range measurement with INS knowledge about the platform attitude and post-processed GPS position, the range can be converted into latitude, longitude and ellipsoidal height of the surface target. The absolute height accuracy of this determination is typically 20-30 cm, mainly limited by long-wavelength kinematic GPS errors.

The laser and INS instruments are rigidly mounted to the aircraft floor, but it is impossible to avoid a small misalignment between the laser coordinate system and the INS reference system. The misalignment angles – typically constant throughout a survey – are determined by over-flights of GPS positioned objects, for instance a building in an airport. At the same time a possible range bias may be found from comparisons to known runway heights (typically from car GPS surveys). We typically fly a clover-leaf pattern in order to get good control of all directions. Figure 4 shows data from one such calibration survey. The misalignment angles are typically less than one degree, and can be determined with an accuracy better than 0.01 degrees. We also in some instances have used crossing tracks during flights for an additional control of lidar misalignments and possible 1-sec time offsets, inherent to the specific Riegl system we use.

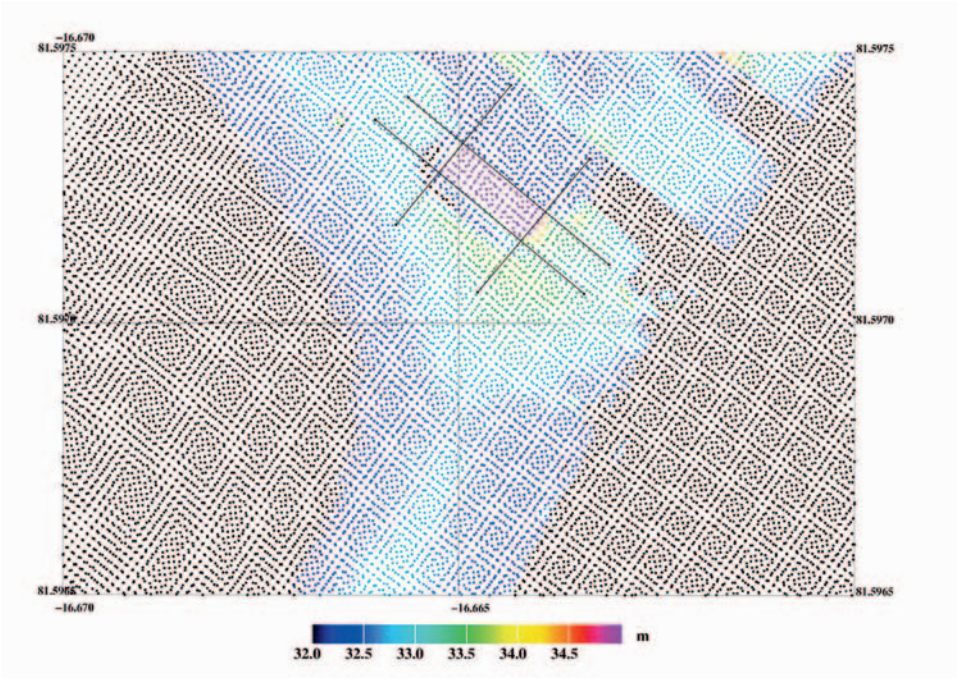

Figure 4. Lidar data from a calibration flight at Station Nord, May 2005.

For sea ice the basic parameter of interest is the sea ice freeboard height F, i.e. the height above the instantaneous sea-surface, which to first order is approximated by a geoid model. The measurement of ice freeboard height, F, relies on laser measurements of range to the surface, r^{laser}, combined with precise kinematic GPS aircraft positioning, attitude determination by INS, and a geoid model; the freeboard is given by

$$F = h^{GPS} - r^{laser} \cos p \cos r - N + e \tag{1}$$

In this equation e is the measurement error and the neglected effects of dynamic sea-surface topography and tides. The GPS height (h^{GPS}) of the aircraft is determined by differential GPS relative to several ground base stations; the range (r^{laser}) from the aircraft to the surface is measured by a scanning laser; pitch (p) and roll (r) by the INS, and the geoid

height (N) is obtained from an updated model based on gravity measurements from previous projects, compiled in the Arctic Gravity Project combined with GRACE data (Forsberg and Skourup, 2005).

The laser scanner freeboard data are affected both by random errors and systematic errors from GPS solution biases, biases in geoid heights, and mean ocean dynamic topography. This bias may be removed by "lowest-level" filtering. For the 2003 to 2005 data a generalised collocation version of the polynomial lowest-level filtering scheme (Hvidegaard and Forsberg, 2002) has been used. The method divides a segment of lidar data into 0.01 hr intervals (approximately 2 km). The minimum value in each interval is averaged over 0.04 hr intervals, and a minimum surface is fitted to the average minimum points using least-squares collocation. Subtracting this fitted curve minimizes the possible bias in the freeboard data at half-wavelengths longer than approximately 8 km.

The sea ice freeboard heights F (in this paper including the snow) were converted to ice thickness T using an approximate ratio between the freeboard and the thickness expressed as

$$T = K \times F \tag{2}$$

K is derived from an assumption of isostatic balance between ice floes and the surrounding seawater. For the 2003 flights K=5 were derived from observations of snow depth and ice density close to *Polarstern*. For 2004 and 2005 a value K=6 was used, based on a climatological model by Wadhams et al. (1992), as no representative in situ information was available.

Table 2. Ratio between sea ice thickness and freeboard, K, for varying values of ice density and snow depth.

Ice density\snow depth	0 m	0.30 m	Relative error (metre)
850 kg/m^3	5.89	4.67	0.6
900 kg/ m^3	7.26	6.31	0.5
Relative error (metre)	0.7	0.8	Max. error: 1.3

For typical values: 3 m ice thickness, 350 kg/ m^3 snow density, and 1024 kg/m^3 seawater density.

The uncertainty in the freeboard data is in the order of 10-15 cm (see for instance Hvidegaard and Forsberg, 2002) and this together with errors in the K-factor comprises the larges error sources in the method. The dominant error in K arises from the fact that K in reality is a function of ice density, sea water density, snow depth, and snow density. The main uncertainty comes from lack of knowledge of the sea ice density and the snow depth on top of the ice. A qualitative look at the influence of the two parameters is gathered in Table 2. Typical ranges of the two parameters are used (0-30 cm snow and 850-900 kg/m^3) in order to look at the maximum influence of using a constant number for K for a specific survey. The K values in the table are found for assumed sea ice thickness of 3 m, snow density of 350 kg/ m^3, and seawater density of 1024 kg/ m^3. It is seen that the maximum error is in the order of one metre.

Typical errors in the laser scanner derived sea ice thickness data sets is therefore expected to be less than one metre. For a typical ice thickness of 3 metres in the Arctic Ocean this is still more than a 30 % uncertainty and work is ongoing to improve models of the conversion from freeboard to thickness; especially coincident observations of laser and radar

altimetry is expected to give more information on the snow depth. In-situ observations of the snow and ice condition will also be valuable for future measurements.

3 RESULTS OF THE AIRBORNE LIDAR MEASUREMENTS

The 2003-5 airborne laser scanner data sets have been analysed as described above. The resulting sea ice thickness is illustrated in Figure 5. In all three years the thickest ice was found close to Greenland's north coast, in accordance with the general packing of sea ice against the coast by the Transpolar Drift stream.

Differences between the years are also seen, for instance the thicker ice north of Ellesmere Island in 2005 compared to 2004. The observations can be used to describe the interannual variability, as data were collected at approximately the same time of year. It should be pointed out that Figure 5 is based on only a small, averaged fraction of the lidar data; the full data set, of a resolution of approximately 1 x 1 m, is very "rich" in showing surface roughness, leads and ridging etc. Figure 6 shows an example of a part of a typical scan. The total volume of the full scanner data is around 200 MB/hour (typically collected in hourly files with a small data gap for file opening and closure).

4 VALIDATION OF THE LIDAR THICKNESS MEASUREMENTS BY INDEPENDENT OBSERVATIONS

The laser scanner derived thickness data have been analysed together with coincident data sets from other experiments, first and foremost the helicopter-borne electromagnetic induction method of the Alfred Wegener Institute, Germany (Haas et al., this volume). The independent comparisons studied include helicopter EM in 2003; ground-truth ice thickness measurements in 2003; and coincident EM-lidar flights in 2005. We utilize the main results of other GreenICE partners mainly with a view to validating the lidar method; joint papers are currently in preparation with more details of the method, and the snow/ice physics implications.

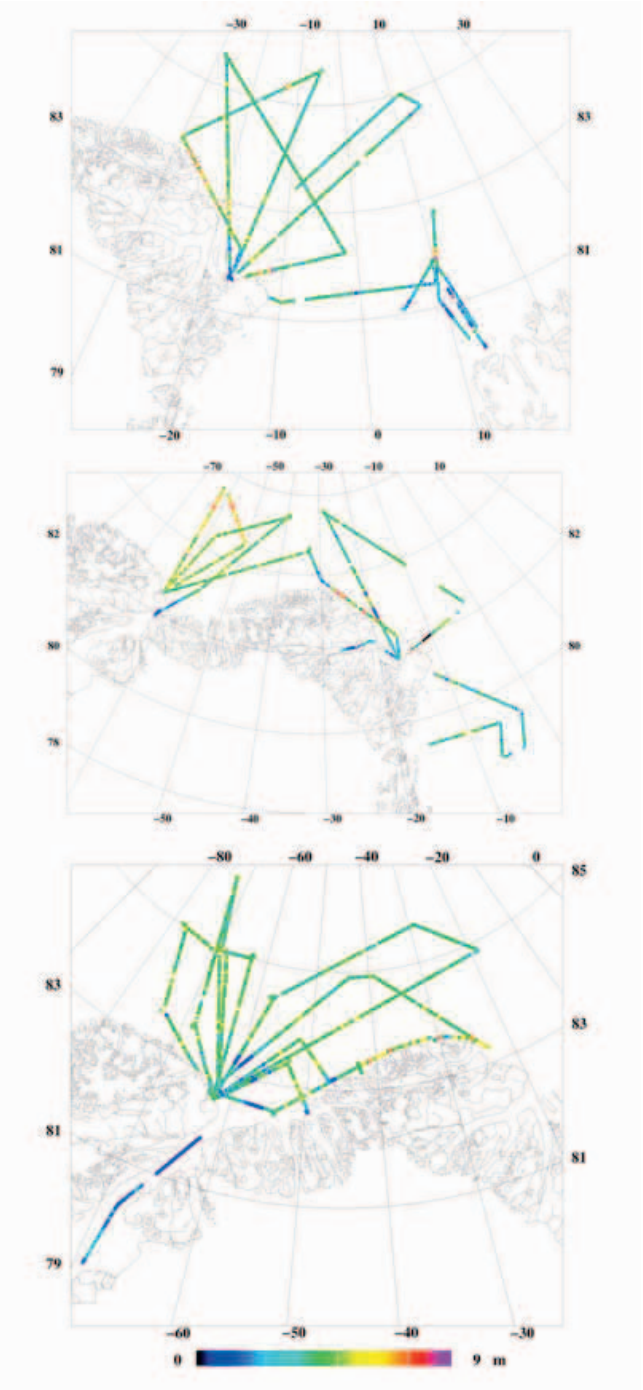

Figure 5. Sea ice thickness derived from DNSC airborne laser scanner measurements April 2003 (top), May 2004 (centre), and May 2005 (bottom).

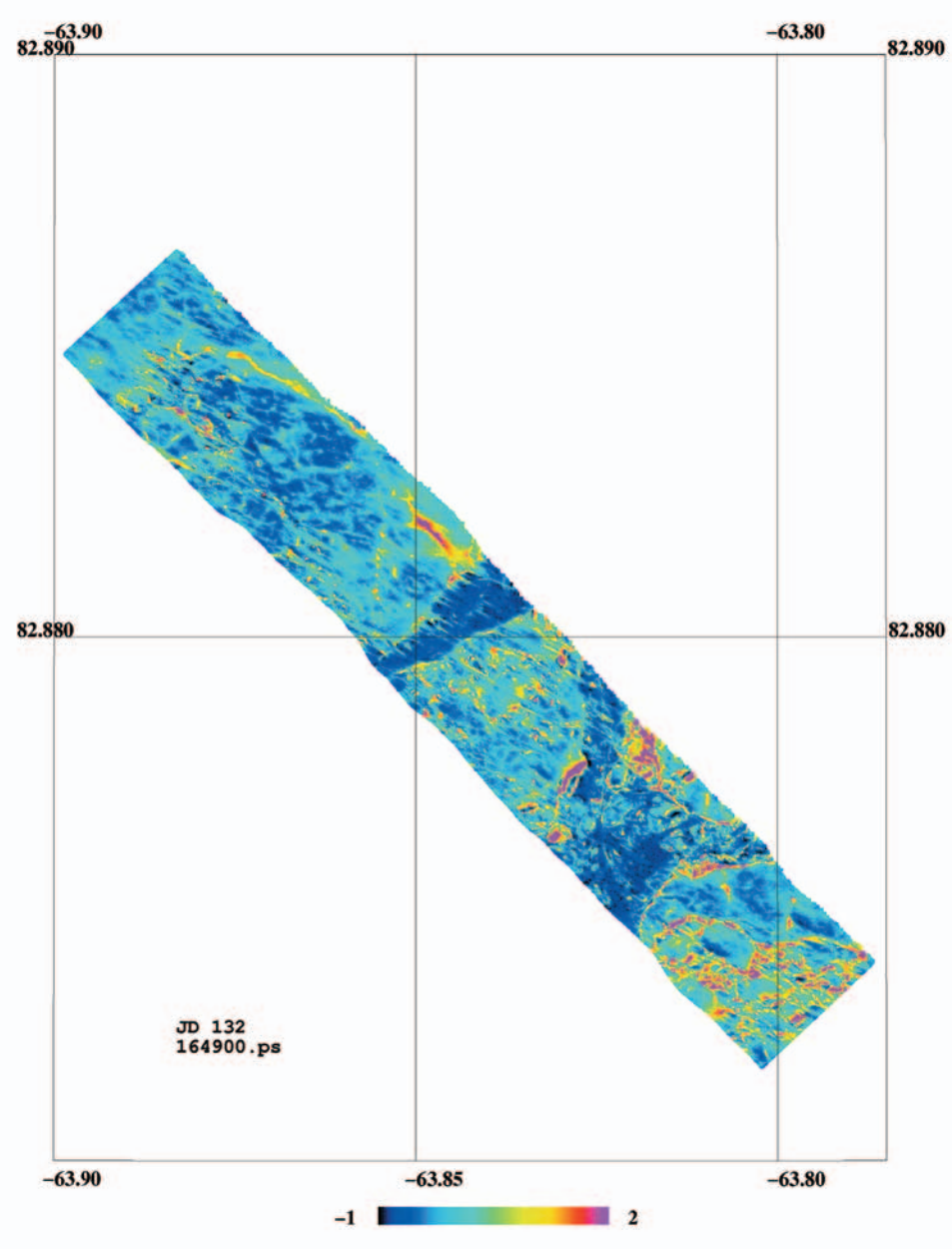

Figure 6. Example of a 2005 laser scan scene. Width of track is approx. 200 m. The snow on the ice shows a dune pattern and refrozen leads are also seen.

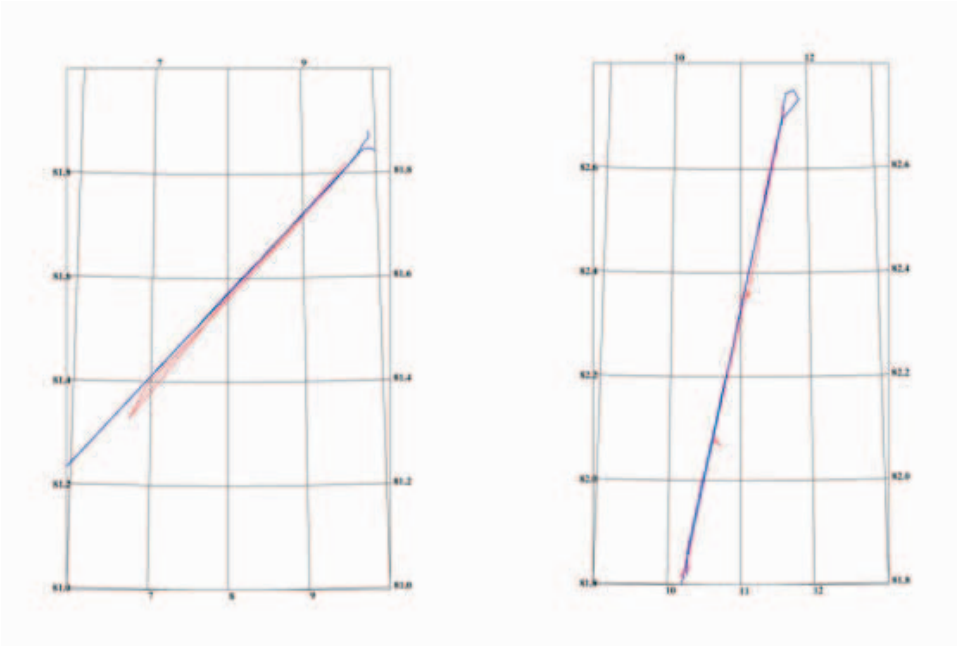

Figure 7. Coincident Twin Otter laser scanner (blue) and helicopter EM (red) flights, Cryovex-2003.

Laser scanning and HEM from the 2003 GreenICE/CryoVEx experiment

During the 2003 campaign, two 100 km tracks of coincident Twin-Otter laser scanner and helicopter EM data were obtained on April 11 and April 15. The coincident lines are shown in Figure 7. For the April 11 flight only a few sections actually overlap, caused by a miscommunication between the operators of the helicopter system on *Polarstern* (in the Fram Strait), and the Twin Otter operators based in Greenland and Svalbard. The April 15 flight gave a significantly better overlap. The flight tracks were aligned slightly differently for the helicopter and the Twin Otter, to account for the ice drift between observations from the two aircraft, flying at different velocities.

The data have been matched after a correction for ice drift, based on the GPS-recorded drift of *Polarstern* during the experiment. The ice drift in the Fram Strait is swift, and the drift between the measurements was too large to be neglected. Figure 8 shows an example of matching laser scanner and HEM data. It can be seen that both sensors measure the same ice, and that the deviations are mainly in the height of the ridge sails, as the laser measures their real height, while the HEM system likely underestimates the maximum ridge thickness due to saltwater intrusion. It should be noted that the conversion of the laser scanner data from freeboard to thickness has a relatively large uncertainty, and that the EM method may in fact be used to provide this calibration (for 2003 we used the ground measurements for the K-factor).

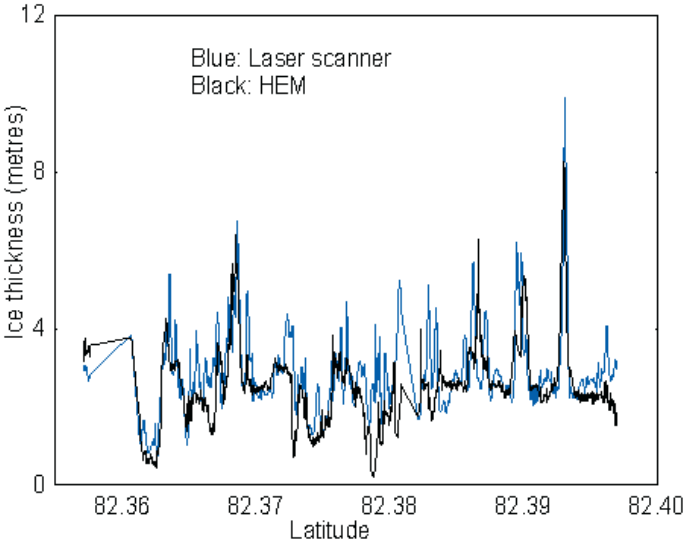

Figure 8. Example of matched laser scanner and HEM data. Date: May 15 2003.

Table 3 compares mean and modal ice plus snow thickness thus obtained from the laser and HEM measurements. The agreement is generally good and within the accuracy of the method of obtaining thickness from laser scanner freeboard data (of the order of 0.5 to 1 metre, assuming a freeboard height error around 10-15 cm, cf. Hvidegaard and Forsberg, 2002).

Table 3. Data comparison for coincident flights April 2003.

Data type	Mean Thickness (m)	Modal Thickness (m)	Std. dev. (m)
Lidar April 11	2.12	1.3	1.56
HEM April 11	2.05	2.5 (0.4/1.3)`	1.24
Lidar April 15	3.83/3.67*	3.3/3.1	1.77/1.66
HEM April 15	3.40	2.5	1.44

* Two flights performed along the same track, out and back
` The thickness distribution shows several distinct modes

Laser scanning and in situ observations near Polarstern 2003

Polarstern was anchored to an ice floe in the Fram Strait for approximately one week when the coincident helicopter and Twin Otter flights were carried out. On April 17 the Twin Otter laser system was used to map this floe as is seen in Figure 9. Taking the ice drift and floe rotation into account, this survey of the floe can be used to compare the laser data to observations performed directly on the ice. Two examples are given here.

The first is a comparison of a grid of drillings on the centre of the ice floe. Unfortunately the overlap between the airborne data and the grid is far from optimal. Therefore the drillings are compared to all data within a circle of radius 50 m surrounding the grid. The statistics are found in Table 4.

Table 4. Comparison of laser scanner and in situ sea ice thickness data near Polarstern.

Data type	Mean Thickness (m)	Modal Thickness (m)	Std. dev. (m)
Laser scanner pred. to EM31 pos.*	2.87	2.2(2.0/3.1)	0.99
EM31	3.65	3.0	1.01
Laser scanner Circle: 50 m	3.14	3.1	0.59
Drillings	2.62	2.5	0.29

* Data has been matched by predicting a laser scanner derived thickness at the position of the EM31 obserations

The second example is a comparison of laser scanner measurements to a ground EM survey carried out with an EM31 pulled over the ice in a kayak. The data have been matched and the statistics are found in Table 3. The time difference between these two observations is large and makes it difficult to match the data sets accurately. Overall the laser scanner thickness data agree with the in situ observations within the expected accuracy.

Laser scanning and HEM from the GreenICE/SITHOS flights 2005

In the May 2005 campaign two flights were carried out to gather coincident helicopter EM and airborne lidar data from Arctic Ocean sea ice. The coincident tracks were selected in order to survey different ice types. The lines were selected from investigation of a Radarsat ScanSAR scene of the area, Figure 10 (left). The two lines were surveyed on May 13 (line heading north) and on May 14 (line from the southern part of the Lincoln Sea, heading northeast). The helicopter and Twin Otter tracks are shown in Figure 10 (right). The overlap of the two observations was almost perfect, as the ice drift in the area is small and can be neglected, and as the data acquisition was separated by less than half an hour.

The lidar data sets have been analysed as outlined earlier, and compared to EM data provided by AWI. Table 5 compares the statistical properties of the selected data from the two tracks (only spatially coincident points have been selected). A good agreement is found, and the differences are within the accuracy of the laser scanner derived thickness data. Figure 11 shows an example of comparing the laser scanner derived sea ice thickness and the HEM data. As in 2003 the differences are likely caused by the underestimation of ridges by the EM system, and the different footprint size of the two systems.

Table 5. Lidar and EM-derived sea ice thickness statistics from coincident tracks.

Data type	Mean Thickness (m)	Modal Thickness (m)*	Std. dev. (m)
Laser scanner May 13	5.94	1.0/4.8	2.95
Helicopter EM	5.20	0.0/4.2	2.52
Laser scanner May 14	3.73	2.4/4.8	2.04
Helicopter EM	2.90	1.8/3.8	1.75

* The distributions have two discrete modes

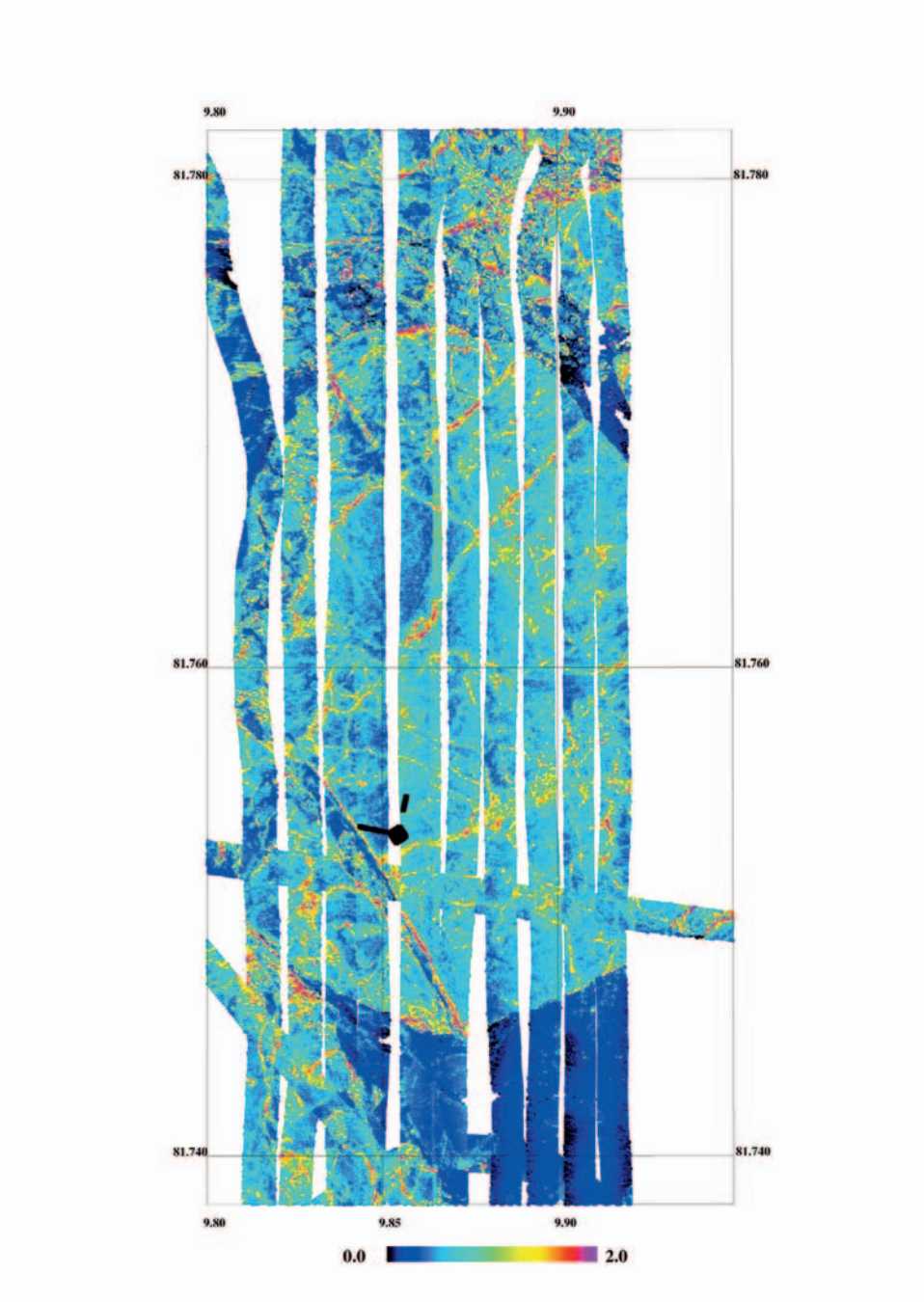

Figure 9. Dense laser scanner survey of the ice floe next to Polarstern May 17 2003. The black dots show the grid of drillings on the floe. Gaps between laser strips occurred because of bad weather, necessitating a very low Twin Otter flight elevation.

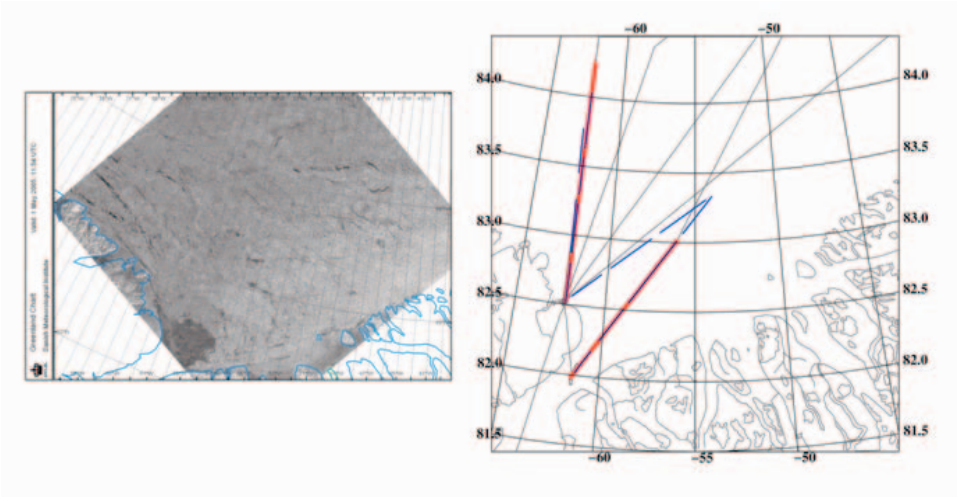

Figure 10. Left: Radarsat ScanSAR scene from May 1, 2005 (provided by the Danish Meteorological Institute); Right: Flight tracks from coincident EM (blue) and laser scanner (red) observations. The background grey lines are the complete set of Twin-Otter flight tracks.

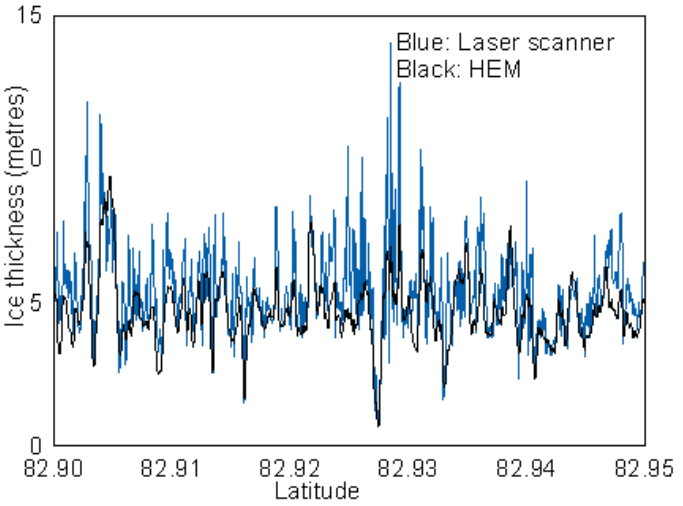

Figure 11. Example of May 14 2005 sea ice thickness comparison with data derived from laser scanner elevations and helicopter EM measurements.

5 CONCLUSIONS

We have outlined the basic principles of airborne lidar freeboard determination, and described the large field campaigns carried out in the Arctic Ocean north of Greenland, Ellesmere Island and Svalbard 2003-5. Based on cross validation with the GreenICE helicopter EM and in-situ ice thickness data, a reasonable agreement was proved, and thus has the potential to do long-range Arctic Ocean sea ice thickness monitoring, to supplement future satellite missions such as CryoSat-2.

The current errors of the lidar method are assumed to be 0.5-1 m in thick ice, as evidenced from the HEM and ground data validations. A further investigation of these coincident data sets may provide more knowledge, as will utilization of more advanced models and satellite data to replace the currently used climatological snow depth estimates. In future surveys, the combined use of airborne radar and laser might provide in-situ snow depth data, such as use of the ESA ASIRAS 13 GHz CryoSat-type radar instrument, currently being installed in the Twin Otter. Repeated comparisons between lidar and EM in other parts of the Arctic Ocean may provide additional constraints on the K-factor variability, as will compilation of basin-wide historical and present measurements of sea ice thickness, density and freeboard.

6 ACKNOWLEDGEMENTS

Data for the EM and ground truth campaigns were provided by C. Haas and A. Pfaffling of the Alfred Wegener Institute of Polar and Marine Research, Germany, and M. Doble, Scottish Association of Marine Science. Support for the airborne Twin Otter operations were provided by the EU through the GreenICE and SITHOS projects (for comparison and regional sea ice flights, respectively), by ESA (campaigns unit, M. Davidson), and by the Danish Natural Science Research Council. A. V. Olesen, K. Keller, and N. S. Dalå, DNSC, have participated in the field operations and subsequent processing.

7 REFERENCES

Forsberg, R., and, H. Skourup: *Arctic Ocean Gravity, Geoid and Sea ice Freeboard Heights from ICESat and GRACE*. Geophysical Research Letters, vol. 32, L21502, 2005.

Hvidegaard, S. M., and R. Forsberg: Sea ice thickness from airborne laser altimetry over the Arctic Ocean north of Greenland, *Geophysical Research Letters*, 29, no. 20, pp.1952-1955, 2002.

Laxon , S., N. Peacock, and D. Smith, High Inter-Annual Variability of Sea Ice Thickness in the Arctic Region, *Nature*, 425, 947-950, 2003.

Wadhams, P., W. B. Tucker, W. B. Krabill, R. N. Swift, J. C. Comiso, and N. R. Davis: Relationship between sea ice freeboard and draft in the Arctic Basin, and implications for ice thickness monitoring. *J. Geophys. Res.*, 97 (C12), 20,325-20,334, 1992.

Effect of the Physical Description of Sea Ice on the Modelled Mean Sea Ice Thickness on the Arctic Ocean

Jari Haapala
Finnish Institute of Marine Research, Erik Palménin aukio 1, PL 2, 00561, Helsinki, Finland

Keywords: sea ice, dynamics, modelling, climate, Arctic Ocean

ABSTRACT: A multi-category sea-ice model with the prescribed atmospheric and oceanic conditions has been used to examine an effect of the physical description of sea ice on its modelled mean state. The evolution of the ice pack has been simulated with a thermodynamics-only model (TDM), a free drift model (FDM), a viscous-plastic model (VPM), a viscous-plastic model with an island at the North Pole (VP-NPM), and with a multicategory model (MCM). It was found that the modelled annual maximum ice extent is rather insensitive to the ice dynamics or the ice thickness distribution model used. This indicates that the maximum annual ice extent is determined by the thermodynamics of the growth of new ice, and that the most important factor is the correct modelling of sea surface temperature. However, minimum ice extent is sensitive to the modelled ice thickness, which in turn is highly dependent on the ice dynamics and the thickness distribution used. Overestimation/underestimation of the dynamical growth of sea ice leads to overestimation/underestimation of ice mass, and to a situation where ice is not melting/surviving during the summer stage. This clearly shows that a mass-momentum coupling is essential for modelling sea ice, and only models that take plasticity into account are physically realistic in climate simulations. All other models generate highly unrealistic ice thicknesses. Sensitivity experiments show that the response of the sea-ice model to changes in thermal forcing depends on the modelled mean state of the control climate and the thickness distribution used. In particular, beyond a certain degree of warming, the two-level model may predict the total disappearance of sea ice in the Arctic while the multicategory ice model may predict the existence of thick ridged ice even during the summer season.

1 INTRODUCTION

Global climate models predict maximum warming in the high latitudes of the Northern Hemisphere. Polar amplification is mainly due to the positive feedback mechanisms related to the insulation and albedo effects of snow and sea ice. The true magnitude of the feedback effect of the ice/snow surface is still unknown because of our incomplete knowledge of snow and ice physics, and of several other unresolved processes of the Arctic climate. A clear indicator of this is the fact that the projected changes exhibit the largest range of warming scenarios in the Arctic (Räisanen, 2002, Walsh and Timlin, 2003). Holland and Bitz (2003) found that the modelled mean sea ice state under the present climate has a considerable influence on the polar warming in the various climate models. In this chapter we analyze in detail the effect of the physical description of sea ice on its modelled mean state, and discuss the influence of simplifications of the sea ice physics on the climate predictions.

Horizontal variability of sea-ice thickness on a continuum scale is described by the ice thickness distribution function g(h) (Thorndike, et al. 1975). Besides direct discretization of g(h), it can approximated by solving evolution equations of several ice thickness categories (Bitz et al., 2001) as

$$\frac{\partial A_i}{\partial t} = -\nabla \bullet \left(\vec{u} A_i\right) + \psi_i + O_i^A \tag{1}$$

$$\frac{\partial \bar{h}_i}{\partial t} = -\nabla \bullet \left(\vec{u} h_i\right) + \Omega_i + O_i^h \tag{2}$$

where A_i is the concentration (i.e. area fraction) of a particular ice category, $\vec{u}$ is the ice velocity, ψ_i is the change of ice concentration due to redistribution (i.e. deformations) and O_i^A denotes thermodynamical changes. $\bar{h}_i$ is the mean ice thickness per unit area, Ω_i and O_i^h are its changes due to redistribution and thermodynamics. Floe thickness h_i is not an independent variable since $\bar{h}_i$ -H_iA_i.

The most common approximation in the climate models, commonly called the two-level model, is that only one thickness and concentration category is resolved and redistribution terms are neglected (Hibler, 1979). More advanced sea-ice models resolve the evolution of the ice thickness distribution function g(h) (Hibler, 1980: Flato and Hibler, 1995) or the evolution of several ice categories and types (Bitz et al., 2001; Haapala et al., 2005).

Ice motion is determined by the momentum balance equation, which reads,

$$m\left(\frac{D\vec{u}}{Dt} + f\hat{k}x\vec{u}\right) = A\left(\vec{\tau}_a + \vec{\tau}_w\right) + mg\nabla H + \nabla \bullet \sigma \tag{3}$$

where m is the total ice and snow mass, $\vec{u}$ is the horizontal ice velocity, f is the Coriolis parameter, $\hat{k}$ is the upward unit vector, $\vec{\tau}_a$ is the air stress vector, $\vec{\tau}_w$ is the water stress vector, g is the gravitational acceleration, ∇H is the sea surface tilt, and σ is the internal stress tensor.

The first order approximation to the momentum balance is that the acceleration, sea surface tilt and internal stress terms are assumed to be negligible, which leads to the free drift model. The cavitating fluid model assumes that the internal stress depends only on the bulk stress of the ice. In the viscous-plastic model (Hibler, 1979), the internal stress is determined by the nonlinear bulk and shear stresses and the ice strength. In the two-level model ice strength is proportional to ice mass and concentration, while in the multi-category model ice strength is directly related to the energy consumed during deformation (Rothrock et al., 1975).

The simplifications of sea-ice physics made in the climate models have considerable differences. None of the models selected for the Arctic Climate Impact Assessment (ACIA) resolve sea-ice physics on the basis of the full primitive equations. Those models are the Canadian Climate model (CCCma, Flato et al, 2000), the Geophysical Fluid Dynamics Laboratory model (GFDL, Knutson et al., 1999), the Max-Planck model (ECHAM/OPYC3, Roeckner et al., 1999), the Hadley Centre model (HadCM3, Gordon et al., 2000) and the Climate System Model of the National Center for Atmospheric Research (NCAR/CSM-1, Boville et al. 2000) The sea-ice physics of those models are described in Table 1.

Table 1. Sea ice physics of the climate models used in the ACIA.

model	ocean component	ice thermodynamics	ice dynamics
CCCma	MOM-1	energy balance	modified free drift
GFDL	MOM-1	simple thermodymics	free drift
ECHAM	OPYC3	simple thermodynamics	viscous-plastic
HadCM3	Cox-Semtner	0-layer Semnter	modified free drift
NCAR/CSM-1	MOM-1	3-layer Semtner	cavitating fluid

2 NUMERICAL EXPERIMENTS

In order to determine how far the modelled mean ice state is sensitive to the simplifications of ice physics we studied a multi-category sea ice model with prescribed atmospheric and oceanic conditions (Haapala et al., 2005). The model has a global coverage but the focus is on the Arctic Ocean and it therefore employs orthogonal curvilinear coordinates. The co-ordinate system is equivalent to MPI-OM1 where the poles are located over Canada and Western Siberia (Marsland et al. 2002).

Atmospheric forcing was obtained from the German ocean model inter-comparison project OMIP (Röske, 2001). The OMIP data provides the mean annual cycles of daily surface fields, superimposed with a synoptic scale variability. The data are derived from the ECMWF 15-years re-analysis (Gibson et al., 1997). The ocean surface temperature and currents were obtained from the previous MPI-OM1 simulations.

The evolution of the ice pack was simulated with the thermodynamics-only model (TDM), the free drift model (FDM), the viscous-plastic model (VPM), the viscous-plastic model with an island at the North Pole (VP-NPM), and with a multicategory model (MCM). In the multicategory model five undeformed and two deformed ice categories were used. All simulations begin from the same initial conditions and stationary conditions were obtained after ten years' integration.

In order to analyze the uncertainties of the modelled future mean ice conditions under the different climate predictions, the sensitivity of the model to change in the thermal forcing was tested. In those simulations air temperature was increased by 4 K, and all other forcing factors were kept the same as in the control simulations.

3 RESULTS

Comparison of the results of different ice models (Figure 1) shows that the physical description of ice dynamics does not have a significant effect on the modelled maximum ice extent. Some differences are noticeable in the coastal regions, on the ice edge, and, in particular, in the Barents Sea. Major differences are found in the modelled ice thickness fields. TDM produces a uniform slab of 3.5 m thick ice in the Central Arctic. FDM generates ice thicker than 20 metres in the coastal regions. VPM and VP-NPM produce an ice thickness pattern that has a horizontal distribution roughly similar to the observed one (Bourke and Garrett, 1987), but the ice is thinner. An artificial North Pole has some blocking effect, especially on the Siberian side of the island. At this resolution the ice can still drift from the Central Arctic to Fram Strait, and hence heavy accumulation of ice in the Arctic is not possible.

For September, the models produce rather different results for both the extent and the thickness of the ice. It should be noted that the ice extent of FDM is much larger than that predicted by other models. In the FDM simulation, the Siberian coastal region is completely covered with ice 2 metres thick, while the other models predict almost ice-free conditions in those regions. The bias of FDM is certainly due to the overestimation of the dynamical thickening of ice.

The mean ice thickness of the MCM in March and September is shown in Figure 3. The ice extent is very similar to VPM but in the Central Arctic MCM produces ice about a metre thicker than VPM. That is probably due to the explicit description of thin and ridged ice growths.

The thermodynamical response of sea ice to increased thermal forcing is shown in Figure 4. The maximum annual ice extent is only slightly smaller. However, with these forcing conditions the annual thermal growth and melting of ice are nearly in balance, and thus the TDM predicts almost completely ice-free conditions during the summer minimum. With minor changes in the thermodynamical parameters of the model, TDM would predict a totally ice-free Arctic.

Figures 5 and 6 depict the response of the MCM to change in the thermal forcing. Again, the annual maximum ice extent is rather similar to the TDM results, but in the MCM simulations in large parts of the Arctic in September the ice concentration is 0.3-0.5. The modelled ice concentration of the different ice classes shows that thick undeformed ice is most common on the Central and Eurasian side of the Arctic. The concentration of deformed ice is largest around Northern Greenland, in the Canadian Archipelago and on the Chucki Sea. Until the occurrence of a minimum ice extent, all undeformed ice melts but the deformed ice survives into the following season.

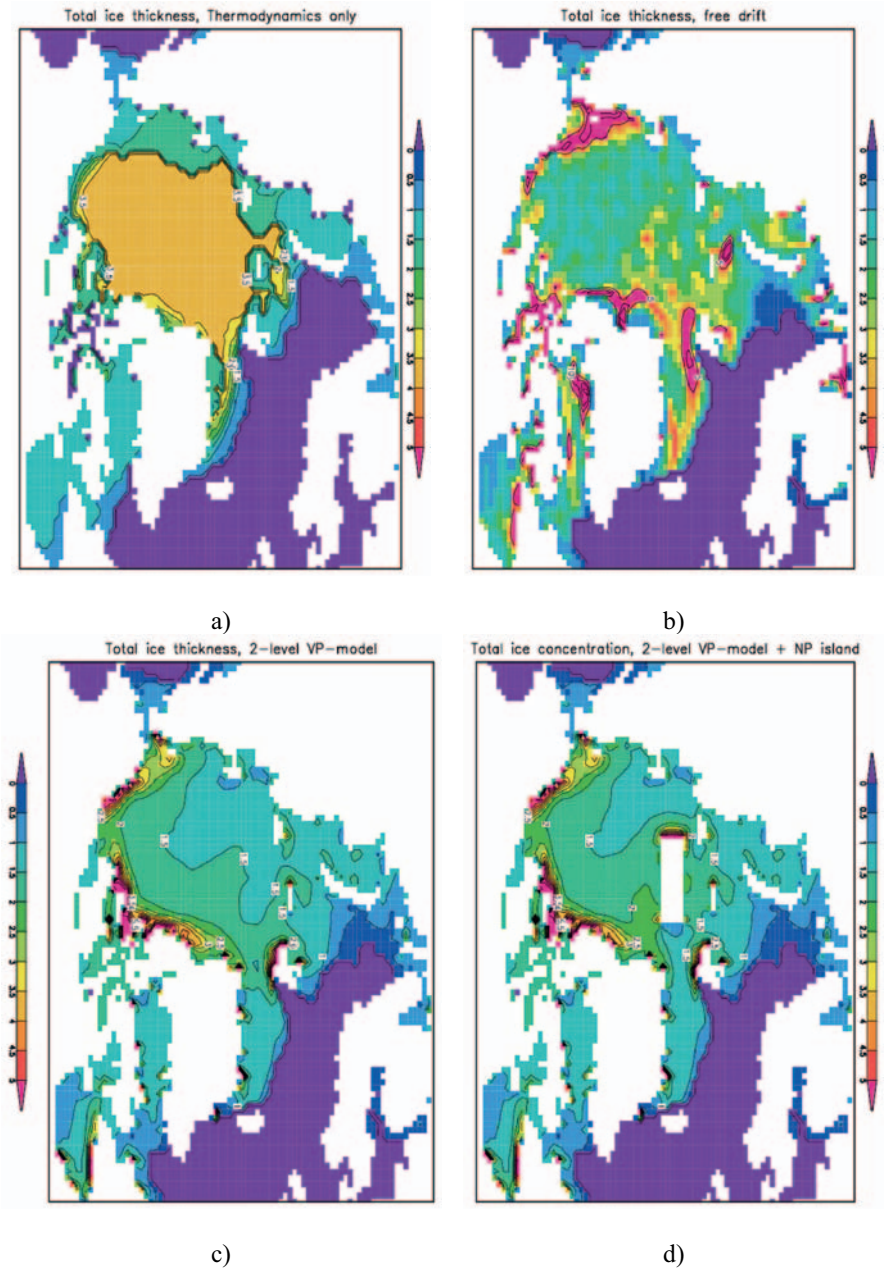

Figure 1. Modelled ice thickness on March 1 for a) thermodynamic only b) free drift c) two-level and d) two-level with island in the North Pole models.

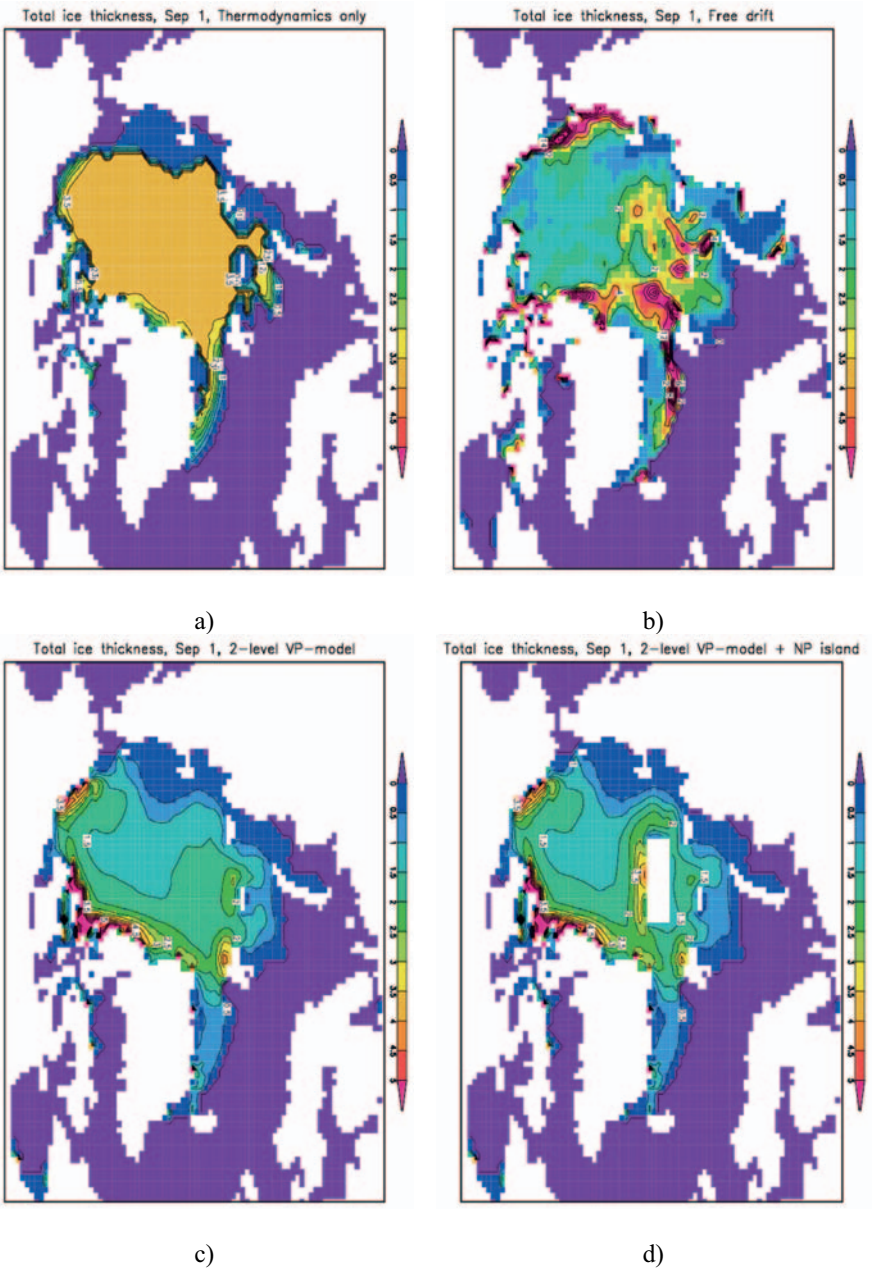

Figure 2. Modelled ice thickness on September 1 for a) thermodynamic only b) free drift c) two-level and d) two-level with island in the North Pole models for the present climate.

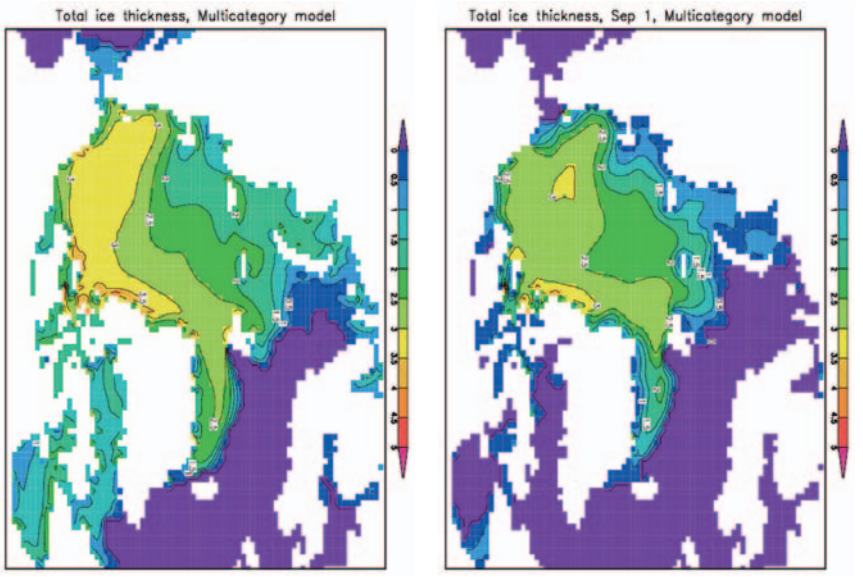

Figure 3. Modelled ice thickness with the multi-category sea ice model on March.

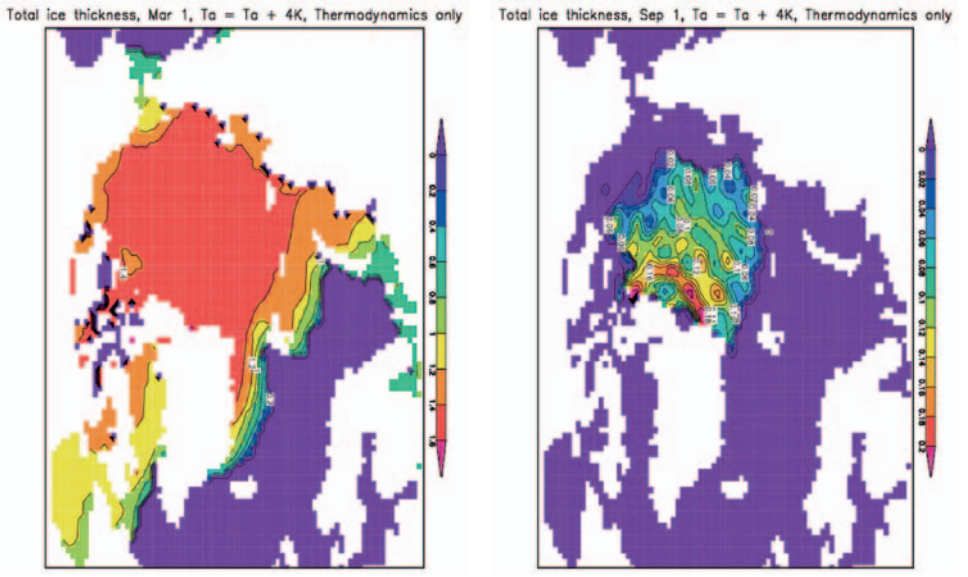

Figure 4. Sea ice response to air temperature change with the thermodynamics only model, a) ice thickness on March 1 and b) ice thickness on September 1.

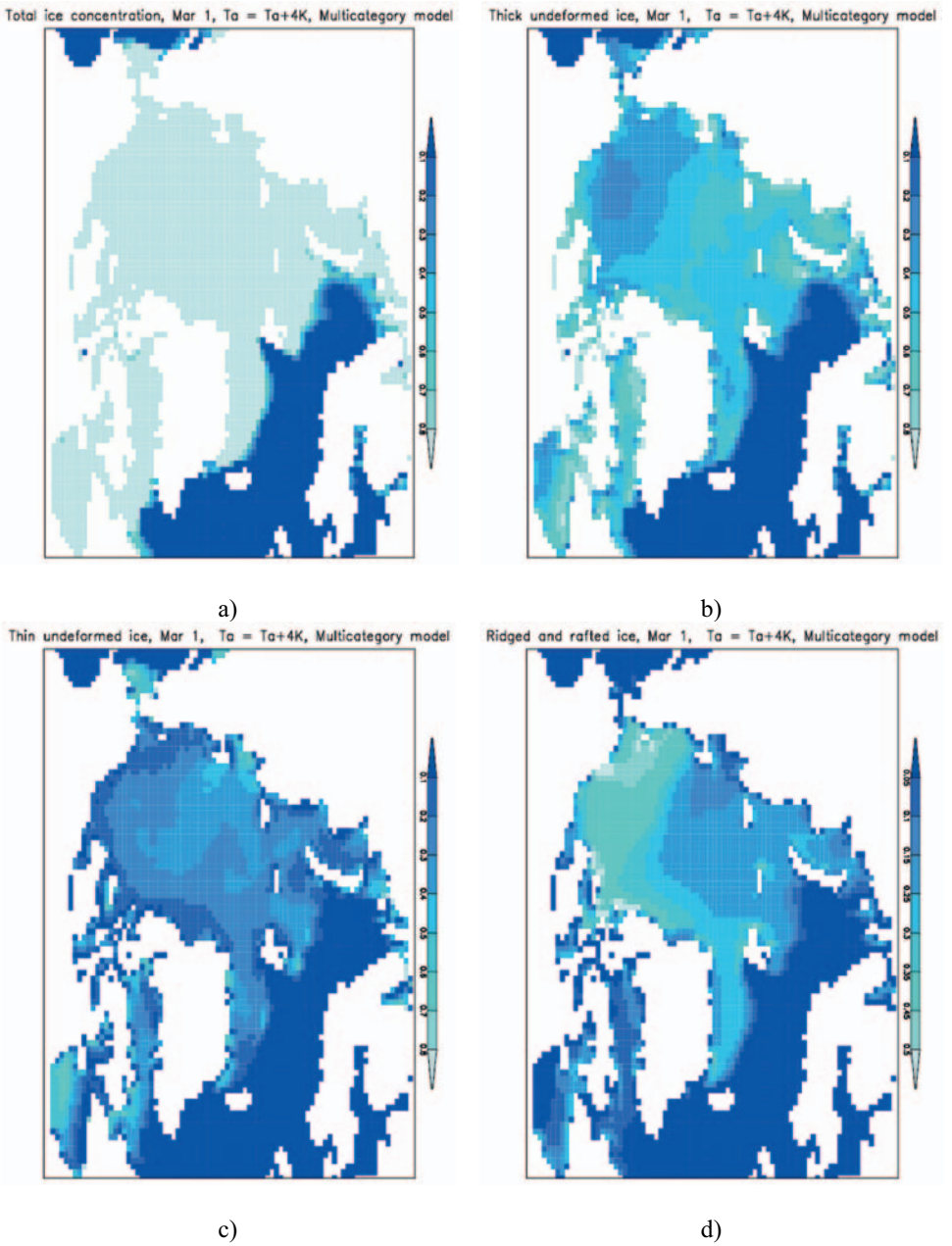

Figure 5. Sea ice response to air temperature change with the multi-category sea ice model, a) total ice concentration b) thick undeformed ice concentration c) thin undeformed ice concentration and d) deformed ice concentration on March 1.

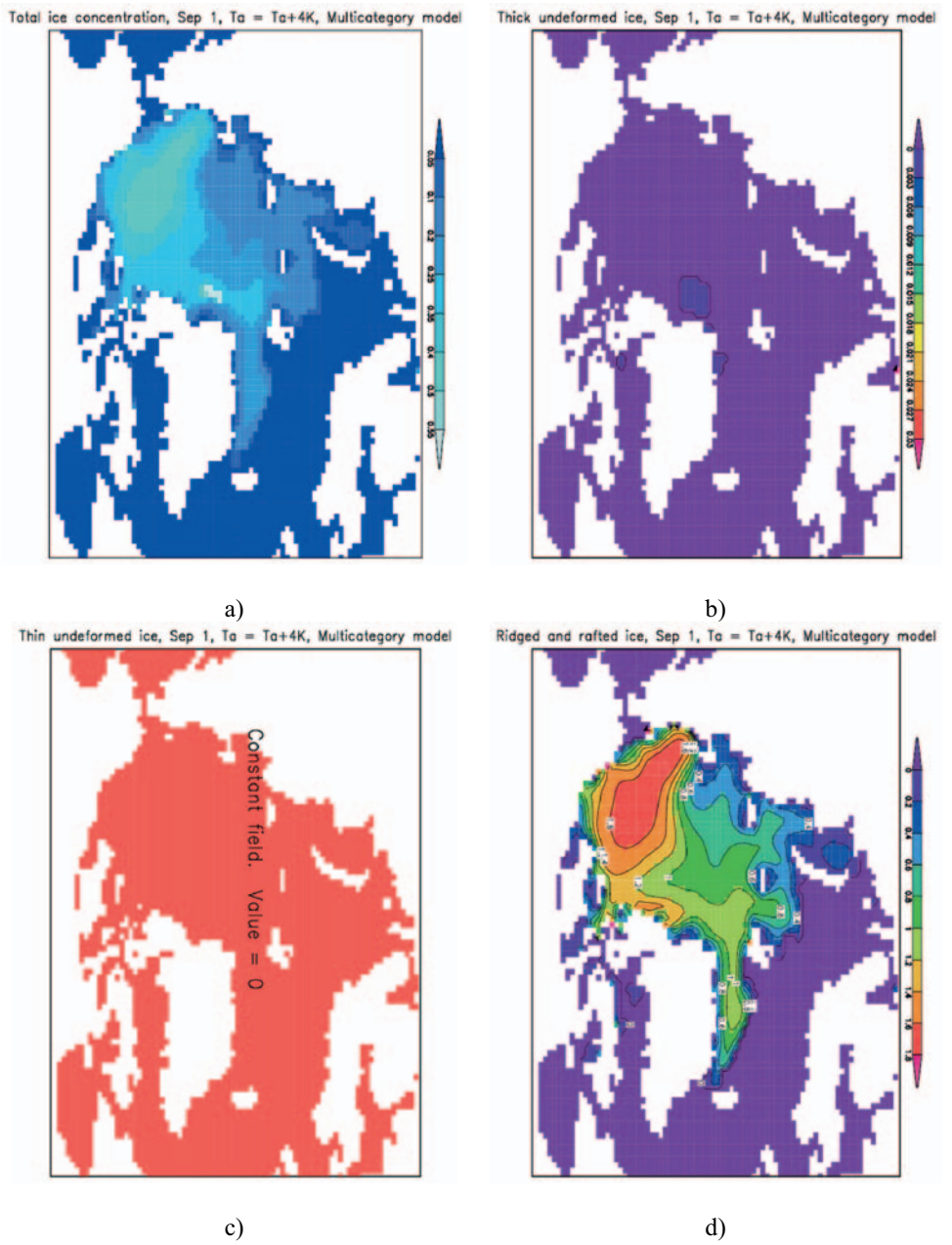

Figure 6. Sea ice response to air temperature change with the multi-category sea ice model, a) total ice concentration b) thick undeformed ice thickness c) thin undeformed ice thickness and d) deformed ice thickness on September 1.

4 CONCLUSIONS

The modelled annual maximum ice extent is rather insensitive to the ice dynamics or ice thickness distribution used. This indicates that the maximum annual ice extent is determined by the thermodynamical growth of new ice, and a correct modelling of sea surface temperature is the most important factor. In addition to the inaccuracies in the surface heat balance, an overestimation of the modelled ice extent in climate models can be caused by an underestimation of the Atlantic heat transport or vertical mixing.

The minimum ice extent is sensitive to the modelled ice thickness, which in turn is highly dependent on the ice dynamics and thickness distribution used. Overestimation/underestimation of the dynamical growth of sea ice leads to an overestimation/underestimation of ice mass, and to a situation where ice is not melting/surviving during the summer stage. This clearly shows that a mass-momentum coupling is essential for the dynamics of sea ice, and only models that take plasticity into account are physically realistic in climate simulations. All other models generate highly unrealistic ice thicknesses that are commonly hidden away by introducing a numerical diffusion or an artificial upper limit for ice thickness.

The response of the sea-ice model to changes in the thermal forcing depends on the modelled mean state of the control climate, and on the thickness distribution used. In particular, beyond a certain degree of warming, two-level models may predict a total disappearance of sea ice in the Arctic, but multicategory ice models may predict the existence of thick ridged ice also during the summer season.

In coarse-resolution models, an artificial north pole island may cause accumulation of ice, but its effect on the modelled ice extent is minor. That problem can be overcome by utilizing regional climates or MPI-OM1 type models, which will also provide more detailed information on the future changes in the Arctic.

The bottleneck of the development of multi-category sea ice models has been the lack of proper data for the model validation. However, this situation has considerably changed during recent years when the new in situ and remote sensing datasets, like ice thickness data from upward looking sonars and submarines, experimental EM ice thickness and laser altimeter measurements, Envisat and ICESat altimetry data, SAR-based ice motion and deformation data and satellite derived ice type data have become available.

5 REFERENCES

Bourke, R.H. and R.P. Garrett. 1987. Sea ice thickness distribution in the Arctic Ocean. *Cold Reg. Sci. Technol.*, 13, 259-280.

Boville, B.A., J.T. Kiehl, P.J. Rasch and F.O. Bryan. 2001. Improvements to the NCAR CSM-1 for transient climate simulations. *J. Climate*, 14, 164-179.

Gibson J.K., Kållberg, P., Uppala, S., Hernandez, A., Nomura, A., and E. Serrano. 1997. ERA description. ECMWF Re-analysis Project Report Ser. 1, Eur. Cent. for Medium-Range Weather Forecast, Reading, England.

Flato, G.M., and W.D. Hibler III. 1995. Ridging and strength in the modelling the thickness distribution of Arctic sea ice. *J.Geophys.Res*., 100(C9), 18 611-18 626.

Flato, G.M., G.J. Boer, W.G. Lee, N.A. McFarlane, D. Ramsden, M.C. Reader and A.J. Weaver. 2000. The Canadian Centre for Climate Modelling and Analysis global coupled model and its climate. *Climate Dynamics*, 16, 451-467

Gordon, C., C. Cooper, A. Senior, H. Banks, J.M. Gregory, T.C. Johns, J.F.B. Mitchell and R.A. Wood. 2000. The simulation of SST, sea ice extent and ocean heat transports in a version of Hadley Centre coupled model without flux adjustments. *Climate Dynamics*, 16, 147-168.

Haapala, J., Lönnroth, N. and A. Stössel. 2005. A numerical study of open water formation in sea ice. *J. Geophys. Res.*,Vol. 110,No. C9, C0901110.1029/2003JC002200

Hibler, III, W.D. 1979. A dynamic thermodynamic sea ice model. *J. Phys. Oceanogr.*, 9: 815-846.

Hibler III, W.D. 1980. Modelling a variable thickness sea ice cover. *Monthly Weather Review*, 108, 1943-1973.

Holland, M.M. and Bitz, C.M. 2003. Polar amplification of climate change in coupled models. *Climate Dynamics*, 21, 221-232.

Knutson, T.R., T.L. Delworth, K.W. Dixon and R.J. Stouffer. 1999. Model assessment of regional surface temperature trends. *J. Geophysical Res.*, 104(D24), 30981-30996.

Roeckner, E., L. Bengtsson, J. Feichter, J. Lelieveld and H. Rodhe. 1999. Transient climate simulations with a coupled atmosphere-ocean GCM including the tropospheric sulfur cycle. *J. Climate*, 12, 3004-3032.

Rothrock, D.A., 1975. The energetics of the plastic deformations of pack ice by ridging. *J. Geophys. Res.*, 80, 4514-4519.

Räisänen, J. 2002. CO2-induced changes in inter-annual temperature and precipitation variability in 19 CMIP2 experiments. *Journal of Climate*, 15, 2395-2411

Röske, F. 2001. An atlas of surface fluxes based on the ECMWF Re-analysis - a climatological dataset to force global ocean general circulation models. Report 323, Max-Planck-Institute für Meteorologie, Hamburg, Germany.

Thorndike, A.S., D.A. Rothrock, G.A. Maykut and R. Colony. 1975. The thickness distribution of sea ice. *J. Geophys. Res.*, 80(33), 4501-4513.

Walsh, J.E and M. S. Timlin. 2003. Northern Hemisphere sea ice simulations by global climate models. *Polar Research*, 22(1), 75-82.

PART 3. SEA ICE EXTENT CHANGES AND IMPLICATIONS FOR SOCIETY

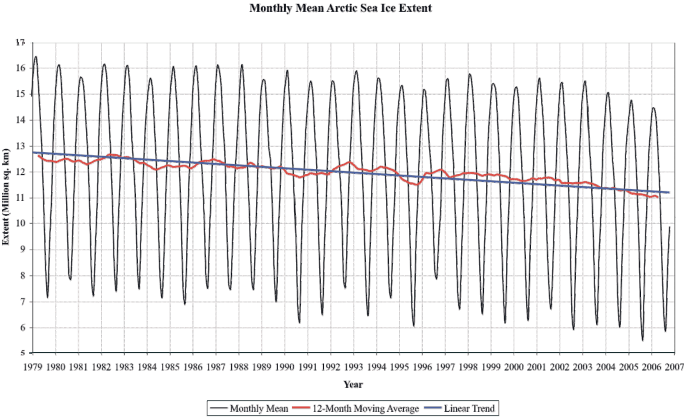

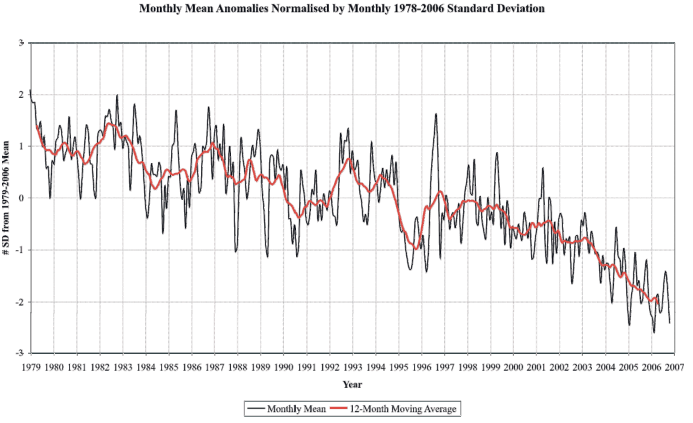

Arctic sea ice extent from 1979 to 2006 and anomaly extent when compared to monthly means.
(Data Source: Fetterer, F., and K. Knowles. 2002, updated 2006. Sea ice index.
Boulder, CO: National Snow and Ice Data Center. Digital media.)

The Arctic Marine Shipping Assessment: Changing Marine Access and a Critical Need for Improved Sea Ice Thickness Information

Lawson W. Brigham,
U.S. Arctic Research Commission, Anchorage, Alaska, USA
Chair, Arctic Marine Shipping Assessment of the Arctic Council

Keywords: Arctic shipping, Arctic Council, PAME, Arctic sea ice, climate change, ice thickness and extent

ABSTRACT: The Arctic Council Ministers in November 2004 requested that PAME (Protection of the Arctic Marine Environment Working Group) conduct a comprehensive Arctic marine shipping assessment (AMSA) with Canada, Finland and the United States as lead countries. The Arctic Council acted because the Arctic sea ice cover is undergoing an unprecedented transformation (sea ice thinning, extent reduction, and a reduction in the area of multi-year ice in the central Arctic Ocean). Sea ice simulations for the 21st century indicate increasing ice-free areas and suggest plausible increases in marine access throughout the Arctic Ocean. However, these simulations have yet to provide robust sea ice thickness distributions. AMSA's initial task will be to conduct an inventory of current Arctic shipping and marine activity. Shipping is defined broadly in AMSA to include all possible ship activities and types: tankers, container ships, bulk carriers, fishing vessels, drilling ships, research ships, offshore supply/support vessels, and others. AMSA will assess the current (2004) and future (2020 & 2050) social, economic and environmental impacts of these Arctic marine activities on Arctic communities, large marine ecosystems (LMEs), and all Arctic coastal states. The final AMSA effort will be development of a suite of strategic directions and recommendations from the findings for use by the Arctic Council member states, all Arctic stakeholders, and the global maritime community. Quite clearly one key requirement to ensure the safety and effectiveness of future Arctic shipping is greater knowledge of sea ice extent, thickness and multi-year ice changes.

1 INTRODUCTION

The Arctic Council is embarked on a comprehensive assessment of Arctic marine activity ~ the Arctic Marine Shipping Assessment or AMSA. The Council's working group Protection of the Arctic Marine Environment (PAME) was tasked to conduct AMSA during 2005-2008 with Canada, Finland, and the United States as lead countries. The remaining Arctic States – Denmark (Greenland and the Faroe Islands), Iceland, Norway, Russia, and Sweden – all have significant maritime interests and will have key roles in the assessment. AMSA will be working closely with the Arctic Council's expert groups, the Permanent Participants (Arctic indigenous residents) and the Council's observers including the Netherlands, France, Germany and the United Kingdom. AMSA will be inclusive, circumpolar in focus, and will promote collaboration with a wide range of stakeholders and relevant marine organizations. The three lead countries recognize the importance of contributions from the broader, global maritime community; such key stakeholders include the International Maritime Organization, shipping companies, non-Arctic states, ship designers, shipbuilders, ship classification societies, and marine insurers.

Figure 1. Key marine routes in the Arctic Ocean and coastal sub-arctic seas. Shown is the minimum extent of Arctic sea ice on 16 September 2002 derived from satellite passive microwave observations. Not identified are the regional and local areas where indigenous marine use is extensive.

2 RECENT ARCTIC MARINE OPERATIONS

Icebreaker access to nearly all of the regions of the Arctic Ocean was attained by the end of the 20th century. During 1977-2005, 61 transits have been made to the Geographic North Pole by the icebreakers of Russia (49), Sweden (5), USA (3), Germany (2), Canada (1), and Norway (1). Remarkably, 17 successful transits by surface ships to the North Pole were conducted during the summers of 2004 and 2005. Seventeen of the 61 voyages were in support of scientific research and the remaining 44 were devoted to tourist voyages to the North Pole and across the Arctic Ocean. Only a single voyage of the 61 did not occur during summer and that was the Soviet nuclear icebreaker *Sibir's* celebrated voyage which supported scientific operations during 8 May to 10 June 1987 and reached the North Pole 25 May (*Sibir* operated in ice thickness 3 m and greater). During the decade of the 1990's, five historic trans-Arctic voyages were accomplished: a transit across the central Arctic Ocean by the nuclear icebreaker *Sovetskiy Soyuz* (Russia) with tourists in August 1991; transits by the *Louis S. St. Laurent* (Canada) and the *Polar Sea* (USA) during July and August 1994 from the Bering Strait to the North Pole and to Svalbard – the first scientific transect of the Arctic Ocean conducted by surface ship with sea ice thicknesses of 1.0-2.7 m observed along the trackline (Tucker and Cate, 1996); and, two crossings by the nuclear icebreaker *Yamal* (Russia) with tourists in 1996. During the late summer of 2004, a small 'armada' consisting of the nuclear icebreaker *Sovetskiy Soyuz*, the icebreaker *Oden* (Sweden) and the icebreaking ship *Vidar Viking* (Norway), outfitted for drilling, conducted a unique scientific drilling

voyage in the most remote reaches of the Arctic Ocean; and, in summer 2005 the U.S. Coast Guard icebreaker *Healy* and *Oden* completed a second scientific transect of the Arctic Ocean. A review of these pioneering voyages provides substantial confirmation that marine access in summer throughout the Arctic Ocean has been achieved by highly capable icebreaking ships. A snapshot of summer 2004 Arctic marine operations shows a diversity of ships operating in all regions of the Arctic Ocean. Canadian Coast Guard reports indicate 107 ships sailing in the Canadian Archipelago; however, only five full transits of the Northwest Passage were conducted: two Canadian Coast Guard ships, one foreign tourist ship (Russian-flag icebreaker) and two foreign yachts. Although there were no reported full transits of the Northern Sea Route (NSR) in 2004, an estimated 165 voyages (by 52 vessels) carried 1.75 million tons of cargo along the western sector of the NSR. At least 27 cruise ships and expedition ships sailed around the coasts of Greenland in the summer of 2004 (increased to a reported 53 cruise ships during summer 2005). In addition to the three icebreakers operating in the central Arctic Ocean and drilling into the deep seabed, six icebreaking ships carried out scientific operations in other regional Arctic seas. While there is currently no complete record of marine activity in the Barents region, there were hundreds of transits and many marine operations in the Barents Sea and in the waters around Svalbard. There were also high numbers of fishing vessels operating during 2004 in the Bering and Barents seas, and around Iceland. Thus, a cursory review shows a significant number of ships and transits in all Arctic waters during 2004.

3 ARCTIC CLIMATE IMPACT ASSESSMENT

The Arctic Climate Impact Assessment (ACIA) released in November 2004 was called for by the Arctic Council and the International Arctic Science Committee. ACIA found that the Arctic is extremely vulnerable to observed and projected climate change and its impacts. The Arctic is now experiencing some of the most rapid and severe climate change on earth. During the 21st century, climate change is expected to accelerate, contributing to major physical, ecological, social and economic changes, many of which have already begun. Changes in Arctic climate will also affect the rest of the planet through increased global warming and rising sea levels. Of direct relevance to AMSA is that potentially accelerating Arctic sea ice retreat improves marine access throughout the Arctic Ocean (ACIA, 2005).

ACIA documented that declining Arctic sea ice is a key climate change indicator. During the past five decades the observed extent of Arctic sea ice has declined in all seasons, with the most prominent retreat in summer (see figure 2). Each of the five Global Climate Models (GCMs) used in ACIA project a continuous decline in Arctic sea ice coverage throughout the 21st century. One of the models projects an ice-free Arctic Ocean in summer by 2050, a future scenario of great significance for Arctic marine shipping since multi-year ice could plausibly disappear in the Arctic Ocean (all the next winter's sea ice would be first-year). GCM projections to 2100 suggest that Arctic sea ice in summer will retreat further and further away from most Arctic coasts, potentially increasing marine access and extending the season of navigation in nearly all Arctic regional seas (figure 3). One limitation of the GCMs is that they are not useful at determining the state of sea ice in the Northwest Passage region. Their resolution is much too coarse to be applied to the narrow straits and sounds of the Canadian Arctic Archipelago. In ACIA the only reliable observed data for the region comes from the Canadian Ice Service and this information, archived since the late 1960s, shows a mean negative trend of sea ice coverage in the Canadian Arctic Archipelago, but very high

inter-annual variability. The ACIA models, however, could be applied to the more open coastal seas of the Russian Arctic. ACIA sea ice projections for Russia's Northern Sea Route indicate an increasing length of the navigation season throughout the 21st century (ACIA, 2005).

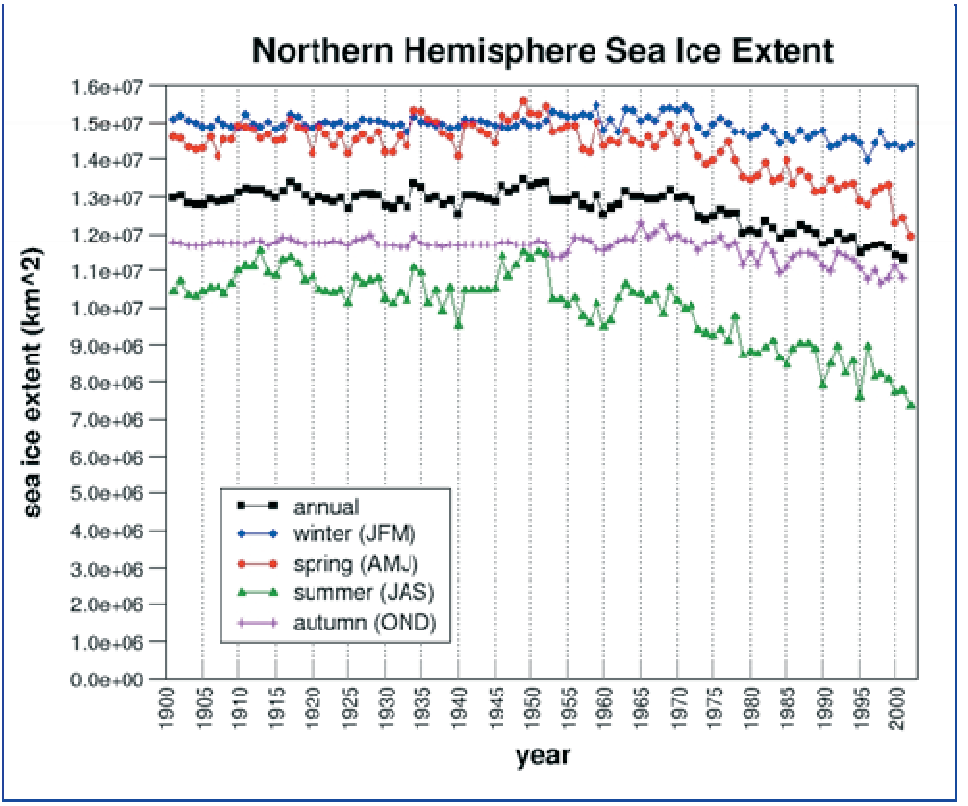

Figure 2. Arctic sea ice extent 1900-2002 (Arctic Climate Impact Assessment).

In summary, ACIA confirms that the observed retreat of Arctic sea ice is a real phenomenon. The GCM projections to 2100 show extensive open water areas in summer around the Arctic Basin. Thus, it is highly plausible there will be increasing regional marine access in all the Arctic coastal seas. However, the projections show only a modest decrease in winter Arctic sea ice coverage; there will always be an ice-covered Arctic Ocean in winter although the ice may be thinner and may contain a smaller fraction of multi-year ice. The very high, inter-annual variability of observed sea ice in the Northwest Passage and non-applicability of the GCMs to the region, prevent an adequate assessment of this complex region. Although the ACIA projections indicate an increasing length of the navigation season for the Northern Sea Route, detailed quantification of this changing marine access is testing the limitations of today's GCMs. There is a definite need for improved Arctic regional models to adequately assess future changes in sea ice extent and thickness, and their considerable implications for expanded marine uses of the Arctic Ocean.

4 ARCTIC MARINE STRATEGIC PLAN

The Arctic Council's vision for the Arctic marine environment is expressed in the Arctic Marine Strategic Plan (AMSP) approved by the Arctic Ministers in November 2004: 'A healthy and productive Arctic Ocean and coasts that support environmental, economic and socio-cultural values for current and future generations.' AMSP is a strategic guide that addresses emerging issues such as oil, gas and shipping activities, employing a risk assessment approach. It takes into account the special needs and requirements of indigenous communities while maintaining an overall objective of sustainable development. AMSP aims to improve how the Arctic coastal and marine environment is managed given accelerated changes due to climate change and increasing economic activity. Four goals for the marine environment are outlined by the Arctic Council in this plan (AMSP, 2004):

- Reduce and prevent pollution in the Arctic marine environment.
- Conserve Arctic marine diversity and ecosystem functions.
- Promote the health and prosperity of all Arctic inhabitants.
- Advance sustainable Arctic marine resource use.

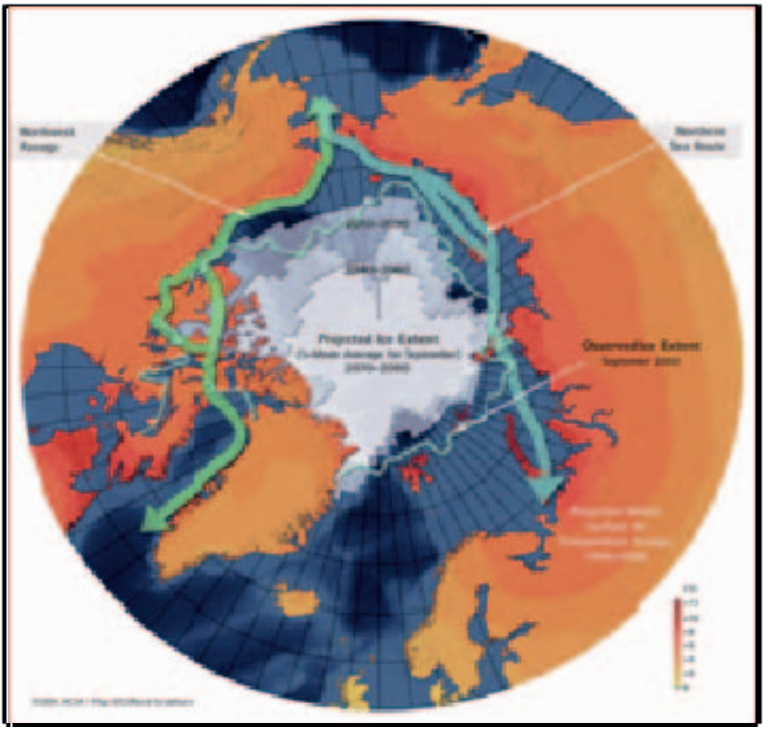

Figure 3. Arctic sea ice simulations for the 21st century. Note the projected ice-free coastal regions in September. No sea ice thickness simulations are provided in these projections (Arctic Climate Impact Assessment).

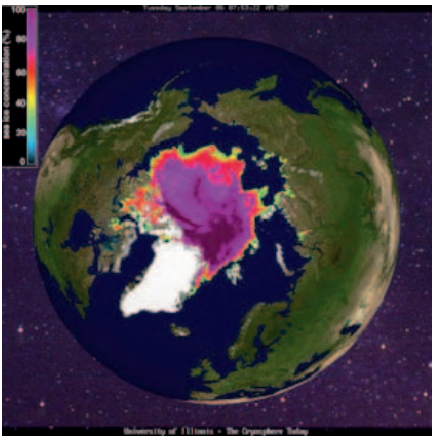

Figure 4. The summer extent of Arctic sea ice on 6 September 2005. This data represents the minimum coverage of Arctic sea ice in the satellite era of observations. The false colors represent sea ice concentrations as determined by satellite passive microwave sensors. Notable for this date are large ice-free areas across the Russian Arctic coastal seas, an ice edge position north of Svalbard, and an historic retreat of the ice edge in the Chukchi Sea (University of Illinois & NOAA).

One key 'strategic action' outlined in the AMSP is the conduct of a comprehensive assessment of Arctic marine shipping at current and projected levels. AMSA will be guided by the AMSP principles including a major opportunity for the future application of an ecosystem approach to management of the Arctic marine environment. A PAME-led experts group is identifying the large marine ecosystems (LMEs) of the Arctic based on the best available ecological information. The LMEs ~ ocean areas characterized by distinct bathymetry, hydrography, productivity and trophic relationships; they produce 95 percent of the world's fish catch ~ are critical elements for AMSA as they can serve as key environmental and socioeconomic indicators of the state of the Arctic Ocean. A key AMSA task will be to determine the environmental impacts of current and projected marine activity on the Arctic marine regions defined by LMEs.

5 AMSA GENERAL WORK PLAN

In 2005 the AMSA lead country and PAME representatives agreed that:

- The assessment would cover all ship-based activity and all ship types.
- The geographical areas would be defined by the Arctic states.
- The LME approach would be used in the assessment.
- An attempt would be made to project Arctic marine activity to 2020 and 2050.

The initial data requirements for AMSA include: a marine activity database for calendar year 2004 (the 'official' activity data requested from the six Arctic coastal states); information on indigenous (traditional) marine use of Arctic waterways; an Arctic shipping accident database (including ship type, location and severity); and, a comprehensive 2004 ice conditions database (derived from Arctic sea ice data held by the national ice centers of the

Arctic states). These data sets are necessary to define a baseline for Arctic marine activity, and to conduct key risk analyses and appropriate social, economic, and environmental assessments. During these initial data captures, the environmental conditions of today's Arctic LMEs will also be determined. The second major AMSA effort will be to project the levels of Arctic marine activity to 2020 and 2050. Determining the plausible scenarios for these future years will require merging regional economic development trends with the changing nature of Arctic sea ice (and the increased marine accessibility in the Arctic Ocean). One of the significant challenges to AMSA will be the evaluation of regional Arctic economic development that may impact future shipping and all Arctic transportation systems.

Determining the environmental impact of current Arctic marine activity will require assessing the condition and bearing capacity for each of the LMEs, narrow Arctic straits, and local regions of known marine traffic. The current impacts of emission volumes (and additional impacts such as noise and wildlife disruptions) will be described within the LMEs and other sensitive areas. AMSA will also conduct a first-order assessment of the environmental impacts of the emissions and accidental releases for 2020 and 2050. Risk analysis will be conducted to estimate the potential for accidents in Arctic marine operations. AMSA will also describe the social and economic impacts of increased marine traffic on local and regional residents. Of particular importance will be the impacts of increased marine accessibility on traditional ways of living in Arctic coastal communities. Improved knowledge of changing sea ice thickness in local regions will be critical to accessing the impacts on Arctic communities.

AMSA will review the relevance of current international marine regulations for Arctic marine operations. Recommendations for a future regulatory framework will be consistent with the many analyses conducted during AMSA. The findings of AMSA will be presented to the PAME representatives and Senior Arctic Officials for their development of recommendations for consideration by the Arctic Ministers. A final AMSA report is planned for presentation at the Arctic Council ministerial meeting to be held in Norway during late autumn 2008.

6 FUTURE ARCTIC SEA ICE THICKNESS NEEDS

The changing nature of marine access throughout the Arctic Ocean requires the availability of enhanced sea ice information. Of particular significance to the conduct of AMSA and to future Arctic marine transport are increased observations and improved simulations of Arctic sea ice thickness. Historical sea ice thickness maps, developed from an integration of basin and coastal seas observations, would be useful in the evaluation of Arctic marine regions where indigenous uses and shipping may overlap. Detailed regional ice thickness observations for regional transport and regulatory efforts are critical since they can highlight annual cycles and inter-annual variability issues. Future GCM simulations of Arctic sea ice to 2100 are required for more robust strategic planning of marine systems; it is expected that these simulations will provide plausible extent and thickness information. Airborne sea ice thickness measurements (electromagnetic sounding) will continue to be quite useful when adapted to regional and local marine operations. Such measurements also provide the basis for regional sea ice thickness monitoring programs. However, real-time satellite observations of thickness will be required in the future for routine, basin-wide coverage. Future satellite systems may rely on co-incident observations of sea ice freeboard for estimates of sea ice thickness; improved estimates of thin ice thickness may also depend in the future on enhanced multiple sensor analyses.

Future Arctic marine activity will require new and improved user products related to sea ice thickness: long-term series of thickness from historical records; maps of GCM simulations of sea ice thickness to 2100; multi-year ice maps indicating extent, thickness, and change rates; regional maps of the location, extent and thickness of landfast ice; and, maps of ice deformation and ridging indicating ranges of thickness (Hutchings and Bitz, 2005).

7 SUMMARY

Responding to the findings of the Arctic Climate Impact Assessment, the Arctic Council is addressing the issue of increased marine access by initiating the Arctic Marine Shipping Assessment. Much of the work of the assessment – for example, future projections of marine activity to 2020 and 2050; risk analyses for Arctic marine operations; and, the environmental, social and economic impacts of expanded use of the Arctic Ocean – is highly dependent on a comprehensive understanding of sea ice coverage and thickness. Future sea ice thickness observations and simulations are crucial to enhancing marine safety and environmental protection in the Arctic Ocean.

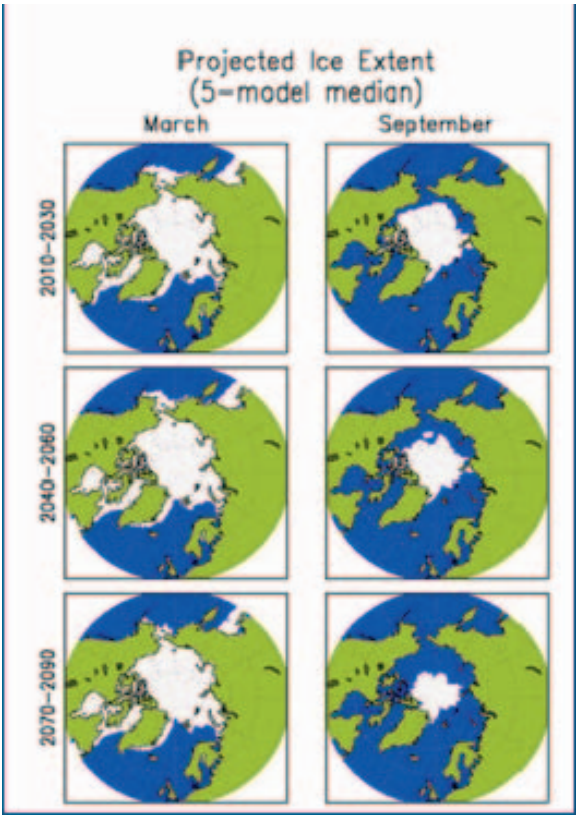

Figure 5. ACIA Key Finding #6 is 'Reduced sea ice is very likely to increase marine transport and access to resources.' This figure includes potential marine routes, projected sea ice extent changes, and projected surface air temperatures (Arctic Climate Impact Assessment).

8 REFERENCES

Arctic Climate Impact Assessment (ACIA), 2005: *Impacts of a warming climate: Arctic climate impact assessment*. University of Cambridge Press, Cambridge, UK, 139 pp.

Arctic Marine Strategic Plan (AMSP), 2004: *Arctic Council Arctic Marine Strategic Plan*, PAME Secretariat, Akureyri, Iceland, 14 pp.

Hutchings, J. and C. Bitz, 2005: *Sea ice mass budget of the Arctic (SIMBA) Workshop – Bringing regional to global scales*. University of Alaska, Fairbanks, 80 pp.

Tucker, W. and D. Cate (editors), 1996: The 1994 Arctic Ocean Section: The First Major Scientific Crossing of the Arctic Ocean. *CRREL Special Report 96-23*, Hanover, New Hampshire, p. 81.

Arctic Sea Ice Thickness: Implications for Arctic Tourism

John M. Snyder*
President, Strategic Studies, Inc. 1789 E. Otero Ave. Centennial, Colorado 80122 USA,

Keywords: Polar tourism, ice extent, tourist access to Arctic

ABSTRACT: Tourism is now the single largest human activity in the Arctic. The number of tourists visiting the Arctic each year far exceeds their host populations. Additionally, polar tourism is the fastest growing segment of the world tourism market, in percentage terms, and the Arctic is increasingly reliant upon this economic activity. As a result of these circumstances, any changes in Arctic ice cover that would facilitate improved tourist access will potentially have significant effects upon Arctic resources. The purpose of this paper is to briefly identify key relationships between tourism and its environmental, cultural, and economic setting; then introduce probable ways in which those relationships will be influenced by Arctic sea ice conditions; and finally suggest why the resource management implications of those events deserve vital consideration when assessing adaptive responses to Arctic environmental change.

1 INTRODUCTION

Two Centuries of Arctic Tourism

The Arctic has been a tourist destination since the early 1800's. The earliest Arctic tourists were individual anglers, hunters and adventurers attracted to abundant fisheries, exotic wildlife species, and remote regions. Several of these individuals published travel journals that became popular guide books for future Arctic travellers. Sportsmen published articles for the growing genre of hunting and fishing periodicals that emerged in the 1800's.

Mass tourism in the Arctic has thrived since the mid-1800's. Steamships and railroads aggressively expanded their transportation networks and thus permitted access to a variety of regions throughout the Arctic. Tourism entrepreneurs, such as Thomas Cook, formed partnerships with railroad and steamship companies and thereby initiated popular tourism. The transport companies accurately foresaw the profits associated with this form of travel. By 1850, steamships and railroads enabled popular, mass tourism to occur throughout the Arctic. The "Land of the Midnight Sun" in the Scandinavian Arctic, the natural wonders of Alaska, and the popular excitement associated with the Alaska and Klondike Gold Rushes firmly established a regular mass tourism market in the Arctic by the 1880's.

During the past two centuries numerous advances in transport technologies have contributed to the steady growth of Arctic tourism. Improved ship technologies together with improved marine charts and navigational aids have allowed cruise ship travel to increase exponentially. Diesel locomotives, four wheel drive and tracked vehicles using expanded transport systems have opened access to vast regions of the Arctic. And, most importantly, air transport in all of its form, is providing immediate and comfortable travel to the Arctic.

* E-mail: sssieti@aol.com, Tel.: +1 303 347 2095.

Collectively, these improved transport technologies not only add numbers of tourists, but also expand the seasonal and geographical reach of tourism.

Reduced "Barriers to Entry"

Since its inception, Arctic tourism has benefited from a continuous reduction in what economists call "barriers to entry". The barriers consist of various constraints that either prohibit or restrict tourism. As the constraints are progressively reduced or eliminated, greater participation in Arctic tourism is able to occur. The most prominent barriers to Arctic tourism and reasons for their continuous decline include the following.

Access

Historically, the Arctic was one of the most inaccessible regions of the globe. As previously stated, a variety of improved transport technologies have progressively improved access to the entire Arctic region. The advanced transport modes have made travel safer, quicker, more convenient, and more comfortable.

Physical barriers, particularly sea ice and severe weather, have represented daunting challenges for Arctic travel. Since the 1980's, the cruise ship industry has responded positively to decreased amounts and duration of sea ice. Expanded cruise ship operations, Northwest Passage transits, cruises to the North Pole, and growing seasonal use of the Arctic exemplify that response. Simultaneously, Arctic governments and native people have sought to take advantage of more moderate weather by lengthening their tourism seasons.

Environmental Conditions - both real and perceived

During the last century, the public's perception of the Arctic steadily transformed from dreadful to increasingly alluring. As the tragic histories of polar exploration recede from popular memory and the attraction of the Arctic as an extraordinary wilderness area takes its place, people are demonstrating a keen interest to visit the region. Their motivations are substantially aided by improved clothing, equipment, accommodation, and diverse support services that facilitate safe and enjoyable Arctic tourism experiences. All of these appurtenances are further enhanced by progressively improving weather conditions.

Cost of Travel

Throughout most of human history, leisure travel was exclusively reserved for the wealthiest strata of society. From the mid-1800's to the present, the cost of travel has precipitously dropped and this has offered abundant opportunities to people throughout the world to travel for the primary purpose of pleasure. Mass tourism provides an opportunity for persons in virtually all strata of society to travel. Transportation companies and tour providers, recognizing the enormous value of tourism, have catered to every conceivable facet of the tourism market. Today, tourism is universally regarded as the world's single largest industry.

Accompanying reduced travel costs is the increase of personal wealth and prosperity. Personal and household income, disposable income, and estate inheritances have all contributed to the wide distribution of economic prosperity. With more people having more money available to spend, the effects upon tourism have been predictably positive. Again, the tourism industry ambitiously seeks to tap this wealth and offers a myriad of tourism

products. The Arctic tourism market is consistently one of the tourism industry's most aggressively promoted markets.

Time to Travel

Sufficient time to enjoy leisure pursuits can be a significant barrier to travel, especially to remote destinations such as the Arctic. Travel to the Arctic traditionally required a considerable amount of time and relatively few people could afford to spend their leisure time in this way. However, since the latter half of the twentieth century reductions in the hours worked per week, guaranteed vacation time, and flexible time scheduling provide growing numbers of people with more leisure time. Additional leisure time, in combination with the availability of fast transport services, now make destinations such as the Arctic a plausible travel choice for increased numbers of people.

One especially important demographic event currently contributing to more leisure time is the enormous number of persons now entering retirement age. The world is currently on the threshold of experiencing the largest growth in retirement aged persons in its history. The consequence of this demographic event is that a large percentage of the world's population has both the time and the money needed to travel. The Arctic, with its comfortable and often luxurious transport modes has always been a desirable destination for this age group.

Jurisdictional Regulations

Jurisdictional regulations can either encourage tourism by means of allowable entries or block access by means of prohibited entry. Both circumstances have occurred in the Arctic. But the current trends provide strong evidence of growing tourist access resulting from the elimination or reduction of prohibited entry to Arctic regions.

Arctic governments at all levels directly influence tourism travel. In recent decades allowable tourism access has not only been permitted but promoted. All of the governments encircling the Arctic now encourage tourism as a desirable form of economic development. All Arctic governments have also established protected areas such as national parks, wildlife refuges, wilderness areas, forests, wild and scenic rivers, and heritage sites. One of the rationales for their creation is the hope of attracting tourists to a diversity of outdoor recreational activities. Additionally, government laws and regulations allowing sport fishing and hunting also encourage tourism and thus provide access to unique tourism experiences.

Some of the Arctic's most stringent and long lasting barriers to tourist entry have been removed. Most notably, the Russian Federation's promotion of tourism in their Arctic regions of Siberia and the Far East represents a significant paradigm shift. The world's largest Arctic land mass is now accessible to tourists. Denial of entry and the prohibitions of a half century have been formally removed by the Russian Government. The implications of this policy reversal remain to be seen, but its significance deserves attention.

For several generations a primary role of the Arctic was its strategic military significance. Consequently, many military installations, support facilities, and security zones were established. Given security considerations, public access to these areas was prohibited. As a result of a new world order caused by the end of the Cold War, the Arctic became a region in which the geopolitical landscape was literally transformed. Numerous military installations not only became accessible, but their infrastructure became valuable assets for

future tourism development. Certainly one of the most remarkable examples of the geopolitical changes resulting from the end of the Cold War is the use of Russian ice breakers as tourist cruise ships in the Arctic.

2 ECONOMIC CHARACTERISTICS OF ARCTIC TOURISM

Diversity of the Arctic Tourism Market

The Arctic tourism market has evolved to become a very large, diversified and sophisticated collection of economic activities. Arctic tourism consists of distinct market segments that are best defined in terms of their primary attractions and the ways in which those attractions are experienced. This approach to classifying tourist markets explicitly acknowledges the highest expectations of the tourist and the service delivery methods used to realize those expectations. Given this organizational approach, there are five polar tourism experiences that currently dominate the polar tourism market. Those five market segments include:

1. The mass market comprised of tourists primarily attracted to sightseeing within the pleasurable surroundings of comfortable transport and accommodation.
2. The sport fishing and hunting market whose participants pursue unique fish and game species within a wilderness setting.
3. The nature market consisting of those people who want the opportunity to observe wildlife species in their natural habitats, and persons who seek the solitude of natural areas.
4. The adventure tourism market is comprised of persons who derive a sense of personal achievement and exhilaration from meeting the challenges and potential perils of outdoor sport activities.
5. The culture and heritage tourism market is a very distinct market comprised of tourists who want to experience personal interaction with the lives and traditions of native people, learn more about a historical topic that interests them, and personally experience historic sites and artifacts.

Each of the five polar tourism markets has their own distinguishing visitor experiences and economic dimensions. The tourist's motivations, expectations, on-site behavior, and resource uses are distinctly different among each of the groups. Sophisticated tourist industries have evolved to provide each market with travel and support services, equipment, clothing, transport, and accommodations. And these markets are energized by promotional campaigns and specialized publications dedicated to sustaining special interests and active involvement. All of these distinctions and associated information provide a useful organizational framework for better understanding Arctic tourism in terms of economic activity, visitor behavior, and resource uses. Of course, the tourists themselves are not constrained by this type of classification and they freely participate in as many types of activities as they wish.

Economic Dimensions of Arctic Tourism

In percentage terms, polar tourism is the fastest growing segment of the world tourism industry. Given the fact that tourism is acknowledged to be the world's largest industry, the implications for Arctic economies are significant. In many instances the increased economic role and dimensions of Arctic tourism have been beneficial to the people of the north.

However, there have also been legitimate concerns expressed regarding the impacts of tourism in the Arctic world.

Arctic economies are increasingly dependent on tourism. To the extent that this has improved economic stability and resource conservation, the effects are considered to be quite positive. By example, the volatile economic history of the Arctic exemplified by a great reliance on resource exploitation and extraction. Fisheries, minerals, timber, energy, and other natural resources were removed from the Arctic and exported to lower latitudes. The environmental effects of early extraction processes caused great damage to ecological systems and produced only short term benefits for Arctic people. Tourism practices that place value on environmental quality and sustaining Arctic wildlife offer a more benign approach to sustainable economic development.

A review of the composition of Arctic economies, their labor force, and their public sector demonstrates a growing economic dependency upon tourism. Private sector businesses increasingly rely on tourism for sales revenue and profit. Households either rely or supplement personal income from the jobs tourism provides, and the market outlet for locally made products and services. The public sector, government, increasingly relies upon tourism for diverse types of revenue and as a means for accomplishing infrastructure and community development.

Diversifying Arctic Economies

Mature Arctic markets are attempting to diversify by means of expanded seasons and new visitor attractions. For example, Alaska and Canada are attempting to establish a winter season. New recreational venues, especially those associated with the adventure tourism market are rapidly being created. New recreation technologies are contributing to this form of diversification. Emerging Arctic markets such as Greenland and Nunavut in the Canadian Arctic are seeking to diversify their economies by means of tourism.

External Economies Increasingly Reliant on Arctic Tourism

The Arctic tourism market continues to be a very lucrative segment of the world tourism industry. Economic gains measured in terms of expenditures per person and consistently high demand create attractive business opportunities for tourism providers. Consequently, the world tourism industry in general, and the multi-billion dollar cruise ship industry in particular, consider Arctic tourism a key market. For example, in 2004 a total of 1.2 million passengers travelled to traditional Arctic cruise markets such as Norway and Alaska. This represented an extremely valuable market for the cruise ship industry that realized 15.6 billion dollars net profits during 2004. Wildlife and nature tour operators as well as cultural tour providers share a keen desire to economically benefit from the expansion of Arctic tourism.

3 SOCIAL CHARACTERISTICS OF ARCTIC TOURISM

Magnitude and Immediate Impacts

Tourism is now the single largest human activity in the Arctic. Significantly, the number of tourists visiting the Arctic far exceeds their host populations at ALL destinations. And its presence is growing.

Arctic communities experience numbers of tourists that not only exceed their permanent resident population, but also challenge the capacities of their physical and human infrastructure. Utility requirements for the seasonal tourism population exceed the resident population's "normal" needs for electrical power, water supplies, wastewater treatment, solid waste disposal, and a wide range of emergency response services such as medical care and law enforcement. Collectively, this places an extraordinary burden on the public finance and human resource capacities of the Arctic's host communities.

Mitigation of the social impacts of Arctic tourism can be influenced by the terms and conditions of collaborative agreements between the tour operators and local community as well as by the optimization of the tourist season. In some instances tax revenues and special fees derived from the tour industry offset local costs. To the extent that tourist seasons can be expanded, there are greater economies of scale and efficiencies resulting from the use of infrastructure as well as an extension of employment and income benefits. The actual effects result from mutual willingness to cooperate and negotiating strengths and skills. Given this variability, a diversity of industry / community relationships has been established throughout the Arctic.

4 CULTURAL CHARACTERISTICS OF ARCTIC TOURISM

Seeking Balance – a Difficult Challenge

The ability of the Arctic's indigenous people to survive has always been dependent upon their ability to adapt to change. Now, as they witness the changes wrought by reduced Arctic sea ice, they are anxiously considering ways in which they will have to adapt to this potentially enormous change. Both negative and positive impacts arising from the sea ice changes are readily perceived. It is also apparent that changes are proceeding quickly and indigenous people are displaying a sense of urgency to find a response. This situation was accurately summarized by Warren Matumeak, Alaska Native Elder:

> *"These (reduced sea ice) changes I and other indigenous people see, can be perceived as positive and negative. The Inupiaq welcome the warmer temperatures but do not appreciate the lack of multiyear pack ice and the increased difficulty of whaling these temperatures bring. The subsistence way of life has to adapt to the environment. The world is changing and I and other indigenous people are bearing witness."*

The Arctic environment is not merely a setting within which indigenous people live, but rather the vital resources upon which their lives depend. Consequently, the loss of Arctic sea ice with its attendant effects on wildlife habitat, numbers, and migratory behavior; the transport routes needed to subsist; the duration of seasons; and the condition of fisheries are of critical importance to the cultural and economic well-being of Arctic people. According to a 2005 statement made by Sheila Watt Cloutier, International Chair, Inuit Circumpolar Conference:

> *"What is at stake here is not just the extinction of animals but the extinction of Inuit as a hunting culture. Climate change in the Arctic is a human issue, a family issue, a community issue, and an issue of cultural survival. The joining of circumpolar peoples with Pacific Island and Caribbean States is surely part*

> *of the answer in addressing these issues. Many small voices can make a loud noise"*

Specific concerns regarding the loss of fast ice include:

1. Fast ice permits travel along the shore by dog sled or snow machine. It enables people to circumvent mountain travel and hazardous sea routes.
2. The sea ice provides access to seals, polar bears, whales, and fish that sustain traditional ways of life and value systems.
3. The loss of fast ice clearly endangers traditional ways of life and increased tourist ship traffic that contributes to further breaking fast ice may exacerbate this situation.

The significance of the third factor was graphically described by George Porter, Inuit leader of the community of Gjoa Haven on King William Island in the central part of the Northwest Passage when he stated:

> *"You know for Inuit people the land and the water are the same thing – here the sea is frozen over for most of the year. So to us driving a ship through the ice is like driving a bulldozer across a field with the blade down."*

Tourism's Role in a Dynamic Setting

Within their highly dynamic environmental setting, the Arctic's indigenous people are attempting to balance the economic benefits of tourism with their vulnerability to negative cultural impacts. There are distinct economic and educational benefits that indigenous people can derive from Arctic tourism. Tourism employment provides an important source of personal income and skills development. The tourist's attraction to culture and heritage also provides critical support for language preservation, the practice of traditional ceremonies, and the perpetuation of ancient customs and art forms. Associated benefits of this form of tourism include an immediate market for art and other native manufactures and services. Additionally, indigenous peoples throughout the Arctic seek economic benefits from increased tourism to offset income losses from other sources due to environmental change. Tourism represents one of the few acceptable ways in which indigenous people can successfully participate in a market economic system.

It must also be acknowledged, however, that tourists can be highly intrusive as a consequence of either their sheer numbers or their personal behavior. Large numbers of tourists arriving at a native site can quickly overwhelm the local people and intrude upon their essential subsistence activities. The personal behavior of tourists, either wittingly or not, can offend local cultural practices and values. Tour operators who specialize in heritage tours are aware of these potential conflicts and normally instruct their clients about appropriate behavior. Some other types of tours do not include this educational practice and the resultant conflicts can damage both the native people's quality of life and the tourist experience. Both parties lose when this occurs, but as previously stated, there are successful techniques for avoiding or mitigating this situation.

The importance of tourism's economic benefits is continuously compared with cultural impacts that it inevitably produces. Additional tourists will further stress increasingly scarce natural resources. Stressed natural resources result in a variety of pressures exerted on indigenous subsistence practices and value systems. Finally, as

traditional indigenous lifestyles succumb to change resulting from reduced Arctic sea ice, there will be fewer opportunities for tourists to experience authentic cultural traditions.

5 EFFECTS OF REDUCED ARCTIC SEA ICE ON "BARRIERS TO TOURIST ENTRY"

Expanding Tourist Access

The combination of reduced Arctic sea ice, improved transport technologies, more infrastructure, and aggressive economic development will enable Arctic tourism access to expand in a variety of ways. The most significant impacts will include: (1) increased numbers of Arctic destinations; (2) an expansion of the seasonal tourism use of the Arctic; and (3) the increased duration of the tourist visit. The cumulative impacts of reduced Arctic sea ice will result in larger numbers of Arctic tourists spending more time in more locations.

New Tourist Destinations: The Northwest Passage and North Pole

Tourist travel in the Arctic is characterized as being both a pioneering and dominant type of travel in the region. The pioneering traits of tourism travel are readily apparent in the transits of the Northwest Passage and cruises to the North Pole. Since the transit of the Northwest Passage by the Lindblad Explorer in 1984, the passage has been successfully navigated by vessels ranging from cruise ships to private charter vessels. North Pole tourist travel is regularly occurring aboard icebreakers and, occasionally, by submersibles.

Arctic routes of tourism travel and the number of vessels participating in this form of tourism are documented in various publications authored by Brigham, Armstrong, and Ellis. The especially noteworthy characteristic of Arctic travel is that most of the traffic is comprised of tourist ships. Quoting a recent study by Lawson Brigham, "During 1977 to 2004, 52 successful voyages have been made to the North Pole by the icebreakers of Russia (42), Sweden (4), Germany (2), United States (2), Canada (1), and Norway (1); remarkably eight surface ships reached the North Pole during the summer of 2004. Thirteen of the voyages were in support of scientific research and the remaining 39 were devoted to tourist voyages to the North Pole and across the Arctic Ocean."

Examination of Arctic transportation in terms of numbers of passengers, ship transits, commercial air flights, and private vessel traffic reveals that tourists are increasingly gaining access to the region. Given this well documented record, it is reasonable to suggest that reduced Arctic sea ice will contribute to additional tourism access.

Changing Environmental Conditions - Both Real and Perceived

A host of dynamic events are causing environmental changes in the Arctic. Among these, the well documented evidence of substantial reductions in sea ice presence and thickness is prominent. From the tourism perspective, the ecological transformations occurring in the Arctic represent a re-characterization of tourist attractions and tourism experiences. In some instances, the attractions are more popular because of the greater numbers of wildlife viewing, sport fishing, and hunting opportunities. In others diminishing numbers of wildlife achieve notoriety, and thus popularity, because of their scarcity. As ecological systems transform and wildlife adapt to their changing habitats, the recreation

experiences associated with those environments are inevitably altered. A few examples of the way in which sea ice changes are re-defining Arctic tourism experiences deserve mention.

Wildlife Tourist Attractions – More Or Less

Ecological changes in the Arctic, particularly those associated with diminished sea ice and relatively warmer weather enable certain wildlife species to thrive while simultaneously creating stressed conditions for others. Increased ice free areas, plant succession, and the extension of woodlands contribute to the viability of many land and bird wildlife species. At the same time, the declining extent and amounts of Arctic sea ice produce habitat loss for selected wildlife species that may eventually lead to their extinction. As the range, nesting areas, migratory patterns, and habitat boundaries of Arctic wildlife continue their transition, tourist wildlife experiences and opportunities will also be transformed.

Warming climatic conditions enable woodland and wetland environments to host increased numbers of wildlife species such as moose, brown bears, and migratory birds. Shorelines freed from ice provide habitat for wildlife and enable plant communities to colonize. The growing availability of nutrients, prey species, and nesting areas in coastal areas enable a diversity of wildlife to exist. As both the inland and coastal areas provide more sustenance larger populations of resident and migratory wildlife will be sustained. It is also probable that wildlife migratory routes will be changed by these sea ice and climatic changes. The greater abundance of wildlife and certainty of experiencing these Arctic species will contribute to the growth of both nature based and, where legally permitted, hunting tourism.

Fishery stock locations and fish migratory behavior will be strongly influenced by Arctic sea ice changes. The lucrative Arctic sport fishing market is very sensitive to those changes. Any changes in the size, location, and seasons of fish species sought by the sport angler will have a considerable impact on Arctic economies. Reduced sea ice conditions that allow improved access to the fisheries will permit this form of tourism to flourish.

Although numerous species of land, bird and marine species will benefit from reduced sea ice and warming conditions, there are certain Arctic wildlife species that are at risk. Most prominent among those are the polar bear, Arctic fox, and seals dependent upon sea ice as their primary habitat. Based on decades of wildlife science research it is now evident that these wildlife species are vulnerable to extinction due to a loss of habitat caused by sea ice changes. By example, Ian Stirling's decades-long research on the polar bear and the ecological integrity of its Canadian Arctic habitat led him to report that: "There is a significant positive relationship between the time of breakup and the condition of adult males and females (i.e., the earlier the breakup, the poorer the condition of adult males and females). . . . Ultimately, if sea ice disappeared altogether, polar bears would become extinct".

The demise of the polar bear, an icon of the Arctic world, would be a tragic loss. One aspect of this deteriorating situation is the negative impact that would have on Arctic tourism. The vibrant tourist industry developed around viewing polar bears in locations such as Churchill, Manitoba, and Wager Bay, Northwest Territories would be adversely affected.

As the Arctic marine environment responds to reduced sea ice, populations of seals and whales that inhabit or migrate through Arctic waters will modify their predation and migratory behavior. Some species will become more vulnerable, some alter migratory routes,

others will thrive on increased nutrients and prey species. These modifications will be reflected in numerous human activities as well. Subsistence practices of native people, commercial harvesting, and tourism viewing opportunities will all be affected by the dynamic changes in the Arctic marine environment.

Other Environmental Changes Affecting Arctic Tourism

The reduction in extent and thickness of Arctic sea ice, accompanied by climatic and ecological changes, will not only affect recreational opportunities but also the personal comfort of visitors. By example, the establishment of pioneer plant communities along coastal zones is initiating a process of plant succession. Accelerated plant succession resulting from the recession of the glacial and fast ice offers tourists more plants to view and a dynamic process to witness. Research confirms that tundra plants are generating their own microclimate and ground temperatures may be as much as 10° C higher than the air temperature. It is possible that plant succession will not only have a multiplier effect on the climate of the Arctic, but on visitation. Tourism comfort will most certainly be enhanced by more tolerable climatic conditions.

Increased vegetation in the Arctic will increasingly contribute to a variety of visitor discomforts and potential hazards. Two notable examples of these effects include the greater prevalence of insects that predictably diminishes tourist comfort, and the growing potential and incidence of wildfire in Arctic regions. The emergence of a host of new environmental events will create the need to re-think traditional resource management practices and calculations of potential hazards. The environmental and climatic transformations now occurring in the Arctic will impact wildlife viewing, sport fishing, hunting, wildlife photography, backpacking, kayaking, and river rafting recreation activities throughout the region.

Re-Defining the Roles of Protected Areas

Protected Areas such as national parks, wildlife refuges, wilderness areas, World Heritage Sites, and marine sanctuaries were established with the explicit intent of conserving a unique collection of environmental resources. Substantial national and international law, monetary and human resources are being dedicated to the conservation of those unique environmental features. What happens when those features no longer exist? Protected areas through the Arctic are now confronting this dilemma.

Rapid changes in sea ice and climate render Protected Areas, such as national parks, unable to protect the representative elements of the landscape for which they were designated. When the physical and biological elements that provide the backdrop for recreation are altered by climatic change, then surely the recreation experience will also be affected. Thus the retreat of Arctic sea ice and the environmental changes created by that event pose not only ecological problems for park managers, but also recreation management problems.

The future management of Protected Areas will involve a thorough re-evaluation of the purpose of those areas. By example, Glacier Bay National Park, Alaska was created for the specific purpose “of providing the opportunity afforded here for the scientific study of glacial action”. The current and foreseeable reality is that the vast majority of the tidewater glaciers in the United States largest marine park are retreating at an extraordinary rate. The salient glacial features that served as rationale for park designation, such as the Muir Glacier,

are now mere remnants. Given circumstances such as these occurring in many parts of the Arctic, the preservation of the "environmental integrity" of Protected Areas must be thoughtfully re-considered.

Environmental Contaminants – New Exposures

One environmental implication of greater tourist access to Arctic sites is the potential for increased exposure to environmental contamination. Not only is the Arctic environment potentially exposed to pollution caused by increased visitation, but the tourists themselves will be exposed to dangerous contaminants located at numerous destinations that were previously off limits. The first scenario has received a considerable amount of well deserved attention. The second threat, tourist exposure to contaminants, has garnered very little.

The existence of significant environmental hazards at Arctic sites that have recently become tourist attractions warrants serious consideration. One of the entirely unanticipated implications of reduced Arctic sea ice and the improved access it provides is the introduction of tourists to dangerously contaminated sites. Three prominent examples include:

1. An unfortunate legacy of the Cold War is the presence of very large numbers of ageing fuel drums, often located in isolated caches, to provide emergency supplies. Leakage is a potentially serious environmental hazard and exposure to those toxins is hazardous.

2. Historic structures, such as abandoned canneries, explorers' huts, and whaling and sealing stations, are simultaneously tourist attractions and health threats. Building materials such as asbestos, chemicals used to process ores, caustic cleaners, machinery lubricants, pesticides, and variety of abandoned supplies comprise a hazardous mixture of environmental contaminants that pose significant health threats.

3. The former Soviet Union's catastrophic environmental impacts on the Arctic's water resources should be addressed now that the Arctic's largest land mass seeks to attract tourism. According to former Soviet authorities, the 155,000 Siberian rivers delivered freshwater to the wrong destinations and as a consequence they decided to impound and divert as much of that water as possible for alternative uses. One of these rivers, the Angara River flows from the southern end of Lake Baikal to the Arctic Ocean across a distance of 2,500 miles. As one distinguished authority has warned, the Angara River "has become the aqueduct for poisons. Yearly it carries 257,000 tons of chlorides, 140,000 tons of sulfates, over 30,000 tons of organic wastes, and 10,000 tons of nitrates from factories built in the 1960's and 1970's along its banks".

Tourist's Environmental Perceptions

Tourist's perceptions of the Arctic have radically transformed during the last century. The public's attitude towards the Arctic in the early 1900's was dominated by stories of the perils, hardships, and lives lost during polar explorations. That perception has been very nearly replaced by the opinion that the Arctic is a safe destination that offers an attractive alternative to an increasingly dangerous world. Two major events in the mid-1980's accelerated this thought process. The Achille Lauro terrorist event in 1985 and the Chernobyl RBMK reactor explosion in 1986 caused the tourism industry to expand polar travel. Recoiling from the risks associated with terrorism and nuclear disaster, cruise ship and other tour operators sought destinations in the Arctic. These strategic decisions were strongly supported by tourists who increasingly perceived the Arctic as a safe destination.

The success associated with those decisions contributed substantially to increased Arctic tourism.

More recently, the impacts of international terrorism on the tourism industry, together with the extensive publicity associated with Arctic climate change, have reinforced perceptions that the Arctic is a desirable tourism venue. The tourist views safety as an increasingly important travel consideration. For the tourist industry, safe destinations reduce their economic risk. In contrast with competitive tourism destinations, Arctic markets are perceived to be less congested. Simultaneously, nature based tourism is growing rapidly and improved clothing and equipment are providing warmer, safer, and more reliable ways to enjoy that type of travel. All of these factors combine to increase the popularity of Arctic tourism.

Jurisdictional Changes – Allowable Entry Replaces Prohibited Access

As previously stated, allowable tourism entry, primarily motivated by economic development, is strongly promoted in Arctic regions that were previously inaccessible. Reduced sea ice in combination with favorable government policies have either expanded or recently permitted tourist entry to vast Arctic regions.

The Russian Federation's endeavors to create an Arctic tourism market in combination with reduced sea ice conditions that enable improved transits of the Northern Sea Route now open the single largest geographic expanse of the Arctic to tourism.

Greenland's new Home Rule Government initiated an ambitious economic development strategy to create a tourism market. Results of this jurisdictional change have substantially accelerated travel to Greenland. During the last decade Greenland has evolved from an obscure, minor player in world tourism to hosting 57 cruise ship entries in 2005. Greenland now offers a diversity of quality land based tourism experiences in multiple seasons.

Another enormous region now transformed as a result of jurisdictional change is Nunavut in the Canadian Arctic. The Nunavuts' economic development endeavors have paralleled their work to attain and strengthen their sovereign status. Tourism plays a central role in the Nunavuts' economic development strategy.

6 RESOURCE MANAGEMENT IMPLICATIONS

Resource Policy Implications

Reduced Arctic sea ice and the accessibility it progressively provides has already started discussions concerning jurisdictional boundaries and foreign policy. From a tourism management viewpoint the resolution of those issues will be critical. Issues regarding sovereignty and jurisdictional boundaries determine the terms and conditions for allowable uses of Arctic resources. International wildlife management cooperative agreements, such as those for Polar Bears, migratory birds, and marine mammals will affect tourism activities. And, of course, fishery laws and regulations will impact take limits, management practices, seasons, and boundaries.

Environmental Management Implications

Alteration of the Arctic's ecological systems will result in the gain and loss of tourism attractions. Accurately discerning tourism's role in these dynamic processes will be essential for understanding how tourism should be managed. The range of tourist impacts on the Arctic's dynamic processes extends from nearly nonexistent to potentially injurious. By example, visitor attractions now influenced by climatic change, such as reduced sea ice and glaciers, will be minimally influenced by onlooking tourists. In contrast, the survival of increasingly endangered wildlife species dependent on sea ice can be further threatened by stresses caused by tourism activities. Identifying allowable tourist uses of the Arctic's resources including types of activities, their location, season of use, and resource vulnerability require assessment and the design of appropriate management techniques.

Wildlife habitat changes will necessitate reconsideration of wildlife management practices in the Arctic. This will influence several types of tourism recreation activities such as wildlife viewing, photography, and sport hunting. Likewise, fisheries management will affect rules and regulations regarding sport fishing activities, season, and limits.

Hydrological changes in the Arctic will affect adventure tourism activities such as river rafting, kayaking, and float plane operations. One of the most popular international recreation activities is coastal sea kayaking. Reduced Arctic sea ice may in fact allow more persons to participate in this activity. Longer ice free seasons are anticipated to benefit river rafting throughout the Arctic.

Improved access to emergent ice free areas will fuel economic competition for the Arctic's natural resources. It should be recognized that commercial tourism and outdoor recreational pursuits will not be the only uses of the increasingly accessible Arctic environment. Competitive zeal to discover and extract commercially viable natural resources and promises of wealth will force several Arctic communities to re-evaluate the economic role of tourism. As tourism competes with resource extraction industries, particularly oil, gas, and minerals the positive and negative impacts of tourism will steadily be viewed from this perspective. The resource management implications of those evaluations and decisions will have long term effects on the Arctic.

The mission statement (management goals and objectives) of Arctic Protected Areas and other natural resource management zones must be re-evaluated. If fidelity to the environmental integrity of those areas is important then resource management policies and practices influenced by reduced Arctic sea ice will have to be re-defined.

Social and Cultural Resource Management Implications

The ways in which Arctic communities allow their natural resources to be used affects the character of those communities. The jobs, businesses, personal wealth, and quality of life derived from the specific uses of natural resources affect not only the community's well-being but their attitude toward their environment and themselves. Arctic communities, motivated by self determination, will decide how to utilize their resources and this will ultimately determine how those resources are managed. Tourism offers a variety of economic and social benefits to Arctic communities, but also warrants numerous safeguards. The implications of community decisions regarding resource management cannot be overestimated.

Native People are confronting numerous issues concerning the conservation of their heritage. It is important to note that indigenous people throughout the world have struggled with similar issues and thus there are numerous case studies that offer valuable lessons learned. The experiences presented in the case studies evaluate resource management issues in a holistic manner. The shared sense of urgency is also present in those experiences.

7 CONCLUSION – ADAPTING TO A NEW PARADIGM

The Arctic's "new realities", particularly reduced sea ice and the complexity of effects associated with it are not merely producing changes; they are creating a new paradigm. In the face of this new paradigm, it is not certain that continuation of traditionally appropriate resource management techniques will meet the Arctic's future resource management challenges in general, and tourism management needs in particular. Significant modification of the Arctic environment, structural transition of Arctic economies, and significant threats to traditional Arctic cultures will demand resource management policies, programmes, and implementation techniques that facilitate adaptation to those changes.

Tourism's role as the largest and fastest growing human activity in the Arctic will be a catalyst in the Arctic's transformation process. Key relationships between tourism and its environmental, cultural, and economic setting need to be identified and the probable ways in which those relationships will be influenced by reduced Arctic sea ice deserve vital consideration when assessing adaptive responses to Arctic environmental change.

8 FURTHER READING

Armstrong, Terence E. 1972: International Transport Routes in the Arctic. *Polar Record*, 16, No. 102, Cambridge University Press, 357-382.

Armstrong, Terence E. 1972: The Northern Sea route, 1971. *Polar Record*, 16, No. 102, Cambridge University Press, 421-422.

Armstrong, Terence E. 1991: Tourist visits to the North Pole, 1990. *Polar Record*, Vol. 27, No. 161, Cambridge University Press, 130.

Brigham, Lawson and Ellis, Ben (Editors). 2005: Arctic marine transport workshop 28 – 30 September 2004. Held at Scott Polar Research Institute, Cambridge University, United Kingdom, Institute of the North, U.S. Arctic Research Commission, International Science Committee, Northern Printing, Anchorage, Alaska.

Capps, Chris. Jan/Feb 1996: Assault on the last frontier. *National Parks*, Vol. 70, No. 1-2., 30-35.

Division of tourism, Government of the Northwest Territories. 1972: Tourism in Canada's Northwest Territories. *Polar Record*, Vol. 16, No. 102, Cambridge University Press, 424-425.

Domanverket (Forest Service) of Sweden. 1972: National Parks in Swedish Lapland. *Polar Record*, Vol. 16, No. 102, Cambridge University Press, 92-93.

Dowdeswell, Julian and Hambrey, Michael. 2002: *Islands of the Arctic*. Cambridge University Press, Cambridge, England, 280.

Du Chaillu, Paul B. 1881: *The Land of the Midnight Sun - Summer and Winter Journeys Through Sweden, Norway, Lapland and Northern Finland* in Two Vols. Harper & Brothers, New York.

Emmet, W.T. 1890: Alaskan Notes of a Fly Fisherman. Outing Publishing Company in Oppell, Frank compiled by, 1986. *Tales of Alaska and the Yukon*. Book Sales, Inc., Secaucus, New York, 469.

Feazel, Charles T. 1990: *White Bear – Encounters with the Master of the Arctic Ice*. Henry Holt and Company, New York, 240.

Feshback, Murray and Friendly Jr., Alfred. 1992: *Ecocide in the USSR Health and Nature Under Siege*. Basic Books a Division of Harpers Collins Publishers Inc., New York, 376.

Koth, B., Field, D., and Clark, R. 1985: An Analysis of Cruiseship Passenger Characteristics, Activity Patterns and Evaluation of Recreation Opportunities in Southeast Alaska, National Park Service Cooperative Park Studies Unit, College of Forestry, Oregon State University, Corvallis, Oregon, 125

Mitchell, John G. April, 1997: Oil on ice. *National Geographic Magazine*, Vol. 191, No. 4, 104-131.

National and Historic Parks Branch, Department of Indian Affairs and Northern Development, Ottowa. 1972: New National Parks for Northern Canada. *Polar Record*, 16, No. 102, Cambridge University Press, 426-427.

National Park Service, September 1984: General Management Plan Glacier Bay National Park and Preserve. National Park Service, U.S. Department of the Interior, U.S. Government Printing Office, Washington, D.C., 109.

Parks Canada. 2004: *Parks Canada Agency Annual Report 2002 - 2003*. Parks Canada, Ottawa, Canada, 105.

Pryde, Phillip R. 1991: *Environmental Management in the Soviet Union*. Cambridge University Press, Cambridge, UK, 314.

Richardson, Jeffrey R. Sept./October 1992: Persistent poison three years after Exxon Valdez spill, oil and politics still taint National Parks in Alaska. National Parks, National Parks and Conservation Association. Vol. 66 No. 9-10, 24-30.

Scidmore, E. Ruhamah, 1896: *Appleton's Guide Book to Alaska and the Northwest Coast*. D. Appleton and Company, New York, 151.

Staple, Tamara and Wall, Geoffrey. 1996: Climate change and recreation in Nahanni National Park Preserve, *The Canadian Geographer*, Vol. 40, No. 2, 109 – 120.

Stirling, Ian and Derocher, Andrew E. 1993: Possible impacts of climatic warming on polar bears, *Arctic*, Vol. 46 No. 3, 240-245.

Stonehouse, Bernard. 1977: *Animals of the Arctic - The Ecology of the Far North*. Book Associates, London, 172 p.

Viken Arvid and Jorgensen, Frigg. 1998: Tourism in Svalbard, *Polar Record*, Vol. 34, No. 189, 123-128.

Yard, Robert Sterling. 1925: *The National Parks Portfolio*. National Park Service, Department of the Interior, U.S. Government Printing Office, Washington, D.C., 270.

Recent Changes in the Sea Ice Distribution in the Russian Arctic: Ice Extent, Area and Length of the Ice-free Season

João Rodrigues
Polar Oceans Physics Group, Department of Applied Mathematics and Theoretical Physics, University of Cambridge, Cambridge, UK.

Keywords: Russian Arctic, ice extent, ice area, ice-free season, Northern Sea Route

ABSTRACT. Using sea ice concentration data obtained from satellite passive microwave imagery we determine the monthly averaged position of the sea ice edge, the values of the sea ice extent and area for the White, Barents, Kara, Laptev, East Siberian, Chukchi and Bering Seas and for the Sea of Okhotsk, and investigate how they have changed during the 1979-2003 period. From the daily sea ice concentrations we derive the length of the ice-free season in each of these seas and find how this quantity has evolved in the same period.

1 INTRODUCTION

Microwave satellite data indicate that the annual average sea ice extent and area in the Northern Hemisphere as a whole has decreased by about 8% in the past 30 years [ACIA, 2004], a value compatible with an average rate of decline of 2-3% per decade calculated by Comiso and Parkinson [Comiso and Parkinson, 2004] for the 1978-2003 period. The global retreat of the summer sea ice is even more striking: over the past 30 years there was a loss of 15-20% in the summer sea ice extent [ACIA, 2004; Comiso, 2002] and in a joint press release of NSIDC, NASA and University of Washington (28/09/2005) the present rate of shrinkage of the sea ice cover at the time of the year when the minimum is reached is estimated as 8% per decade. Based on the current sea ice distribution and its current rate of decline, most climatic models predict that there will be no ice in the Arctic Ocean in the month of September by late this century.

It is the aim of this paper to describe in detail the current spatial sea ice distribution and its recent changes in each of the Russian Arctic seas – White, Barents, Kara, Laptev, East Siberian and Chukchi Seas – and in their peripheral seas – Bering Sea and Sea of Okhotsk (whose exact boundaries and approximate dimensions are given in Appendix A). Such a study may be relevant not only for regional or global climatic models but also to evaluate how a warming Arctic can modify the marine transport and the access to natural resources in the Russian Arctic. In fact, shipping through key marine routes such as the Northern Sea Route is likely to increase due to the reduction of the amount of sea ice in the traditional navigation season and to the extension of the length of the ice-free season. In eastern Siberia, which is only accessible by ship in the summer, a decrease in sea ice will help reaching remote ports such as Tiksi in the Laptev Sea and Pevek in the East Siberian Sea in longer periods. Regular trans-arctic shipping via the over-the-pole route may become a reality in the 21st century instead of just a theoretical possibility, as it is considered today.

In order to give a quantitative description of the main modifications in the ice cover of the Russian Arctic, we study the evolution of the local ice distributions in each of the Siberian seas and extract from them values for the rate of change and relative change of the sea ice extent and area; we describe the shifts in the position of the ice edge, we identify the

regions where the changes in the ice concentration are more important and quantify those changes; finally, we discuss how the length of the ice-free season has varied in some specific points (mostly along the Northern Sea Route).

We limit ourselves to report the modifications that have occurred in the recent past and avoid projections for future changes. There is not sufficient evidence to support the idea that the approximately linear decline of the sea ice extent and area will continue in coming years. In fact, a collaboration between NSIDC and NASA found a stunning reduction in Arctic sea ice at the end of the summer for the fourth consecutive year, which led the group to conclude that Arctic sea ice is probably on an accelerating, long-term decline.

The reader who is less familiar with the geography of the Russian Arctic may find useful information in the appendices. We keep the original Russian, Norwegian or English names of most geographic features, following the conventions adopted by the United Kingdom Hydrographic Office. Although the White Sea is often considered an inlet of the Barents Sea, we shall separate it from the rest of the Barents Sea because of its specific ice conditions. Consequently, when referring to the latter, we exclude the White Sea. We shall comment on the ice situation on the W coast of Spitsbergen though, strictly speaking, it belongs to the shores of the Greenland Sea.

2 ICE CONCENTRATION, EXTENT AND AREA

From Satellite Data to Sea Ice Concentrations

Thanks to the satellites that NASA has put in polar orbits since the early 1970s, we have today a vast amount of data on sea ice concentrations in the polar regions from where the recent changes in sea ice extent and area can be calculated with satisfactory accuracy for any particular portion of the ocean. The first systematic measurements of sea ice concentrations by remote sensing were performed between 1973 and 1976 by the Electrically Scanning Microwave Radiometer on board the Nimbus 5 satellite. They were followed by observations by the Scanning Multichannel Microwave Radiometer (SMMR) on board the Nimbus 7 satellite from 1978 to 1987. More recently, several satellites of the United States Defense Meteorological Satellite Program carried on board the more advanced Special Sensor Microwave Imagers (SSM/I): the satellites F8, F11 and F13 obtained data during the periods 1987 to 1991, 1991 to 1995, and 1995 to 2003, respectively. In this article we consider the data collected between January 1979 and December 2003.

In passive microwave imagery the sea ice concentration of each pixel is obtained from the corresponding brightness temperature. The extraction of the latter from the actually measured intensities at different frequencies (and, sometimes, at different polarisations) is non-trivial and requires a sophisticated algorithm. The study presented in this article uses the sea ice concentrations generated with the Bootstrap Algorithm. The latter is described in [Comiso, 1986; Comiso, 1990; Comiso, 1995], while the actual sea ice concentration data sets [Comiso, 1999] are archived and distributed by the National Snow and Ice Data Center. According to [Comiso, 1999], the overall retrieval accuracy is estimated as 5-10%, except in some unusual circumstances such as the presence of a large fraction of thin ice or meltponding within the cell or the occurrence of stormy weather conditions, especially near the ice edge. Other commonly used algorithms include the AES [Swift et al., 1985], the NORSEX [Svendsen et al., 1983] and the NASA Team [Cavalieri et al., 1990] algorithms.

Although in general the results from different algorithms are in reasonably good agreement, there are non-negligible discrepancies in some regional distributions.

The calculated concentrations are projected onto a 25km x 25km polar stereographic grid which we shall call the NSIDC grid. SSMR data were collected every other day and SSM/I data every day. The NSIDC data sets include files with daily and monthly averaged sea ice concentrations.

Trends in Ice Extent and Area

We assume that the sea ice concentrations have been derived from satellite data and mapped onto a grid with equal area cells and adopt the following definitions of sea ice extent and sea ice area, as in [Zwally et al., 1990]. The sea ice extent E in a limited portion of the ocean is the sum of the areas of the cells within the boundaries of that portion of the ocean with at least a sea ice concentration of 0.15. If Ci is the ice concentration of the cell (or pixel) i, of area a=625km^2, then the total sea ice extent can be written as

$$E = \sum_i a\theta(C_i - 0.15) \tag{1}$$

where the sum runs over all the cells within the boundaries of that portion of the ocean and the function $\theta(x)$ is such that $\theta(x)$=0 for x<0 and $\theta(x)$=1 for x≥0. The effects of taking a different value for the lower cutoff in the previous equation will be considered. The sea ice area A in a certain portion of the ocean, which is the area of that portion of the ocean actually covered by sea ice, is given by

$$A = \sum_i aC_i \tag{2}$$

where the sum runs over all the cells within the boundaries of that portion of the ocean and the concentrations C_i are in the range (0,1).

For the calculation of the extent and area of the sea ice cover in each region we use the NSIDC monthly averaged sea ice concentrations. Thus, for each month m and for each year y between 1979 and 2003, we define the quantities $E_m(y)$ and $A_m(y)$.

For a given month, sea ice distributions normally exhibit a strong year-to-year variability. In most cases, though, it is possible to detect long term trends in the sea ice extent and area by finding the best linear fit to the extent-time and area-time graphs. In this work we determine the best straight line that fits a graph with a linear least squares regression. With this method we construct the new functions $E'_m(y)$ and $A'_m(y)$ which, for each month m, vary linearly with the year y. Although these functions have, in general, different values from the actually observed ones, they are more adequate than the latter to identify long term trends.

For each month m, we assume that the gradient of the linear functions $E'_m(y)$ and $A'_m(y)$ gives the rate of change of the extent and area, respectively, during the 1979-2003 period. It is measured in km^2/year and, together with the value of the total area of the sea; it should give a clear idea on how fast the ice is retreating (or advancing, as it happens in a few particular cases). For each month m and for each sea, the *relative change* of the sea ice extent between 1979 and 2003 is defined as the ratio

$$\frac{\Delta E'_m}{E'_m(1979)} \equiv \frac{E'_m(2003) - E'_m(1979)}{E'_m(1979)} \tag{2}$$

with a similar definition for the relative change in sea ice area. Throughout this paper the quantities $E'_m(1979)$ and $E'_m(2003)$ are often referred to as early and late ice extents, with analogous definitions for early and late ice areas.

The above definitions are not unique. In Section 3, while attempting to describe the evolution of the edge of the ice pack between 1979 and 2003, we will be naturally led to define those quantities in a different way, and to find slightly different values for some of them. In view of such ambiguities, the tables presented in the next section must be considered with caution (especially in what concerns the ice extent).

Tables of Ice Extent and Area

Tables 1-8 summarise the changes in sea ice extent and area in each of the eight Siberian seas between 1979 and 2003. The rate of change and relative change were calculated from linear regression of the actually observed ice extent and area as explained in the previous section. The ice extent was defined with the 0.15 threshold.

Table 1. Changes in the sea ice extent and area in the White Sea. The cases where linear regression is not valid are marked with (*).

Month	EXTENT		AREA	
	Rate of change (10^2 km^2/year)	Relative change (%)	Rate of change (10^2 km^2/year)	Relative change (%)
January	-1.1	-2.8	-4.3	-13.8
February	0	+0.1	-2.3	-6.6
March	+0.1	+0.2	-2.8	-8.5
April	+0.1	+0.4	-4.2	-14.7
May	-9.2	-28.8	-8.2	-49.5
June	(*)	(*)	(*)	(*)
July	(*)	(*)	(*)	(*)
August	0	0	0	0
September	0	0	0	0
October	(*)	(*)	(*)	(*)
November	-12.4	-65.1	-5.6	-70.8
December	-5.2	-15.7	-5.6	-30.4

Table 2. Changes in the sea ice extent and area in the Barents Sea.

Month	EXTENT		AREA	
	Rate of change (10^2 km^2/year)	Relative change (%)	Rate of change (10^2 km^2/year)	Relative change (%)
January	-6.2	-16.1	-6.7	-21.0
February	-4.5	-11.3	-5.4	-16.1
March	-4.6	-11.2	-5.6	-16.3
April	-7.0	-16.3	-8.4	-22.6
May	-6.4	-16.4	-7.3	-23.3
June	-9.1	-27.6	-7.9	-34.8
July	-7.6	-36.7	-4.7	-39.3
August	-2.0	-24.5	-1.4	-29.6
September	+0.4	+6.8	-0.1	-4.2
October	-1.1	-8.1	-0.7	-8.4
November	-0.8	-3.1	-0.5	-2.9
December	-3.2	-9.9	-4.3	-16.7

Table 3. Changes in the sea ice extent and area in the Kara Sea.

Month	EXTENT		AREA	
	Rate of change (10^2 km^2/year)	Relative change (%)	Rate of change (10^2 km^2/year)	Relative change (%)
January	0	0	-0.1	-0.4
February	0	0	-0.2	-0.6
March	0	0	-0.3	-1.0
April	0	0	-0.6	-1.9
May	0	0	-1.4	-4.3
June	-0.5	-1.5	-3.0	-10.0
July	-5.7	-17.3	-5.6	-23.9
August	-5.0	-24.9	-3.5	-28.8
September	-0.6	-5.2	-1.8	-21.5
October	-1.2	-4.7	-1.4	-7.6
November	0	0	-0.8	-2.6
December	0	0	-1.0	-3.2

Table 4. Changes in the sea ice extent and area in the Laptev Sea.

Month	EXTENT		AREA	
	Rate of change (10^2 km^2/year)	Relative change (%)	Rate of change (10^2 km^2/year)	Relative change (%)
January	0	0	0	0
February	0	0	-0.1	-0.4
March	0	0	-0.2	-0.9
April	0	0	-0.2	-0.7
May	0	0	-0.3	-0.9
June	-0.5	-1.9	-2.0	-7.7
July	-2.2	-7.8	-4.5	-19.8
August	-6.7	-31.1	-5.4	-36.4
September	-5.3	-25.9	-4.0	-30.3
October	0	0	-2.8	-10.8
November	0	0	-0.1	-0.5
December	0	0	0	0

Table 5. Changes in the sea ice extent and area in the East Siberian Sea.

Month	EXTENT		AREA	
	Rate of change (10^2 km^2/year)	Relative change (%)	Rate of change (10^2 km^2/year)	Relative change (%)
January	0	0	+0.1	+0.2
February	0	0	-0.2	-0.5
March	0	0	-0.2	-0.5
April	0	0	-0.2	-0.4
May	0	0	-0.3	-0.8
June	0	0	-2.0	-5.6
July	-0.3	-0.7	-6.1	-18.7
August	-8.3	-24.2	-10.5	-39.3
September	-11.9	-36.8	-12.1	-46.5
October	-0.1	0	-6.6	-18.3
November	0	0	0	0
December	0	0	+0.2	+0.6

Table 6. Changes in the sea ice extent and area in the Chukchi Sea.

Month	EXTENT		AREA	
	Rate of change (10^2 km^2/year)	Relative change (%)	Rate of change (10^2 km^2/year)	Relative change (%)
January	0	0	0	+0.1
February	0	0	0	0

March	0	0	0	-0.1
April	0	0	0	-0.1
May	0	0	-1.3	-5.6
June	-2.6	-10.9	-3.5	-17.4
July	-4.0	-21.3	-4.5	-32.0
August	-3.6	-29.4	-4.0	-48.8
September	-7.1	-62.0	-5.9	-73.8
October	-6.3	-39.0	-5.8	-49.0
November	-4.5	-18.4	-5.5	-28.0
December	0	0	-0.4	-1.8

Table 7. Changes in the sea ice extent and area in the Bering Sea.

Month	**EXTENT**		**AREA**	
	Rate of change (10^2 km^2/year)	Relative change (%)	Rate of change (10^2 km^2/year)	Relative change (%)
January	+8.4	+32.5	+6.8	+36.9
February	+4.3	+13.2	+4.5	+18.7
March	-0.6	-1.7	+0.5	+1.7
April	+0.9	+2.9	+0.6	+2.4
May	-0.4	-2.1	-0.6	-6.2
June	+0.5	+23.5	+0.2	+21.7
July	0	0	0	0
August	0	0	0	0
September	0	0	0	0
October	0	0	0	0
November	-0.7	-11.2	-0.3	-9.4
December	+3.7	+20.4	+1.9	+16.4

Table 8. Changes in the sea ice extent and area in the Sea of Okhotsk.

Month	**EXTENT**		**AREA**	
	Rate of change (10^2 km^2/year)	Relative change (%)	Rate of change (10^2 km^2/year)	Relative change (%)
January	-7.1	-15.5	-8.0	-24.1
February	-5.7	-9.9	-6.3	-13.4
March	-4.5	-7.5	-5.9	-12.2
April	-9.6	-19.6	-10.7	-31.5
May	-6.4	-33.6	-3.2	-32.6
June	-2.2	-50.1	-1.0	-51.3
July	0	0	0	0
August	0	0	0	0
September	0	0	0	0
October	0	0	0	0
November	-0.1	-3.3	-0.2	-20.6
December	+2.8	+16.0	+1.7	+18.0

3 CHANGES IN ICE EXTENT AND IN THE POSITION OF THE ICE EDGE

Introductory Remarks

In this section we describe the recent changes in the values of the ice extent as well as in the position of the ice edge in each of the Russian Arctic seas, in the Bering Sea and in the Sea of Okhotsk. We present plots with the values of the observed ice extents from 1979 to 2003 for some chosen months, together with the corresponding best linear fits (dashed lines). In the Kara, Laptev, East Siberian and Chukchi Seas it is natural to select the summer months (the navigation season) because in all others the ice extent is trivial (100% or near 100% of the total area of the sea). In the White Sea, Bering Sea and Sea of Okhotsk there is normally no ice in the summer and thus we illustrate the changes in some winter, spring and autumn months. In the Barents Sea we chose to show the situation at the end of each season.

We also offer maps with the typical positions of the edge of the ice pack, here defined as the 0.15 concentration contour, at the beginning and at the end of the 1979-2003 period, which were constructed in the following way. For a certain month m we find the best linear fit (using the least squares fitting technique) of the $C_{i,m}(y)$ curves (one for each pixel i); the result is a new set of functions $C'_{i,m}(y)$, one for each pixel i, that vary linearly with y. The early and late concentrations for each pixel i are then defined as $C'_{i,m}(1979)$ and $C'_{i,m}(2003)$, respectively. For each sea, the *early* and *late* ice edges are defined as the set of points j for which $C'_{j,m}(1979)=0.15$ and $C'_{j,m}(2003)=0.15$, respectively. The early and late positions of the ice edge are shown in the diagrams as red and blue contours, respectively. Its average position during the 1979-2003 period is represented by the green line.

Early and late ice extents can now be determined from the position of the early and late 0.15 concentration contours and early and late ice areas from the new distributions $C'_{j,m}(1979)$ and $C'_{j,m}(2003)$. The values of the early and late ice extents obtained with this method (hereafter referred to as method two) do *not* coincide with $E'_m(1979)$ and $E'_m(2003)$, respectively, and, consequently, the corresponding rate of change and the relative change in ice extent are *different* from the ones that appear in Tables 1-8, which were calculated in a different way. Close agreement (within the margin of error estimated for the retrieval of the ice concentrations) is found in most cases but there are a few situations where the discrepancies are non-negligible. The two methods lead to identical values for the ice area, though.

The fact that different methods lead to different results for the ice extent is not surprising. The root of the discrepancy lies on the presence of the non-linear θ function in the definition of extent. Because the definition of extent requires a lower cutoff, to calculate the ice extent first and then find the best linear fit does not yield the same result as to find the best linear fit for the ice concentrations first and *then* calculate the extent. We consider that both approaches are valid and refrain from eliminating one in favour of the other. It is also worth noting that, although in general there is a good agreement between the results obtained for rates of change and relative variations with a lower threshold of 0.15 and one of 0.30, in some cases, the differences are significant. This discussion suggests that, in order to avoid ambiguities, the determination of the changes in ice extent based on a process of linearisation of the data must specify the procedure used.

White Sea

The White Sea is always totally clear of ice in August and September and almost always totally clear of ice in October. Since 1991 no large portions of the White Sea froze in October.

Ice formation is likely to start in November near the shores, although in six seasons no ice was present at this time of the year, all of them between 1991 and 2003. The relative change in sea ice extent in November between 1979 and 2003 was the highest observed in the Siberian seas at any time of the year. Values for the ice extent close to 90% were commonly observed in December in the early 1980s but presently it is not rare to find the central part of the White Sea free of ice. In every January, February, March and April ice is essentially everywhere.

The May ice cover has large fluctuations: the probability of an ice extent above 95% is 40% but, for instance, in 1995 the White Sea was already totally free of ice. The changes in the ice distribution occurred especially in the central White Sea, a vast portion of which can now be free of ice at this time of the year, something unlikely around 1979.

The changes in the sea ice extent in the months of June and July are clearly non-linear. Instead, there is a striking contrast between the ice extent in the first and second halves of the 1979-2003 period. While before 1989 there was always some ice in June, normally in more than 75% of the total area of the sea, in the 1989-2003 period there was no ice in ten seasons. Between 1980 and 1987 there was always some ice in July, with the ice extent reaching 71% in 1982, but since 1988 no ice has been observed in July.

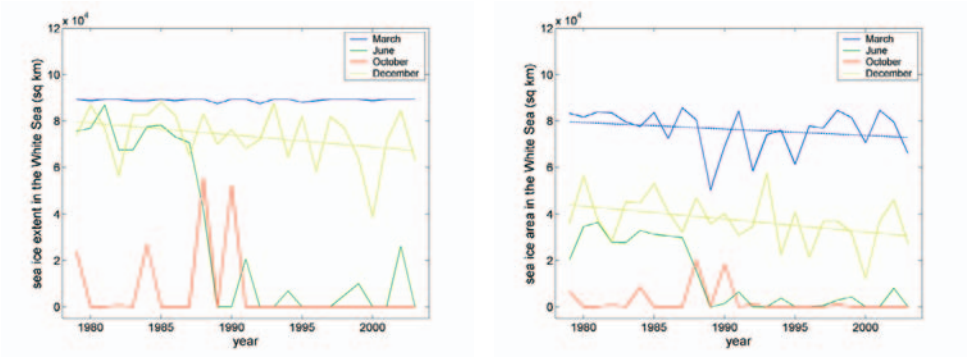

Figure 1. Sea ice extent (left) and sea ice area (right) in the White Sea the 1979-2003 period.

Barents Sea

In September, normally the month of minimum extent, when most of the Barents Sea is free of ice, the changes in ice extent and in the position of the ice edge are small compared to the changes that occurred in the other months (with the possible exception of November). When calculated with the first method (described in Section 2.2) the relative change in ice extent is positive, while when calculated with the second method (described in Section 3.1), it is negative (approximately –9%). This is one of the four cases in which different methods lead to opposite changes in ice extent (the others are in the Kara Sea and in the Bering Sea) and it illustrates the ambiguities associated in the calculation of the ice extent changes based on linear regression. It is also worth noting that taking a cutoff of 0.30 (instead of the usual

0.15) we find a reduction in ice extent (relative change about –1.5%) with method one and no variation with method two. This is the only case among all eight seas in which the relative variation in ice extent changes sign when the cutoff is raised from 0.15 to 0.30.

The changes in the October ice extent and ice edge are also comparatively small and in November the position of the ice edge has been stable.

The boundary of the December ice-pack in the central Barents Sea moved northwards since 1979 except in the region between Bjørnøya and 28°E, where it has been stable. Changes have also been observed in the W boundary of the ice pack; the sea between Bjørnøya and the S tip of Spitsbergen is now likely to be free of ice, which was not the case in the late 1970s, when the W ice edge was clearly W of the line joining Bjørnøya and Sørkappøya.

January exhibits the largest variation in ice extent of the winter months. Modifications in the boundaries of the pack occurred everywhere except in the region between Bjørnøya and 28°E, where the ice edge has been stationary. In the central Barents the ice limit is now located at approximately 76°N while in the early years of the 1979-2003 period it was as far S as 73°N at a longitude of 38°E.

In February and March there are essentially no changes in the W limit of the ice pack. The main changes occurred in the central part of the Barents Sea, mostly in the region between 36°E and 48°E, where the edge of the pack is now at around 75°N. In the early years of the 1979-2003 period the boundary of the pack was at about 73°N roughly between 38°E and 44°E and there was ice all over the portion of the Barents Sea E of the latter meridian.

April is statistically the month of greatest ice extent (with February and March coming very close). The largest changes took place in the S and central Barents Sea. In the S sector, say from 68°N to 72°N, the boundary of the ice pack moved eastwards from about 40°E to 43°E at about 70°N and to 47°E at about 72°N. The ice limit is now just 70 miles off the W coast of Novaya Zemlya at a latitude of 73°N. In the central Barents Sea, approximately between 72°N and 75°N, there was a big shift in the position of the edge of the pack in the NE direction, in some areas as large as 170 miles. The qualitative changes in the May ice boundaries are similar to those of April.

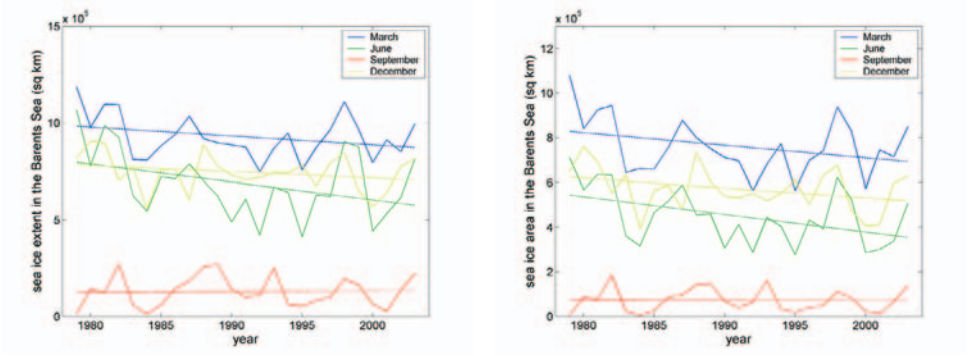

Figure 2. Sea ice extent (left) and sea ice area (right) in the Barents Sea during the 1979-2003 period.

In June the Barents Sea had the second highest rate of loss in ice extent in the Russian Arctic in any month, mostly because of an improvement in the ice conditions in the E sectors. Large portions with ice in the S Barents are currently restricted to the areas between the S coast of Novaya Zemlya and the coast of mainland Russia and between the SE coast of Ostrov Kolguyev and the coast of Malozemel'skaya Tundra.

The absolute decrease in ice extent in July since 1979 was also comparatively large, which led to the greatest relative change of all months, between 31 and 39%, depending on the method used and on the choice of the cutoff. The main changes occurred in the vast area between Svalbard and Novaya Zemlya, where the ice edge was earlier roughly at 76°30'N (except in the vicinity of the W coast of Novaya Zemlya, where it was as low as 75°N) while now it lies normally above 77°N (except, again, the waters near the W coast of Novaya Zemlya, where it is approximately at 76°30'N) and, in particular, at 78°N between 38°E and 46°E.

In August the rate of change in ice extent is more modest than in all previous months since January but the relative change is the third most important. The average position of the ice edge and its changes between 1979 and 2003 are similar to those described above for the month of September except in the region between Zemlya Frantsa Iosifa and Novaya Zemlya. The whole W coast of Novaya Zemlya is now likely to be ice-free in August. In fact, at the longitude of Mys Zhelaniya the ice edge lies now at about 78°N, meaning that the passage N of Novaya Zemlya is expected to be free of ice.

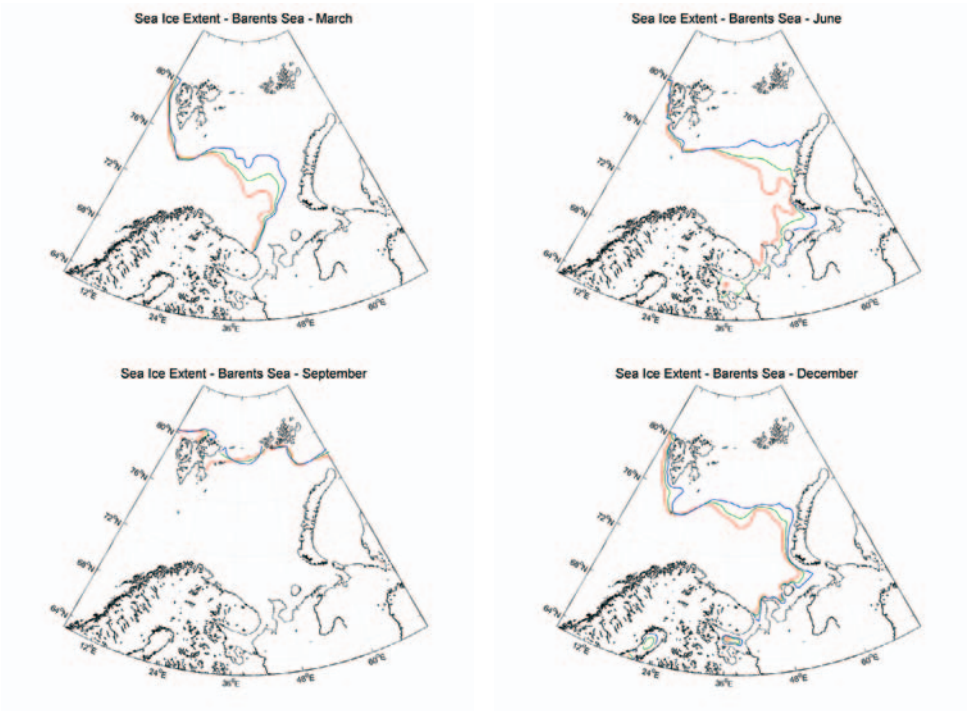

Figure 3. Changes in the sea ice edge in the Barents and White Seas.

Kara Sea

Ice fills the Kara Sea from December to May. The average ice extents in November and June are 97% and 99%, respectively, with no particular trends observed. The significant changes occur in the summer months.

The 25-year averaged ice extent in July is 89% but while earlier there was ice essentially all over the Kara Sea there is now a large region of the S Kara Sea which is likely to be free of ice. In July (as well as in the other summer months) there are comparatively large discrepancies between the results for the ice extent obtained with the two different methods. When calculated with the second method, the rate of change and the relative change drop to about $-3x10^3$ km^2/y and –8%.

August is when the relative variation of the ice extent calculated with method one has its largest value, for both values of the cutoff. However, when calculated with method two (and, for instance, a cutoff of 0.15), its value is about 10% lower than the value shown in Table 3, and, in fact, lower than the value obtained for September with the same method. One of the most interesting changes in the position of the August ice edge took place on the E coast of Novaya Zemlya; the latter was earlier free of ice S of 75°N but now ice is likely to be present in a band (less than 30 miles wide) that extends from Mys Men'shikova (at the entrance of Proliv Karskiye Vorota) to Mys Sporyy Navolok (at approximately 76°20'N). This feature makes the E coast of Novaya Zemlya one of the few regions of the Russian Arctic where the amount of ice has increased in the past 25 years. The N tip of Novaya Zemlya and the direct route from that point to Dikson are likely to be free of ice at this time of the year.

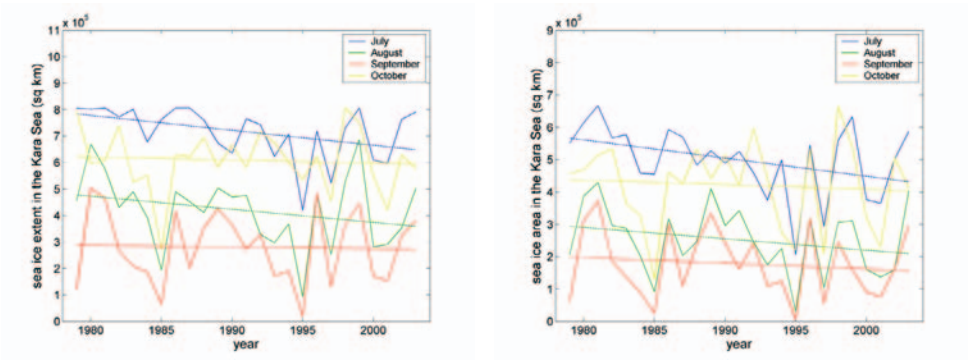

Figure 4. Sea ice extent (left) and sea ice area right) in the Kara Sea during the 1979-2003 period.

September is by far the month of minimum ice extent: in an average season 35% of the total area of the sea, much less than in August (52%) and in October (75%). The most significant feature of the modifications of the September ice edge between 1979 and 2003 is its displacement in the NE direction by 40-80 miles.

There is a clear contradiction between the limits of the October ice pack depicted in Figure 5 and the values shown in Table 3; this is, again, one of the few cases where the two methods produce results with opposite signs. In fact, it can be seen in the October ice diagram that the edge of the pack has shifted southwards, a variation which is not compensated by the

reduction in ice extent in Baidaratskaya Guba. This observation is compatible with the value +2% calculated for the overall relative variation in ice extent with method two.

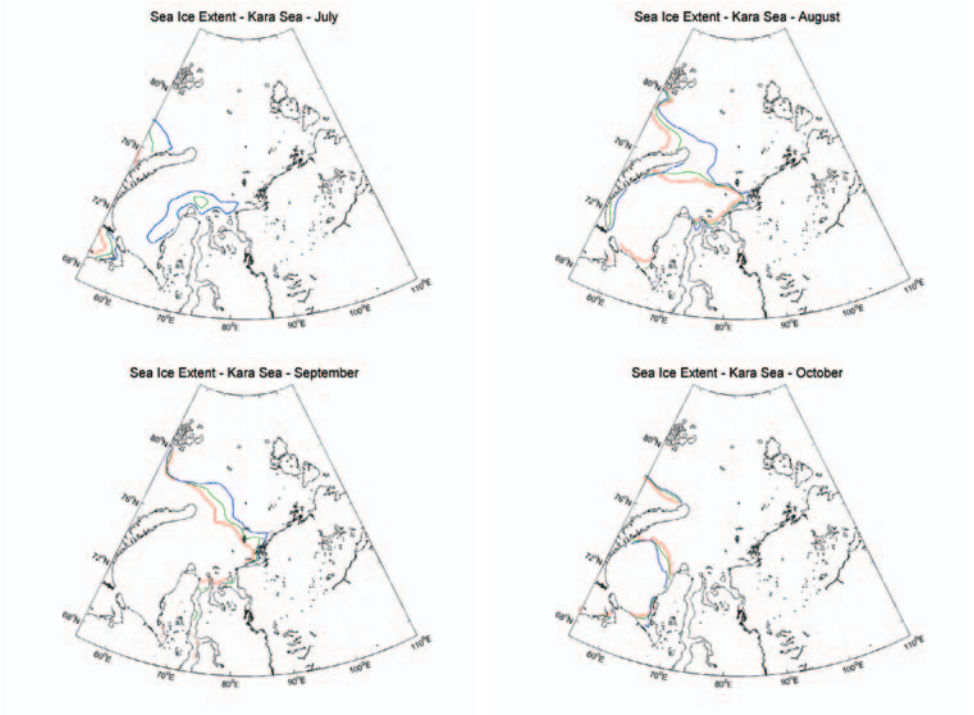

Figure 5. Changes in the sea ice edge in the Kara Sea.

Laptev Sea

Every year there is ice over the whole Laptev Sea from October to May. In June the ice extent can sporadically reach values as low as 90% of the total area of the Laptev Sea but almost every year it is above 95%. In July the ice extent is above 90% in four out of five seasons.

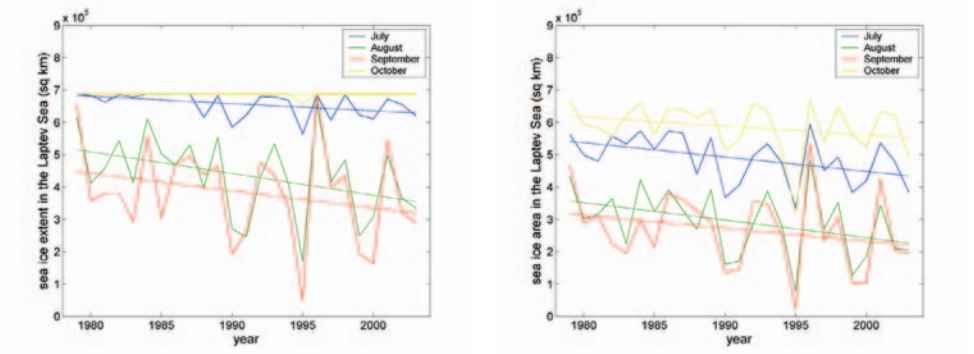

Figure 6. Sea ice extent (left) and sea ice area (right) in the Laptev Sea during the 1979-2003 period.

The average ice extent in August between 1979 and 2003 was 63% but values between 25% (in 1995) and 96% (in 1996) were observed during this period. The rate of decrease and the relative decrease were larger than in all other months for both methods and values of the cutoff. The size of the ice-free portion of the Laptev Sea is today about twice the size it was in the late 1970s at this time of the year.

September is almost always the month of minimum extent. The average value between 1979 and 2003 was 56% but, as in the previous months, large fluctuations occurred; in 1995, for instance, the extent was as low as 7% while in the following year it was 100%. Overall, the changes are less striking than in August, especially when the second method of calculation is used: then the rate of change drops to –0.4x103 km2/y and the relative extent to –2%. In fact, as the diagrams show, there is little change in the position of the September ice edge.

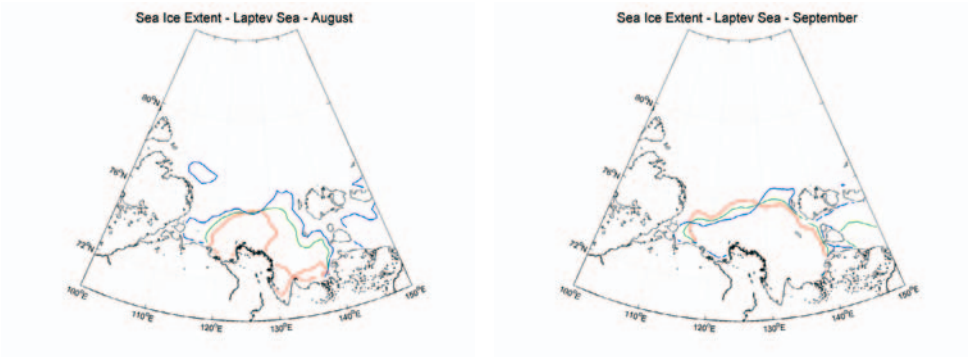

Figure 7. Changes in the ice edge in the Laptev Sea.

East Siberian Sea

In every year ice covers the whole East Siberian Sea from October to June. In July the 25-year averaged ice extent was 98% of the total area of the sea.

The average sea ice extent in August was 79% (it was 100% on three occasions, all of them before 1986, and just 20% in 1990). The current position of the August ice edge is completely different from its position in 1979, in agreement with observed very large average loss of ice per year (the largest among all seas in this month). However, because the N boundary of the East Siberian Sea lies quite far N, most of the sea remains ice-covered throughout the year. This is the reason why the relative variation in ice extent quoted in Table 5 is not particularly large. Around 1979 almost the whole East Siberian Sea used to be covered with ice at this time of the year, the exception being a comparatively small region near the shores, roughly between 160°E and 163°E. Now the whole N coast of Russia from the E entrance of Proliv Dmitriya Lapteva to Mys Shelagskiy (70°06'N, 170°25'E) is likely to be free of ice except, possibly, in a band a few miles wide adjacent to the coast between the mouth of Reka Kolyma and Ostrov Ayon. The edge of the pack is expected to be at least 50 miles away from the coast.

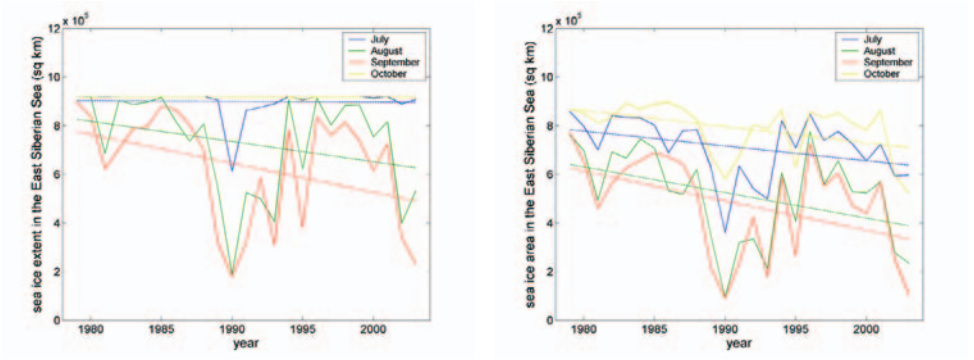

Figure 8. Sea ice extent (left) and sea ice area (right) in the East Siberian Sea during the 1979-2003 period.

In September the East Siberian Sea had the highest rate of decrease in ice extent of all eight seas and, as a consequence, the position of the September ice edge showed an immense change during the 25-year period. While earlier in that period there was ice in almost all East Siberian Sea except in the region next to the mouth of Reka Kolyma, now one expects the presence of a very wide band free of ice along the N coast of Russia from the Severnaya Zemlya Straits to the W entrance of Proliv Longa. This band has its smallest width (about 40 miles) at approximately 160°E. From that point eastwards to the entrance of Proliv Longa its width is roughly 70-100 miles.

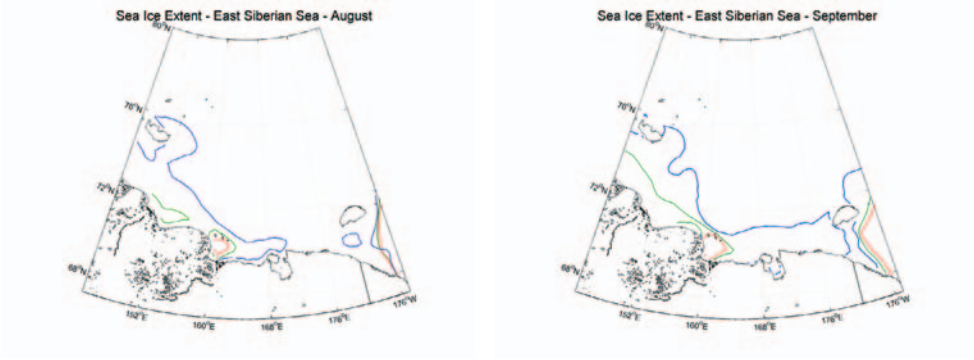

Figure 9. Changes in the sea ice edge in the East Siberian Sea.

Chukchi Sea

The ice cover in the Chukchi Sea is total from December to May and 92% in November. In all other months there was a decrease whose magnitude depends (more than anywhere else) on the method used. Typically, method two leads to smaller values for the rate of change and relative change in ice extent, with differences of about 10% for the latter quantity in August and October and as high as 18% in November.

The 0.15 ice concentration contour throughout the summer and autumn resembles an arc of a circle joining a point on the coast of Russia to a point on the coast of Alaska. The exception is the current ice edge in September, which clearly diverges from an arc on the E sectors.

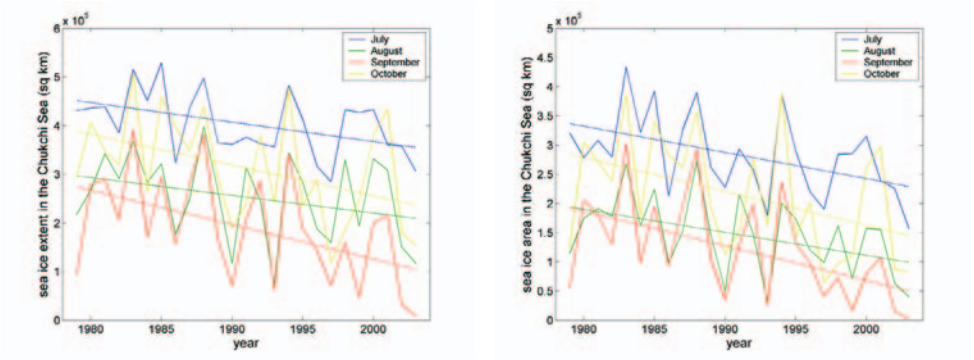

Figure 10. Sea ice extent (left) and sea ice area (right) in the Chukchi Sea during the 1979-2003 period.

In an average June ice is present in 92% of the area of the Chukchi Sea. In the early years of the period under study the ice extent was almost total, leaving only the Bering Strait and its immediate vicinity without ice. Presently the ice-free zone at this time of the year extends further N up to 67°30'N but it does not include any portion of the coasts of Russia or Alaska N of the Bering Strait or Kotzebue Sound.

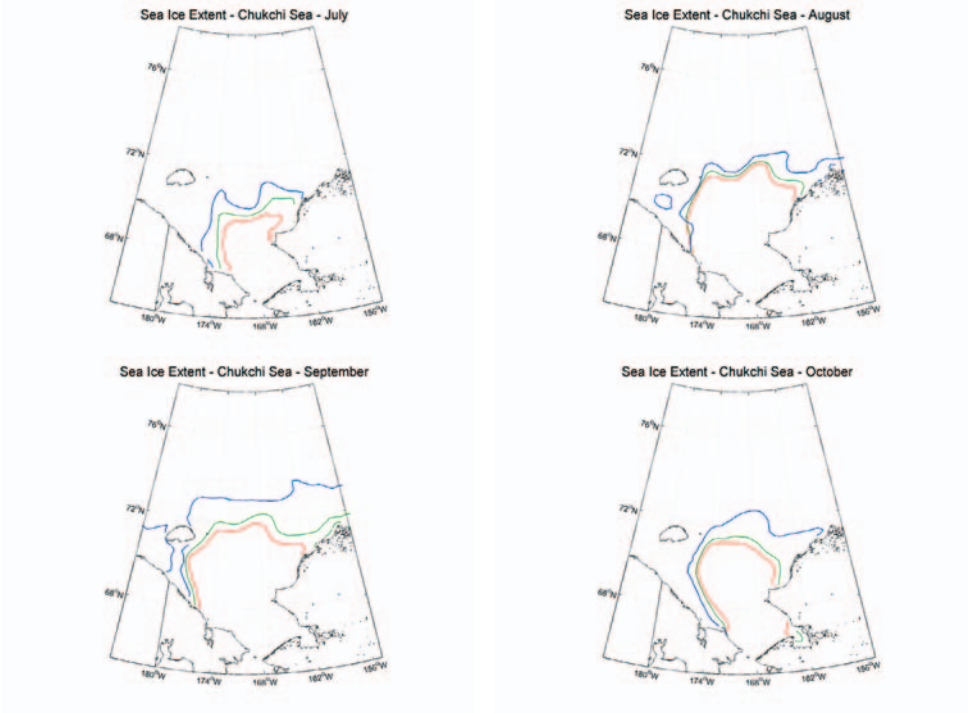

Figure 11. Changes in the ice edge in the Chukchi Sea.

We can describe the main modification in the limits of the ice-free waters in July as an increase in the radius of the arc of circumference mentioned above with a magnitude such that the NW coast of Alaska is now likely to be free of ice up to about 162°W. In August the changes in the position of the ice edge are qualitatively similar to those of the previous month

but with a less striking outwards displacement. The main differences lie in the E Chukchi; in the early years of the period under study the ice edge met the coast of Alaska near Icy Cape while now the whole coast of Alaska W of Point Barrow is likely to be free of ice.

September, statistically the month of least extent (on average 33% of the total area of the sea), has the largest relative reduction in ice extent of all Siberian seas in all months for both values of the cutoff and methods of calculation (with the possible exception of the White Sea in June, July or October where, however, the amount of ice is much smaller). In September 2003 the ice extent had its minimum value for 25 years, when ice was found in just 1.5% of the Chukchi Sea. The whole coast of Alaska is now likely to be free of ice while earlier ice would be expected E of Icy Cape.

In October the Chukchi Sea exhibits both the largest rate of change and the largest relative change in ice extent among the eight seas. The qualitative trends are the same as in the previous months.

Bering Sea

There is no ice in the Bering Sea between July and October. In November, the average ice extent is just 6%.

In December there was a 30-40 miles shift in the boundary of the ice pack in the southwards direction, which is reflected in an overall relative increase in sea ice extent higher than 20%, the largest of the two positive variations observed in this month (the other took place in the Sea of Okhotsk). In January one observes the greatest increase in the rate of change and in the relative change in ice extent of all Siberian seas at any time of the year, a result which is independent of the choice of threshold and method. This increase is the result of a southwards shift of the ice edge estimated in 50-80 miles in the region of the central Bering Sea between 180° and 160°W. In February there was also a southwards shift of the same order of magnitude in the position of the ice edge between 170°E and 170°W.

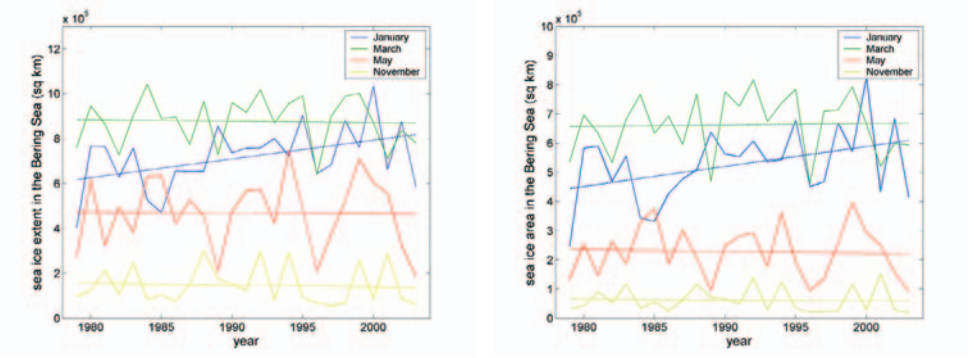

Figure 12. Sea ice extent (left) and sea ice area (right) in the Bering Sea during the 1979-2003 period.

March is on average the month of maximum extent (with February and April close runners-up). The only interesting changes occurred in the region between 170°E and 178°E where the boundary of the ice pack was displaced in the southwards direction by 25-40 miles. Altogether the variation of the ice extent is minimal. In April the ice edge remained approximately stationary during the 1979-2003 period.

There are only minor changes in the position of the ice edge and in the value of the ice extent in May. In June the ice extent is approximately 2% of the total area of the Bering Sea and no trends are detected.

The above observations imply that the Bering Sea is the only one of the eight Siberian seas where there has been a recent significant increase in sea ice extent in several periods of the year.

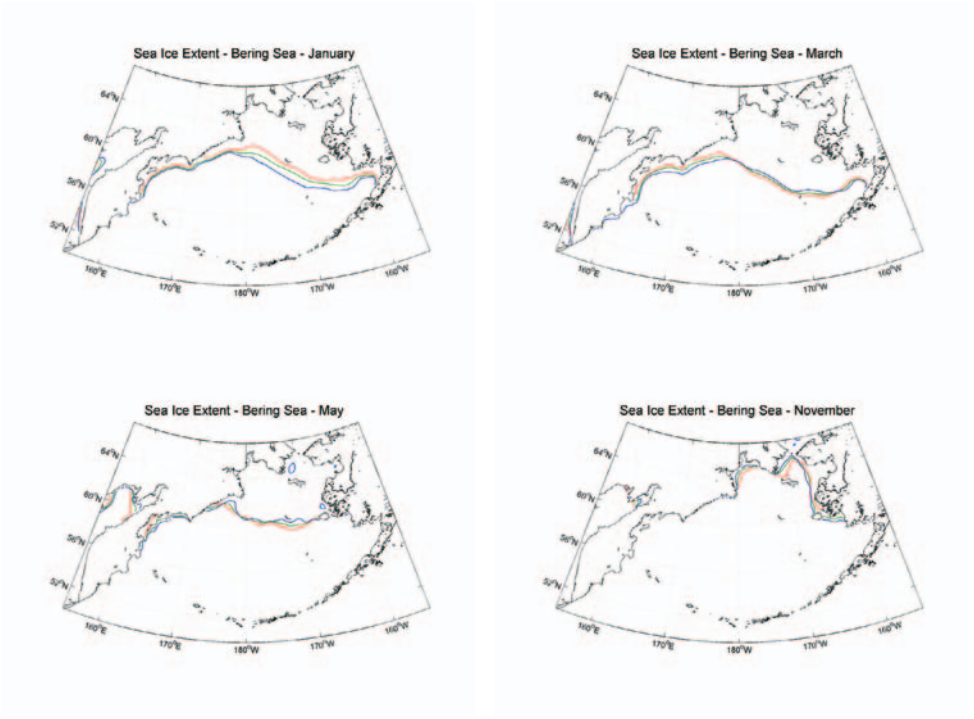

Figure 13. Changes in the ice edge in the Bering Sea.

Sea of Okhotsk

There is no ice in the Sea of Okhotsk between July and October and the average ice extent in November is just 3% of the total area of the sea. In December there was a small increase in ice extent, mostly due to changes that occurred near the E coast of Sakhalin, where the ice edge extends now further away from the coast and further S than in 1979. In January, on the contrary, there was a significant reduction in ice extent from 1979 to 2003 mainly because of the changes that took place in the central Sea of Okhotsk, which is now likely to be (partly) free of ice.

February and March have similar ice conditions (average extent 71% and 75% respectively), similar positions of the ice edge, similar values for the rate of change and relative change of ice extent and similar changes in the position of the boundaries of the ice pack, the most noticeable of which is the westwards displacement of the ice edge in the SE sector.

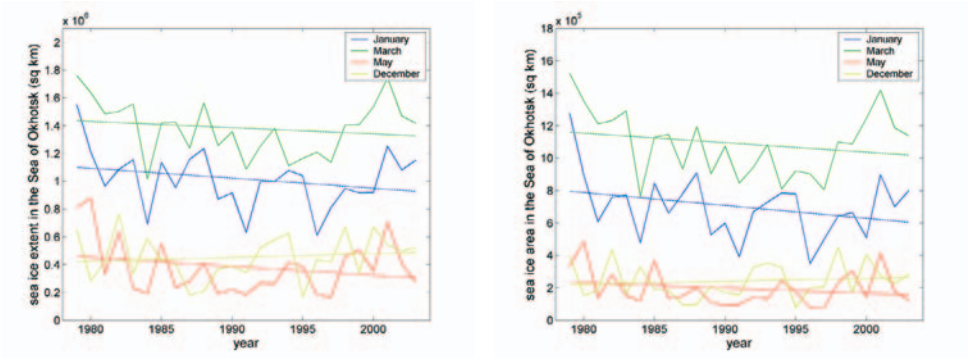

Figure 14. Sea ice extent (left) and sea ice area (right) in the Sea of Okhotsk during the 1979-2003 period.

The rate of change in ice extent in April is higher than in all other Siberian seas in the same month. In the late 1970s the boundary of the ice pack was typically a line joining a point on the W coast of Kamchatka at approximately 56°N to the NE tip of Iturup and most of the NE coast of Hokkaido was still ice-covered. Now the ice edge lies much further W (between 70 and 170 miles) in such a way that the whole chain of the Kuril Islands and most of the coast of Hokkaido are likely to be ice-free.

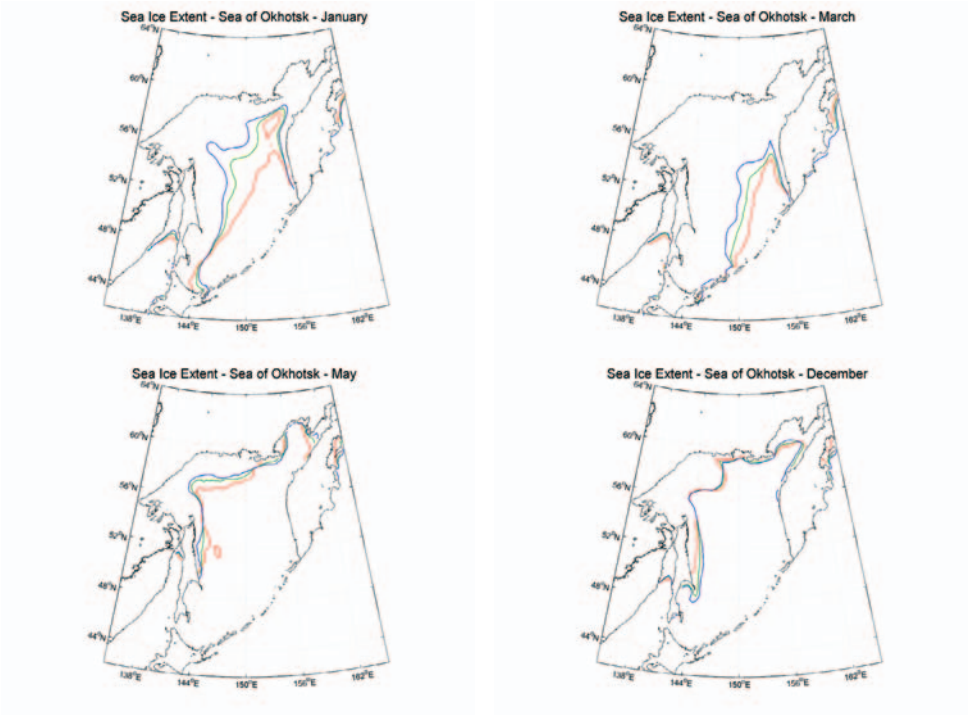

Figure 15. Changes in the sea ice edge in the Sea of Okhotsk.

In May we note a northwards displacement of 35-70 miles in the position of the ice edge in the NW sector and a reduction of about 50% in the width of the band of ice adjacent to the E coast of Sakhalin. In June the Sea of Okhotsk is again almost totally free of ice.

4 CHANGES IN ICE CONCENTRATIONS AND AREA

Introductory Remarks

From C'i,m(1979) and C'i,m(2003), the early and late sea ice concentrations defined in Section 3.1, we can derive the early and late ice areas which, as mentioned before, coincide with the ones obtained by linear regression of the actually measured ice areas throughout the period in study. Thus, the rate of change and the relative change in ice area don't suffer from the severe problems that affect the determination of the rate of change and relative change in ice extent due to the presence of the lower cutoff in the definition of the latter. From the purposes of identifying trends, the ice area appears as a cleaner variable.

In order to easily visualise the current distribution of the sea ice concentrations and the way this distribution changed between 1979 and 2003 we present contour diagrams for the functions $C'_m(2003)$ and $\Delta C'_m \equiv C'_m(2003) - C'_m(1979)$ in some selected months. When labelling the ice concentration contour lines, we use percentages instead of absolute values from zero to one.

Since almost all variations of the ice concentrations (and, accordingly, those of the ice areas) are negative, we shall often omit the word negative. In the rare situations where there is an increase in concentration or area we shall clearly state that the variation is positive.

White Sea

As stated in Section 3.2, there is no ice in the White Sea in August and September and no linear trends can be identified in October or July, when ice was present only four and eight times, respectively, in 25 years.

In November and December the White Sea has the largest relative decrease in ice area of all Siberian seas. The main modifications in the distribution of the ice concentrations took place in the inner parts of Onezhskaya Guba and Dvinskaya Guba, where around 1979 they were typically in the interval 0.40-0.70 and now they are below 0.30. Such impressive changes are only matched (at this time of the year) by those that were observed in the central and W Chukchi Sea. In December, a decrease of about 0.20 occurred essentially all over the White Sea with the exception of the S coast of Kol'skiy Poluostrov, where no appreciable alterations in the ice distribution occurred.

In January, February and March there was a reduction in ice concentration of approximately 0.10 all over the White Sea. In April the average decrease was in the interval 0.10-0.20.

The largest variations in May, between 0.20 and 0.30, took place in Onezhskaya Guba, Dvinskaya Guba and Kandalakshskiy Zaliv, while in the central White Sea the change was of the order of 0.10. The June ice cover in the White Sea is disappearing fast: from 1979 to 2003 there was a decrease of approximately 0.20 in the ice concentrations in the central areas and above 0.50 in Onezhskaya Guba, Dvinskaya Guba and Kandalakshskiy Zaliv. The White Sea is now likely to be totally or almost totally ice-free in June.

The relative loss of ice in the White Sea in spring and autumn has been higher than anywhere else in the Russian Arctic.

Barents Sea

September, with an average ice cover of about 5% of the total area of the sea, is normally the month with the least amount of ice, most of which is to be found beyond 80°N. It is also the month with the smallest loss of ice per year in the 1979-2003 period. Ice starts forming in October in the N Barents. The rate of change and the relative change in ice area in October are amongst the smallest of the year and only small regional changes in the position of the ice concentration contours were observed.

November is the month with the smallest relative change in ice area. In most points of the Barents Sea the changes in ice concentration have been smaller than 0.10. The largest negative variations occurred on the N coast of Nordaustlandet, where the typical concentrations were in the range 0.60-0.70 at the beginning of the period in study and are now in the range 0.40-0.50.

In December there is an overall northwards shift in the position of the ice concentration contours. The 0.50 contour, for example, is now above 76°N in the waters between Svalbard and Novaya Zemlya while earlier it was as low as 75°N in the region between Svalbard and Bjørnøya and near the coast of Novaya Zemlya. The most striking changes are observed precisely in the region between Svalbard and Bjørnøya, where the ice concentration decreased in some areas by more than 0.50.

January has the largest loss of ice per year and relative variation in ice area of the winter months. Generally, there is a northwards shift in the ice concentration contours in the central and N Barents, an eastwards shift (towards the coast of Novaya Zemlya) in the E Barents and a southeastwards shift (towards the coast of Malozemel'skaya Tundra) in the SE sector. The largest variations, above 0.30, occurred in vast areas in the central Barents E of 36°W, in the region between Spitsbergen and Bjørnøya, and on and near the N coast of Spitsbergen.

The situation is very similar in February and March with respect to average ice area (52% and 53% of the total area of the sea, respectively), rate of change and relative change in ice area, but there are some differences in the locations where the changes occur. In February, variations of at least 0.10 occurred essentially all over the Barents Sea S of 77°N with the exceptions of the area NE of Bjørnøya, where there was actually a small increase in ice concentration and, obviously, in the SW sectors which do not freeze in the winter. Variations larger than 0.30 occurred in disjoint regions of the central Barents, and the highest ones, above 0.40, in a region about 100 miles W of the W coast of Novaya Zemlya at about 75°N.

April is statistically the month with the biggest amount of ice (mean ice area 55%) and the one with the highest rate of change in ice area. In the central Barents the current 0.50 concentration contour oscillates between 75°30'N and 76°30'N from the S tip of Spitsbergen to longitude 50°E, where it turns S; on the E it lies 20-40 miles away from the coast of the S island of Novaya Zemlya. Around 1979 this contour was always S of 76°N and W of 48°E, meaning that it was typically at least 75 miles away from the coast of Novaya Zemlya. The most significant variations, above 0.40, are found in the central Barents at about 76°N and in the vicinity of the NE coast of Ostrov Kolguyev. The only points where there was an increase in the amount of ice are those just NE of Bjørnøya.

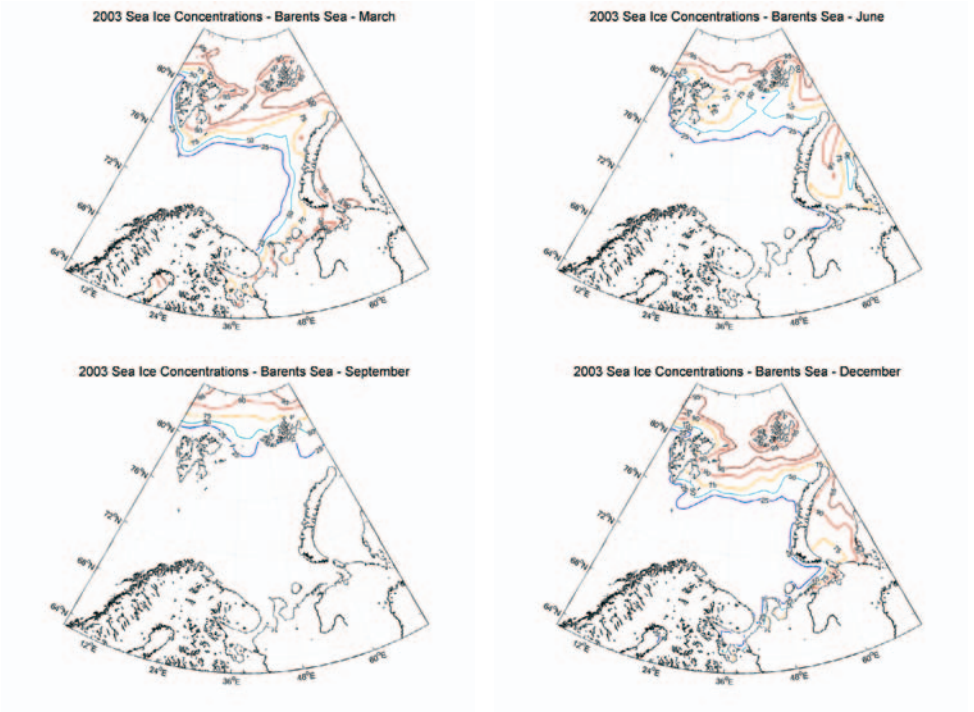

Figure 16. Current distribution of the sea ice concentrations in the Barents and White Seas.

In May there is a decrease of at least 0.10 in the ice concentrations in almost all the Barents Sea. Particularly striking is the loss of ice that occurred in the waters between Ostrov Kolguyev and the SW coast of Novaya Zemlya, where the ice concentrations dropped by 0.40-0.50. Equally high variations were only observed, at this time of the year, in certain areas of the Chukchi Sea. Variations in the interval 0.25-0.40 occurred in the portion of the Barents Sea E of the 46°E meridian from the S shore up to 76°N. This means that the ice situation on the W coast of Novaya Zemlya is now much milder than it used to be. The 0.75 contour, which is now above 76°30'N in the central Barents, passes through the N tip of Novaya Zemlya.

In June the loss of ice in the Barents Sea is the highest among all Siberian seas. Generally, all ice concentration contours in the central, N and E Barents moved northwards as a consequence of variations above 0.10 in the ice concentrations. The 0.50 concentration contour, which was approximately at 76°N in the vast region between Svalbard and Novaya Zemlya in the early years of the 1979-2003 period, is now above 76°30'N in all its length and it touches the SW coast of the archipelago of Zemlya Frantsa Iosifa. Concentrations above 0.75 are nowadays restricted to the NW and NE sectors while previously they were everywhere N of 76°30'N. Negative shifts in the ice concentration just above 0.40 are found on the W coast of the N island of Novaya Zemlya and in the central Barents around position (77°N, 42°E). These are the highest variations observed in this month in the Russian Arctic. A decrease in the range 0.25-0.50 was observed in the waters between Ostrov Kolguyev and SW Novaya Zemlya. The only exception to this global loss of ice is the N coast of Zemlya Frantsa Iosifa, where data show an increase in ice concentration between 1979 and 2003.

In July the relative changes are quite important but, because the amount of ice is much smaller than in the previous months, losses per year are also smaller. Concentrations above 0.50 are now restricted to the far N, typically above 80°, while in the beginning of the 1979-2003 period they could be found as far S as 77°N in the vicinity of Svalbard and Novaya Zemlya. The largest variations, above 0.25, occurred in the region between Novaya Zemlya and Zemlya Frantsa Iosifa. The loss of ice is felt, however, in most points N of 76°N.

In August the ice is restricted to the N Barents. Concentrations above 0.5 are now above 81°N while around 1979 they could be found as low as 80°N in the area between Nordaustlandet and Zemlya Frantsa Iosifa.

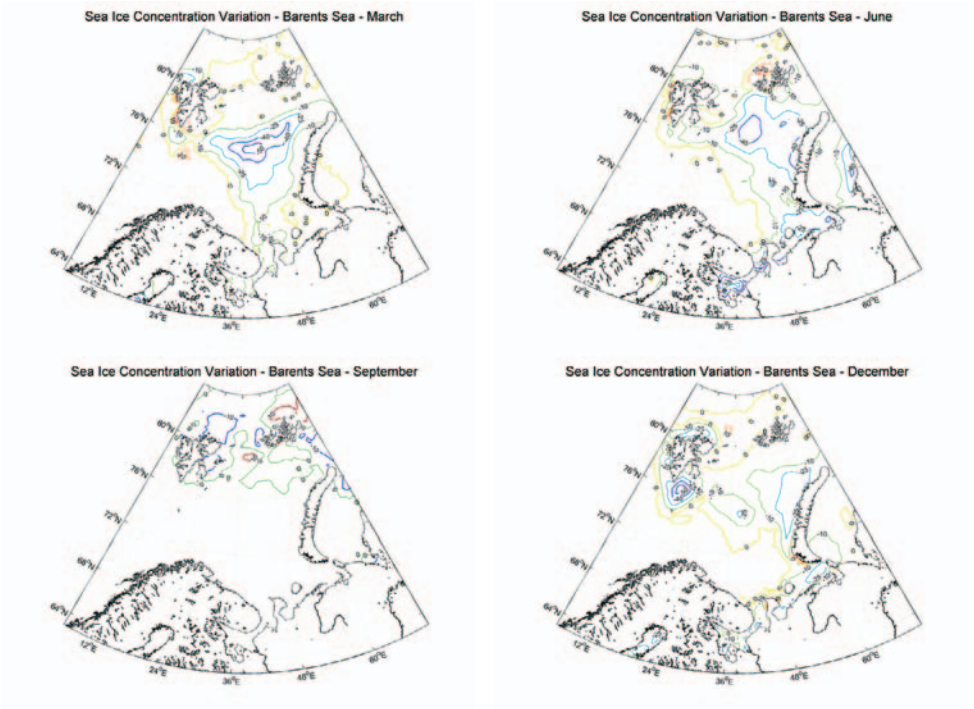

Figure 17. Variation in the distribution of the sea ice concentration in the Barents and White Seas.

Kara Sea

There were only minor variations in the ice distribution in the winter and spring months in the Kara, Laptev and East Siberian seas. We thus limit ourselves to a description of the main changes that have occurred between June and October.

With rare exceptions, there was a modest decrease in the ice concentrations all over the Kara Sea in June, in general slightly above 0.10 in the W Kara and between 0 and 0.10 in the E Kara. The most visible variations, in the interval 0.25-0.40, occurred near the W coast of Poluostrov Yamal, on the NE coast of Ostrov Belyy and in the vicinity of Dikson.

A decrease in the amount of ice was observed in July more or less all over the Kara Sea, with the largest differences in ice concentration between 1979 and 2003 taking place in the W Kara and in the vicinity of Dikson, where they were mostly in the range 0.25-0.40.

Between 1979 and 2003 there was a general northwards shift of the August ice concentration contours, especially in the N and E sectors of the Kara Sea. The 0.25 contour, for instance, is now at least 60 miles away from Mys Zhelaniya, which signals a great improvement in the ice conditions in the stretch of the Northern Sea Route round the N tip of Novaya Zemlya. The largest alterations in ice concentration, between 0.25 and 0.40, happened NE of the N tip of Novaya Zemlya and in the area of the N Kara between Novaya Zemlya and Zemlya Frantsa Iosifa.

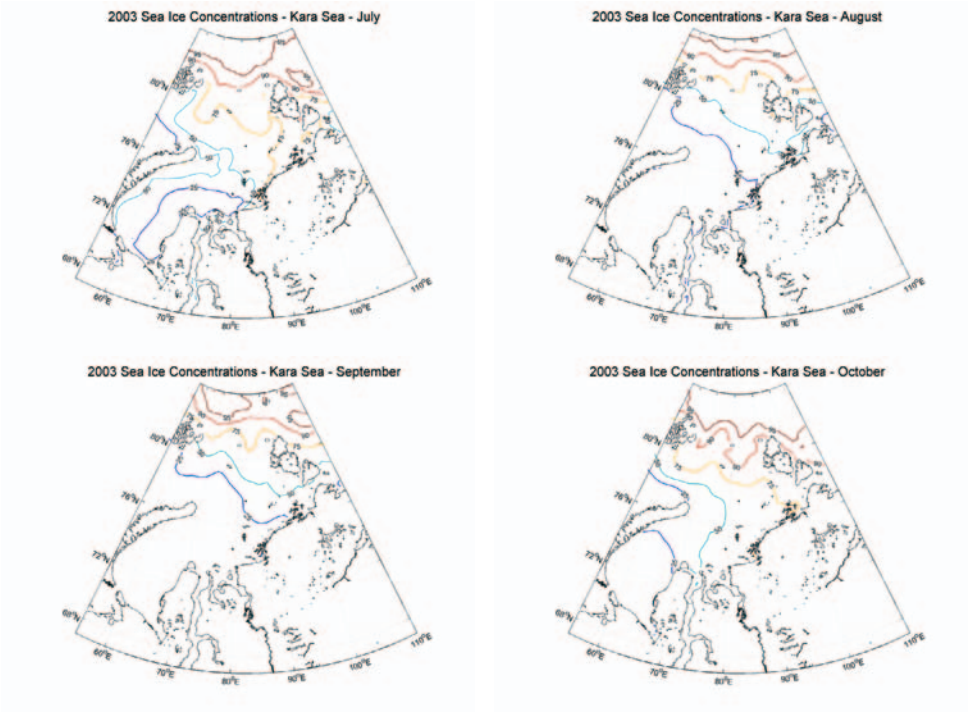

Figure 18. Current distribution of the sea ice concentrations in the Kara Sea.

In September the W Kara is essentially free of ice and thus the alterations in the ice distribution, smaller than those registered in the previous months, were mostly observed in the N and E sectors of the Kara Sea. The largest loss of ice took place in an area about 100 miles NE of Mys Zhelaniya, about half way between Novaya Zemlya and Ostrov Vize, which is now likely to be free of ice. Between 1979 and 2003 there was a general northwards displacement (of less than one degree) in the contour lines for values of the ice concentration below 0.50. For concentrations above 0.50 the contours moved northwards in some points and southwards in others. Accordingly, a small increase in the amount of ice was detected on the NE and E coasts of Zemlya Frantsa Iosifa, as well as in a large region W of Severnaya Zemlya.

The only remarkable changes in the ice distribution in the Kara Sea in October were in Baydaratskaya Guba. In an average season some 25 years ago, the bay would have had ice from entrance to head, with variable concentrations, reaching 0.75 at the head; now the ice is normally limited to the innermost parts of the bay and in smaller concentrations.

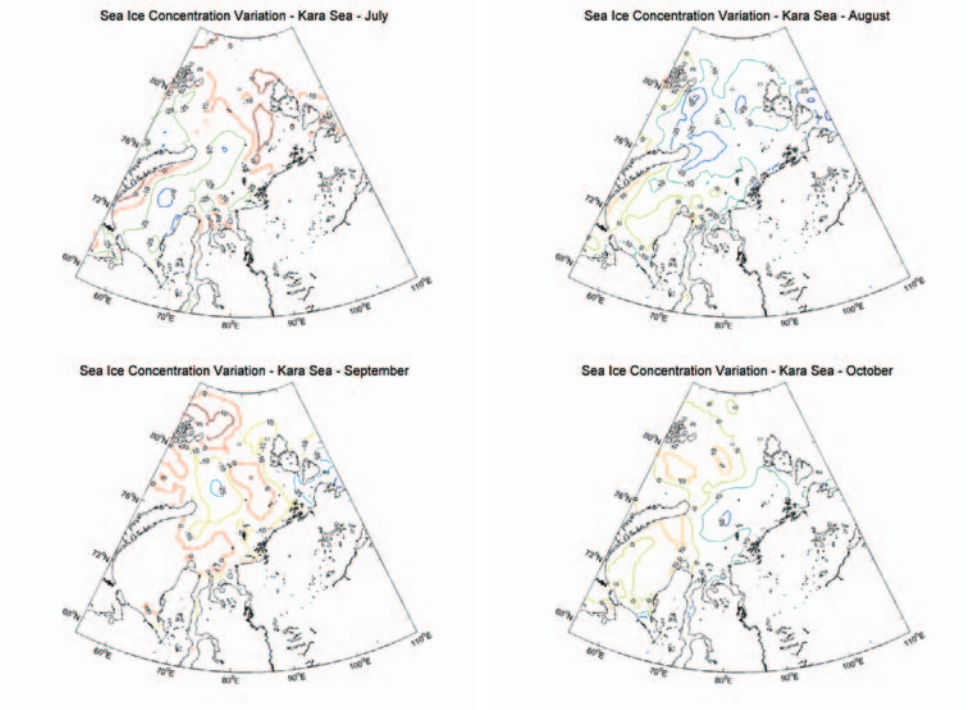

Figure 19. Variation in the distribution of the sea ice concentrations in the Kara Sea.

Laptev Sea

There are three areas of the Laptev Sea where a significant decrease in the amount of ice took place in the months that form the navigation season: the E coast of Poluostrov Taymyr (where, in some seasons, the Taymyr Massif can be found), the S Laptev near the Lena Delta and the N coast of Ostrov Kotel'nyy. In June, the variations in ice concentration in these regions, mostly in the interval 0.25-0.40, were among the largest observed in the Russian Arctic in this month.

In July, changes in the sea ice distribution occurred more or less all over the Laptev Sea, making the present ice conditions much more favourable than in the late 1970s. High or very high ice concentrations are now restricted to the northernmost sectors, while earlier in the 1979-2003 period they were present in more than half of the Laptev Sea.

The loss of ice in August also happened all over the Laptev Sea except in a comparatively small area in the central Laptev where a modest increase in ice concentration was detected. The S Laptev is now likely to be totally free of ice, whereas around 1979 the presence of low concentration ice would be normal. Large variations were observed all over the NW Laptev, in a small region in the S Laptev and off the N coasts of Ostrov

Faddeyevskiy and Ostrov Novaya Sibir'. The most dramatic changes, however, are found near the E coast of Poluostrov Taymyr, where the ice concentrations decreased by more than 0.40; only small quantities of ice may be expected now in that region.

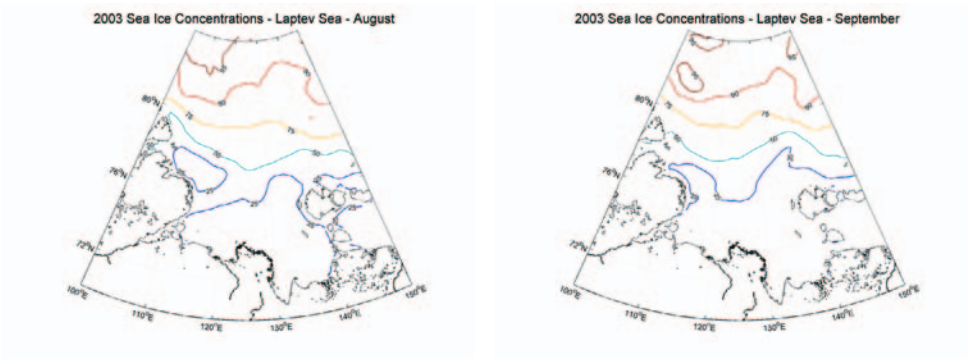

Figure 20. Current distribution of the sea ice concentrations in the Laptev Sea.

September is the month with the minimum average amount of ice. In 1995 only 3% of the Laptev Sea was covered with ice (while in the following year the ice cover was 78%). Between 1979 and 2003 ice disappeared in most points N of 76°N (at lower latitudes there is not much ice at this time of the year). The reduction in the amount of ice was particularly remarkable in the vicinity of the NE coast of coast of Poluostrov Taymyr, where the early ice concentrations were higher than 0.75 and the late ones are lower than 0.50, and in a region NW of Ostrov Kotel'nyy.

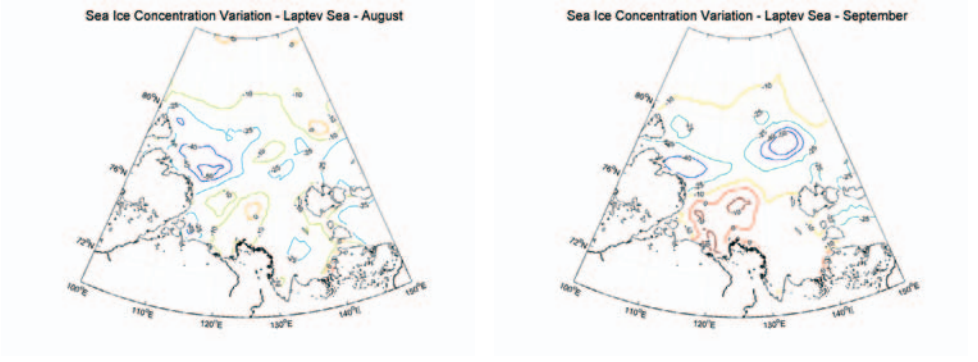

Figure 21. Variation in the distribution of the sea ice concentrations in the Laptev Sea.

In a typical October in the late 1970s the Laptev Sea used to have concentrations higher than 0.90 in the portion N of 76°30'N and in the interval 0.75-0.90 S of that latitude. Now the concentrations are below 0.90 S of 78°N and values above 0.75 are only found in the W Laptev, namely off the E coast of Poluostrov Taymyr and on the E coast of Severnaya Zemlya.

East Siberian Sea

From July to October the East Siberian Sea had the greatest loss of ice per year of all Siberian seas. In all other months the changes in the ice distribution were minimal.

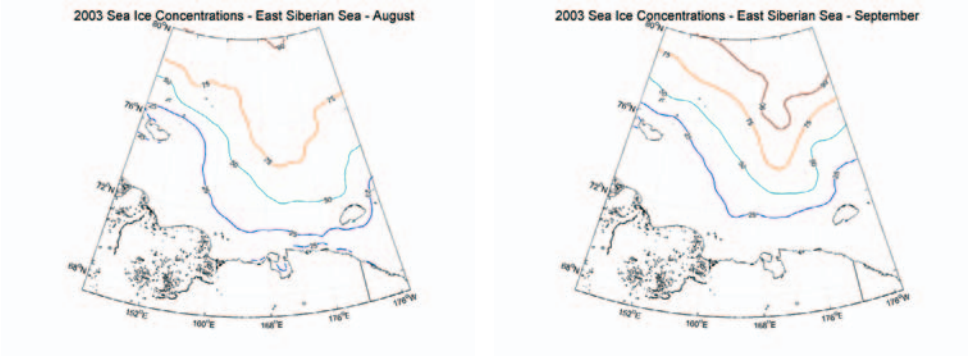

Figure 22. Current distribution of the sea ice concentrations in the East Siberian Sea.

In July there was a decrease in the quantity of ice in the whole East Siberian Sea between 1979 and 2003. The variations in ice concentration were mostly in the interval 0.10-0.25 but between 0.25 and 0.40 in the following areas: E of Ostrov Novaya Sibir', on the coast of Russia between 156°E and 164°E, on the coast of Russia E of Mys Shelagskiy (70°06'N, 170°25'E) and in Chaunskaya Guba.

In August there was a massive loss of ice in the East Siberian Sea (only surpassed by that of September). The most striking changes took place E of Novo Sibirskiye Ostrova, where the early ice concentrations were around 0.75 and are now around 0.25, the largest variations observed in the Russian Arctic at this time of the year. Strong differences between the early and late ice distributions also occurred on the SW East Siberian Sea and in the S sector around 168°E.

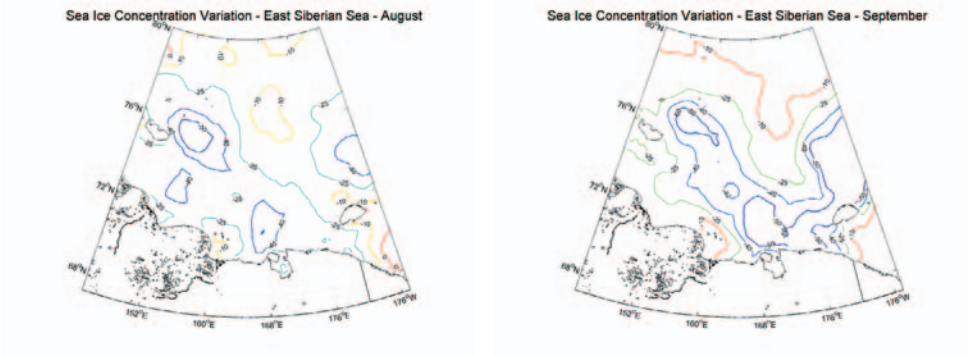

Figure 23. Variation in the distribution of the sea ice concentrations in the East Siberian Sea.

The loss of ice in the East Siberian Sea in September was by far the largest of all Siberian seas in all months. Around 1979 concentrations below 0.25 were mostly expected along the coast of Russia from the E entrance of Proliv Dmitriya Lapteva to the mouth of Reka Kolima; now the whole portion of the East Siberian Sea S of 72°N is likely to be free of

ice while in the W sector the ice-free zone extends from the coast of Russia to beyond the N coast of Ostrov Novaya Sibir'.

In October, the largest variation in ice concentration, above 0.40, one the highest values in the Russian Arctic at this time of the year, took place in the area SW of Ostrov Vrangelya. In most points of the central East Siberian Sea the variation was around 0.30, while in the N sector and in the vicinity of the S shore it was below 0.25.

Finally, we note that one of the regions of the East Siberian Sea where the ice conditions are now much more favourable than in the late 1970s is located near Ostrov Ayon, precisely where the Ayon Massif, when present, constitutes a formidable obstacle to the navigation due to its large amounts of old ice.

Chukchi Sea

During the winter the ice-free portion of the Chukchi Sea occupies invariably less than 3% of the total area of the sea. It is only at the beginning of the melting season that trends in the ice distribution become visible. The most striking losses of ice in May (only comparable to those that took place in some areas of the Barents Sea) occurred near the NE coast of Chukotskiy Poluostrov, roughly between the Bering Strait and the 172°W meridian, where the ice concentrations decreased between 0.25 and 0.40. In June the decrease in ice concentration was felt all over the Chukchi Sea, with variations below 0.10 N of 71°30'N, between 0.10 and 0.25 in most of the central Chukchi, between 0.25 and 0.40 in most of the S Chukchi (except in the vicinity of the Bering Strait, where there is not much ice at this time of the year) and on the coast of Alaska between Point Hope and Icy Cape, and above 0.40 in some points near the coast of Russia between 172°W and 177°W.

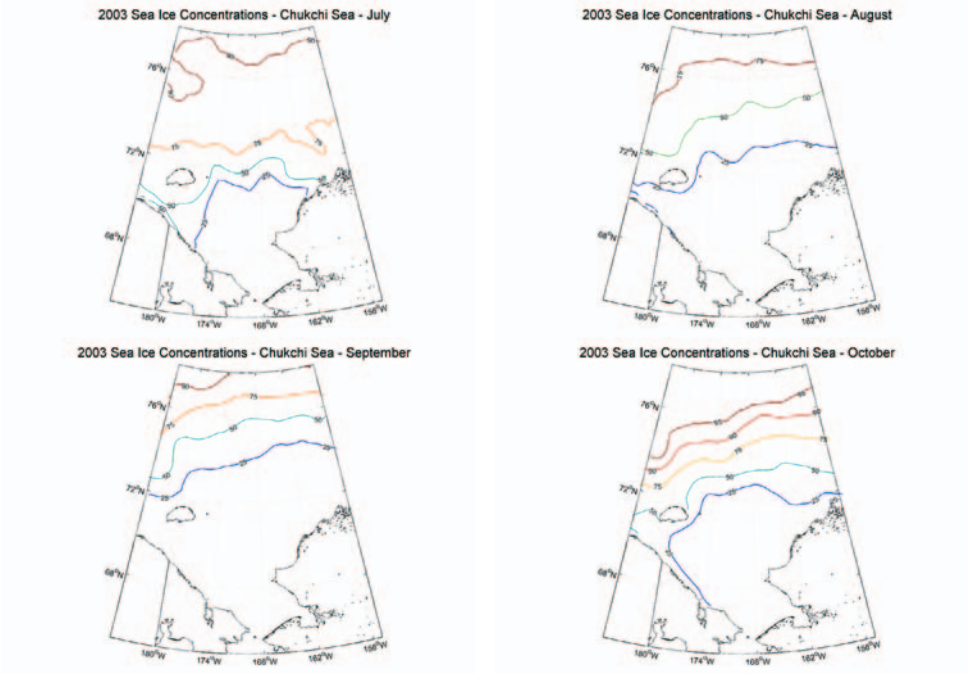

Figure 24. Current distribution of the sea ice concentrations in the Chukchi Sea.

When July comes the alterations in ice area and in the ice concentration distribution become larger. Because there is little ice in the S sector in this month, the loss of ice occurred mostly in the central Chukchi, notably in the vast area between Ostrov Vrangelya and the NW coast of Alaska.

In August, September and October the Chukchi Sea has the largest relative decrease in ice area of all Siberian seas. In August the drop in ice concentration is felt almost everywhere N of 70°N, with the largest variations, above 0.40, taking place in the band of latitudes between 72°N and 75°N. The most dramatic changes in the ice cover in the Chukchi Sea occurred in September, traditionally the month with the least amount of ice. The Chukchi Sea lost almost 74% of its ice cover in 25 years, by far the largest relative loss of all Siberian seas in all months. All contour lines were displaced northwards by several degrees of latitude; the 0.90 concentration contour, for instance, which around 1979 lay between 73°N and 74°N, lies now mostly beyond 78°N.

In October the overall picture is similar, with a loss of almost 50% of the ice between 1979 and 1983. The heaviest loss took place along the coast of Alaska E of Icy Cape, with a drop in ice concentration of more than 0.50.

There are significant differences between the November ice cover around 1979 and around 2003 except near the Bering Strait, where the ice concentrations are typically low at this time of the year, and in the far N, where they are invariably very high. The largest variations, above 0.40, occurred off the coast of Alaska, approximately between Cape Lisburne and Icy Cape.

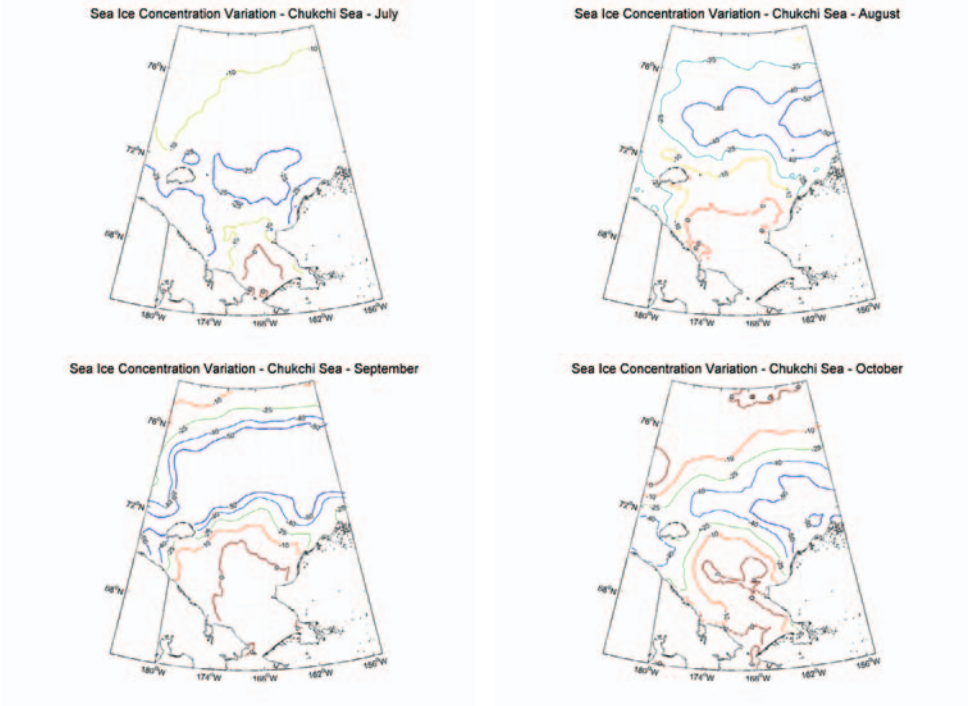

Figure 25. Variation in the distribution of the sea ice concentrations in the Chukchi Sea.

Bering Sea

There is no ice in the Bering Sea between July and October. A global increase in the amount of ice occurred in January, February, March, April, June and December. Together with the increase observed in the Sea of Okhotsk in December, these are the only positive variations registered in the Siberian seas in the 1979-2003 period.

There is normally little ice here in November (the average ice area is approximately 2.5% of the total area of the sea). In December there was a striking increase in the amount of ice on the W shore between Mys Navarin and Kamchatskiy Poluostrov, and on the E shore S of Nunivak Island. In the first of these regions the increase in ice concentration was above +0.40 and in the second it was in the range (+0.20,+0.30), but above +0.40 in the innermost parts of Bristol Bay. Such large positive variations are almost unique in the Northern Hemisphere (they also occurred on the E coast of Sakhalin in the Sea of Okhotsk).

The largest increase in the amount of ice per year and the largest relative increase in ice area occurred in January, a month in which positive variations took place in the whole portion of the Bering Sea where there is normally ice at this time of the year. This is the largest area with a significant increase in the amount of ice in this month in the Northern Hemisphere).

In February there are no appreciable trends in the N or E sectors but there are strong differences between the ice concentrations around 1979 and around 2003 in the central Bering Sea and on its W shore. The central part of the Bering Sea, where the rise in ice concentration was typically over 0.20, is the biggest region in the Arctic to exhibit such an increase. The largest variations, in some points higher than +0.40, were registered off the coast of Russia between 60°N and 63°N. In general, the ice concentration contours moved southwards, in contrast to what happened in most of the peripheral seas of the Arctic Ocean.

As a consequence of a balance between worsening ice conditions on the W shore and improving ice conditions on parts of the central and SE sectors, the rate of change and the relative change in ice area in the Bering Sea in March are much smaller than in February. The positive variations on the W shore, almost as large as those that occurred in February, are the most significant ones in the whole Arctic at this time of the year. The ice situation on the westernmost parts of the Bering Sea, especially on the coast of Kamchatka between 54°N and Mys Navarin, is now worse than it was around 1979.

In April there were only small changes in the ice distribution. In May the ice cover of the Bering Sea is much smaller than in the winter months. Between 1979 and 2003 there was an overall decrease in the amount of ice. Variations of -0.25 were observed near the Bering Strait but large positive variations (which reached values higher than +0.30) were found in Anadyrskiy Zaliv and on the E coast of Kamchatka between 57°N and 60°N. The amount of ice in the Bering Sea in June is very small (ice covers larger than 1% were observed only five times).

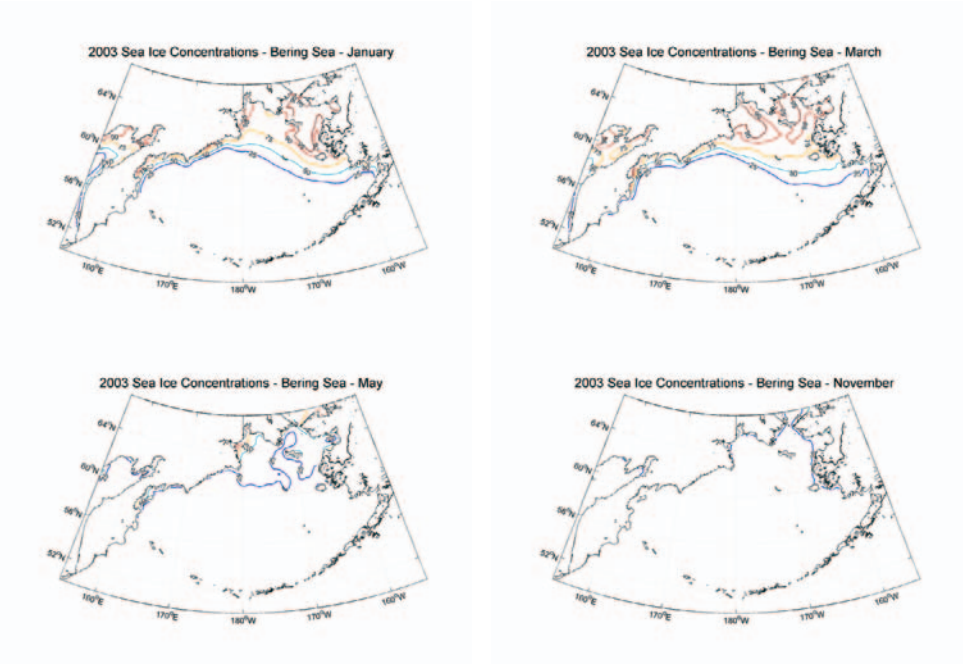

Figure 26. Current distribution of the sea ice concentrations in the Bering Sea.

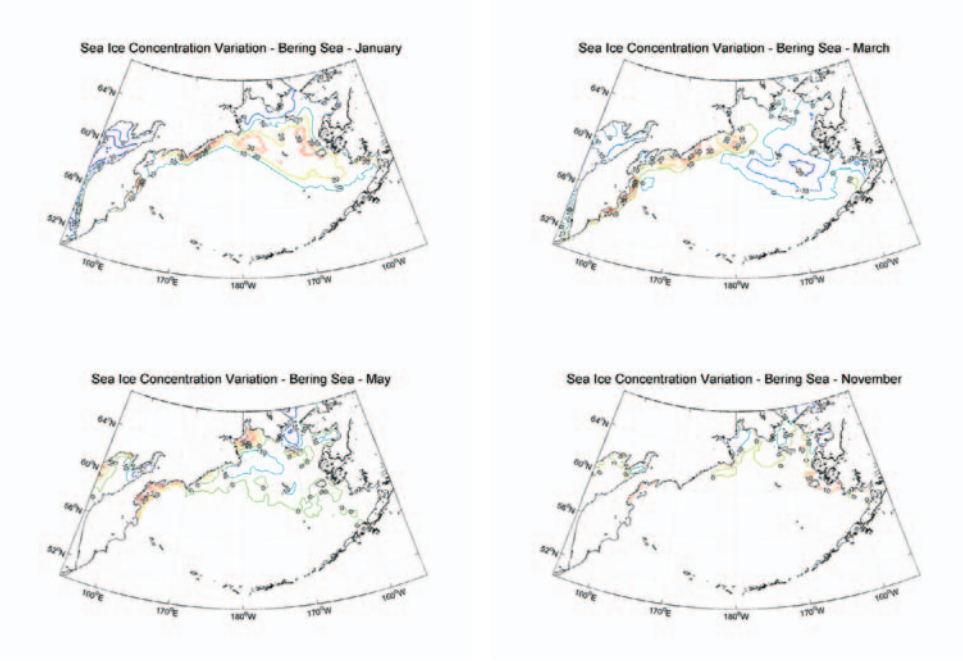

Figure 27. Variation in the distribution of the sea ice concentrations in the Bering Sea.

Sea of Okhotsk

There is no ice in the Sea of Okhotsk between July and October. In an average season sea ice covers about 1% of the total area of the Sea of Okhotsk in November. In December the average ice cover is 13%. There was a global increase in the amount of ice in December during the period under study, due to larger ice concentrations in recent years along most of the shores.

In January there are positive variations along the shores of the Sea of Okhotsk and negative variations almost everywhere else (excluding, obviously, the waters near the Kuril Islands, where there is no chance of ice at this time of the year). The most significant increases in the amount of ice took place along the NE coast of Hokkaido, on the W coast of Kamchatka between the entrance of Zaliv Shelikova and Mys Lopatka, and along the E coast of Sakhalin. In the central Sea of Okhotsk the ice concentrations decreased by 0.25-0.40 (slightly more than 0.40 in some points).

In February and March, with similar ice distributions, trends are less evident than in the other months of the ice season. Generally, the highest variations in the ice concentrations, between 0.25 and 0.40, were observed in the central Sea of Okhotsk.

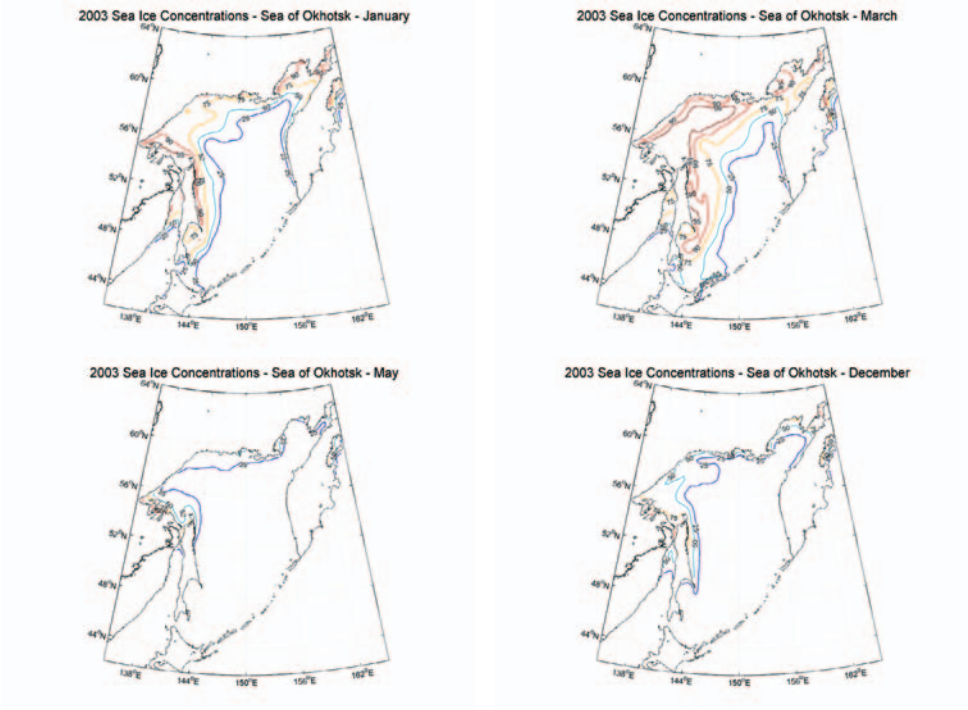

Figure 28. Current distribution of the sea ice concentrations in the Sea of Okhotsk.

April is the month with the largest rate of decrease in ice cover in spite of the amount of ice being usually much smaller than in the previous two months. With the exception of a few scattered points on the NE coast of Hokkaido and on the E coast of Sakhalin (where there was an increase in the amount of ice), the ice concentrations decreased everywhere (except in

points where there is no chance of ice at this time of the year). The largest variations, in the range 0.30-0.40, occurred in Zaliv Shelikova, notably on its E shore. Variations between 0.25 and 0.30 were found in many areas of the central Sea of Okhotsk.

In an average month of May ice is only present in 11% of the sea. Positive variations between 0.20 and 0.30 occurred on the N shore between Mys Yenkan and Mys Tolstoy. Everywhere else the concentrations decreased (except where there is never ice at this time of the year). The most striking alterations took place in the region of Shantarskiye Ostrova, in Penzhinskaya Guba, and, generally, in most of the W part of the Sea of Okhotsk. In June, the average ice cover is about 2%.

5 CHANGES IN THE LENGTH OF THE ICE-FREE SEASON

Introductory Remarks

We derive the length of the ice-free season (LIFS) in each point for each year between 1979 and 2003 from the NSIDC daily sea ice concentrations [Comiso, 1999] (before 1988 records were taken every other day). In days when data are missing, an average between the ice concentrations recorded on the previous and following days is assigned. Instead of using the original ice concentration time series, we work with smooth ice concentration time series, which are obtained from the former by replacing the value of the ice concentration $C_i(d,y)$ for day d in the original time series for year y by the average over the five day period $\{C_i(d-2,y), C_i(d-1,y), C_i(d,y), C_i(d+1,y), C_i(d+2,y)\}$. With this procedure we minimise possible isolated errors in the recording of the concentrations by the satellite.

We define the LIFS at a certain point i in a particular year y, and denote it by $L_i(y)$, as the number of days between the clearance of the ice and the formation (or, more exactly, the appearance) of the ice in that point in that year. If the number of clearances and formations is larger than one the LIFS is defined as the sum of the lengths of all periods between an ice clearance and the following ice formation. If there is only one ice clearance and no ice formations the LIFS is given by the number of days between the date of ice clearance and the end of the year. If there is only one ice formation and no ice clearances the LIFS is given by the number of days from the beginning to the year until the date of ice formation.

The criteria to identify dates of ice clearance and ice formation are as follows. We assume that there is clearance in day d if the ice concentration is 0.15 or higher in days $d-4$, $d-3$, $d-2$ and $d-1$ and below 0.15 in days d, $d+1$, $d+2$, $d+3$ and $d+4$. We consider that there is formation in day d if the ice concentration is below 0.15 in days $d-4$, $d-3$, $d-2$ and $d-1$ and 0.15 or higher in days d, $d+1$, $d+2$, $d+3$ and $d+4$. With these criteria we ignore contributions from periods of less than five days without ice which lie between two periods of five days or more with ice and from periods of less than five days with ice between two periods of five days or more without ice. We consider that the LIFS as defined above is more relevant for an analysis of the trends in the ice cover (and for navigational purposes) than the number of days without ice in the year.

In this paper we limit ourselves to study the recent changes in the LIFS and do not discuss shifts that may have occurred in the dates of clearance or formation. While when there is only one ice clearance and one ice formation in one year these dates are easy to identify, the situation is less clear when more than one clearance or formation takes place.

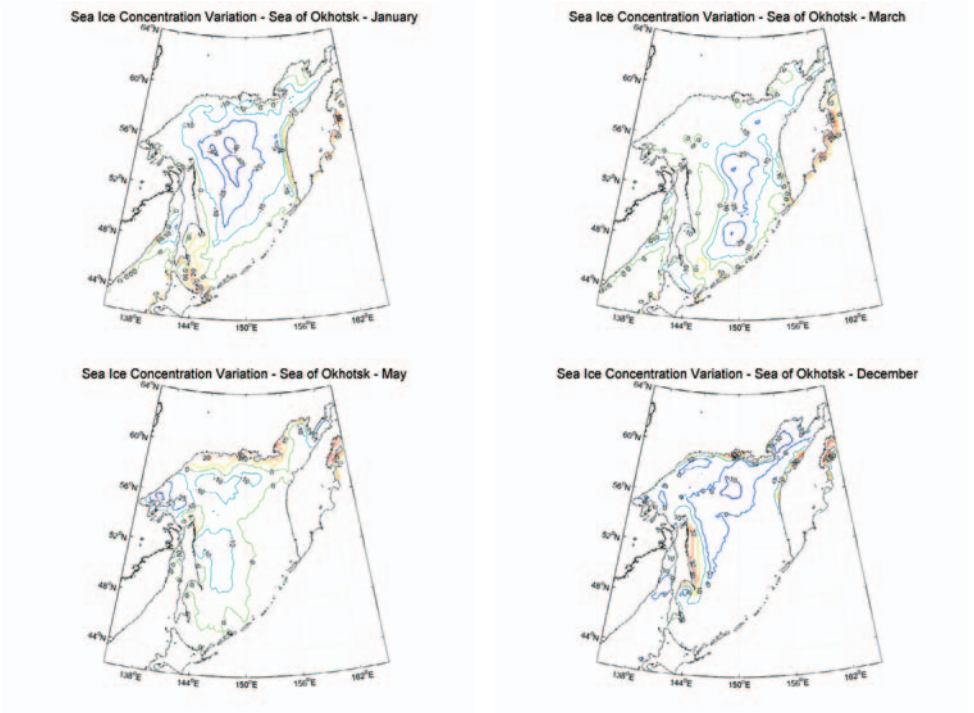

Figure 29. Variation in the distribution of the sea ice concentrations in the Sea of Okhotsk.

The functions $L_i(y)$, one for each point i are, in general, not monotonic with y because the LIFS has large inter-annual variations. In order to find long-term trends, we perform a linear regression of each $L_i(y)$ as a function of y to obtain a new set of functions $L'_i(y)$, one for each pixel i, which vary linearly with y. The functions $L'_i(1979)$ and $L'_i(2003)$ which we call, respectively, *early* and *late* LIFS, are expected to give the approximate values of the LIFS around 1979 and 2003, respectively. The most suitable quantity to study the trends is $\Delta L'_i \equiv L'_i(2003) - L'_i(1979)$, which, we assume, represents the change in the LIFS between 1979 and 2003.

In the next pages we depict contour diagrams with the present spatial distribution of the LIFS for each of the eight Siberian seas, $L'(2003)$, as well as for its variation, $\Delta L'$, in the period of 25 years between 1979 and 2003, and we identify the areas where the changes are more dramatic.

We present tables with the numerical values of $L'(1979)$, $L'(2003)$ and $\Delta L'$ for some particular locations, namely along the Northern Sea Route. Almost every selected location covers more than one pixel in the NSIDC grid, in which case the values shown are spatial averages taken over the cells that correspond to the region. In this section's tables the term *coast* designates the area between the coastline and a line approximately 75km away (which corresponds to three cells in the NSIDC grid).

White Sea

This inlet of the Barents Sea possesses the most dramatic increase in the LIFS of all Russian Arctic seas, with an average of 75 days. In the southernmost sectors the increase in the LIFS exceeds 100 days while at the entrance the change is more modest (24 days). There are only two locations where the ice-free season is decreasing in length: near Mys Svyatoy Nos and near Mys Kanin Nos, both at the entrance of the White Sea.

Table 9. Changes in the length of the ice-free season in the White Sea. The first row is a spatial average over the whole White Sea and the second row is for the entrance only.

Location	*L'*(1979)	*L'*(2003)	*ΔL'*
White Sea	137	212	+75
Entrance of White Sea	224	248	+24

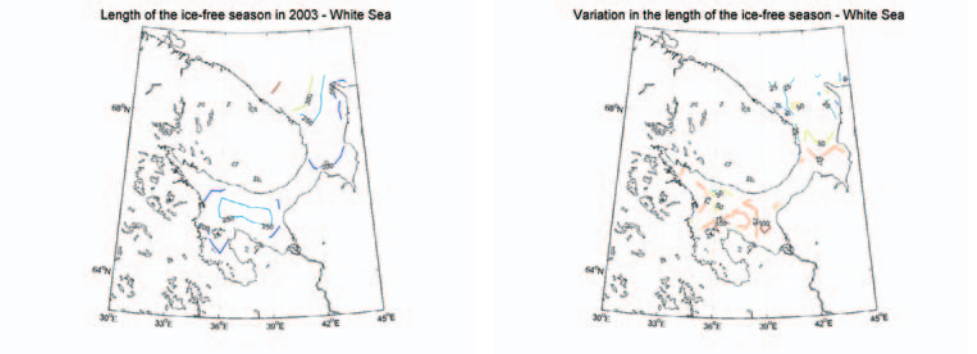

Figure 30. Current length of the ice-free season (left) and its variation between 1979 and 2003 (right) in the White Sea.

Barents Sea

In almost every part of the Barents Sea where ice formation normally occurs there was an increase in the LIFS. This increase was particularly significant in Cheshskaya Guba (65-85 days), in the passage between Malozemel'skaya Tundra and Ostrov Kolguyev (65-85 days) and in the central Barents Sea, where it reached values above 75 days in a large region situated at approximately 75°N (and above 90 days at certain points). With the exception of the White Sea, no such large variations were observed in the Russian Arctic Seas, Bering Sea or Sea of Okhotsk. Exceptionally high values for the variation of the LIFS (around 100 days) were also observed in some points near the N coast of Spitsbergen.

Table 10. Changes in the length of the ice-free season in selected locations in the Barents Sea.

Location	*L'*(1979)	*L'*(2003)	*ΔL'*
Around Bjørnøya	245	244	-1
E coast Edgeøya	63	83	+20
Nordkapp (Nordaustlandet)	39	61	+22
S boundary of Zemlya Frantsa Iosifa (approximately 80°N)	58	59	+1
W coast N Novaya Zemlya (74°N–76°N)	158	191	+33
W coast S Novaya Zemlya (71°N–73°N)	197	209	+12
Pechorskoy More	141	177	+36
Central Barents Sea (72°N–76°N, 30°E–45°E)	230	286	+56

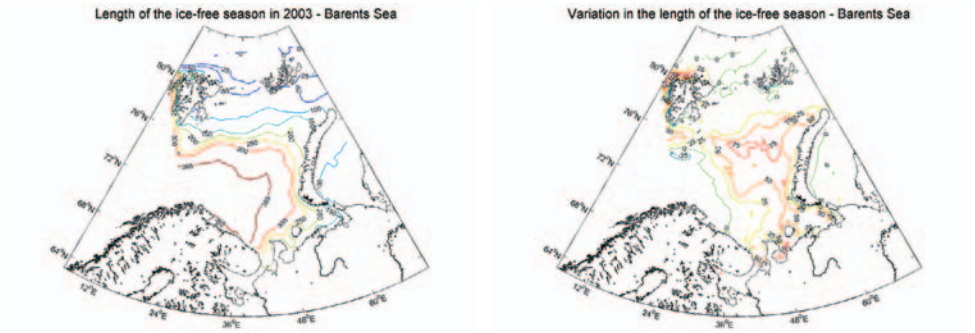

Figure 31. Current length of the ice-free season (left) and its variation between 1979 and 2003 (right) in the Barents Sea.

The only points of the Barents Sea where the data show a small reduction in the LIFS are located in a comparatively small region E of Bjørnøya and on the S coast of Zemlya Frantsa Iosifa. There are also negative trends in some places on the W coast of Spitsbergen.

Kara Sea

In most points of the Kara Sea the ice-free season is longer now than in the late 1970s. The most striking changes occur in three regions. The first one is a relatively narrow band (20-40 miles wide) that stretches in the SW-NE direction between the E coast of Poluostrov Yavay and the vicinity of Dikson, where in some points the increase in the LIFS exceeds 50 days. The second one is a broad band (75-100 miles wide) that extends from the N tip of Novaya Zemlya to the proximity of Ostrova Arkticheskogo Instituta, where the increase is 30-40 days. The last one is Baydaratskaya Guba, where it is around 40 days.

Table 11. Changes in the length of the ice-free season in selected locations in the Kara Sea.

Location	*L'*(1979)	*L'*(2003)	*ΔL'*
Proliv Karskiye Vorota	97	94	-3
E coast of S Novaya Zemlya (71°N–73°N)	100	100	0
E coast of N Novaya Zemlya (74°N–76°N)	70	68	-2
Vicinity of Mys Zhelaniya	61	79	+18
W coast of O. Oktyabr'skoy Revolyutsii	4	11	+7
Dikson and outer Yeniseyskiy Zaliv	55	86	+31
Central W Kara Sea	97	110	+13
Central E Kara Sea	33	54	+21

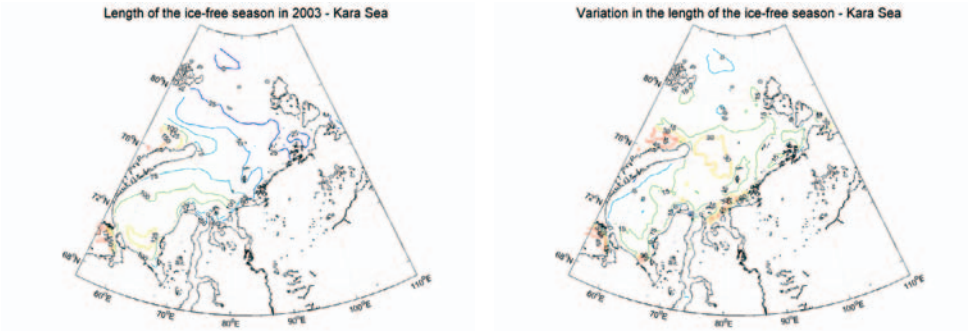

Figure 32. Current length of the ice-free season (left) and its variation between 1979 and 2003 (right) in the Kara Sea.

The regions where the variations are slightly below zero are Proliv Karskiye Vorota and the coast of Novaya Zemlya S of 76°N. In the latter the ice-free season lost between one and ten days (15 in some small stretches) from 1979 to 2003. The largest reductions in the LIFS, around 30 days, took place in Proliv Malygina (the passage between the N coast of Poluostrov Yamal and Ostrov Belyy).

Laptev Sea

The LIFS increased over almost all the Laptev Sea. The largest positive variations were observed in a region centred at the approximate position 74°30'N, 128°E, about 60 miles N of the N sector of the Lena Delta, with typical values in the range 45-60 days and exceeding 60 days at some points. Near the NE coast of Poluostrov Taymyr the increase was generally between 30 and 40 days but as high as 45 days at some particular points. An increase of 30-40 days, occasionally 50 days, took place in the vicinity of the NW coast of Ostrov Kotel'nyy.

Small negative variations (0-10 days) occurred in some stretches of the W coast of Ostrov Kotel'nyy and large ones (of the order of 20 days) in Sellyakhskaya Guba (in the SE sector of the Laptev Sea).

The location designated “SE Laptev Sea” in Table 12 is the portion of the Laptev Sea S of a line joining Antipinskiy, on the Lena Delta, and Mys Svyatoy Nos, at the entrance of Proliv Dmitriya Lapteva; this region includes the approaches to the port of Tiksi and the approaches to Proliv Dmitriya Lapteva from the SW.

Table 12. Changes in the length of the ice-free season in selected locations in the Laptev Sea.

Location	*L'*(1979)	*L'*(2003)	*ΔL'*
Proliv Borisa Vil’kitskogo	1	8	+7
Vicinity of the N tip of Severnaya Zemlya	0	2	+2
SE Laptev Sea	49	65	+16
Tiksi	48	64	+16
Vicinity of the Lena delta	50	81	+31
E coast of Poluostrov Taymyr	9	36	+27
Central Laptev Sea (region of approx. 104 km2 centred at (76°N, 122°30'E))	29	53	+24

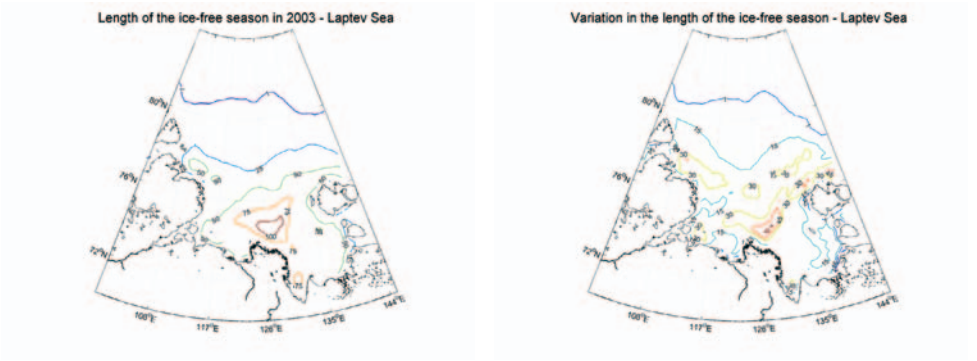

Figure 33. Current length of the ice-free season (left) and its variation between 1979 and 2003 (right) in the Laptev Sea.

East Siberian Sea

There are essentially no points in the East Siberian Sea where the ice-free season became shorter between 1979 and 2003. We note, however, an average decrease of eight days in the LIFS in Proliv Dmitriya Lapteva (as opposed to an average raise of seven days in Proliv Sannikova).

The most significant positive variations occurred near the coast of Siberia between the 164°E meridian and the W entrance of Proliv Longa. Typically, the variations were in the range 45-60 days in a wide band (roughly 50-100 miles wide) between those two meridians, and reached values in the interval 60-70 days near the N coast of Ostrov Ayon. This evolution may prove especially favourable for navigation because the vicinity of Ostrov Ayon is considered one of the most problematic stretches of the Northern Sea Route due to the frequent presence of the Ayon Ice Massif.

The other region with a remarkable increase in the LIFS is the N boundary of Novo Sibirskiye Ostrova, where the average increase is around 40 days (50 days near the N coast of Ostrov Novaya Sibir').

The region designated by Ayon in Table 13 (where the Ayon Ice Massif often appears) is the portion of the East Siberian Sea bounded on the S by the coast of mainland Russia and the N coast Ostrov Ayon, on the N by the 72°N parallel, on the W by the 166°E meridian and on the E by the 172°E meridian (excluding Chaunskaya Guba).

Table 13. Changes in the length of the ice-free season in selected locations in the East Siberian Sea.

Location	*L'*(1979)	*L'*(2003)	*ΔL'*
Proliv Dmitriya Lapteva	34	26	-8
Proliv Sannikova	28	35	+7
N coast of Ostrov Kotel'nyy	16	45	+29
N coast of Ostrov Vrangelya	2	29	+27
Pevek	13	32	+19
Ayon	9	49	+40
Central E. S. S. (region of approx. 76x103 km2 centred at (72°30'N,163°30'E))	9	37	+28

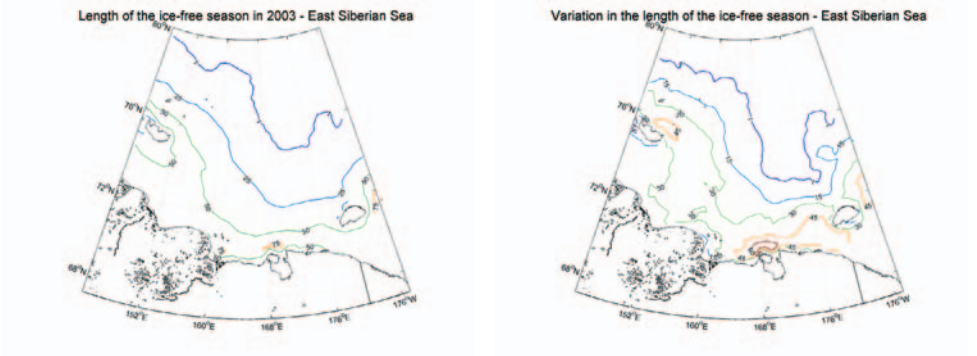

Figure 34. Current length of the ice-free season (left) and its variation between 1979 and 2003 (right) in the East Siberian Sea.

Chukchi Sea

The most striking changes in the Chukchi Sea took place on the N coast of Alaska between 160°W and 163°W where the increase in the LIFS was in the range 70-90 days. More modest, but still remarkable, variations occurred in a region with an approximate area of 104 km2 situated E of Ostrov Vrangelya, with an increase of 50-55 days, and in the central part of Proliv Longa, with an increase of 50-60 days. The LIFS decreased only in a small number of isolated points.

We estimate that positive variations in the LIFS occurred in about 90% of the total area or the Chukchi Sea, a fraction higher than in any other Russian Arctic sea (with the exception of the White Sea).

Table 14. Changes in the length of the ice-free season in selected locations in the Chukchi Sea.

Location	*L'*(1979)	*L'*(2003)	*ΔL'*
Proliv Longa	16	55	+39
Point Barrow	20	65	+45
Bering Strait	156	171	+15
Central Chukchi Sea (region of approximately 76x103 km2)	110	142	+32

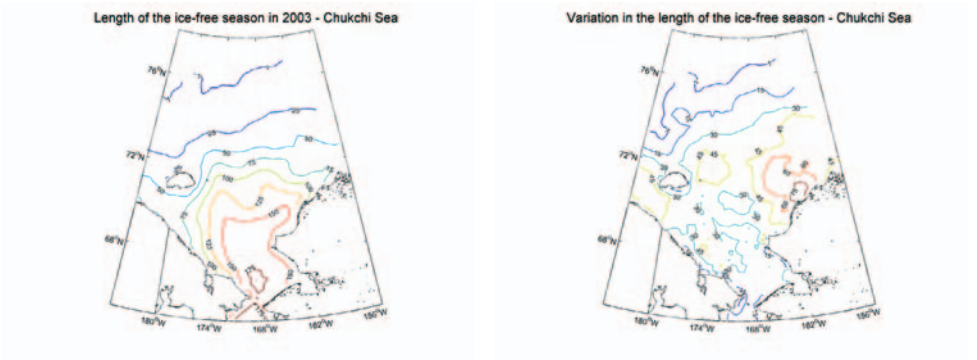

Figure 35. Current length of the ice-free season (left) and its variation between 1979 and 2003 (right) in the Chukchi Sea.

Bering Sea

The fraction of the Bering Sea where the LIFS decreased is greater than the fraction where it increased. Such a negative balance is unique among the northern seas.

The strongest positive variations occurred in the region between St. Lawrence Island and the Bering Strait, with increases of 10-20 days, and in Anadyrskiy Zaliv, with an average increase of just a few days but as high as 30 days in its central part.

A striking shrinking of the LIFS, between 40 and 80 days, depending on the location, was found on the E coast of Kamchatka between Mys Navarin and approximate latitude 55°N. Our data indicate that between 60°N and 61°N and in Kamchatskiy Zaliv the reduction may have been even larger. On the W coast of Alaska S of 60°N and in the inner parts of Bristol Bay the decrease of the LIFS is in the range 40-60 days.

Table 15. Changes in the length of the ice-free season in selected locations in the Bering Sea.

Location	*L'*(1979)	*L'*(2003)	*ΔL'*
N Bering Sea (between St Lawrence Is. and Bering St.)	180	198	+18
N Bering Sea (immediately S of St Lawrence Is.)	215	211	-4
Bristol Bay	298	284	-14
Anadyrskiy Zaliv	173	180	+7

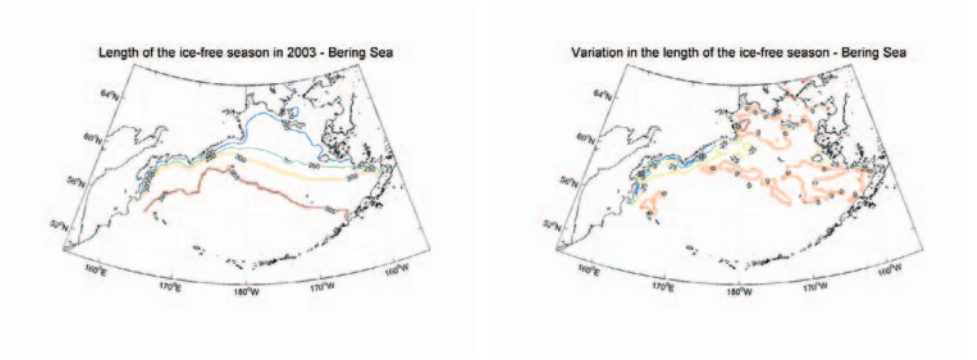

Figure 36. Current length of the ice-free season (left) and its variation between 1979 and 2003 (right) in the Bering Sea.

Sea of Okhotsk

The greatest changes in the LIFS took place in the central Sea of Okhotsk, namely in the vicinity of 53°30'N, 149°E, where the increase was in the range 55-60 days.

In many stretches of the shores of the Sea of Okhotsk there was a decrease in the LIFS, with the largest values, between 60 and 70 days, observed on the S coast of Sakhalin, notably in Zaliv Aniva. Other places where there were comparatively large reductions in the LIFS are La Perouse Strait, Zaliv Terpeniya (30-35 days at the head of the bay), the whole E coast of Sakhalin N of Mys Terpeniya (48°38'N, 144°45'E), the N shore of the Sea of Okhotsk between Mys Yenkan (57°46'N, 140°19'E) and Mys Tolstoy (59°10'N, 155°12'E) and the W coast of Kamchatka S of 56°N.

Table 16. Changes in the length of the ice-free season in selected locations in the Sea of Okhotsk.

Location	*L'*(1979)	*L'*(2003)	*ΔL'*
La Perouse Strait	297	273	-24
E coast of Sakhalin (49°30'N–53°30'N)	219	203	-16
Sakhalinskiy Zaliv	154	174	+20
Tauyskaya Guba	217	178	-39
Zaliv Shelikova (incl. Gizhiginskaya Guba and Penzhinskaya Guba)	208	215	+7
W coast Kamchatka (56°N–58°N)	270	275	+5
NE coast Hokkaido	244	238	-6
Central S. of Okhotsk (region of approx. 290x103 km2 centred at (54°N, 150°E)	292	323	+31

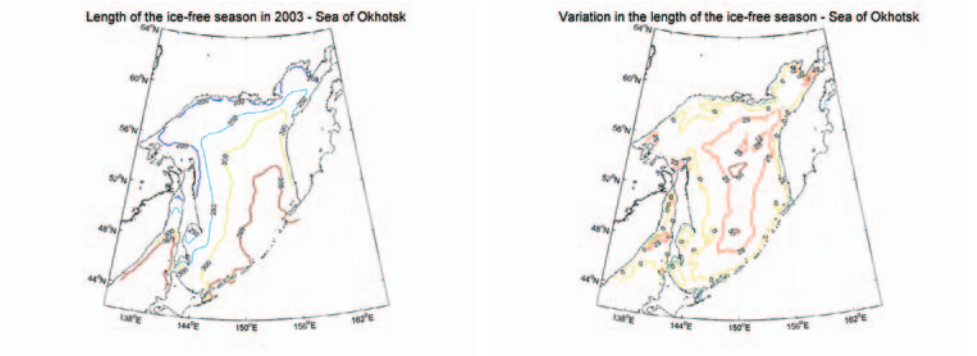

Figure 37. Current length of the ice-free season (left) and its variation between 1979 and 2003 (right) in the Sea of Okhotsk.

6 CONCLUSIONS

The reduction in sea ice extent and area that has been observed during the past few decades in the Russian Arctic, more rapid than anywhere else in the Northern Hemisphere, is one of the most striking environmental changes that have occurred on our planet.

The analysis of the sea ice concentration data between 1979 and 2003 shows that the rate of change and the relative change of the ice extent and area are almost always negative, null or approximately null. The largest relative reductions in ice extent took place in June, July and October in the White Sea (where the decline with time was faster than linear) and in September in the Chukchi Sea. Other large reductions occurred in the Barents Sea in July, in the Laptev Sea in August, in the East Siberian Sea in September, in the Chukchi Sea in October and in the Sea of Okhotsk in May. Exceptions happened in the Barents Sea in September, in the Bering Sea in December, January, February and June, and in the Sea of Okhotsk in December, where there is a significant increase in the relative ice extent. Modifying the lower threshold from 0.15 to 0.30 in the definition of ice extent induces only small changes in the position of the ice edge and small variations in the rate of change and relative change in ice extent.

Based on daily records of sea ice concentrations, we found that there was a considerable increase in the length of the ice-free season during the 1979-2003 period almost everywhere in the Russian Arctic. In the White, East Siberian and Chukchi Sea there are remarkable differences between the current figures and those of the late 1970s. In some points the increase in the length of the ice-free season was faster than linear. A reduction was observed in some parts of the Bering Sea and Sea of Okhotsk only.

This apparently long term decline in the ice-covered area and in the length of the ice season in the Russian Arctic Seas opens new opportunities for the Northern Sea Route, which in the coming decades may become a real alternative to more traditional routes that connect the Atlantic and the Pacific.

7 ACKNOWLEGMENTS

This work was partly supported by the GreenICE Project of the EU Fifth Framework Environment and Sustainable Development Programme.

8 APPENDIX A. BOUNDARIES OF THE SIBERIAN SEAS

The boundaries of the Russian Arctic seas were provided by the Arctic and Antarctic Research Institute in St. Petersburg while those of the Bering Sea and Sea of Okhotsk were obtained from the International Hydrographic Organisation [1973].

White Sea

The White Sea is an inlet of the Barents Sea whose N boundary is the line that joins Mys Svyatoy Nos (68°08'N, 39°50'E) to Mys Kanin Nos (68°40'N, 43°18'E).

The area of the White Sea is approximately 9.0×10^4 km^2.

Barents Sea

The Barents Sea is bounded on the W by a line joining Nordkapp (71°10'N, 25°48'E), the N extremity of Norway, to Kapp Bull (74°21'N, 19°05'E), the S extremity of Bjørnøya; thence by the E coast of the latter; thence by a line joining Nordkapp (74°31'N, 19°07'E), the N extremity of Bjørnøya, to Sørkappøya (76°29'N, 16°39'E); thence by a line joining the latter to the nearby S extremity of Spitsbergen; thence by the E coast of the Svalbard Archipelago up to Kapp Leigh Smith (80°06'N, 27°35'E), on the E coast of Nordaustlandet.

The N boundary is the line joining Kapp Leigh Smith to the northernmost point of Kvitøya to Mys Mary Harmsworth, in Zemlya Aleksandra; thence the N shores of Zemlya Frantsa Iosifa, passing by Mys Fligeli (81°52'N, 59°00'E), the northernmost point of Ostrov Rudopha, up to Mys Kohlsaat (81°01'N, 65°22'E), the easternmost point of Ostrov Graham Bell.

On the E side, the Barents Sea is bounded by the line joining Mys Kohlsaat to Mys Zhelaniya (76°57'N, 68°35'E), just a few miles away from the N tip of Novaya Zemlya; thence by the W coast of Novaya Zemlya from Mys Zhelaniya to Mys Kusov Nos (70°28'N, 57°07'E); thence by the SW entrance of Proliv Karskiye Vorota, a line that joins Mys Kusov Nos to Mys Lapin Nos (70°04'N, 58°36'E); thence by the SW coast of Ostrov Vaygach; thence by the SW entrance of Proliv Yugorskiy Shar, a line that joins Mys Greben' (69°39'N, 59°59'E) to Mys Belyy Nos (69°36'N, 60°11'E).

The limits on the S are the N coast of mainland Russia from Mys Belyy Nos to Mys Kanin Nos; thence the N boundary of the White Sea; thence the N coast of Kol'skiy Poluostrov from Mys Svyatoy Nos to the Russia-Norway border; thence the N coast of Norway to Nordkapp.

The area of the Barents Sea is estimated as 1.4×10^6 km^2.

Kara Sea

The Kara Sea is bounded on the W by the NE entrance of Proliv Yugorskiy Shar, the line joining Mys Yarossel (69°51'N, 60°27'E) to Mys Belyy (69°54'N, 60°28'E); thence by the NE coast of Ostrov Vaygach; thence by the NE entrance of Proliv Karskiye Vorota, the line joining Mys Bolvanskiy Nos (70°28'N, 59°04'E) to Mys Men'shikova (70°42'N, 57°36'E); thence by the E coast of Novaya Zemlya up to Mys Zhelaniya; thence by a line joining the latter to Mys Kohlsaat; thence by a line joining the latter to the easternmost point of Ostrov Belaya Zemlya, in Zemlya Frantsa Iosifa, which has approximate coordinates 81°38'N, 63°51'N.

The N boundary is the line joining the easternmost point of Ostrov Belaya Zemlya to Mys Molotova (81°16'N, 95°40'E), the N tip of Ostrov Komsomolets, in Severnaya Zemlya. In some Russian charts Mys Arkticheskiy (81°16'N, 95°43'E) is used instead of Mys Molotova to define the N boundary of the Kara Sea.

On the E, the Kara Sea is bounded by the W coast of Ostrov Komsomolets; thence by the W entrance of Proliv Yungshturm; thence by the W coast of Ostrov Pioner; thence by the W entrance of Proliv Krasnoy Armii; thence by the SW coast of Ostrov Oktyabr'skoy Revolyutsii; thence by the W entrance of Proliv Shokal'skogo, the line joining Mys Sverdlova (78°46'N, 98°18'E) to Mys Neupokoyeva (77°55'N, 99°33'E), on Ostrov Bol'shevik; thence by the W entrance of Proliv Borisa Vil'kitskogo, the line joining Mys Neupokoyeva to Mys Poluostrovnoy (77°23'N, 102°07'E), on the coast of Poluostrov Taymyr.

The limits on the S are the N coast of Russia between Mys Poluostrovnoy and Mys Yarossel. For the calculation of the extent and area of the sea ice cover of the Kara Sea we include the outer part of Yeniseyskiy Zaliv and the N part of Obskaya Guba. The former is the portion of Yeniseyskiy Zaliv NW of the line joining Ostrov Krestovskiy (72°26'N, 80°46'E) to position (72°20'N, 80°00'E). The latter is the portion of Obskaya Guba N of Mys Taran (71°25'N, 73°02'E).

The above definitions imply that the Novaya Zemlya straits (Proliv Karskiye Vorota, Proliv Yugorskiy Shar and Proliv Matochkin Shar) are not included in the Barents Sea or in the Kara Sea.

It is sometimes convenient to make a distinction between W, E and N Kara as the ice conditions can be remarkably different in each of these three divisions. The boundaries of the W Kara are the E coasts of Ostrov Vaygach and Novaya Zemlya, a line joining Mys Zhelaniya and Dikson and the coast of mainland Russia between Dikson and the E entrance of Proliv Karskiye Vorota. The E Kara is bounded on the W by the line joining Mys Zhelaniya and Dikson, on the N by a line joining Mys Zhelaniya to Mys Molotova, on the E by the W coast of Severnaya Zemlya and on the S by the coast of Russia between the W entrance of Proliv Borisa Vil'kitskogo and Dikson. The N Kara Sea is the triangle defined by Mys Zhelaniya, the easternmost point of Ostrov Belaya Zemlya and Mys Molotova.

The area of the Kara Sea (including the Severnaya Zemlya straits) is approximately 8.8×10^5 km^2.

Laptev Sea

The Laptev Sea is bounded on the W by the E entrance of Proliv Borisa Vil'kitskogo, the line that joins Mys Pronchishcheva (77°34'N, 105°55'E) to Mys Vaygacha (78°19'N, 104°57'E); thence by the E coast of Ostrov Bol'shevik; thence by the NE entrance of Proliv Shokal'skogo, between Mys Peschanyy (79°26'N, 102°30'E) and Mys Anuchina, on the E coast of Ostrov Oktyabr'skoy Revolyutsii, (79°40'N, 100°22'E); thence by the NE coast of Ostrov Oktyabr'skoy Revolyutsii up to Mys Voroshilova (80°10'N, 97°40'E); thence by the E entrance of Proliv Krasnoy Armii; thence by the E coast of Ostrov Komsomolets up to Mys Molotova.

The N boundary is the line drawn from Mys Molotova to a point on the edge of the continental shelf at 79°00'N, 139°00'E.

On the E, the boundary of the Laptev Sea is the line joining the position 79°00'N, 139°00'E to Mys Anisiy (76°13'N, 139°05'E), the N extremity of Ostrov Kotel'nyy; thence the W coast of Ostrov Kotel'nyy down to Mys Medvezhiy (74°40'N, 139°07'E); thence the W entrance of Proliv Sannikova, the line that joins Mys Medvezhiy to position (74°14'N, 140°18'E) on the W coast of Ostrov Malyy Lyakhovskiy; thence the W coast of the latter island; thence the line joining the S tip of Ostrov Malyy Lyakhovskiy to Mys Vagina (73°26'N, 139°50'E), the W extremity of Ostrov Bol'shoy Lyakhovskiy; thence a small portion of the coast of this island between Mys Vagina and Mys Kigilyakh (73°20'N, 140°00'E); thence the W entrance of Proliv Dmitriya Lapteva, the line that joins Mys Kigilyakh to Mys Svyatoy Nos (72°51'N, 140°50'E) on mainland Siberia.

The S limit is the coast of Russia between Mys Svyatoy Nos and Mys Pronchishcheva.

Notice that these boundaries imply that the Severnaya Zemlya straits (Proliv Borisa Vil'kitskogo, Proliv Shokal'skogo, Proliv Krasnoy Armii and Proliv Yungshturm) are not included in the Kara Sea or in the Laptev Sea. In some Russian charts, however, Proliv Borisa Vil'kitskogo and Proliv Shokal'skogo are considered part of the Kara Sea. These definitions also imply that the Novo Sibirskiye Ostrova straits (Proliv Dmitriya Lapteva, Proliv Eterikan and Proliv Sannikova) are not part of the Laptev Sea.

The area of the Laptev Sea is approximately 6.6×10^5 km^2 (slightly higher when using the NSIDC grid of resolution 25km).

East Siberian Sea

The East Siberian Sea is bounded on the W by the E entrance of Proliv Dmitriya Lapteva, the line that joins the mouth of Reka Kondrat'eva (72°41'N, 143°50'E), in mainland Siberia, to Mys Shalaurova (73°10'N, 143°11'E), the S extremity of Ostrov Bol'shoy Lyakhovskiy; thence by the portion of the E coast of the latter island up to mouth of Reka Ort-Yuryakh, at approximately 73°28'N, 143°34'E; thence by the line joining this point to Mys Blagoveshchenskiy (75°39'N, 145°00'E), the NE extremity of Ostrov Kotel'nyy; thence by the N coast of the latter up to Mys Anisiy; thence by the line joining the latter to position 79°00'N, 139°00'E.

The N boundary is the line drawn from position (79°00'N, 139°00'E) to position (76°00'N, 180°00').

On the E, the boundary of the East Siberian Sea is the portion of the 180° meridian from position (76°00'N, 180°00') down to the N coast of Ostrov Vrangelya; thence the NW and the W coasts of Ostrov Vrangelya down to Mys Blossom (70°47'N, 178°46'E), the S extremity of the island; thence the line joining the latter to Mys Yakan (69°35'N, 177°28'E).

The S limit is the N coast of Russia between Mys Yakan and the mouth of Reka Kondrat'eva.

Proliv Dmitriya Lapteva, Proliv Eterikan, Proliv Sannikova and Proliv Longa are excluded from the East Siberian Sea. However, Proliv Blagoveshchenskiy (that separates Ostrov Kotel'nyy from Ostrov Novaya Sibir') and the waters around Ostrov Novaya Sibir' are part of it.

The area of the East Siberian Sea is evaluated as 9.2×10^5 km^2.

Chukchi Sea

The Chukchi Sea is bounded on the W by the coast of Siberia from Mys Yunkyn (66°22'N, 170°35'W) to Mys Yakan; thence by the line joining Mys Yakan to Mys Blossom; thence by the S, E and NE coasts of Ostrov Vrangelya; thence by the portion of the 180°meridian from the point it intercepts the N coast of this island to position (76°00'N, 180°00').

The N boundary is the line joining position (76°00'N, 180°00') to position (72°00'N, 156°00'W).

On the E, the boundary of the Chukchi Sea is the line joining position (72°00'N, 156°00'W) to Point Barrow (71°20'N, 156°20'W); thence the coast of Alaska down to Shishmaref Bay (66°10'N, 165°55'W).

The S limit of the Chukchi Sea is the line joining Shishmaref Bay to Mys Yunkyn.

Proliv Longa is considered part of the Chukchi Sea.

The area of the Chukchi Sea is approximately 5.9×10^5 km^2.

Bering Sea

The Bering Sea is bounded on the W by the coast of Siberia from Mys Kamchatskiy (56°01'N, 163°04'E), on the E coast of Poluostrov Kamchatskiy, to Mys Yunkyn.

The N boundary is the line joining Mys Yunkyn to Shishmaref Bay.

On the E, the boundary of the Bering Sea is the coast of Alaska from Shishmaref Bay to Kabuch Point (54°48'N, 163°21'W), the W extremity of the Alaska Peninsula.

The S limit of the Bering Sea is a line running from Kabuch Point through the Aleutian Islands to the S extremes of Komandorskiye Ostrova and on to Mys Kamchatka in such a way that all the narrow waters between Alaska and Poluostrov Kamchatskiy are included in the Bering Sea.

The area of the Bering Sea is estimated as 2.3×10^6 km^2.

Sea of Okhotsk

The Sea of Okhotsk, of irregular shape, is bounded by the following set of lines: the line joining Söya Misaki (45°31'N, 141°26'E), the northernmost point of Hokkaido, to Mys Kril'on (45°54'N, 142°05'E), the southernmost point of Sakhalin; the E coast of Sakhalin from Mys Kril'on to Mys Marii (54°20'N, 142°15'E), the NW extremity of the island; the SE shore of Sakhalinskiy Zaliv from Mys Marii to latitude 53°20'N; the N entrance of the Strait of Tartary, which lies at approximately 53°20'N; the SW shore of Sakhalinskiy Zaliv from latitude 53°20'N to Mys Aleksandra (54°18'N, 139°47'E); the coast of Siberia between Mys Aleksandra and Mys Lopatka (50°52'N, 156°40'E), the S extremity of Poluostrov Kamchatskiy; a line running from the latter to Nosappu Misaki (43°23'N, 145°49'E), the easternmost point of Hokkaido, through the chain of Kuril Islands in such a way that all the narrow waters between the two points are included in the Sea of Okhotsk.

The Sea of Okhotsk has an approximate area of 1.6×10^6 km^2.

9 APPENDIX B. THE NORTHERN SEA ROUTE

In 1991 the Administration of the Northern Sea Route defined legally the Northern Sea Route (NSR) as the marine passage across the seas of the Russian Arctic beginning at the *western entrance of the Novaya Zemlya and Ostrov Vaygach straits and the meridian north through Mys Zhelaniya* and ending *by the 66°N parallel and the 168°58'37"W meridian.*

Far from being unique, the NSR is generally regarded as any possible route from the E Barents Sea to the Pacific Ocean through several straits and open seas N of mainland Russia. It is possible to distinguish four routes, referred to as *coastal* (traditional or conventional), *central* (or mid), *high latitude* (or transit) and *close-to-the-pole* (or over-the-pole) routes. The traditional route can be considered as a portion of the historical Northeast Passage that follows the Eurasian coastline between the Atlantic and the Pacific Oceans. The high-latitudinal route is in most instances blocked by ice but at least parts of it have occasionally been used. The close-to-the-pole route, which connects Murmansk to the Bering Strait across the Arctic Ocean, is not a plausible option with present technology.

Details of sailing directions along the NSR can be found elsewhere. In this Appendix we limit ourselves to a brief overview of the route.

The conventional starting points of the Coastal Route are Murmansk and Arkhangel'sk. From these points the route passes N of Ostrov Kolguyev and leads directly to Proliv Yugorskiy Shar or Proliv Karskiye Vorota. The Central and the High-latitudinal routes set off from Murmansk and head for the N tip of Novaya Zemlya.

Proliv Yugorskiy Shar separates Poluostrov Yugorskiy from Ostrov Vaygach and is the southernmost of the three straits that connect the Barents Sea to the Kara Sea. Proliv Karskiye Vorota separates the SE coast of the S island of Novaya Zemlya from the NW coast of Ostrov Vaygach. Proliv Matochkin Shar separates the N and S islands of Novaya Zemlya. At the time of writing the latter strait is barred to foreign vessels and it has been closed to all commercial navigation in recent years due to radioactive contamination from the nuclear tests that have been conducted in the area since the early 1950s [Brubaker, 2005]. If it is opened to navigation in the future, it could be considered as an alternative to the southern Proliv Yugorskiy Shar and Proliv Karskiye Vorota if the latter are obstructed at the Kara Sea end by

ice carried southwards by the current that flows along the E coast of Novaya Zemlya [Barnett, 1991]. According to the *Guide to Navigation through the Northern Sea Route* [1996], in June, July and August the passage through the S straits is preferred while in September and October the passage N of Novaya Zemlya is more frequently used.

Having entered the Kara Sea through Proliv Yugorskiy Shar or Proliv Karskiye Vorota, a vessel following the Coastal Route heads to a position off the NW coast of Ostrov Belyy, from where the route can diverge into two branches. One branch, called offshore route, leads directly to Severnaya Zemlya. It passes SE of Ostrov Uedineniya (77°30'N, 82°16'E), N of Ostrova Sergeya Kirova and S of Ostrov Voronina (78°12'N, 93°50'E). From a position S of Ostrov Voronina, the route leads either to Proliv Borisa Vil'kitskogo or to Proliv Shokal'skogo. The other branch heads E towards Dikson and then continues to Severnaya Zemlya. Between Ostrov Belyy and Dikson diversions to Obskaya Guba, Gydanskiy Zaliv and Yeniseyskiy Zaliv are possible. Between Dikson and one of the Severnaya Zemlya straits vessels usually navigate in a coastal strip up to 100 miles wide [Brubaker, 2005].

The Central Route proceeds eastwards from the N tip of Novaya Zemlya to Proliv Borisa Vil'kitskogo. The High Latitude Route takes a NE direction towards the N tip of Severnaya Zemlya.

Vessels that enter the Kara Sea through one of the southern straits may find their route in the SW Kara obstructed by the ice of the Novaya Zemlya Massif, especially at the beginning of the navigational season. A massif is a large ice field that is observed in most summers at the same place which normally contains a significant percentage of multi-year and hummocked ice. The location of the main ice massifs in the Russian Arctic can be found in [Mulherin, 1994]. Some of the major obstacles to the transit in the NSR during the navigational season are the Severnaya Zemlya Massif (near the SW side of Severnaya Zemlya, in the Kara Sea), the Taymyr Massif (on the E coast of Poluostrov Taymyr, in the Laptev Sea), the Ayon Massif (in the East Siberian Sea) and the Vrangelevskiy Massif (near Ostrov Vrangelya, in the Chukchi Sea).

Proliv Borisa Vil'kitskogo is the southernmost of the straits that link the Kara and the Laptev Seas. It separates the S coast of Ostrov Bol'shevik from Poluostrov Taymyr in mainland Siberia. Proliv Shokal'skogo, another possibility to enter the Laptev Sea, separates Ostrov Bol'shevik from Ostrov Oktyabr'skoy Revolyutsii. Proliv Krasnoy Armii separates the NW coast of Ostrov Oktyabr'skoy Revolyutsii from Ostrov Pioner and the N coast of the former from Ostrov Komsomolets. Proliv Yungshturm lies between Ostrov Pioner and Ostrov Komsomolets.

In theory the Coastal and the Central Routes may use either Proliv Borisa Vil'kitskogo or Proliv Shokal'skogo. In practice, Proliv Borisa Vil'kitskogo is used at least 95% of the times, according to the Guide to Navigation through the Northern Sea Route [1973]. Proliv Krasnoy Armii and Proliv Yungshturm are not used at all [Bondarenko, 1995].

The High Latitude Route passes N of the Severnaya Zemlya archipelago. This route may be considered as an alternative primarily at the beginning of the navigational season when the S straits are still frozen. In August and September, however, it is an unlikely choice due to the possible presence of large amounts of ice near Mys Molotova and, especially, off the NE coast of Ostrov Komsomolets.

There are three possible branches of the Coastal Route in the Laptev Sea: the first one leads from Proliv Borisa Vil'kitskogo to Khatangskiy Zaliv, the second one to Proliv Dmitriya Lapteva and the third one to Proliv Sannikova. The Central Route leads from Proliv Borisa Vil'kitskogo eastwards to the N coast of Ostrov Kotel'nyy. The High Latitude Route crosses the N Laptev Sea from the N of Severnaya Zemlya to the N of Novo Sibirskiye Ostrova.

In the region of Novo Sibirskiye Ostrova there are three different routes that lead from the Laptev Sea to the East Siberian Sea. The first route uses Proliv Dmitriya Lapteva, which separates the S coast of Ostrov Bol'shoy Lyakhovskiy from mainland Siberia. The second route is through Proliv Sannikova, the channel that separates the N coasts of Ostrov Malyy Lyakhovskiy and Ostrov Bol'shoy Lyakhovskiy from the S coast of Ostrov Kotel'nyy. A third alternative (frequently used in the beginning of the navigational season) is the passage northward of Novo Sibirskiye Ostrova along the N coasts of Ostrova Anjou.

The Coastal Route uses Proliv Dmitriya Lapteva (rarely) and Proliv Sannikova (frequently). The Central and the High Latitude Routes use the passage northward of Novo Sibirskiye Ostrova. In the beginning of the summer the route that passes N of Ostrova Anjou is always used, a choice that is supported by the fact that in an average June or July the ice concentrations are remarkably lower in the waters N of the archipelago than in either of the two S straits. In August and September the situation is reversed.

Vessels following the Coastal Route in the East Siberian Sea may pass well off Ostrova Medvezh'i or may traverse Proliv Kolymskaya (between this archipelago and the mainland). Vessels using the Central or the High Latitude Route sail approximately ESE from the N coast of Ostrov Novaya Sibir' towards Pevek or the W entrance of Proliv Longa.

Even in normal summers, drifting ice from the Arctic Ocean may be pushed southwards by the northerly winds creating an accumulation of old and new ice near the coast roughly between 166°E and 172°E known as the Ayon Massif.

To enter the Chukchi Sea from the East Siberian Sea all three routes use Proliv Longa (which separates Ostrov Vrangelya from the mainland). Once in the Chukchi Sea ships navigate along the coast until they reach the Bering Strait.

10 REFERENCES

ACIA (2004); *Impacts of a Warming Arctic: Arctic Climate Impact Assessment*; Cambridge University Press.

Barnett, D. (1991); Sea Ice Distribution in the Russian Arctic; in *The Soviet Maritime Arctic*; Ed. by L.W. Brigham; Belhaven Press.

Bondarenko, V. (1995); *The Northern Sea Route*; INSROP discussion paper.

Brubaker, R.D. (2005); *The Russian Arctic Straits*; Martinus Nijhoff Publishers.

Cavalieri, D.J., P. Gloersen and J. Zwally (1990); *DMSP SSM/I daily polar gridded sea ice concentrations*; Ed. by J. Maslanik and J. Stroeve; National Snow and Ice Data Center, Boulder, CO; Digital Media (updated current year);

Comiso, J. (1986); Characteristics of Arctic winter sea ice from satellite multispectral microwave observations; *J. Geophys. Res.*, 91, 975-994.

Comiso, J. (1990); *DMSP SSM/I daily polar gridded sea ice concentrations*; Ed. by J. Maslanik and J. Stroeve; National Snow and Ice Data Center, Boulder, CO; Digital Media (updated current year);

Comiso, J. (1995); SSM/I Sea ice concentrations using Bootstrap Algorithm; *NASA Ref. Publ. 1380*.

Comiso, J. (2002); A rapidly declining perennial sea ice cover in the Arctic; *Geophys. Res. Lett.*, 29, 1956.

Comiso, J. (1999); *Bootstrap sea ice concentrations from Nimbus-7 SMMR and DMSP SSM/I*; National Snow and Ice Data Center, Boulder, CO; Digital Media (updated 2003).

Comiso, J. and C. Parkinson (2004); Satellite Observed Changes in the Arctic; *Physics Today* (August 2004).

The Head Department of Navigation and Oceanography of the Ministry of Defence of the Russian Federation (1996); *Guide to Navigation through the Northern Sea Route*; St Petersburg.

International Hydrographic Organisation (1973); *Limits of Oceans and Seas* (Special Publication 23); Third Edition.

Mulherin, N., D. Sodhi and E. Smallidge (1994); *Northern Sea Route and Icebreaking Technology*; US Army Corps of Engineers; Cold Regions Research and Engineering Laboratory.

Svendsen, E. et al. (1983); Norwegian remote sensing experiment: Evaluation of the Nimbus 7 scanning multichannel microwave radiometer for sea ice research; *J. Geophys. Res.*, 88, 2781-2991.

Swift, C.T., L.S. Fedor and R.O. Ramseier (1985); An Algorithm to Measure Sea Ice Concentrations with Microwave Radiometers; *J. Geophys. Res.*, 90, 1087-1099.

Zwally, J., J.C. Comiso, C.L. Parkinson, D.J. Cavalieri and P. Gloersen (2002); Variability of Antarctic Sea Ice 1979-1998; *J. Geophys. Res.*, 107, C5, 3041.

CLIMATE CHANGE AND NATURAL HAZARDS SERIES

N°	Title	EUR
1	EUROPEAN RESEARCH ON CLIMATE CHANGE Catalogue of 6th Framework Programme Projects - Volume 1	21935
2	EUROPEAN RESEARCH ON NATURAL HAZARDS Catalogue of selected 5th Framework Programme and 6th Framework Programme Projects - Volume 1	21936
3	EUROPEAN RESEARCH ON FLOOD RISK MANAGEMENT - A contribution to the concerns generated by the summer 2005 floods in Europe - Proceedings of a Workshop on 10 October 2005 in Brussels	22024
4	EUROPEAN RESEARCH ON CLIMATE CHANGE Catalogue of 5th Framework Programme and 6th Framework Programme projects on Carbon Cycle and GreenHouse Gases	22063
5	Scientific report on the International Symposium on Climate Change Research Challenges, Brussels, 2-3 February 2006	22042
6	European research on POLAR ENVIRONMENT AND CLIMATE Results and information from FP-5 and FP-6 projects	22415
7	EUROPEAN RESEARCH ON CLIMATE CHANGE Catalogue of 6th Framework Programme Projects – Volume 2	22421
8	Scientific report on the International Workshop on Climate Change Impacts on the Water Cycle, Resources and Quality, Brussels, 25-26 September 2006	22422
9	Proceedings of the International Conference on Transport, Atmosphere and Climate (TAC), Oxford, UK, 26-29 June 2006	22428
10	Proceedings of the International Workshop on Arctic Sea Ice Thickness: Past, Present and Future, Rungstedgaard, Denmark, 8-9 November 2005	22416